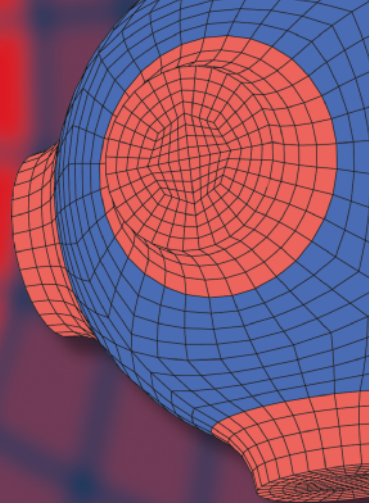


Advanced Structured Materials

Holm Altenbach
Marco Amabili
Yuri V. Mikhlin *Editors*



Nonlinear Mechanics of Complex Structures

From Theory to Engineering Applications

 Springer


Advanced Structured Materials

Volume 157

Series Editors

Andreas Öchsner, Faculty of Mechanical Engineering, Esslingen University of Applied Sciences, Esslingen, Germany

Lucas F. M. da Silva, Department of Mechanical Engineering, Faculty of Engineering, University of Porto, Porto, Portugal

Holm Altenbach , Faculty of Mechanical Engineering, Otto von Guericke University Magdeburg, Magdeburg, Sachsen-Anhalt, Germany

Common engineering materials reach in many applications their limits and new developments are required to fulfil increasing demands on engineering materials. The performance of materials can be increased by combining different materials to achieve better properties than a single constituent or by shaping the material or constituents in a specific structure. The interaction between material and structure may arise on different length scales, such as micro-, meso- or macroscale, and offers possible applications in quite diverse fields.

This book series addresses the fundamental relationship between materials and their structure on the overall properties (e.g. mechanical, thermal, chemical or magnetic etc.) and applications.

The topics of *Advanced Structured Materials* include but are not limited to

- classical fibre-reinforced composites (e.g. glass, carbon or Aramid reinforced plastics)
- metal matrix composites (MMCs)
- micro porous composites
- micro channel materials
- multilayered materials
- cellular materials (e.g., metallic or polymer foams, sponges, hollow sphere structures)
- porous materials
- truss structures
- nanocomposite materials
- biomaterials
- nanoporous metals
- concrete
- coated materials
- smart materials

Advanced Structured Materials is indexed in Google Scholar and Scopus.

More information about this series at <http://www.springer.com/series/8611>


Holm Altenbach · Marco Amabili · Yuri V. Mikhlin
Editors


Nonlinear Mechanics of Complex Structures

From Theory to Engineering Applications

 Springer

Editors

Holm Altenbach 
Fakultät für Maschinenbau
Otto-von-Guericke-Universität Magdeburg
Magdeburg, Germany

Marco Amabili 
Mechanical Engineering
McGill University
Montreal, QC, Canada

Yuri V. Mikhlin 
National Technical University “Kharkiv
Polytechnic Institute”
Kharkiv, Ukraine

ISSN 1869-8433

ISSN 1869-8441 (electronic)

Advanced Structured Materials

ISBN 978-3-030-75889-9

ISBN 978-3-030-75890-5 (eBook)

<https://doi.org/10.1007/978-3-030-75890-5>

© The Editor(s) (if applicable) and The Author(s), under exclusive license to Springer Nature Switzerland AG 2021

This work is subject to copyright. All rights are solely and exclusively licensed by the Publisher, whether the whole or part of the material is concerned, specifically the rights of translation, reprinting, reuse of illustrations, recitation, broadcasting, reproduction on microfilms or in any other physical way, and transmission or information storage and retrieval, electronic adaptation, computer software, or by similar or dissimilar methodology now known or hereafter developed.

The use of general descriptive names, registered names, trademarks, service marks, etc. in this publication does not imply, even in the absence of a specific statement, that such names are exempt from the relevant protective laws and regulations and therefore free for general use.

The publisher, the authors and the editors are safe to assume that the advice and information in this book are believed to be true and accurate at the date of publication. Neither the publisher nor the authors or the editors give a warranty, expressed or implied, with respect to the material contained herein or for any errors or omissions that may have been made. The publisher remains neutral with regard to jurisdictional claims in published maps and institutional affiliations.

This Springer imprint is published by the registered company Springer Nature Switzerland AG
The registered company address is: Gewerbestrasse 11, 6330 Cham, Switzerland

Preface

The book covers different topics of nonlinear mechanics in complex structures, such as the appearing of new nonlinear phenomena, the behavior of finite dimensional and distributed nonlinear systems, including numerous systems directly connected with important technological problems. We suppose that the book will be of significant interest to Ph.D. students, researchers, practitioners and engineers working with modern technological processes. It shows the importance to take into account effects and phenomena exciting in nonlinear models and engineering systems, which does not necessarily exist in the linear ones. Modern analytical and numerical modeling techniques permit to describe the complexity of the nonlinear systems under consideration. A wide thematic score of the book can stimulate an extensive exchange of opinions among researchers dealing with different branches of nonlinear mechanics and its applications. It can promote effective solutions of different problems, which are current for both nonlinear theory and engineering.

Part I of the book “*Investigation of Advanced Structures in Engineering*” contains papers devoted to the analysis of statics or dynamics of structures from modern materials, in particular, composite materials or constructions like as sandwiches or multilayer ones. Chapter 1 by Cveticanin “On Mechanical Metastructures Applied in Vibration Suppression—A Review” presents an overview on the mechanical metastructures applied for vibration suppression. Although the existing metastructures are very suitable for vibration absorption or suppression, tests have also shown a major anisotropy in vibration absorption, depending on the excitation force action. Hence, the overview states that there is a need to harmonize the type of material and structure into a single whole. Chapter 2 “Debonding Resistance Evaluation in Virtual Testing of Sandwich Specimens” of Burlayenko et al. is dedicated to the simulation of the fracture testing for sandwich panels which are studied in the context of providing an assessment of face sheet-to-core interface strength. The models exploit both the framework of linear elastic fracture mechanics in combination with analytical consideration and numerical simulation results and one-dimensional beam theories. In Chap. 3 “Modeling of Mechanical Properties of Composite Materials Under Different Types of Loads” written by Kryshchuk et al., the modern numerical and analytical methods for determining the effective elasticity characteristics of layered composite materials are presented. The effective finite element models are chosen

based on the data of the stress–strain state of the composite structures under power loads. In Chap. 4 by Kurpa et al. “Nonlinear Dynamic Analysis of FGM Sandwich Shallow Shells with Variable Thickness of Layers,” the application of the R-functions method is used to study the dynamics of the sandwich functionally gradient materials (FGM) shallow shells with variable thickness of layers and complex shapes. Mathematical formulation of the problem has been done in the framework of the refined shear deformation theory of the first order. In Chap. 5 by Lvov and Kostromitskaya “Residual Stresses in Plastic Deformed Composites,” the residual stresses at the micro-level in a unidirectional reinforced composite that arise after rate-independent plastic deformation are analyzed. Micromechanical analysis was performed by the finite element method for the case of a plane stress state. Determination of residual stresses and plastic strains at different loading paths distribution is used to identify parameters of the model. Chapter 6 “Dynamics of Curved Laminated Glass Composite Panels Under Impact Loading” presented by Sukhanova et al. is devoted to the analysis of dynamic state of the shallow shell laminated glasses (LG) composites under impact loading. A modeling of a rigid ball drop on LG with polyvinyl butyral inter-layer is considered using the FEM within an explicit dynamics approach in 3D statement. Chapter 7 by Ugrimov et al. “Modeling of Response of Multilayer Glazing on Distributed and Localized Force Loading” is devoted to modeling of the multilayer glazing response to dynamically distributed and localized loading. The dynamic behavior of glazing is described by equations of the layerwise generalized model that accounts for the spatial strain character and inertial loads. The responses of the flat glazing to a shock wave and to shocks caused by a solid, soft bodies and a bullet are considered.

Part II “*Nonlinear Dynamics of Distributed Systems*” contains works on nonlinear dynamics of shells and the shrouded blade assemblies. In Chap. 8 by Zippo et al. “Synchronicity Phenomena in Circular Cylindrical Shells Under Random Excitation,” an experimental study on the nonlinear dynamics of a thin polymeric circular cylindrical shell, carrying a top mass, subjected to both thermal gradients and random excitation is presented. Tests have been performed in controlled temperature conditions, and the shell has been excited through an electrodynamic shaker. The experimental results pointed out that a broadband random excitation at the base of the shell can give rise to the synchronicity of the response. Chapter 9 “Investigation of the Nonlinearity Effect of the Shrouded Blade Assemblies on Their Forced Vibrations” by Zinkovskii et al. presents a study of the forced vibrations of the shrouded blades with nonlinearity due to the interaction of contact surfaces of the shrouds and the presence of fatigue crack by the FEM. The comparative analysis of the obtained results shows a significant difference of the linearized and nonlinear FEM models.

Part III “*Nonlinear Dynamics of Discrete Systems*” contains investigations on the complex dynamic behavior of some nonlinear discrete systems. Chapter 10 “Influence of Linear and Nonlinear Electromechanical Couplings on Vibration Absorber—Harvester System” by Kecik and Smagala presents the analysis of the electromechanical problem for the pendulum absorber–harvester system containing the oscillator with the attached pendulum tuned mass absorber. In the absorber, a special mechanism consisting of the oscillating magnet in the coil is applied. The system

response and recovered energy of the absorber–harvester system with the fixed, linear and nonlinear electromechanical coupling models are studied. A comparison with experimental results is made. In Chap. 11 “Crisis-Induced Intermittency and Other Nonlinear Dynamics Phenomena in Vibro-impact System with Soft Impact” by Bazhenov et al., the dynamics of a platform vibrator with shock are examined. The system is described by 2-DOF vibro-impact model, where the soft impact is simulated by the nonlinear contact force in accordance with the Hertzian contact theory. The model demonstrates a complex behavior in different ranges of the control parameters, namely sustained (permanent) and transient chaos, boundary and interior crises, crisis-induced intermittency and coexisting regimes in the hysteresis zone.

Part IV “*Interaction of Structures and Flow*” contains three papers. In Chap. 12 “Aeroelastic Interactions Between Plates and Three-Dimensional Inviscid Potential Flows” by Avramov et al., the method for analysis of dynamic interactions between plates and three-dimensional potential inviscid gas is suggested. The system of the singular integral equations with respect to aerodynamic derivatives of the pressure drop is obtained and analyzed by the numerical method for singular integral equations solutions. Loss of the plate dynamic stability is analyzed numerically. In Chap. 13 “Hydroelastic Vibrations of Circular Sandwich Plate Under Inertial Excitation” (Kondratov et al.), the bending vibrations of the circular sandwich plate, which is the top wall of a narrow channel, under the action of inertial excitation are considered. It is assumed that the channel bottom wall is a rigid disk mounted on a vibrating foundation; the channel is filled with a viscous incompressible liquid, and its movement is studied as a creeping one. The circular sandwich plate hydro-elastic response for the main vibration mode is determined. Chapter 14 “Effect of Finite Vessel Stiffness on Transition from Two-Dimensional Liquid Sloshing to Swirling: Reduced-Order Modeling” by Zusman and Gendelman presents an analysis of the liquid sloshing in partially filled tanks. The proposed reduced-order model describes the transition from two-dimensional to three-dimensional motion, including swirling when a finite stiffness of the vessel itself is considered. It permits to analyze the interaction between the sloshing liquid and the tank structural modes in conditions of the simple horizontal harmonic forcing.

Part V “*Longtime Behavior of Engineering Structures*” contains three papers. Chapter 15 “Analysis of Creep, Shrinkage and Damage in Armored Concrete Dome at Static and Seismic Loading” by Breslavsky and Chuprynin is devoted to study the creep and long-term strength of thin-walled structures made of concrete and reinforced concrete. A mathematical formulation and a method for solving the creep damage problem of thin-walled concrete elements under short-term and long-term loading, which makes it possible to determine their bearing capacity and long-term strength, are presented. Chapter 16 “Stress–Strain State of Nuclear Reactor Core Baffle Under the Action of Thermal and Irradiation Fields” by Breslavsky et al. contains a description of the method for numerical simulation of stress–strain state variation in the structural elements of nuclear reactor in conditions of creep and swelling. The constitutive equations account for radiation swelling, creep and damage accumulation in reactor steel and are solved by FEM. Nuclear reactor’s baffle initially is regarded as 3D solid object, and subsequently the problem is reduced to a 2D one.

In Chap. 17 “Application of Data-Driven Yield Surface to Prediction of Failure Probability for Centrifugal Pump” by Shapovalova and Vodka, the probability of the centrifugal pump failure-free operation is studied. Finding the probability of model failures is based on the data-driven yield surface application taking into account the different behavior of composite materials under tensile and compressive loads. It is analyzed at the micro-level using the FEM. Going beyond the yield surface indicates the possibility of transition into a plastic state.

In Part VI “*Rotating Systems*,” there are three papers dedicated to nonlinear dynamics of mentioned systems. In Manevich’s paper Chap. 18 “Self-Synchronization of Rotational Regimes of Vibro-exciter on Oscillatory Systems,” the steady-state synchronous rotations of vibro-exciter (unbalanced rotors), mounted on a linear oscillator (elastic base) and driven by different rotating torques, are studied employing some analytical procedure. The obtained solution yields to essential corrections in characteristics of the synchronized regimes in comparison with some previous publications. Stability of the synchronized motions is also studied. Chapter 19 “Stability Analysis of Rotor Motion in Nonlinear Systems with Passive and Active Magnetic Bearings” by G. Martynenko presents an approach to analyze the rotor motion stability in systems with passive and active magnetic bearings. The rotor dynamics are described by the Lagrange–Maxwell magneto-mechanical system of differential equations. The analytical–numerical approach based on simulation modeling and stability analysis by vibrograms, spectrograms, phase trajectories and Poincaré sections is proposed. It permits to realize the analytical–numerical modeling of various dynamic modes and to study stability of rotors of complex magneto-mechanical systems. Chapter 20 “Computational-Experimental Evaluation of Stiffness Response in Elastic Supports of Rotor Systems” by Tkachuk et al. contains an analysis of the stiffness response in elastic supports found in rotor systems such as superchargers of heavy-duty engines. Several computational models for the response evaluation are proposed. The obtained results permit to conclude that the force–displacement response is essentially nonlinear due to the contact.

Part VII “*Satellites and Spacecrafts*” contains two papers. In Chap. 21 “A Brief Analysis of Artificial Satellites Solar Panels Deployment Considering a Nonlinear Dynamic Model” by Avanço et al., the present analysis is focused on the nonlinear dynamics of a solar panel opening during the motion of the satellite around the Earth. The interaction between energy sources and the panels is taken into account. A numerical simulation is made for the panel directly connected to the DC engine and for a torsion spring connected to the motor shaft and the solar panel. Chapter 22 “The Optimal in Terms of Fuel Consumption Approach to Reorientation of a Spacecraft Based on the Nonlinear Boundary-Value Problem Solution” by Uspenskiy et al. presents a study of the nonlinear boundary problem connected with the reorientation of the rigid body along the trajectory of inertial rotation. The problem solution is given in the form of decomposition in the power series. The obtained solution can be used to calculate the initial conditions of the inertial maneuver in the onboard control system of the spacecraft.

Part VIII “*Nonlinear phenomena and Methods of Investigation*” contains papers on modern analytical and numerical methods of investigation of complex dynamical problems in different kinds of nonlinear systems. In Kovalev’s paper Chap. 23 “Asymptotic Methods for Soliton Excitations,” an asymptotic method of determination of two-parameter dynamic envelope solitons in media with a different character of linear wave spectrum is demonstrated for few examples. Particular attention is paid to a method of constructing such solutions for nonlinear weakly dispersive media with a sound-type spectrum of linear waves. Chapter 24 “Method of Superimposed Meshes for Solving Nonlinear Dynamic Problems” by Martynenko is devoted to the justification and application of the method of superimposed meshes for solving continuous dynamic problems with different types of nonlinearities. Modeling of anisotropic nonlinear mechanical properties of solid deformable bodies using finite element codes is considered. Rearranging the Lagrangian functional shows a possibility to construct any level of anisotropy of viscoelastic properties for the solution of the dynamic problems of the polymer composites. In Chap. 25 by Shvets and Donetskyi “New Types of Limit Sets in the Dynamic System “Spherical Pendulum–Electric Motor””, the nonlinear interaction of a spherical pendulum and a source of excitation is discussed. A number of unusual limit sets of the system, which can be both regular and chaotic, have been constructed and analyzed. It is shown that these limit sets are not attractors in the traditional sense of this term. Some scenarios of transitions from regular limit sets to chaotic ones, as well as scenarios of transitions from one type of the chaotic limit sets to other types are considered. In Chap. 26 “Exact Solutions to the Four-Component Merola–Ragnisco–Tu Lattice Equations” by Zemlyanukhin et al., a class of exact kink solutions of integrable four-component Merola–Ragnisco–Tu lattice equations is constructed. To this aim, a modification of the geometric series method adapted for differential–difference equations is used. This algorithm involves the analysis of a sequence of linear ordinary differential equations, which forms a geometric progression, the sum of which is found using the Padé approximants and gives the exact solution to the lattice equations.

The editors would like to thank Mrs. Dr. Gayane Rudnyeva and Dr. Ivan Breslavsky sincerely for their valuable work and support in the book preparation. In addition, we have to thank Mrs. Mayra Castro and Ashok Arumairaj (Springer Nature) for their support.

During the preparation of the book, Prof. Arkadiy I. Manevich passed away. After the Preface, one can find some information about this world-renowned specialist in the field of nonlinear mechanics.

Magdeburg, Germany
Kharkiv, Ukraine
Montreal, Canada
April 2021

Holm Altenbach
Yuri V. Mikhlin
Marco Amabili

Obituary

Professor Arkady Isaakovich Manevich (1940–2021)



Arkady Manevich was born on January 2, 1940, in the city of Mogilev, USSR (now Belarus) to a family of physicians. In 1962, he graduated (diploma with honors) from Oles Honchar Dnipro National University, where he majored in mechanics. From 1962 to 1966, he worked as a senior engineer at the Rybinsk aircraft engine plant (now UEC Saturn). In 1966, he moved back to Dnipro, where he worked until 1974 as a senior engineer and a team leader at the Institute of Engineering Mechanics.

In 1967, A. Manevich received his Candidate of Sciences degree (equivalent to Ph.D.). His thesis was devoted to the stability of cylindrical shells reinforced by circumferential ribs. In 1974, A. Manevich became an associate professor—and later a full professor—at the Department of Mathematics of the Ukrainian State University of Chemical Technology, where he worked until 1990. A. Manevich received his Doctor of Sciences degree (equivalent to the German habilitation) in 1989 from Leningrad Polytechnic Institute (now Peter the Great St. Petersburg Polytechnic University) with a thesis on the nonlinear theory of coupled buckling in reinforced thin-walled structures. In 2001, A. Manevich joined the faculty of the Oles Honchar

Dnipro National University, where he worked as a full professor at the Department of Computational Mechanics and Structural Strength, and from 2015, he was a full professor at the Department of Theoretical and Applied Mechanics of this university.

Professor A. Manevich's scientific interests lay in the mechanics of deformable solids as well as in computational mathematics. He published more than 250 scientific papers, as well as two books. Prof. Manevich made major contributions toward theoretical and experimental studies of the stability of reinforced shells. He developed several analytical formulas that account for the influence of various factors (such as initial imperfections, the eccentricity of ribs, pre-buckling deformations and the discrete nature of reinforcing elements) on the critical values of pressure, axial compression, torsion and bending loads. He is the founder of the nonlinear theory of coupled buckling of reinforced thin-walled structures (such as ribbed plates and shells). In addition, he developed a conjugate directions algorithm with orthogonalization for unconstrained minimization as well as a linearized reduced gradient method for nonlinear programming problems. It must be mentioned his contribution into non-classical theories of beams and plates, as well to the optimal design of thin-walled structures. He made major contributions into the study of the dynamics of nonlinear systems with internal resonances and nonlinear interactions of rotations and oscillations in mechanical systems with inertial excitations.

Manevich's work exhibits a keen understanding of the essence of physical phenomena without unnecessary generalizations and overcomplicated formulas. His drive to explore the nature of phenomena of stability led him to develop the concept of coupled buckling forms, and he published several groundbreaking works in this area. The German chemist and philosopher Wilhelm Ostwald proposed a classification of creative scientific minds that divides them into "classics" and "romantics." The "classics" dive deep, aiming for full comprehension of their chosen field. The "romantics" contribute instead in the breadth of their work, initiating many independent threads of study without committing fully to any one of them. Although this dichotomy is not universally applicable, a better case for it could not be made than through the works of Arkady Manevich, the classic, and his late brother Leonid Manevich (1938–2020), the romantic (whose scientific achievements are described in [1]).

A.I. Manevich passed away on February 8, 2021, in Dnipro, Ukraine. He will always be remembered as a brilliant scientist, a devoted teacher and a loving father.



Professors A.I. Manevich and L.I. Manevich

Selected Publications by A. I. Manevich

Books

1. Andrianov I.V., Manevich A.I., Mikhlin Yu.V., Gendelman O.V. (Eds.). *Problems of Nonlinear Mechanics and Physics of Materials*. Cham, Springer Nature, 2019
2. Manevich A.I., Manevitch L.I. *The Mechanics of Nonlinear Systems with Internal Resonances*. Imperial College Press, 2005
3. Manevich A.I. *Stability and Optimal Design of Reinforced Shells*. Kiev-Donetsk, Vishcha Shkola, 1979 (in Russian)

Papers

4. Manevich A.I. Stability of synchronous regimes in unbalanced rotors on elastic base. *Proc. Inst. Mech. Eng. Part C. J. Mech. Eng. Sci.*, 1–14, 2020
5. Manevich A.I. Discontinuities in viscoelastic Timoshenko beam under moving concentrated loads. In [1], 425–434
6. Manevich A.I. An oscillator-rotator system: vibrational maintenance of rotation, stationary synchronous regimes, stability, vibration mitigation. *J. Sound Vib.* 437(22), 223–241, 2018

7. Manevich A.I. Dynamics of Timoshenko beam on linear and nonlinear foundation: phase relations, significance of the second spectrum, stability. *J. Sound Vib.* 344, 209–220, 2015
8. Manevich A.I., Kolakowsky Z. Revisiting the theory of transverse vibrations of plates with shear deformation. *Int. Appl. Mech.* 50, 196–205, 2014
9. Manevich A.I., Kolakowsky Z. Free and forced oscillations of Timoshenko beam made of viscoelastic material. *J. Theor. Appl. Mech.* 49(1), 3–16, 2011.
10. Manevich A.I., Boudinov E.A. An efficient conjugate direction method with orthogonalization for large-scale quadratic optimization problems. *Optim. Meth. Soft.* 22(2), 309–328, 2007
11. Manevich A.I. Coupled instability of cylindrical shells stiffened with thin ribs. *Thin-Walled Structures: Advances and Developments. Third Intern. Conf. Amsterdam, New York, Elsevier*, 683–691, 2001
12. Manevich A.I. Interaction of coupled modes accompanying non-linear flexural vibrations of a circular ring. *J. Appl. Math. Mech.* 58(6), 1061–1068, 1994
13. Ladygina Ye.V., Manevich A.I. Free oscillations of a non-linear cubic system with two degrees of freedom and close natural frequencies. *J. Appl. Math. Mech.* 57(2), 257–266, 1993
14. Manevich A.I. Coupled stability loss of a compressed stiffened panel. *Mech. Solids* 23(5), 152–159, 1988
15. Manevich A.I., Polyanchikov P.I. A one-step method of conjugate directions. *Sov. J. Computer Systems Sc.* 23(2), 1985
16. Manevich A.I. On the theory of coupled loss of stability in stiffened thin-walled structures. *J. App. Math. Mech.* 46(2), 261–267, 1983
17. Manevich A.I. Loss of stability of compressed longitudinally stiffened cylindrical shells at finite displacements with account of ribs-plates local buckling. *Mech. Solids* 18(2), 136–145, 1983
18. Manevich A.I., Zaidenberg A.I. Linearized reduced gradient procedure for the solutions of nonlinear programming problems. *Izv. Akad. Nauk USSR, Tekh. Kibern.* 6, 13–18, 1974 (in Russian)

Holm Altenbach
Igor V. Andrianov
Yuri V. Mikhlin

Contents

Part I Investigation of Advanced Structures in Engineering

1	On Mechanical Metastructures Applied in Vibration Suppression—Review	3
	Livija Cveticanin	
1.1	Introduction	3
1.2	Elastic Metastructure	6
1.3	Mechanical Metastructure as Vibration Isolator	9
1.4	Auxetic Structure	11
1.5	Conclusion and Future Investigation	14
	References	15
2	Debonding Resistance Evaluation in Virtual Testing of Sandwich Specimens	19
	Vyacheslav N. Burlayenko, Holm Altenbach, and Svetlana D. Dimitrova	
2.1	Introduction	19
2.2	Fracture Test Methods	21
2.3	Sandwich Specimens with Finite Crack	22
	2.3.1 Fracture Mechanics Approach	23
	2.3.2 1-D Beam Theory-Based Approach	26
	2.3.3 2-D Finite Element Modeling	27
2.4	Results and Discussion	30
2.5	Conclusions	34
	Appendix 1	35
	Appendix 2	36
	References	36
3	Modeling of Mechanical Properties of Composite Materials Under Different Types of Loads	39
	Mykola Kryshchuk, Sergiy Shukayev, and Viktor Rubashevskiy	
3.1	Introduction	39
3.2	Determination of Elastic Properties of Layered Composites	41
3.3	Phenomenological Failure Criteria of Composite Materials	43

3.3.1	Tsai–Wu Criterion	44
3.3.2	Maximum Stress Criterion	46
3.3.3	Maximum Principal Strain Criterion	47
3.3.4	Tsai–Hill Criterion (or Modified Hill Criterion) (Azzi and Tsai 1965)	48
3.4	Estimation of Strength and Modal Analysis of a Standard Structure of a Space-Use Honeycomb Panel	49
3.5	Comparative Analysis of Strength Assessment Methods for Layered Composites	52
3.6	Conclusions	54
	References	54
4	Nonlinear Dynamic Analysis of FGM Sandwich Shallow Shells with Variable Thickness of Layers	57
	Lidiya Kurpa, Tetyana Shmatko, and Galina Timchenko	
4.1	Introduction	57
4.2	Formulation Problem	59
4.3	Solution Method—Free Vibration Problem	63
4.4	Numerical Results	64
4.5	Conclusions	73
	References	73
5	Residual Stresses in Plastic Deformed Composites	75
	Gennadiy Lvov and Olga Kostromitskaya	
5.1	Introduction	76
5.2	Numerical Simulation of Residual Stress Accumulation	81
5.3	The Governing Equations of Plastic Deformation of a Composite	85
5.4	Conclusions	88
	References	89
6	Dynamics of Curved Laminated Glass Composite Panels Under Impact Loading	91
	Olha Sukhanova, Oleksiy Larin, Konstantin Naumenko, and Holm Altenbach	
6.1	Introduction	91
6.2	Formulation of the Problem	92
6.3	Simulation Model	93
6.4	Calculation of Nonlinear Dynamics of the Laminated Glass	94
6.5	Conclusions	98
	References	101
7	Modeling the Response of Multilayer Glazing to Distributed and Localized Force Loading	103
	Sergey Ugrimov, Natalia Smetankina, and Vladislav Kobynik	
7.1	Introduction	103

- 7.2 Mathematical Model of Multilayer Glazing and the Governing Equations 106
- 7.3 Investigation of the SSS in Glazing Under Dynamic Force Loading 109
 - 7.3.1 Distributed and Localized Loading. Transient Dynamic Analysis 109
 - 7.3.2 Blast Loading 115
 - 7.3.3 Bird Collision 116
 - 7.3.4 Low-Velocity Impact Loading 117
 - 7.3.5 Bullet Resistance 119
- 7.4 Conclusions 121
- References 122

Part II Nonlinear Dynamics of Distributed Systems

- 8 Synchronicity Phenomena in Circular Cylindrical Shells Under Random Excitation 127**
Antonio Zippo, Giovanni Iarriccio, and Francesco Pellicano
 - 8.1 Introduction 127
 - 8.2 Description of the Experimental Setup 130
 - 8.3 Natural Frequencies and Modes 132
 - 8.4 Test Procedure 136
 - 8.5 Experimental Results: Excitation and Dynamic Response 137
 - 8.5.1 Case 1. Standard Homogeneous Temperature, 30 °C, Broadband Excitation, 10–2000 Hz 137
 - 8.5.2 Case 2. Homogeneous Temperature 25 °C, 900–3000 Hz, $45\text{--}273 \frac{m}{s^2}$ 139
 - 8.5.3 Case 3. 20 °C Homogeneous Temperature 141
 - 8.5.4 Case 4. Thermal Gradient, 20 °C Outside, 48 °C Inside, 900–3000 Hz, $43\text{--}298 \frac{m}{s^2}$ 148
 - 8.5.5 Case 6. Gradient Temperature (Inner 48 °C, Outer 20 °C), Narrow Band Excitation, 900–1500 Hz 149
 - 8.6 Conclusions 155
 - References 156
- 9 Investigation of the Nonlinearity Effect of the Shrouded Blade Assemblies on Their Forced Vibrations 159**
Anatoliy Zinkovskii, Kyrylo Savchenko, and Yevheniia Onyshchenko
 - 9.1 Introduction 159
 - 9.2 Approaches to Finite Element Modelling of the Object Nonlinearity 160
 - 9.2.1 Shrouded Flange Coupling of the Blades 160
 - 9.2.2 Fatigue Crack 161
 - 9.3 Calculation of the Forced Vibrations of the Blade Assemblies 162
 - 9.4 Results of the Computational Experiments 164

9.5 Conclusions 167
 References 168

Part III Nonlinear Dynamics of Discrete Systems

10 Influence of Linear and Nonlinear Electromechanical Couplings on Vibration Absorber–Harvester System 171

Krzysztof Kecik and Arkadiusz Smagala
 10.1 Introduction 171
 10.2 Absorber-Harvester Architecture 173
 10.2.1 Model of Vibration Absorber System with Energy Harvester 174
 10.2.2 Electromechanical Coupling Modeling 175
 10.3 Results 178
 10.3.1 Parameters Identification 178
 10.3.2 Comparison of Electromechanical Coupling Models 178
 10.3.3 Analysis of Linear Electromechanical Coupling Model 179
 10.3.4 Analysis of Nonlinear Electromechanical Coupling Model 180
 10.4 Conclusions 181
 References 182

11 Crisis-Induced Intermittency and Other Nonlinear Dynamics Phenomena in Vibro-impact System with Soft Impact 185

Victor Bazhenov, Olga Pogorelova, and Tatiana Postnikova
 11.1 Introduction 185
 11.2 Brief Description of Platform-Vibrator Mathematical Model 187
 11.3 Soft Impact Simulation 190
 11.3.1 With Linear Force 190
 11.3.2 With Nonlinear Hertz’s Force 192
 11.4 About the Model Verification and Validation 193
 11.5 Coexisting Regimes—Hysteresis 194
 11.5.1 When the Exciting Frequency Ω is Varied 195
 11.5.2 When the Technological Mass m_2 is Varied 196
 11.5.3 When the Stiffness of Vibro-isolating Spring k_1 is Varied 196
 11.6 Interior Crisis. Crisis-Induced Intermittency 198
 11.7 Permanent and Transient Chaos 199
 11.7.1 Permanent (Sustained) Chaos 199
 11.7.2 Transient Chaos 199
 11.8 Conclusions 201
 References 202

Part IV Interaction of Structures and Flow

12 Aeroelastic Interactions Between Plates and Three-Dimensional Inviscid Potential Flows 207
 Konstantin V. Avramov, Darkhan S. Myrzaliyev,
 and Kazira K. Seitkazenova

12.1 Introduction 207
 12.2 Equations of Plate Motions 209
 12.3 System of Singular Integral Equations with Respect
 to Aerodynamic Derivatives of Pressure Drop 210
 12.4 Finite Degrees of Freedom Model of Plates Vibrations 215
 12.5 Numerical Methods of Singular Integral Equation Solution 217
 12.6 Results of Numerical Analysis 219
 12.7 Conclusions 224
 References 224

13 Hydroelastic Vibrations of Circular Sandwich Plate Under Inertial Excitation 227
 Dmitry V. Kondratov, Lev I. Mogilevich, Victor S. Popov,
 and Anna A. Popova

13.1 Introduction 228
 13.2 The Problem Statement 230
 13.3 Solving the Hydroelasticity Problem 233
 13.4 Calculation Results 239
 13.5 Summary and Conclusion 240
 References 240

14 Effect of Finite Vessel Stiffness on Transition from Two-Dimensional Liquid Sloshing to Swirling: Reduced-Order Modeling 243
 Dar Zusman and Oleg V. Gendelman

14.1 Introduction 243
 14.2 Description of the Model 246
 14.2.1 Introducing the Model 246
 14.2.2 Equations of Motion 246
 14.3 Numerical Study 248
 14.3.1 Effect of Finite Vessel Stiffness on the Critical
 Excitation Amplitude 248
 14.3.2 Effect of Finite Vessel Stiffness and Finite Liquid
 Depth on the Sloshing Modes 249
 14.3.3 3:1 Internal Resonance 250
 14.3.4 Effect of Finite Vessel Stiffness on the Formation
 of Chaotic Response 251
 14.4 Analytical Treatment 253
 14.5 Discussion and Concluding Remarks 258
 Appendix 259
 References 260

Part V Longtime Behavior of Engineering Structures

15	Analysis of Creep, Shrinkage, and Damage in Armored Concrete Dome at Static and Seismic Loading	265
	Dmytro Breslavsky and Aleksandr Chuprynin	
15.1	Introduction	265
15.2	Problem Statement and Constitutive Equations	267
15.2.1	Problem Description	267
15.2.2	Constitutive Equations	268
15.2.3	Method of Numerical Modeling	271
15.3	Numerical Simulation of Spherical Dome Loaded by Long-Term Static and Seismic Actions	271
15.4	Conclusions	275
	References	276
16	Stress–Strain State of Nuclear Reactor Core Baffle Under the Action of Thermal and Irradiation Fields	279
	Dmytro Breslavsky, Alyona Senko, Oksana Tatarinova, Victor Voevodin, and Alexander Kalchenko	
16.1	Introduction	280
16.2	Solution Procedure	281
16.2.1	Problem Statement	281
16.2.2	Solution of Heat Conductivity Problem	284
16.2.3	FEM Calculation Scheme	285
16.3	Results of Numerical Simulation	287
16.3.1	Deformation of a Thick Tube of Equivalent Dimensions	288
16.3.2	Long-Term Behavior of Core Baffle	289
16.4	Conclusions	291
	References	292
17	Application of Data-Driven Yield Surface to Prediction of Failure Probability for Centrifugal Pump	295
	Mariya Shapovalova and Oleksii Vodka	
17.1	Introduction	296
17.2	Objectives	297
17.3	Modeling of Centrifugal Pump WD 16/25	297
17.4	Application of Data-Driven Yield Surface to Prediction of Failure Probability for Centrifugal Pump	302
17.5	Conclusions	307
	References	308

Part VI Rotating Systems

18 Self-synchronization of Rotational Regimes of Vibro-exciters on Oscillatory Systems 313
 Arkadiy I. Manevich

18.1 Introduction 313

18.2 The Model and Governing Equations 314

18.3 Solution in the First Approximation: Averaged Synchronous Regimes 316

18.3.1 Averaged Characteristics of the Synchronous Regimes 316

18.3.2 Stability of the Synchronous Regimes in the First Approximation 320

18.4 Solution in the Second Approximation: Non-uniform Synchronous Regimes 322

18.4.1 Analytical Solution 322

18.4.2 Instability of Stationary Synchronous Regimes Caused by the Translational Inertia Forces 324

18.5 Results of the Numerical Analysis and Comparison with the Numerical Simulation 325

18.5.1 The Averaged Characteristics of the Synchronous Regimes 325

18.5.2 Verification by Numerical Simulation 326

18.5.3 Checking the New Stability Criterion (18.33) 328

18.6 Conclusions 331

References 332

19 Stability Analysis of Rotor Motion in Nonlinear Systems with Passive and Active Magnetic Bearings 333
 Gennadii Martynenko

19.1 Introduction 333

19.2 Object and Aim of Research 335

19.2.1 Analyzed Design and Initial Data 335

19.2.2 Research Objectives 337

19.3 Mathematical Modeling of the Nonlinear Rotor Dynamics in Magnetic Bearings 338

19.3.1 Formation of a System of Electromechanical Equations 338

19.3.2 Solving the Nonlinear Differential Equation System 340

19.4 Numerical-Graphical Analysis of Rotor Motion Stability in Magnetic Bearings 341

19.4.1 Estimation of the Parameters of the Linearized Oscillatory System 341

19.4.2 Simulation of the Nonlinear Dynamics of a Rotor in Magnetic Bearings 341

19.4.3 Stability Rating of the Rotor Motion in MBs
Using Numerical and Graphical Data 346

19.4.4 Validation of the Proposed Approach
to the Stability Analysis 346

19.5 Conclusions 347

References 348

20 Computational–Experimental Evaluation of Stiffness

Response in Elastic Supports of Rotor Systems 353
Mykola M. Tkachuk, Andriy Grabovskiy, Mykola A. Tkachuk,
and Olexandr Shut

20.1 Introduction 353

20.2 Literature Overview 354

20.3 The Design of the Flexible Ring with Intermeshed Inner
and Outer Flanges 355

20.4 Computational Models for the Elastic Ring 356

20.5 Numerical Evaluation of Elastic Supports Stiffness
and Critical Velocities 356

20.5.1 Stiffness of Elastic Supports for Various Number
of Grooves on the Elastic Ring 357

20.5.2 Critical Rotation Velocities of the Cantilever
Rotor Depending on the Stiffness of the Elastic
Supports 361

20.6 Experimental Measurement of Elastic Support Stiffness 363

20.7 Results Analysis 364

20.8 Conclusions 364

References 365

Part VII Satellites and Spacecrafts

21 A Brief Analysis of Artificial Satellites Solar Panels

Deployment Considering a Nonlinear Dynamic Model 369
Rafael Avanço, Raibel Arias, José Manoel Balthazar,
Ângelo Marcelo Tuset, Maurício Aparecido Ribeiro,
Frederic Conrad Janzen, and Átila Madureira Bueno

21.1 Introduction 370

21.2 The Non-ideal and Ideal Model for the Simplified Solar
Panel 371

21.2.1 The Non-ideal (RNIS) and Ideal (IS) Model
for the Dynamics in the Opening of the Simplified
Solar Panel 371

21.2.2 Ideal (IS) Model for the Dynamics of the Simplified
Model of the Solar Panel 374

21.3 Numerical Results from the Non-ideal (RNIS) and Ideal
(IS) of the Simplified Model of the Solar Panel 375

- 21.3.1 Results from the Non-ideal Model (RNIS) of the Simplified Model of the Solar Panel 375
- 21.3.2 Results from the Ideal (IS) Model of the Simplified Solar Panel 378
- 21.3.3 Non-ideal (RNIS) with Constant Sinusoidal Voltage from the Motor 380
- 21.4 Conclusions 382
- References 383

22 The Optimal in Terms of Fuel Consumption Approach to Reorientation of a Spacecraft Based on the Nonlinear Boundary Value Problem Solution 385

Valerii B. Uspenskiy, Natalia V. Shyriaieva, and Mariia V. Nekrasova

- 22.1 Introduction 385
- 22.2 Formulation of the Problem 388
- 22.3 Results of Modeling 393
- 22.4 Discussion of the Solution Practical Implementation 398
- 22.5 Conclusions 400
- References 400

Part VIII Nonlinear Phenomena and Methods of Investigation

23 Asymptotic Methods for Soliton Excitations 405

Alexander Kovalev

- 23.1 Introduction 405
- 23.2 Asymptotic Method for Envelop Solitons 406
- 23.3 Asymptotic Method for Solitons in Weakly Dispersive Media 411
- 23.4 Conclusions 420
- Appendix 420
- References 421

24 Method of Superimposed Meshes for Solving Nonlinear Dynamic Problems 423

Volodymyr Martynenko

- 24.1 Introduction 423
 - 24.1.1 The Sources of Anisotropy of Polymer Composite Properties 424
 - 24.1.2 The Different Degrees of Anisotropy of Elastic and Viscoelastic Properties 424
 - 24.1.3 Effects and Methods in Modeling of Nonlinear Dynamic Anisotropic Viscoelastic Properties 425
 - 24.1.4 The Reasons and Benefits of Using the Method of Superimposed Meshes 426
 - 24.1.5 The Insight of the MSM 426
- 24.2 Formulation of the MSM for the Elasticity Problem 428

24.2.1	Lagrangian Functional of the Elastic Material	428
24.2.2	Subdivision into Several Finite Element Meshes	429
24.2.3	Combination of Superimposed Meshes	430
24.2.4	Total Stress–Stain State Basing on Stress–Strain States in Superimposed Meshes	431
24.2.5	Extension of MSM to Nonlinear Nonstationary Problems	432
24.3	Calculation Using the MSM	433
24.3.1	Benchmarking	433
24.3.2	Verification	434
24.4	Conclusions	437
	References	439
25	New Types of Limit Sets in the Dynamic System “Spherical Pendulum—Electric Motor”	443
	Aleksandr Shvets and Serhii Donetskyi	
25.1	Introduction	443
25.2	Equations of Motion of Spherical Pendulum with the Limited Excitation	444
25.3	Results of Numerical Constructions of Limit Sets	445
25.4	Scenarios of Transitions Between Limit Sets of Various Types	451
25.5	Conclusion	453
	References	454
26	Exact Solutions to the Four-Component Merola–Ragnisco–Tu Lattice Equations	457
	Aleksandr I. Zemlyanukhin, Andrey V. Bochkarev, and Aleksandr V. Ratushny	
26.1	Introduction	457
26.2	Linear Stability Analysis of Constant Solutions	458
26.3	Continualization	460
26.4	Exact Solution to the System	462
26.5	Combined Kink Wave	466
26.6	Conclusions	467
	References	468

Contributors

Holm Altenbach Institut für Mechanik, Otto-von-Guericke-Universität Magdeburg, Magdeburg, Germany

Raibel Arias Federal University of Maranhão, Balsas, State of Maranhão, Brazil

Rafael Avanço Federal University of Maranhão, Balsas, State of Maranhão, Brazil

Konstantin V. Avramov National Academy of Science of Ukraine, Podgorny Institute for Mechanical Engineering, Kharkiv, Ukraine;
National Technical University “Kharkiv Polytechnic Institute”, Kharkiv, Ukraine;
Department of Technical Systems, Kharkiv National University of Radio Electronics, Kharkiv, Ukraine

José Manoel Balthazar UNESP-Universidade Estadual Paulista, Bauru, SP, Brazil

Victor Bazhenov Kyiv National University of Construction and Architecture, Kyiv, Ukraine

Andrey V. Bochkarev Department of Applied Mathematics, Yuri Gagarin State Technical University of Saratov, Saratov, Russia

Dmytro Breslavsky Department of Computer Modelling of Processes and Systems, National Technical University “Kharkiv Polytechnic Institute”, Kharkiv, Ukraine

Átila Madureira Bueno UNESP-Universidade Estadual Paulista, Sorocaba, SP, Brazil

Vyacheslav N. Burlayenko Department of Applied Mathematics, National Technical University “Kharkiv Polytechnic Institute”, Kharkiv, Ukraine

Aleksandr Chuprynin Department of Theoretical and Building Mechanics, O.M. Beketov National University of Urban Economy, Kharkiv, Ukraine

Livija Cveticanin Faculty of Technical Sciences, University in Novi Sad, Novi Sad, Serbia;
Doctoral School of Safety and Security Sciences, Obuda University, Budapest, Hungary

Svetlana D. Dimitrova Department of Higher Mathematics, National Technical University “Kharkiv Polytechnic Institute”, Kharkiv, Ukraine

Serhii Donetskyi National Technical University of Ukraine “Igor Sikorsky Kyiv Polytechnic Institute”, Kyiv, Ukraine

Oleg V. Gendelman Faculty of Mechanical Engineering, Technion, Israel Institute of Technology, Haifa, Israel

Andriy Grabovskiy Department of Theory and Computer-Aided Design of Mechanisms and Machines, National Technical University “Kharkiv Polytechnic Institute”, Kharkiv, Ukraine

Giovanni Iarriccio Department of Engineering Enzo Ferrari, University of Modena and Reggio Emilia, Modena, Italy

Frederic Conrad Janzen Federal University of Technology, Ponta Grossa, Paraná, Brazil

Alexander Kalchenko Institute of Solid-State Physics, Materials Science and Technologies, National Scientific Center ‘Kharkiv Institute On Physics and Technics’ NAS of Ukraine, Kharkiv, Ukraine

Krzysztof Kecik Department of Applied Mechanics, Lublin University of Technology, Lublin, Poland

Vladislav Kobylnik Department of Vibration and Thermostability Studies, A. Pidhorny Institute for Mechanical Engineering Problems National Academy of Sciences of Ukraine, Kharkiv, Ukraine

Dmitry V. Kondratov Institute of Precision Mechanics and Control, Russian Academy of Sciences, Saratov, Russia

Olga Kostromitskaya Department of Dynamics and Strength of Machines, National Technical University “Kharkiv Polytechnic Institute”, Kharkiv, Ukraine

Alexander Kovalev B.I. Verkin Institute for Low Temperature Physics and Engineering of NANU, Kharkov, Ukraine;
V.N. Karazin Kharkiv National University of MESU, Kharkov, Ukraine

Mykola Kryshchuk Department of Dynamics and Strength of Machines and Strength of Materials, National Technical University of Ukraine “Igor Sikorsky Kyiv Polytechnic Institute, Kyiv, Ukraine

Lidiya Kurpa Department of Applied Mathematics, National Technical University “Kharkiv Polytechnic Institute”, Kharkiv, Ukraine

Oleksiy Larin Department of Dynamics and Strength of Machines, National Technical University “Kharkiv Polytechnic Institute”, Kharkiv, Ukraine

Gennadiy Lvov Department of Dynamics and Strength of Machines, National Technical University “Kharkiv Polytechnic Institute”, Kharkiv, Ukraine

Arkadiy I. Manevich Department of Theoretical and Computational Mechanics, Dniepr National University, Dniepr, Ukraine

Gennadii Martynenko Department of Dynamics and Strength of Machines, National Technical University “Kharkiv Polytechnic Institute”, Kharkiv, Ukraine

Volodymyr Martynenko Dynamics and Strength of Machines Department, National Technical University “Kharkiv Polytechnic Institute”, Kharkiv, Ukraine

Lev I. Mogilevich Department of Applied Mathematics and System Analysis, Yuri Gagarin State Technical University of Saratov, Saratov, Russia

Darkhan S. Myrzaliyev Department of Mechanics and Engineering, M. Auezov South Kazakhstan State University, Shymkent, Republic of Kazakhstan

Konstantin Naumenko Institut für Mechanik, Otto-von-Guericke-Universität Magdeburg, Magdeburg, Germany

Mariia V. Nekrasova National Technical University “Kharkiv Polytechnic Institute”, Kharkiv, Ukraine

Yevheniia Onyshchenko Department of Oscillations and Vibration Reliability, G.S. Pisarenko Institute for Problems of Strength of the National Academy of Sciences of Ukraine, Kyiv, Ukraine

Francesco Pellicano Department of Engineering Enzo Ferrari, University of Modena and Reggio Emilia, Modena, Italy;
Centre InterMech MoRe, University of Modena and Reggio Emilia, Modena, Italy

Olga Pogorelova Kyiv National University of Construction and Architecture, Kyiv, Ukraine

Victor S. Popov Institute of Precision Mechanics and Control, Russian Academy of Sciences, Saratov, Russia;
Department of Applied Mathematics and System Analysis, Yuri Gagarin State Technical University of Saratov, Saratov, Russia

Anna A. Popova Department of Applied Mathematics and System Analysis, Yuri Gagarin State Technical University of Saratov, Saratov, Russia

Tatiana Postnikova Kyiv National University of Construction and Architecture, Kyiv, Ukraine

Aleksandr V. Ratushny Department of Applied Mathematics, Yuri Gagarin State Technical University of Saratov, Saratov, Russia

Maurício Aparecido Ribeiro Federal University of Technology, Ponta Grossa, Paraná, Brazil

Viktor Rubashevskiy Department of Dynamics and Strength of Machines and Strength of Materials, National Technical University of Ukraine “Igor Sikorsky Kyiv Polytechnic Institute, Kyiv, Ukraine

Kyrylo Savchenko Department of Oscillations and Vibration Reliability, G.S. Pisarenko Institute for Problems of Strength of the National Academy of Sciences of Ukraine, Kyiv, Ukraine

Kazira K. Seitkazenova Department of Mechanics and Engineering, M. Auezov South Kazakhstan State University, Shimkent, Republic of Kazakhstan

Alyona Senko Department of Computer Modelling of Processes and Systems, National Technical University “Kharkiv Polytechnic Institute”, Kharkiv, Ukraine

Mariya Shapovalova Department of Dynamics and Strength of Machines, National Technical University “Kharkiv Polytechnic Institute”, Kharkiv, Ukraine

Tetyana Shmatko Department of Higher Mathematics, National Technical University “Kharkiv Polytechnic Institute”, Kharkiv, Ukraine

Sergiy Shukayev Department of Dynamics and Strength of Machines and Strength of Materials, National Technical University of Ukraine “Igor Sikorsky Kyiv Polytechnic Institute, Kyiv, Ukraine

Olexandr Shut Department of Theory and Computer-Aided Design of Mechanisms and Machines, National Technical University “Kharkiv Polytechnic Institute”, Kharkiv, Ukraine

Aleksandr Shvets National Technical University of Ukraine “Igor Sikorsky Kyiv Polytechnic Institute”, Kyiv, Ukraine

Natalia V. Shyriaieva National Technical University “Kharkiv Polytechnic Institute”, Kharkiv, Ukraine

Arkariusz Smagala Department of Applied Mechanics, Lublin University of Technology, Lublin, Poland

Natalia Smetankina Department of Vibration and Thermostability Studies, A. Pidhorny Institute for Mechanical Engineering Problems National Academy of Sciences of Ukraine, Kharkiv, Ukraine

Olha Sukhanova Department of Dynamics and Strength of Machines, National Technical University “Kharkiv Polytechnic Institute”, Kharkiv, Ukraine

Oksana Tatarinova Department of Computer Modelling of Processes and Systems, National Technical University “Kharkiv Polytechnic Institute”, Kharkiv, Ukraine

Galina Timchenko Department of Applied Mathematics, National Technical University “Kharkiv Polytechnic Institute”, Kharkiv, Ukraine

Mykola A. Tkachuk Department of Theory and Computer-Aided Design of Mechanisms and Machines, National Technical University “Kharkiv Polytechnic Institute”, Kharkiv, Ukraine

Mykola M. Tkachuk Department of Theory and Computer-Aided Design of Mechanisms and Machines, National Technical University “Kharkiv Polytechnic Institute”, Kharkiv, Ukraine

Ângelo Marcelo Tusset Federal University of Technology, Ponta Grossa, Paraná, Brazil

Sergey Ugrimov Department of Vibration and Thermostability Studies, A. Pidhorny Institute for Mechanical Engineering Problems National Academy of Sciences of Ukraine, Kharkiv, Ukraine

Valerii B. Uspenskyi National Technical University “Kharkiv Polytechnic Institute”, Kharkiv, Ukraine

Oleksii Vodka Department of Dynamics and Strength of Machines, National Technical University “Kharkiv Polytechnic Institute”, Kharkiv, Ukraine

Victor Voevodin Institute of Solid-State Physics, Materials Science and Technologies, National Scientific Center ‘Kharkiv Institute On Physics and Technics’ NAS of Ukraine, Kharkiv, Ukraine

Aleksandr I. Zemlyanukhin Department of Applied Mathematics, Yuri Gagarin State Technical University of Saratov, Saratov, Russia

Anatoliy Zinkovskii Department of Oscillations and Vibration Reliability, G.S. Pisarenko Institute for Problems of Strength of the National Academy of Sciences of Ukraine, Kyiv, Ukraine

Antonio Zippo Department of Engineering Enzo Ferrari, University of Modena and Reggio Emilia, Modena, Italy;
Centre InterMech MoRe, University of Modena and Reggio Emilia, Modena, Italy

Dar Zusman Faculty of Mechanical Engineering, Technion, Israel Institute of Technology, Haifa, Israel

Part I
Investigation of Advanced Structures
in Engineering

Chapter 1

On Mechanical Metastructures Applied in Vibration Suppression—Review



Livija Cveticanin

Abstract This paper is an overview of the mechanical metastructures applied for vibration suppression. The metastructures are usually the micro version of metamaterials which are artificially produced to satisfy certain physical requirements. Mechanical metastructures are periodical with various unit cells connected into a complex one, two, or three-dimensional structure. Three groups of mechanical metastructures are considered: with negative effective mass, negative effective stiffness, and negative Poisson's ratio. The first group of metastructures are also named elastic and the third group auxetics. The elastic metamaterials form the frequency stopband for vibration. The mechanical metastructure are often utilized as vibration isolator.

Keywords Elastic metamaterial · Auxetics · Effective stiffness · Effective mass · Negative Poisson's ration

1.1 Introduction

Vibration is one of the worst pollutants with negative effects in the living and working environment. Engineering structures, special lightweight ones, often suffer from environmental vibration that is difficult to suppress due to its low frequency and multiple polarizations. Decades of research have been conducted on vibration suppression, cancellation and absorption methods. In the most cases the vibration suppression is done after the structure is fabricated and settled in its function. The problem is solved by implementation required masses to the structure (vibration absorbers) or by adding viscoelastic material with certain damping properties (vibration isolators). The main lack of the suggested procedures is that the weight of the structure is increased, the stiffness of the system is changed and the effect of vibration suppression is not

L. Cveticanin (✉)

Faculty of Technical Sciences, University in Novi Sad, Trg D. Obradovica 6, 21000 Novi Sad, Serbia

e-mail: cveticanin@uns.ac.rs; cpinter.livia@uni-obuda.hu

Doctoral School of Safety and Security Sciences, Obuda University, Nepszinhaz u. 8, H-1081 Budapest, Hungary

constant but variable due to the temperature (damping properties of the viscoelastic material depend on the temperature).

To overcome the problem, the application of the newly developed mechanical metastructures is suggested. The emerging field of metastructure offers a practical solution for the low frequency vibration reduction without introducing extra isolators that have gigantic size and heavy weight.

Metastructure is an arrangement of artificial structural elements, designed to achieve advantages and unusual physical properties. It is an artificial man-made structure which is the macro version of the metamaterial (a composite containing periodic unit cells whose configuration affects the material properties rather than the inherent attributes of solid materials). Metamaterial research began when the modification of material in the molecular and nanometer scales were introduced. It was found that the unique properties of metamaterials (optical, electric, mechanic, wave propagation, etc) result from their designed periodic structures rather than chemical reactions

Fig. 1.1 Mass-in-mass two degree-of-freedom system

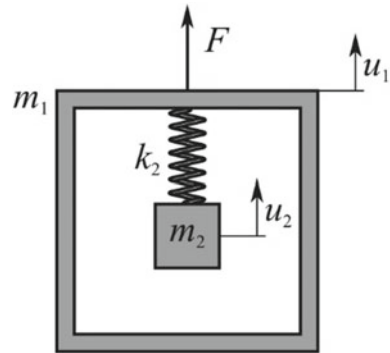
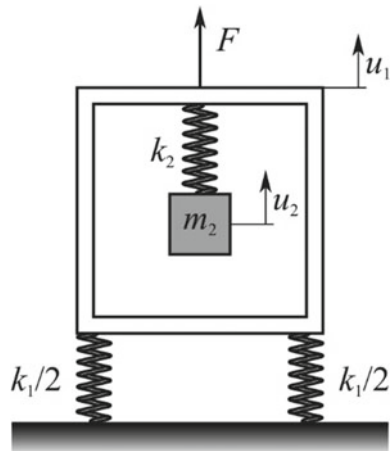


Fig. 1.2 Mass-in-spring two degree-of-freedom system



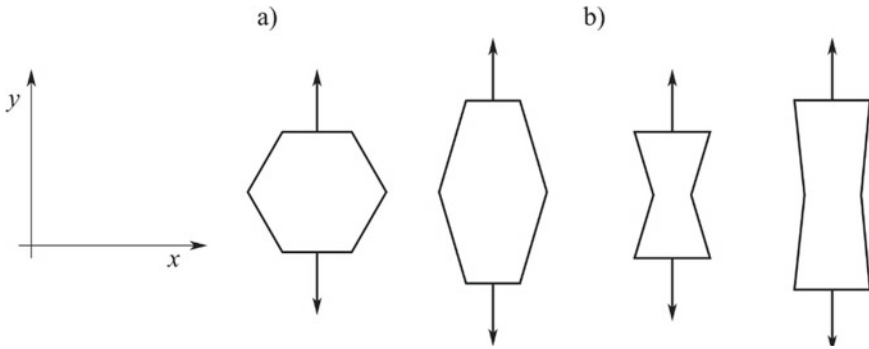


Fig. 1.3 a Nonauxetic structure deformation, b auxetic (re-entrant) structure deformation

during manufacturing. The advantage of metamaterials over their conventional counterparts comes from their designability. First, the electromagnetic metamaterials were investigated. There is a significant number of publication considering these metamaterials (see reviews Liu and Zhang, 2011; Priyanka, 2014; Liu et al. 2015; Singh et al. 2015; Buriak 2016; Zhang et al. 2018; Kadic et al. 2019). The material exhibited a negative permittivity and/or negative permeability and stop the propagation of the electro-magnetic waves. The achievements in metamaterials in the electromagnetic field inspired other researchers branching the concept out to acoustics, water waves, plasmonics, etc. which are governed by different mechanisms and equations. The concept was extended to acoustic metamaterials. The metamaterial utilizes the theory of Bragg scattering and exhibits some type of periodicity: the lattices are created such that when the acoustic wave reflect off the structure they destructively interfere with each other. Mechanical metastructure, as the metamaterial inspired concept, was developed for vibration elimination (Reichl, 2018). Mechanical or elastic metamaterial are combination of geometries and material properties which are integrated into a host structure with physical property of suppression of mechanical effects: vibration, impacts, etc. Due to excellent flexibility in design the mechanical metastructure brings a new perspective in understanding physical properties of structures. Thus, macroscopic structures can exhibit counterintuitive response characteristics, such as: negative effective mass density, negative stiffness and negative Poisson's ratio. Depending on these properties three types of mechanical metastructures are considered: 1. Metastructure with continually distributed vibration absorbers for elimination vibration for certain frequency band, 2. Metastructure as vibration isolator which decreases the amplitude of vibration and 3. Auxetic metastructure. The mechanical metastructures with negative effective mass, negative stiffness and negative Poisson's ratio need to have periodical structure and to have unit cells with the same property as the whole structure. The corresponding theoretical explanation is given in papers reported in reviews Cveticanin et al. (2016) and (2017).

Based on the theoretical investigation, in this review, the three aforementioned groups of mechanical metastructures are considered.

In general, it is found that the mechanical metastructures can be employed for vibration attenuation, energy absorption and flexible engineering structures. The application of mechanical metamaterial is very wide: in military, automobile, aerospace industry, civil infrastructure etc., in lightweight structures, where excellent rigidity, strength, heat isolation, vibration suppression and impact energy absorption, are required. The structures bear large global flexibility, large local deformation within elastic limits. Metastructures are also proposed for impact energy absorption, which enables their use in packaging, protective systems and crash mitigation. The structures are used for flexible electronics, deformable smart phone, expandable vascular metallic stent, etc. Auxetic metastructures can be applied for designing: body armor, packing material, knee and elbow pads, robust shock absorbing material and sponge mops. Mechanical metastructures can be employed against impact damages, for flexible industrial components, vibration attenuation of engineering structures etc.

1.2 Elastic Metastructure

Milton (2007) was the first to conceive the idea of using local absorbers to create structures with negative effective mass that varies with frequency. It was found that the requirement of negative effective mass of the structure requires the same for the unit cells which form the structure, i.e. to have the effective negative effective mass of the unit (Sun et al. 2010). The unit cell is modeled as a mass-in-mass two-degree-of-freedom system shown in Fig.1.

The system contains a basic mass m_1 and an absorber. The absorber contains a mass m_2 and a spring with rigidity k_2 . The absorber is connected with the basic mass. On the basic mass an external excitation force $F=F_0\exp(i\Omega t)$, with amplitude F_0 and frequency Ω , acts. The system has two degrees of freedom. Introducing the two generalized coordinates are motion u_1 and u_2 , the mathematical model of the mass-in-mass system is

$$\begin{aligned} m_1\ddot{u}_1 + k_2(u_1 - u_2) &= F \\ m_2\ddot{u}_2 + k_2(u_2 - u_1) &= 0 \end{aligned} \quad (1)$$

The closed form solution of (1) is $u_1 = a_1\exp(i\Omega t)$ and $u_2 = a_2\exp(i\Omega t)$, where

$$a_1 = \frac{F_0(k_2 - m_2\Omega^2)}{(k_2 - m_1\Omega^2)(k_2 - m_2\Omega^2) - k_2^2}, a_2 = \frac{F_0k_2}{(k_2 - m_1\Omega^2)(k_2 - m_2\Omega^2) - k_2^2} \quad (2)$$

Let us introduce the effective mass m_{eff} which satisfies the relation $F = m_{eff}\ddot{u}_1$ i.e. $F_0 = -m_{eff}\Omega^2 a_1$ and $F_0 = m_{eff}\Omega^2 a_2 \left(\frac{\Omega^2}{\omega^2} - 1 \right)$ where $\omega = \sqrt{\frac{k_2}{m_2}}$. Substituting (2), the relation for the effective mass is obtained

$$m_{eff} = m_1 + \frac{m_2}{1 - \Omega^2/\omega^2} \quad (3)$$

Analyzing the expression (3) it is obvious that the effective mass is negative for $\Omega > \omega$ and $\frac{m_2}{\frac{\Omega^2}{\omega^2} - 1} > m_1$. For that case $a_1 = -\frac{F_0}{m_{eff}\Omega^2} > 0$ and $a_2 = \frac{F_0}{m_{eff}\Omega^2\left(\frac{\Omega^2}{\omega^2} - 1\right)} < 0$, i.e. u_1 and u_2 are 180° out of phase. Then the downward pulling spring force acts on m_1 which satisfies the relation $k_2(a_1 - a_2) = F_0(m_{eff} - m_1)/m_{eff} > F_0$. The consequence of action of this force is the negative effective mass of the unit.

According to suggestion given in Milton (2007) this units are suggested to be connected into 1D beam, 2D plate and even into 3D space form. The concept of metastructure beam (Pai et al. 2014; Wang et al. 2016) and plate (Pend and Pai, 2014; Peng and Pai, 2015) is based on the principle of conventional vibration absorbers. Metamaterials employ mass-spring-damper subsystems as local resonators. Metamaterials are designed by building mechanical subunits into a natural material to resonate with mechanical waves propagating in it. An elastic wave in a structure may resonance with the structure's subunits and its spread and wavelength can be changed. This local mechanical resonance can be used to design metamaterials with dynamic-dependent negative effective mass and stiffness.

Using the theoretical consideration for the unit cell, Cheng et al. (2008) created the first metastructure with negative effective mass that gives a band gap at a certain frequency. The metastructure contained the basic lattice structure in which lead spheres coated in a silicone rubber within an epoxy matrix are settled. The lead balls in the rubber are referred to as local resonators or local absorbers. The local resonator mechanism is the same mechanism used for vibration suppression. Namely these local resonators suppress vibration. The metastructure, usually called elastic one, represents the structure with distributed vibration absorbers. In opposite to the conventional materials, in the metastructure absorbers are integrated and there is the geometry and material change on the centimeter level (Reichl, 2018). The benefit of using elastic metastructures as opposed to traditional added absorbers is that the structure is initially designed including the absorbers instead of adding them after creation. Elastic metastructures provide advanced control of elastic wave propagation particularly through their ability to exhibit frequency band gaps where elastic waves cannot propagate. The band gap frequencies are fixed at design time by the metastructure geometry and constituent materials.

Zhu et al. (2014) designed the chiral-lattice-based elastic metamaterial with multiple embedded local resonators with the aim to achieve broadband vibration suppression. Chiral lattice is selected due to its capability for load bearing and feasibility for inner resonators implementation. In an aluminum chiral beam with macro dimensions 470x91x10 mm and frame thickness 0.5 mm, rubber-coated metal cylinders are placed. Experimental measurements of the vibration characteristics of the structure with and without inserted absorbers were done. According to different layouts, different frequency responses are indicated, and the existence of a vibration gap i.e. absence of vibration for certain frequencies is evident. A theoretical explanation of this phenomenon is given in Cveticanin and Zukovic (2017). It was concluded

that each of the basic units of the metastructure has a negative effective mass. The area of existence of the negative effective mass is directly related to the elimination of oscillations at a certain frequency. The larger the area of the negative effective mass, the larger the area for which this absorber ensures the absence of oscillations (Cveticanin et al. 2018₁). This area has been shown to be larger if the nonlinearity of the absorber is larger (Cveticanin et al. 2018₂).

In Reichl (2017) and Reichl (2019) a metamaterial is investigated where an array of small resonators is built to a host structure and tuned by design to eliminate all vibration within a desired frequency band. 1D metastructure is composed by adding absorbers in the hollow square cross-section tube. The sample has the length of 450 mm and cross section area of 900 mm² and 10 absorbers are added. It is obtained that this metamaterial concept allows structural members to fulfill their overall mass, stiffness, strength and geometric requirements and also act on vibration suppression. The structure eliminates the need for conventional vibration suppression.

The previously mentioned metamaterials have the disadvantage due to their complexity in fabrication.

Hence, the new requirement was set: the basic structure and absorbers have to be made of the same material and the metastructure has to be made as a single unit with negative effective mass.

3D printing technique allows to create structures with extremely complex geometries tuned for broadband vibration suppression. The unit in Hobek et al. (2015) is a square structure inside which a mass as an absorber acts. Distributed arrays of resonators have been implemented in host structure creating mechanical metastructures. The 3D-printed metastructure is suitable for passive vibration suppression. In addition, the structures remain capable of bearing loads without adding additional mass. The structure is made of polyurethane material on the 3D printer. Printing the part material properties such as compliance and density can be varied throughout a single structure and interfaces can be created. The metastructure is comprised of a distributed system of integrated internal oscillators. Results of utilizing metastructures can be quite effective at vibration suppression even with fairly simple geometries. Each oscillator serves to absorb vibration from the entire host structure.

The improvement to elastic metamaterial is reported in Pierce et al. (2020). The elastic metastructure is made of magneto-active elastomers which enable active control of frequency band gaps. The magneto-active elastomers are composite materials consisting of ferro magnetic particles dispersed in an elastometric matrix. The structure of the metamaterial is lattice-based designed and filled to form lattice-resonator structure. The metastructure has the ability to exhibit frequency band gaps where elastic waves cannot propagate. Control of elastic wave propagation is due to variation of a magnetic field. By remote application of a magnetic field the band gap can be tuned over a continuous frequency range. However, the band gap tenability depends not only on the strength of the applied magnetic field, but also on the interaction of the magnetic field and the metastructure geometry.

In Essink and Inman (2020) the device capable of vibration suppression under excitation in three directions: longitudinal, transverse and torsional are designed. This accommodation is necessary for devices to be implemented in non-laboratory

settings to account for excitation from multiple directions. In Essink and Inman (2020) the 3D printer is used to create the metastructure. With this manufacturing the absorbers and main beam can be created as a single structure. The structure is printed out of a stiff polymer material and additional damping is incorporated using material with higher viscoelastic effect. Comparing the beams with and without this absorbers it is concluded that metastructures reduce vibrations in all directions of excitation. Further increases to design bandwidth can be made by optimizing the absorbers for each degree of freedom of vibration.

A special type of elastic metamaterial for vibration suppression of a shaft is presented in Fan et al. (2020). An elastic metamaterial shaft with stack-like resonators is investigated. Resonator consists of bonded periodically sticking annular lead rings and annular soft rubber rings. Due to discretized rubber rings the stiffness is reduced. The metastructure support the formation of ultra-low-frequency vibration band gap. In the paper it is suggested that this structure can be used to reduce vibrations of shaft-like structures at low frequencies in the practical environment.

Finally, it is concluded that the elastic metamaterial has an unusual low-frequency bandgap behavior. Because of that it is applied in engineering for low-frequency vibration attenuation. Increasing the absorber's damping can increase the stopband's width and reduce low frequency vibration amplitudes, but too much damping can deactivate the stopband effect. Further investigation is necessary.

1.3 Mechanical Metastructure as Vibration Isolator

Vibration isolators are widely used in engineering systems to separate objects of interest from external vibration excitation. In order to provide effective isolation a low natural frequency is desirable for the vibration isolators. In Sun et al. (2010) it is explained that the metastructure with effective negative stiffness satisfies the suggested requirement. The effective negative stiffness is defined as arising from an applied force that is antiparallel to the displacement direction in the pre strained object. This characteristics is different from that for most of elastic materials.

In Sun et al. (2010) it is found that the metamaterial with effective negative stiffness need to have unit cells with the same property. The unit cell is modeled as a mass-in-spring two degrees of freedom system (Fig.2). Mass m_2 is with a spring whose rigidity is k_2 connected to a massless beam with symmetrical rigidity $k_1/2$. For the excitation force $F=F_0\exp(i\Omega t)$, with amplitude F_0 and frequency Ω , motion of the mass is u_2 and of the massless beam u_1 . Mathematical model of the mass-in-spring system is

$$\begin{aligned} m_2\ddot{u}_2 + k_2(u_2 - u_1) &= 0 \\ (k_1 + k_2)u_1 - k_2u_2 &= F \end{aligned} \quad (4)$$

The closed form solution of (4) is $u_1 = a_1\exp(i\Omega t)$ and $u_2 = a_2\exp(i\Omega t)$, where

$$a_1 = \frac{F_0(k_2 - m_2\Omega^2)}{(k_1 + k_2)(k_2 - m_2\Omega^2) - k_2^2}, \quad a_2 = \frac{F_0k_2}{(k_1 + k_2)(k_2 - m_2\Omega^2) - k_2^2} \quad (5)$$

Let us define the effective stiffness k_{eff} which satisfies the relation $F = k_{eff}u_1$ i.e. $F_0 = k_{eff}a_1$ and $F_0 = k_{eff}a_2\left(1 - \frac{\Omega^2}{\omega^2}\right)$ where $\omega = \sqrt{\frac{k_2}{m_2}}$. Substituting (5) into the previous relation the effective stiffness follows

$$k_{eff} = k_1 + \frac{k_2}{1 - \Omega^2/\omega^2} \quad (6)$$

For $\Omega < \omega$ the effective stiffness becomes negative for $\frac{k_2}{\frac{\omega^2}{\Omega^2} - 1} > k_1$. For $\Omega < \omega$ and $k_{eff} < 0$ we obtain that $a_1 = \frac{F_0}{k_{eff}} < 0$ and $a_2 = \frac{F_0}{k_{eff}\left(1 - \frac{\Omega^2}{\omega^2}\right)} < 0$ and u_1 and u_2 motions are in phase. For that case the downward pulling spring force against the excitation force F is $k_2(a_1 - a_2) = \frac{F_0(k_{eff} - k_1)}{k_{eff}} > F_0$. The existence of this force explains why the effective stiffness is negative.

Vuyk and Harne (2020) suggested the metastructure made with elastomeric polymers to be utilized for shock mitigation and crash absorption. Elastomeric metastructure is fabricated using thermoset silicon rubber where the microstructure contains vertical beams separated by horizontal elastomer beams. Subjected to uniaxial compression in the metastructure lateral buckling of the vertical beams occur leading to elastic energy mitigation. Unfortunately, bifurcation occurs between left and right lateral motion of the central horizontal beam and the intuition of dynamic stiffness is very complex. Experiments on relationships among metastructure design, material deformation and vibration mitigation are done. It is obtained that the large amplitude excitation force changes the slope in transmitted force and causes a total compaction of the metastructure voids which results by extreme collapse.

It is known that multi-stable structures are able to achieve significant geometric change and retain specific deformed configurations after the loads have been removed. Hua et al. (2019) introduced a new type unit for a metastructure convenient for vibration isolation based on bistable unit cells. The bistable unit cell contains an elastic ring between two elastic ones. The unit has two stable positions. Due to force action the rings in unit change their positions and it causes variation of the stiffness. By parallel connection of certain number of bistable units, a multistable mechanical metastructure with negative stiffness is developed. The basic cell is a bistable structure which exhibits two different stable shapes or positions where its elastic energy reaches a local minimum. Elastic deformation of metamaterial cylinder produces reversible energy absorption and it is a good candidate for vibration isolation and protecting structure from impact. The cylindrical structure is multistable and contain multiple unit cells.

In Zhang et al. (2020) a multistable mechanical metastructure is designed. This structure has multiple stable morphologies and is able to achieve significant geometrical changes by switching between different stable configurations. These stable

configurations do not require external loads to be maintained. The multi-stability has been utilized in energy absorbers with tunable stiffness. The basic element of the metastructure is a 3D bi-stable unit cell which contains 2 rigid frames connected with elastic ligaments. By specific assembly (parallel or serial) of a number of unit cells, the resulting multi-stable metastructure is able to exhibit translational and rotational motion. The resulting structure possess multiple equilibrium states including tilted stable configurations. These configurations offer the possibility to control the multi-stable property of metamaterial.

To achieve the ultra-low frequency vibration isolation metastructures with quasi-zero dynamic stiffness (QZS) are designed (Fan et al. 2020). The lightweight elastic metastructure consists of numerous unit cells with QZS. The unit cell, which possesses QZS, is realized by designing the sinusoidal beam and semicircular arches. The unit cells compose the metastructure. The vibration isolation properties of the metastructure are considered. It is concluded that the continuous structure has very good vibration isolation performance (much better than the linear isolator) and has great potential in the vibration isolation applications for the small scale equipment. Vibration amplitude of the isolated object has been significantly reduced by the metastructure. Better isolation properties are achieved for smaller damping and high vibration excitation frequency.

Finally, metamaterials with negative stiffness have advantages in vibration isolation and energy absorption due to their unique deformation behavior which cause them to be suitable for use as deformation control devices and sensors (Duos et al. 2014).

1.4 Auxetic Structure

Usually, the conventional material has the property when it is stretched it becomes longer in the direction of stretch and thinner in cross-section. Then the ration of the lateral contractile strain to the longitudinal tensile strain, called Poisson ratio, is positive. Nevertheless, an artificial material i.e. metastructure is designed with negative Poisson ratio. When stretched the structure become thicker perpendicular to the applied force. This phenomena occur due to the way of deformation of the sample which is uniaxially loaded: the overall structure expands when stretched and contracts when compressed. The metastructure is also called auxetic structure, auxetic material or auxetics. Auxetics has a special property to expand its dimension perpendicular to load direction. Auxetics are realized by creating periodic lattice structures which consist of a number of unit cells. The unit cells have to satisfy the condition of negative Poisson ration. In Fig.3 unit cells with conventional convex and artificial concave hexagonal geometry are plotted. Thus, if the unit cell has conventional hexagonal geometry, the cell elongates along the y -axis and close up in x -direction if the stretching is in y -direction. Thus, the common conventional material with such units has positive Poison's coefficient. By maintaining the same deformation mechanism by modifying the geometry of cell to adopt the re-entrant

structure, the unit undergoes elongation in both directions. This structure has the negative Poisson coefficient and is called auxetic structure. In addition, it is worth to say that the structure made of such units is anisotropic: Poisson ratio differs when loaded along x and when loaded along y direction. If the material is linear elastic and isotropic it is found that the Poisson ratio cannot be less than -1 (see Mir et al. 2014).

Based on the deformation of the unit cells and due to its internal structure which can be of micro (auxetic material) or of macro (auxetic structure) scale, the structures can be classified into (Xia et al. 2018):

1. Re-entrant structures, where the diagonal ribs move in such a way that leads to auxetic effect in the direction perpendicular to loading one,
2. Chiral structure, where the coupled deformation of node rotation and ligament bending gives the auxetic behavior,
3. Rigid or semi-rigid structures, where rotation of rigid polygons joined with each other through hinges (rotating squares, rectangles, parallelograms, triangles, tetrahedral, etc.) give as the result the auxetic behavior.

In the paper of Mir et al. (2014) the review of mechanics and applications of all three groups of auxetic structures is presented.

1. The design of auxetic structure with negative Poisson's ration is inspired from nature. Namely, it is found that, for example, the skin of salamander or snake has quite different properties than materials which are usually in engineering. The skin contracts or expands in any spatial direction when exposed to a stress. Analyzing the skin structure it is seen that the macrostructure contains concave hexagonal units. Deformation of units causes the skin to give the effect of auxetics (Santulli and Langella, 2016).

Based on this observation the auxetic metamaterial with concave hexagonal unit cells is designed (Proffit and Kennedy, 2020). The obtained metamaterial is the hexagonal re-entrant structure. It is one of the most commonly studied one as it can be defined with very few parameters unlike other more complex structures. The main property of the structure is that the ratio between the transverse and the longitudinal strain produced by the application of load F orthogonal to its section is negative. This geometry was first invented in 2D but with the development of additive manufacturing was extended to 3D. However, this design of auxetic structure suffers from design limitation arising out of the numerous sharp corners and joints. Consequently, the more joints, the higher the possible points of high-stress concentration and the higher the chances of failure of the structures due to critical stresses generated at joints. Further, additive manufacturing, though of great help in building 2D and 3D complex structures may result in surface defects, often leading to stress concentration issues. It is in particular true with metal powders consolidated.

A couple of trials were made attempting to resolve the stress concentration aspects through local modification of sharp concerns by filtering. New and novel unit cell configuration is given in (Meena and Singamneni, 2019), which gives auxetic responses, and in comparison with standard re-entrant form greatly

reduces degree of stress concentration. Using the SolidWorks 2015 the CAD models of the re-entrant and the S shaped structures were designed. The S structure was optimized numerically by varying the geometrical parameters application but maintaining the balance between the negative Poisson's ratio and the stresses generated under loading. Comparing the re-entrant and S unit structure it is found that the stress concentration is two times higher in the first in comparison to the second. Nevertheless, for both types of structures it is common that they have attractive acoustic, vibration suppression and impact properties.

2. The auxetic with chiral structure of the honeycomb type is designed as a combination of unit cells containing rigid nodes (rigs or cubes) interconnected with elastic ligaments or ribs. Namely, rigid nodes are linked to each other by ligaments. Depending on the geometrical spatial relation between ligaments and nodes chiral and antichiral systems exist. If the nodes are on the opposite side of the ligament, the system is called chiral, while if nodes are on the same side of the ligament the system is antichiral. Hexachiral, tetrachiral, antitetrachiral and antitrichiral structures are formed (Alderson et al. 2010) depending on the number of ligament connections in the node. Under exterior loading the main deformation features are node rotation and ligament bending. In the chiral structure the deformation of ligament is of full-wave shape, and in antichiral structure it of a half-wave shape. Chiral structures consisting of circular ring nodes and tangentially connected ligaments are engineered systems that exhibit excellent flexibility, vibration attenuation, impact resistance performance, etc. In Li et al. 2017, a hybrid tetrachiral and antitetrachiral metastructure is considered (Fig.15). The nodes are assumed to be circular. The in-plane mechanical properties are studied numerically and experimentally.

Using this structure an auxetic stent is designed (Li et al. 2017). Deformation in axial and circumferential direction is controlled through adjusting the spaces of unit cell along axial and circumferential direction of the stent.

In Ma et al. (2018) novel chiral-type cylindrical shells were designed and fabricated via 3D printing method. Cylindrical shells were with various categories of chiral-type cells. Results revealed that the anti-chiral shell and chiral-axial shell can achieve auxetic behavior, namely, negative Poison ration behavior and compressive-twist response, which are beneficial for energy absorption and vibration isolation performance. Given the distinction in the geometrical configuration of unit cell, the cylindrical shells exhibited extremely diverse mechanical properties.

In Wu et al. (2017) an innovative hierarchical anti-tetrachiral structures based on the auxetic deformation behaviors of anti-tetrachiral unit cell at different structural hierarchical levels is proposed. The in-plane mechanical properties of hierarchical anti-tetrachiral metastructures are deduced. And can be remarkably enhanced and manipulated through combining the auxetic deformation behaviors of chiral structures and the mechanical benefits of structural hierarchy, and its tunable mechanical properties can be designed within very large range of modulus and Poisson's ratio value. Finally, an innovative hierarchical

anti-tetrachiral stent is proposed, and the interaction between stent and artery vessel are studied, demonstrating the promising industrial application potential of hierarchical chiral metastructures. The proposed chiral geometry represents a new family of chiral hierarchical structures, and the extent of auxeticity and its in-plane mechanical properties can be tuned through manipulating node ring size and shape, length and thickness, and the hierarchy level, thus achieving desired extreme mechanical properties.

Based on the rigid cubic node rotation and deformation relations of ligaments and nodes, in Xia et al. (2018) the analytical expression for the modulus of 3D isotropic antitetrachiral structure is derived and compared with experimentally obtained one, finite element analysis and theoretical studies. Mechanical properties of 3D antitetrachiral structure can be controlled and tuned with two independent dimensionless geometrical parameters.

3. Zhao et al. 2019 presented the 3D printed subwavelength-scale microstructures embedded into a honeycomb structure to form a lightweight metastructure which can suppress vibrations with different polarizations at targeted frequencies. Moreover, by simply he fabricated resonators from horizontal embedment into vertical embedment, the band gaps as well as the vibration isolations can be easily switched for different vibration sources. The deformation mechanism is based on rotation of the rigid units. The multi-polarization vibration suspensions have are realized with strategically positioned resonators following interval and segment arrangements. The theory of elasticity and also Poisson's ratio are scale-independent properties and so the structure that is deforming may be at a macroscopic or microstructural level.

Because of the periodic nature of this auxetic, it affects how waves propagate through it and thus can be used for vibration suppression among other applications. Namely, auxetics have mechanical properties such as high energy and vibration absorption, fracture resistance, negative stiffness and energy dissipation.

1.5 Conclusion and Future Investigation

This paper is a review on the mechanical metastructures applied for vibration suppression and absorption. Three groups of metastructures are considered: the elastic metastructures, metastructures for isolation and auxetic structures. Elastic metamaterials exhibit negative effective mass, metastructures for isolation have negative effective stiffness and the auxetic structures have negative Poisson's coefficient. For all structures is common that they are periodical and that they contain unit cells which properties required for the whole structure. It is concluded that these man-made structures have significant mechanical benefits: enhanced indentation resistance, enhanced fracture toughness, enhanced porosity variation when stretched or compressed, enhanced energy and vibration absorption. Although the existing metastructures are shown to be very suitable for vibration absorption or suppression (depending on the structure),

tests have also shown a major drawback. Namely, the structures show anisotropy in vibration absorption, depending on the action of the excitation force, i.e. when a force acts in one direction the metastructure shows good absorption property, but if the direction of the force changes the absorption property disappears. In addition, the characteristics of the slab with metastructure do not meet some of the requirements that designers usually set before it: they do not have sufficient strength, resistance to temperature changes, thermal conductivity, sufficient rigidity, etc. Hence, there is a need to harmonize the type of material and structure into a single whole in order to ensure: isotropy, suitability for load transfer, easy technical implementation i.e. production, resistance to temperature changes, but also low cost of fabrication. Mechanical properties, thermal properties, environmental properties and manufacturing restriction would give the trends for future development. Practical implementation would take a front seat with the advent of the additive processing technologies.

Extention of the freedom to design is necessary and development of new technologies for fabrication of more complex forms is necessary. It is time new unit cell configurations to develop.

There is no doubt that controllable metamaterials, upon which smart structures will be built upon, will be the trend of the next phase of metamaterial development. In the future, metastructure design will be more challenging than ever before. Structural and functional properties will be bound more and more closely together.

References

- Alderson, A., Alderson, K.L., Attard, D., Evans, K.E., Gatt, R., Grima, J.N., Miller, W., Ravirala, N., Smith, C.W., Zied, K.: Elastic constants of 3-, 4- and 6-connected chiral and anti-chiral honeycombs subject to uniaxial in-plane loading. *Composite Science and Technology* **70**(7), 1042–1048 (2010)
- Buriak, I.A., Zhurba, V.O., Vorobjov, G.S., Kulizhko, V.R., Kononov, O.K., Rybalko, O.: Metamaterials: Theory, classification and application strategy, *Journal of Nano- and electronic Physics*, 8(4(2)). Article ID **04088**, 1–11 (2016)
- Cheng, Y., Xu, J.Y., Liu, X.J. (2008) One-dimensional structured ultrasonic metamaterials with simultaneously negative dynamic density and modulus, *Physical Review B*, 77(4), Article ID 045134, 6 pages.
- Cveticanin, L., Mester, Gy: Theory of Acoustic Metamaterials and Metamaterial Beams: An Overview. *Acta Polytechnica Hungarica* **13**(7), 43–62 (2016)
- Cveticanin, L., Cveticanin, D.: Application of the acoustic metamaterial in engineering: An overview. *Romanian Journal of Mechanics* **2**(1), 29–36 (2017)
- Cveticanin, L., Zukovic, M.: Negative effective mass in acoustic metamaterial with nonlinear mass-in-mass subsystems. *Communications in Nonlinear Science and Numerical Simulation* **51**, 89–104 (2017)
- Cveticanin, L., Zukovic, M., Cveticanin, D.: ₁ On the elastic metamaterial with negative effective mass. *Journal of Sound and Vibration* **436**, 295–309 (2018a)
- Cveticanin, L., Zukovic, M., Cveticanin, D.: ₂ Influence of nonlinear subunits on the resonance frequency band gaps of acoustic metamaterial. *Nonlinear Dynamics* **93**(3), 1341–1354 (2018b)

- Duoss, E., Weisgraber, T., Hearon, K., Zhu, C., Small, W., Metz, T., Vericella, J., Barth, H., Kuntz, J., Maxwell, R., Soadaccini, C.: Three-dimensional printing of elastomeric, cellular architectures with negative stiffness. *Advanced Functional Materials* **24**(31), 4905–4913 (2014)
- Essink, B.C., Inman, D.J. (2020) Three-dimensional mechanical metamaterial for vibration suppression, *Special Topics in Structural Dynamics & Experimental Techniques* (Ed. N. Dervilia), 5, 43–48.
- Fan, L., He, Y., Chen, X., Zhao, X.: Elastic metamaterial shaft with a stack –like resonator for low-frequency vibration isolation, *Journal of Physics D, Applied Physics*, 53. Article ID **105101**, 1–9 (2020a)
- Fan, H., Yang, L., Tian, Y., Wang, Z.: Design of metastructures with quasi-zero dynamic stiffness for vibration isolation, *Composite Structures*, 243. Article ID **112244**, 1–13 (2020b)
- Hobeck, J.D., Laurent, C.M.V., Inman, D.J. (2015) 3D printing of metastructures for passive broadband vibration suppression, *20th Int. Conf. on Composite Materials*, Copenhagen, 19–24 July, 1–8.
- Hua, J., Lei, H., Zhang, Z., Gao, C., Fang, D.: Multistable cylindrical mechanical metastructures: Theoretical and experimental studies, *Journal of Applied Mechanics*, 86. Article ID **071007**, 1–10 (2019)
- Kadic, M., Milton, G.W., van Hecke, M., Wegener, M.: 3D metamaterials, *Nature Reviews. Physics* **1**, 198–210 (2019)
- Li, H., Ma, Y., Wen, W., Wu, W., Lei, H., Fang, D.: In plane mechanical properties of tetrachiral and antitetrachiral hybrid metastructures, *Journal of Applied Mechanics*, 84. Article ID **081006**, 1–11 (2017)
- Liu, R., Ji, C., Zhao, Z., Zhou, T.: Advanced materials and materials genome – review metamaterials: Reshape and rethink. *Engineering* **1**(2), 179–184 (2015)
- Liu, Y., Zhang, X.: Metamaterials: a new frontier of science and technology. *Chemical Society Reviews* **40**, 2494–2507 (2011)
- Ma, C., Lei, H., Liang, J., Wu, W., Wang, T., Fang, D.: Macroscopic mechanical response of chiral-type cylindrical metastructures under axial compression loading. *Materials & Design* **158**, 198–212 (2018)
- Meena, K., Singamneni, S.: A new auxetic structure with significantly reduced stress concentration effects, *Materials and Design*, 173. Article ID **107779**, 1–11 (2019)
- Milton, G.W.: New metamaterials with macroscopic behavior outside that of continuum elastodynamics. *New Journal of Physics* **9**(359), 1–13 (2007)
- Mir, M., Ali, M.N., Sami, J., Ansaari, U. (2014) Review of Mechanics and applications of auxetic structures, *Advances in Materials Science and Engineering*, Article ID 753496, 17 pages
- Pai, P.F., Peng, H., Jiang, S.: Acoustic metamaterial beams based on multi-frequency vibration absorbers. *International Journal of Mechanical Sciences* **79**, 195–205 (2014)
- Peng, H., Pai, P.F.: Acoustic metamaterial plates for elastic wave absorption and structural vibration suppression. *International Journal of Mechanical Sciences* **89**, 350–361 (2014)
- Peng, H., Pai, P.F., Deng, H.: Acoustic multi-stopband metamaterial plates design for broadband elastic wave absorption and vibration suppression. *International Journal of Mechanical Sciences* **103**, 104–114 (2015)
- Pierce, C.D., Willey, C.L., Chen, V.W., Hardin, J.O., Berrigan, J.D., Juhl, A.T., Matlack, K.H.: Adaptive elastic metastructures from magneto-active elastomers. *Smart Materials and Structures* **29**(6), (2020)
- Priyanka, A. (2014) A review paper on metamaterial, *International Journal of Engineering Sciences and Research Technology, IJESRT*, 3(12), 8 pages.
- Proffit, K., Kennedy, J.: Dynamic response of auxetic structures. *Vibroengineering Procedia* **31**, 1–6 (2020)
- Reichl, K.K., Inman, D.J.: Lumped mass model of a 1D metastructure for vibration suppression with an additional mass. *Journal of Sound and Vibration* **403**, 75–89 (2017)
- Reichl, K.K. (2018) *Active metastructures for light-weight vibration suppression*, PhD thesis, Aerospace Engineering, The University of Michigan.

- Reichl, K.K., Inman, D.J.: Lumped mass model of a 1D metastructure with vibration absorbers with varying mass, in Sensors and Instrumentation, *Aircraft/Aerospace and Energy Harvesting* (eds. E.W. Sit). Conf. Proceedings of the Society for Experimental Mechanics Series **8**, 49–56 (2019)
- Santulli, C., Langella, C.: Study and development of of concept of auxetic structures in bio-inspired design. *International Journal of Sustainable Design* **3**(1), 20–37 (2016)
- Singh, G., Rajni, I., Marwaha, A.: A review of metamaterials and its applications. *Journal of Engineering Trends and Technology, IJETT* **19**(6), 1–6 (2015)
- Sun, H., Du, X., Pai, R.R.: Theory of metamaterial beams for broadband vibration absorption. *Journal of Intelligent Material Systems and Structures* **7**, 1085–1101 (2010)
- Vuyk, P., Harne, R.L.: Collapse characterization and shock mitigation by elastomeric metastructures, *Extreme Mechanics Letters*, 37. Article ID **100682**, 1–6 (2020)
- Wang, T., Sheng, M.P., Qin, Q.H.: Multi-flexural band gaps in an Euler-Bernoulli beam with lateral local resonators. *Physics Letters A* **380**, 525–529 (2016)
- Wu, W., Tao, Y., Xia, Y., Chen, J., Lei, H., Sun, L., Fang, D.: Mechanical properties of hierarchical anti-tetrachiral metastructures. *Extreme Mechanics Letters* **16**, 18–32 (2017)
- Xia, R., Song, X., Sun, L., Wu, W., Li, C., Cheng, T., Qian, G. Mechanical properties of 3D isotropic anti-tetrachiral metastructure, *Physica Status Solidi B*, 255, 1700343, 1-9.
- Zhang, W., Song, Q., Zhu, W., Shen, Z., Chong, P., Tsai, D.P. (2018) Metafluidic metamaterial: a review, *Advances Physics: X*, 3(1), 6 pages.
- Zhang, Y., Wang, Q., Tichem, M., van Keulen, F.: Design and characterization of multi-stable mechanical metastructures with level and tilted stable configurations, *Extreme Mechanics Letters*, 34. Article ID **100593**, 1–9 (2020)
- Zhao, W., Wang, Y., Huang, G., Zhu, R. (2019) Isolating vibrations with different polarizations via lightweight embedded metastructure, *Proceedings of SPIE The International Society for Optical Engineering*, Article ID 109720, 6 pages.
- Zhu, R., Liu, X.N., Hu, G.K., Sun, C.T., Huang, G.L.: A chiral elastic metamaterial beam for broadband vibration suppression. *Journal of Sound and Vibration* **333**(10), 2759–2773 (2014)

Chapter 2

Debonding Resistance Evaluation in Virtual Testing of Sandwich Specimens



Vyacheslav N. Burlayenko, Holm Altenbach, and Svetlana D. Dimitrova

Abstract Three different experimental methods used in fracture testing sandwich panels are studied in the context of providing an assessment of face sheet-to-core interface strength. For this reason, strain energy release rate (ERR), complex stress intensity factors (SIFs) and mode mixity phase angle are computed. The analytical models exploit both the framework of linear elastic fracture mechanics (LEFM) in a combination of analytical considerations and numerical results and one-dimensional (1D) beam theories, whereas the finite element predictions are conducted using the capabilities of the ABAQUS package and a standalone subroutine developed in MATLAB environment for post-processing the results of two-dimensional (2D) finite element analysis. The results presented in this research allow drawing conclusions on the accuracy of fracture analysis predictions for each of the three different specimens by comparing 2D numerical calculations with semi-analytical results and 1D analytical solutions.

Keywords Face sheet/core interface debonding · Sandwich fracture specimens · Fracture mechanics analysis · Finite element analysis

2.1 Introduction

An assembly of two relatively stiff, strong layers (face sheets) and a soft, lightweight material (core) separating them in a single sandwich material has opened up new

V. N. Burlayenko (✉)

Department of Applied Mathematics, National Technical University “Kharkiv Polytechnic Institute”, Kharkiv 61002, Ukraine
e-mail: burlayenko@yahoo.com

H. Altenbach

Institut für Mechanik, Otto-von-Guericke-Universität Magdeburg, 39106 Magdeburg, Germany
e-mail: holm.altenbach@ovgu.de

S. D. Dimitrova

Department of Higher Mathematics, National Technical University “Kharkiv Polytechnic Institute”, Kharkiv 61002, Ukraine
e-mail: s.dimitrovaburlayenko@gmail.com

possibilities in creating constructions that require an effective combination of high rigidity and low weight (Altenbach et al. 2018; Amabili 2018). This, along with improved acoustic and thermal insulation, enhanced protection against impacts, high corrosion and wear resistance have already made sandwich composites indispensable structural elements for many engineering applications (Fu and Sadeghian, 2020; Chatterjee et al. 2020; Sivaram et al. 2020). However, since the sandwich concept suggests an abrupt change in mechanical and geometrical properties at the interfaces of basic layers, failure related to debonding of the face sheet from the core is the most encountered life-limiting damage mode of sandwich-type constructions. Existing debonding in sandwich panels is insidious and may result in their premature buckling, excessive vibrations and loss of load-bearing capacity (Burlayenko et al. 2020a; Szekrényes 2021). Therefore, intensive experimental and theoretical studies have been carried out to research debonding problems of sandwich composites for their durability and safe exploitation (Burlayenko and Sadowski 2011a, 2011b; Davidson et al. 2012; Odessa et al. 2018; Funari et al. 2018) to name a few.

To assess the debonding resistance in sandwich composites, specific tests should be done for measuring face sheet-to-core interfacial fracture parameters such as stress intensity factors (SIFs), energy release rate (ERR) and mode mixity phase angle. Among a variety of testing configurations available in the literature as discussed in Quispitupa et al. (2009), the double cantilever beam (DCB) (Prasad and Carlsson 1994), single cantilever beam (SCB) (Ratcliffe and Reeder 2011; Adams et al. 2012) and double cantilever beam subjected to uneven bending moments (DCB-UBM) (Sorensen et al. 2006; Berggreen et al. 2018) specimens are frequently accepted in dominated mode I and mixed-mode I/II laboratory tests. These test methods are superior to others due to their adaptability to a large number of sandwich material systems and relatively easy implementation. Herewith, the reliability of measurements depends also on the accuracy of methods used for data reduction procedures to estimate the fracture parameters.

The structural theories are often adopted to develop analytical and semi-analytical solutions appropriate for extraction of the ERR and SIFs in DCB, SCB and DCB-UBM laboratory specimens. Closed-form solutions based on a beam on elastic foundation model have been obtained for DCB and SCB sandwich specimens in Avilés and Carlsson (2008) and Yoshida and Aoki (2018), respectively. Semi-analytical solutions with additional coefficients determined via a numerical approach have been provided by Østergaard and Sørensen (2007); Kardomateas et al. (2013) without accounting for shear deformation and by Li et al. (2004); Andrews and Massabò (2007); Barbieri et al. (2018) including shear effect. 2D exact elasticity solutions occur for very limited cases (Ustinov 2019), whereas numerical methods, in particular, the finite element method (FEM) have found a wide application. In the context of the FEM, virtual crack extension (VCE), interaction integral (M -integral), crack surface displacement (CSD) methods and virtual crack closure technique (VCCT) have been used in fracture analyses of the sandwich specimens as carried out in Davis et al. (2014); Burlayenko et al. (2019b); Farkash and Banks-Sills (2020); Burlayenko et al. (2020b).

This work focuses on the accuracy assessment of fracture analysis predictions of DCB, SCB and DCB-UMB sandwich specimens. The energy release rates, mode mixity angles and stress intensity factors in the specimens are obtained using different computation techniques. The semi-analytic approach combining analytical considerations within the linear elastic fracture mechanics and numerical estimations of unknown coefficients based on the finite element method, the closed-form expressions derived relying on the beam-like models and the results of 2D finite element analyses exploiting either the J-integral method or the crack surface displacement method are used in the study. Also, the strength of the face sheet-to-core interface for each specimen has been discussed in detail.

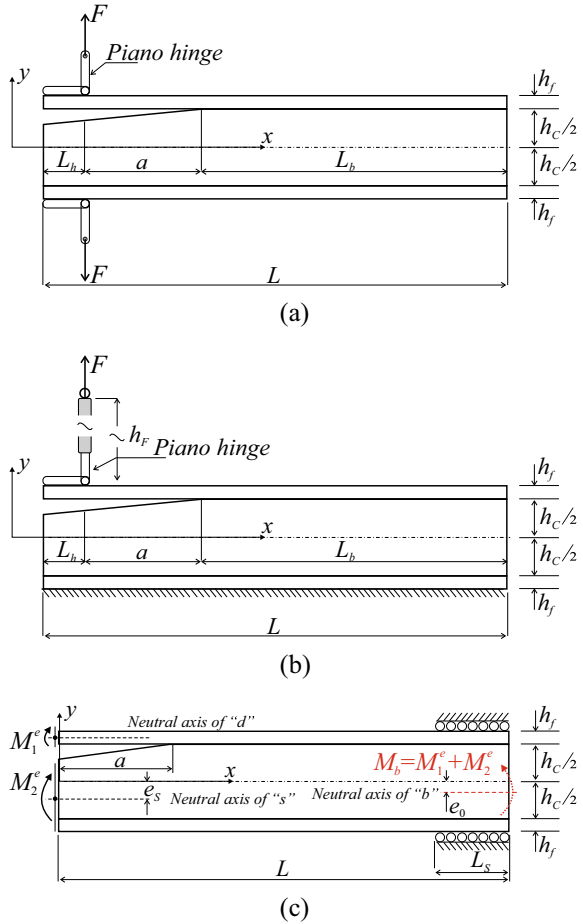
2.2 Fracture Test Methods

We consider three different test methods DCB, SCB and DCB-UMB, chosen due to their popularity in the experimental practice of debonding resistance testing and their scientific rigor among academics. All the test methods are designed to result in the debonding growth at the pre-cracked edge of the coupons as shown in Fig. 2.1. The specimen preferred in most mode I loading tests is the DCB (Fig. 2.1a). In this test, two piano hinges are usually used to transfer the loading to the edges of the specimen's cracked region. The DCB sandwich specimen is subjected to an opening displacement by applying to the grip plates either two opposite transverse loads or one upward load and appropriate boundary constraints (Prasad and Carlsson, 1994; Avilés and Carlsson, 2008).

Since it has been experimentally shown and theoretically proven that during the DCB test, the debonding may sometimes kink into the core (Prasad and Carlsson 1994; Burlayenko et al. 2019a), the SCB specimen (Fig. 2.1b) has been reported as an alternative test configuration for predominately mode I loading (Adams et al. 2012). Unlike the DCB test, the lower part of the SCB specimen is affixed to a rigid base to prevent its bending deformation, and only an upward force is applied to a steel hinge mounted on the upper debonded face sheet. Moreover, to provide an accurate interface toughness measurement and to ensure that bending is the primary form of loading, the dimensions of the SCB specimen and the load rod length h_F have to satisfy sizing requirements defined in Ratcliffe and Reeder (2011).

Of special interest for the debonding analysis is the case of mixed-mode loading. Some test methods have been developed for testing sandwich specimens under conditions of simultaneous opening and shearing as discussed by Quispitupa et al. (2009). However, in most cases, either they have a limited capability for mode mixities or the mode mixity changes with growing the crack. In contrast to this, the DCB-UMB test (see in Fig. 1c) allows producing a wide range of I/II mode mixity conditions by changing the ratio of the moments applied to the specimen's cracked edges, $MR = M_1^c/M_2^c$. Also, this method keeps constant mode mixity during the test (Berggreen et al. 2018).

Fig. 2.1 Schemes of the fracture sandwich specimens: **a** DCB; **b** SCB; and **c** DCB-UMB



2.3 Sandwich Specimens with Finite Crack

In this section, modeling aspects used to determine the energy release rate and mode mixity phase angle in DCB, SCB and DCB-UBM specimens are discussed. The sandwich specimens are considered as tri-layer structures, where each layer is defined by an elastic orthotropic material. We assume that face sheets are of equal thickness, h_f , and are made of the same materials no. 1, whereas a much thicker core layer of thickness, h_c , is made of another material no. 2. Herewith, the principal axes of each orthotropic material are aligned with the reference coordinate axes.

2.3.1 Fracture Mechanics Approach

Semi-analytic solutions based on the fracture mechanics approach are obtained for the energy release rate and mode mixity phase angle in terms of forces and moments acting at the debonded section of sandwich beam-like specimens. The derivation of these quantities for a symmetric sandwich beam subjected to the general system of loads has been done in Andrews and Massabò (2007); Barbieri et al. (2018). Following these authors, the stress resultants of an elementary segment of the beam containing the crack front shown in Fig. 2a are presented by superposition of four independent self-equilibrium systems. Figure 2b shows a decomposition of the load subsystem, determined only by pure bending moments and axial forces, into the two simple load cases, while a sum of the other two basic load cases related to the shear resultants only is illustrated in Fig. 2c.

Using the original notations in Andrews and Massabò (2007); Barbieri et al. (2018), the generalized crack tip loads in Fig. 2b and c are defined as follows:

$$\begin{aligned}
 P &= N_1 - N_3 C_1 - \frac{C_2}{h_f} M_3 \\
 M &= M_1 - C_3 M_3 \\
 M^* &= M + h_f \left(\frac{1}{2} + \frac{1}{2\eta} + \tilde{e}_s \right) P \\
 V_D &= -V_2 \\
 V_S &= V_3,
 \end{aligned}
 \tag{2.1}$$

where the coefficients C_1 , C_2 and C_3 the geometrical and material dimensionless parameters η , \tilde{e}_s are presented in the Appendix 1.

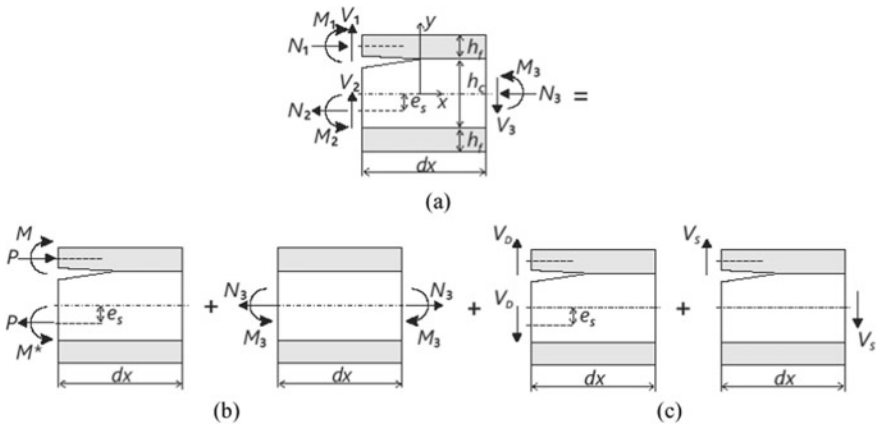


Fig. 2.2 **a** General loading of a sandwich beam elementary segment with a crack front; **b** load subsystem defined by pure bending moments and axial forces; and **c** load subsystem defined by the shear resultants

Following the methodology proposed by Li et al. (2004); Østergaard and Sørensen (2007); Barbieri et al. (2018), the ERR is computed within the context of plane stress or plane strain by taking the J -integral over the closed counter around the crack tip cross section. In doing so, the stress components σ_{yy} , σ_{xx} and σ_{xy} caused by the crack tip loads in each particular load case shown in Fig. 2b and c are to be calculated first. By superimposing the solutions of all the individual load cases with M , P , V_D , $V_S \neq 0$, the result is a positive definite quadratic form containing terms proportional to the squared crack tip loads and their cross products as follows:

$$\begin{aligned} \mathcal{G} = & f_M^2 \frac{M^2}{E_f h_f^3} + f_P^2 \frac{P^2}{E_f h_f} + 2f_M f_P \sin \gamma_M \frac{PM}{E_f h_f^2} + f_{V_D}^2 \frac{V_D^2}{E_f h_f} + f_{V_S}^2 \frac{V_S^2}{E_f h_f} \\ & + 2f_{V_D} f_{V_S} \sin(\psi_{V_D} - \psi_{V_S}) \frac{V_D V_S}{E_f h_f} + 2f_M f_{V_D} \sin(\psi_M - \psi_{V_D}) \frac{M V_D}{E_f h_f^2} \\ & + 2f_M f_{V_S} \sin(\psi_M - \psi_{V_S}) \frac{M V_S}{E_f h_f^2} + 2f_P f_{V_D} \sin \gamma_{V_D} \frac{P V_D}{E_f h_f} + 2f_P f_{V_S} \sin \gamma_{V_S} \frac{P V_S}{E_f h_f}, \quad (2.2) \end{aligned}$$

where the phase angles $\psi_M = \gamma_M + \omega - \pi/2$, $\gamma_{V_D} = \psi_{V_D} - \omega + \pi/2$ and $\gamma_{V_S} = \psi_{V_S} - \omega + \pi/2$, the positive dimensionless functions $f_M(\Sigma, \eta)$, $f_P(\Sigma, \eta)$ and the phase angle $\gamma_M(\Sigma, \eta)$ are given by analytical equations in Appendix 2, and the positive dimensionless functions $f_{V_D}(\alpha, \beta)$, $f_{V_S}(\alpha, \beta)$ and the phase angles $\psi_{V_D}(\alpha, \beta)$, $\psi_{V_S}(\alpha, \beta)$ and $\omega(\alpha, \beta)$ calculated for different values of α and β are tabulated in Barbieri et al. (2018).

The mode mixity angle associated with the ratio of the imaginary and real parts of the complex stress intensity factor $K = K_1 + iK_2$, where $i = \sqrt{-1}$ is derived based on dimensional considerations and linearity as discussed in Li et al. (2004); Østergaard and Sørensen (2007). In the general loading case at the characteristic length defined by h_f , it takes a form:

$$\psi = \tan^{-1} \left(\frac{f_M M \sin \psi_M + f_P P h_f \sin \omega + f_{V_D} V_D h_f \sin \psi_{V_D} + f_{V_S} V_S h_f \sin \psi_{V_S}}{f_M M \cos \psi_M + f_P P h_f \cos \omega + f_{V_D} V_D h_f \cos \psi_{V_D} + f_{V_S} V_S h_f \cos \psi_{V_S}} \right) \quad (2.3)$$

The general relationships of the ERR and the mode mixity phase angle in (2.2) and (2.3), respectively, are used to determine the particular forms of these expressions for DCB, SCB and DCB-UBM sandwich specimens.

In a DCB sandwich specimen, a transverse force F is applied to the cracked ends of the beam (Fig. 1a). Hence, the elementary load systems are defined by the zero loads P and V_S and nonzero loads $M = Fa$ and $V_D = F$. Consequently, the ERR and the mode mixity angle are reduced to the forms:

$$\begin{aligned} \mathcal{G}^{DCB} = & f_M^2 \frac{M^2}{E_f h_f^3} + f_{V_D}^2 \frac{V_D^2}{E_f h_f} + 2f_M f_{V_D} \cos(\psi_M - \psi_{V_D}) \frac{V_D M}{E_f h_f^2} \\ \psi^{DCB} = & \tan^{-1} \left(\frac{f_M M \sin \psi_M + f_{V_D} V_D h_f \sin \psi_{V_D}}{f_M M \cos \psi_M + f_{V_D} V_D h_f \cos \psi_{V_D}} \right) \quad (2.4) \end{aligned}$$

Unlike the DCB test method, in an SCB sandwich specimen, an upward transverse force F is applied only to the end of the debonded face sheet of the beam as shown in Fig. 1b. Moreover, the fixity of the SCB specimen on the bottom face sheet may also affect the stress field near the crack tip along with the shear effect caused by the transverse force itself.

For analyzing the SCB sandwich beam, we propose for consideration two cases of decomposition of the general load conditions into the elementary load subsystems demonstrated in Fig. 2.2. The first one is a simplified situation when it is assumed that the fixture has a negligible influence on the near crack tip stresses. This can be considered as an approximation of SCB specimens with a very thick core layer, $h_c \gg h_f$. Then, all the resultants except V_D are nonzero and equal to $P = -\frac{C_2}{h_f}Fa$, $M = Fa - C_3Fa$ and $V_S = F$. It results in the following reduction of the general expressions for the ERR and the mode mixity angle:

$$\begin{aligned} \mathcal{G}^{SCB_1} &= f_M^2 \frac{M^2}{E_f h_f^3} + f_P^2 \frac{P^2}{E_f h_f} + 2f_M f_P \sin \gamma_M \frac{PM}{E_f h_f^2} + f_{V_S}^2 \frac{V_S^2}{E_f h_f} \\ &\quad + 2f_M f_{V_S} \cos(\psi_M - \psi_{V_S}) \frac{V_S M}{E_f h_f^2} + 2f_P f_{V_S} \sin \gamma_{V_S} \frac{V_S P}{E_f h_f^2} \\ \psi^{SCB_1} &= \tan^{-1} \left(\frac{f_M M \sin \psi_M + f_P P h_f \sin \omega + f_{V_S} V_S h_f \sin \psi_{V_S}}{f_M M \cos \psi_M + f_P P h_f \cos \omega + f_{V_S} V_S h_f \cos \psi_{V_S}} \right) \end{aligned} \quad (2.5)$$

An improvement to the accuracy of fracture analysis of the SCB specimen is to account for the fixity at the bottom face sheet on the near crack tip stresses. Following by Kardomateas and Yuan (2020), the reaction on the bottom face sheet is assumed to be such as linear distributed force, with intensities q_1 and q_2 at the left and right ends of the sandwich beam, respectively. Then, the force and moment equilibrium gives the shear force Q_S and the moment M_S acting at the crack front cross section of the substrate as follows:

$$\begin{aligned} Q_S &= -\frac{Fa}{L^*} \left(4 - \frac{3a}{L^*} \right) \\ M_S &= -\frac{Fa^2}{L^*} \left(2 - \frac{a}{L^*} \right), \end{aligned} \quad (2.6)$$

where $L^* = L - L_h$ is a length of the SCB specimen without the hinge length as shown in Fig. 1b.

Therefore, the general load system at the crack tip cross-section is not reduced to a simplified case, and it is decomposed into the elementary load subsystems with $P = -\frac{C_2}{h_f} \left(Fa - \frac{Fa^2}{L^*} \left(2 - \frac{a}{L^*} \right) \right)$, $M = Fa - C_3 \left(Fa - \frac{Fa^2}{L^*} \left(2 - \frac{a}{L^*} \right) \right)$, $V_D = \frac{Fa}{L^*} \left(4 - \frac{3a}{L^*} \right)$ and $V_S = F - \frac{Fa}{L^*} \left(4 - \frac{3a}{L^*} \right)$, which are further used to compute the ERR and the mode mixity angle in (2.2) and (2.3), respectively.

In a DCB-UBM sandwich specimen, external two moments M_1^e and M_2^e acting at the cracked ends of the beam (Fig. 1c) lead to the nonzero resultants $P =$

$-\frac{C_2}{h_f}(M_1^e + M_2^e)$ and $M = M_1^e - C_3(M_1^e + M_2^e)$ in the elementary load cases, whereas V_D and V_S are zeros there. Thereby, the ERR and the mode mixity angle have the following forms:

$$\begin{aligned} \mathcal{G}^{DCB-UBM} &= f_M^2 \frac{M^2}{E_f h_f^3} + f_P^2 \frac{P^2}{E_f h_f} + 2f_M f_P \sin \gamma_M \frac{PM}{E_f h_f^2} \\ \psi^{DCB-UBM} &= \tan^{-1} \left(\frac{f_M M \sin \psi_M + f_P P h_f \sin \omega}{f_M M \cos \psi_M + f_P P h_f \cos \omega} \right) \end{aligned} \quad (2.7)$$

2.3.2 1-D Beam Theory-Based Approach

The energy release rate generated by the interface crack in the DCB test method (Fig. 1a) is analytically derived base on the 1D beam theory in Avilés and Carlsson (2008). The model considers the upper (debonded) face sheet as a Euler–Bernoulli beam partially supported by a Winkler elastic foundation representing the core. Only Young’s moduli coinciding with the axial direction of sandwich beam are considered for the orthotropic face sheets and core in the formulation. The final expression for the ERR of the DCB beam of the width b takes the form:

$$\mathcal{G}^{DCB} = \frac{F^2}{2b^2} \left\{ \frac{1}{G_{xz}^c h_c} + \frac{a_0^2}{\left(D - \frac{B^2}{A}\right)} + \frac{12}{E_f h_f^3} \left(a^2 + 2a\xi^{\frac{1}{3}} + \xi^{\frac{1}{3}}\right) \right\}, \quad (2.8)$$

where the parameter $\xi = \frac{bh_f^3 E_f}{3K}$ and the elastic foundation coefficient $K = \frac{2bE_c}{h_c}$. The 1D extensional, coupling and bending stiffness coefficients A , B and D are computed as follows:

$$A = E_f h_f + E_c h_c, \quad B = \frac{h_f h_c}{2} (E_c - E_f)$$

and

$$D = \frac{1}{12} \{ E_f (h_f^3 + 3h_f h_c^2) + E_c (h_c^3 + 3h_f^2 h_c) \}$$

The kinematics of the SCB specimen of the width b (Fig. 1b) described by the Timoshenko beam—Winkler foundation model in Ratcliffe and Reeder (2011) leads to an analytical estimation of the ERR in the SCB test method in the form:

$$\mathcal{G}^{SCB} = \frac{4\zeta F^2}{2bK} \left\{ \zeta^3 a^2 + 2\zeta^2 a + \zeta + \frac{K}{4b\zeta k G_{xy}^f h_f} \right\}, \quad (2.9)$$

where the parameter $\zeta = \left(\frac{K}{4D_f}\right)^{1/4}$ with bending stiffness of the face sheet $D_f = \frac{bh_f^3}{12}$ and the foundation coefficient $K = \frac{bE_c}{h_c}$ identical to that in (2.8), k is the shear correction factor equal to 5/6.

The Euler–Bernoulli beam theory is also utilized to model the DCB-UBM specimen of the width b . Based on the beam assumptions and the J -integral calculated along the outer boundaries of the specimen (Fig. 1c), the ERR is calculated in Burlayenko et al. (2019c) as follows:

$$\mathcal{G}^{DCB-UBM} = \frac{1}{2b} \left\{ \frac{N^2}{(EA)_d} + \frac{N^2}{(EA)_s} + \frac{M^2}{(EI)_d} + \frac{M^{*2}}{(EI)_s} \right\}, \quad (2.10)$$

where $N = \gamma_2 M_b$, $M = M_1 - \gamma_3 M_b$ and

$$M^* = N \left(e_s + \frac{h_c}{2} + \frac{h_f}{2} \right) - M$$

are the equivalent axial load and bending moments, respectively, with

$$\gamma_2 = \frac{(EA)_d}{(EI)_b} \left(e_0 + \frac{h_c}{2} + \frac{h_f}{2} \right)$$

and

$$\gamma_3 = \frac{(EI)_d}{(EI)_b}$$

the parameters e_0 and e_s locate neutral axes of the intact part of specimen and the substrate, Fig. 1c; $(EA)_i$ and $(EI)_i$ are generalized axial and flexural rigidities of the debonded portion “ d ,” substrate “ s ” and intact part of the specimen “ b ,” i.e., $i = \{d, s, b\}$.

It should be noticed that all the expressions from (2.8) to (2.10) for the ERR derived based on 1D beam theories do not account for the core shearing in the specimens in contrast to those obtained within the fracture mechanics concept in (2.2), (2.4), (2.5) and (2.7).

2.3.3 2-D Finite Element Modeling

The 2D finite element models of the studied specimens have been developed with the commercial package ABAQUS (2016). The specimens’ geometries were discretized with 8-node full integration solid plane stress quadrilateral elements. The debond as an interfacial crack was modeled by duplicate nodes between finite elements placed along the crack flanks. The region near the crack tip was covered by a “spider-web”

mesh refinement as shown in Fig. 3a. Typically, about 30,000 degrees of freedom were employed in the model. Also, to capture the square root singularity in the mesh with 8-node isoparametric elements, the elements with the mid-side nodes on the sides connected to the crack tip moved to the $\frac{1}{4}$ -point nearest the crack tip were used in a ring around the crack tip.

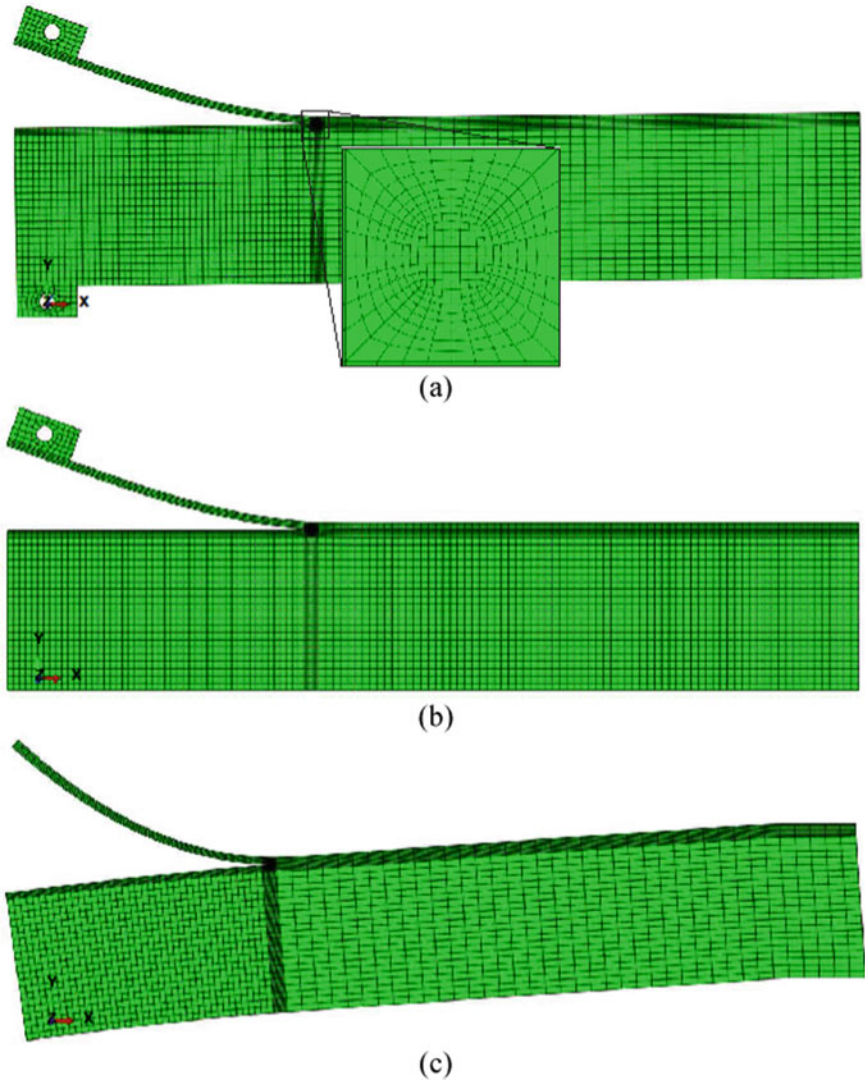


Fig. 2.3 Deformed configurations of the fracture specimens: **a** the DCB specimen; **b** the SCB specimen; and **c** the DCB-UBM specimen

By using the J -integral option available in ABAQUS (2016), the ERR and the complex stress intensity factors associated with mode mixity phase angle relating to a local mode I/II mixity at the near tip stress field were calculated in all the specimens. Herewith, an assumption of reducing the orthotropic properties of the laminated face sheet into the equivalent isotropic ones has been done. While such finite element predictions with ABAQUS built-in capabilities enable to give accurate enough results, they do not account for the actual orthotropy of the material constituents. For this reason, an add-on MATLAB subroutine was developed to compute the fracture parameters of crack at bi-material orthotropic interfaces (Burlayenko et al. 2019c, 2020b). The routine implements the CSD method by handling a displacement field on the crack flanks, extracted from the post-processing part of finite element analysis in accordance with the formulas:

$$\mathcal{G} = \frac{H_{11}|K|^2}{4\cosh^2\pi\epsilon} = \frac{\pi(1+4\epsilon^2)}{8H_{11}\left(\frac{r}{\tilde{l}}\right)} \left(\frac{H_{11}}{H_{22}}\Delta_2^2 + \Delta_1^2 \right) \quad (2.11)$$

and

$$\psi = \tan^{-1} \left(\sqrt{\frac{H_{11}}{H_{22}}} \frac{\Delta_1}{\Delta_2} \right) - \epsilon \ln \left(\frac{r}{\tilde{l}} \right) + \tan^{-1} 2\epsilon, \quad (2.12)$$

where $\Delta_j = u_j(r, \pi) - u_j(r, -\pi)$, $j = 1, 2$ represents the relative crack flank displacements (shearing and opening modes) at distance r behind the crack tip, and H_{11} and H_{22} are components of the Hermitian matrix \mathbf{H} , which is defined for the orthotropic materials with material axes aligned with the coordinate axes as follows:

$$\begin{aligned} H_{11} &= [2n\lambda^{1/4}\sqrt{s_{11}s_{22}}]_{\#1} + [2n\lambda^{1/4}\sqrt{s_{11}s_{22}}]_{\#2} \\ H_{22} &= [2n\lambda^{-1/4}\sqrt{s_{11}s_{22}}]_{\#1} + [2n\lambda^{-1/4}\sqrt{s_{11}s_{22}}]_{\#2} \\ H_{12} = \bar{H}_{21} &= i[\sqrt{s_{11}s_{22}} + s_{12}]_{\#1} - i[\sqrt{s_{11}s_{22}} + s_{12}]_{\#2} \end{aligned} \quad (2.13)$$

Here s_{ij} , $i, j = 1, 2, 6$, $s_{16} = s_{26} = 0$ are components of the compliance matrix of the orthotropic materials (#1 or #2) in plane stress; the compliance coefficients in plane strain are

$$\tilde{s}_{ij} = s_{ij} - \frac{s_{i3}s_{j3}}{s_{33}}$$

Note that the parameters of anisotropy are

$$\lambda = s_{11}/s_{22} \text{ and } \varrho = \frac{(2s_{12} + s_{66})}{2\sqrt{s_{11}s_{22}}}$$

and the coefficient $n = \sqrt{\frac{(1+\varrho)}{2}}$.

The expressions (2.11) and (2.12) are only valid at the limit $r \rightarrow 0$. Since the finite element model is not able to provide this situation, the crack flank displacements very close to the crack tip are calculated instead. Then, the values of \mathcal{G} and ψ are estimated by linear extrapolation of the results in the interval $10^{-3} \leq r/\hat{l} \leq 10^{-2}$ to $r = 0$. The characteristic length is accepted as $\hat{l} = h_f$.

Finally, given the \mathcal{G} and ψ parameters, the components of the complex stress intensity factor can be found as follows:

$$\begin{aligned} K_1 &= \Re \left\{ K \hat{l}^{i\epsilon} \right\} = |K| \cos \psi \\ K_2 &= \Im \left\{ K \hat{l}^{i\epsilon} \right\} = |K| \sin \psi \end{aligned} \quad (2.14)$$

2.4 Results and Discussion

The numerically and analytically obtained results for the fracture parameters of the fracture specimens are considered in this section. The finite element fracture analysis was carried out using the capacities of software ABAQUS (2016). All the specimens of an equal length of 280 mm and width of 25 mm with pre-crack of 90 mm were assumed to be made up of the PVC H100 core of thickness 50 mm and the same laminated glass/epoxy face sheets of thickness 2.4 mm. The material properties of the specimen's constituents are summarized in Table 2.1.

The specimens were subjected to loads in accordance with the test methods shown schematically in Fig. 2.1. The loads induced approximately equal levels of the ERR about 4.0×10^{-4} N/mm in each test. That is, $F = 1$ N and $M_1^e = 75$ N mm and $M_2^e = 1125$ N mm have been accepted for comparisons in what follows.

Figure 2.3 illustrates the deformed configurations of the considered specimens resulting from the finite element analysis. The specimens' kinematics highlights and confirms some issues that may arise in their laboratory testing. For instance, the asymmetry of the DCB specimen caused by the fact that the lower part (below the crack plane) being more rigid in flexure than the upper one (above the crack plane)

Table 2.1 Material properties of the sandwich specimens

Constituents	Material constants
Glass/epoxy face sheet	$E_x = E_z = 16.5$ GPa; $E_y = 3.8$ GPa; $G_{xy} = G_{xz} = 1.3$ GPa; $G_{yz} = 6.6$ GPa; $\nu_{xy} = 0.05$; $\nu_{xz} = \nu_{yz} = 0.25$
PVC H 100 foam core	$E_x = E_y = E_z = 0.105$ GPa; $G_{xy} = G_{xz} G_{yz} = 0.0389$ GPa; $\nu_{xy} = \nu_{xz} = \nu_{yz} = 0.325$

may result in a slight rotation of the specimen at large opening displacements as shown in Fig. 3a and mentioned in Avilés and Carlsson (2008).

To provide a mode I dominated debonding associated with a face sheet peeling from the core in a SCB specimen, the bending of the debonded face sheet has to be the primary form of loading. It can be provided by keeping the applied force as more perpendicular as possible to the crack plane during the testing as illustrated in Fig. 3b. In actual tests, this condition is implemented by satisfying the load rod length, h_F (Fig. 1b) to sizing requirements defined in Ratcliffe and Reeder (2011).

Finally, the major concern of the DCB-UBM test method is to provide a proper application of the loads producing pure bending moments at the cracked ends of the specimen as shown in Fig. 3c. The research focusing on establishing suitable test loading as well as a new recommended methodology for that in DCB-UBM specimens can be found in Berggreen et al. (2018).

Figure 2.4 demonstrates the distributions of near tip stress components in the specimens analyzed in the simulations. As general for all the contour plots, the high stressed regions spread to large influence zones in all the specimens due to the soft-core layer adjacent to the crack tip. The longitudinal normal stresses σ_{xx} are mainly developed in the debonded face sheet due to its high bending resistance and play some role in determining the values of maximum principal stresses in the vicinity of the crack tip. In turn, the transverse normal stresses σ_{yy} achieve their maximum in the crack tip regions as well as the shear stresses σ_{xy} , but with values an order of magnitude smaller than the transverse normal stresses. It is also found that though the transverse normal stresses in each specimen under dominated mode I loading are more severe than the shear stresses, the latter ones surely exist providing mode mixity at the crack tip. As suggested by the results of Adams et al. (2012), the sign of shear stress is a factor that explains the debonding path direction in sandwich structures, and the degree of mode mixity defines the elevation of fracture toughness.

Analyzing the stress distributions for each of the specimen separately, one can see that all the plots for DCB (Fig. 4a–b) and SCB (Fig. 4c–e) samples exhibit similar trends in contrast to their counterparts for DCB-UBM beam shown in Fig. 4f–i. Thus, differences in fracture characteristics as design parameters of the DCB, SCB and DCB-UBM test methods are expected.

Given the material properties of actually orthotropic face sheet and core reduced to equivalent isotropic materials, the specimens are analyzed with analytical expressions presented in Sects. 3.1 and 3.2. Also, the numerical predictions with both the orthotropic and isotropic constituents of the specimens are carried out for comparisons. In the numerical predictions, to compute the complex stress intensity factors, the CSD method is used for the specimens with orthotropic constituents, while the interaction integral method as a built-in option of the ABAQUS code is activated in the case of constituents with equivalent isotropic properties.

Comparisons between the ERR and mode mixity phase angle values obtained by the analytical formulas and those calculated numerically with the 2-D FEA are listed in Table 2.2. One can see good agreement between the numerical and analytical solutions. The analytical expressions based on the elastic foundation models for calculation of the ERR in the DCB and SCB specimens a little overestimate those

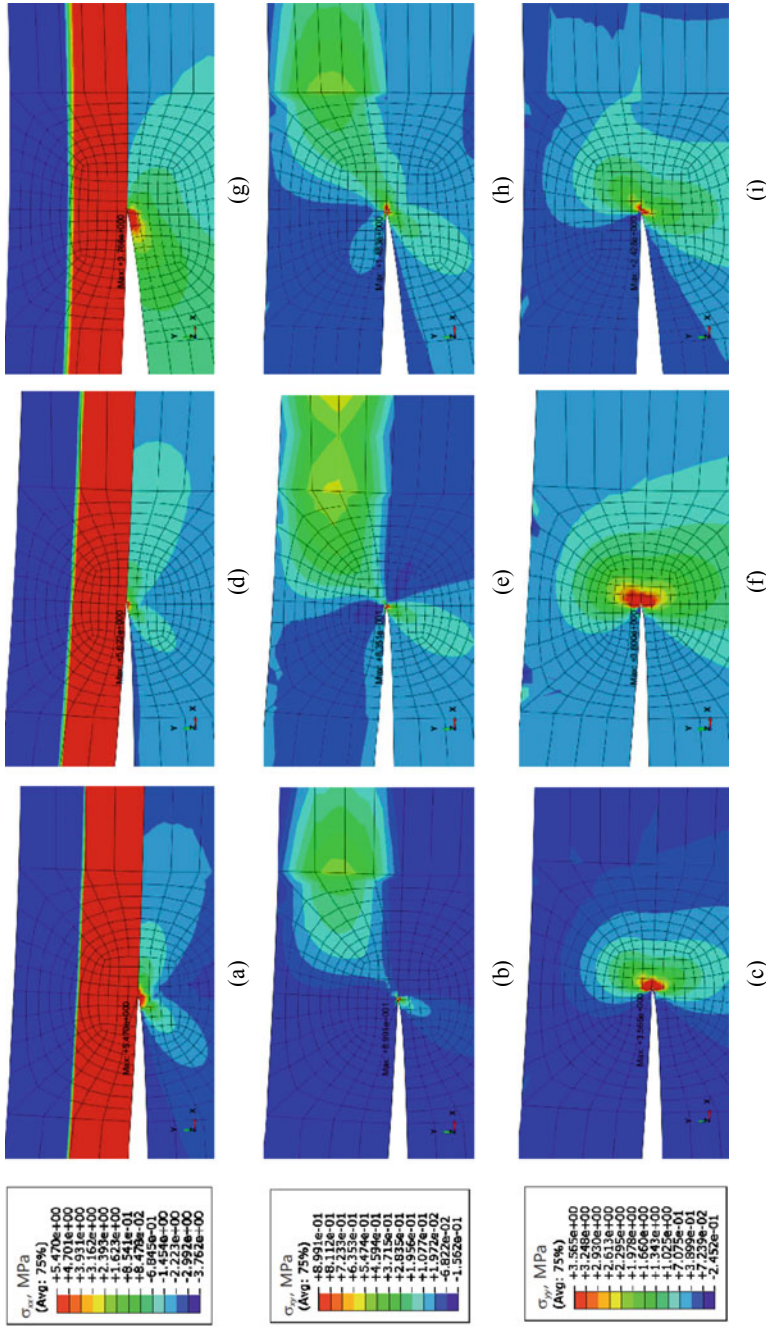


Fig. 2.4 Contour plots of near tip stress components—the longitudinal normal stress σ_{xx} , the shear stress σ_{xy} , and the transverse normal stress σ_{yy} , in: **a–c** the DCB specimen; **d–f** the SCB specimen; and **g–i** DCB-UBM specimen

Table 2.2 Comparisons for the SERR calculated for the DCB, SCB and DCB-UBM sandwich specimens

Specimen	Parameter	Analytic		2D FEA	
		Section 3.1	Section 3.2	Isotropic	Orthotropic
DCB	$\mathcal{G} \times 10^{-4}$, N/mm	4.0334	4.3636	4.0452	4.0501
	ψ , deg	-19.11	-	-9.23	-14.69
	$\Re\{Kh_f^{i\epsilon}\}$, N/mm ^{3/2}	0.2778	-	0.3039	0.2966
	$\Im\{Kh_f^{i\epsilon}\}$, N/mm ^{3/2}	-0.0927	-	-0.0494	-0.0778
SCB	$\mathcal{G} \times 10^{-4}$, N/mm	4.0004	4.3445	4.0293	4.0254
		4.0157			
	ψ , deg	-22.98	-	-12.23	-17.60
		-20.66			
	$\Re\{Kh_f^{i\epsilon}\}$, N/mm ^{3/2}	0.2696	-	0.3003	0.2913
		0.2745			
	$\Im\{Kh_f^{i\epsilon}\}$, N/mm ^{3/2}	-0.1081	-	-0.0651	-0.0926
		-0.0990			
DCB-UBM	$\mathcal{G} \times 10^{-4}$, N/mm	4.5660	4.5660	4.5524	4.5568
	ψ , deg	19.48	-	29.82	23.44
	$\Re\{Kh_f^{i\epsilon}\}$, N/mm ^{3/2}	0.2949	-	0.2835	0.2984
	$\Im\{Kh_f^{i\epsilon}\}$, N/mm ^{3/2}	0.1003	-	0.1625	0.1294

numerical and semi-analytical results. In turn, the analytical ERR derived using the linear elastic fracture mechanics for the DCB-UBM specimen gives a value identical to the semi-analytic result and very close to the numerical predictions. Also, it needs to notice good compliance between the results predicted for the samples with orthotropic material properties and those assuming properties of equivalent isotropic materials. However, the latter case does not provide accurate values of the mode mixity phase angle. Nevertheless, both of the numerical predictions related to the stress intensity factors are close to each other and agree satisfactory with the analytical results. Thus, the anisotropic properties of the bi-material interface affect the accuracy of the fracture characteristics evaluation. Herewith, since the ERR is an integral parameter, this value is less disturbed by the material anisotropy than the mode mixity angle, which is very sensitive to a localized state at the crack tip. Also, due to this fact, the essential difference in the mixity phase angles calculated by the analytical and numerical methods occurs as the methods use different techniques in modeling the near crack tip stress field. In Table 2.2, the parameters for the SCB specimen in the upper parts of the cells are determined by simplified formulas (2.5), whereas those in the lower parts of the cells are defined by (2.2) and (2.3).

This comparison, first, confirms the accuracy and efficiency of the proposed 2D numerical models, and second, it emphasizes the differences in the sandwich specimens' responses dependent on the test method used for estimation of the fracture parameters. It is obvious from Table 2.2 that remote mode I loading in the specimens leads to local mixed I/II mode in terms of transversal normal and shear stresses simultaneously existing at the crack tip. Also, one can see that the mode mixity increases from the DCB to DCB-UBM specimen types as shown in Fig. 2.4. Moreover, in contrast to the DCB and SCB specimens with an assumed crack path inside the face sheet-to-core interface due to the negative factor $K_2 < 0$, the DCB-UBM beam exhibits a positive factor $K_2 > 0$, i.e., the crack may kink into the core. Therefore, these observations following from the considered analytical, semi-analytical and numerical models may serve high fidelity estimations of the fracture parameters in actual fracture specimens as well as the combination of these models with experimental data may provide data reductions in such tests.

2.5 Conclusions

In this research, efforts have been focused on the evaluation of the fracture parameters in virtual tests related to the assessment of face sheet-to-core interface strength in sandwich panels. Both the analytical methods based on beam-like models and the semi-analytical approach combining analytical considerations and numerical results, and two-dimensional finite element analyses carried out with ABAQUS have been used for computing ERR, SIFs and mode mixity phase angle in three popular DCB, SCB and DCB-UBM sandwich fracture specimens. The numerically obtained results have been handled in the post-processing part of the finite element analysis to evaluate mode mixity. The J -integral method as a built-in option of the ABAQUS code was used for solving interfacial problems of two dissimilar isotropic materials, while the crack surface displacement method programmed in the MATLAB environment was applied to for analyzing a general bi-material configuration of the interfaces.

In general, good agreement between the results of the numerical calculations based on 2D modeling and those following from the semi-analytical approach and the 1D analytical solutions is observed for all the sandwich specimens with the same material and geometrical properties. However, the inability of the beam theories to account for crack tip shear deformation results in overestimated values of the ERR of the specimens, and the beam models also do not provide closed-form solutions for the mode mixity phase angle. On the other hand, the semi-analytical technique, which allows enforcing the root rotation compatibility at the crack tip, gives results very close to the finite element predictions for all the fracture parameters. Herewith, a coupling between the interfacial shear and transverse normal stresses at a crack tip is a direct outcome of the finite element solution of the 2D elastic problem.

Comparing the results of the semi-analytical technique and those obtained with the FEM, the computational aspects of the 2D numerical models in terms of their accuracy and efficiency have been evaluated to put them into perspective of the interface

strength assessments of sandwich panels. It was found out that, first, the orthotropic constituencies of the interfaces can be replaced by their equivalent isotropic counterparts with small deviations from the semi-analytical results for the ERR and SIFs, but with a rough estimation of the mode mixity angle. Second, the simplified model of the SCB sandwich should be used with strong limitations due to a high influence of the reaction on the fixed bottom face sheet on the near tip stress field, i.e., the foundation reaction should be taken into account in general. Third, given the same material and geometrical parameters and under mode I loading conditions, the responses of the DCB and SCB specimens are similar, but the DCB-UBM sample distinguishes much from them. The former two specimens have mode I dominated state with a small negative mode II component, while the latter one in such mode I dominated regime possesses a larger positive mode II component.

Acknowledgements The first author would like to mention that this research has been started during his stay at the Institute of Mechanics of Otto-von-Guericke-Universität Magdeburg, which was supported by the German Academic Exchange Service (DAAD) Funding Program ID no.~57440915.

Appendix 1

Following the original notations in Østergaard and Sørensen (2007); Andrews and Massabò (2007); Barbieri et al. (2018), the geometrical and material dimensionless parameters of the sandwich beam cross-section are defined as follows:

$$\begin{aligned}\eta &= \frac{h_f}{h_c} \\ \alpha &= \frac{\Sigma-1}{\Sigma+1}, \text{ with } \Sigma = \frac{\bar{E}_f}{\bar{E}_c} \\ \beta &= \frac{G_f(\bar{\kappa}_c-1)-G_c(\bar{\kappa}_f-1)}{G_f(\bar{\kappa}_c+1)+G_c(\bar{\kappa}_f+1)} \\ \varepsilon &= \frac{1}{2\pi} \ln\left(\frac{1-\beta}{1+\beta}\right)\end{aligned}\quad (2.15)$$

where $\bar{E}_i = E_i$ for plane stress and $\bar{E}_i = \frac{E_i}{1-\nu_i^2}$ for plane strain with E_i and ν_i the Young's modulus and the Poisson's ratio of the layer $i = \{f, c\}$ and the shear modulus, $G_i = \frac{E_i}{2(1+\nu_i)}$; α and β stand for the Dundur's parameters with $\bar{\kappa}_i = \frac{3-\nu_i}{1+\nu_i}$ for plane stress and $\bar{\kappa}_i = 3 - 4\nu_i$ for plane strain; ε is the oscillatory index.

The dimensionless distance of the neutral axis of the substrate at crack tip cross-section of unit width is defined by

$$\tilde{e}_s = \frac{e_s}{h_f} = \frac{\bar{E}_f h_f}{\bar{E}_c h_c + \bar{E}_f h_f} \frac{h_f + h_c}{2h_f} = \frac{\Sigma(\eta + 1)}{2(\Sigma\eta + 1)}, \quad (2.16)$$

whereas the dimensionless bending stiffnesses of the substrate and fully bonded part (the base) of unit width cross-section are given by

$$\begin{aligned}\tilde{D}_s &= \frac{D_s}{\bar{E}_f h_f^3} = \frac{1}{12} + \left(\frac{\eta + 1}{2\eta} - \tilde{e}_s \right)^2 + \frac{1}{\Sigma\eta} \left(\frac{1}{12\eta^2} + \tilde{e}_s^2 \right) \\ \tilde{D}_b &= \frac{D_b}{\bar{E}_f h_f^3} = \left(\frac{1}{6} + \frac{1}{2\eta^2} (\eta + 1)^2 \right) + \frac{1}{12\Sigma\eta^3}\end{aligned}\quad (2.17)$$

The coefficients in (2.1) are calculated in the forms:

$$\begin{aligned}C_1 &= \frac{\Sigma\eta}{1+2\Sigma\eta} \\ C_2 &= \frac{1}{\tilde{D}_b} \left(\frac{1}{2} + \frac{1}{2\eta} \right) \\ C_3 &= \frac{1}{12\tilde{D}_b}\end{aligned}\quad (2.18)$$

Appendix 2

The positive dimensionless functions $f_M(\Sigma, \eta)$, $f_P(\Sigma, \eta)$ and the phase angle $\gamma_M(\Sigma, \eta)$ define the energy release rates for arbitrary combinations of bending moments and axial forces (Fig. 2b). In terms of the dimensionless parameters they take the form (Barbieri et al. 2018):

$$\begin{aligned}f_M(\Sigma, \eta) &= \left(\frac{1}{2} \left(12 + \frac{1}{\tilde{D}_s} \right) \right)^{\frac{1}{2}} \\ f_P(\Sigma, \eta) &= \left(\frac{1}{2} \left(1 + \frac{\Sigma\eta}{1+\Sigma\eta} + \frac{1}{\tilde{D}_s} \left(\frac{1}{2} + \frac{1}{2\eta} + \tilde{e}_s \right)^2 \right) \right)^{\frac{1}{2}} \\ \gamma_M(\Sigma, \eta) &= \sin^{-1} \left(\frac{1}{2\tilde{D}_s f_P f_M} \left(\frac{1}{2} + \frac{1}{2\eta} + \tilde{e}_s \right) \right)\end{aligned}\quad (2.19)$$

References

- ABAQUS: User's Manual, ver. 2016. Dassault Systèmes Simulia Corp., Providence, RI, USA (2016)
- Adams, D.O., Nelson, J., Bluth, Z.: Development and evaluation of fracture mechanics test methods for sandwich composites. In: Proceedings of the 2012 Aircraft Airworthiness and Sustainment Conference, Baltimore, MD, US (2012)
- Altenbach, H., Altenbach, J., Kissing, W.: Mechanics of Composite Structural Elements, 2nd edn. Springer (2018)
- Amabili, M.: Nonlinear Mechanics of Shells and Plates in Composite Soft and Biological Materials. Cambridge University Press, Cambridge (2018)
- Andrews, M.G., Massabò, R.: The effects of shear and near tip deformations on energy release rate and mode mixity of edge-cracked orthotropic layers. Eng. Fract. Mech. **74**(17), 2700–2720 (2007)
- Avilés, F., Carlsson, L.A.: Analysis of the sandwich DCB specimen for debond characterization. Eng. Fract. Mech. **75**(2), 153–168 (2008)

- Barbieri, L., Massabò, R., Berggreen, C.: The effects of shear and near tip deformations on interface fracture of symmetric sandwich beams. *Eng. Fract. Mech.* **201**, 298–321 (2018)
- Berggreen, C., Saseendran, V., Carlsson, L.: A modified DCB-UBM test method for interfacial fracture toughness characterization of sandwich composites. *Eng. Fract. Mech.* **203**, 208–223 (2018)
- Burlayenko, V.N., Sadowski, T.: Dynamic analysis of debonded sandwich plates with flexible core— Numerical aspects and simulation. In: Altenbach, H., Eremeyev, V.A. (eds.) *Shell-like Structures: Non-classical Theories and Applications*, Advanced Structured Materials, vol. 15, pp. 415–440. Springer, Berlin Heidelberg (2011)
- Burlayenko, V.N., Sadowski, T.: Numerical modeling of sandwich plates with partially dedonded skin-to-core interface for damage detection. In: DeRoeck G, Degrande G, Lombaert G, Müller G (eds) *Proceedings of the 8th International Conference on Structural Dynamics (EURODYN)*, pp 2242–2249. Leuven, Belgium (2011b)
- Burlayenko, V., Pietras, D., Sadowski, T.: Influence of geometry, elasticity properties and boundary conditions on the mode I purity in sandwich composites. *Compos. Struct.* **223**, 110942 (2019)
- Burlayenko, V.N., Altenbach, H., Sadowski, T.: Dynamic fracture analysis of sandwich composites with face sheet/core debond by the finite element method. In: Altenbach, H., Belyaev, A., Eremeyev, V.A., Krivtsov, A., Porubov, A.V. (eds.) *Dynamical Processes in Generalized Continua and Structures*, Advanced Structured Materials, vol. 103, pp. 163–194. Springer, Cham (2019)
- Burlayenko, V.N., Sadowski, T., Pietras, D.: Influence of dynamic loading on fracture behaviour of DCB sandwich specimen. *ITM Web Conf.* **29**, 02003 (2019)
- Burlayenko, V.N., Altenbach, H., Dimitrova, S.D.: Interface strength assessments of sandwich panels with a face sheet/core debond. In: Altenbach, H., Chinchaladze, N., Kienzler, R., Müller, W.H. (eds.) *Analysis of Shells, Plates, and Beams: A State of the Art Report*, pp. 95–122. Springer, Cham (2020)
- Burlayenko, V.N., Sadowski, T., Dimitrova, S.D.: Nonlinear fracture dynamic analysis of double cantilever beam sandwich specimens. In: Lacarbonara, W., Balachandran, B., Ma, J., Tenreiro Machado, J.A., Stepan, G. (eds.) *New Trends in Nonlinear Dynamics*, pp. 89–97. Springer, Cham (2020)
- Chatterjee, V.A., Saraswat, R., Verma, S.K., Bhattacharjee, D., Biswas, I., Neogi, S.: Embodiment of dilatant fluids in fused-double-3D-mat sandwich composite panels and its effect on energy-absorption when subjected to high-velocity ballistic impact. *Compos. Struct.* **249**(112), 588 (2020)
- Davidson, P., Waas, A.M., Yerramalli, C.S.: Experimental determination of validated, critical interfacial modes I and II energy release rates in a composite sandwich panel. *Compos. Struct.* **94**(2), 477–483 (2012)
- Davis, B., Wawrzynek, P., Hwang, C., Ingrassia, A.: Decomposition of 3-D mixed mode energy release rates using the virtual crack extension method. *Eng. Fract. Mech.* **131**, 382–405 (2014)
- Farkash, E., Banks-Sills, L.: Quarter-point elements are unnecessary for the VCCT. *J. Appl. Mech.* **87**(8), 081009 (2020)
- Fu, Y., Sadeghian, P.: Flexural and shear characteristics of bio-based sandwich beams made of hollow and foam-filled paper honeycomb cores and flax fiber composite skins. *Thin-Walled Structures* **153**, 106834 (2020)
- Funari, M.F., Greco, F., Lonetti, P.: Sandwich panels under interfacial debonding mechanisms. *Compos. Struct.* **203**, 310–320 (2018)
- Kardomateas, G.A., Berggreen, C., Carlsson, L.A.: Energy-release rate and mode mixity of face/core debonds in sandwich beams. *AIAA j.* **51**(4), 885–892 (2013)
- Kardomateas, G.A., Yuan, Z.: Closed form solution for the energy release rate and mode partitioning of the single cantilever beam sandwich debond from an elastic foundation analysis. *J. Sandwich Struct. Mater.* (2020). <https://doi.org/10.1177/1099636220932900>
- Li, S., Wang, J., Thouless, M.D.: The effects of shear on delamination in layered materials. *J. Mech. Phys. Solids* **52**(1), 193–214 (2004)
- Odessa, I., Frostig, Y., Rabinovitch, O.: Modeling of interfacial debonding propagation in sandwich panels. *Int. j. Solids Struct.* **148–149**, 67–78 (2018)

- Østergaard, R.C., Sørensen, B.F.: Interface crack in sandwich specimen. *Int. j. Fract.* **143**(4), 301–316 (2007)
- Prasad, S., Carlsson, L.A.: Debonding and crack kinking in foam core sandwich beams—I. Analysis of fracture specimens. *Eng. Fract. Mech.* **47**(6), 813–824 (1994)
- Quispitupa, A., Berggreen, C., Carlsson, L.A.: On the analysis of a mixed mode bending sandwich specimen for debond fracture characterization. *Eng. Fract. Mech.* **76**(4), 594–613 (2009)
- Ratcliffe, J.G., Reeder, J.R.: Sizing a single cantilever beam specimen for characterizing facesheet–core debonding in sandwich structure. *J. Compos. Mater.* **45**(25), 2669–2684 (2011)
- Sivaram, A., Manikandan, N., Krishnakumar, S., Rajavel, R., Krishnamohan, S., Vijayaganth, G.: Experimental study on aluminium based sandwich composite with polypropylene foam sheet. *Mater. Today Proc.* **24**, 746–753 (2020)
- Sorensen, B., Jorgensen, K., Jacobsen, T., Ostergaard, R.: DCB-specimen with uneven bending moments. *Int. j. Fract.* **141**, 163–176 (2006)
- Szekrényes, A.: Mechanics of shear and normal deformable doubly-curved delaminated sandwich shells with soft core. *Compos. Struct.* **258**(15), 113196 (2021)
- Ustinov, K.: On semi-infinite interface crack in bi-material elastic layer. *Eur. j. Mech. Solids* **75**, 56–69 (2019)
- Yoshida, K., Aoki, T.: Beam on elastic foundation analysis of sandwich SCB specimen for debond fracture characterization. *Compos. Struct.* **195**, 83–92 (2018)

Chapter 3

Modeling of Mechanical Properties of Composite Materials Under Different Types of Loads



Mykola Kryshchuk, Sergiy Shukayev, and Viktor Rubashevskiy

Abstract This study examines the calculation methods used to predict the load bearing capacity of composite structures. Specifically, examined are the numerical and analytical methods of determining the effective elastic properties of layered composites. Presented are the results of a stress analysis performed on a space-use honeycomb panel under different types of loads. The results of numerical experiments conducted on models of the honeycomb panel were obtained in APDL ANSYS. Recommendations regarding the application of efficient finite element models were proposed based on the stress–strain state data of composite structures under loading, obtained via simulation models of different types. Examined are the approaches to assessing the limit state of composites under uniaxial and biaxial loading. Also discussed are the advantages and disadvantages of using finite element models and analytical models.

Keywords Composite materials · Honeycomb panels · Elastic properties · Stress–strain state · Strength · Modal analysis · Finite element models

3.1 Introduction

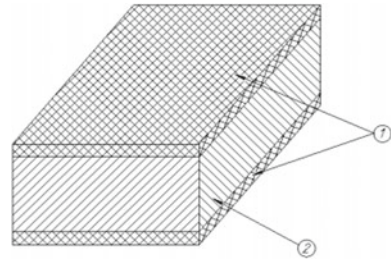
Due to the rapid spread of usage of composite materials in the manufacturing of various structures, the objective of rational design of such items—for instance, of honeycomb structures—has become increasingly relevant. The honeycomb panel is a three-layer structure consisting of two skins and a honeycomb core sandwiched between them (Fig. 3.1).

M. Kryshchuk (✉) · S. Shukayev · V. Rubashevskiy
Department of Dynamics and Strength of Machines and Strength of Materials, National Technical University of Ukraine “Igor Sikorsky Kyiv Polytechnic Institute, Kyiv, Ukraine
e-mail: krys@ukr.net

S. Shukayev
e-mail: shukayev@ukr.net

V. Rubashevskiy
e-mail: viktorrub21@ukr.net

Fig. 3.1 Honeycomb panel:
1 fiber-reinforced epoxy
skin, 2 honeycomb core



Structures of this type are widely used in the aerospace industry due to their high level of technical and economic efficiency.

The calculation of the load bearing capacity of composite honeycomb panels is an important task in modern mechanical engineering. Such calculations include the determination of the elastic properties of the honeycomb panel components. This task is often approached by applying analytical methods, which can be used to determine both the properties of a monolayer and the effective elastic properties of the composite structure as a whole.

Methods employed to determine the stress–strain state include both those developed for multilayer plates and the approaches designed to use equivalent single-layer plates. Computer simulation models of structural components have also been extensively utilized in recent times. The combined use of analytical and numerical methods allows for a reduction of experimental research, while it also leads to an early discovery of design defects in the item being manufactured.

This study presents the results of a stress analysis performed on a space-use honeycomb panel under different types of loads. A standard honeycomb panel structure, the particulars of which are described above, serves here as the simulation model example. Reported are the results of numerical experiments conducted on three models of the honeycomb panel, all of which were created in APDL ANSYS using finite elements. A comparison of the convergence and accuracy of these results was carried out based on an evaluation of the amounts of displacement in static tests and the calculation of ten first eigenfrequencies and mode shapes. Provided are the examples of numerical calculations of mechanical properties and of strength assessment for composite honeycomb panels. Based on these calculations, the maximum deflection values for the panel under thermal and mechanical loading in low earth orbits ranging from 200 to 400 km were determined.

Determined also was the stress-strained state of the target honeycomb panel under self-weight. The transition from a multilayer to a three-layer structure was possible due to the determination of the effective elastic properties of the panel skins. The results obtained were verified by finite element method calculations in the ANSYS Workbench software environment.

Additionally, a comparison was made of the numerical and analytical approaches to assessing the limit state of a layered *AS4/3501-6 carbon/epoxy laminate* under uniaxial and biaxial loading. The analytical model of the mechanical properties

degradation of a composite layer (Kucher and Zarazovskii 2009) and the numerical simulation method in ANSYS Workbench were applied.

3.2 Determination of Elastic Properties of Layered Composites

Owing to the fact that the physical and mechanical properties of composites are required for calculating strength, frequency and fatigue, their determination with the help of numerical and analytical methods is not only an urgent task, but also a viable alternative to experimental research.

The effective modulus of elasticity of a layered composite is one of the most important characteristics. Numerical and analytical methods for determining the effective modulus of elasticity of a layered composite both for the carbon fiber-reinforced plastics (CFRP) (EDT-10/TC 36S-12 K, AS4/3501-6 carbon/epoxy, T300/BSL914C epoxy) and for the glass-fiber reinforced plastics (E-glass 21xK43Gevetex/LY556/HT907/DY063 epoxy and Silenka E-Glass1200tex/MY750/HY917/ DY063 epoxy) are described in a number of recent studies (Rubashevskiy et al. 2017; Maslei and Rudakov 2019). The comparisons of calculated and experimental data for composites of these types were conducted by means of rule of mixtures (Voigt and Reuss models) (Altenbach et al. 2018), coaxial cylinder methods (Christensen 1980), Vanin's method (Vanin 1985), Kilchinskyi model (Kilchinsky 1965) and methods developed by other authors Jones, Förster/Knappe, Puck, Schneider (ECSS-E-HB-32-20 2011) and the finite element method. Based on the research findings, it can be concluded that finite element models of a composite monolayer produce good results for the above-mentioned task, whereas recommended formulas do not always produce a satisfactory result. The analysis and comparison of analytical approaches showed a certain superiority of the methods of coaxial cylinders and Vanin's method, which gave the best correlation of calculated and experimental data.

Once the elastic properties of a composite monolayer have been determined, it is possible to proceed to predicting the effective elastic properties of the composite structure as a whole. To determine the effective elastic properties of the entire layered composite, this study used the approach developed in (Khoroshun and Maslov 1980). In accordance with this approach, the components of the effective stiffness tensor of a layer, which are represented by the respective elastic parameters E_1, E_2, G_{12}, G_{23} and ν_{12} , were averaged by volume for the target combination of layers of the composite. As a result of the conversion of the effective stiffness tensor to the effective stiffness matrix, effective elastic constants of the material are obtained.

$$[A] = \begin{bmatrix} \frac{1}{E_1} & \frac{-\nu_{21}}{E_2} & \frac{-\nu_{31}}{E_3} & 0 & 0 & 0 \\ \frac{-\nu_{12}}{E_1} & \frac{1}{E_2} & \frac{-\nu_{32}}{E_3} & 0 & 0 & 0 \\ \frac{-\nu_{13}}{E_1} & \frac{-\nu_{23}}{E_2} & \frac{1}{E_3} & 0 & 0 & 0 \\ 0 & 0 & 0 & \frac{1}{G_{23}} & 0 & 0 \\ 0 & 0 & 0 & 0 & \frac{1}{G_{13}} & 0 \\ 0 & 0 & 0 & 0 & 0 & \frac{1}{G_{12}} \end{bmatrix} \quad (3.1)$$

Here, $[A] = [\lambda]^{-1}$ is the effective compliance tensor and $[\lambda]$ is the effective stiffness matrix.

As an example, shown below is the calculation of the effective elasticity modulus E_x of the layered composite AS4/3501-6 carbon/epoxy, which was carried out based on the experimentally determined elastic constants of a monolayer (Soden et al. 2002).

$$E_1 = 126 \text{ GPa}, \quad E_2 = E_3 = 11 \text{ GPa}, \quad G_{12} = G_{23} = G_{31} = 6.6 \text{ GPa},$$

$$\nu_{12} = \nu_{13} = \nu_{23} = 0.28$$

$$\langle \lambda_{ij} \rangle = \left[2\lambda_{ij}^{90} + 2\lambda_{ij}^{-45} + 2\lambda_{ij}^{45} + 2\lambda_{ij}^0 \right] \Delta h / H \quad (3.2)$$

$$\lambda_{11}^\theta = m^4 \lambda_{11} + 2m^2 n^2 (\lambda_{12} + 2\lambda_{66}) + 4mn(m^2 \lambda_{16} + n^2 \lambda_{26}) + n^4 \lambda_{22} \quad (3.3)$$

Here, Δh and H are the thicknesses of the monolayer and the composite, respectively; λ_{ij}^θ is the stiffness parameters of layers ($i, j = 1, 2, \dots, 6$), which are turned at an angle of θ relative to the local coordinate frame; $\langle \lambda_{ij} \rangle$ is the components of the averaged stiffness matrix; and $n = \sin(\theta)$, $m = \cos(\theta)$, $\Delta h = 0.125 \text{ mm}$, $H = 1 \text{ mm}$

$$\lambda_{ij} = \begin{bmatrix} 126 & 4,36 & 4,36 & 0 & 0 & 0 \\ 4,36 & 11 & 3,49 & 0 & 0 & 0 \\ 4,36 & 3,49 & 11 & 0 & 0 & 0 \\ 0 & 0 & 0 & 6,6 & 0 & 0 \\ 0 & 0 & 0 & 0 & 6,6 & 0 \\ 0 & 0 & 0 & 0 & 0 & 6,6 \end{bmatrix} \quad (3.4)$$

$$E_x = [2 \cdot 126 + 2 \cdot 45.68 + 2 \cdot 45.68 + 2 \cdot 11] \cdot 0,125 = 57.09 \text{ GPa} \quad (3.5)$$

Other effective elastic constants are determined in the same manner as above. This method was used to calculate the effective elastic constants for other composites, for instance, T300/BSL914C epoxy, E-glass 21xK43Gevetex/LY556/HT907/DY063 epoxy and Silenka E-Glass1200tex/ MY750/HY917/DY063 epoxy. The errors between the experimental and calculated results ranged between 2.1 and 9.8% for Young's modulus, between 1.1 and 31.2% for the shear modulus, and between 1.7 and 31.5% for Poisson's ratio.

In order to determine the effective properties of the three-layer honeycomb panel shown in Fig. 3.1, a combination of two methods was used. The panel consists of two layers of composite skins (each 0.8 mm thick) with a layup schedule of $[0^\circ/90^\circ/\pm 45^\circ]$. The skins are bonded to a 76 mm thick honeycomb core made of 5056-6-23 aluminum foil. L-Khoroshun's analytical method shown in work (Khoroshun and Maslov 1980) was used in combination with the rule of mixtures. The resulting data was compared to data obtained from calculations, which were performed using the Layups module in the FEMAP v11.0.1 software environment (Kryshchuk et al. 2019). As indicated by the comparison of the results of elastic orthotropic properties calculations for the target structure, the maximum discrepancy between the results produced by the analytical and the numerical methods does not exceed 11%.

3.3 Phenomenological Failure Criteria of Composite Materials

To estimate the strength of composite materials, it is necessary to know the criteria that specify the permissible limits of stresses and strains in which the material can operate under specified conditions without failure. In Lepikhin and Romashchenko (2013), a review of some of the prevalent phenomenological criteria applied to assess the strength of composite materials is given.

The phenomenological failure criteria describe the macromechanical behavior of composite materials as a whole, without taking into account the micromechanical features that arise as a result of deformation of the composite.

The phenomenological approach makes it possible to use the general design requirements for materials that are different in composition and technology, but have the same symmetry properties, as well as for materials with significant anisotropy, for which the same stress state can lead to different limit states if the stress signs are reversed or the stress orientation is changed.

Phenomenological failure criteria are not derived analytically; they are postulated or proposed on the basis of generalization of experimental data. The choice of a criterion depends on the nature of the material, its composition, the degree of anisotropy, the chosen calculation concept, and the available amount of experimental data.

As noted in (Kollar and Springer 2003), the relative frequency of use of the phenomenological criteria is as follows: maximum deformations account for 30% of calculations, maximum stresses for 23%, Tsai–Hill for 18%, Tsai–Wu for 13%, and all other for 19%. It is worth noting that the Tsai–Wu criterion more accurately describes the failure of composite materials as compared to the maximum principal strain criterion, the maximum stress criterion, and the Tsai–Hill criterion.

One of the most general formulations of the anisotropic failure criterion for the three-dimensional case has the following form (Goldenblat and Kopnov 1965)

$$(F_i \sigma_i)^\alpha + (F_{ij} \sigma_i \sigma_j)^\beta + (F_{ijk} \sigma_i \sigma_j \sigma_k)^\gamma + \dots \leq 1, (i, j, k \dots = 1, 2, \dots, 6) \quad (3.6)$$

where F_i , F_{ij} , F_{ijk} are the so-called strength-surface tensors of the second, fourth, sixth, and subsequent even ranks; σ_l is the stress tensor; and the exponents α , β , γ , etc., are determined from experimental data. Working solely with the first two components of the inequality, the authors of (Goldenblat and Kopnov 1965) most fully developed a version of this criterion, in which it is assumed that $\alpha = 1$, $\beta = \frac{1}{2}$.

More convenient for practical application was a variant of the criterion in which the exponents were taken to be equal to unity (Alfutov et al. 1984; Wu 1974; Tsai and Wu 1971)

$$\alpha = \beta = \gamma = \dots = 1 \text{ and } F_i\sigma_i + F_{ij}\sigma_i\sigma_j + F_{ijk}\sigma_i\sigma_j\sigma_k + \dots \leq 1 \quad (3.7)$$

This form of notation is called **the tensor-polynomial failure criteria** (Alfutov et al. 1984; Wu 1974; Tsai and Hahn 1975).

3.3.1 Tsai–Wu Criterion

Owing to the large number of material constants that need to be determined experimentally, the third and subsequent components in this expression are usually disregarded. The indicated polynomial criterion is then reduced to the Tsai–Wu criterion (Tsai and Wu 1971) of the following form

$$F_i\sigma_i + F_{ij}\sigma_i\sigma_j \leq 1 \quad (3.8)$$

According to the data presented in (Kollar and Springer 2003), under strict equality, this equation can describe the failure surface, if the magnitude of mixed components F_{ij} ($i \neq j$) is constrained by the following inequality:

$$F_{ii}F_{jj} - F_{ij}^2 \geq 0 \quad (3.9)$$

The Tsai–Wu criterion generally takes into account the difference in tensile and compressive strengths, and the dependence of the shear strength on the direction of shear stresses. It also has the maximum possible flexibility. This criterion does not contain excessive parameters and facilitates the determination of the principal axes of strength, etc. (Wu 1974).

Strength-surface tensor components can only be determined experimentally. For a material with a general type of anisotropy of properties, 27 experiments are required to instantiate the above inequality (Wu 1974). This leads to the fact that it is practically impossible to apply the criterion for such materials. It is thus only practically applicable to orthotropic and transversally isotropic materials.

According to (Kollar and Springer 2003), for an orthotropic material, the criterion in the principal axes of orthotropy of the material takes the following form

$$F_1\sigma_1 + F_2\sigma_2 + F_3\sigma_3 + F_{11}\sigma_1^2 + F_{22}\sigma_2^2 + F_{33}\sigma_3^2$$

$$\begin{aligned}
& + F_{44}\sigma_4^2 + F_{55}\sigma_5^2 + F_{66}\sigma_6^2 \\
& + 2F_{12}\sigma_1\sigma_2 + 2F_{13}\sigma_1\sigma_3 + 2F_{23}\sigma_2\sigma_3 \leq 1
\end{aligned} \tag{3.10}$$

The unmixed components of strength-surface tensors in the formula are expressed as $F_1, F_2, F_3, F_{11}, F_{22}, F_{33}, F_{44}, F_{55}, F_{66}$. The values of these components are uniquely determined by uniaxial tensile or compression experiments and pure shear experiments. The mixed components of the strength-surface tensor are designated as F_{12}, F_{13}, F_{23} . The main problem with the practical application of the Tsai–Wu criterion is the difficulty of experimental determination of the mixed components of the strength-surface tensor. Finding them requires biaxial experiments or the use of complex shape specimens, which entails considerable costs. The value of F_{ij} depends heavily on the scatter of experimental data. At the same time, its minute changes have a noticeable effect on the appearance of the failure surface.

As their first approximation, the authors of (Tsai and Hahn 1980) proposed the following expression

$$F_{ij} = c\sqrt{(F_{ii}F_{jj})}, \text{ where } |c| \leq 1 \tag{3.11}$$

In this case, there is no need to carry out biaxial experiments to determine, F_{ij} , which greatly simplifies the practical application of the criterion. At $c = -\frac{1}{2}$, the specified approach has been recently widely applied to failure analysis of composites (Evans and Zhang 1987; Benzeggagh et al. 1995; Manne and Henriksen 1998; Sleight 1999; Paepegem and Degrieck 2003). Moreover, in the case of isotropic materials, this criterion coincides with the von Mises criterion.

Due to this, the authors of (Mises 1913; Yang 1980) named the variant of the criterion for $c = -\frac{1}{2}$ **the generalized von Mises criterion**.

According to the data of (Kollar and Springer 2003; Reddy and Pandey 1987), the components of the strength-surface tensors for the generalized von Mises criterion can be determined as follows

$$\begin{aligned}
F_1 &= \frac{1}{X_T} - \frac{1}{X_C}, F_2 = \frac{1}{Y_T} - \frac{1}{Y_C}, F_3 = \frac{1}{Z_T} - \frac{1}{Z_C}, F_{11} = \frac{1}{X_T X_C}, \\
F_{22} &= \frac{1}{Y_T Y_C}, F_{33} = \frac{1}{Z_T Z_C}, F_{44} = \frac{1}{R^2}, \\
F_{55} &= \frac{1}{S^2}, F_{66} = \frac{1}{T^2}, F_{12} = -\frac{1}{2}\sqrt{X_T X_C Y_T Y_C}, F_{13} = -\frac{1}{2}\sqrt{X_T X_C Z_T Z_C}, \\
F_{23} &= -\frac{1}{2}\sqrt{Y_T Y_C Z_T Z_C}
\end{aligned} \tag{3.12}$$

Hereinafter X_T, Y_T, Z_T represent the ultimate tensile strength in principal directions 1, 2 and 3, respectively; X_C, Y_C, Z_C represent the ultimate compressive strength in principal directions 1, 2, and 3, respectively; and R, S, T represent the ultimate shear strength in 2–3, 1–3, and 1–2 principal planes, respectively.

To instantiate the generalized von Mises criterion, it is necessary to determine 12 coefficients through 9 experiments (6 experiments for tension and compression in three principal directions of orthotropy, and 3 experiments for shear in three principal planes).

For a transversely isotropic material with a 2–3 plane of isotropy, according to the data of (Kollar and Springer 2003), the following equation can be derived

$$F_1\sigma_1 + F_2(\sigma_2 + \sigma_3) + F_{11}\sigma_1^2 + F_{22}(\sigma_2^2 + \sigma_3^2) + 2(F_{22} - F_{23})\sigma_4^2 + F_{66}(\sigma_5^2 + \sigma_6^2) + 2F_{12}(\sigma_1\sigma_2 + \sigma_1\sigma_3) + 2F_{23}\sigma_2\sigma_3 \leq 1 \quad (3.13)$$

The corresponding seven components of the strength-surface tensors in the equation are determined as follows

$$F_1 = \frac{1}{X_T} - \frac{1}{X_C}, F_2 = \frac{1}{Y_T} - \frac{1}{Y_C}, F_{11} = \frac{1}{X_T X_C}, F_{22} = \frac{1}{Y_T Y_C}, F_{66} = \frac{1}{T^2}$$

$$F_{12} = -\frac{1}{2}\sqrt{X_T X_C Y_T Y_C}, F_{23} = -\frac{1}{2}\sqrt{Y_T Y_C Z_T Z_C} \quad (3.14)$$

To instantiate these components, it is necessary to carry out 5 tension–compression experiments in directions 1 and 2, and a pure shear experiment in the 1–2 plane. It should be mentioned that for any transversely isotropic body with a 2–3 plane of isotropy, when applying quadratic failure criteria, the equality is as follows

$$F_{44} = 2(F_{22} - F_{23}) \quad (3.15)$$

According to (Evans and Zhang 1987), the generalized von Mises criterion corresponds well with experimental data for materials with a high degree of anisotropy.

3.3.2 Maximum Stress Criterion

According to this criterion, failure occurs when any of the following conditions is not satisfied (Yang 1980)

$$-X_C \leq \sigma_1 \leq X_T, -Y_C \leq \sigma_2 \leq Y_T, -Z_C \leq \sigma_3 \leq Z_T, |\sigma_4| \leq R, |\sigma_5| \leq S, |\sigma_6| \leq T \quad (3.16)$$

The maximum stress criterion can be expressed in terms of the tensor-polynomial criterion as follows (Benzeggagh et al. 1995)

$$(\sigma_1 - X_T)(\sigma_1 + X_C)(\sigma_2 - Y_T)(\sigma_2 + Y_C)(\sigma_3 - Z_T)(\sigma_3 + Z_C)(\sigma_4 - R) \times (\sigma_4 + R)(\sigma_5 - S)(\sigma_5 + S)(\sigma_6 - T)(\sigma_6 + T) \leq 0 \quad (3.17)$$

Disregarding terms of higher than the second order, an approximate criterion for maximum stress is obtained in a quadratic form, for which the nonzero components of the strength-surface tensors are as follows

$$\begin{aligned} F_1 &= \frac{1}{X_T} - \frac{1}{X_c}, F_2 = \frac{1}{Y_T} - \frac{1}{Y_c}, F_3 = \frac{1}{Z_T} - \frac{1}{Z_c}, F_{11} = \frac{1}{X_T X_c}, \\ F_{22} &= \frac{1}{Y_T Y_c}, F_{33} = \frac{1}{Z_T Z_c}, F_{44} = \frac{1}{R^2}, F_{55} = \frac{1}{S^2}, F_{66} = \frac{1}{T^2}, F_{12} = -\frac{F_1 F_2}{2}, \\ F_{13} &= -\frac{F_1 F_3}{2}, F_{23} = -\frac{F_2 F_3}{2} \end{aligned} \quad (3.18)$$

All other strength constants are equal to zero.

For a transversely isotropic material with a 2–3 plane of isotropy, taking into account the data of (Kollar and Springer 2003), the following is true

$$\begin{aligned} F_1 &= \frac{1}{X_T} - \frac{1}{X_c}, F_2 = F_3 = \frac{1}{Y_T} - \frac{1}{Y_c}, F_{11} = \frac{1}{X_T X_c}, F_{22} = F_{33} = \frac{1}{Y_T Y_c} \\ F_{55} &= F_{66} = \frac{1}{T^2}, F_{12} = F_{13} = -\frac{F_1 F_2}{2}, F_{23} = -\frac{F_2^2}{2} \end{aligned} \quad (3.19)$$

3.3.3 Maximum Principal Strain Criterion

For the maximum principal strain criterion, it is assumed that failure occurs when any of the following conditions is not met (Reddy and Pandey 1987)

$$\begin{aligned} -X_{\varepsilon C} \leq \varepsilon_1 \leq X_{\varepsilon T}, -Y_{\varepsilon C} \leq \varepsilon_2 \leq Y_{\varepsilon T}, -Z_{\varepsilon C} \leq \varepsilon_3 \leq Z_{\varepsilon T}, |\varepsilon_4| \leq R_\varepsilon, |\varepsilon_5| \leq S_\varepsilon, \\ |\varepsilon_6| \leq T_\varepsilon \end{aligned} \quad (3.20)$$

where $\varepsilon_1, \varepsilon_2, \varepsilon_3$ are tensile strains in directions 1, 2, and 3, respectively; $\varepsilon_4, \varepsilon_5, \varepsilon_6$ are shear strains in the 2–3, 1–3, and 1–2 planes, respectively; $X_{\varepsilon T}, Y_{\varepsilon T}, Z_{\varepsilon T}$ are ultimate tensile strains in principal directions 1, 2, and 3, respectively; $X_{\varepsilon C}, Y_{\varepsilon C}, Z_{\varepsilon C}$ are ultimate compressive strains in principal directions 1, 2, and 3, respectively; and R, S, T are ultimate shear strains in 2–3, 1–3, and 1–2 principal planes, respectively.

The criterion is expressed in a tensor-polynomial form as follows (Reddy and Pandey 1987)

$$\begin{aligned} (\varepsilon_1 - X_T)(\varepsilon_1 + X_{\varepsilon C})(\varepsilon_2 - Y_T)(\varepsilon_2 + Y_{\varepsilon C})(\varepsilon_3 - Z_T)(\varepsilon_3 + Z_{\varepsilon C}) \\ \times (\varepsilon_4 - R_\varepsilon)(\varepsilon_4 + R_\varepsilon)(\varepsilon_5 - S)(\varepsilon_5 + S)(\varepsilon_6 - T)(\varepsilon_6 + T) \leq 0 \end{aligned} \quad (3.21)$$

For a transversely isotropic material with a 2–3 plane of isotropy, taking into account the data of (Kollar and Springer 2003), the following equations are obtained

$$\begin{aligned}
F_1 &= F_1^A + \left(\frac{S_{12}}{S_{22}} + \frac{S_{13}}{S_{33}} \right) F_2^A, F_2 = F_3 = \frac{S_{12}}{S_{11}} F_1^A + \left(1 + \frac{S_{23}}{S_{33}} \right) F_2^A, \\
F_{66} &= \frac{1}{T^2}, \\
F_{11} &= \frac{1}{X_T X_C} + \left(\left(\frac{S_{12}}{S_{22}} \right)^2 + \left(\frac{S_{13}}{S_{33}} \right)^2 \right) \frac{1}{Y_T Y_C} - \left(\frac{S_{13}}{S_{33}} + \frac{S_{12}}{S_{22}} \right) F_1^A F_2^A \\
&\quad - \frac{S_{12} S_{13}}{S_{22} S_{33}} (F_2^A)^2, \\
F_{22} &= \left(1 + \left(\frac{S_{23}}{S_{33}} \right)^2 \right) \frac{1}{Y_T Y_C} + \left(\frac{S_{12}}{S_{11}} \right)^2 \frac{1}{X_T X_C} - \left(\frac{S_{12}}{S_{11}} + \frac{S_{12} S_{23}}{S_{11} S_{33}} \right) F_1^A F_2^A \\
&\quad - \frac{S_{23}}{S_{33}} (F_2^A)^2, \\
F_{12} &= \frac{S_{12}}{S_{11}} \frac{1}{X_T X_C} + \left(\frac{S_{12}}{S_{22}} + \frac{S_{13} S_{23}}{S_{33}^2} \right) \frac{1}{Y_T Y_C} \\
&\quad - \frac{1}{2} \left(1 + \frac{S_{12}}{S_{11}} \left(\frac{S_{12}}{S_{22}} + \frac{S_{13}}{S_{33}} \right) + \frac{S_{23}}{S_{33}} \right) F_1^A F_2^A \\
&\quad - \frac{1}{2} \left(\frac{S_{12} S_{23}}{S_{22} S_{33}} + \frac{S_{13}}{S_{33}} \right) (F_2^A)^2, \\
F_{23} &= S_{23} \left(\frac{1}{S_{22}} + \frac{1}{S_{33}} \right) \frac{1}{Y_T Y_C} + \frac{S_{12} S_{13}}{S_{11}^2} \frac{1}{X_T X_C} \\
&\quad - \frac{1}{2} \left(1 + \frac{S_{23}}{S_{22}} \left(\frac{S_{23}}{S_{33}} + \frac{S_{12}}{S_{11}} \right) + \frac{S_{13}}{S_{11}} \right) F_1^A F_2^A \\
&\quad - \frac{1}{2} \left(\frac{S_{23} S_{13}}{S_{11} S_{33}} + \frac{S_{12}}{S_{11}} \right) (F_2^A)^2
\end{aligned} \tag{3.22}$$

In the above equations, S_{ij} is the components of the compliance matrix.

3.3.4 Tsai–Hill Criterion (or Modified Hill Criterion) (Azzi and Tsai 1965)

According to (Reddy and Pandey 1987), this criterion can be expressed as follows

$$\begin{aligned}
&\left(\frac{\sigma_1}{X_i} \right)^2 + \left(\frac{\sigma_2}{Y_i} \right)^2 + \left(\frac{\sigma_3}{Z_i} \right)^2 - \left(\frac{1}{X_i^2} + \frac{1}{Y_i^2} - \frac{1}{Z_i^2} \right) \sigma_1 \sigma_2 - \left(\frac{1}{Z_i^2} + \frac{1}{X_i^2} - \frac{1}{Y_i^2} \right) \sigma_1 \sigma_3 \\
&\quad - \left(\frac{1}{Y_i^2} + \frac{1}{Z_i^2} - \frac{1}{X_i^2} \right) \sigma_2 \sigma_3 + \left(\frac{\sigma_4}{R} \right)^2 + \left(\frac{\sigma_5}{S} \right)^2 + \left(\frac{\sigma_6}{T} \right)^2 \leq 1
\end{aligned} \tag{3.23}$$

In this criterion, stress components do not occur in the first degree; therefore, F_1 , F_2 , and F_3 are equal to zero. The values X_i , Y_i , and Z_i take on the values of either X_T , Y_T , Z_T or X_C , Y_C , Z_C depending on the sign of normal stresses σ_1 , σ_2 , σ_3 , respectively.

The strength-surface tensor components for this criterion are as follows

$$\begin{aligned} F_i &= 0, & F_{22} &= \frac{1}{Y_i^2}, & F_{33} &= \frac{1}{Z_i^2}, & F_{44} &= \frac{1}{R^2}, & F_{55} &= \frac{1}{S^2}, & F_{66} &= \frac{1}{T^2} \\ F_{12} &= -\frac{1}{2} \left(\frac{1}{X_i^2} + \frac{1}{Y_i^2} - \frac{1}{Z_i^2} \right), & F_{13} &= -\frac{1}{2} \left(\frac{1}{Z_i^2} + \frac{1}{X_i^2} - \frac{1}{Y_i^2} \right), \\ F_{23} &= -\frac{1}{2} \left(\frac{1}{Y_i^2} + \frac{1}{Z_i^2} - \frac{1}{X_i^2} \right) \end{aligned} \quad (3.24)$$

For a transversely isotropic material with a 2–3 plane of isotropy, taking into account the data of (Kollar and Springer 2003), the following is true

$$\begin{aligned} F_i &= 0, & F_{11} &= \frac{1}{X_i^2}, & F_{22} &= F_{33} = \frac{1}{Y_i^2}, & F_{66} &= \frac{1}{T^2}, \\ F_{12} &= F_{13} = -\frac{1}{2} \left(\frac{1}{X_i^2} \right), & F_{23} &= -\frac{1}{2} \left(\frac{2}{Y_i^2} - \frac{1}{X_i^2} \right) \end{aligned} \quad (3.25)$$

Many works have been devoted to the analysis of phenomenological criteria. For instance, it is noted in (Lepikhin and Romashchenko 2013) that, among the most widely used criteria, the Tsai–Wu criterion and the generalized von Mises criterion are the most accurate and general, while the generalized von Mises criterion does not require complex experiments to be instantiated. Also, basing on the analysis of the applicability of various phenomenological failure criteria for modeling the failure of multilayer composites, the conclusion is made that the same criterion can be the most accurate in some cases and produce low accuracy results in other cases.

3.4 Estimation of Strength and Modal Analysis of a Standard Structure of a Space-Use Honeycomb Panel

A standard honeycomb panel structure (Fig. 3.2) with known topological arrangements of aluminum cells, and of upper and lower composite skins, will serve here as the simulation model example.

To verify the data obtained from numerical experiments (Maslei et al. 2018; Rubashevskiy and Shukayev 2019), three types of finite element models were developed using the APDL ANSYS v12.1 software package (ANSYS Structural Analysis Guide ANSYS Release 12.1 xxxx), which is designed to determine the structural dynamics

Fig. 3.2 Simulation model of a honeycomb panel showing the arrangement of kinematic supports (1)

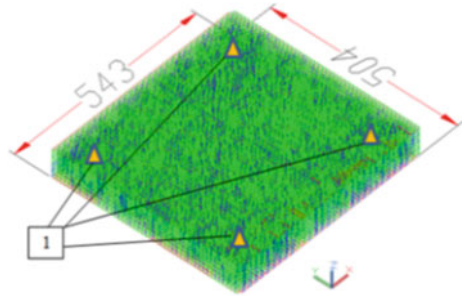


Table 3.1 Calculated values of the effective elastic constants of the honeycomb panel on the basis of the Cartesian coordinates shown in Fig. 3.2

E_x , GPa	E_y , GPa	E_z , GPa	G_{xy} , GPa	G_{yz} , GPa	G_{zx} , GPa	μ_{xy}	μ_{yz}	μ_{zx}
1	1	462	1e-5	59.65	87.86	0.49	0.001	0.001

and assess the structural strength of a three-layer honeycomb panel. Each finite element model type represented a different approach to displaying the elastic and mass properties of the honeycomb core material with isotropic properties and the multilayer anisotropic carbon fiber skins rigidly connected to the upper and lower surfaces of the cells.

The basic model of the honeycomb panel was designed considering a just identification of the geometric structure of the honeycomb core with diamond-shaped 6 mm edged cells and 0.8 mm thick composite skins with a $[0^\circ/90^\circ/\pm 45^\circ]$ carbon fiber layup. The refined model of the honeycomb panel preserved the geometric structure of the honeycomb core, but with a 12 mm cell edge of equivalent stiffness. In order to design the through-thickness layup schedule of the upper and lower skins with CFRP and to reproduce the cell topology of the honeycomb structure in the basic and refined models, the SHELL181 multilayer plate finite element (FE) was used.

The equivalent model of a honeycomb panel was simulated by means of replacing the honeycomb core structure with solid orthotropic material with effective elastic properties. These properties were determined by numerical experiments, which involved simple loading of the model with axial and transverse unit forces under compression and shear deformations (Table 3.1). The procedure of discretization of the honeycomb core was performed using SOLID185 FEs. SHELL181 FEs were used to approximate the reinforced fiber material with known elastic properties, which constituted the upper and lower skins of the honeycomb panel. The joining of FEs of different types in the discrete model of the honeycomb panel was done using the “node to node” scheme. In the discrete models corresponding to each of the three design schemes of the honeycomb panel (basic, refined and equivalent), there were 29,880/7585/29880 nodes and 47,056/11760/17454 FEs, respectively.

When modeling the deformation of honeycomb structures and the equivalent elastic layer of a three-layer honeycomb panel with an upper and lower skin under

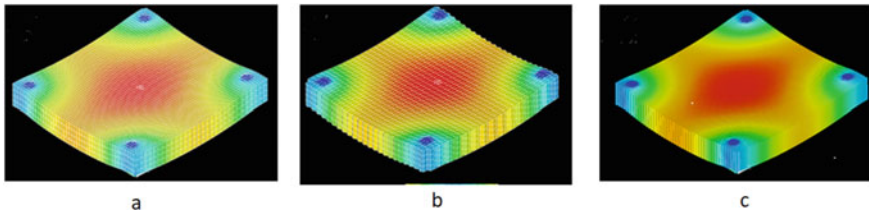


Fig. 3.3 Strain of the basic (a), refined (b), and equivalent (c) models of the honeycomb panel under a self-weight load

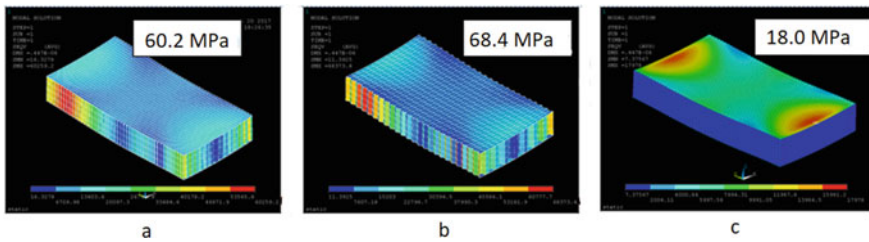


Fig. 3.4 Distribution of von Mises equivalent stresses for the core parts of discrete FE models under a self-weight load: basic (a), refined (b), and equivalent (c). The numerical values represent the maximum von Mises equivalent stresses

self-weight, the calculation results for different FE approximations correlated within a reasonable margin (Fig. 3.3). In Fig. 3.4, the distribution of von Mises equivalent stresses is shown for the core part of the honeycomb panel.

As compared to the basic model, the stress calculation error for the refined model was 12%. With regard to the equivalent model, a direct comparison of its stress distribution to those of the basic and refined models (Fig. 3.3 a, b) is not appropriate, the more so since the equivalent model does not provide for determining the adhesive bond strength of the honeycomb core to the composite plates.

A comparison of the convergence and accuracy of the results obtained when choosing adequate finite element approximations of the honeycomb panel model was also made by means of evaluating the calculations of the first 10 eigenfrequencies and mode shapes. The error in calculating the eigenfrequencies for the three dynamic models of the honeycomb panel, with each of them employing different algorithms for calculating the elastic and mass properties of the conjugate elements of the panel's structure, ranged from 0.8 to 8% (Fig. 3.5). This finding allows for the conclusion that in the design calculations of such structures, the dynamic model of the honeycomb panel that includes the replacement of its structures with solid orthotropic material with effective properties is sufficient to make design and technological decisions.

To carry out a preliminary strength assessment of the honeycomb panel under the action of deterministic and stochastic loads, equivalent stresses σ_e were determined by von Mises criterion. The σ_e stresses were obtained as the sum of the static $\sigma_{sp,static}$ and dynamic $\sigma_{sp,ry}$ values of von Mises stresses

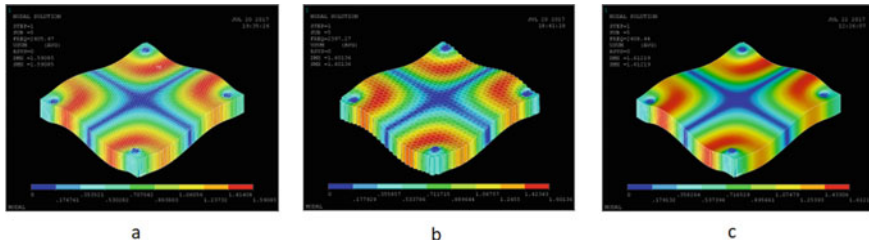


Fig. 3.5 Modal analysis. The fifth form of natural oscillations for the basic (a), refined (b), equivalent, and (c) discrete FE models and their respective frequencies: 2405/2397/2408 Hz

$$\sigma_e = \sigma_{sp,static} + 3\sigma_{sp,ry} \quad (3.26)$$

The following strength condition was used

$$\sigma_e < [\sigma] = \min(\sigma_y/\eta_y, \sigma_u/\eta_u) \quad (3.27)$$

where $[\sigma]$ are allowable stresses equal to the smaller of the values determined by offset yield strength σ_y or by ultimate tensile strength σ_u at safety factors η_y and η_u .

Using the above methods of mathematical modeling, other examples of numerical calculations of mechanical properties and strength assessment were carried out for composite honeycomb panels in space- and civilian-use structures under various loads. Because of these calculations (Kryshchuk et al. 2019), maximum deflection values were determined for the honeycomb panel under thermomechanical loading in low earth orbits ranging from 200 to 400 km.

3.5 Comparative Analysis of Strength Assessment Methods for Layered Composites

The comparative analysis of strength assessment methods for layered composites (Soden et al. 2002; Rubashevskiy and Shukayev 2019; Hinton et al. 2004) was carried out using 0.125 mm thick 8 ply AS4/3501-6 carbon/epoxy laminate with a $[90^\circ/45^\circ/-45^\circ/0^\circ/0^\circ/-45^\circ/45^\circ/90^\circ]$ layup schedule under uniaxial and biaxial stress-state conditions. For the analysis, the analytical and numerical methods were applied.

Applying the analytical model of the mechanical properties degradation of the composite layer, which was proposed in Kucher and Zarazovskii (2009), and building on the assumptions made in (Maslei and Rudakov 2019), failure stress assessment was carried out for CFRP under complex stress-state conditions using elastic constants, whose definition is provided in paragraph 2 of the present article.

To determine the stress tensor components of the composite, the following relations were applied

$$\begin{cases} \langle \sigma_i \rangle = \lambda_{ij} \langle \varepsilon_i \rangle \\ \langle \varepsilon_i \rangle = A_{ij} \langle \sigma_i \rangle \end{cases} \quad (3.28)$$

where $\langle \sigma_i \rangle$ is through-thickness averaged stresses of the composite, λ_{ij} is the components of effective stiffness properties, A_{ij} is the components of effective compliance properties, and $\langle \varepsilon_i \rangle$ is through-thickness averaged strains of the composite.

The main principles of the analytical model for assessing the failure stresses of a composite plate are based on the maximum stress criterion for an orthotropic body under biaxial stress-state conditions. It is assumed that failure begins when the stress in one of the layers reaches critical value, under which value at least one of the following conditions is not satisfied

$$\tilde{\sigma}_{-1} < \sigma_1 < \tilde{\sigma}_{+1}; \tilde{\sigma}_{-2} < \sigma_2 < \tilde{\sigma}_{+2}; -\tilde{\sigma}_{12} < \sigma_{12} < \tilde{\sigma}_{12} \quad (3.29)$$

where $\tilde{\sigma}_{12}$ is the ultimate shear strength of the layer in the reinforcement plane; $\tilde{\sigma}_{-1}$ and $\tilde{\sigma}_{+1}$ are the ultimate compressive and tensile strengths in the reinforcement direction, respectively; $\tilde{\sigma}_{-2}$ and $\tilde{\sigma}_{+2}$ are the ultimate compressive and tensile strengths in the transversal direction, respectively. It is considered that the layered composite loses its load bearing capacity once all layers have failed.

Using the numerical simulation method, tubular specimens were modeled in the ANSYS Workbench software environment in accordance with the experiment (Soden et al. 2002), the required CFRP properties were set, and, with the application of the ACP (Pre) and ACP (Post) modules (which are specifically designed for composite calculations) and the maximum stress criterion, strength assessment was performed.

A comparison of errors for both approaches to solving this problem is shown in Fig. 3.6. The problem area for both approaches, namely $C = -5 \dots 0$, is clearly

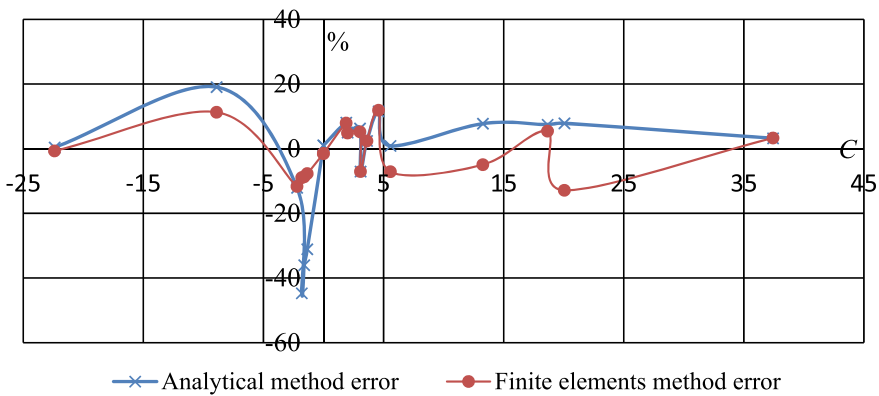


Fig. 3.6 Comparison of calculated and experimental data. The error between the experiment and calculation is plotted on the vertical axis as a percentage, while the ratio (C) between the highest and lowest stress values in composites under biaxial stress-state conditions is plotted on the horizontal axis

visible on the graph; outside this area, errors take on either nearly identical or opposing values.

Based on the above results, it can be concluded that the degradation model for the mechanical properties of a composite layer produces good results under biaxial stress-state conditions with a positive C . The accuracy of the analytical method (for which the maximum error does not exceed 12%) is close to that of the numerical method, which is based on the algorithm for by-layer calculation of elastic properties. It must be noted here that for the application of the analytical model, only the mechanical characteristics of the monolayer components (i.e., fiber and matrix) are required, while the numerical method requires the specification of mechanical properties of the monolayer as a whole.

It was discovered that the application of the degradation model for the mechanical properties of a composite layer to assess strength under biaxial stress-state conditions with a negative C may lead to a significant error (up to 45%). Therefore, in order to make it possible for the model to be applied under such conditions, it needs to be further improved.

As a result of this study, the efficiency of the application of ACP (Pre) and ACP (Post) modules in the ANSYS Workbench software environment for assessing the limit state of a layered composite under uniaxial and biaxial stress-state conditions was confirmed for all modes of loading (the maximum error does not exceed 13%).

3.6 Conclusions

1. The research findings showed that the combined use of finite element models and analytical approaches yields good result in determining the effective elastic properties and assessing the stress–strain state of composite structures.
2. It was demonstrated that, in design calculations, a dynamic model of the honeycomb panel, which includes the replacement of its structures with a solid orthotropic material with effective properties, is sufficient to make design and technological decisions.
3. For the solution of strength problems in composite structures, the existing analytical approaches require improvement or a setting of reasonable limits to their application on a case-by-case basis.

References

- “ANSYS Structural Analysis Guide ANSYS Release 12.1.” available at: www.ansys.com/
- Alfutov, N.A., Zinoviev, P.A., Popov, B.G.: Raschet mnogosloynuh plastin i obolochek iz kompozicionnuh materialov. Mashinostroenie, Moscow (1984)
- Altenbach, H., Altenbach, J., Kissing, W.: Mechanics of Composite Structural Elements, 2nd edn. Springer Nature Singapore Pte Ltd (2018)

- Azzi, V.D., Tsai, S.W.: Anisotropic strength of composites. *Exp. Mech.* **5**(5), 283–288 (1965)
- Benzeggagh, M.L., Khellil, K., Chotard, T.: Experimental determination of Tsai failure tensorial terms for unidirectional composite materials. *Compos. Sci. Technol.* **55**(2), 145–156 (1995)
- Christensen, R.: *Mechanics of Composite Materials*. Wiley, New York (1980)
- ECSS-E-HB-32–20. Part 1A. *Structural Materials Handbook—Part 1: Overview and Material Properties and applications*. (2011), available at: https://www.ecss.nl/wp-content/uploads/handbooks/ecss-e-hb/ECSS-E-HB-32-20_Part1A.pdf
- Evans, K.E., Zhang, W.C.: The determination of normal interaction term in the Tsai-Wu tensor polynomial strength criterion. *Compos. Sci. Technol.* **30**(4), 251–262 (1987)
- Goldenblat, I.I., Kopnov, V.A.: Strength of glass-reinforced plastics in the complex stress state. *Mekhanika Polymerov (poly. Mech.)* **1**(2), 54–59 (1965)
- Hinton, M.J., Kaddour, A.S., Soden, P.D. (eds.): *Failure Criteria in Fibre-Reinforced Polymer Composites: The Worldwide Failure Exercise*. Elsevier, Amsterdam et al. (2004)
- Khoroshun, L.P., Maslov, B.P.: *Metody avtomatizirovanogo rascheta fiziko-mekhanicheskikh postojannykh kompozicionnykh materialov*. Naukova Dumka, Kiev (1980)
- Kilchinsky, A.A.: On a model for determining the thermoelastic characteristics of materials reinforced by fibers. *Prikladnaya Mekhanika* **1**(12), 65–74 (1965)
- Kollar, L.P., Springer, G.S.: *Mechanics of Composite Structures*. Cambridge University Press, Cambridge (2003)
- Kryshchuk, M.G., Maslei, V.M., Shukayev, S.M., Lavendels, J.: The dimensional stability assessment of the composite honeycomb panel for the conditions of thermal and gravitational loading in a Near-Earth Orbit. *Mech. Adv. Technol.* **86**(2), 130–137 (2019)
- Kucher, M.K., Zarazovskii, M.M.: Otsinka mitsnosti sharuvatych plastykiv iz vrachuvannjam degradatsii mekhanichnykh haracterystyk v protsesi deformuvannya (in Ukrainian). (Estimation of Strength of Laminates of Plastics With Treatment of Degradation of Mechanical Characteristics in The Process of Deformation), No. 57, pp. 174–179. *Visnyk NTUU «KPI» Mashynobuduvannya* (2009)
- Lepikhin, P.P., Romashchenko, V.A.: Methods and findings of stress-strain state and strength analyses of multilayer thick-walled anisotropic cylinders under dynamic loading (Review). Part 3. Phenomenological strength criteria. *Streng. Mater.* **45**(3), 271–283 (2013)
- Manne, P.M., Henriksen, T.K.: Composites failure criteria for industrial applications. In: *Proceedings European Conference on Spacecraft Structures, Materials and Mechanical Testing*, pp. 371–376. Braunschweig, Germany, (ESA SP-428) (1998)
- Maslei, V.N., Rudakov, K.N.: To definition of elasticity modules of plate from unidirectional highmodules carbon fiber. *Mech. Adv. Technol.* **87**(3), 7–15 (2019)
- Maslei, V.N., Krishchuk, N.G., Tsybenko, A.S.: Analysis of harmonic vibration characteristics for a composite honeycomb panel of the spacecraft scanner. *Strength Mater.* **50**(4), 655–664 (2018)
- Mises, R.V.: *Mechanik der festen Körper im plastisch-deformablen Zustand*. Nachrichten von der Gesellschaft der Wissenschaften zu Göttingen, Mathematisch-Physikalische Klasse 582–592 (1913)
- Paepegem, W.V., Degrieck, J.: Calculation of damage-dependent directional failure indices from the Tsai-Wu Static failure criterion. *Compos. Sci. Technol.* **63**(2), 305–310 (2003)
- Reddy, J.N., Pandey, A.K.: A first-ply failure analysis of composite laminates. *Comput. Struct.* **25**(3), 371–393 (1987)
- Rubashevskiy, V.V., Shukayev, S.M.: Estimation of limit state for quasi-isotropic $[90^\circ/\pm 45^\circ/0^\circ]$ AS4/3501-6 carbon/epoxy under uniaxial and biaxial loads. *Mech. Adv. Technol.* **86**(2), 7–13 (2019)
- Rubashevskiy, V.V., Shukayev, S.M.: Stress-Strain state of the honeycomb panel with carbon fiber reinforced polymer facings under its own weight. In: *Materials of the XX International Scientific and Technical Conference “Progressive engineering, technology and engineering education*. Kyiv-Kherson, pp. 11–14 (2019)

- Rubashevskiy, V.V., Zarazovskii, M.M., Shukayev, S.M.: Analysis of methods for determination of the constants of elasticity unidirectional layer composite materials. *Mech. Adv. Technol.* **80**(2), 107–112 (2017)
- Sleight, D.W.: *Progressive Failure Analysis Methodology for Laminated Composite Structures*. NASA/TR-1999-209107 (1999)
- Soden, P.D., Hinton, M.J., Kaddour, A.S.: Biaxial test results for strength and deformation of a range of E-glass and carbon fiber reinforced composite laminates: failure exercise benchmark data. *Compos. Sci. Technol.* **62**(12–13), 1489–1514 (2002)
- Tsai, S.W., Hahn, H.T.: Failure analysis of composite materials inelastic behavior of composite materials. *ASME AMD* **13**, 73–96 (1975)
- Tsai, S.W., Hahn, H.T.: *Introduction to Composite Materials*. Lancaster, Technomic (1980)
- Tsai, S.W., Wu, E.M.: A general theory of strength for anisotropic materials. *J. Compos. Mater.* **5**(1), 58–80 (1971)
- Vanin, G.: *Mikromekhanika kompozicionnykh materialov* (in Russ., *Micromechanics of Composite Materials*). Naukova Dumka, Kiev (1985)
- Wu, E.M.: Phenomenological Anisotropic Failure Criterion, Part 2 Composite Materials. In: Sendekyj, G.P. (ed) *Mechanics of Composite Materials*, pp. 353–431. Academic Press (1974)
- Yang, W.H.: A Generalized von Mises criterion for yield and fracture. *Trans. ASME. J. Appl. Mech.* **47**(2), 297–300 (1980)

Chapter 4

Nonlinear Dynamic Analysis of FGM Sandwich Shallow Shells with Variable Thickness of Layers



Lidiya Kurpa, Tetyana Shmatko, and Galina Timchenko

Abstract This paper considers the application of the R-functions method to a new class of problems: the study of vibrations of sandwich FGM shallow shells with variable thickness of layers and complex shape. The core is fabricated of FGM, and the face sheets are made of metal. Mathematical formulation of the problem has been done in the framework of the refined shear deformation theory of the first order. To calculate the effective characteristics of the material, Voigt's law was applied. Analytical expressions have been obtained for coefficients depended on thickness. These coefficients are to calculate the stress and moment resultants. Comparisons of the obtained results with known ones for a special case (bi-layered object) are carried out. Dynamic analysis is fulfilled for the shells and plates with parabolic thickness of layers and different constituent materials of FGM. Effect of materials and layers thickness on the natural frequencies and backbone curves of the shells is shown.

Keywords R-functions theory · Complex plan form · Timoshenko's theory · FGM · Sandwich shallow shell · Free nonlinear vibrations · Variable thickness of layers

4.1 Introduction

Sandwich plates and shells are widely employed in many industries: aerospace, satellite, industrial construction, medicine, internal combustion engines and others. The manufacture of modern sandwich structures is often carried out from new advanced

L. Kurpa (✉) · G. Timchenko

Department of Applied Mathematics, National Technical University "Kharkiv Polytechnic Institute", Kharkiv 61002, Ukraine
e-mail: kurpalidia@gmail.com

G. Timchenko

e-mail: gntimchenko2000@gmail.com

T. Shmatko

Department of Higher Mathematics, National Technical University "Kharkiv Polytechnic Institute", Kharkiv 61002, Ukraine
e-mail: ktv_ua@yahoo.com

composite materials, called as functionally graded materials (FGM). It is connected with the following reasons. These materials provide lightness and strength of the construction and restrain a sharp change in the mechanical properties of the layers. Therefore, they prevent stress concentration, destruction and delamination of layers. Due to these reasons, the study of the static and dynamic behavior of FGM structures draws an attention of many researchers since the issue of FGM structures calculation is among the most important problems of modern mechanics. A huge number of works devoted to this problem and, in particular, to vibration of the sandwich plates and shells is known (Alijani and Amabili 2014; Swaminathan et al. 2015; Thai et al. 2014; Zenkour 2005; Bennoun et al. 2016; Li et al. 2008, Malekzaden and Ghaedsharaf 2014). New theory and models were developed (Thai et al. 2014; Bennoun et al. 2016) to study a nonlinear vibration of FG sandwich plates and shells. Recently, Birman and Kardomateas (2018) have been made a current analysis in research of sandwich FGM structures. Thai and Kim (2015) made a comprehensive analysis of different theories for studying FGM plates and shells. Authors analyze the theories used widely in the modeling FGM plates and shells: the classical plate theory, first- and higher-order shear deformation theories, simplified and mixed theories, which are equivalent to single-layer theories. The work of Thai et al. 2017 is devoted to wide-ranging review on the development of higher-order continuum models in predicting the behavior of small-scale structures. In particular, the finite element solutions for size-dependent analysis of beams and plates were also developed. Great interest for many modern engineering FGM sandwich structures leads to the development of new theories (Arshid et al. 2020). For example, in Arshid et al. (2020), the vibrational behavior of rectangular micro-scale sandwich plates resting on a visco-Pasternak foundation is studied by a novel quasi-3D hyperbolic shear deformation theory.

It should be noted that number of papers devoted to research of the nonlinear vibration of FGM sandwich shells with variable thickness is limited enough. Some reviewer of these works was presented in Tornabe et al. (2017). The authors employed several higher-order shear deformation theories, defined by a unified formulation in order to study FGM sandwich shell structures with variable thickness. The generalized differential quadrature method is used as numerical tool. Due to developed approach, the structural models can be considered as two-dimensional ones. It is one of the advantages of the proposed method.

Awrejcewicz et al. (2013) analyze geometrically nonlinear vibrations of single-layer shallow shells of variable thickness and complex shape using the R-functions theory (Rvachev 1982) and variational methods (RFM). The mathematical formulation of the problem is carried out within the framework of the classical theory. A distinctive feature of the proposed approach was also an original construction of approximate solutions to the nonlinear problem. Later in Awrejcewicz et al. (2015), Kurpa and Shmatko (2014), this approach was developed for multilayer shallow shells, provided that the layers had a variable thickness, but the total thickness was constant. The mathematical formulation is based on the first-order shear deformation theory of the shallow shells. These works have shown that this approach allows to study the dynamic behavior of shallow shells with an arbitrary shape of their plans and various types of boundary conditions.

In this article, we consider the issue of geometrically nonlinear vibrations of the FGM sandwich shallow shells, provided that the FGM core has a variable thickness. The method proposed in Awrejcewicz et al. (2015, Kurpa and Shmatko (2014), Kurpa et al. (2018), Awrejcewicz et al. 2018 is generalized to solve the problem under consideration. Software has been developed to implement RFM for the problem. Numerical results are presented for shallow shells with square and complex planform for parabolic law of changing layers thickness. Effect of the different parameter (gradient index, type of FGM, boundary conditions and others) on dynamic behavior of the structures is shown.

4.2 Formulation Problem

Consider a three-layered shallow shell with variable thickness of layers if total thickness is constant. Assume that face-sheet layers are made of metal and core is made of functionally graded materials. The layers are symmetric relative to the middle plane as it is shown in Fig. 4.1a and b. The functionally graded layer is made from a mixture of two phases (metal and ceramics). The effective material properties of the FGMs are calculated by power law (Voigt’s model). According to this model, elastic modulus E , Poisson’s ratio ν and the density ρ of the composite are defined by the following relations

$$E = (E_c - E_m)V_c + E_m, \quad \nu = (\nu_c - \nu_m)V_c + \nu_m, \quad \rho = (\rho_c - \rho_m)V_c + \rho_m. \tag{4.1}$$

Here, E_c, ν_c, ρ_c are elastic modulus, Poisson’s ratio and the density of ceramics relatively; E_m, ν_m, ρ_m are corresponding characteristics of metal. Fraction of ceramic V_c and metal phases V_m are related by formula

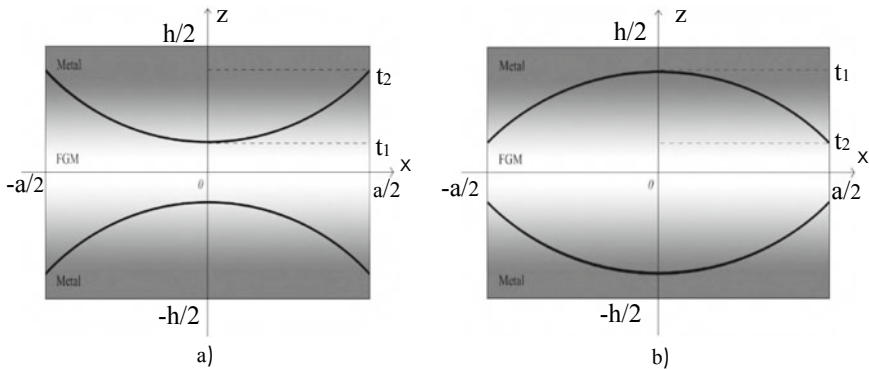


Fig. 4.1 Material variation along the thickness of FGM plate

$$V_c + V_m = 1. \quad (4.2)$$

Take into account that thickness of FGM layers changes symmetrically relative to the middle surface, let us present the expressions V_c for the given case:

$$\begin{cases} V_c = 0, & z \in \left[-\frac{h}{2}, -h_1(x, y)\right], \\ V_c = \left(\frac{z+h_1(x, y)}{h_1(x, y)}\right)^p, & z \in [-h_1(x, y), 0], \\ V_c = \left(\frac{h_1(x, y)-z}{h_1(x, y)}\right)^p, & z \in [0, h_1(x, y)], \\ V_c = 0, & z \in \left[h_1(x, y), \frac{h}{2}\right]. \end{cases} \quad (4.3)$$

In formula (4.3), index $p(0 \leq p < \infty)$ denotes the volume fraction exponent (gradient index), z is the distance between a current point and the shell mid-surface. Note that if $h_1(x, y) = h/2$, then we have so-called bi-layered object.

Solution of the problem is carried out within the first-order shear deformation theory of shallow shells (FSDT).

According to this theory, the displacements components u_1, u_2, u_3 at a point (x, y, z) are expressed as functions of the middle surface displacements u, v and w in the Ox, Oy and Oz directions and the independent rotations ψ_x, ψ_y of the transverse normal to middle surface about the Oy and Ox axes, respectively (Zenkour 2005, Bennoun et al. 2016, Li et al. 2008, Malekzaden and Ghaedsharaf 2014):

$$u_1 = u + z\psi_x, \quad u_2 = v + z\psi_y, \quad u_3 = w.$$

Strain components $\varepsilon = \{\varepsilon_{11}; \varepsilon_{22}; \varepsilon_{12}\}^T$, $\chi = \{\chi_{11}; \chi_{22}; \chi_{12}\}^T$ and $\gamma = \{\gamma_{yz}; \gamma_{xz}\}^T$, an arbitrary point of the shallow shell are:

$$\varepsilon = \begin{Bmatrix} \varepsilon_{11} \\ \varepsilon_{22} \\ \varepsilon_{12} \end{Bmatrix} = \begin{Bmatrix} u_{,x} + \frac{w}{R_x} + \frac{1}{2}w_{,x}^2 \\ v_{,y} + \frac{w}{R_y} + \frac{1}{2}w_{,y}^2 \\ u_{,y} + v_{,x} + w_{,x}w_{,y} \end{Bmatrix}, \quad \chi = \begin{Bmatrix} \chi_{11} \\ \chi_{22} \\ \chi_{12} \end{Bmatrix} = \begin{Bmatrix} \psi_{x'x} \\ \psi_{y'y} \\ \psi_{x'y} + \psi_{y'x} \end{Bmatrix},$$

$$\gamma = \begin{Bmatrix} \gamma_{yz} \\ \gamma_{xz} \end{Bmatrix} = \begin{Bmatrix} \psi_y + w_{,y} - \frac{v}{R_y} \\ \psi_x + w_{,x} - \frac{u}{R_x} \end{Bmatrix}.$$

In-plane force resultant vector $N = (N_{11}, N_{22}, N_{12})^T$, bending and twisting moments resultant vector $M = (M_{11}, M_{22}, M_{12})^T$ and transverse shear force resultant $Q = (Q_x, Q_y)^T$ are calculated by integration along the Oz -axes and defined as:

$$\begin{aligned} N &= [A]\{\varepsilon\} + [B]\{\chi\}, \\ M &= [B]\{\varepsilon\} + [D]\{\chi\}, \end{aligned} \quad (4.5)$$

where

$$\begin{aligned}
[A] &= \begin{bmatrix} A_{11} & A_{12} & 0 \\ A_{12} & A_{22} & 0 \\ 0 & 0 & A_{33} \end{bmatrix}, \\
[B] &= \begin{bmatrix} B_{11} & B_{12} & 0 \\ B_{12} & B_{22} & 0 \\ 0 & 0 & B_{33} \end{bmatrix}, \\
[D] &= \begin{bmatrix} D_{11} & D_{12} & 0 \\ D_{12} & D_{22} & 0 \\ 0 & 0 & D_{33} \end{bmatrix}.
\end{aligned} \tag{4.6}$$

Elements A_{ij} , B_{ij} , D_{ij} of the square matrices A , B and D in relations (4.5, 4.6) are calculated by formulas:

$$\begin{aligned}
A_{ij} &= \sum_{r=1}^3 \int_{z_r}^{z_{r+1}} Q_{ij}^{(r)} dz, \\
B_{ij} &= \sum_{r=1}^3 \int_{z_r}^{z_{r+1}} Q_{ij}^{(r)} z dz, \\
D_{ij} &= \sum_{r=1}^3 \int_{z_r}^{z_{r+1}} Q_{ij}^{(r)} z^2 dz,
\end{aligned} \tag{4.7}$$

where $z_1 = -h/2$, $z_2 = -h_1(x, y)$, $z_3 = h_1(x, y)$, $z_4 = h/2$, $r = 1, 2, 3$ define a number of the layers. Values $Q_{ij}^{(r)}$ ($i, j = 1, 2, 3$) in formulas (4.7) are determined by the following expressions:

$$Q_{11}^{(r)} = Q_{22}^{(r)} = \frac{E^{(r)}}{1 - (\nu^{(r)})^2}, \quad Q_{12}^{(r)} = \frac{\nu^{(r)} E^{(r)}}{1 - (\nu^{(r)})^2}, \quad Q_{66}^{(r)} = \frac{E^{(r)}}{2(1 + \nu^{(r)})}. \tag{4.8}$$

Transverse shear force resultants Q_x , Q_y are defined as:

$$Q_x = K_s^2 A_{33} \gamma_{xz}, \quad Q_y = K_s^2 A_{33} \gamma_{yz}, \tag{4.9}$$

where K_s^2 denotes the shear correction factor. In this paper, it is taken by 5/6.

Further, we will consider materials with the same Poisson's ratio for ceramics and metal, i.e., $\nu_m = \nu_c$. Then, elements A_{ij} , B_{ij} , D_{ij} of matrices (6) $[A]$, $[B]$, $[C]$ can be calculated in a direct way. Analytical expressions of these elements for shells with variable thickness of layers are obtained and presented below

$$A_{11} = \frac{1}{1 - \nu^2} \left(E_m h + 2E_{cm} \frac{h_1(x, y)}{p + 1} \right), \quad B_{11} = 0,$$

$$D_{11} = \frac{1}{1-\nu^2} \left(\frac{E_m}{12} h^3 + 2E_{cm} h_1^3(x, y) \left(\frac{1}{p+1} - \frac{2}{p+2} + \frac{1}{p+3} \right) \right), \quad (4.10)$$

where E_{cm} denotes the difference between E_c , E_m , that is,

$$E_{cm} = E_c - E_m.$$

Note that values

$$\{A_{22}, B_{22}, D_{22}\} = \{A_{11}, B_{11}, D_{11}\}, \quad (4.11)$$

and values A_{12} , A_{66} , B_{12} , B_{66} , D_{12} , D_{66} are defined as:

$$\begin{aligned} \{A_{12}, B_{12}, D_{12}\} &= v\{A_{11}, B_{11}, D_{11}\}, \\ \{A_{66}, B_{66}, D_{66}\} &= \frac{1-\nu}{2}\{A_{11}, B_{11}, D_{11}\}. \end{aligned} \quad (4.12)$$

The governing differential motion equations for a free vibration of shear deformable shallow shell can be presented as

$$\begin{aligned} \frac{\partial N_{11}}{\partial x} + \frac{\partial N_{12}}{\partial y} - \frac{Q_x}{R_x} &= I_0 \frac{\partial^2 u}{\partial t^2} + I_1 \frac{\partial^2 \psi_x}{\partial t^2}; \\ \frac{\partial N_{22}}{\partial y} + \frac{\partial N_{12}}{\partial x} - \frac{Q_y}{R_y} &= I_0 \frac{\partial^2 v}{\partial t^2} + I_1 \frac{\partial^2 \psi_y}{\partial t^2}; \\ \frac{\partial Q_x}{\partial x} + \frac{\partial Q_y}{\partial y} + \frac{N_{11}}{R_x} + \frac{N_{22}}{R_y} + N_{11} \frac{\partial^2 w}{\partial x^2} \\ + 2N_{12} \frac{\partial^2 w}{\partial x \partial y} + N_{22} \frac{\partial^2 w}{\partial y^2} &= I_0 \frac{\partial^2 w}{\partial t^2}; \end{aligned} \quad (4.13)$$

$$\begin{aligned} \frac{\partial M_{11}}{\partial x} + \frac{\partial M_{12}}{\partial y} - Q_x &= I_2 \frac{\partial^2 \psi_x}{\partial t^2} + I_1 \frac{\partial^2 u}{\partial t^2}; \\ \frac{\partial M_{22}}{\partial y} + \frac{\partial M_{12}}{\partial x} - Q_y &= I_2 \frac{\partial^2 \psi_y}{\partial t^2} + I_1 \frac{\partial^2 v}{\partial t^2}, \end{aligned}$$

where

$$(I_0, I_1, I_2) = \sum_{r=1}^3 \int_{z_r}^{z_{r+1}} (\rho)_r (1, z, z^2) dz, \quad (4.14)$$

here $(\rho)_r$ is a mass density of the r th layer.

Analytical expressions of coefficients I_0, I_1, I_2 for shells provided that $v_m = v_c$ are presented below.

$$I_0 = \rho_m h + 2\rho_{cm} \frac{h_1(x, y)}{p+1}, \quad \rho_{cm} = \rho_c - \rho_m,$$

$$I_1 = 0, \quad I_2 = \frac{\rho_m}{12} h^3 + 2\rho_{cm} h_1^3(x, y) \left(\frac{1}{p+1} - \frac{2}{p+2} + \frac{1}{p+3} \right). \quad (4.15)$$

4.3 Solution Method—Free Vibration Problem

To solve the formulated problem, we apply a variational method combined with the R-functions theory (RFM methods). Let us indicate the main steps of developed approach. First, we solve the linear vibration problem, applying Ritz's method in order to find eigenfunctions. Solution of the linear vibration problem for laminated shells by RFM is described in works (Awrejcewicz et al. 2013, 2015, 2018; Rvachev 1982; Kurpa and Shmatko 2014; Kurpa et al. 2018, 2007). The main difference of the considered problem is dependence of the elements A_{ij}, B_{ij}, D_{ij} on matrices (6) $[A], [B], [C]$ of variables x and y . But due to an application of Ritz's method, the variational formulation of the linear problem is formally the same and is reduced to finding the minimum of the total energy functional

$$J = U_s - T, \quad (4.16)$$

here, strain energy U_s can be written as

$$U_s = \frac{1}{2} \int_{\Omega} N_s^T \varepsilon_s d\Omega, \quad (4.17)$$

where $N_s^T = \{N, M, \gamma\}$, $\varepsilon_s^T = \{\varepsilon, \chi, \gamma\}$.

Kinetic energy T in (16) is defined as

$$T = \frac{1}{2} \int_{\Omega} I_0(\dot{u}^2 + \dot{v}^2 + \dot{w}^2) + 2I_1(\dot{u}\dot{\psi}_x + \dot{v}\dot{\psi}_y) I_2(\dot{\psi}_x^2 + \dot{\psi}_y^2) d\Omega,$$

$$I = U(u, v, w, \psi_x, \psi_y) - \lambda^2 V(u, v, w, \psi_x, \psi_y), \quad (4.18)$$

where λ is a vibration frequency.

Now the expressions for U and V in Eq. (4.16) are defined by relations:

$$U = \frac{1}{2} \iint_{\Omega} N_s^T \varepsilon_s dx dy, \quad (4.19)$$

$$V = \frac{1}{2} \iint_{\Omega} I_0(u^2 + v^2 + w^2) + 2I_1(u\psi_x + v\psi_y) + I_2(\psi_x^2 + \psi_y^2) dx dy. \quad (4.20)$$

According to Ritz' approach, unknown functions are presented as

$$\begin{aligned} u &= \sum_{i=1}^{N_1} a_i u_i, & v &= \sum_{i=N_1+1}^{N_2} a_i v_i, & w &= \sum_{i=N_2+1}^{N_3} a_i u_i, \\ \psi_x &= \sum_{i=N_3+1}^{N_4} a_i \psi_{xi}, & \psi_y &= \sum_{i=N_4+1}^{N_5} a_i \psi_{yi}. \end{aligned} \quad (4.21)$$

Here, $\{u_i\}$, $\{v_i\}$, $\{w_i\}$, $\{\psi_{xi}\}$, $\{\psi_{yi}\}$ are admissible functions that in case of a complex shape can be constructed by the R-functions theory (Rvachev 1982).

Coefficients of this expansion $\{a_i\}$, $i = \overline{1, N_5}$ is found from Ritz's system

$$\frac{\partial I}{\partial a_i} = 0, \quad i = \overline{1, N_5}.$$

To solve the nonlinear problem, the approach proposed by authors earlier and described in detail in (Awrejcewicz et al. 2015, 2018; Kurpa and Shmatko 2014; Kurpa et al. 2018) is used. Note that the obtained nonlinear differential equations of the second order are solved by Runge–Kutta method of the 7–8-th order.

4.4 Numerical Results

To verify an accuracy of the present results obtained by the proposed approach, we consider the solution of several test problems.

Problem 1 Simply supported square FG bi-layered plates are considered. The following material properties for metal and ceramic constituents are used (Li et al. 2008, Malekzaden and Ghaedsharaf 2014):

$$\begin{aligned} E_m &= 70 \text{ GPa}, E_c = 380 \text{ GPa}, \rho_m = 2707 \text{ kg/m}^3, \\ \rho_c &= 3800 \text{ kg/m}^3, \nu_m = 0.3, \nu_c = 0.3. \end{aligned}$$

Table 4.1 Comparison of non-dimensional natural frequency of square FGM plate

h/a	Method	$p = 0$	$p = 0.5$	$p = 1$	$p = 5$	$p = 10$
0.01	Present	1.8885	1.4827	1.2718	0.9658	0.9506
	Li et al. (2008)	1.888.3	1.4824	1.2716	0.9656	0.9504
	Malekzaden and Ghaedsharaf (2014)	1.8882	1.4826	1.2716	0.9657	0.9505
0.1	Present	1.8244	1.4416	1.2403	0.9425	0.9251
	Li et al. (2008)	1.8268	1.4461	1.2447	0.9448	0.9273
	Malekzaden and Ghaedsharaf (2014)	1.8268	1.4462	1.2447	0.9443	0.9258
0.2	Present	1.6697	1.3395	1.1606	0.8835	0.8613
	Li et al. (2008)	1.6771	1.3536	1.1749	1.8909	0.8637
	Malekzaden and Ghaedsharaf (2014)	1.6772	1.3536	1.1748	0.8894	0.8683

Comparison of non-dimensional natural frequency parameter $\Lambda = a^2\omega/h$ for different thickness-to-length ratio h/a , and material graded index (p) is shown in Table 4.1.

Table 4.1 shows that results presented in Li et al. (2008), Malekzaden and Ghaedsharaf (2014) are in a good agreement with the obtained results.

Problem 2 Consider a three layer rectangular plate with layers of the variable thickness (Fig. 4.1). Layers arrangement is symmetric about the middle plane. The thickness of the middle layer (core) is varied.

$$h_1(x) = -\left(t_1 + \frac{4}{a^2}(t_2 - t_1)x^2\right), \quad h_2(x) = -h_1(x). \tag{4.22}$$

If $t_2 > t_1$, then middle layer has a form, as shown in Fig. 4.1a. If $t_2 < t_1$, then form of the core is presented in Fig. 4.1b. If $t_1 = t_2$, then we have three-layered plate with layers of constant thickness. But if $t_1 = t_2 = \frac{h}{2}$ types, then plate is bi-layered. There are studied all cases in the paper. Three of FGMs for a core are considered: M1 is a mixture of Al/ZrO₂; M2 is a mixture of Si₃N₄/SUS304; M3 is a mixture of Al₂O₃/Al.

Mechanical properties of the constituent materials of the mixtures are taken from Alijani and Amabili (2014), Swaminathan et al. (2015) and presented in Table 4.2.

where $E_0 = 1 \text{ GPa}$, $\rho_0 = 1 \text{ kg/m}^3$.

Table 4.2 Mechanical properties of the constituent materials

Material	E	ν	ρ
Al	$70E_0$	0.3	$2707\rho_0$
Al ₂ O ₃	$389E_0$	0.3	$3800\rho_0$
Si ₃ N ₄	$322.27E_0$	0.3	$2370\rho_0$
SUS304	$207.78E_0$	0.3	$8166\rho_0$
ZrO ₂	$200E_0$	0.3	$5700\rho_0$

Suppose that rectangular plate is clamped or simply supported along a whole border. Introduce the geometrical parameters $\alpha = \frac{2t_1}{h}$; $\beta = \frac{2t_2}{h}$. Let these parameters and ratio $\frac{a}{b}$ be varied, but the total thickness is constant and is equal to $\frac{h}{2a} = 0.1$. Two types of FGMs are taken $\text{Al}_2\text{O}_3/\text{Al}$ and $\text{Si}_3\text{N}_4/\text{SUS304}$.

Non-dimensional parameters of the natural frequency are defined as:

$$\Lambda = a^2\omega\sqrt{\frac{\rho_c}{E_c}}/h. \tag{4.23}$$

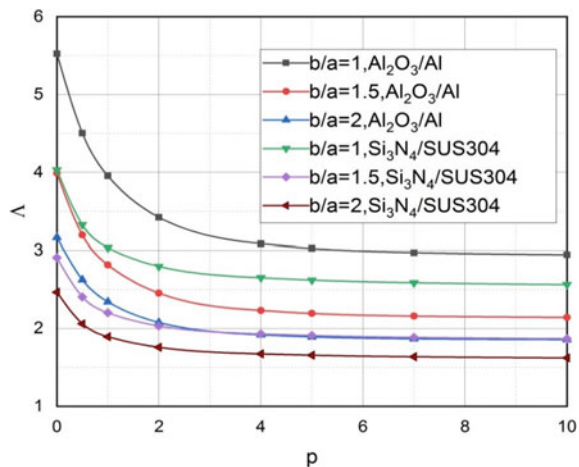
Table 4.3 shows the results of non-dimensional fundamental frequency parameter for clamped rectangular sandwich plates with FGM core of the variable thickness.

Figure 4.2 depicts the fundamental frequencies parameters for different values of

Table 4.3 Effect of gradient index p on non-dimensional natural frequency of clamped rectangular plates ($\alpha = 0.4, \beta = 0.8, \text{Fig. 4.1a}$)

p	$\text{Al}_2\text{O}_3/\text{Al}$			$\text{Si}_3\text{N}_4/\text{SUS304}$		
	$\frac{b}{a} = 1$	$\frac{b}{a} = 1.5$	$\frac{b}{a} = 2$	$\frac{b}{a} = 1$	$\frac{b}{a} = 1.5$	$\frac{b}{a} = 2$
0	9.3482	8,2697	7.9771	6.7077	5.5478	5.2322
0.5	7,7944	6.735	6.4543	5.6455	4.5442	4.2421
1	6.9428	5.8783	5.5904	5.1821	4.1033	3.8057
2	6.0741	4.9744	4.6754	4.7819	3.7321	3.4291
4	5.4466	4.2989	3.9832	4.5269	3.4871	3.1970
5	5.3197	4.1599	3.8396	4.4744	3.4404	3.1316
7	5.1903	4.0183	3.6931	4.4154	3.3893	3.1025
10	5,1132	3.9353	3.6075	4.3723	3.3523	3.0683

Fig. 4.2 Effect of gradient index p on non-dimensional natural frequency (23) for simply supported rectangular plates ($\alpha = 0.4, \beta = 0.8$)



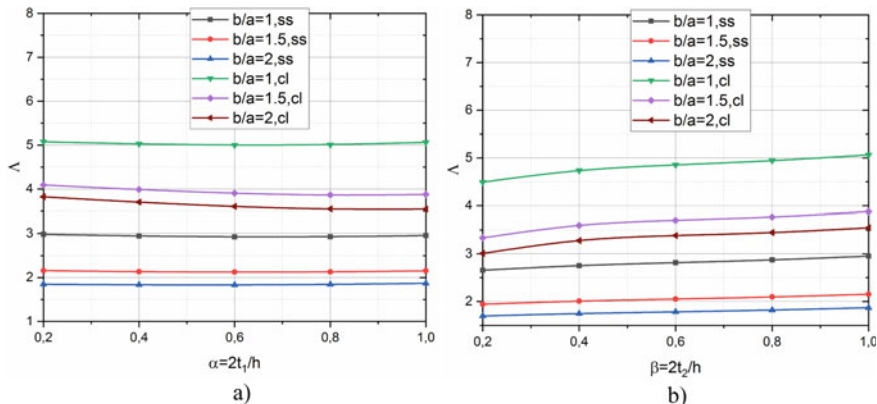


Fig. 4.3 Effect of parameters $\alpha = \frac{2t_1}{h}$, $\beta = 1$ (Fig. 4.3a) and parameters $\beta = \frac{2t_2}{h}$, $\alpha = 1$ (Fig. 4.3b) on non-dimensional natural frequency of rectangular plates (FGM is $\text{Si}_3\text{N}_4/\text{SUS304}$)

gradient index p of two types of FGM simply supported sandwich rectangular plates for values $\alpha = 0.4$, $\beta = 0.8$ and different ratios a/b .

Effect of parameters α and β on behavior of the non-dimensional fundamental frequencies is shown in Fig. 4.3.

Note that for different ratio $\frac{b}{a}$ the frequencies are changing slightly, when the parameters α and β vary from 0.2 to 1.

Problem 3 Vibration of the shallow shells with a complex planform. Let us consider the FGM sandwich shallow shells with a complex planform are shown in Fig. 4.4. Assume that thickness of layers is varied by parabolic law according to Eq. (4.22).

To construct a system of admissible functions, let us use the R-functions theory. Equation of the border is $\omega(x, y) = 0$. For the given domain function, $\omega(x, y)$ can be constructed as:

$$\begin{aligned} \omega(x, y) &= (f_1 \wedge_0 f_2) \wedge_0 (f_3 \vee_0 f_4) \wedge_0 (f_5 \vee_0 f_6), \\ f_1 &= (a^2 - x^2)/2a, \quad f_2 = (b^2 - y^2)/2b, \\ f_3 &= (b_1 - y) \geq 0; \quad f_4 = (a_1 - x) \geq 0; \\ f_5 &= (b_2 - y) \geq 0; \quad f_6 = (a_2 - x) \geq 0. \end{aligned}$$

The signs \wedge_0 and \vee_0 define the R-operators: R-conjunction and R-disjunction relatively (Rvachev 1982). So, we have

$$f_1 \wedge_0 f_2 = f_1 + f_2 - \sqrt{f_1^2 + f_2^2},$$

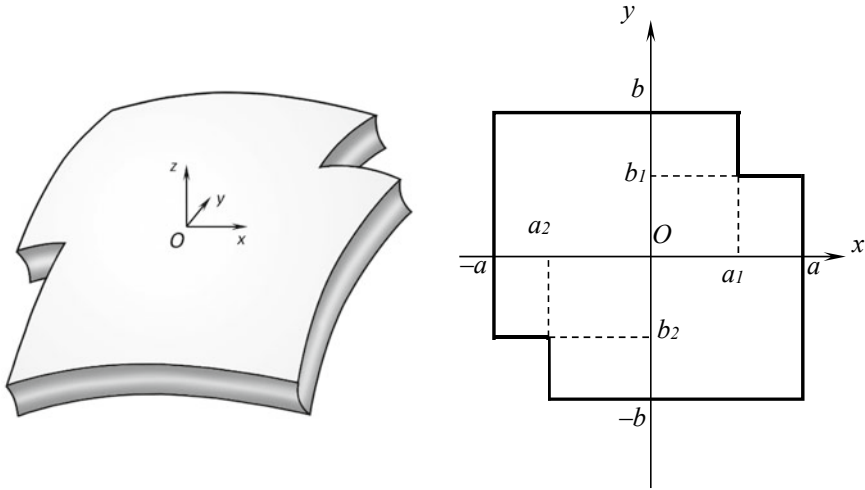


Fig. 4.4 Sandwich shallow shell and its planform

$$f_3 \vee_0 f_4 = f_1 + f_2 + \sqrt{f_1^2 + f_2^2}.$$

For clamped shells, the system of admissible functions can be chosen in the following form:

$$\begin{aligned} u_k &= \omega(x, y)\phi_k^{(u)}, k = \overline{1, N_1}, \\ v_k &= \omega(x, y)\phi_k^{(v)}, k = \overline{N_1 + 1, N_2}, \\ w_k &= \omega(x, y)\phi_k^{(w)}, k = \overline{N_2 + 1, N_3}, \\ \psi_{xk} &= \omega(x, y)\phi_k^{(\psi_x)}, k = \overline{N_3 + 1, N_4}, \\ \psi_{yk} &= \omega(x, y)\phi_k^{(\psi_y)}, k = \overline{N_4 + 1, N_5}, \end{aligned}$$

where $\phi_k^{(r)}$, $r = u, v, w, \psi_x, \psi_y$ are terms of some complete system functions Φ_i , $i = 1, 2, 3, 4, 5$. System of power polynomials is taken for the given problem. Geometrical parameters for shell are put as:

$$\begin{aligned} \frac{h}{2a} &= 0.1; \frac{b}{a} = 1, \frac{a_1}{2a} = 0.3; \frac{b_1}{2a} = 0.25; \frac{a_2}{2a} = -0.3; \\ \frac{b_2}{2a} &= -0.25; k_1 = \frac{2a}{R_x} = 0.1; k_2 = \frac{2a}{R_y} = 0.1. \end{aligned}$$

Parameters $\alpha = \frac{2t_1}{h}, \beta = \frac{2t_2}{h}$ and gradient index p vary. Non-dimensional parameters of the natural frequency are defined as:

$$\Lambda = (2a)^2 \omega \sqrt{\frac{\rho_c}{E_c}} / h. \tag{4.24}$$

Table 4.4 shows the influence of the gradient index on linear frequencies of the clamped plates and spherical shells for parabolic law (see Fig. 4.1a).

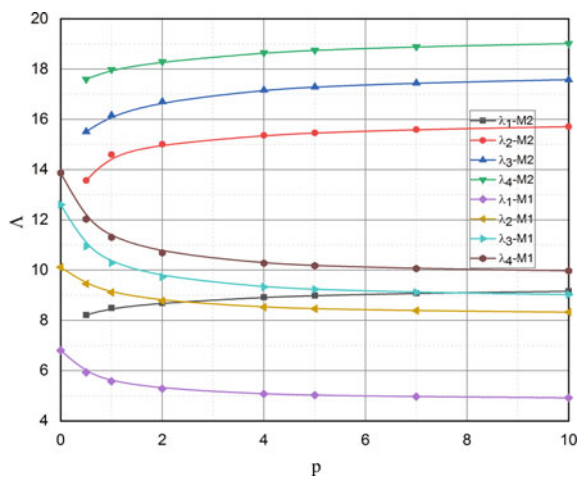
All natural frequencies $\Lambda_i (i = 1, 2, 3, 4)$ are decreasing when gradient index p increases. The difference between frequencies of the plate and shallow spherical shell is not essential. It may be explained by boundary conditions and small curvatures of the shell.

Effect of the gradient index on the first four natural frequencies of the clamped spherical shells for different FGMs (M1-Al/ZrO₂ and M2-Si₃N₄/SUS304) is shown in Fig. 4.5. Parabolic law of thickness variation corresponds to Fig. 4.1b, parameters

Table 4.4 Effect of gradient index p on non-dimensional natural frequencies (24) of clamped plate and spherical shell with complex shape ($\alpha = \frac{2l_1}{h} = 0.4, \beta = \frac{2l_2}{h} = 0.8$); FGM is Si₃N₄ /SUS304

p	Plate				Spherical shell ($k_1 = k_2 = 0.1$)			
	λ_1	λ_2	λ_3	λ_4	λ_1	λ_2	λ_3	λ_4
0	7.247	12.166	13.372	15.336	7.299	12.183	13.385	15.347
0.5	6.169	10.615	11.683	12.892	6.218	10.630	11.695	12.902
1	5.704	9.886	10.827	11.843	5.751	9.900	10.839	11.852
2	5.303	9.201	10.046	10.961	5.3477	9.215	10.057	10.970
4	5.043	8.719	9.492	10.394	5.086	8.732	9.503	10.402
5	4.988	8.612	9.365	10.270	5.031	8.625	9.576	10.279
7	4.926	8.487	9.212	10.125	4.967	8.500	9.223	10.134
10	4.880	8.393	9.092	10.014	4.920	8.4055	9.102	10.022

Fig. 4.5 Effect of gradient index p on non-dimensional natural frequencies (24) for clamped spherical shell with complex shape made of different material FGMs ($\alpha = \frac{2l_1}{h} = 0.8, \beta = \frac{2l_2}{h} = 0.4$)



$$\alpha = \frac{2t_1}{h} = 0.8; \beta = \frac{2t_2}{h} = 0.4.$$

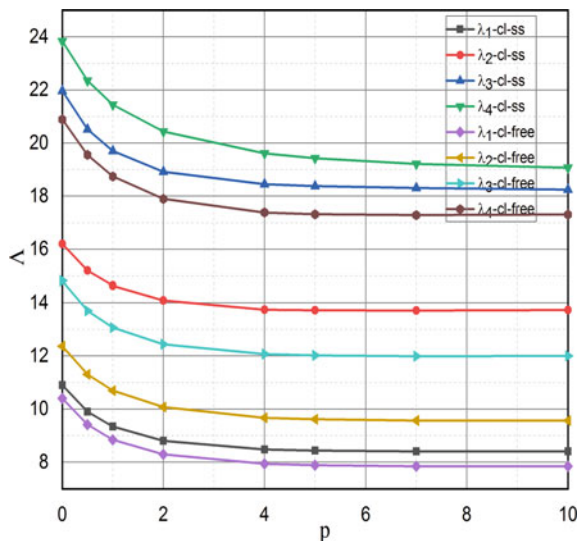
As follows from Fig. 4.5, frequencies for core made of Al/ZrO₂ (M1) are decreasing, and they are increasing for FGM Si₃N₄/SUS304 (M2) if gradient index *p* increases.

Table 4.5 and Fig. 4.6 show an influence of boundary conditions on the natural frequencies while the gradient index is increasing. Two types of the mixed boundary conditions are considered: clamped simply supported and clamped-free. It is assumed that sides $y = \pm b$ are simply supported or free and remain part of the boundary is clamped. Values parameters α, β are taken the following: $\alpha = 0.4, \beta = 0.8$, Fig. 4.1a, FGMs is Al/ZrO₂.

Table 4.5 Effect of gradient index *p* on non-dimensional natural frequency (24) of spherical shell (Fig. 4.4) and different boundary condition for FGMs Al/ZrO₂ (M1)

<i>p</i>	Clamped-simply supported				Clamped-free			
	λ_1	λ_2	λ_3	λ_4	λ_1	λ_2	λ_3	λ_4
0	10.904	16.204	21.970	23.837	10.409	12.366	14.831	20.895
0.5	9.903	15.205	20.516	22.358	9.413	11.308	13.702	19.557
1	9.347	14.646	19.702	21.452	8.851	10.698	13.069	18.744
2	8.806	14.090	18.919	20.439	8.292	10.075	12.446	17.899
4	8.483	13.746	18.454	19.615	7.943	9.676	12.076	17.386
5	8.437	13.726	18.378	19.426	7.890	9.616	12.026	17.320
7	8.405	13.716	18.305	19.213	7.851	9.573	11.999	17.290
10	8.404	13.739	18.249	19.069	7.844	9.569	12.007	17.310

Fig. 4.6 Effect of gradient index *p* on non-dimensional natural frequency parameter (24) of spherical shell (Fig. 4.4) with different boundary condition ($\alpha = \frac{2t_1}{h} = 0.4$; $\beta = \frac{2t_2}{h} = 0.8$; Fig. 4.1a)



Comparison analysis of the behavior of the natural frequency for different FGMs and mixed boundary conditions for values of parameters $\alpha = \frac{2r_1}{h} = 0.8, \beta = \frac{2r_2}{h} = 0.4$ (Fig. 4.1b) is presented in Table 4.6 and Fig. 4.7. It is observed that frequencies are essentially greater for material Al/ZrO₂ than for Si₃N₄/SUS304.

Nonlinear behavior of the sandwich FGM spherical clamped shallow shells with planform drawn in Fig. 4.4 for different FG materials was studied for two values of the parameter $\alpha, \beta \alpha = (0.4; 0.8); \beta = (0.8; 0.4)$ and two values of the gradient index $p = (0.5; 2)$. The remain geometric parameters are the same with linear problem.

In Fig. 4.8, backbone curves are presented for case $\alpha = 0.4; \beta = 0.8$ that corresponds to Fig. 4.1a. The obtained results for ratio of nonlinear frequency to linear frequency for case $\alpha = 0.8; \beta = 0.4$ corresponding to Fig. 4.1b are shown in Fig. 4.9.

Table 4.6 Effect of gradient index p on non-dimensional natural frequency parameter (24) of spherical shell with complex shape and different boundary condition made of different materials; FGM is $Si_3N_4/SUS304$ (M2) and Al/ZrO_2 (M1)

p	Clamped		Clamped-simply supported		Clamped-free	
	Si ₃ N ₄ /SUS304 λ_1	Al/ZrO ₂ λ_1	Si ₃ N ₄ /SUS304 λ_1	Al/ZrO ₂ λ_1	Si ₃ N ₄ /SUS304 λ_1	Al/ZrO ₂ λ_1
0	7.299	11.551	7.965	10.904	6.861	10.409
0.5	6.218	10.603	6.830	9.903	5.763	9.413
1	5.751	10.08 9	6.339	9.347	5.283	8.851
2	5.3477	9.605	5.909	8.806	4.865	8.292
4	5.086	9.3367	5.626	8.483	4.595	7.943
5	5.031	9.303	5.566	8.437	4.539	7.890
7	4.967	9.288	5.496	8.405	4.476	7.851
10	4.920	9.297	5.443	8.404	4.430	7.844

Fig. 4.7 Effect of gradient index p on non-dimensional natural frequency parameter (24) for spherical shell with complex shape and different boundary condition made of different FGM materials ($\alpha = \frac{2r_1}{h} = 0.8; \beta = \frac{2r_2}{h} = 0.4$)

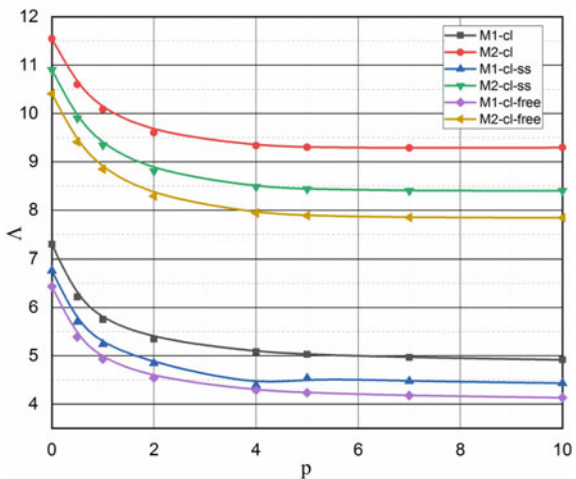


Fig. 4.8 Effect of gradient index and FGMs on nonlinear to linear frequency ratio of clamped spherical shells with variable thickness of layers defined by law (22) for values $\alpha = 0.4$; $\beta = 0.8$ and planform is shown in Fig. 4.4

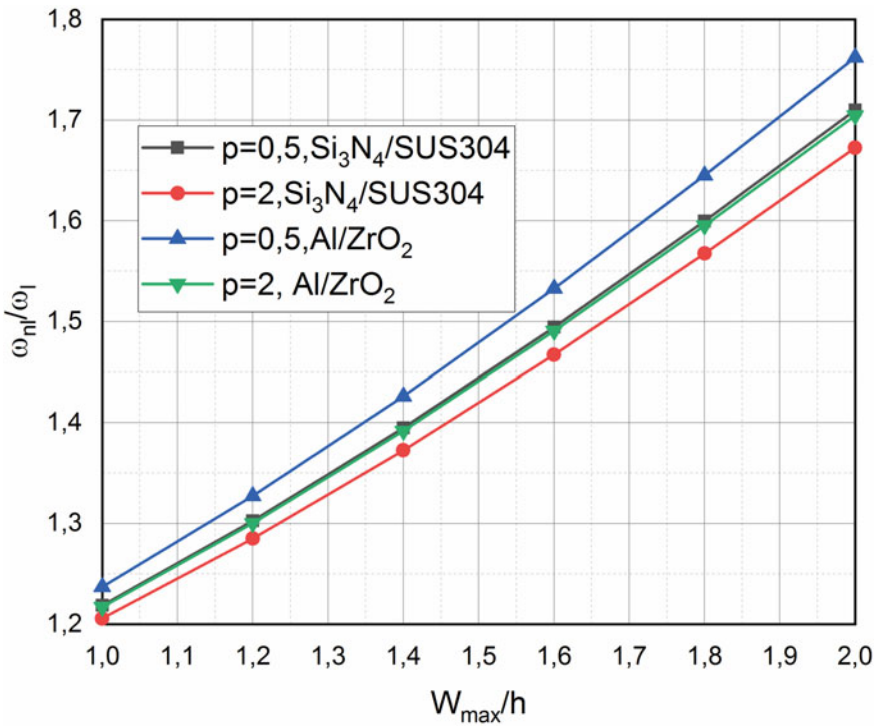
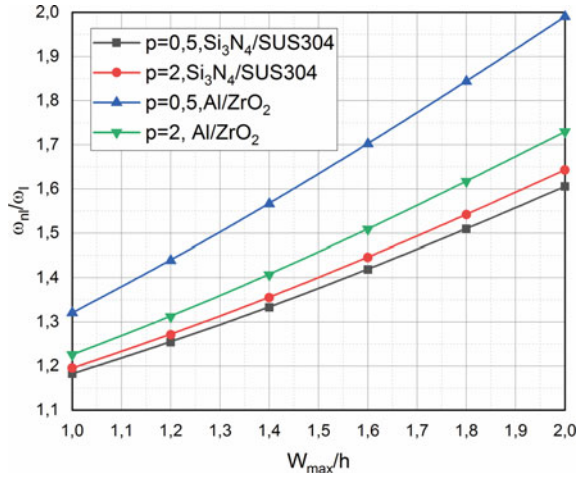


Fig. 4.9 Effect of gradient index p and FGMs on nonlinear to linear frequency ratio of clamped spherical shells with variable thickness of layers defined by law (22) for values $\alpha = 0.4$; $\beta = 0.8$ and planform is shown in Fig. 4.4

From these plots, it follows that effect on backbone curves is more essential for layers arrangement corresponding to Fig. 4.1a. The ratio $\frac{\omega_N}{\omega_L}$ for FGM Al/Zr O₂ greater than for FGM Si₃N₄/SUS304 in both the cases.

4.5 Conclusions

The linear and geometrically nonlinear free vibration of functionally graded shallow shells of sandwich type with a complex planform is investigated using the R-functions theory and variational methods. The considered shell consists of the layers of variable thickness that are symmetrical about the middle surface, but the total thickness is constant. The effective material properties are calculated according to the power law. Analytical expressions have been obtained for dependent on thickness coefficients needed for calculation of the stress and moment resultants.

The developed algorithm and corresponding software have been applied to plate and shallow shells with rectangular and complex planforms with different boundary conditions and various FGMs. As example, the parabolic law of the thickness change of layers has been considered. Effect of different parameters (form of the parabola, type of FGMs, boundary conditions, value of gradient index) on natural frequencies and response curves is shown.

References

- Alijani, F., Amabili, M.: Non-linear vibration of shells: a literature review from 2003 to 2013. *Int. J. Non-Linear Mech.* **58**, 233–257 (2014)
- Arshid, H., Khorasani, M., Soleimani-Javid, Z., Dimitri, R., Tornabene, F.: Quasi-3D hyperbolic shear deformation theory for the free vibration study of honeycomb microplates with graphene nanoplatelets-reinforced epoxy skins. *Molecules* **25**(21), 5085, (21 p.) (2020)
- Awrejcewicz, J., Kurpa, L., Shmatko, T.: Large amplitude free vibration of orthotropic shallow shells of complex form with variable thickness. *Lat. Am. J. Solids Struct.* **10**, 147–160 (2013)
- Awrejcewicz, J., Kurpa, L., Shmatko, T.: Investigating geometrically nonlinear vibrations of laminated shallow shells with layers of variable thickness via the R-functions theory. *J. Compos. Struct.* **125**, 575–585 (2015)
- Awrejcewicz, J., Kurpa, L., Shmatko, T.: Linear and nonlinear free vibration analysis of laminated functionally graded shallow shells with complex plan form and different boundary conditions. *Int. J. Non-Linear Mech.* **107**, 161–169 (2018)
- Bennoun, M., Houari, M.S.A., Tounsi, A.: A novel five-variable refined plate theory for vibration analysis of functionally graded sandwich plates. *Mech. Adv. Mater. Struct.* **23**(4), 423–431 (2016)
- Birman, V., Kardomateas, G.A.: Review of current trends in research and applications of sandwich structures. *Compos. B* **142**, 221–240 (2018)
- Kurpa, L., Pilgun, G., Amabili, M.: Nonlinear vibrations of shallow shells with complex boundary: R-functions method and experiments. *J. Sound Vib.* **306**, 580–600 (2007)
- Kurpa, L.V., Shmatko, T.V.: Nonlinear vibrations of laminated shells with layers of variable thickness. In: Pietraszkiewicz, W., Górski, J. (eds) *Shell Structures: Theory and Applications*, 305–308. Taylor & Francis Group, London, UK

- Kurpa, L., Timchenko, G., Osetrov, A., Shmatko, T.: Nonlinear vibration analysis of laminated shallow shells with clamped cutouts by the R-functions method. *J. Nonlinear Dyn.* **93**(1), 133–147 (2018)
- Li, Q., Iu, V.P., Kou, K.P.: Three-dimensional vibration analysis of functionally graded material sandwich plates. *J. Sound Vib.* **311**, 498–515 (2008)
- Malekzadeh, P., Ghaedsharaf, M.: Three-dimensional free vibration of laminated cylindrical panels with functionally graded layers. *J. Compos. Struct.* **108**, 894–904 (2014)
- Rvachev, V.L.: *The R-Functions Theory and Its Some Application* (in Russ.). Kiev: Naukova Dumka (1982)
- Swaminathan, K., Naveencumar, D.T., Zenkour, A.M., Carrera, E.: Stress, vibration and buckling analyses of FGM plates A State-of-the-Art Review. *J. Compos. Struct.* **120**, 10–31 (2015)
- Thai, H.T., Nguen, T.K., Vo, T.P., Lee, J.: Analysis of functionally graded sandwich plates using a new first-order shear deformation theory. *Eur. J. Mech.-A/solids* **45**, 211–225 (2014)
- Thai, H.T., Kim, S.E.: A review of theories for the modeling and analysis of functionally graded plates and shells. *J. Compos. Struct.* **128**, 70–86 (2015)
- Thai, H.-T., Vo, T., Nguyen, T.-K., Kim, S.-E.: A review of continuum mechanics models for size-dependent analysis of beams and plates. *J Compos. Struct.* **177**, 196–219 (2017)
- Tornabe, F., Fantuzzi, N., Baccocchi, M., Viols, E., Reddy, J.: A numerical investigation on the natural frequencies of FGM sandwich shells with variable thickness by the local generalized differential quadrature method. *Appl. Sci.* **7**(2), 131 (39 p.) (2017)
- Zenkour, A.M.: A comprehensive analysis of functionally graded sandwich plates: part 2- Buckling and free vibration. *Int. J. Solids Struct.* **42**(18), 5243–5258 (2005)

Chapter 5

Residual Stresses in Plastic Deformed Composites



Gennadiy Lvov and Olga Kostromitskaya

Abstract In this paper, we study the residual stresses at the microlevel in a unidirectional reinforced composite that arises after rate-independent plastic deformation. Micromechanical analysis was performed on a representative volume by the finite element method for the case of a plane stress state. A series of basic numerical experiments were carried out, which made it possible to determine the distribution of residual stresses and plastic strains at different loading paths. The results of these experiments were used to identify the parameters of the developed plastic deformation model of the composite. As governing relations for an equivalent orthotropic material, a modification of the Chaboche theory is used. Translational hardening is described by a plasticity function including parameters of residual micro stresses. In known plasticity models, translational hardening is reflected by introducing parameters depending on the accumulated plastic deformation. Sometimes they are formally interpreted as micro stresses. In contrast to such models, in the proposed approach, the residual micro stresses have real physical meaning. They are done by analyzing the stress state of a representative volume. The advantage of this approach is the possibility of theoretical determination of all model parameters, based on the known properties of the matrix and reinforcing components. Numerical results were obtained for unidirectional reinforced boron-aluminum composite.

Keywords Residual stresses · Metal matrix composite · Plasticity

G. Lvov (✉) · O. Kostromitskaya
Department of Dynamics and Strength of Machines, National Technical University “Kharkiv Polytechnic Institute”, 2 Kyrpychova Str, Kharkiv 61002, Ukraine
e-mail: lvovdpm@ukr.net

O. Kostromitskaya
e-mail: kostrom_olga@ukr.net

5.1 Introduction

Residual stresses at the micro and macro levels of composite can have a significant effect on the accumulation of continuous damage and the initiation of macro cracks. They can also cause delamination and contact failure between the matrix and the fibers. Thus it is important to account for residual stresses when designing composite structures.

The processing induced thermal residual stresses in metal-ceramic and metal matrix composites are a result from the difference in the coefficients of thermal expansion of the constituent materials. Residual stresses in cured epoxy composites mostly arise due to chemical shrinkage of resin.

Thermal residual stresses. Thermal stresses induced during the cooling of Cr–Al₂O₃ metal-ceramic composites are experimentally investigated and modeled numerically in Węglewski et al. (2019); Węglewski et al. (2014). Microscopic residual stresses remaining in the composites after cooling are mainly caused by the difference in thermoelastic properties of alumina and chromium. Thermal residual stresses were measured by three experimental methods: photoluminescence piezo spectroscopy, X-ray diffraction, and neutron diffraction. Identical samples were used to measure residual stresses using three methods. The gauge areas were chosen so that the residual stress results obtained by different methods could be compared. When constructing a geometric model of representative volume contours and positions in the ceramic phase are obtained from the μ CT images. Then this model is transformed into a finite element model using a commercial software package ScanIP/FE. The residual stresses are calculated assuming the linear elastic model for the alumina phase and two alternative models for the chromium phase: linear elastic and elastoplastic. The qualitative influence of the size of reinforcements on the residual stresses in the alumina matrix was found by experimental measurements and numerical modeling.

Węglewski et al. (2012) is devoted to investigation of the thermal residual stresses in Cr–Al₂O₃ composite induced upon cooling from the temperature of the powder metallurgy process to room temperature. The thermal stress was calculated numerically using the finite element method (FEM) analysis with considering the porosity and microcracking. The numerical results were obtained for two material models, one taking into account plastic deformations, the other for linear elastic material. Numerical analysis showed that taking into account plastic deformation of chromium slightly affects the residual stresses in the composite.

To validate the theoretical results, Cr–Al₂O₃ composite was produced. On samples with parameters similar to the calculated the residual stresses were experimentally measured using the X-ray diffraction method. Experimental results show that thermal stresses did not lead to a high level of microcracking. The decrease of elastic modulus was mainly caused by the initial porosity.

Internal residual stresses arise in metal matrix composites when they are produced at a high temperature followed by cooling to room temperature. Thermal residual stresses are resulted from mismatch of the coefficients of thermal expansion between

matrix and reinforcement phases. In Bouafia et al. (2012) the FEM was used to analyze the residual stresses in composites with aluminum matrix reinforced by silicon carbide particles. Rectangular parallelepipeds with one or two spherical inclusions are selected as representative volumes. The particle (SiC) was considered as an isotropic material and the aluminum matrix was defined as elastoplastic material. A constant rate cooling down process was considered with the initial and final temperature are 320 °C and 20 °C, respectively. The calculations were performed using commercial software package ABAQUS. The finite element model consisted of 45,641 4-node linear tetrahedron elements. As a result of numerical studies, qualitative and quantitative features of residual stresses are established. In particular, it was found that the volume fraction of particles plays an important role regarding the generation of residual stresses. On models with two particles, it is shown that the internal residual stresses increase with a decrease in spacing.

In Sharma et al. (2016) an elastoplastic finite element model for studying the thermomechanical behavior of aluminum–alumina particle reinforced composites is proposed. Thermal residual stresses generated while cooling the composites from sintering temperature to room temperature are simulated. Three-dimensional representative volumes of composites were generated using special software that uses a random sequential adsorption algorithm for particle distribution. To model the irregular-shaped alumina particles this work is carried out using icosahedron-shaped particles for the reinforcement particles. The geometrical models were exported to the commercial software Abaqus for meshing and structure analysis. As a result of calculations, it was found that the stress concentration within the microstructure causes the yielding of the aluminum matrix. The matrix was modeled as elastoplastic material with material properties adopted from literature. Alumina particles in reinforcement phase were modeled as elastic material with temperature-independent properties. Comparative analysis showed that the thermal residual stresses generated considering the elastic deformation of the matrix is much higher as compare to that considering elastoplastic deformation.

Unlike numerical simulation in Sevostianov and Bruno (2019) Maxwell homogenization scheme was used to evaluate residual stresses in an aluminum matrix composite with SiC particle reinforcement. The effect of interaction between the matrix and particles is reduced to calculation of the additional field acting on an inhomogeneity due to the stress-free strains in its neighbors. The method is illustrated by examples with a material reinforced with spherical particles with a parallel mustache and a metal matrix containing flat randomly oriented short fibers. For validation of the proposed approach, the model prediction was compared with the data for Al–SiC composite reported by other authors. This comparison showed that Maxwell scheme, being applied to the calculation of the residual stresses in composites, shows good agreement with the experimental results.

Residual stresses in polymer matrix composites. In the process of curing composite materials with polymer matrices technological residual stresses arise. Several factors cause residual stresses formation. Residual stresses in cured epoxy composites arise because fiber and resin have different linear expansion coefficients. In addition changes in resin volume can result from chemical shrinkage and thermal expansion.

Numerical analysis was used in (Agius et al. 2016) to predict the development of residual thermal stresses in carbon-epoxy laminates. The RVE has been highlighted from hexagonal fiber packing structure. The experimentally measured chemical shrinkage and thermal expansion properties of the resin were used as inputs to a finite element analysis to calculate the residual stresses in the composite.

The analysis found that the chemical shrinkage contribution to residual stress dominates the thermal contribution for low initial cure temperatures.

To predict residual stress development in carbon fiber composite due to curing a multiscale thermo-viscoelastic processing model is developed in Chen and Zhang (2019). This model includes the heat transfer analysis, the governing equation for the resin cure kinetics, and stress analysis to determine curing-induced stress development using a viscoelastic constitutive law. The multiscale modeling approach is used, which includes a mesoscale model at the lamina level and a micromechanics model at the fiber and matrix scale. At the mesoscale level, the composite laminate is considered as discrete layers of transversely isotropic laminae. At the microstructure level, the lamina is represented as an assemblage of fiber-matrix concentric cylinders. Residual stress prediction performed using different material models. Comparison of residual stresses predicted by the viscoelastic and elastic processing models shows that the viscoelastic processing model can provide an improved prediction on curing-induced residual stresses because the viscoelastic model accounts for the stress relaxation of the composite during curing.

Multiscale modeling was used in Yuan et al. (2018) to predict the curing residual stresses in fiber-reinforced thermosetting composite Hexcel AS4/3501-6. At the macroscale modeling, the laminate is assumed as a continuum media. The governing equations for heat transfer and macro residual stresses are solved with respect to the realistic initial and boundary conditions. A linear viscoelastic constitutive equation has been used to predict the curing residual stresses and curing deformation in composite structures. The temperatures, degree of cure and macro residual strains calculated by macroscale model are used in the RVE model as boundary conditions in the microscale modeling. Geometrical micro model was considered as a single fiber-matrix structure with the interphase between them. Three different composite structures are established: a square, a hexagonal, and a diamond fibre arrangement. Numerical results were obtained by the FEM using a software package ABAQUS. Numerical analysis showed that the maximum micro residual stresses calculated in diamond fiber arrangement model are larger than that in hexagonal and square fiber arrangement.

The micromechanical model was used in Tsai and Chi (2008) to calculate the thermal residual stress of the unidirectional fiber composite. The repeating unit cell containing fiber and matrix phase was employed for different structures: square edge packing, square diagonal packing, and hexagonal packing. The fiber was assumed to be linear elastic material, and the matrix was regarded as a nonlinear elastoplastic material. The microthermal residual stresses induced during curing were calculated. Calculations were carried out under the condition that during cooling there is no mechanical loading applied and the macro stress state of the composites should be equal to zero.

A new viscoelastic constitutive model was proposed in (Zhang et al. 2016) for numerical investigation of cure-induced residual stresses in polymer matrix composites. The constitutive equations were used in the form of the hereditary integrals for relaxation of residual stresses. The proposed viscoelastic constitutive equations were implemented in the ABAQUS finite element code with considering the thermal and the chemical shrinkage strains. For residual stress simulation was created three-dimensional geometry model of cross-ply laminate [0/90]_s.

Numerical analysis made it possible to predict residual stresses resulting from various physical processes. During the curing process, stresses are caused by shrinkage during chemical curing. At the cooling stage, they arise from thermal contraction. Residual stress relaxation is associated with the viscoelasticity of the composite matrix.

The thermal and cure-induced residual stresses were numerical modeled in (Zhang et al. 2018) for variable-stiffness curvilinear fiber panels. The temperature distribution in the composites was described by the 3D heat conduction equation taking into account the anisotropy of the thermal conductivity properties. The resin curing process was described by phenomenological cure kinetic equation with Arrhenius temperature dependence. The mechanical properties of the composites were determined by elastic constants of the fiber and linear thermo-viscoelasticity model of resin. A numerical study of the distribution of residual stresses in composite panels was performed by the finite element method on a 3D model of a variable stiffness panel with various reinforcement angles using ABAQUS software.

As a result of numerical studies, it was found that a higher temperature and the curing degree distribution of the panel are determined by the direction of reinforcement. The distribution of the degree of cure is similar to the distribution of temperature because the cure rate is highly dependent on heat release. Obtained results also indicate that the residual stresses of the composite panels depend significantly on the angle of reinforcement.

Experimental investigations. The experimental study of residual stresses is a complex technical problem even for structures made of traditional homogeneous materials. The review of residual stress measurement methods is given in Guo et al. (2019) on the basis of modern publications. Destructive and non-destructive testing methods for homogeneous materials are reflected. A few publications are devoted to experiments on determining residual stresses in composite materials.

In Niu et al. (2019) residual micro stresses after the fabrication of SiC fiber-reinforced Ni–Cr–Al alloy composites were investigated by Raman spectroscopy method. The fabrication temperatures of composites are very high. The difference between coefficients of thermal expansion of SiC fibers and Ni–Cr–Al alloys causes great residual stress at the interface during fabrication of the composites. Laser Raman method allows to determine the microscopic residual stress distribution in the interface of the composite material. Raman spectroscopy was performed using a LabRam HR 800 Raman spectrometer. The interface morphologies of the composite material were observed by scanning electron microscopy. As a result of Raman spectrum analysis, it was founded that the SiC fibers are under residual compressive

stress. But after the process that the SiC fibers are fabricated to the precursor wires, the compressive stress inside the fibers is reduced, and the stress at the portion near the C-rich coating becomes tensile stress.

The article (Xie et al. 2016) is devoted to experimental investigation of compressive residual stress distribution caused by shot peening in the deformed surface layer of titanium matrix composite. Shot peening treatment was performed using an air blast machine. The shot media was cast steel balls with average diameter of 0.6 mm. The residual stresses along the depth from the surface were measured using X-ray diffraction method by X-ray stress analyzer. To obtaining the stress distribution deeper inside the material, the thin top surface was removed layer by layer via chemical etching. The experimental results show the average residual stresses of the composite because the irradiation area of X-ray is larger than the dimension of reinforcement. The experimental results indicated that the residual stress formed in the surface layer and the maximum appeared on the subsurface. The range of residual stresses found in experiments correspond the simulated results obtained by 3D finite element analysis.

Residual stresses in composite materials manufactured by the method of pultrusion were studied experimentally in Yuksel et al. (2019) by the hole drilling method. The reasons for the residual stresses in pultrusion are non-uniform curing and heating/cooling in the manufacturing process. A pultruded rectangular composite bar of unidirectional glass fiber with polyester resin was investigated in this study. The hole drilling with digital image correlation (Harrington and Schajer 2017; Baldi 2014; Kashfuddoja et al. 2014) have been employed by comparing two images taken before and after drilling. The Aramis 4 M system with 2048×2048 pixels camera was used to measure the strain field obtained after drilling. The FEM model was used to interpret the measured strain distribution after hole drilling and estimate the initial stress state locked in the profile after the manufacturing process and before hole drilling. The residual strain obtained experimentally was compared with the simulated strain field. The corresponding residual stress was calculated using the measured strains in a numerical model. A good agreement was obtained for the measured and predicted strain distribution of the drilling affected-zone.

Plasticity models of fiber composites. One of the reasons for the appearance of residual stresses in composite materials is the difference in the elastoplastic properties of their components. When loading such materials beyond the yield limits and the subsequent complete removal of external loads, stresses remain within the cells of the heterogeneity. These micro stresses are self-balanced within the cell boundaries, and there are no statically equivalent macro stresses. Existing phenomenological plasticity theories of fiber composites describe the observed effects using the concept of kinetic hardening. The displacement of the plasticity surface is determined by internal variables (called back-stress), which are associated with accumulated plastic macro strains. Overview of various evolution models of the kinematic variable made by Chaboche (2008) for homogenous materials.

For polymer matrix and metal matrix composites, there are many plasticity theories. In Spencer (1992) the theory of anisotropic plasticity proposed with the assumption that yielding is not affected by a tension in the fibre direction. The generalized anisotropic elastoplastic constitutive model was proposed in Car et al. (2000) for the large strain analysis of fiber-reinforced composite materials. With micromechanical approaches fibers are assumed to be linear elastic anisotropic solids and the matrix is modeled as an isotropic elastoplastic solid.

Constitutive thermodynamically consistent models were formulated (Nagaraja et al. 2019) for anisotropic plasticity of polymer composites reinforced by unidirectional fibers. Two nonquadratic yield functions with nonlinear isotropic hardening are proposed. These functions are governed by three anisotropic coefficients. In conjunction with an associated flow rule, this was enough to predict experimental data on the plastic deformation of composites. All variants of the constitutive models were calibrated according to experimental results for various types of stress state.

In the considered plasticity models translational hardening is reflected by introducing parameters depending on the accumulated plastic deformation. Sometimes they are formally interpreted as micro stresses. The disadvantage of this theoretical approach is the neglect of residual micro stresses when assessing the strength of structural elements from composites. In contrast to such models, in the proposed approach, the residual micro stresses have real physical meaning.

In the framework of the homogenization concept of the composite material mechanical properties, its state is determined by the average values in the representative volume element—macro stresses $\bar{\sigma}_{ij}$ and macro strains $\bar{\varepsilon}_{ij}$

$$\bar{\sigma}_{ij} = \frac{1}{V} \int_V \sigma_{ij} dV, \quad \bar{\varepsilon}_{ij} = \frac{1}{V} \int_V \varepsilon_{ij} dV \quad (5.1)$$

where σ_{ij} , ε_{ij} —stress and strains within representative elements. In this article, all characteristics within a representative cell will be called micro quantities.

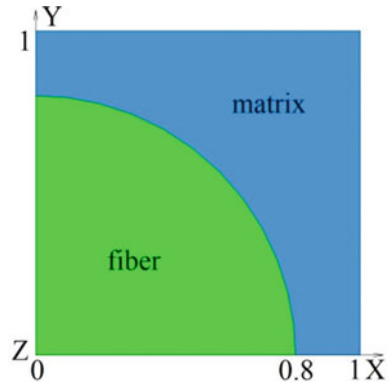
5.2 Numerical Simulation of Residual Stress Accumulation

As a result of plastic deformation of the metal matrix composites, they accumulate residual strains and stresses. With complex deformation programs, accompanied by unloading and alternating loads, the determination of residual stresses requires an analysis of the entire history of deformation. A feature of composite materials is the heterogeneity of residual stresses and strains at the microlevel, i.e., within a representative cell. The results of such an analysis could be the basis for the development of a phenomenological model of plasticity at the macro level. The material parameters of such a model are predicted based on the known mechanical properties of the composite components.

Table 5.1 Mechanical properties of composites components

Characteristic	Fiber	Matrix
Elastic modulus, GPa	$E = 420$	$E = 70$
Poisson ratios	$\nu = 0.25$	$\nu = 0.34$
Yield strength, MPa		$\sigma_{ys} = 260$
Tangential modulus, GPa		$E_T = 8.75$

Fig. 5.1 A representative element



In this section, the methodology for the numerical analysis of plastic deformation processes is described on the example of boron-aluminum composite with unidirectional reinforcement. The mechanical properties of the fibers and matrix are presented in Table 5.1.

Plastic deformation of the matrix was described by a time-independent model with linear isotropic hardening. Due to the double periodic structure of the composite with the tetragonal reinforcement scheme, numerical analysis was performed on a representative element (Fig. 5.1). All calculations were performed by the finite element method in the ANSYS software package.

The main feature of the numerical simulation of the cell stress state is the adequate formation of boundary conditions. These conditions should ensure that the micro stresses within the representative element are fully consistent with the state that occurs when the unlimited array of the composite is uniformly deformed. For simple loading programs, when all the components of the stress tensor only increase in proportion to one parameter, the procedure for setting the boundary conditions is described in Lvov and Kostromitskaya (2020). This procedure is described below for complex programs of alternating loading on the example of uniaxial tension/compression in the direction perpendicular to the fibers.

At the first stage of the loading program, uniaxial elastoplastic extension is simulated, when the macro stress $\bar{\sigma}_x$ monotonically increases from zero to a certain value. An analysis of the generalized plane strain state is performed at zero force in the direction of reinforcement, which is equivalent to the absence of macro stress $\bar{\sigma}_z = 0$. At the boundaries $x = 0$ and $y = 0$, the symmetry conditions are set, and at

the other two boundaries the following conditions are set:

$$\begin{aligned} x = 1 : \quad u_x &= C_1, \quad \tau_{xy} = 0 \\ y = 1 : \quad u_y &= C_2, \quad \tau_{xy} = 0 \end{aligned} \tag{5.2}$$

At each loading step the value of the constant C_1 increases sequentially, which corresponds to an increase in macro strain, and the value of C_2 is determined by the method of successive approximations. The goal of the iterative procedure is to simulate a uniaxial macro stressed state. At each iteration, the average stresses $\bar{\sigma}_x$ and $\bar{\sigma}_y$ are determined. The process of successive approximations continues until the specified accuracy is reached when $\bar{\sigma}_y < \varepsilon \cdot \bar{\sigma}_x$. After reaching the specified accuracy $\varepsilon < 10^{-3}$ at each step of loading, the values of macro stresses $\bar{\sigma}_x$ and the corresponding value of macro strain $\bar{\varepsilon}_y$ are found, which determines one point in the stress–strain diagram of composite.

At the second stage of the unloading program is simulated. The restart of the calculation is made from the last point of the first stage of the program with the saving of all analysis data. At each step of unloading, the value of the constant C_1 decreases at each restart. In this case, the constant C_2 is determined by the method of successive approximations to satisfy the condition $\bar{\sigma}_y < \varepsilon \cdot \bar{\sigma}_x$, similarly to the procedure used at the first stage of the program. Numerical simulation of the unloading process continues until the macro stress $\bar{\sigma}_x$ becomes equal to zero. This state corresponds to the unloading of the composite when all the components of the macro stress tensor are equal to zero. But within the representative cell, residual micro stresses are retained. The distribution of equivalent residual micro stresses and plastic micro strains is shown in Fig. 5.2. The presented results correspond to uniaxial pre-tension at the first stage of the program to the value of macro strain $\varepsilon = 10^{-2}$ and plastic strains **(b)**

The values of residual macro strains depend on the degree of preliminary tension of the composite. Figure 5.3 shows the dependences of residual macro strains $\tilde{\varepsilon}_x$, $\tilde{\varepsilon}_y$ and $\tilde{\varepsilon}_z$ on the magnitude of the preliminary macro stress $\bar{\sigma}_x$.

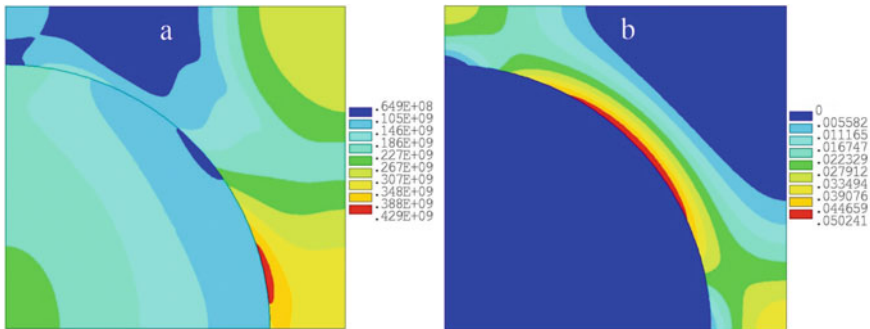


Fig. 5.2 The second stage. Equivalent von Mises residual micro stresses **(a)**

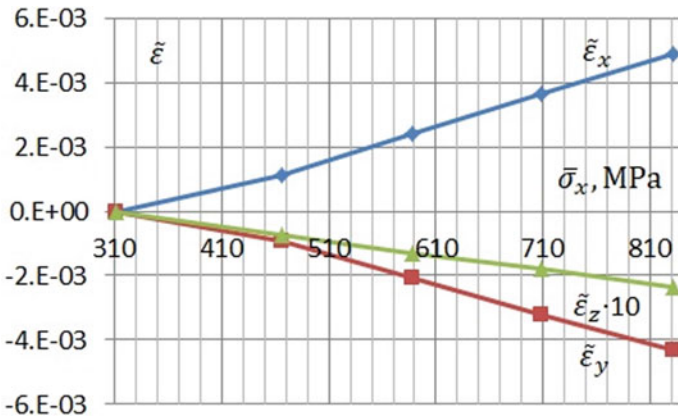


Fig. 5.3 Dependences of residual macro strains $\tilde{\epsilon}_x$, $\tilde{\epsilon}_y$ and $\tilde{\epsilon}_z$ on preliminary macro stress $\bar{\sigma}_x$

At the third stage of the loading program, the process of compressing the composite after tension and full unloading is simulated. To simulate uniaxial compression after complete unloading, the calculation is performed starting from the end-point of the second stage. In the boundary conditions (5.1), the value of the constant C_1 is successively reduced to zero, and the value of C_2 at each step is determined by the method of successive approximations using the above algorithm. The distribution of equivalent micro stresses and plastic micro strains at the end of the third stage of loading program is shown in Fig. 5.4.

A numerical analysis performed in the first two stages simulates a stress-closed uniaxial tension cycle. And the results of the analysis at all three stages simulate the strain-closed cycle of tensile and compression. The combination of these results is presented in Fig. 5.5, which shows the relationship between macro stresses and macro strains under uniaxial stress state of the composite.

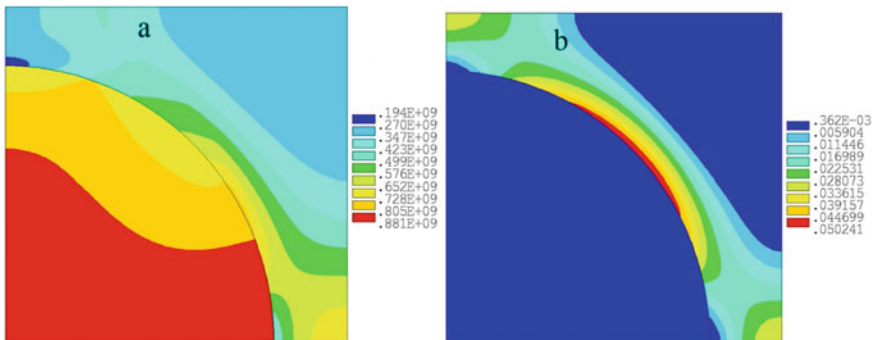
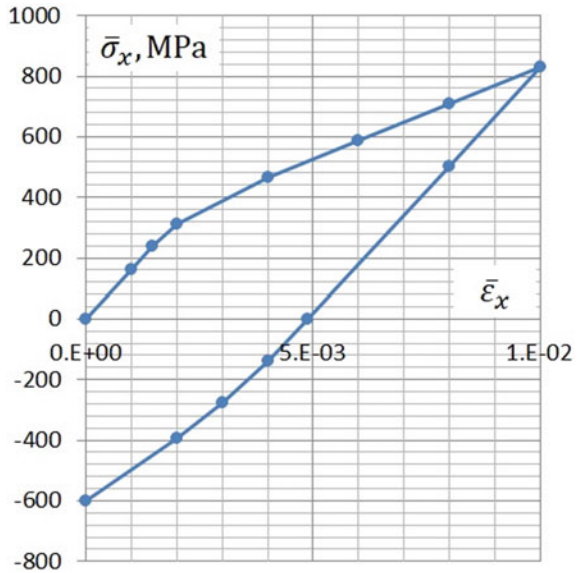


Fig. 5.4 The third stage, Equivalent von Mises residual micro stresses (a) and plastic strains (b)

Fig. 5.5 Macro stresses and macro strains under uniaxial stress state of the composite



Numerical modeling of the process of pre-tension beyond elasticity and subsequent compression before the appearance of secondary plastic deformations showed that the Bauschinger effect is detected in the composite at the macro level. A detailed analysis of strain-closed cycles with various values of pre-tension allows us to conclude that hardening is close to translational. The difference between the yield strengths for tensile and compression of the hardened composite differs from the doubled yield strength of the composite in the initial state by 3–4%. For the investigated material, it is possible not to take into account the expansion of the yield surface.

5.3 The Governing Equations of Plastic Deformation of a Composite

The traditional way of constructing physical relations connecting strains or their increment with stresses is based on a generalization of experimentally established properties of materials at various loading paths. For composites, a useful alternative is the theoretical modeling of plastic deformation processes based on the known properties of matrix and fibers materials.

A numerical analysis of the plastic deformation of a unidirectional reinforced composite revealed the possibility of the appearance of residual micro stresses and the anisotropic character of hardening associated with them. The variant of physical relations described below is based on the data of this analysis. The yield criterion of the composite in the initial undeformed state is adopted in the form of a quadratic

form relative to macro stresses:

$$A_{ijkl}\bar{\sigma}_{ij}\bar{\sigma}_{kl} = 1 \quad (5.3)$$

where A_{ijkl} are the components of the fourth-rank tensor, the values of which are determined by the yield strengths of the composite in different directions. As such limits, macro stresses are taken at which the equivalent (according to von Mises) micro stresses in the matrix reach the yield strength. The procedure for determining the coefficients in the yield criterion (5.3) is developed in Małachowski et al. (2017) for orthogonally reinforced composites. To reflect the combined (translational and isotropic) hardening, yield surface equation can be taken in the form

$$2f \equiv A_{ijkl}(\bar{\sigma}_{ij} - \sigma_{ij}^r)(\bar{\sigma}_{kl} - \sigma_{kl}^r) - \varphi^2(W) = 0 \quad (5.4)$$

where σ_{ij}^r are the components of the tensor reflecting the influence of residual stresses, $\varphi(W)$ is the scalar function of isotropic hardening, which depends on the work of plastic deformation. In the particular case of translational hardening $\varphi^2(W) = 1$.

The quadratic invariant form of the plasticity function is written for the general case of anisotropy. For transversally anisotropic and orthotropic materials, the book (Naumenko and Altenbach 2007) contains systems of invariants for quadratic creep potentials.

Under the conditions of active loading

$$f = 0, \quad \frac{\partial f}{\partial \bar{\sigma}_{ij}} d\bar{\sigma}_{ij} > 0 \quad (5.5)$$

the increments of plastic strains are determined by the flow rule associated with the equation of the yield surface (5.4):

$$d\bar{\varepsilon}_{ij}^p = d\lambda \frac{\partial f}{\partial \bar{\sigma}_{ij}} = d\lambda A_{ijkl}(\bar{\sigma}_{kl} - \sigma_{kl}^r) \quad (5.6)$$

In case of unloading: $f = 0$, $\frac{\partial f}{\partial \bar{\sigma}_{ij}} d\bar{\sigma}_{ij} < 0$, or neutral loading: $f = 0$, $\frac{\partial f}{\partial \bar{\sigma}_{ij}} d\bar{\sigma}_{ij} = 0$, no plastic strain increments $d\bar{\varepsilon}_{ij}^p = 0$.

Residual micro stresses are of great importance in the analysis of the strength of a composite since destruction processes are initiated within representative cells. For the formation of physical dependencies at the macro level, changes in the properties of the material during plastic deformation should be reflected by irreversible macro parameters. The simplest way to take into account translational hardening can be the proportional dependence $\sigma_{ij}^r = c\bar{\varepsilon}_{ij}^p$. In this case, the scalar factor $d\lambda$ can be expressed in terms of macro stresses increments. Under active loading, accompanied by an increase in plastic strains, condition (5.2) is satisfied. Therefore, the total differential of the yield function f is equal to zero:

$$df = \frac{\partial f}{\partial \bar{\sigma}_{ij}} d\bar{\sigma}_{ij} + \frac{\partial f}{\partial \bar{\varepsilon}_{ij}^p} d\bar{\varepsilon}_{ij}^p = 0 \quad (5.7)$$

Taking into account the form of the yield function (5.2) in the case of only translational hardening, the equality (5.4) is reduced to

$$A_{ijkl}(\bar{\sigma}_{kl} - c\bar{\varepsilon}_{kl}^p) d\bar{\sigma}_{ij} - c A_{ijkl}(\bar{\sigma}_{kl} - c\bar{\varepsilon}_{kl}^p) d\bar{\varepsilon}_{ij}^p = 0 \quad (5.8)$$

Now, taking into account the associated flow rule (5.6), we can obtain the explicit dependence $d\lambda$ from increments of macro stresses

$$d\lambda = \frac{A_{ijkl}(\bar{\sigma}_{kl} - c\bar{\varepsilon}_{kl}^p) d\bar{\sigma}_{ij}}{c A_{ijkl}(\bar{\sigma}_{kl} - c\bar{\varepsilon}_{kl}^p) (A_{ijmn}(\bar{\sigma}_{mn} - c\bar{\varepsilon}_{mn}^p))} \quad (5.9)$$

The elastic components of the macro strain tensor are related to macro stresses by Hooke's law for anisotropic bodies:

$$\bar{\varepsilon}_{ij}^e = a_{ijkl} \bar{\sigma}_{kl} \quad (5.10)$$

Identification of material parameters of the governing equations. The proposed physical relationships include a number of material parameters of the composite material. These are the elastic constants a_{ijkl} in the Hooke law, the components of the tensor A_{ijkl} in the yield criterion (5.1) and parameter c in the yield surface Eq. (5.2). A numerical technique for determining effective elastic constants is described in Zadeh and Lvov (2015) for unidirectionally reinforced composites. This technique is used in processing the results of numerical modeling of complex loading programs described in the second section of the article. To determine the constant c , it is convenient to use the processing of the results of numerical modeling of a pure shear in a plane perpendicular to the direction of reinforcement. A numerical experiment simulating a pure composites shear was carried out using the following boundary conditions:

$$\begin{aligned} x = 0 : \quad & u_y = 0, \quad \sigma_x = 0 \\ y = 0 : \quad & u_x = 0, \quad \sigma_y = 0 \\ x = 1 : \quad & u_y = 0, \quad \sigma_x = 0 \\ y = 1 : \quad & u_x = C_1, \quad \sigma_y = 0 \end{aligned} \quad (5.11)$$

The value of the constant C_1 was increasing in the interval $0 \leq C_1 \leq 10^{-2}$, which made it possible to obtain the transverse shear diagram shown in Fig. 5.6.

Under continuously increasing loading for pure shear conditions, the yield surface Eq. (5.4) leads to the following dependence of the shear stresses on the plastic component of the shear strain:

$$A_{1212}(\bar{\sigma}_{12} - c\bar{\varepsilon}_{12}^p) = 1 \quad (5.12)$$

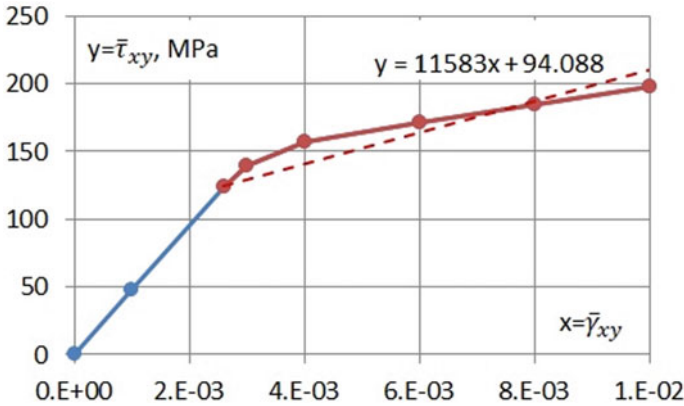


Fig. 5.6 Macro stresses vs macro strains under pure shear of the composite

If we take into account the elastic component of the shear strain:

$$\bar{\varepsilon}_{12}^e = a_{1212} \bar{\sigma}_{12} \tag{5.13}$$

then the theoretical dependence of shear stresses on shear deformations beyond elasticity will have the form:

$$\bar{\sigma}_{12} = \frac{1}{\sqrt{A_{1212}}} + E_k \left(\bar{\varepsilon}_{12} - \frac{a_{1212}}{\sqrt{A_{1212}}} \right) \tag{5.14}$$

where— E_k is the tangent module of the deformation diagram in the yield area. This module is found as a result of approximation of the calculated strain diagram (Fig. 5.6) by a bilinear function. Now we can find the parameter c in the yield surface equation:

$$c = \frac{E_k}{1 - E_k a_{1212}} \tag{5.15}$$

5.4 Conclusions

The effect of the appearance of residual micro stresses after plastic deformation was revealed as a result of numerical simulation of unidirectional reinforced composites. The study was performed by analyzing the microstress state within a representative cell by the finite element method. Systems of boundary conditions are compiled that ensure full correspondence of the loads on the representative volume element under various programs for changing macro stresses in the composite.

It is established that after a cycle closed by macro stresses, residual micro stresses can reach 50% of the maximum macro stresses. For a linearly hardening matrix, the relationship between macro stresses and macro strains can be approximated by a bilinear function. Similar properties of residual micro stresses were also revealed as a result of numerical modeling of a pure shear in a plane perpendicular to the direction of reinforcement.

The features of plastic deformation and the development of residual micro stresses revealed as a result of numerical modeling served as the basis for the construction of the governing equations of macro plasticity of a unidirectional reinforced composite. The theoretical model assumes a general anisotropy of the mechanical properties of an equivalent homogeneous material and the translational character of hardening. The developed numerical methods make it possible to determine all the material parameters of the model based on the known mechanical properties of the matrix and fibers. Numerical results are given for a composite with elastic boron fibers and a plastic aluminum matrix. The calibrated homogenized model was evaluated by comparison to micromechanics simulations for transversal shear.

References

- Agius, S.L., Joosten, M., Trippitt, B., Wang, C.H., Hilditch, T.: Rapidly cured epoxy/anhydride composites Effect of residual stress on laminate shear strength. *Compos. A* **90**, 125–136 (2016)
- Baldi, A.: Residual stress measurement using hole drilling and integrated digital image correlation techniques. *Exp. Mech.* **54**(3), 279–291 (2014)
- Bouafia, F., Serier, B., Bouiadjra, B.A.B.: Finite element analysis of the thermal residual stresses of SiC particle reinforced aluminum composite. *Comp. Mater. Sci.* **54**, 195–203 (2012)
- Car, E., Oller, S., Oñate, E.: An anisotropic elastoplastic constitutive model for large strain analysis of fiber reinforced composite materials. *Comput. Methods Appl. Mech. Eng.* **185**, 245–277 (2000)
- Chaboche, J.L.: A review of some plasticity and viscoplasticity constitutive theories. *Int. J. Plasticity* **24**, 1642–1693 (2008)
- Chen, W., Zhang, D.: Improved prediction of residual stress induced warpage in thermoset composites using a multiscale thermo-viscoelastic processing model. *Compos. A* **126**, 105575 (2019)
- Guo, J., Fu, H., Pan, B., Kang, R.: Recent progress of residual stress measurement methods: a review. *Chin. J. Aeronaut.* (2019). <https://doi.org/doi:10.1016/j.cja.2019.10.010>
- Harrington, J.S., Schajer, G.S.: Measurement of structural stresses by hole-drilling and DIC. *Exp. Mech* **57**(4), 559–567 (2017)
- Kashfuddoja, M., Prasath, R.G.R., Ramji, M.: Study on experimental characterization of carbon fiber reinforced polymer panel using digital image correlation a sensitivity analysis. *Opt. Lasers Eng.* **62**, 17–30 (2014)
- L'vov G.I., Kostromitskaya O.A.: Numerical modeling of plastic deformation of unidirectionally reinforced composites. *Mech. Compos. Mater.* **56**, 1–24 (2020)
- Małachowski, J., L'vov, G., Daryazadeh, S.: Numerical prediction of the parameters of a yield criterion for fibrous composites. *Mech. Compos. Mater.* **53**(5), 589–600 (2017)
- Nagaraja, S.G., Pletz, M., Schuecker, C.: Constitutive modeling of anisotropic plasticity with application to fiber-reinforced composites. *Int. J. Solids Struct.* **180–181**, 84–96 (2019)
- Naumenko, K., Altenbach, H.: *Modeling of Creep for Structural Analysis*. Springer, Berlin, Heidelberg (2007)

- Niu, X., Zhang, H., Pei, Z., Shi, N., Sun, C., Gong, J.: Measurement of interfacial residual stress in SiC fiber reinforced Ni–Cr–Al alloy composites by Raman spectroscopy. *J. Mater. Sci. Technol.* **35**, 88–93 (2019)
- Sevostianov, I., Bruno, G.: Maxwell scheme for internal stresses in multiphase composites. *Mech. Mater.* **129**, 320–331 (2019). <https://doi.org/10.1016/j.mechmat.2018.12.005>
- Sharma, N.K., Mishra, R.K., Sharma, S.: 3D micromechanical analysis of thermo-mechanical behavior of Al₂O₃/Al metal matrix composites. *Comp. Mater. Sci.* **115**, 192–201 (2016)
- Spencer, A.J.M.: Plasticity theory for fiber-reinforced composites. *J. Eng. Math.* **26**, 107–118 (1992)
- Tsai, J.L., Chi, Y.K.: Investigating thermal residual stress effect on mechanical behaviors of fiber composites with different fiber arrays. *Compos. B* **39**, 714–721 (2008)
- Węglewski, W., Basista, M., Chmielewski, V., Pietrzak, K.: Modeling of thermally induced damage in the processing of Cr–Al₂O₃ composites. *Compos. B* **43**(2), 255–264 (2012)
- Węglewski, W., Basista, M., Manescu, A., Chmielewski, M., Pietrzak, K., Schubert, Th.: Effect of grain size on thermal residual stresses and damage in sintered chromium–alumina composites measurement and modeling. *Compos. B* **67**, 119–124 (2014)
- Węglewski, W., Krajewski, M., Bochenek, K., Denis, P., Wyszomolek, A., Basista, M.: Anomalous size effect in thermal residual stresses in pressure sintered alumina-chromium composites. *Mat. Sci. Eng. A* **762**, 138111 (2019)
- Xie, L., Wang, C., Wang, L., Wang, Z., Jiang, C., Lu, W., et al.: Numerical analysis and experimental validation on residual stress distribution of titanium matrix composite after shot peening treatment. *Mech. Mater.* **99**, 2–8 (2016)
- Yuan, Z., Wang, Y., Yang, G., Tang, A., Yang, Z., Li, S., et al.: Evolution of curing residual stresses in composite using multi-scale method. *Compos. B* **155**, 49–61 (2018)
- Yuksel, O., Baran, I., Ersoy, N., Akkerman, R.: Investigation of transverse residual stresses in a thick pultruded composite using digital image correlation with hole drilling. *Compos. Struct.* **223**, 110954 (2019)
- Zadeh, S.D., Lvov, G.I.: Numerical procedure of determining the effective mechanical characteristics of an aligned fiber composite. *Strength Mater.* **47**, 536–543 (2015)
- Zhang, J.T., Zhang, M., Li, S.X., Pavier, M.J., Smith, D.J.: Residual stresses created during curing of a polymer matrix composite using a viscoelastic model. *Compos. Sci. Technol.* **130**, 20–27 (2016)
- Zhang, G., Wang, J., Ni, A., Li, S.: Process-induced residual stress of variable-stiffness composite laminates during cure. *Compos. Struct.* **204**, 12–21 (2018)

Chapter 6

Dynamics of Curved Laminated Glass Composite Panels Under Impact Loading



**Olha Sukhanova, Oleksiy Larin, Konstantin Naumenko,
and Holm Altenbach**

Abstract The study presents the results of an analysis of dynamic state of shallow shell laminated glasses (LG) composites under impact loading. The work considers modeling of a rigid ball drop on LG with polyvinyl butyral (PVB) interlayer. The aim of the work is to study the dependence of LG dynamic deformation on the glass curvature. The study carries out the dynamic strains and stress state analysis in LG under different loading conditions. The work performs computations using a finite element method (FEM) within an explicit dynamics approach in 3D statement. The investigation includes a mesh-size convergence analysis.

Keywords Laminated glass · Impact loading · Polyvinyl butyral interlayer · Dynamic deformed state · Explicit dynamics

6.1 Introduction

Glass laminated panels are widely used in modern mechanical and structural engineering. For example portholes, vehicle windows, outer parts of solar panels, elements of building structures, etc. Their functional purpose is to protect other sensitive elements from external factors. Laminated glass (LG) consists of two or more glasses laminated together with one or more layers of polymeric film (interlayers). The interlayer improves mechanical properties, e.g. impact strength, fracture toughness, and failure mode. As the area of impact increases, there is the possibility of improved impact resistance (Vedrtnam and Pawar 2017a, b).

O. Sukhanova (✉) · O. Larin
Department of Dynamics and Strength of Machines, National Technical University “Kharkiv Polytechnic Institute”, Kharkiv, Ukraine
e-mail: olha.sukhanova@khpi.edu.ua

K. Naumenko · H. Altenbach
Institut für Mechanik, Otto-von-Guericke-Universität Magdeburg, Magdeburg, Germany
e-mail: konstantin.naumenko@ovgu.de

H. Altenbach
e-mail: holm.altenbach@ovgu.de

The effect of the interlayer material on the stiffness, impact strength, fracture pattern, and load-bearing capacity of LG plate is well known. Polyvinyl butyral film (PVB), Ethyl Vinyl Acetate (Cross-Linked EVA), Ionoplast Polymers, Cast in Place (CIP) liquid resin, and Thermoplastic polyurethane (TPU) are used as interlayers most commonly.

The impact resistance of the LG plate is higher than that glass plate of the same thickness. Studying LG dynamic behavior features under the impact loading is an important practical task, the result of which are recommendations on internal structure, technical instructions on the operating modes, limits of use, etc. The destructive impact behavior of the LG is complex (Naumenko and Eremeyev 2014; Eisenträger et al. 2015; Weps et al. 2013; Schulze et al. 2012; Aßmus 2019). The combined effects of the brittleness of glass, the nonlinear characteristic of interlayer, and the adhesive bonding make the impact damage behaviors of LG much more complicated. Impact failure analysis of LG is commonly performed experimentally followed by numerical simulations or vice versa (Vedrtam and Pawar 2017a, b, 2018; Keller and Mortelmans 1999).

Experimental studies are quite expensive and complicated due to the high fragility, optical transparency, high smoothness of the glass surface, have significant limitations on the possibilities for the use of experimental equipment. Preliminary computational modeling allows reducing the number of necessary experimental analyses, formulating practical recommendations, and defining restrictions.

Most of the studies known in the literature have been done for straight panels. However, curvilinear ones are of particular interest since they have been able to exhibit improved additional functional/operational characteristics such as aerodynamics, high load capacity, etc. Their usage becomes quite spread in modern structural engineering, in transport engineering since it is possible to mold them into various bending shapes. It should be claimed that a curved LG differs from a straight LG in its static and especially dynamic behavior (Aşık et al. 2014).

Thus, the current paper deals with the study of the dynamic behavior of curved composite glass packets under impact loading, which is motivated by practical interest.

6.2 Formulation of the Problem

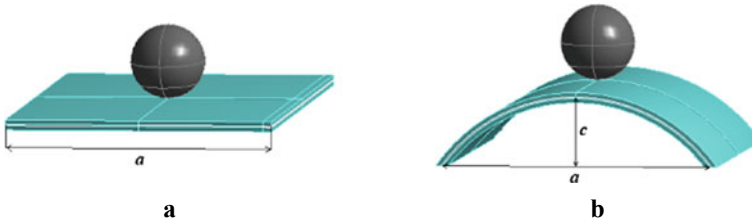
The aim of this work is to study the dynamic response of laminated multilayer glass composites with different LG curvatures arising under the rigid ball impact loading and to study the dependence of dynamic deformations level, occurring in the elements of these composites on the conditions of the influence.

The following tasks are set in this study:

- (1) to model a three-layer LG with different curvatures.
- (2) to develop a computer mathematical model that allows studying the impact interaction of an absolutely rigid spherical body with LG models;

Table 6.1 Material properties

Material	Density, ρ (kg/m^3)	Young's modulus, E (Pa)	Poisson ratio, ν
Steel	7850	2×10^{11}	0.3
Glass	2500	7×10^{10}	0.23
PVB	1100	2.2×10^8	0.495

**Fig. 6.1** LG with different curvatures **a** straight LG, **b** curved LG

- (3) to carry out a complex of numerical studies concerning definition of influence parameters regularity of ball falling on the laminates.

In current work, the different curvatures of three-layer LG have been modeled. The curvature parameter has been varying from 0 to 152.5 mm (i.e. from flat LG up to the curved as cylindrical shell with radius equal to half the side length). Curved LG, which was subjected to impact loading through contact with the 83 mm diameter smooth solid steel ball (2.3 kg), is considered. The laminate is a combination of two skin glass layers of thickness 5 mm each with a PVB interlayer of 1.52 mm thicknesses. The size of beams is 305×305 mm. The material properties of the glass and interlayers are taken from manufacturer's data tables and verified by the initial properties considered in (Zhang et al. 2013) and shown in Table 6.1. The geometric models are shown in Fig. 6.1.

6.3 Simulation Model

The behavior of the impact of LG samples with PVB interlayer was modeled using Explicit Dynamics analysis in the framework of 3D modeling by the finite element method (FEM). Hexagonal FE with 8 nodes with 3 degrees of freedom in each was used.

The geometric models of LG with different curvatures are presented in Fig. 6.1. The straight LG is a special case of curved glasses with a zero curvature parameter ($c = 0$ mm) in Fig. 6.1a, and one of the curved LG ($c = 76$ mm) in Fig. 6.1b, as an example. The side sizes in all models are equal ($a = 305$ mm).

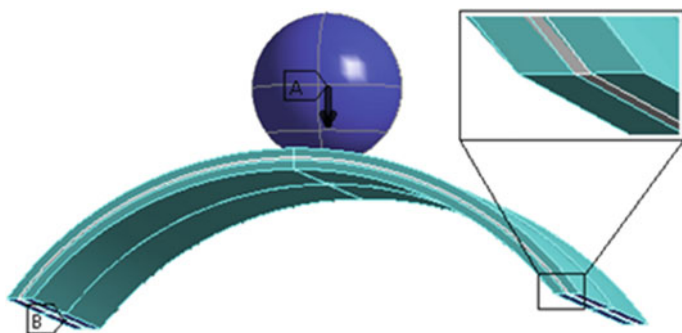


Fig. 6.2 Boundary conditions **a** vector of initial velocity, **b** fixed support of composite

As a boundary condition, LG was clamped on two sides, and the impact of the ball was simulated in the center of the LG, as shown in Fig. 6.2. The ball was modeled as an absolutely rigid body. The laminate was modeled in a three-dimensional setting as part of a physical linear-elastic state. The interaction of the ball and the laminate was carried out in the framework of solving the problem of one-way contact by the “surface to surface” (STS) algorithm. The resistance caused by air during impact was neglected.

For the studied straight LG, FE mesh with elements of different sizes was created. For each mesh size, the calculations of maximum magnitude of the displacement vector and maximum Equivalent (von Mises) Stress were performed to determine the computational error. The LG-PVB model with different height of ball-free fall was analyzed. Similar computational studies for the laminate with the same dimensions and conditions have been studied in the work of Vedrtam and Pawar (2017a, b). The closest value of the mesh size is 2 mm. The error between the values of magnitude of the displacement vector for calculations with FE meshes with dimensions of 5 and 4 mm is quite large—24%, but then it is significantly reduced to 3% between meshes of 4 and 3 mm and between 2 and 1 mm is 2.8%.

6.4 Calculation of Nonlinear Dynamics of the Laminated Glass

The impact loading of a steel ball on LG with different curvatures and the height of the ball fall (h_{bff}) were calculated. The results of maximum magnitude of the displacement vector (lu_{max}), Intensity Stress (σ_{int} is defined as the largest of the absolute values of $|\sigma_1 - \sigma_2|$, $|\sigma_2 - \sigma_3|$ or $|\sigma_3 - \sigma_1|$) and Intensity Strain (ε_{int} is defined as the largest of the absolute values of $|\varepsilon_1 - \varepsilon_2|$, $|\varepsilon_2 - \varepsilon_3|$ or $|\varepsilon_3 - \varepsilon_1|$) at characteristic points (Fig. 6.3) at time t_0 (corresponding to the maximum displacement) and t_{max} (corresponding to the maximum value of stresses over the entire time period) are

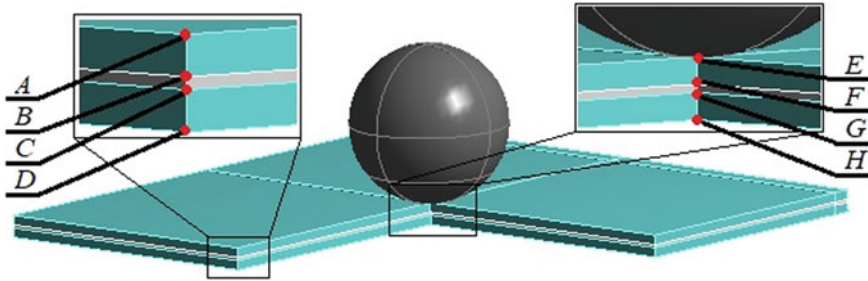


Fig. 6.3 Main investigated points of the model

derived. The characteristic point *H* is chosen, where the largest maximum displacement and high-stress localization are observed, but there is no singularity of stress concentration, as at the point of direct interaction of the LG with the rigid ball. The obtained values as a result of the calculation are shown in Table 6.2.

Figures 6.4 and 6.5 show the magnitude of the displacement vector and Intensity Stress in LG with different curvatures under the impact loading of a solid ball with 490 mm height of the ball fall. For LG with other ball heights, it was also evaluated similarly. The maximum magnitude of the displacement vector is observed in the center of impact zone, and the minimum displacement—in the fixed sides of the model. With a curvature parameter increasing, the distribution of maximum magnitude of the displacement vector can be traced along the LG. The Intensity Stress distribution reflects that the maximum values are placed in the center of impact zone of the LG. It can be found that starting approximately from the 40 mm of curvature parameter *c* (i.e. from 15% of shell width) a distribution of the elastic wave has been considered.

Additional calculations were done with different mesh sizes (1.5, 2, 2.5 mm) for a height of 490 mm of the ball fall. A fitting analysis of the data was performed to analyze the dependence of magnitude of the displacement vector and Intensity Stress on the curvature parameter. The magnitude of the displacement vector data was approximated by an exponential function:

$$u_{\max} = y_0 + S \cdot \exp(R_0 \cdot c) \tag{6.1}$$

where

- y*₀ is the offset,
- S* is the initial value and
- R* is the rate.

The Intensity Stress data were approximated by a cubic polynomial function:

$$\sigma_{\text{int}} = A_0 + A_1 \cdot c + A_2 \cdot c^2 + A_3 \cdot c^3 \tag{6.2}$$

Table 6.2 The results of the simulation

c (mm)	FE mesh size (mm)	h_{bfff} (mm)	u_{max} (mm)	Point	σ_{int} in t_0 (MPa)	σ_{int} in t_{max} (MPa)	$\varepsilon_{int} 10^{-3}$ in t_0	$\varepsilon_{int} 10^{-3}$ in t_{max}
0	2	490	1.8789	H	214.28	240.17	3.7653	4.2202
		1200	2.9755		360.96	398.85	6.3426	7.0084
		1450	3.2372		395.51	438.48	6.9496	7.7047
		1900	3.6405		449.52	500.01	7.8988	8.7859
19.06	2	490	1.2923	H	299.98	305.72	5.271	5.3719
		1200	2.0797		494.5	502.58	8.6891	8.831
		1450	2.2811		539.55	550.38	9.4806	9.671
		1900	2.5877		608.72	623.92	10.696	10.963
23.8	2	490	1.2227	H	301.43	312.5	5.2966	5.4911
		1200	1.9582		496.13	510	8.7177	8.9614
		1450	2.1558		541.49	557.25	9.5148	9.7918
		1900	2.4458		615.9	635.95	10.822	11.175
28.6	2	490	1.179	H	309.31	317.98	5.4351	5.5874
		1200	1.8959		498.78	520.05	8.7643	9.138
		1450	2.076		559.38	570.12	9.8291	10.018
		1900	2.356		626.09	650.24	11.001	11.426
38.13	2	490	1.1002	H	290.82	294.53	5.1102	5.1752
		1200	1.7662		480.99	481.33	8.4516	8.4576
		1450	1.9343		528.41	528.41	9.285	9.285
		1900	2.198		601.07	601.07	10.562	10.562
57.2	2	490	1.0252	H	280.5	294.28	4.9289	5.1709
		1200	1.6508		451.96	485.63	7.9416	8.5333
		1450	1.8249		496.73	532.87	8.7282	9.3633
		1900	2.0768		559.7	601.42	9.8348	10.568
76.25	2	490	0.99523	H	286.54	303.66	5.035	5.3357
		1200	1.6272		451.57	494.92	7.9347	8.6964
		1450	1.7839		494.41	542.8	8.6875	9.5379
		1900	2.0285		561.57	616.37	9.8676	10.831
114.4	2	490	1.0196	H	210.43	262.25	3.6975	4.6081
		1200	1.6515		352.15	420.84	6.1877	7.3948
		1450	1.8099		366.22	461.93	6.435	8.1167
		1900	2.0566		418.07	525.45	7.346	9.2328
152.5	2	490	1.0588	H	150.044	212.59	2.6434	3.7354
		1200	1.7085		239.75	349.89	4.2128	6.1481
		1450	1.8677		258.59	383.46	4.5437	6.7379

(continued)

Table 6.2 (continued)

c (mm)	FE mesh size (mm)	h_{bff} (mm)	u_{max} (mm)	Point	σ_{int} in t_0 (MPa)	σ_{int} in t_{max} (MPa)	$\varepsilon_{int} 10^{-3}$ in t_0	$\varepsilon_{int} 10^{-3}$ in t_{max}
		1900	2.1184		294.76	434.61	5.1794	7.6367

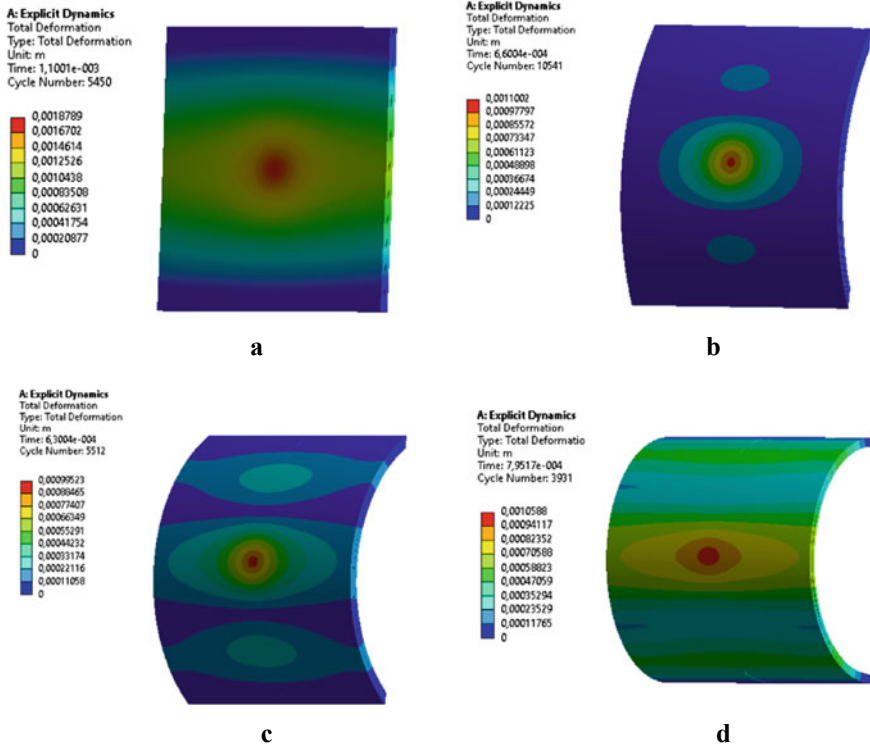


Fig. 6.4 Magnitude of the displacement vector in LG with the ball free fall height 490 (mm) **a** $c = 0$ (mm), **b** $c = 38$ (mm), **c** $c = 76$ (mm), **d** $c = 152.5$ (mm)

where A_0 is the offset and A_1, A_2, A_3 —are coefficients. The values of the regression parameters are shown in Table 6.3. The maximum magnitude of the displacement vector decreases with increasing the curvature parameter, but with a high curvature parameter, it can increase slightly (Fig. 6.6). The Intensity Stress was considered at point H at t_{max} . It increases with increasing curvature parameter until about 45 mm and then decreases (Fig. 6.7).

The Intensity Strain distribution, especially in the PVB interlayer, reflects that the maximum values are placed in the impact zone of the LG, and the minimum strain

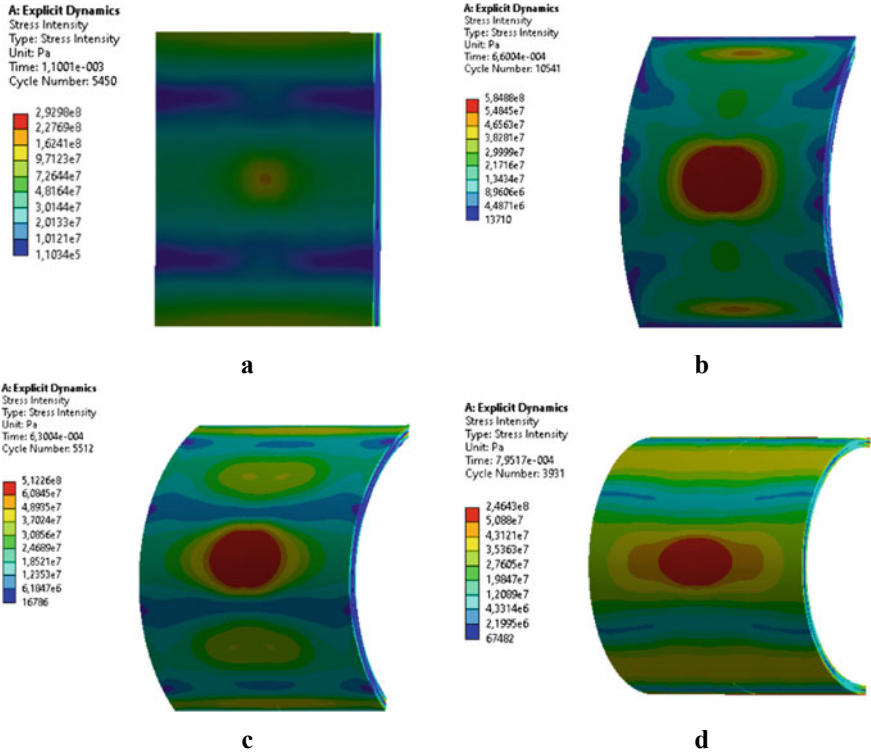


Fig. 6.5 Intensity Stress in LG with the ball free fall height 490 (mm) **a** $c = 0$ (mm), **b** $c = 38$ (mm), **c** $c = 76$ (mm), **d** $c = 152.5$ (mm)

Table 6.3 Regression parameters

Parameter	y_0 (mm)	S (mm)	R_0 (1/mm)	A_0 (MPa)	A_1 (MPa/mm)	A_2 (MPa/mm ²)	A_3 (MPa/mm ³)
Value	1.049	0.922	-0.095	245.468	3.223	-0.045	1.435×10^{-4}

can be observed at the edges of the model. With increasing a curvature parameter, the distribution of Intensity Strain can be observed along the LG (Fig. 6.8).

6.5 Conclusions

This work investigates the dynamics of the stress–strain state in LG with different curvatures, which consisted of two glasses with a thickness of 5 mm, laminated together with PVB interlayer thickness of 1.52 mm. The curvature parameter has been varying from 0 to 152.5 mm (i.e. from straight LG up to the curved as cylindrical shell with radius equal to half the side length). The dynamic excitation was formed

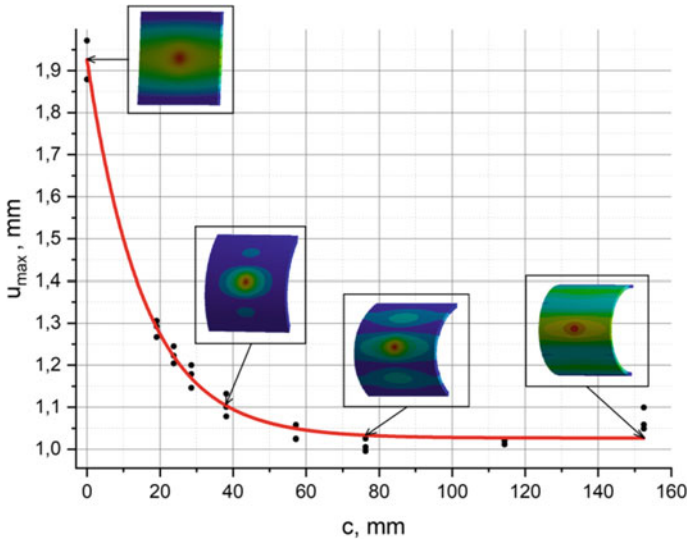


Fig. 6.6 Dependence of maximum magnitude of the displacement vector on the curvature parameter with the ball free fall height 490 (mm)

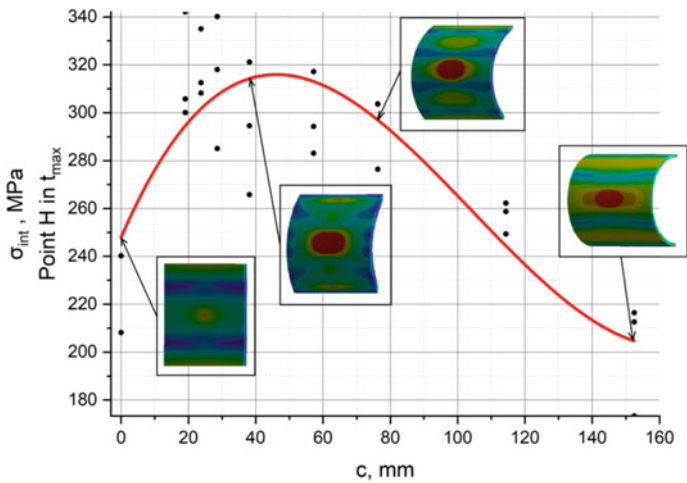


Fig. 6.7 Dependence of Intensity Stress at point H at t_{max} on the curvature parameter with the ball free fall height 490 (mm)

due to the impact loading on the composite, which was modeled as a dynamic one-way interaction with a rigid spherical body with a diameter of 83 mm (2.3 kg) to simulate a ball impact test on the composite with different free ball fall heights.

The computer model was developed within the FEM in a three-dimensional setting with explicit dynamic modeling of each structural element of the composite. The

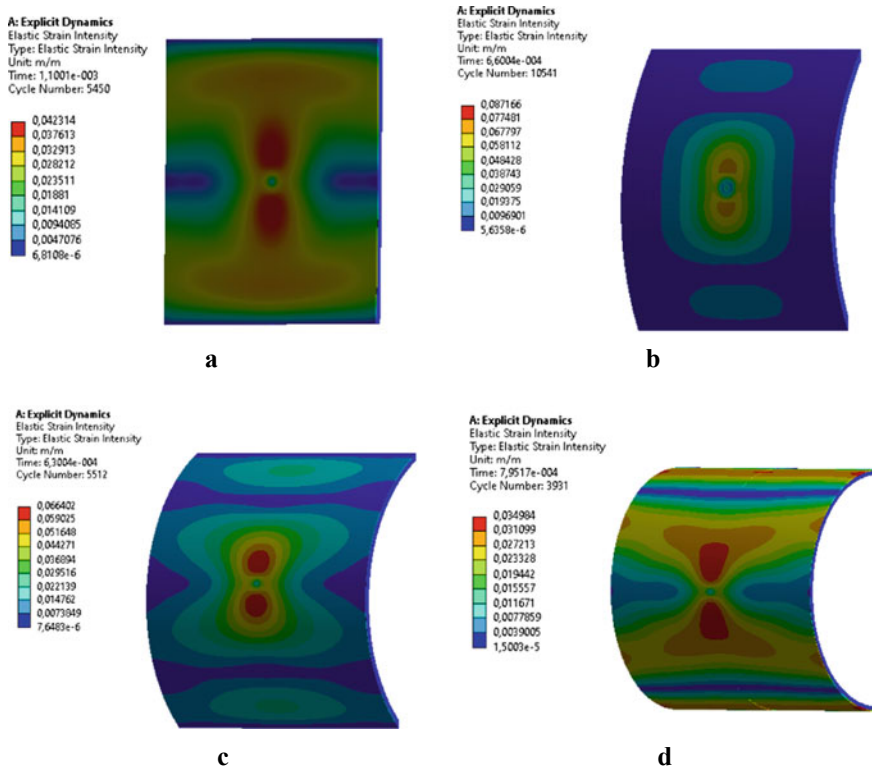


Fig. 6.8 Intensity elastic strain in PVB interlayer with the ball free fall height 490 (mm) **a** $c = 0$ (mm), **b** $c = 38$ (mm), **c** $c = 76$ (mm), **d** $c = 152.5$ (mm)

curvature parameter and the height of free ball fall are varied. The results of maximum displacements, intensity stresses, and strains are obtained and analyzed. The results showed that the distribution of maximum magnitude of the displacement vector, Intensity Stress, and Strain can be traced along the LG, with a curvature parameter increasing.

A fitting analysis of the data was performed to analyze the dependence of magnitude of the displacement vector and Intensity Stress on the curvature parameter. The maximum magnitude of the displacement vector decreases with increasing the curvature parameter, but with a high curvature parameter, it can increase slightly. The Intensity Stress was considered at point H at t_{\max} . It increases with increasing curvature parameter until about 45 mm and then decreases.

Acknowledgements This work has been supported by the Ministry of Education and Science of Ukraine in the framework of the realization of the research project “Development of methods for mathematical modeling of the behavior of new and composite materials aims to structural elements lifetime estimation and prediction of engineering designs reliability” (State Reg. Num. 0117U004969).

References

- Aşik, M.Z., Dural, E., Yetmez, M., Uzhan, T.: A mathematical model for the behavior of laminated uniformly curved glass beams. *Compos. B Eng.* **58**, 593–604 (2014)
- Aßmus, M.: *Structural Mechanics of Anti-Sandwiches—An Introduction*. SpringerBriefs in Continuum Mechanics. Springer (2019)
- Eisentträger, J., Naumenko, K., Altenbach, H., Meenen, J.: A user-defined finite element for laminated glass panels and photovoltaic modules based on a layer-wise theory. *Compos. Struct.* **133**, 265–277 (2015)
- Keller, U., Mortelmans, H.: Adhesion in Laminated Safety Glass—What makes it work? *Glass Processing Days*, pp. 13–16 (1999)
- Naumenko, K., Eremeyev, V.A.: A layer-wise theory for laminated glass and photovoltaic panels. *Compos. Struct.* **112**, 283–291 (2014)
- Schulze, S., Pander, M., Naumenko, K., Altenbach, H.: Analysis of laminated glass beams for photovoltaic applications. *Int. J. Solids Struct.* **49**(15–16), 2027–2036 (2012)
- Vedrtnam, A., Pawar, S.J.: Experimental and simulation studies on fracture of laminated glass having polyvinyl butyral and ethyl vinyl acetate interlayers of different critical thicknesses due to impact load. *Glass Technol. Eur. J. Glass Sci. Technol. Part A* **58**(6), 169–178 (2017)
- Vedrtnam, A., Pawar, S.J.: Laminated plate theories and fracture of laminated glass plate—a review. *Eng. Fract. Mech.* **186**, 316–330 (2017)
- Vedrtnam, A., Pawar, S.J.: Experimental and simulation studies on fracture and adhesion test of laminated glass. *Eng. Fract. Mech.* **190**, 461–470 (2018)
- Weps, M., Naumenko, K., Altenbach, H.: Unsymmetric three-layer laminate with soft core for photovoltaic modules. *Compos. Struct.* **105**, 332–339 (2013)
- Zhang, X., Hao, H., Ma, G.: Laboratory test and numerical simulation of laminated glass window vulnerability to debris impact. *Int. J. Impact Eng.* **55**, 49–62 (2013)

Chapter 7

Modeling the Response of Multilayer Glazing to Distributed and Localized Force Loading



Sergey Ugrimov, Natalia Smetankina, and Vladislav Kobylnik

Abstract The problems of modeling the response of multilayer glazing to dynamic distributed and localized force loading are considered. The dynamic behavior of glazing is described by equations of the layerwise generalized model that accounts for the spatial strain character and inertial loads. The stress distribution pattern is shown to be essentially nonlinear for localized loading. The response of flat glazing to a shock wave and to shocks caused by a solid, soft bodies and a bullet is considered. Computational results are compared to experimental data, as well as to those of similar computations by other investigators.

Keywords Multilayer glazing · Transient vibrations · Impact · Blast loading · Bird strike collision · Bullet resistance

7.1 Introduction

Transparent multilayer structural elements are used widely in modern civil engineering and transport machine building. The multilayer imparts the required strength, and thermal and weight properties to the glazing and it ensures its nonshattering destruction. Both static and dynamic forces affect the glazing. Dynamic loads are meant to be impulse loading, and impact with various solid and soft bodies (Dharani and Wei 2004; Larcher et al. 2012; Mohagheghian et al. 2017; Shim et al. 2016). Special-purpose glazing must meet additional requirements imposed on bullet resistance and on resistance to impact with splinters and other strike elements.

S. Ugrimov (✉) · N. Smetankina · V. Kobylnik
Department of Vibration and Thermostability Studies, A. Pidhorny Institute for Mechanical Engineering Problems National Academy of Sciences of Ukraine, 2/10 Pozharskogo St., Kharkiv 61046, Ukraine
e-mail: sugrimov@ipmach.kharkov.ua

N. Smetankina
e-mail: nsmetankina@ukr.net

V. Kobylnik
e-mail: kobylnikvlad@gmail.com

Glazing can be made of silica glass (SG), organic glass (OG) and polycarbonate layers joined together by polymer adhesive layers. SG reinforced by chemical etching, ion hardening, and thermal hardening is used widely in the glazing of transport vehicles. The mechanical properties of the layers differ significantly (by a factor of hundreds to tens of thousands). The adhesive layers can be thin as well as commensurable to the thickness of the load-bearing layer. The total package thickness can be substantial. Therefore, a qualitative description of the process of layerwise glazing strain calls for using discrete-structural shell models that account for transverse strains. When space-localized loads act on the glazing, higher-order shell theories or three-dimensional models must be used.

Existing multilayer glazing design methods are based on two-dimensional models developed for laminated structures (Amabili and Reddy 2020; Carrera et al. 2011; Carrera and Cinefra 2013; Demasi 2009; Matsunaga 2002; Reddy 2003; Smetankina et al. 2007) or on three-dimensional modeling with the finite element method. As a rule, two-dimensional models use simplified models that approximately describe the transverse shear strain and fail to account for package reduction. In fact, such models can be used effectively only for thin and medium-thickness structures subjected to distributed loading. Problems in theoretical evaluation of multilayer glazing with dynamic localized loading, when the stress-strain state is essentially three-dimensional, have been poorly explored thus far.

Besides, the following problems have been investigated insufficiently: evaluating the strength of multilayer glazing subjected to real dynamic loads; analyzing the process of destruction and penetration of a multilayer glazing. This is due to the mathematical complexity of describing external actions, dynamic response of glazing, and the glass destruction process (Hu et al. 2013; Holmquist and Johnson 2011). Real dynamic loads can be distributed or localized in space. They can also have an intricate, and in some cases, an a priori unknown time behavior. Distributed loads are forces applied to areas whose typical size is significantly greater than the package thickness (or that of the external glazing layer). Local loads are those when the loading area is commensurable with the package thickness. The action of air shock waves and bird strikes are examples of action of distributed loads on a glazing. Impacts with airborne particles, solids, and bullets are examples of local actions. Each of these problems has its own features.

The glazing of motor vehicles and military equipment is designed with account for its being subjected to the action of blast shock loads. The shock wave load affects the external surface of the structure. The loading in this case is a distributed one. As a rule, its time behavior is defined by the mass of the blasting agent and the glazing distance to the blast point. The basic factor involved in assessing the blast danger is the excess pressure on the shock wave front. However, in some cases, it is necessary to account for the influence of not only the increased pressure phase but also of that of the low-pressure phase (Dharani and Wei 2004; Larcher et al. 2012). L. R. Dharani and J. Wei conducted a detailed numerical modeling of the response of architectural three-layer glass to the effects of air shock waves. It was found that, with allowance for the influence of the negative phase, deflection and stress in the

glass can be almost twice as much as the values observed when only the increased pressure phase is considered.

Ensuring aircraft survivability during bird strike collisions is a topical issue (Dolbeer et al. 2011). In 2008–2015, the International Civil Aviation Organization (ICAO) registered 97,751 collisions of aircraft with birds (ICAO 2017). A most dangerous kind of collision is that of a bird with the transparencies, causing their failure and cabin depressurizing. Thereat, transparencies account for 15 to 18% of all collisions of passenger and transport aircraft with birds. All modern aircraft structures are designed with account for likely collision with birds. Thus, aviation standards require that the aircraft glazing would allow the crew to conclude the flight safely after collision with a 1.81-kg bird (Federal Aviation Regulation 2020). Theoretical analysis of the bird strike resistance of aircraft glazing components calls for developing special methods for their strength design to take into account bird strikes (Heimbs 2011; Hedayati et al. 2014). It should be noted that the area of glass loading with a bird strike is large. This is a distributed load (with the exception of a small initial period of glass-bird interaction). The complexity of these problems stems from the difficulty of describing the contact interaction of the bird with an obstacle, and from bird nonuniformity. To date, a number of approaches have been developed to evaluate glazing strength under impact. These approaches are based on the finite-element modeling of both the glazing and the bird. The underpinning of each approach is always a number of assumptions on the form and mechanical parameters of the bird, with one or other equation of state being used. In the general case, these parameters are known poorly and should be found experimentally. In the majority of cases, bird strike action on an obstacle is restricted to considering the hydrostatic pressure (the Hugoniot impulse is neglected). Finite-element modeling can yield qualitative results. However, in the majority of cases, it is computation-intensive. However, in the event of impact with small-deformation obstacles, which in the majority of cases are the glazing of civil aircraft, a no less effective method can be the application of certain semi-empirical relationships that specify the contact interaction parameters. This simplifies computations substantially.

Analysis of glazing strength calls for solving several specific problems related to structural design for low-velocity impact with a solid (Heimbs et al. 2019; Hu et al. 2013). Such problems are as follows: impact on the glazing of buildings by solid particles brought with the wind; impact on the glazing of vehicles by blast fragments; impact on the glazing of aircraft and motorcars by road and airfield pavement fragments; locomotive glazing impact with a solid, and so forth. As a rule, such loadings are localized ones. Thereat the parameters of contact interaction are unknown a priori and must be found when solving the problem. For this purpose, the glazing motion equations are complemented with indenter motion equations and the condition of compatibility of displacement of interacting bodies. Indenter motion is often considered as the motion of a solid, with Hooke's law used to account for deformations in the impact point.

The task of evaluating glazing bullet resistance is one of the most challenging problems (Ben-Dor et al. 2013; Chou et al. 2020; Holmquist and Johnson 2011; Shim et al. 2016). To date, the bullet resistance of multilayer glazing is analyzed, as a rule,

by using finite-element systems. They allow account for glazing deformation and destruction processes with a qualitative result. To achieve this, these systems require the following: a knowledge of the parameters of the state of interacting bodies with allowance for their deformation rates; a consideration of crack propagation processes and methods of reinforcing the glazing. In the majority of cases, these methods have been investigated insufficiently for multilayer glazing materials. A solution to this is the use of semi-empirical relationships for preliminary evaluation of glazing bullet resistance.

The main purpose of this paper is to develop a universal 2-dimensional model of multilayer glass that can be used for transient analysis of the stress–strain state (SSS) of glazing with a different structure and thickness. Another objective is the development of a complex of analytical–numerical methods for analyzing the SSS of multilayer glazing subjected to intense force actions of different origin.

7.2 Mathematical Model of Multilayer Glazing and the Governing Equations

A multilayer glazing is considered, which is secured on the edge and subjected to an external loading force $\bar{P}(p_1, p_2, p_3)$ applied to the first layer. The glazing (Fig. 1) consists of I layers of constant thickness; h_i is the thickness of the i -th layer. The mechanical parameters of the i -th layer of the glazing are designated as follows: E_i is Young’s modulus, ν_i is Poisson’s ratio, ρ_i is density. Contact between layers is assumed to exclude their delamination and mutual slipping.

The behavior of a multilayer glazing is described by equations of the generalized theory of multilayer plates (Ugrimov 2002). It allows choosing the required accuracy of the SSS description, depending on the package composition and loading conditions. The displacements of an i -th layer point are described by the following kinematic relationships:

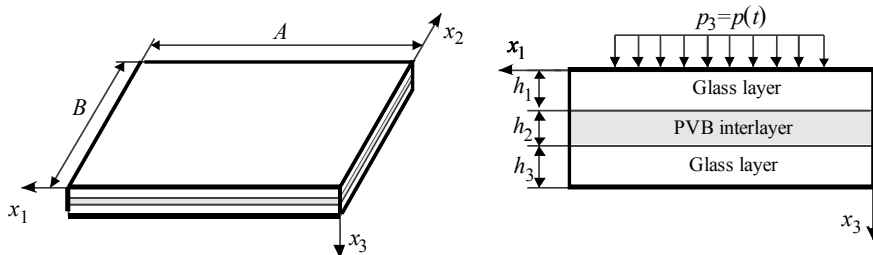


Fig. 1 Multilayer glazing

$$u_{\alpha}^i(x_1, x_2, x_3, t) = u_{\alpha} + \sum_{k=1}^{K_{\alpha}} \left[\sum_{j=1}^{i-1} h_j^k u_{\alpha k}^j + (x_3 - \delta_{i-1})^k u_{\alpha k}^i \right] \quad (1)$$

where $h_j^k = (h_j)^k$; $\delta_i = \sum_{j=1}^i h_j$, $\delta_{i-1} \leq x_3 \leq \delta_i$, $i = \overline{1, I}$; u_{α}^i ($\alpha = \overline{1, 3}$) are displacements of an i -th layer point in the direction of the coordinate axes Ox_{α} ; u_{α} , $u_{\alpha k}^i$ are terms in power series expansions depending on x_1 , x_2 , t ; K_{α} are maximum powers of terms retained in a power series for in plane ($\alpha = 1, 2$) and transverse displacements ($\alpha = 3$), with the values of parameters K_{α} being chosen depending on the required approximation accuracy. In so doing, K_1 and K_2 will be the same and equal to K . Henceforth, the generalized theory will be designated by the number of retained terms in power series (1) for plane and transverse displacements—theory $\{K, K_3\}$.

The accepted kinematic relationships (1) are equivalent to the following hypotheses: for $\{1, 0\}$, of the E. I. Grigoliuk and P. P. Chulkov model; for $\{1, 1\}$, of the first-order refined model that accounts for reduction of each layer; for $\{3, 2\}$, of the higher-order model that enables studying localized loading (Shupikov et al. 1998; Ugrimov 2002).

The strains $\varepsilon_{\alpha\beta}^i$ of the layers are assumed small and are described by Cauchy's formulas. The stresses $p_{\alpha\beta}^i$ in the layers are calculated based on Hooke's law.

$$\begin{aligned} p_{\alpha\beta}^i &= \lambda^i \delta_{\alpha\beta} \varepsilon_{11}^i + 2\mu^i \varepsilon_{\alpha\beta}^i, \varepsilon_{11}^i \\ &= \varepsilon_{11}^i + \varepsilon_{22}^i + \varepsilon_{33}^i, \varepsilon_{\alpha\beta}^i = (u_{\alpha\beta}^i + u_{\beta,\alpha}^i)/2, \\ \lambda^i &= E_i v_i / ((1 + v_i)(1 - 2v_i)), \mu^i \\ &= 0.5 E_i / (1 + v_i), \alpha, \beta = \overline{1, 3}, i = \overline{1, I}, \end{aligned}$$

where $\delta_{\alpha\beta}$ is Kronecker delta; $\varepsilon_{\alpha\beta}^i$ is strain tensor; λ^i , μ^i are Lamé's coefficients of an i -th layer; E_i , v_i are Young's modulus and Poisson's coefficient of an i -th layer.

The equations of motion and the boundary conditions are found using the Ostrogradsky-Hamilton variational principle as this was done for layered plates (Shupikov et al. 1998). The equations of motions in term of the resultant stress have the following form (Ugrimov 2002):

$$\begin{aligned} \sum_{i=1}^I [L_{\alpha}^i - I_{\alpha 1}^i] + p_{\alpha} &= 0, \\ N_{1\alpha,1}^{ik_{\alpha}} + N_{\alpha 2,2}^{ik_{\alpha}} - k_{\alpha} N_{\alpha 3}^{ik_{\alpha}-1} \\ &+ h_i^{k_{\alpha}} \sum_{j=i}^{I-1} [L_{\alpha}^{j+1} - I_{\alpha 1}^{j+1}] - I_{\alpha k_{\alpha}+1}^i = 0 \end{aligned} \quad (2)$$

where $L_1^i = N_{11,1}^{i0} + N_{12,2}^{i0}$, $L_2^i = N_{22,2}^{i0} + N_{12,1}^{i0}$, $L_3^i = N_{13,1}^{i0} + N_{23,2}^{i0}$, $N_{\alpha\beta}^{ik} = N_{\beta\alpha}^{ik} = \int_{\delta_{i-1}}^{\delta_i} (x_3 - \delta_{i-1})^k p_{\alpha\beta}^i dx_3$, $I_{\alpha r}^i = \frac{\rho_i h_i^r}{r} \left(u_{\alpha 0,tt} + \sum_{k=1}^{K_\alpha} \left[\sum_{j=1}^{i-1} h_j^k u_{\alpha k,tt}^j + \frac{r h_i^k}{k+r} u_{\alpha k,tt}^i \right] \right)$, $\alpha = \overline{1, 3}$, $k_\alpha = \overline{1, K_\alpha}$, $i = \overline{1, I}$, $i = \overline{1, I}$.

Thus, the dynamic response of a plate is described by $(2K + K_3)I + 3$ differential equations, with the number of governing equations depending on the number of layers.

The glazing in motorcars, locomotives, and aircraft is secured using a rubber-sealing strip. It is held in place along the perimeter with a polymer or rubber retainer. This allows considering glazing elements as simply supported ones. Therefore, for rectangular glazing ($A \times B$), the components of the external load \overline{P} as well as displacement functions $u_\alpha, u_{\alpha k}^i$ are expanded into a series in terms of functions $B_{amn}(x_1, x_2)$ satisfying the simply supported conditions.

$$\begin{aligned} [u_\alpha, u_{\alpha k}^i, p_\alpha] &= \sum_{m=1}^{\infty} \sum_{n=1}^{\infty} [\Phi_{amn}(t), \Phi_{\alpha kmn}^i(t), p_{amn}(t)] \cdot B_{amn}(x_1, x_2) \\ B_{1mn} &= \cos d_1 x_1 \cdot \sin d_2 x_2, \\ B_{2mn} &= \sin d_1 x_1 \cdot \cos d_2 x_2, \\ B_{3mn} &= \sin d_1 x_1 \cdot \sin d_2 x_2, \\ d_1 &= m\pi/A, d_2 = n\pi/B. \end{aligned}$$

Hence, the problem of non-stationary vibrations of a multilayer glazing for each pair of values m and n is reduced to integrating a system of ordinary differential equations with a constant coefficient.

$$\Omega \cdot \overline{\Phi}_{tt}^{mn} - \Lambda^{mn} \cdot \overline{\Phi}^{mn} = \overline{Q}^{mn}, \overline{\Phi}^{mn} \Big|_{t=0} = 0, \overline{\Phi}_{,t}^{mn} \Big|_{t=0} = 0.$$

where Ω , Λ^{mn} is mass matrix and stiffness matrix (Ugrimov 2002); $\overline{\Phi}^{mn}$, \overline{Q}^{mn} are vectors.

$$(\overline{\Phi}^{mn})^T = (\Phi_{amn}, \Phi_{\alpha kmn}^i), (\overline{Q}^{mn})^T = (p_{amn}, 0, \dots, 0), i = \overline{1, I}, k_\alpha = \overline{1, K_\alpha}.$$

The system obtained is integrated by using the modified method of expanding the solution into Taylor's series.

7.3 Investigation of the SSS in Glazing Under Dynamic Force Loading

7.3.1 Distributed and Localized Loading. Transient Dynamic Analysis

The essentially dissimilar mechanical properties of layers in multilayer glass require that transverse normal and shear strains in the applied mathematical model are accounted for. Localized loading poses yet more strict requirements to the model being used. The limits to the applicability of different glass models obtained in terms of hypothesis (1) for different values of K_α were investigated.

The effect of accounting for transverse reduction (strain ε_{33}) in the mathematical model was studied. The glass was modeled using the E.I. Grigoliuk and P.P. Chulkov model {1, 0}, which fails to account for transverse reduction, and the refined first-order model {1, 1} that takes into consideration the reduction of each layer. Let us consider the dynamic behavior of a three-layer square-shaped simple-supported glazing ($A = B = 0.5$ m, $h_1 = h_3 = 0.015$ m, $h_2 = 0.003$ m) with impulse loading.

$$p_1 = p_2 = 0, p_3 = \frac{1}{2} P_0 [1 + \text{sign}(t_1 - t)] \sin \frac{\pi t}{t_1} \sin \pi \frac{x_1 - x_{11}}{x_{12} - x_{11}} \sin \pi \frac{x_2 - x_{21}}{x_{22} - x_{21}} \quad (3)$$

applied to the outer surface of the first layer over a rectangular area $x_{11} \leq x_1 \leq x_{12}$, $x_{21} \leq x_2 \leq x_{22}$, $t_1 = 4$ ms.

The glazing is composed of two SG bonded by a polyvinyl butyral (PVB) layer. The mechanical properties of layers are: $E_1 = E_3 = 61.2$ GPa, $\nu_1 = \nu_3 = 0.22$, $\rho_1 = \rho_3 = 2500$ kg/m³, $E_2 = 0.28$ GPa, $\nu_2 = 0.38$, $\rho_2 = 1200$ kg/m³.

The SSS in glass under impulse distributed and localized loading (3) is studied. The distributed loading that acts almost over the entire outer layer surface has the following parameters $x_{11} = x_{21} = 0.01$ m, $x_{12} = x_{22} = 0.49$ m, $P_0 = 7.8125$ kPa. The localized loading that is distributed over a square area 0.0048 m \times 0.0048 m has the parameters $x_{11} = x_{21} = 0.2476$ m, $x_{12} = x_{22} = 0.2524$ m, $P_0 = 78.125$ MPa.

Figure 2a, b show the through-the-thickness distribution of normal stresses p_{11}^i at the center of the glazing. The distributions are given for time instances when they achieve their maximum values on the outside surface of the first layer. Figure 2a shows the distributed loading and Fig. 2b, the localized one. The stresses in the polymer material layer ($i = 2$) are not shown in the figures because they are much smaller than the similar values for bearing layers ($i = 1, 3$), and they can be omitted for the graph scale shown.

It is evident from Fig. 2 that, with distributed loading, the results obtained without taking into consideration the transverse reduction of layers are in good agreement with similar computational data obtained by using the suggested refined first-order

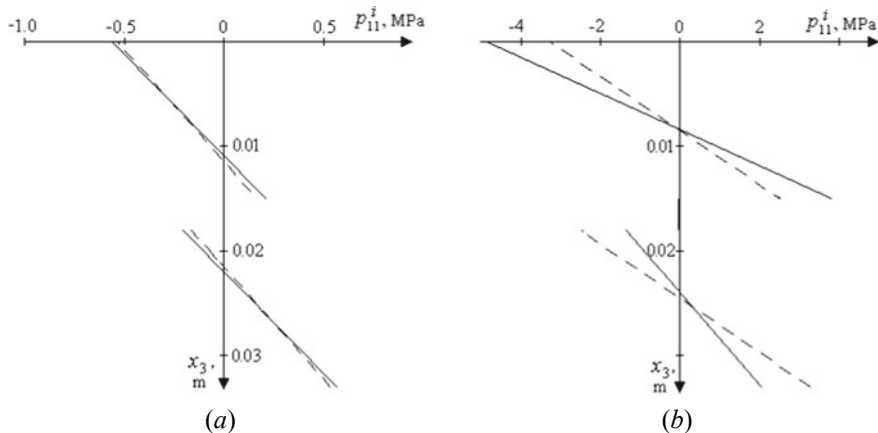


Fig. 2 Through-the-thickness distribution of stresses p_{11}^i for distributed (a) and localized (b) loadings (the solid lines are for the refined first-order theory, and the dashed lines are for the E.I. Grigoliuk and P.P. Chulkov theory)

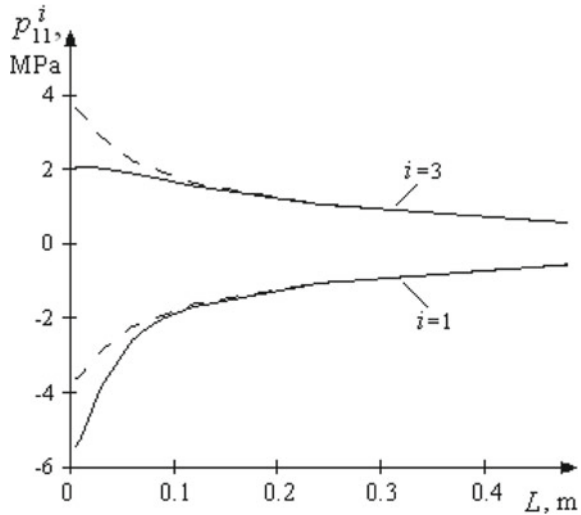
theory (Fig. 2a). When localized loading acts on the glazing, the results obtained with the discussed models differ significantly (Fig. 2b).

The influence of the characteristic size of the loading area (3) on the maximum stresses in glazing was investigated. As before, the load is assumed to be applied to a square area with the sides $L = x_{12} - x_{11} = x_{22} - x_{21}$ arranged symmetrically relative to the center of the outer glass plate surface. The total force applied to the plate is always constant and equal to 1.8 kN. The characteristic size of loading area L varies within 0.48–0.0048 m. The ultimate range values correspond to the cases of distributed and local loading studied earlier.

Figure 3 shows the maximum stresses at the center of the outer surfaces of the bearing layers. The difference in the results obtained by {1, 0} and {1, 1} theories increases with decreasing dimensions of the loading area. The differences become evident for loading area dimensions smaller than 0.1 m. This corresponds to about three glazing thicknesses. According to the E.I. Grigoliuk and P.P. Chulkov theory, which fails to account for transverse strain of layers, the moduli of the stresses found for the glazing on the outer layers were equal. However, under localized loading, the pattern of the through-the-thickness distribution of real stresses is non-symmetrical (see Fig. 2b). As a result, according to the {1, 0} model, the bending stresses on the outer surface of the first layer are smaller than similar values found according to the suggested refined theory. On the outer surface of the third layer, these values are bigger. In the case being discussed, the E. I. Grigoliuk and P. P. Chulkov theory yields averaged values of real stresses.

For the case of localized loading of a square three-layer glazing, $A = B = 0.5$ m with a symmetrical structure ($h_1 = h_3$) and the same mechanical parameters of the layers as those of the glass considered above, the impact of the ratio of the layers' thicknesses were investigated for maximum bending stresses. The thickness of the

Fig. 3 Maximum flexural stresses vs. characteristic size of the loading area (the solid lines show the result for the refined theory, and the dashed lines are for the E. I. Grigoliuk and P. P. Chulkov theory)

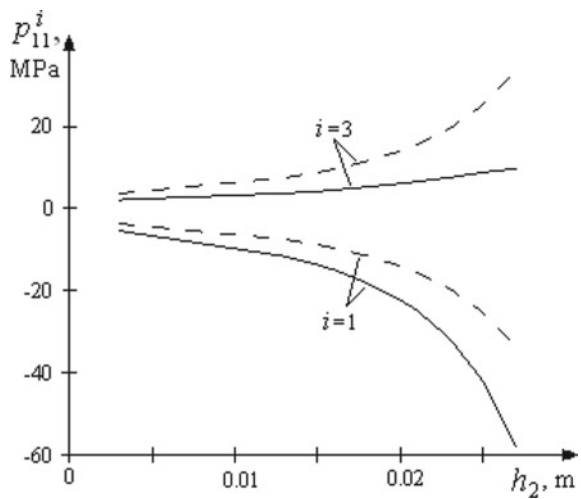


second softer layer was varied within 0.003 m to 0.027 m with a constant glazing thickness of 0.033 m.

Figure 4 shows the variation of the stresses in the outer layers vs. second layer thickness under localized loading. With increasing thickness of the soft layer, glass reduction becomes more pronounced and the difference between the results obtained according to the models, which account and do not account for reduction, increases.

When studying glazing response to force loading, the need to account for nonlinear terms of expansion (1) was also considered.

Fig. 4 Maximum bending stresses vs. second layer thickness under localized loading The solid lines are for the refined theory, and the dashed lines are for the E. I. Grigoliuk and P. P. Chulkov theory



The response of three-layer glazing to impulse load action was investigated. The glazing has the following geometric parameters: $A = 0.47$ m; $B = 0.42$ m, $h_1 = h_3 = 0.012$ m, $h_2 = 0.002$ m. The bearing layers ($i = 1, 3$) are made of SG ($E_1 = E_3 = 66.7$ GPa, $\nu_1 = \nu_3 = 0.22$, $\rho_1 = \rho_3 = 2500$ kg/m³). The adhesive layer ($i = 2$) is made of a polymer ($E_2 = 0.274$ GPa, $\nu_2 = 0.38$, $\rho_1 = \rho_3 = 1200$ kg/m³). The impulse load is applied to a rectangular area $x_1 \leq x \leq x_2$, $y_1 \leq y \leq y_2$ according to the law.

$$p_1 = p_2 = 0, p_3 = P_0H(t).$$

Here P_0 is load intensity and $H(t)$ is Heavyside's function. The value P_0 is selected for the total force to be $P = 2$ kN in all the cases being investigated. Distributed loading acts on the entire external surface of the first layer with the load intensity $P_0 = 10.13$ kPa. Localized loading is distributed evenly over a square with the side 0.005 m at the center of the external surface of the first layer with the load intensity $P_0 = 80$ MPa.

Figure 5a, b shows the through-the-thickness distribution of normal stresses at the glazing center when they reach their maximum values for distributed (Fig. 5a) and localized (Fig. 5b) loading. The stresses in the bearing layers ($i = 1, 3$) significantly exceed those in the adhesive layer ($i = 2$). Therefore, their pictorial presentation for the accepted scale in Fig. 5 is problematic.

A good match of results is achieved based on the first-order theory and the high-order theory for distributed loads. When localized loads act on the glazing, the results differ drastically. In this case, the through-the-thickness stress distribution

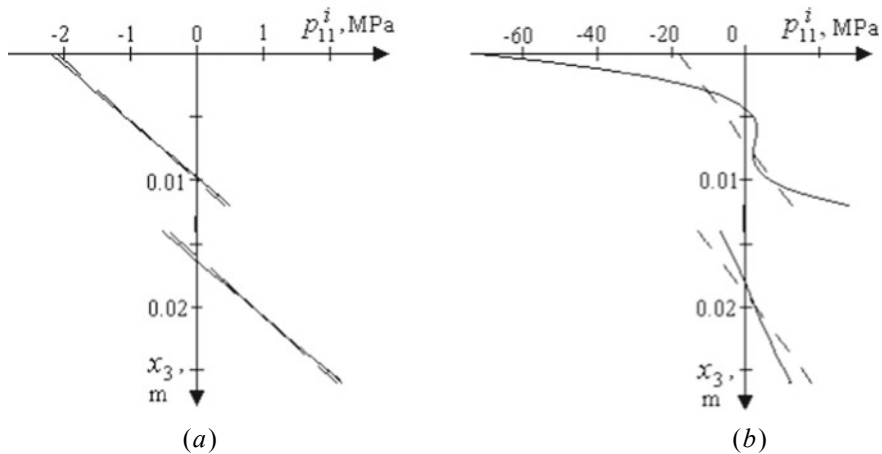


Fig. 5 Through-the- thickness distribution of normal stresses in a three-layer glazing for distributed (a) and localized (b) loadings. The solid lines show the result for the theory {3, 2}, and the dashed lines are for the first-order theory {1, 0}

in the glazing is a nonlinear one (Ugrimov 2002). It is approximated poorly by classical models and models based on the broken normal hypotheses (Timoshenko-type models).

Note that the through-the-thickness distribution of transverse shear stresses in the glazing even for distributed loading is nonlinear and cannot be described using linear approximations.

The three-layer glazing ($A = B = 0.5$ m, $h_1 = h_2 = h_3 = 0.01$ m) subjected to impulse distributed loading was considered. The impulse load has the form.

$$p_3 = P_0 \cdot H(t) \cdot \sin \frac{\pi x_1}{A} \cdot \sin \frac{\pi x_2}{B}, p_1 = p_2 = 0,$$

where $P_0 = 0.1$ MPa.

The character of the through-the-thickness distribution of transverse shear stresses that depend on the filler susceptibility in a three-layer plate whose external layers are made of SG ($E_1 = E_3 = 66.7$ GPa, $\nu_1 = \nu_3 = 0.22$, $\rho_1 = \rho_3 = 2500$ kg/m³) is investigated. The other mechanical characteristics (Poisson's ratio, density) of the inner layer were assumed equal to the SG characteristics ($\nu_1 = \nu_2 = \nu_3$, $\rho_1 = \rho_2 = \rho_3$).

Figure 6 shows the through-the-thickness distribution of transverse stresses p_{13}^i in the glazing being considered for three E_2/E_1 ratios. The stresses are taken in points $x_1 = 0.125$ m, $x_2 = 0.25$ m. The distributions are given for time instances when they achieve their maximum values on the outside surface of the first layer. The results of computations according to the theory described are compared against the exact solution found by the analytic method (Ugrimov 2002).

Figure 6 shows that the generalized theory with parameters {3, 2} and {7, 6} yields a distribution very close to a real one. By applying the {1, 1} theory, which accounts only for shear strains averaged over layer thickness, it is impossible to describe precisely the through-the-thickness stress distribution and to meet, even approximately, the interlayer contact conditions ($p_{13}^i = p_{13}^{i+1}$). For the case of homogeneous glazing ($E_2 = E_1$), the through-the-thickness distribution of stresses is parabolic. With a decreasing elasticity modulus of the middle layer, the external layers take the greater part of the load. The through-the-thickness distribution of stresses in the middle layer becomes close to a linear one, whereas in the external layers it remains nonlinear. At $E_2 = E_1$ and $E_2 = 10^{-3}E_1$, the through-the-thickness distribution of stresses is nearly symmetrical relative to the packet median line; at $E_2 = 10^{-6}E_1$, it is nonsymmetrical. This is because that with a very soft aggregate, the glazing outer layer begins to take the greater part of the external load.

Next, the SSS in a multilayer glazing for real distributed and localized loadings were considered.

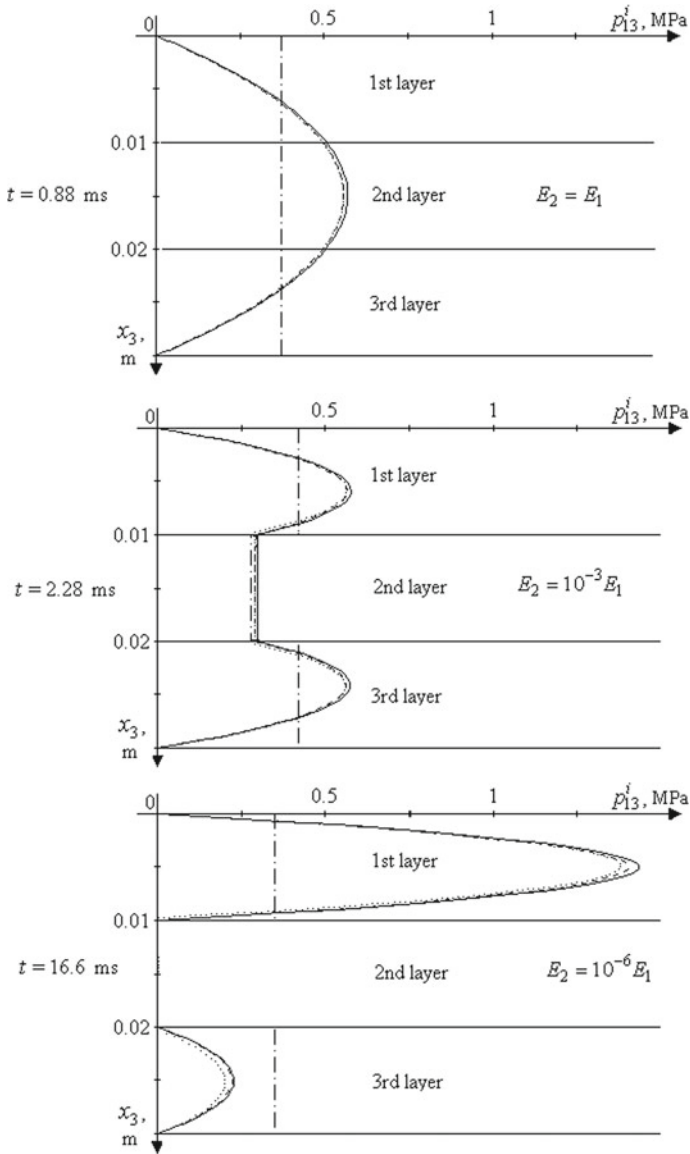


Fig. 6 Through-the-thickness distribution of shear stresses in a three-layer glazing at distributed loadings (the solid lines are for the 3-dimensional solution; the dashed lines are for the theory {7, 6}; the dotted lines are for the theory {3, 2}; the dash-dot lines are for the theory {1, 1})

7.3.2 Blast Loading

Transient analysis of multilayer glazing response to the impact of an air shock is considered. The impulse acting on the structure during a blast is described as follows (Dharani and Wei 2004).

$$p_1 = p_2 = 0, p_3 = \Delta p \cdot (1 - t/\tau_+) \cdot \exp(-\gamma t/\tau_+).$$

Here Δp is maximum pressure at $t = 0$; τ_+ is duration of action of the increased pressure phase; γ is decomposition factor. Here it is assumed that the glazing is arranged perpendicularly to the wave propagation direction and fairly far from the blast point. This allows considering the wave a plane one. The load is applied across the entire outer surface of the first layer.

A numerical study was performed for the impact of an air shock wave on architectural three-layer glazing with the geometrical characteristics $A = B = 1.325$ m, $h_1 = h_3 = 0.00476$ m, $h_2 = 0.00152$ m whose external layers are made of SG with the mechanical properties: $E_i = 72$ GPa, $\rho_i = 2500$ kg/m³, $\nu_i = 0.25$, $i = 1, 3$. The other layer is made of PVB: $E_2 = 0.274$ GPa, $\rho_2 = 1100$ kg/m³, $\nu_2 = 0.38$.

Figure 7 shows the time dependence of deflections at the center of the glazing caused by an air shock wave with and without account for the low-pressure phase. The shock wave parameters are $\tau_+ = 7.7$ ms, $\gamma = 0.55$, $\Delta p = 6894.8$ Pa. Calculation results were compared with data obtained by L. R. Dharani and J. Wei (Dharani and Wei 2004). The close agreement of results confirms the applicability of the suggested approach for distributed loading.

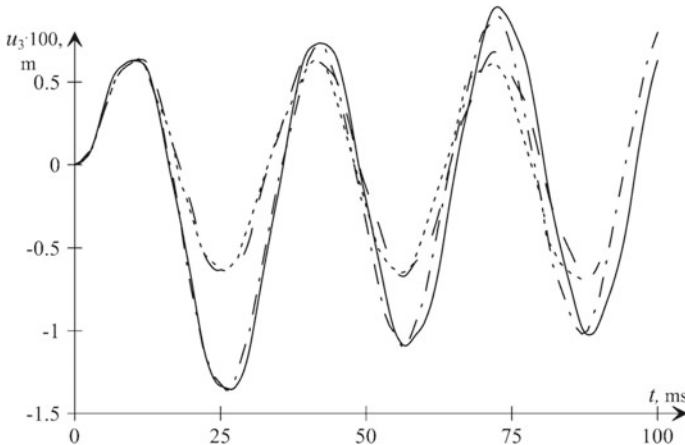


Fig. 7 Deflections in three-layer glazing under blast loading (the solid and dashed lines show the result of deflection for the suggested model with account for the low-pressure phase and without account for it correspondingly, the dot-and-dash and dotted lines are for similar results obtained by L. R. Dharani and J. Wei)

7.3.3 Bird Collision

Transient analysis of a glazing system subjected to bird strike is considered. A bird with mass M collides with the glazing system with velocity V . The bird's trajectory of motion is at angle α to the target plane (Fig. 8). The bird's geometrical and physical body characteristics should be known to describe the parameters of the bird strike impact on the target. As a rule, the bird's body is simulated using a cylinder, a cylinder with mating hemispheres, and an ellipsoid (Shupikov et al. 2013). An ellipsoid describes the shape of the bird's body with best accuracy. This is why the bird's body model was an ellipsoid with axes $2c$, $2a$, $2b$, and with the average body mass density of 0.93 g/cm^3 .

The area of contact of the bird with a flat glazing is elliptical in shape. The components of the vector of the external load acting on the glazing system during a strike are represented as

$$p_1 = p_2 = 0, p_3 = \frac{1}{2}[1 + \text{sign}(\tau_p - t)]F \sin \alpha,$$

where τ_p is time of the bird-and-target interaction; $F = F(x_1, x_2, t)$ is function of contact pressure over the load area. Here it is assumed that, with a bird strike, the values of the load tangential components are much less than those of the normal component, and they can be ignored when the glazing strength is analyzed. This can be justified in part in that the normal load is more dangerous for the glazing, and that bird density is close to that of water.

The distribution of the contact pressure over the load area is assumed to be

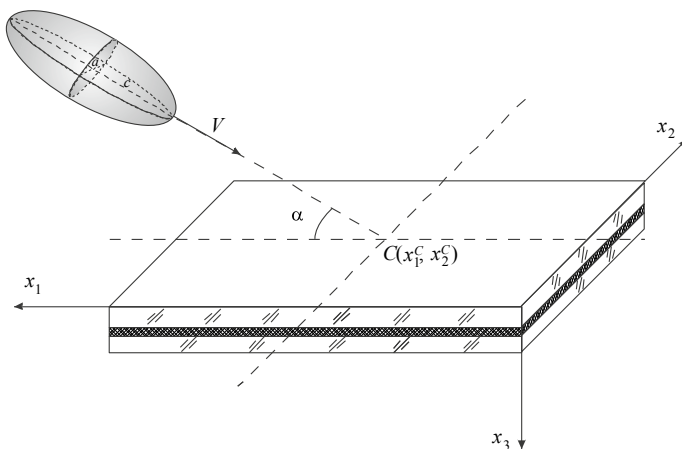


Fig. 8 Bird strike collision with a flat glazing

$$F = P_0 \left[1 - (x_1 - x_1^c - \delta)^2 / u_b^2 - (x_2 - x_2^c)^2 / v_b^2 \right]^{1/2},$$

where $P_0 = P_0(t)$ is load intensity; u_b and v_b are lengths of semiaxes of the elliptical load area; x_1^c , x_2^c are coordinates indicating the point where the trajectory of motion of the bird's center of mass intersects the glazing system; δ is a parameter characterizing the displacement of the center of the load area during oblique strikes.

The force of contact interaction (instantaneous impact force) of the bird and plate relates to load intensity as follows:

$$P_b = \int_{\Omega(t)} p_3(x_1, x_2, t) dx_1 dx_2 = \frac{2}{3} P_0 \pi u_b v_b,$$

where $P_b = P_b(t)$ is contact force; $\Omega(t)$ is the elliptical area of bird and glazing contact.

Values u_b , v_b , δ , P_b vary with time and depend on the bird mass, impact angle, and velocity. In the general case, they should be found from experimental data.

According to the fluid dynamic theory suggested, the first approximation of the contact interaction force P_b is assumed to be represented by the value found from the fluid dynamic theory. During normal impact, it takes the form $P_b(t) = \rho_b V^2 \pi u_b v_b$, where ρ_b is bird tissue density, $\rho_b = 3M/(4\pi abc)$. Variation of u_b , v_b in time is approximated as the dimensions of the ellipsoid section with a plane simulating a flat target. The load action time is known to depend on the impact angle, and it is slightly greater than the squashing time. It can be found approximately using the formula $t_b = 2ck/V$, where k is a coefficient selected from experimental data.

The response of five-layer aircraft glazing ($A = 0.66$ m, $B = 0.33$ m, $h_1 = 0.005$ -m, $h_2 = 0.003$ -m, $h_3 = 0.015$ -m, $h_4 = 0.002$ -m, $h_5 = 0.02$ -m) during collision with a 1.8-kg bird at different impact velocities (134 and 191 m/s) and an impact angle of $\alpha = 30^\circ$ is investigated. The glazing is composed of three PVB-bonded SGs. The mechanical properties of SG are $E = 64$ GPa, $\nu = 0.22$, $\rho = 2500$ kg/m³. The PVB mechanical properties are $E = 0.25$ GPa, $\nu = 0.39$, $\rho = 1200$ kg/m³. Figure 8 shows the theoretical and experimental data of glazing stress p_{22}^5 in point $x_1 = A/2$, $x_2 = B/2$, $x_3 = \delta_5$ at the collision velocities 191 m/s (Fig. 9a) and 134 m/s (Fig. 9b). The solid line is the theoretical curve and the dashed line denotes the experimental data (Onhirskey et al. 2009).

7.3.4 Low-Velocity Impact Loading

The multilayer glazing transient response to low-velocity impact loading was also investigated. In this problem, the system of Eq. (2) is to be complemented with the ball motion equation and the condition of compatibility of displacements of the indenter and the glazing (Smetankina et al. 2007; Shupikov et al. 1998).

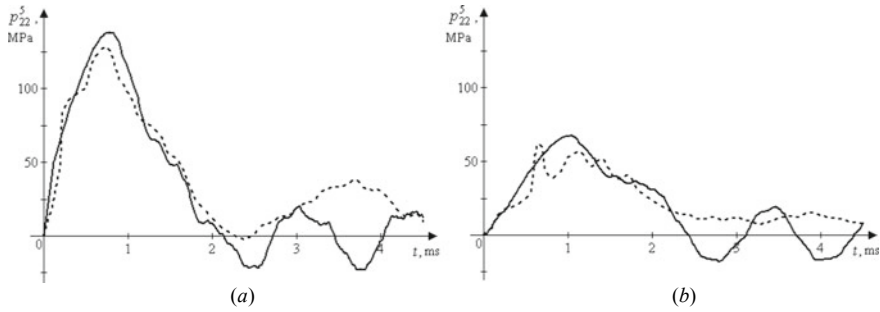


Fig. 9 Response of a glazing element to bird strike at the collision velocities 191 m/s **(a)** and 134 m/s **(b)** (the solid line is the theoretical curve, and the dashed line denotes the experimental data)

$$u_3^1(x_{10}, x_{20}, 0, t) + \chi(t) - z(t) \geq 0,$$

where $\chi(t)$ is contact indentation, $z = z(t)$ are coordinates of the indenter center of mass.

Contact indentation is defined by Hertz law $\chi = kP^{2/3}$, where P is contact force, k is a coefficient, which depends on the material and form of interacting bodies.

The radius of the contact area $r(t)$ in case of impact by a ball of radius R is computed by formula (Smetankina et al. 2007, Shupikov et al. 1998).

$$r(t) = [3P(t) \cdot R \cdot (\theta + \theta_1)/16]^{1/3},$$

$$\theta_1 = 4(1 - \nu_1^2)/E_1, \theta = 4(1 - \nu^2)/E,$$

where E , ν are Young's modulus and the Poisson ratio for the ball material, and E_1 , ν_1 are values of Young's modulus and the Poisson ratio for the first layer.

The contact force is found on the assumption of compatibility of displacements at each time step. This is a nonlinear equation of a relatively unknown contact force. The procedure for solving this problem is described in Smetankina et al. (2007); Shupikov et al. (1998).

The dynamic response of a five-layer aviation glazing to impact loading is considered. The numerical results are compared with experimental data. The geometrical characteristics for a five-layer glazing are as follows: $A = 0.6$ m; $B = 0.28$ m; $h_1 = 0.005$ m; $h_2 = 0.003$ m; $h_3 = 0.015$ m; $h_4 = 0.002$ m; $h_5 = 0.02$ m. The bearing layers ($i = 1, 3, 5$) are made of SG ($E_i = 64$ GPa, $\nu_i = 0.22$, $\rho_i = 2500$ kg/m³) and the adhesive ones ($i = 2, 4$), of a polymer ($E_i = 0.25$ GPa, $\nu_i = 0.39$, $\rho_i = 1200$ kg/m³). Impact loading was effected by an indenter $M = 0.215$ kg, $R = 0.03$ m dropped from the height $h = 1$ m. The indenter was made of OG ($E = 5.59$ GPa, $\nu = 0.38$, $\rho = 1200$ kg/m³). The impact was on the external surface of the first layer at the center of the plate. The strains are calculated for the external surface of the last layer in the impact point.

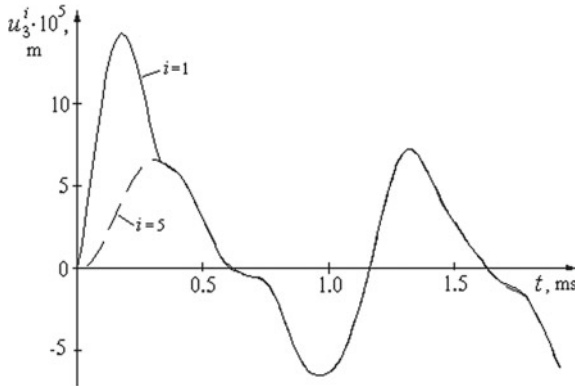


Fig. 10 Deflections in a five-layer glazing under impact

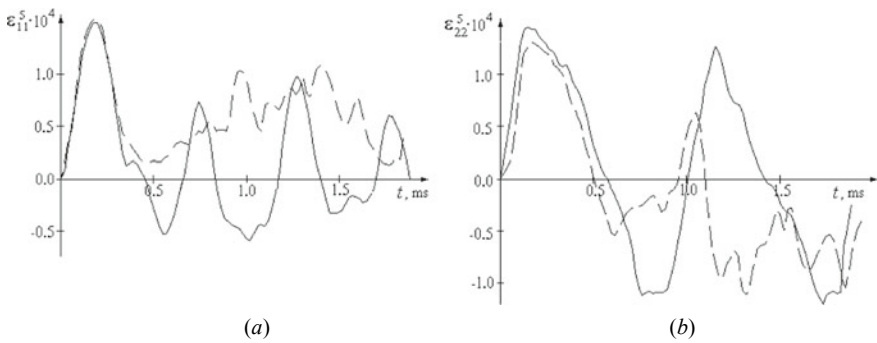


Fig. 11 Strains in a five-layer glazing vs time under impact loading: **a** ϵ_{11} , **b** ϵ_{22} (the solid line designates the numerical result, and the dashed line shows the experimental one (Shupikov et al. 1998))

Figure 10 shows the numerical values of deflections of the external surfaces of the first (solid line) and last (dashed line) layers in the impact point.

Figure 11 shows the strains in a five-layer glazing versus time. A comparison of theoretical and experimental data in Fig. 5 shows that the suggested theory consistently describes the process of transient strain of multilayer glazing under localized loading.

7.3.5 Bullet Resistance

A vital problem for military equipment is to increase the bulletproof performance of aircraft cockpits and glazing of armored ground vehicles. Analyzing the bullet resistance of glazing is a challenging mathematical problem (Shim et al. 2016; Cho et al.

2020). In this case, two processes need to be accounted for, namely, the penetration process and the deformation process in the glazing at impact. Further, in the paper, we will consider only the process of indenter penetration. For simplicity, the process of penetration of a rigid indenter into multilayer glazing at the initial stage can be represented as follows: indenter penetration into an unbounded medium; knockout of the so-called Hertz cones during direct contact with the silica glass layers and involvement of the cones in joint motion. As a result, up to the instance of destruction of the cone proper, the pressure from the indenter is transmitted to the next layers across an area much bigger than that resulting from the bullet diameter. Due to this, the bullet kinetic energy decreases faster. Following cone destruction, the indenter starts penetrating into the glass fragments.

The stresses on the surface of indenter contact with the obstacle are calculated using the above empirical formula. The dynamic penetration of a rigid axisymmetrical body into a plate with impact velocities ($10^2 - 10^3$ m/s) is described by the empirical formula $\sigma = H_d + k\rho V^2$ (Ben-Dor et al. 2014). Here σ is specific penetration resistance force, H_d is dynamic hardness of the medium material, k is shape coefficient of the indenter nose, ρ is density, V is current velocity.

Figure 12 shows how indenters with a conical nose and a truncated cone nose penetrate into a layered medium.

The equation motion of an indenter with a conical nose in the i -th layer is

$$\frac{d(V^2)}{dx} = -4\pi t g^2 \alpha \int_a^x (x - \xi)(H_i + k\rho_i V^2) d\xi - 4\pi t g^2 \alpha \sum_{j=i+1}^{i-1} \int_{\delta_{j-1}}^{\delta_j} (\delta_j - \xi)(H_j + k\rho_j V^2) d\xi$$

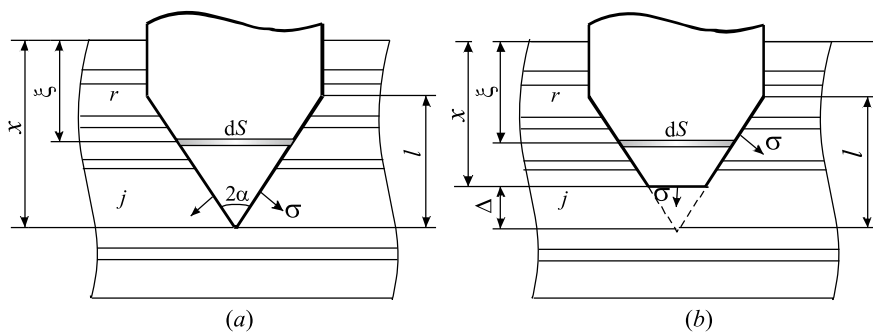


Fig. 12 Indenter penetration into a layered structure: **a** with a conical nose, **b** with a truncated cone nose

Table 1 Glazing composition and bullet penetration depth

No.	Glazing composition	Glazing thickness (m)	Bullet penetration depth (m)
1	4(1) 4(1) 4(1) 4(1) 4(1) 4(1) 4(1) 4(1) 4	0.044	0.0175
2	6(1) 6(1) 6(1) 6(1) 6(1) 6(1) 6	0.048	0.0166
3	10(1) 8(1) 8(1) 6(1) 4(1) 4	0.045	0.0158

$$-\frac{4\pi t g^2 \alpha}{m} \int_{x-l}^{\delta_r} (\delta_r - \xi)(H_r + k\rho_r V^2) d\xi - \frac{2E_{i+1}}{mh_{i+1}}(x - \delta_{i-1})S_i,$$

where H_i is dynamic hardness of the i -th layer material, S_i is area of the bottom surface of the deformed cone in the i -th layer.

The depth of penetration of a 3.4-g bullet with a steel non-heat hardened core into multilayer glazing at an impact velocity of 900 m/s was investigated. Several multilayer compositions of silica glass and filling adhesive were considered. The adhesive layers are made of a polymer ($E = 0.001$ GPa, $\nu = 0.39$, $\rho = 1200$ kg/m³); SG is unreinforced. Table 1 shows the glazing compositions considered and the results of calculating the bullet penetration depth. In the compositions, the thicknesses are shown in millimeters in succession, starting from the face layer. The SG layer thicknesses are without parentheses, and the thicknesses of the adhesive layers are in parentheses. The calculations yield slightly overestimated penetration depth values as compared to real ones.

7.4 Conclusions

Problems in modeling the response of a multilayer glazing to dynamic localized and distributed force loadings were considered. A generalized model was used to describe glazing behavior. This theory is based on a power series expansion of the displacement vector component in each layer for the transverse coordinate.

Analysis of the SSS in glazing under different loading conditions, geometric characteristics, and mechanical parameters of the layers leads to the following conclusions:

- for dynamic distributed load action, analysis of displacements and stresses p_{11} (or p_{22}) in thin and medium-thickness glazing can be based on the refined model {1, 1} variant, whereas for thicker glazing, higher-order models must be used, for instance, the {3, 2} theory, etc.;
- when a localized load acts on the glazing, higher-order models ({3, 2} (or even higher ones) must be used to investigate displacements and stresses p_{11} (or p_{22})

in the load application domain and its neighborhood because the distribution of loads through the glazing thickness is essentially nonlinear;

- when investigating transverse stresses p_{13} (or p_{23} , p_{33}), a generalized more higher-order theory must be applied, for example $\{5, 4\}$ or $\{7, 6\}$ models.

The capabilities of the suggested model are demonstrated by the example of solving a number of real problems in the dynamic loading of glazing. The response of a flat glazing to shock wave action, bird strike collision, and low velocity impact with a ball was analyzed. In the first two cases, a distributed load acts on the glazing, and in the third one, the glazing loading is local. Besides, the problem of glazing penetration at high-velocity bullet impact is given. In this case, at the initial impact stage, the penetration process depends weakly on the boundary support conditions and it is essentially local. The complex nonlinear action of external loads is common for all the problems considered.

References

- Amabili, M., Reddy, J.N.: The nonlinear, third-order thickness and shear deformation theory for statics and dynamics of laminated composite shells. *Compos. Struct.* **244**, 112265–2–112265–16 (2020). <https://doi.org/10.1016/j.compstruct.2020.112265>
- Ben-Dor, G., Dubinsky, A., Alperin, T.: *High-speed Penetration Dynamics: Engineering Models and Methods*. World Scientific Publishing Company (2013)
- Ben-Dor, G., Dubinsky, A., Elperin, T.: Engineering models of high speed penetration into geological shields. *Cent. Eur. j. Eng.* **4**, 1–19 (2014). <https://doi.org/10.2478/s13531-013-0135-4>
- Carrera, E., Cinefra, M.: Classical, refined, zig-zag and layer-wise models for laminated structures. In: Mantic, V. (ed.) *Mathematical Methods and Models in Composites*, pp.135–172. Imperial College Press, London (2013). https://doi.org/10.1142/9781848167858_0004
- Carrera, E., Fazzolari, F.A., Demasi, L.: Vibration analysis of anisotropic simply supported plates by using variable kinematic and Rayleigh-Ritz method. *J. Vib. Acoust.* **133**(6), 061017 (2011). <https://doi.org/10.1115/1.4004680>
- Cho, H., Lee, J., Hong, S., Kim, S.: Bulletproof performance of composite plate fabricated using shear thickening fluid and natural fiber paper. *Appl. Sci.* **10**(1), 88 (2020). <https://doi.org/10.3390/app10010088>
- Demasi, L.: ∞^6 mixed plate theories based on the generalized unified formulation. Part I governing equations. *Compos. Struct.* **87**(1), 1–11 (2009). <https://doi.org/10.1016/j.compstruct.2008.07.013>
- Dharani, L.R., Wei, J.: Dynamic response of laminated glass under blast loading: effect of negative phase. In: Jones, N., Brebbia, C.A. (eds.) *Structures Under Shock and Impact VIII*, pp. 181–190. WIT Press, Southampton (2004)
- Dolbeer, R.A., Wright, S.E., Weller, J.R., Begier, M.J.: *Wildlife Strikes to Civil Aircraft in the United States, 1990–2009*. U.S. Department of Transportation, Federal Aviation Administration, Office of Airport Safety and Standards, Serial Report No. 16, Washington, D.C., USA (2011)
- Federal Aviation Regulation: Part 25. Airworthiness Standards: Transport Category Airplanes. https://www.faa.gov/aircraft/air_cert/airworthiness_certification/std_awcert/std_awcert_regs/regs/. Accessed 19 Dec 2020
- Hedayati, R., Ziaei-Rad, S., Eyvazian, A., Hamouda, A.M.: Bird strike analysis on a typical helicopter windshield with different lay-ups. *J. Mech. Sci. Technol.* **28**, 1381–1392 (2014). <https://doi.org/10.1007/s12206-014-0125-3>

- Heimbs, S.: Computational methods for bird strike simulations: a review. *Comput. Struct.* **89**(23–24), 2093–2112 (2011). <https://doi.org/10.1016/j.compstruc.2011.08.007>
- Heimbs, S., Wagner, T., Viana Lozoya, J.T., Hoenisch, B., Franke, F.: Comparison of impact behaviour of glass, carbon and Dyneema composites. *Proc. Inst. Mech. Eng. Part C J. Mech. Eng. Sci.* **233**(3), 951–966. (2019). <https://doi.org/10.1177/0954406218764509>
- Holmquist, T.J., Johnson, G.R.: A computational constitutive model for glass subjected to large strains, high strain rates and high pressures. *J. Appl. Mech.* **78**(5), 051003-1–051003-19 (2011). <https://doi.org/10.1115/1.4004326>
- Hu, W., Wang, Y., Yu, J., Yen, C., Bobaru, F.: Impact damage on a thin glass plate with a thin polycarbonate backing. *Int. j. Impact Eng.* **62**, 152–165 (2013). <https://doi.org/10.1016/j.ijimpeng.2013.07.001>
- ICAO Electronic Bulletin EB 2017/25: 2008–2015 Wildlife Strike Analyses (IBIS). [https://www.icao.int/safety/IBIS/2008-2015WildlifeStrikeAnalyses\(IBIS\)-EN.pdf](https://www.icao.int/safety/IBIS/2008-2015WildlifeStrikeAnalyses(IBIS)-EN.pdf) (2017). Accessed 19 Dec 2020
- Larcher, M., Solomos, G., Casadei, F., Gebbeken, N.: Experimental and numerical investigations of laminated glass subjected to blast loading. *Int. j. Impact Eng.* **39**(1), 42–50 (2012). <https://doi.org/10.1016/j.ijimpeng.2011.09.006>
- Matsunaga, H.: Assessment of a global higher-order deformation theory for laminated composite and sandwich plates. *J. Composite Mater.* **56**, 279–291 (2002). [https://doi.org/10.1016/S0263-8223\(02\)00013-2](https://doi.org/10.1016/S0263-8223(02)00013-2)
- Mohagheghian, I., Wang, Y., Zhou, J., Yu, L., Guo, X., Yan, Y., Charalambides, M.N., Dear, J.P.: Deformation and damage mechanisms of laminated glass windows subjected to high velocity soft impact. *Int. j. Solids Struct.* **109**(15), 46–64 (2017). <https://doi.org/10.1016/j.ijsolstr.2017.01.006>
- Reddy, J.N.: *Mechanics of Laminated Composite Plates and Shells: Theory and Analysis*. CRC Press, Boca Raton (2003). <https://doi.org/10.1201/b12409>
- Shim, G.I., Kim, S.H., Ahn, D.L., Park, J.K.: Experimental and numerical evaluation of transparent bulletproof material for enhanced impact-energy absorption using strengthened-glass/polymer composite. *Compos. B Eng.* **97**, 150–161 (2016). <https://doi.org/10.1016/j.compositesb.2016.04.078>
- Shupikov, A.N., Ugrimov, S.V., Kolodiazhny, A.V., Yareschenko, V.G.: High-order theory of multilayer plates. The impact problem. *Int. J. Solids Struct.* **35**(25), 3391–3404 (1998). [https://doi.org/10.1016/S0020-7683\(98\)00020-1](https://doi.org/10.1016/S0020-7683(98)00020-1)
- Shupikov, A.N., Ugrimov, S.V., Smetankina, N.V., Yareschenko, V.G., Onhirsky, G.G., Ukolov, V.P., Samoilenko, V.F., Avramenko, V.L.: Bird dummy for investigating the bird strike resistance of aircraft components. *J. Aircraft* **50**(3), 817–826 (2013). <https://doi.org/10.2514/1.C032008>
- Smetankina, N.V., Shupikov, A.N.: Sotrikhin SYu, and Yareschenko VG: dynamic response of an elliptic plate to impact loading: theory and experiment. *Int. j. Impact Eng.* **34**(2), 264–276 (2007). <https://doi.org/10.1016/j.ijimpeng.2005.07.016>
- Ugrimov, S.V.: Generalized theory of multilayer plates. *Int. j. Solids Struct.* **39**(4), 819–839 (2002). [https://doi.org/10.1016/S0020-7683\(01\)00253-0](https://doi.org/10.1016/S0020-7683(01)00253-0)
- Onhirsky, G.G., Shupikov, A.N., Ugrimov, S.V.: Testing the aircraft glazing elements to bird resistance. *Issues Des. Manuf. Flying Vehic.* **1**(57), 7–12 (2009) (in Russian)

Part II
Nonlinear Dynamics of Distributed Systems

Chapter 8

Synchronicity Phenomena in Circular Cylindrical Shells Under Random Excitation



Antonio Zippo, Giovanni Iarriccio, and Francesco Pellicano

Abstract In many engineering areas, the structures are subjected to external forcing with a prevalent harmonic component in conjunction with significant likely non-deterministic contribution; moreover, the coupling between loading conditions and extreme environmental temperatures can lead to complex dynamic phenomena. In this paper, an experimental study on the nonlinear dynamics of a thin polymeric circular cylindrical shell, carrying a top mass, subjected to thermal gradients and random excitation is presented. Tests have been performed in controlled temperature conditions and the shell has been excited through an electrodynamic shaker. The experimental results pointed out that a broadband random excitation at the base of the shell can give rise to the synchronicity of the response to the resonance corresponding to the first axisymmetric mode of the shell; the vibration energy is conveyed to specific harmonics, some of which are outside and far from the excitation band.

Keywords Thin-walled structures · Synchronicity; random vibrations · Experimental · Thermal gradients · Polymers

8.1 Introduction

The vibration behavior of structures excited by non-deterministic dynamic forcing is an important topic for engineers operating in several fields: Aerospace, Nuclear, Naval, Mechanics. The intrinsic difficulty in analyzing and modeling the structural behavior of systems subjected to random excitation is magnified when the system

A. Zippo · G. Iarriccio · F. Pellicano (✉)
Department of Engineering Enzo Ferrari, University of Modena and Reggio Emilia, Modena, Italy
e-mail: francesco.pellicano@unimore.it

A. Zippo
e-mail: antonio.zippo@unimore.it

G. Iarriccio
e-mail: giovanni.iarriccio@unimore.it

A. Zippo · F. Pellicano
Centre InterMech MoRe, University of Modena and Reggio Emilia, Modena, Italy

under investigation presents some peculiarities: modeling complexity, high modal density, nonlinearities. In many applications, vibration problems are joined with a complicating factor, i.e., a significant temperature variability, which can sensibly change the material properties. When shell-like structures are subjected to strong random excitations and exposed to high thermal gradients, the dynamics can be characterized by strong nonlinearity, which leads to the rise of unexpected phenomena that cannot be predicted by standard design tools.

Usually, systems subjected to a random excitation vibrate randomly following the amplitude amplification of the linear transfer function; however, in some particular conditions, like internal or parametric resonances, the presence of nonlinearities in the system can give rise to unexpected phenomena. For example, a chain of nonlinear oscillators subjected to a random forcing could lead to synchronization that induces a harmonic response; this phenomenon has been partially studied in the literature for its remarkable characteristics of conveying a broadband spectral energy to specific frequencies (Ibrahim et al. 1976).

The literature on shell vibration as well as on random vibrations is remarkably extensive, due to the importance of these topics. Nevertheless, the publications containing experimental results related to the topics of the present paper are not so common. A relevant monograph due to Bolotin (1984) is focused on random vibrations of elastic systems; the topic gained attention thanks to the aerospace and marine applications, where the excitation due to the fluid turbulence and waves leads to broadband forcing spectrum acting on the structure. This topic was investigated by the same author in Bolotin (1966), an asymptotic method was used for investigating a broadband excitation on an elastic system; the approach consists in replacing the contribution of each mode with the integration over a defined band in wave number space.

Several aspects of random vibrations have been studied in the past, involving linear and nonlinear behaviors. A recent contribution to the determination of nonlinear response under random excitation is Malara et al. (2018), where a boundary element method in conjunction with a Newmark integration scheme were applied for estimating the response in the time domain with a compatible spectrum of the excitation. In Spanos et al. (2010) the random response of a nonlinear system was analyzed, considering a frequency-dependent restoring force; the authors approached the problem in frequency domain through the method of statistical linearization.

A chain of nonlinear oscillators, subjected to intense periodic forcing, can exhibit the “mode-locking” phenomenon that synchronizes the forcing load with the system response, such phenomenon is described in several textbooks. The *synchronization* of nonlinear oscillators under random excitation is much less known, in this case, the broad band spectral energy of the random forcing is conveyed to specific frequencies, determining large vibration amplitudes.

Jansen (1998, 2002) showed that a single, non-resonant periodic forcing is insufficient to activate the mode-locking phenomenon, but the supplement of a reasonable quantity of broadband noise allows transient mode locking to the original periodic drive to occur. Ibrahim et al. (1976) studied the response of a system with auto-parametric coupling subjected to a broadband random forcing, steady oscillations

were observed in the response moments; the authors claimed: “This suggests the occurrence of entrainment of regular harmonic responses by the system”.

Different synchronization mechanisms in dynamical systems were deeply discussed in Boccaletti et al. (2002), the synchronization of chaos was referred to as a process in which, several chaotic systems adapt a certain property of their dynamics to a common behavior, due to a coupling or a periodic or random forcing. An analytical and numerical work was published in Toral et al. (2001), they discussed the synchronization induced by noise in chaotic systems. Cicek et al. (2002) conducted a set of experiments on a beam tip mass and pendulum system subjected to random excitation, to determine the autoparametric interaction between two modes of the system in the neighborhood of the autoparametric region; in particular, the response behaves as ultra-narrowband process in the neighborhood of exact internal resonance that converge into a periodic response. Some experimental studies on very simple systems can be found in the literature, Ibrahim (1991) presented a review article on experimental investigations of random excitation of dynamic systems; the same author (Ibrahim et al. 1990) presented experimental results regarding a nonlinear two-degree-of-freedom system excited with random loading in the neighborhood of internal resonance.

A study carried out by Roberts (1980) presented an analytical and experimental investigation on a two degree of freedom vibratory system, with nonlinear coupling of autoparametric type, subjected to a broad band random excitation; the system consists of a cantilever beam supporting on its free end another orthogonal beam; the primary beam, is excited by a vibration generator. The transversal vibration of the primary beam imposes an axial motion to the secondary cantilever. The system is a common structural arrangement, representing the fuselage-tail plane coupling in aircraft structures.

In Zippo et al. (2017) thin circular cylindrical shells were experimentally studied. Results showed the coexistence of more than one stable state when the shell is pre-loaded and excited with a moderately large sinusoidal excitation.

The effects of extreme temperature conditions and thermal gradients across a polymeric shell have been studied in Zippo et al. (2019, 2020) and Iarriccio et al. (2020): different dynamic scenarios have been observed due to the strong dependence of the material properties (elastic and dissipative) from the temperature.

In the present study, the dynamic response of a circular cylindrical shell excited by a high-energy random excitation is investigated. The shell is clamped at the base to an electrodynamic shaker, which provides a seismic excitation. On the top of the shell a rigid disk is mounted, it allows only a rigid body motion of the top end of the shell; moreover, due to the seismic motion, the disk inertia exerts axial loads to the shell. The environmental conditions (temperature) are controlled both inside and outside of the shell. Several tests were carried out by varying temperature and excitation parameters; the synchronicity phenomenon was detected for particular thermal and loading conditions: a severe transfer of energy from a broadband excitation to almost harmonic response is experimentally observed; energy transfer to low frequencies was observed as well.

8.2 Description of the Experimental Setup

The experimental setup consists of a specimen mounted on an electrodynamic shaker coupled with a climate chamber and monitored by accelerometers, laser vibrometer, and a telemeter.

The specimen under investigation is a thin cylindrical shell made of Polyethylene terephthalate (P.E.T.), a thermoplastic polymer, obtained by a production batch of plastic bottles; the single bottle has been prepared, to get the testing specimen, cutting the top and the bottom. The whole production batch reduces the presence of geometrical imperfection between different specimens and allows the repeatability of the experimental campaign without undue geometrical errors.

Once the specimen is ready, a disk made of aluminum alloy is glued to the top side of the shell; to avoid the tilt motion of the top mass, a special care was given to the orthogonality of the disk with respect to the longitudinal axis of the shell. The top disk has been designed to be enough rigid in order to achieve its first natural frequency far away from the frequency bandwidth of the test requirements.

The bottom side of the shell is clamped to the vibration table adapter (VTA) through a bolted shaft collar. Those mounting conditions allow a clamped–clamped connection of the shell to the top disk and to the vibration table adapter, respectively. In Table 8.1, the geometrical and material parameters of the shell and the material properties of the fixture and top disk are reported. In Fig. 8.1 a schematic representation of the whole setup and its components is shown; the control system, the shaker, and the climate chamber are described as well.

Inside the shell, a cartridge heater is mounted in order to set the inner temperature and to obtain the desired thermal gradient across the shell thickness, see Fig. 8.2. Eight aluminum foil wings are mounted on the thermal cartridge in order to increase the heat transfer capabilities; the heating group is isolated from the fixture by means of high-temperature-resistant silicon glue in order to avoid interference with the dynamics of the system under investigation. A mirror periscope has been designed and built to reflect the laser beam of the vibrometer and to allow reaching a lateral point of the shell located in a shadow position with respect to the climate chamber window (see the yellow circle in Fig. 8.2). In addition, a laser telemeter measures the

Table 8.1 Geometrical and material parameters of the shell, the fixture, and top disk

Fixture and top disk		Shell			
Material	Aluminum alloy	Material	P.E.T	Diameter	0.080 m
Mass density	2700 kg/m ³	Mass density	1366 kg/m ³	Thickness	0.38 × 10 ⁻³ m
Young's modulus	68.9 GPa	Young's modulus	3.2 GPa at 20 °C	Height	0.160 m
Poisson's ratio	0.33	Poisson's ratio	0.417		

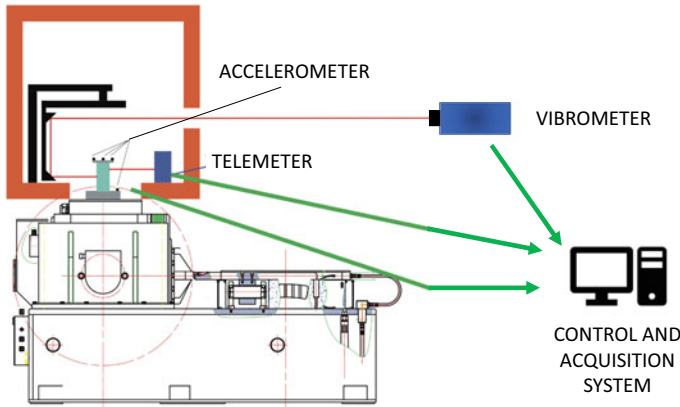
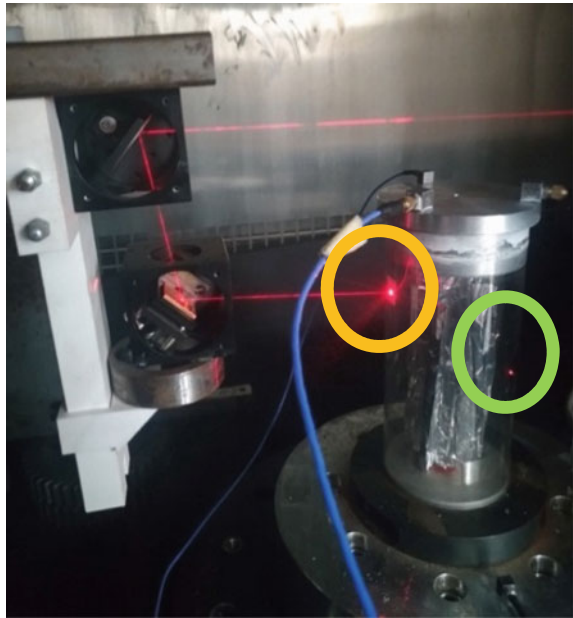


Fig. 8.1 Scheme of the experimental setup

Fig. 8.2 Detail of the specimen inside the climate chamber: laser Doppler Vibrometer spotlight (orange circle) and laser telemeter spotlight (green circle)



displacement of another point of the shell lateral surface, highlighted with a green circle in Fig. 8.2, out of phase of about 135° respect to the vibrometer measurement point (Fig. 8.3).

A detailed drawing of the assembly of the shell and of the top mass is shown in 0a; while in 0b the drawing of the top disk is presented, the top disk mass is 0.200 kg.

In order to complete sensors description, we have to mention an accelerometer located on the base of fixture, such accelerometer is used by the control system of

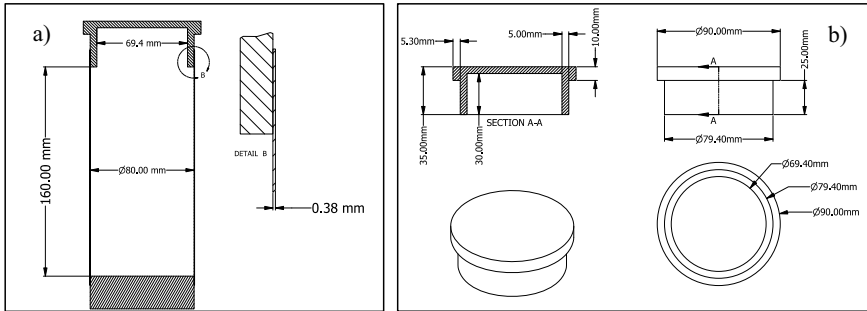


Fig. 8.3 System dimensions and detail of the mechanical constraints. **a** Shell; **b** top disk

the shaker for the closed-loop vibration control; three triaxial accelerometers are located equally spaced on the top disk, they are used to measure all the six dofs of the rigid body motion, this allows to detect axisymmetric modes, asymmetric modes, beam-like modes, and torsional modes. The specimen is mounted on an Es40 Dongling electrodynamic shaker (40,000 N, 1–3000 Hz) coupled with a climate chamber (temperature limits $-70\text{ }^{\circ}\text{C}$ and $+180\text{ }^{\circ}\text{C}$) that allows to set the outer temperature of the shell. Two thermocouples are used to measure the temperature of the inner and outer surface of the shell. The experimental test campaign consists of a random broadband loading that is imposed to the base of the circular cylindrical shell. The electrodynamic shaker is controlled by a Siemens LMS Scadas Mobile, which is used to measure the response and simultaneously to generate the random signal, the controller feedback is based on the signal of a control accelerometer placed at the base of the shell in vertical direction. Each test is carried out with random excitation having a specific bandwidth, different overall RMS levels are considered. As an example, in Fig. 8.4 the time history base acceleration is shown, this clarifies that the random excitation is exerted with increasing amplitude levels, a single time history is recorded for the whole test; this procedure is repeated for each test at different temperatures and gradients as well as different frequency bands. Experimental data were processed with a MATLAB code, where the different levels were separated in order to extract spectra and rms. Different combinations of temperature and forcing load have been tested changing the temperature inside the shell, using the heater, and outside the shell, using the climate chamber; indeed, the setup allows an easy control of environmental conditions, i.e. homogenous temperature and gradients can be accurately set.

8.3 Natural Frequencies and Modes

In order to prepare the basis for interpreting the novel results regarding nonlinear dynamics, which will be shown in the next section, it is useful to have a clear idea

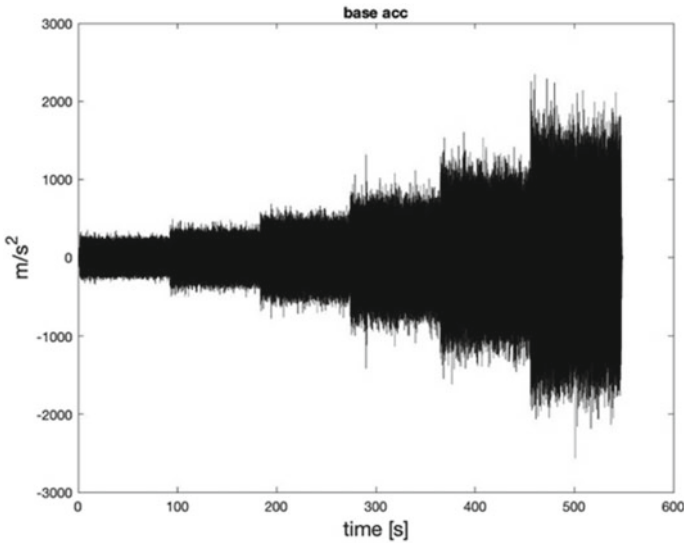


Fig. 8.4 Example of base acceleration time history, 24 °C outer temperature—74 °C inner temperature

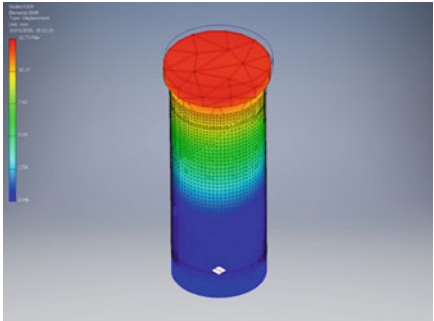
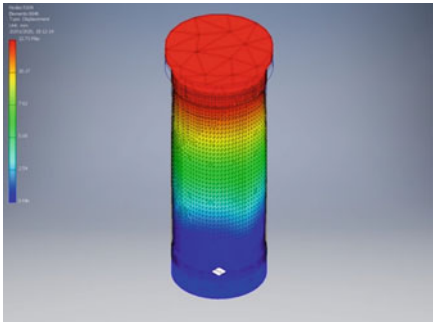
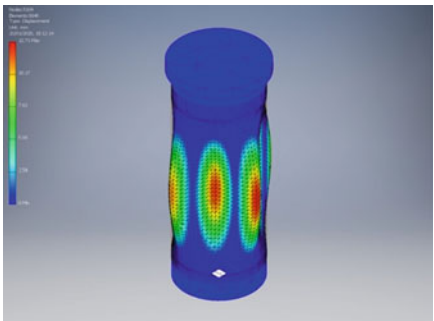
of the natural frequencies and mode shapes of the system under investigation. The analysis is carried out numerically after a validation with experimental data.

Numerical linear modal analysis has been performed using a Finite Element model (Nastran solver), see Tables 8.2 and 8.3. It is important to note that the material properties of the shell are strongly dependent on temperature, Zippo et al. (2019) and Fig. 8.5. In particular, one can see that the behavior of the Young modulus is monotonic and drops down with the temperature, as expected; the damping behaves differently, the polymer displays the lowest damping from 40 to 70 °C, for lower and higher temperatures the damping increases.

Due to the aforementioned dependence of the mechanical properties from the temperature, the natural frequencies obtained from the simulation could be slightly different with respect to the experiments; moreover, the specimen presents a marginal uncertainty in the geometry. The experimental tests are carried out by exciting the shell from the base, using a very low energy random excitation with closed-loop control, the spectrum is flat in the band 0–2000 Hz, see Fig. 8.6. The excitation due to the base motion is mainly the inertia force created by the top disk acceleration; therefore, the base excitation mainly pumps into the first axisymmetric mode, see Table 8.2; the results are summarized in the FRF of 0, where a resonance of the first axisymmetric mode is found at 462.5 Hz. The numerical finite element analysis returns 457.6 Hz, with a difference of the 1%, which is fully satisfactory. The numerical simulation has been performed using, for the shell, the properties of the material (PET) reported in Table 8.1 and the Young modulus at 30 °C from Fig. 8.5a.

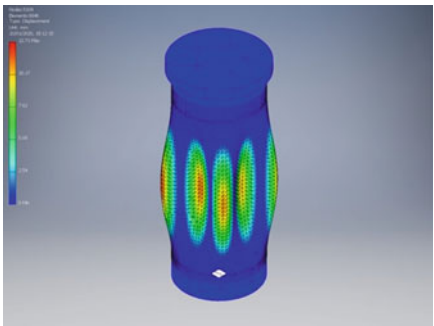
Table 8.2 lists the mode shapes and the corresponding natural frequencies of the shell. The experimental test rig allows the identification of the first axisymmetric mode, only, because the other modes are not excited when the forcing level at the base is very low (as needed for linear vibration analyses). The first modes presented in

Table 8.2 Numerical modal analysis 30 °C homogenous temperature: mode shapes, natural frequencies

Mode	<i>m</i>	<i>n</i>	Natural frequency [Hz]	Mode shapes
1st cantilever beam like			97.57	
1st axisymmetric	1	0	457.56	
1st shell like mode	1	4	504.56	

(continued)

Table 8.2 (continued)

Mode	m	n	Natural frequency [Hz]	Mode shapes
2nd shell like mode	1	5	533.18	

m number of longitudinal half waves, n number of nodal diameters

Table 8.3 Numerical modal analysis 30 °C homogenous temperature: mode shapes, natural frequencies

Mode	m	n	FEM [Hz]
1st cantilever beam like	–	1	97.57
2nd cantilever beam like	–	1	97.60
1st axisymmetric	1	0	457.56
1st shell like mode	1	4	504.56
2nd shell like mode	1	5	533.18
3rd shell like mode	1	3	660.29
4th shell like mode	1	6	684.05

m number of longitudinal half waves, n number of nodal diameters

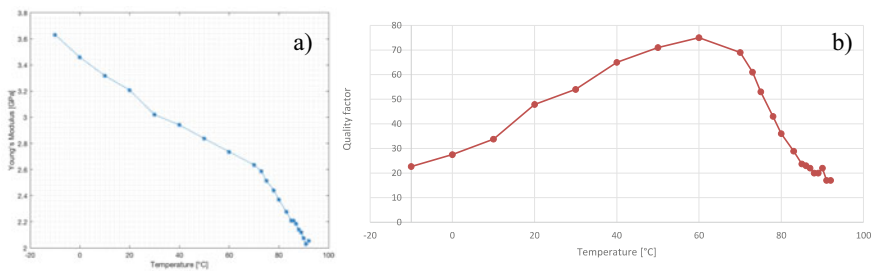


Fig. 8.5 Experimental results reprinted from (Zippo et al. 2019)] with permission from Elsevier: Young modulus (a) and quality factor (b) versus temperature

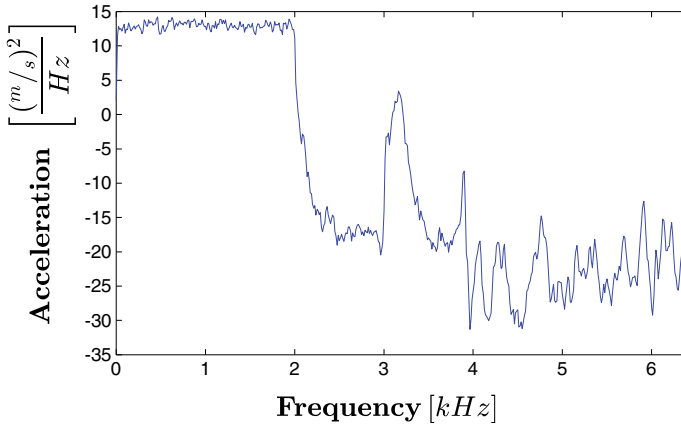


Fig. 8.6 PSD of driven base forcing load, random broadband between 10 and 2000 Hz

Tables 8.2 and 8.3 will be useful for the comprehension of experimental phenomena presented in Sect. 8.5.

8.4 Test Procedure

The test procedure consists of a random base excitation provided by a shaking table (see 0). The excitation is applied at different levels for each test (tests are also called runs), in order to investigate nonlinear phenomena arising at high vibration energies. Several frequency bands of the random spectrum are considered as well as different thermal conditions: homogeneous temperature and thermal gradients between the outer and inner shell surface are considered.

In order to provide a stationary thermal condition, an adequate amount of time has been left to avoid variation of temperatures in time. Two thermocouples were placed inside and outside the shell, the temperature was checked every 10 min for 5 h, this step is fundamental to obtain a uniform temperature along the shell surface.

Table 8.4 reports the environmental and the excitation conditions considered in this work. Note that only the most interesting cases, where unknown phenomena occurred, are reported and analyzed in this paper. Moreover, it is to note that the excitation frequency bandwidths and the intensity levels are not always uniform; in fact, for some cases, the tests could not be completed, due to limitations of the shaker performances and system controller capabilities. The shaking table is a Dongling ET-40-370, 40kN peak force, 100 g maximum acceleration, 500 kg max static payload, 1–2800 Hz frequency band.

Table 8.4 Test campaign schedule

Type	Temperature [°C]			Frequency bandwidth [Hz]	Overall rms [$\frac{m}{s^2}$]	Case
	Inner	Outer	Gradient			
Homogeneous	30	30	0	10–2000	200	1
	25	25	0	900–3000	45–273	2
	20	20	0	10–2000 800–2000 900–2000	25 170–350 180–370	3a 3b 3c
Gradient	48	20	28	900–3000	43–298	4a
					175–515	4b
	74	24	50	900–3000	68–426	5
	48	20	28	900–1500	150–490	6

8.5 Experimental Results: Excitation and Dynamic Response

In this section results of a wide experimental campaign are presented, the excitation is random, following Table 8.4, several bandwidths are investigated as well as several environmental conditions, uniform and differential temperature. The kind of excitation, which is from the base, and the frequency band, from 10 to 3000 Hz, with different sub-intervals, lead to a direct excitation of the first axisymmetric mode; other modes could be indirectly excited when auto-parametric resonances due to high energy excitation, other minor sources of excitation of asymmetric modes are geometric imperfections. The goal is to investigate possible energy transfer and concentration, leading to a synchronization of the system response to a specific frequency or a very narrow band.

8.5.1 Case 1. Standard Homogeneous Temperature, 30 °C, Broadband Excitation, 10–2000 Hz

For this series of tests homogenous temperature of 30 °C is considered, the random excitation presents a uniform spectrum on the bandwidth 10–2000 Hz, the excitation level is $200 \frac{m}{s^2}$ overall rms. The signal is recorded for 1s. It should be noted that the first axisymmetric mode frequency is 462.5 Hz. In Fig. 8.6 the random base excitation PSD (Power Spectral Density) is shown; the shaker controller assures a flat spectrum of $13 \left(\frac{m}{s^2}\right)^2$ in the band 10 – 2000 Hz, corresponding to $200 \frac{m}{s^2}$ overall rms; there is a peak with negligible level at 3162 Hz, 10 decades smaller than the main band. Figure 8.7 shows the PSD of the top disk acceleration, which displays the resonance of the first axisymmetric mode. Figure 8.8 shows the PSD of the electric signal, which

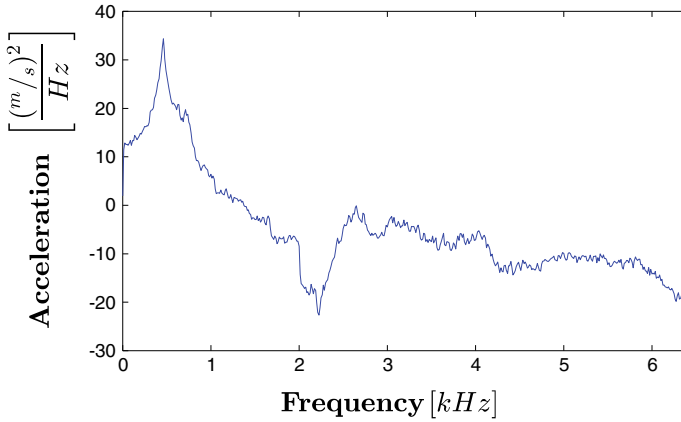


Fig. 8.7 PSD of top acceleration response

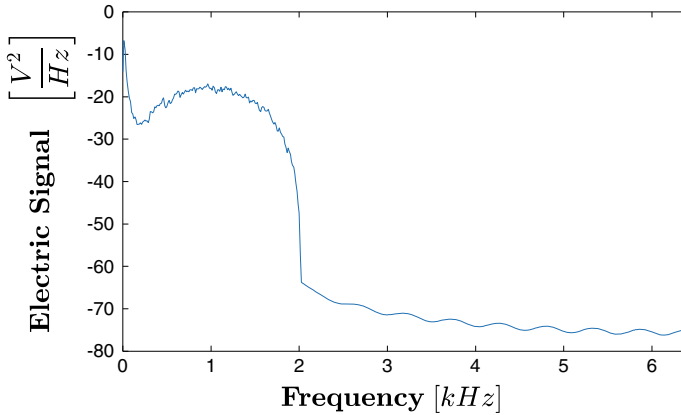


Fig. 8.8 PSD of the electric signal sent to shaker amplifier

is the input of the shaker amplifier, obviously, there is energy only on the band 10–2000 Hz; within this frequency range the spectrum is not flat because the closed-loop controller, checks the base acceleration (controlled signal) and modulates the electric amplifier input (controller signal) in order to maintain flat the base acceleration in the range 10–2000 Hz; the controller cannot have any action in the out of band spectrum (below 10 Hz and over 2000 Hz).

8.5.2 Case 2. Homogeneous Temperature 25 °C, 900–3000 Hz, 45–273 $\frac{m}{s^2}$

In this case, the temperature is uniform 25 °C, the frequency band is 900–3000 Hz, six excitation levels, from 45 to 273 $\frac{m}{s^2}$ overall rms, are considered; Table 8.5 shows the RMS versus time of base, top disk, and lateral vibration, note that the shell is vibrating with a non-negligible amplitude even though shell like asymmetric modes are not directly excited. Table 8.6 summarizes the results; it shows that increasing the amplitude of the excitation produces a proportional increment of the system vibration.

Figures 8.9, 8.10 and 8.11 show the spectra of the base and top acceleration and

Table 8.5 Evolution of rms over time of case 2: 25 °C homogeneous temperature, bandwidth 900–3000 Hz

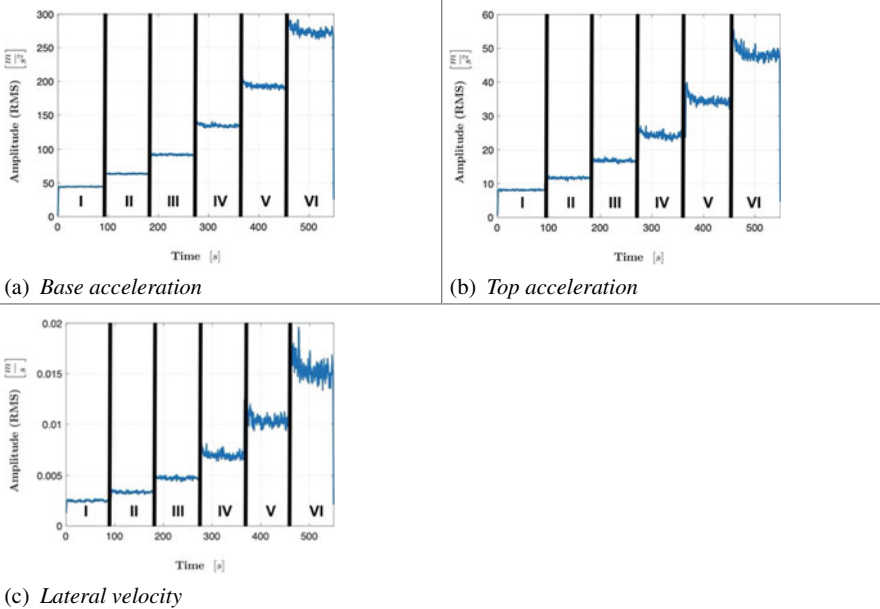


Table 8.6 Case 2: vibration levels

Level	Base (m/s^2)	Top (m/s^2)	Lateral velocity (m/s)
I	45.11	8	0.00239
II	63.09	11.55	0.00336
III	92.78	16.8	0.00463
IV	135.1	23.98	0.00736
V	195.2	34	0.01035
VI	273.4	48	0.01546

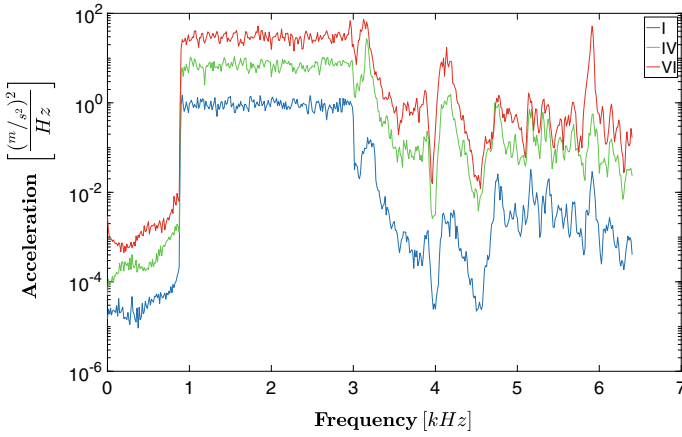


Fig. 8.9 PSD of base acceleration case 2 at uniform temperature at 25 °C and bandwidth 900–3000 Hz

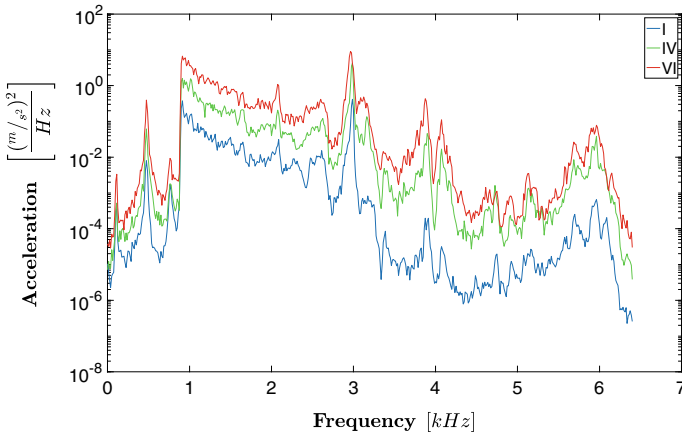


Fig. 8.10 PSD of top acceleration case 2 at uniform temperature at 25 °C and bandwidth 900–3000 Hz

the lateral velocity, two harmonics are present below the excitation band, i.e., at 112.5 and 475 Hz (first beam like mode and first axisymmetric mode). This is an unusual out of band energy transfer to subharmonic frequencies.

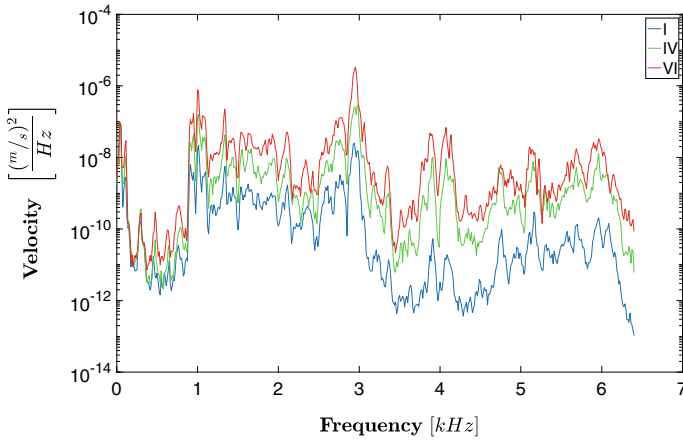


Fig. 8.11 PSD of lateral velocity case 2 at uniform temperature at 25 °C and bandwidth 900–3000 Hz

8.5.3 Case 3. 20 °C Homogeneous Temperature

The goal of this section is to investigate the effect of the excitation level as well as the frequency band. Tests are carried out at uniform 20 °C, three subsections are present, depending on the bandwidth:

- Case (3a) 10–2000 Hz, 25.39 $\frac{m}{s^2}$
- Case (3b) 900–2000 Hz, 180–370 $\frac{m}{s^2}$.

For each case, at same temperature conditions, several tests have been performed: each experiment consists in applying a random signal, controlled through the accelerometer applied at the base in the Z direction (vertical), for a certain period of time and at different levels of rms. The rms levels have been chosen according to the maximum force applicable by the shaker and the bandwidth of the test, therefore, between different tests, the levels and the duration of the same are slightly different.

8.5.3.1 Case 3a. 10–2000 Hz 25.39 m/s²

These tests are carried out using a broadband excitation, the goal is to check the overall system behavior and detect linear resonances of the shell. The use of the broadband signal, including low frequencies, limits the excitation level due to the shaker limitations in terms of max force, max acceleration, max velocity, and max displacement.

Table 8.7 presents the system behavior at low excitation level at 25.39 $\frac{m}{s^2}$ overall rms (base acceleration); the closed-loop controller imposes a flat spectrum of the base vibration (see Table 8.7b), this controller action can be appreciated by noting

Table 8.7 PSD of measured quantities at 20 °C between 10 and 2000 Hz.

Measured	PSD linear scale	PSD log scale
(a) Electrical signal		
(b) Base acceleration (controlled excitation)		

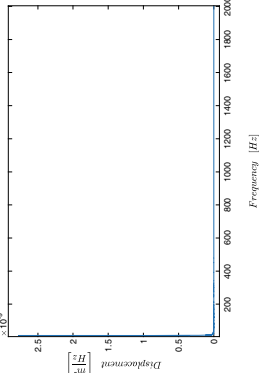
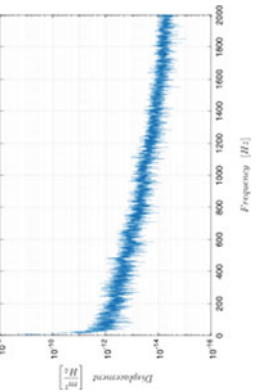
(continued)

Table 8.7 (continued)

Measured	PSD linear scale	PSD log scale
(c) Response of the top acceleration in axial direction		
(d) Lateral velocity		

(continued)

Table 8.7 (continued)

Measured	PSD linear scale	PSD log scale
(e) Lateral displacement		

that, in order to impose the base spectrum, the electric signal provided to the shaker amplifier is suitably adjusted in real-time (Table 8.7c).

From the top acceleration spectrum (Table 8.7c) we can observe the effect of the temperature, the first axisymmetric mode frequency at 20 °C is now 477 Hz, with an increment of 15 Hz with respect to the case at 30 °C (462.5 Hz): a relatively small reduction of temperature (10 °C) induces an increment of the fundamental frequency of 3%.

As expected, the low-level broad band excitation reveals the linear spectrum of the structure, the overall rms of the top disk is $99.37 \frac{m}{s^2}$, four times bigger than the base, this is due to the fact that the resonance of the first axisymmetric mode is inside the excitation frequency band. The PSD of the lateral velocity does not show any interesting aspect, the regular peaks are only due to electric disturbances at 50 Hz and its multiples. The lateral displacement is below the sensor range (Tables 8.8 and 8.9).

Table 8.8 Evolution of rms over time, case 3c at uniform temperature at 20 °C and bandwidth 900–2000 Hz

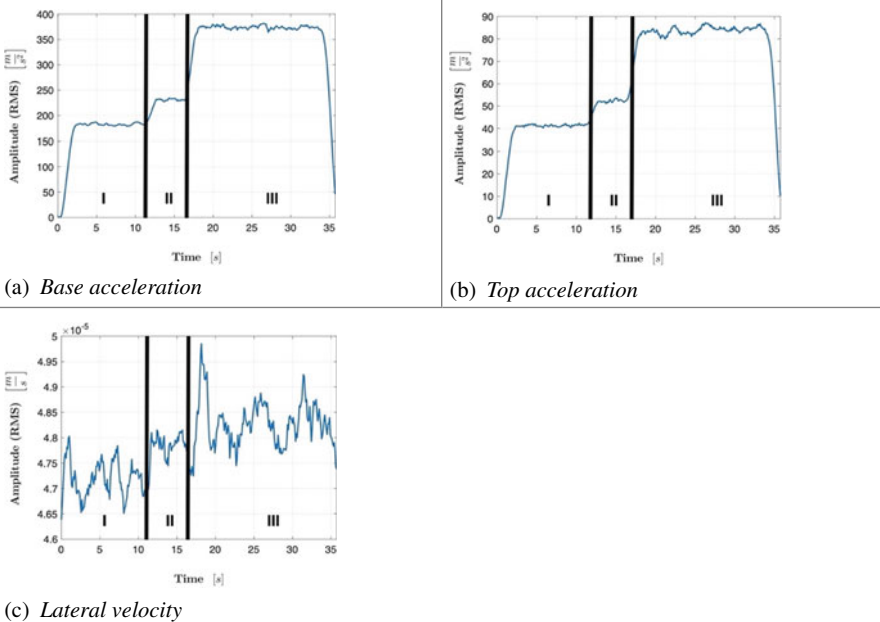


Table 8.9 Case 3c: vibration levels

Level	Base (m/s ²)	Top (m/s ²)	Lateral velocity (m/s)
I	183	41	0.0000474
II	215	51	0.0000479
III	373	84.15	0.0000485

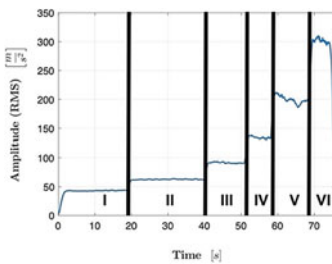
8.5.3.2 Case 3b. Uniform Temperature 20 °C, 900–2000 Hz, 180–370 $\frac{m}{s^2}$

In these tests, the excitation band is reduced of 100 Hz with respect to the Case 3b in order to increase the level of the PSD but avoiding increment of the overall rms that is limited by the shaker max performances.

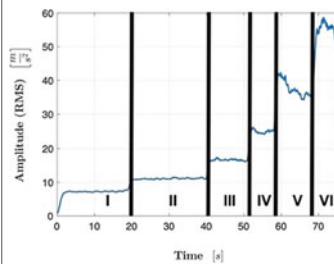
Table 8.10 shows the evolution of RMS of the base acceleration (a), the response of top acceleration (b), and the lateral velocity (c); the evolution shows a regular behavior for the base and the top, while the lateral vibration.

displays an irregular behavior. Three levels of excitation are considered, Table 8.11 summarizes the results and confirm the situation of Case 3b, the lateral vibration is negligible.

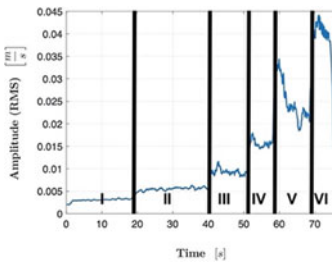
Table 8.10 Evolution of rms over time of case 4a: thermal gradient 20–48 °C, bandwidth 900–3000 Hz



(a) Base acceleration



(b) Top acceleration



(c) Lateral vibration

Table 8.11 Case4a: vibration levels

Level	Base (m/s ²)	Top (m/s ²)	Lateral velocity (m/s)
I	43.12	7.142	0.003
II	62.35	10.96	0.005
III	90.15	16.57	0.009
IV	132.9	24.38	0.014
V	199.4	37.23	0.025
VI	298.2	55.25	0.040

Spectra are shown in Figs. 8.12, 8.13 and 8.14, a small subharmonic at 375 Hz, while the lateral vibration does not reveal any noteworthy phenomenon, just electric disturbances are visible.

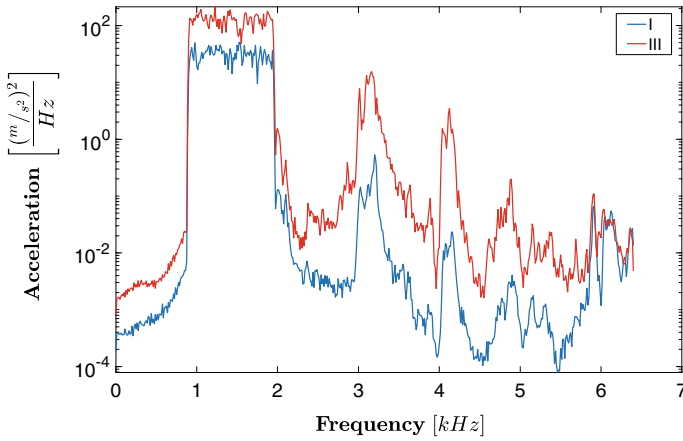


Fig. 8.12 PSD of base acceleration case at uniform temperature at 20 °C and bandwidth 900–2000 Hz

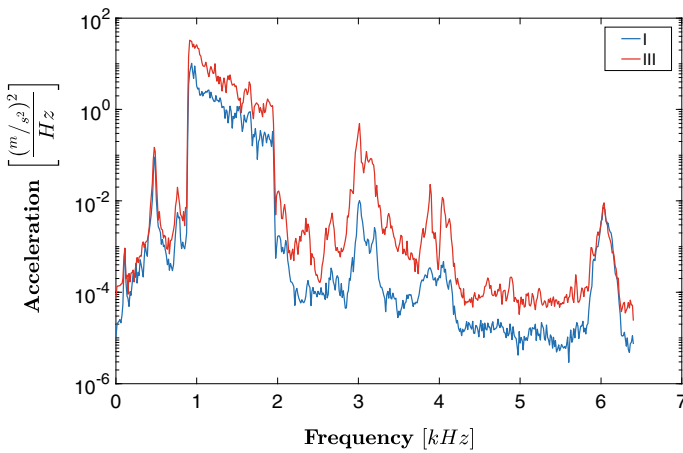


Fig. 8.13 PSD of top acceleration case at uniform temperature at 20 °C and bandwidth 900–2000 Hz

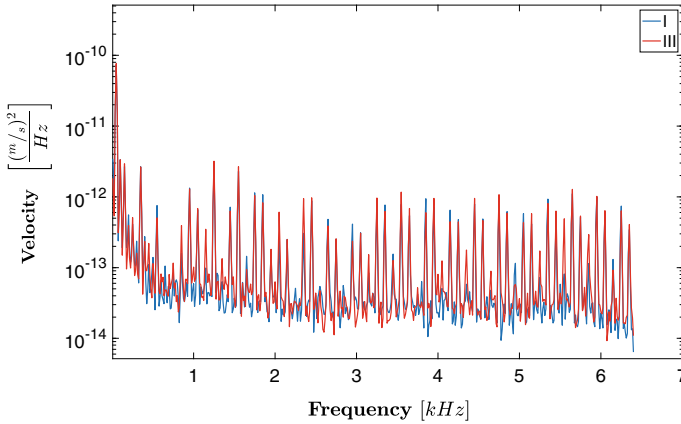


Fig. 8.14 PSD of lateral velocity on case at uniform temperature at 20 °C and bandwidth 900–2000 Hz

8.5.4 Case 4. Thermal Gradient, 20 °C Outside, 48 °C Inside, 900–3000 Hz, 43–298 $\frac{m}{s^2}$

In this section the effect of a thermal gradient is investigated, the shell has been subjected to a 28 °C thermal gradient with 20 °C in the outer surface and 48 °C in the inner surface.

Two series of tests are carried out: case 4a, low medium levels (43–298 $\frac{m}{s^2}$); case 4b, high levels (175–516 $\frac{m}{s^2}$), for sake of brevity only results of case 4a will be shown.

In **case 4a Low medium levels 43–298 $\frac{m}{s^2}$** , six vibration levels are considered from 43 to 298 $\frac{m}{s^2}$, in Table 8.12 shows the different rms levels of the base, top, and lateral vibration. Table 8.13 summarizes the overall vibration levels; note that the lateral shell vibration is not negligible. Spectra of the base vibration for the six levels are shown in Fig. 8.15, the PSD is flat in the frequency band where the controller is active (900–3000 Hz); while the spectrum of the top acceleration. Figure 8.16 presents two sharp peaks below the excitation band, corresponding to the first bending mode (112.5 Hz) and the first axisymmetric mode (475 Hz); an amplification of the response at 3000 Hz is present. The lateral vibration presents a strong sensitivity to the variation of the base vibration amplitude, see Fig. 8.17, where the spectrum is irregular and jagged; in particular, a pure tone of high intensity is present at 2988 Hz and smaller pure tone is visible at 1000 Hz.

Table 8.12 Case 6: evolution of rms versus time

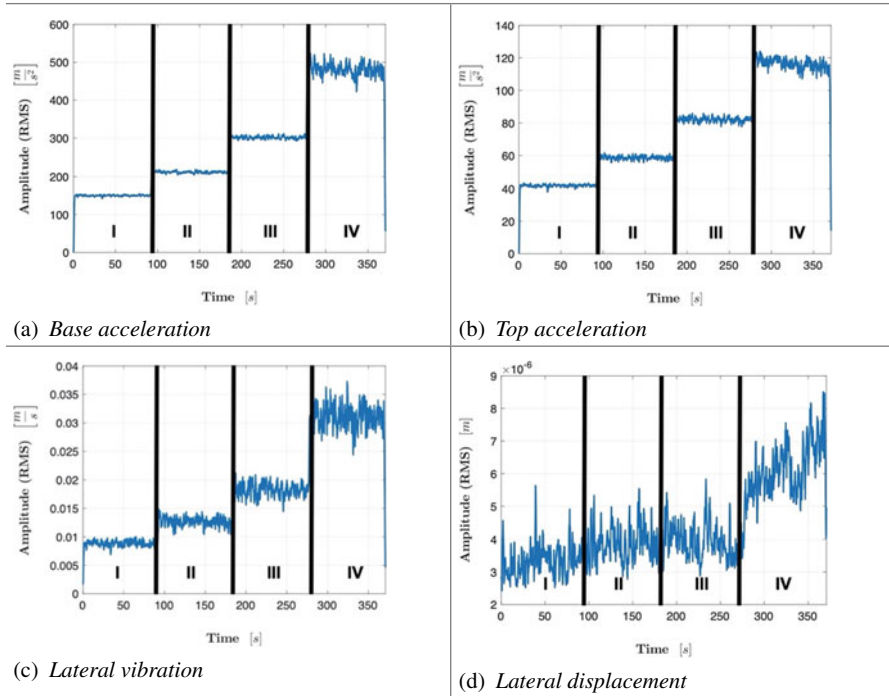


Table 8.13 Case 6: vibration levels

Level	Base (m/s ²)	Top (m/s ²)	Lateral displacement (μm)	Lateral velocity (m/s)
I	150	42	3.92	0.00913
II	212	58	3.72	0.01252
III	301	82	4.65	0.01799
IV	490	116	6.9	0.03303

8.5.5 Case 6. Gradient Temperature (Inner 48 °C, Outer 20 °C), Narrow Band Excitation, 900–1500 Hz

The specimen has been forced with a uniform random signal having a flat spectrum of $15 \frac{(\frac{m}{s^2})^2}{Hz}$ in the band 900 – 1500 Hz, corresponding to $102 \frac{m}{s^2}$ overall rms, see Fig. 8.18; the closed-loop shaking table controller acts only on the aforementioned band. A 28 °C thermal gradient is imposed, 48 °C in the inner surface and 20 °C in the outer surface.

Figures 8.19, 8.20 and 8.21 show the PSD of the top acceleration in vertical direction, lateral displacement, and lateral velocity, respectively. In Fig. 8.19 the PSD

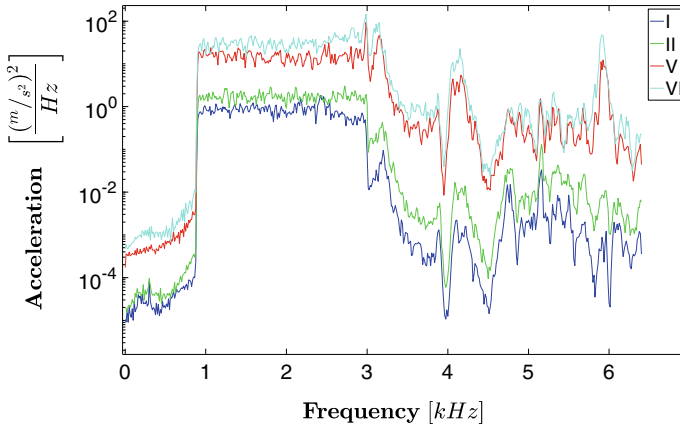


Fig. 8.15 PSD of base acceleration case 4a with thermal gradient at 20–48 °C and bandwidth 900–3000 Hz.

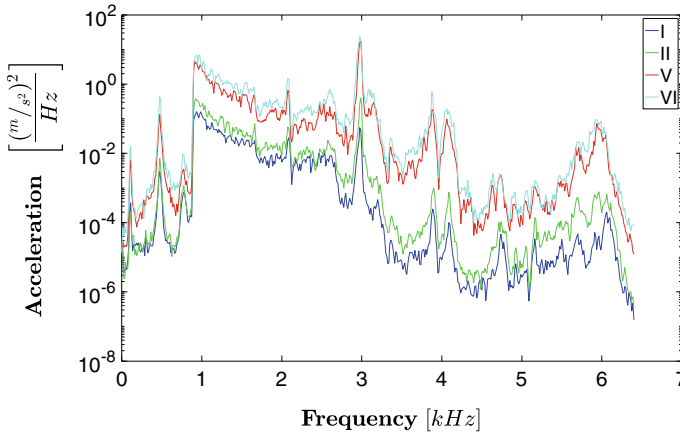


Fig. 8.16 PSD of top acceleration case 4a with thermal gradient at 20–48 °C and bandwidth 900–3000 Hz

of the top acceleration in the axial direction (Z) is presented and the presence of a low-frequency harmonic is clearly visible, which coincides with the first axisymmetric mode (467 Hz); it is important to note that, as shown in Fig. 8.18, in the PSD of the base acceleration no energy is provided below 900 Hz; this proves that there is a transfer of energy from a broadband source to a specific sub-harmonic, i.e., a synchronization; this energy transfer is accompanied by a very annoying single tone noise. In the band 900–1500 Hz, the spectrum of the top acceleration is continuous, but it is not flat, it drops down of three decades; this is perfectly coherent with the transfer function of the shell near the first axisymmetric mode, see the spectrum in Table 8.7 in the range 900–1500 Hz. The spectrum of the lateral vibration is

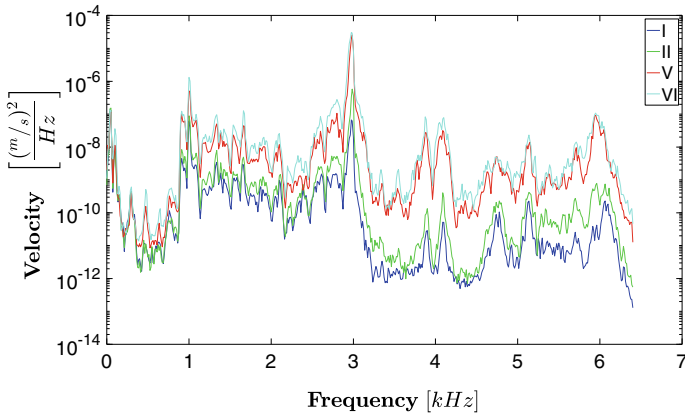


Fig. 8.17 PSD of lateral velocity case 4a with thermal gradient at 20–48 °C and bandwidth 900–3000 Hz

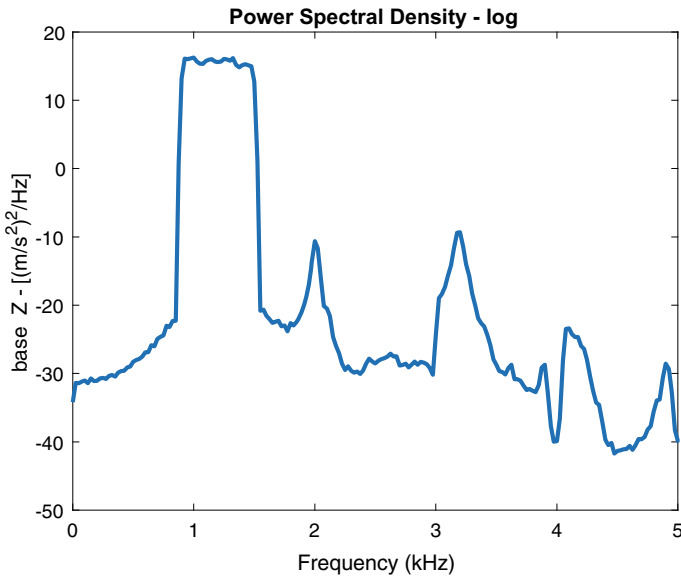


Fig. 8.18 PSD of random forcing load measured at VTA base

represented in Fig. 8.20 (displacement measured by a Laser telemeter) and Fig. 8.21 (velocity measured by a Laser Doppler); in the band 900–1500 Hz both spectra show marked peaks close to the extrema of the excitation band (1000 and 1300 Hz).

Spectra of Figs. 8.18, 8.19, 8.20 and 8.21 are extracted from a test database of about 370 s; the test consists of a random excitation having four different levels, see Table 8.14, the complete dataset is presented in terms of evolution of rms over

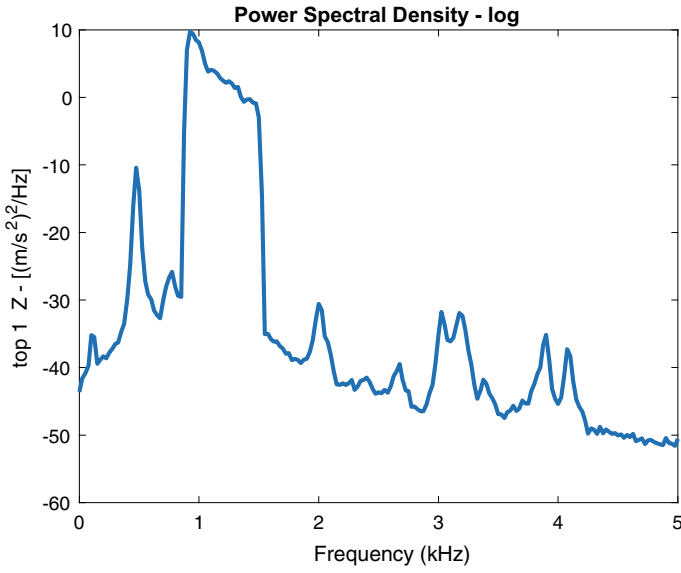


Fig. 8.19 PSD of response of top acceleration in vertical direction of first accelerometer

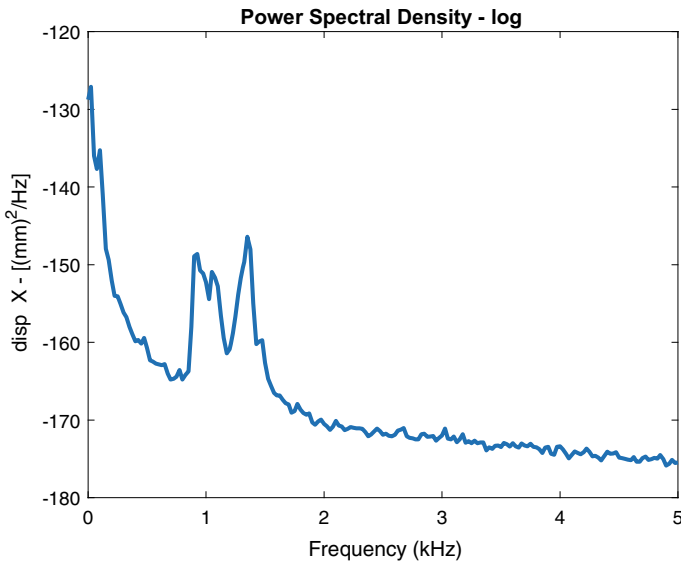


Fig. 8.20 PSD of lateral displacement

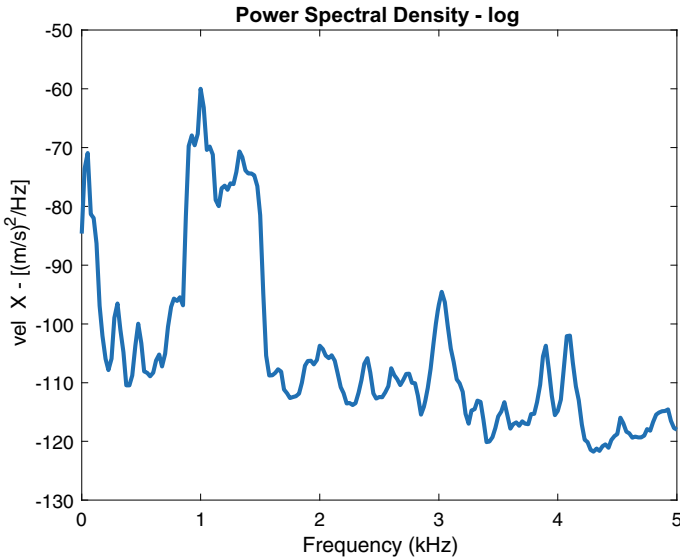


Fig. 8.21 PSD of lateral velocity

the time; the four levels are marked with roman numerals, the black vertical lines indicate the change of amplitude. In Table 8.15 the overall rms value for each level is presented, a subset of 5 s for each level is used for calculating the rms. For sake of brevity, only the vertical measurement of the first accelerometer is shown.

Note that the overall rms level of the top acceleration is about 4 times less than the excitation at the base.

Signals corresponding to rms of Table 8.15 are now analyzed, extracting a subset of 5 s from time histories for each measurement level, in order to compute the PSDs.

Figure 8.13 shows the PSD of the base acceleration for different excitation levels, the light blue strip highlights the excitation band (900–1500 Hz); it is worthwhile to stress the closed-loop control is active only in this band, it can be seen that the levels in the excitation band are several decades higher than other parts of the spectrum. Under 900 Hz no energy is provided to the system, while at higher frequencies peaks are present at about 2 and 3 kHz, it's to point out that this peak can be related to the shaker resonance. For the level IV only (black line of Fig. 8.22) the peak at 3 kHz is of the same order of the level in the excitation band.

Consider now the response of the top mass in vertical direction, Fig. 8.23, it can be seen that the acceleration response presents a subharmonic peak at 462.5 Hz, that corresponds to the first axisymmetric mode, even though no energy is furnished in that frequency band, see Fig. 8.22. In Fig. 8.24 the PSD of the lateral displacement is shown; for the lowest level “I” the spectrum mainly shows energy in the excitation band; for higher forcing levels (II, III, and IV) the lateral response shows out of band peaks, which are more and more evident as the energy increases.

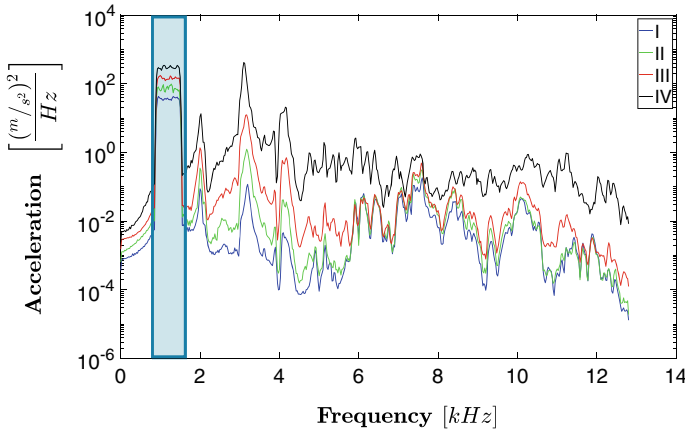


Fig. 8.22 PSD of random forcing load measured at VTA base, highlighted in light blue the controlled bandwidth

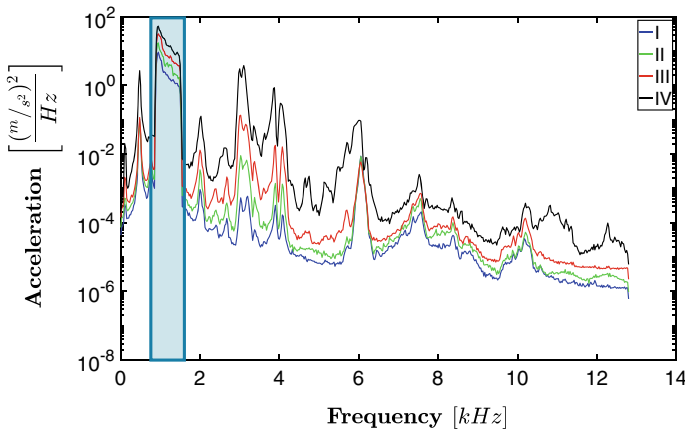


Fig. 8.23 PSD of top acceleration, highlighted in light blue the controlled bandwidth

In Fig. 8.24, yellow color shows two areas A and B where the spectrum presents interesting symmetries with respect to the carrier frequencies 5 and 10 kHz, this could be related to a masked quasiperiodic response originating the sidebands.

In Fig. 8.25, the lateral velocity measured with the Laser Doppler shows an irregular response both in the controlled excitation band; two prominent peaks are present at 1000 and 1325 Hz; below the excitation band a small peak is present, close to the first axisymmetric mode (475 Hz); at higher frequencies, a strong harmonic is present at 3537 Hz, other important harmonics are observed at 3875, 4000 and 6025 Hz.

There is a clear transfer of energy from a broadband input to specific frequencies; this explains the highly annoying single tone structure born sound.

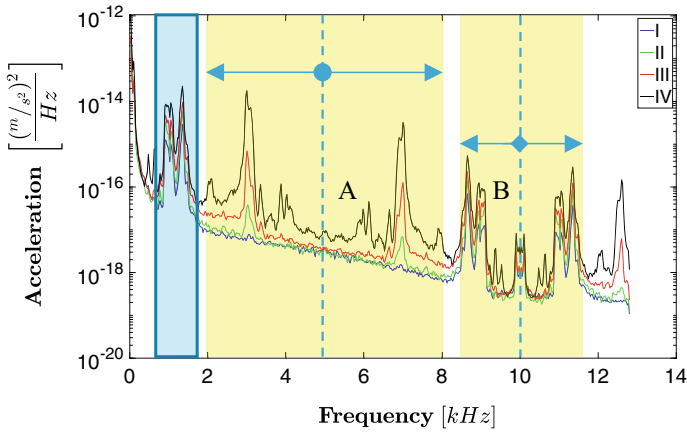


Fig. 8.24 PSD of lateral displacement, highlighted in light blue the controlled bandwidth

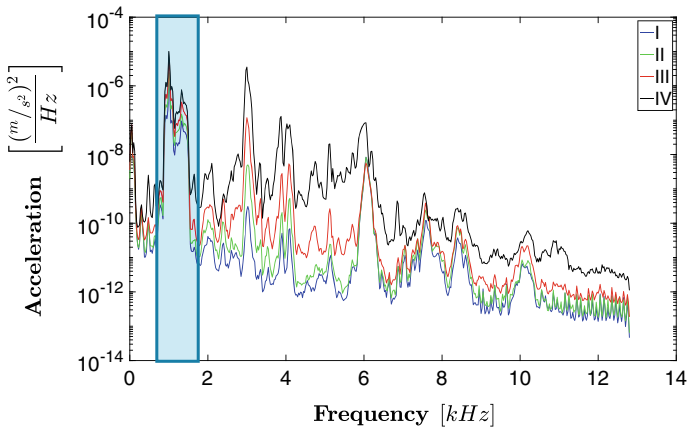


Fig. 8.25 PSD of lateral velocity, highlighted in light blue the controlled bandwidth

8.6 Conclusions

In this work, an experimental investigation on nonlinear dynamics of randomly excited shells is presented; a thin cylindrical shell, carrying a rigid disk on the top is excited from the base through a random excitation. Different excitation bands and levels are considered, as well as different environmental conditions.

Experiments show that the broadband random excitation at the base gives rise to an interesting phenomenon, called in literature “Synchronicity”, i.e. a conveying of the broadband excitation energy to specific frequencies.

An energy transfer to the first axisymmetric mode has been observed, 450 Hz, which is far from the excitation band and no energy is provided at such low frequencies.

The temperature variation and the thermal gradient seems to have a role in the rising of the Synchronicity, a quasiperiodic vibration is observed.

The increment of temperature plays a role in increasing the occurrence of the synchronicity, in particular, the lateral shell vibration seems to be more sensitive to presence of gradients.

References

- Boccaletti, S., Kurths, J., Osipov, G., Valladares, D.L., Zhou, C.S.: The synchronization of chaotic systems. *Phys. Rep.* **366**(1–2), 1–101 (2002). [https://doi.org/10.1016/S0370-1573\(02\)00137-0](https://doi.org/10.1016/S0370-1573(02)00137-0)
- Bolotin, V.: Broad band random vibrations of elastic systems. *Int. J. Solid Struct.* **2**, 105–124 (1966)
- Bolotin, V.: *Random Vibrations of Elastic Systems*. Springer (1984)
- Cicek, I., Ertas, A.: Experimental investigation of beam-tip mass and pendulum system under random excitation. *Mech. Syst. Signal Process.* **16**(6), 1059–1072 (2002). ISSN 0888-3270. <https://doi.org/10.1006/mssp.2001.1475>
- Iarriccio, G., Zippo, A., Pellicano, F., Barbieri, M.: Resonances and nonlinear vibrations of circular cylindrical shells, effects of thermal gradients. *Proc. Inst. Mec. Eng. Part C J. Mech. Eng. Sci.* (2020). <https://doi.org/10.1177/0954406220907616>
- Ibrahim, R.A., Roberts, J.W.: Broad band random excitation of a two-degree-of-freedom autoparametric coupling. *J. Sound Vibration* **44**(3), 335–348 (1976). [https://doi.org/10.1016/0022-460X\(76\)90506-X](https://doi.org/10.1016/0022-460X(76)90506-X)
- Ibrahim, R.A.: Nonlinear random vibration: experimental results. *ASME. Appl. Mech. Rev.* **44**(10), 423–446 (1991). <https://doi.org/10.1115/1.3119487>
- Ibrahim, R.A., Yoon, Y.J., Evans, M.G.: Random excitation of nonlinear coupled oscillators. *Nonlinear Dyn.* **1**(1), 91–116 (1990). <https://doi.org/10.1007/BF01857587>
- Jensen, R.V.: Synchronization of driven nonlinear oscillators. *Am. J. Phys.* **70**(6), 607–619 (2002). <https://doi.org/10.1119/1.1467909>
- Jensen, R.V.: Synchronization of randomly driven nonlinear oscillators. *Phys. Rev. E-Stat. Phys. Plasmas Fluids Related Interdiscip Topics* **58**(6), R6907–R6910 (1998). <https://doi.org/10.1103/PhysRevE.58.R6907>
- Malara, G., Spanos, P.D.: Nonlinear random vibrations of plates endowed with fractional derivative elements. *Probab. Eng. Mech.* **54**, 2–8 (2018). <https://doi.org/10.1016/j.probengmech.2017.06.002>
- Roberts, J.W.: Random excitation of a vibratory system with autoparametric interaction. *J. Sound Vib.* **69**(1), 101–116 (1980). ISSN 0022-460X, [https://doi.org/10.1016/0022-460X\(80\)90437-X](https://doi.org/10.1016/0022-460X(80)90437-X)
- Spanos, P.D., Evangelatos, G.I.: Response of a non-linear system with restoring forces governed by fractional derivatives—time domain simulation and statistical linearization solution. *Soil Dyn. Earthquake Eng.* **30**(9), 811–821 (2010). <https://doi.org/10.1016/j.soildyn.2010.01.013>
- Toral, R., Mirasso, C.R., Hernández-García, E., Piro, O.: Analytical and numerical studies of noise-induced synchronization of chaotic systems. *Chaos* **11**(3), 665–673 (2001). <https://doi.org/10.1063/1.1386397>
- Zippo, A., Barbieri, M., Iarriccio, G., Pellicano, F.: Nonlinear vibrations of circular cylindrical shells with thermal effects: an experimental study. *Nonlinear Dyn.* (2020). <https://doi.org/10.1007/s11071-018-04753-1>

- Zippo, A., Barbieri, M., Pellicano, F.: Temperature gradient effect on dynamic properties of a polymeric circular cylindrical shell. *Compos. Struct.* **216**, 301–314 (2019). <https://doi.org/10.1016/j.compstruct.2019.02.098>
- Zippo, A., Barbieri, M., Pellicano, F.: Experimental analysis of pre-compressed circular cylindrical shell under axial harmonic load. *Int. J. Non-Linear Mech.* **94**, 417–440 (2017). <https://doi.org/10.1016/j.ijnonlinmec.2016.11.004>

Chapter 9

Investigation of the Nonlinearity Effect of the Shrouded Blade Assemblies on Their Forced Vibrations



Anatoliy Zinkovskii, Kyrylo Savchenko, and Yevheniia Onyshchenko

Abstract The paper presents the approaches to finite element studying of the forced vibrations of the shrouded blades with nonlinearity due to the interaction of contact surfaces of the shrouds and the presence of fatigue crack. The dynamic characteristics have been calculated for the developed linearized and nonlinear finite element models of the set of two blades and damaged airfoil. The comparative analysis of the obtained results shows their significant difference for the linearized and nonlinear models in both cases of study.

Keywords Assembly of shrouded blades · Compressor blade airfoil · Breathing crack · Forced vibration · Nonlinearity effects

9.1 Introduction

A peculiar feature of shrouded blade assemblies, which are widely used in the design of turbine machines, is the presence of contact surfaces both between adjacent blades and in their joints with the disc (Petrov and Ewins 2006; Savchenko et al. 2018; Siewert et al. 2010; Szwedowicz et al. 2008; Zucca et al. 2012). This fact determines the nonlinearity of the blade assembly as a vibration system with a structural rotational symmetry, which can become more intense due to fatigue cracks (Dimarogonas 1996; Huang and Kuang 2006; Onishchenko et al. 2018; Shen and Chu 1992).

At present, a computational experiment with modern methods of computer modelling based on their three-dimensional models, one of which is the finite element method (FEM), becomes increasingly important in the determination of the dynamic

A. Zinkovskii (✉) · K. Savchenko · Y. Onyshchenko
Department of Oscillations and Vibration Reliability, G.S. Pisarenko Institute for Problems of Strength of the National Academy of Sciences of Ukraine, Kyiv 01014, Ukraine
e-mail: zinkovskii@ipp.kiev.ua

K. Savchenko
e-mail: savchenko@ipp.kiev.ua

Y. Onyshchenko
e-mail: onyshchenko@ipp.kiev.ua

state of blade assemblies. It is used to solve the problem of determining the dynamic stress state of the objects under investigation.

Despite the actual nonlinearity of blade assemblies, it is common to use both linear (Rzadkowski et al. 2007; Soliman 2019; Zinkovskii et al. 2016) and nonlinear (Dimarogonas 1996; Petrov and Ewins 2006; Onishchenko et al. 2018; Shen and Chu 1992; Siewert et al. 2010; Szwedowicz et al. 2008) approaches to the investigation of their vibration characteristics.

In the first case, the use of linearized finite element models is typical, where the contact conditions are replaced with kinematic constraints (Zinkovskii et al. 2016) or they are neglected (Soliman 2019). The areas with kinematic constraints are mainly specified from the results of the preliminary solution to the static contact interaction between the corresponding surfaces (Szwedowicz et al. 2008). It should be implied that the results of the linearized models often have low sensitivity and noticeable differences as compared with the experimental data.

The nonlinear analysis allows one to consider the dynamic variation in the contact between the surfaces. In turn, this leads to a qualitative and quantitative change in the vibration characteristics of the blade assemblies as compared with those obtained using linearized models, in particular, the occurrence of sub- and superharmonic resonances in the presence of fatigue cracks (Dimarogonas 1996; Matveev et al. 2010; Onishchenko et al. 2018; Shen and Chu 1992).

The analysis of some scientific papers demonstrates that the accuracy of the obtained results depends significantly on the approaches to the modelling of the contact conditions between their constituent elements. Therefore, the aim of this paper lies in the generalization of the test results in the determination of the effect of possible nonlinearity of the shrouded blade assemblies on the characteristics of their forced vibrations.

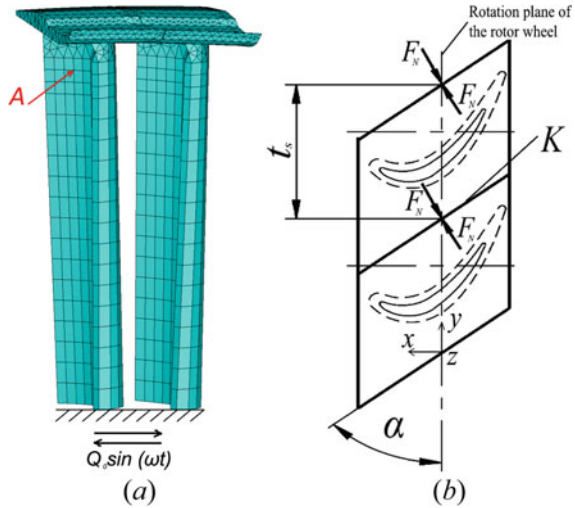
9.2 Approaches to Finite Element Modelling of the Object Nonlinearity

Let us consider two possible sources of the nonlinearity of the blades under study: shrouded coupling between the blades and a crack in the blade airfoil.

9.2.1 *Shrouded Flange Coupling of the Blades*

The analysis of forced vibrations of the blade assemblies is usually performed assuming that they are cyclically symmetric systems, namely all blades have identical geometric and mechanical characteristics. Here, the investigation of the blades is based on the use of their period with the appropriate boundary conditions. Such a period is assumed to have one blade. However, it is required to select a set of two

Fig. 9.1 General view of the FE model of the set of blades (a) and scheme of the interaction between the contact surfaces (b)



blades to consider the conditions of interaction between the shrouded flanges as a period. Noteworthy is that it is also the simplest regular system that allows one to determine the influence of structural and operational force factors on the formation of its vibrations, including the frequency detuning of the blades. Therefore, for computational experiments, a set of two blades with a straight shrouded flange was chosen (see Fig. 9.1a).

In study (Savchenko et al. 2020), you will find a detailed description of the approaches to modelling this set of blades. Therefore, let us concentrate on the basic principles of the solution to this task.

The shrouded flanges interact on the contact surfaces K as shown in Fig. 9.1b, where α is the angle of their inclination relative to the rotation plane; t_s is the blade spacing; F_N is the resultant normal force to the contact surfaces K .

An eight-node finite element and its modifications were used to construct the finite element (FE) model of the set of blades, and a four-node contact element was used to model the contact interaction between the shrouded flanges, which make it possible to track the relative position of the corresponding contact surfaces.

9.2.2 Fatigue Crack

From the previous experience (Onishchenko et al. 2018), the fatigue crack was modelled in the form of a mathematical cut, which allows one to consider both its closing and opening during blade deformation. It should also be noted that the mass of the blade is the same, and only its stiffness undergoes variations on the deformation cycles. The edges of the open crack do not interact with each other. In case of a breathing crack, the mutual non-penetration of its edges is ensured by

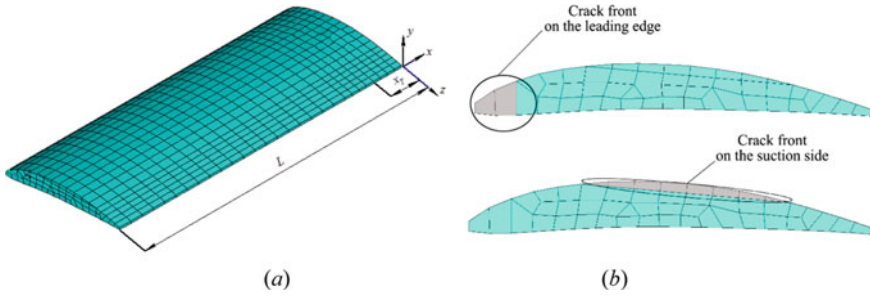


Fig. 9.2 General view of the FE model of the compressor blade airfoil (a) and its cross section with a fatigue crack (b)

the introduction of the surface contact finite elements and the solution to the contact problem as in the modelling of the interaction between the shrouded flanges of rotor blades.

Figure 9.2 illustrates the example of the FE model of the compressor blade airfoil and its cross section with a fatigue crack.

9.3 Calculation of the Forced Vibrations of the Blade Assemblies

As noted earlier, the dynamic variation in the contact interaction along the flanges arises under the action of structural and operational factors and leads to the nonlinearity of the assemblies. This is corroborated both by the results of the analysis of the static stress state (Szwedowicz et al. 2008) and from the data of full-scale experiments (Savchenko et al. 2018).

The matrix equation of forced vibrations of arbitrary nonlinear systems has the following form:

$$[M]\{\dot{u}\} + [D]\{\dot{u}\} + ([K_l] + [K_{nl}])\{u\} = \{F(t)\}, \quad (9.1)$$

where $[M]$, $[D]$ are the inertia and dissipative matrices of the system, correspondingly; $[K_l]$, $[K_{nl}]$ are the linear and nonlinear components of its stiffness matrix $[K]$; $\{F(t)\}$ is the column vector of the generalized forces acting on the system $\{u\}$; $\{\dot{u}\}$ $\{\ddot{u}\}$ are the column vectors of displacements, velocities and accelerations, respectively.

All matrices and column vectors of Eq. (9.1) are presented as units. The order of the matrix units is determined by the dimension of the FE mesh of the system under investigation.

The size of $[K_{nl}]$, which is due to the contact interaction (Wriggers 2006), depends on the number of contact nodes where each element is presented as:

$$\begin{vmatrix} k_s & 0 & -k_s & 0 \\ 0 & k_n & 0 & -k_n \\ -k_s & 0 & k_s & 0 \\ 0 & -k_n & 0 & k_n \end{vmatrix}, \quad (9.2)$$

where k is the coefficient in q -th node; n, s are the indexes characterizing the normal and tangential components of the stress state characteristics.

The components k_s of the stiffness coefficient k should satisfy the following conditions:

$$\begin{cases} k_s \neq 0, & \text{if } \eta|F_n| > |F_s|; \\ k_s = 0, & \text{if } \eta|F_n| = |F_s|, \end{cases} \quad (9.3)$$

Here F is the internal force in the considered node; η is the friction factor of the contact surfaces of the shrouded joint.

To determine the nonlinear component $[K_{nl}]$ of the stiffness matrix $[K]$, let us use the Newton–Raphson method (Zienkiewicz 1972), which is based on the solution to the static nonlinear contact task described as follows:

$$([K_I] + [K_{BN}])\{u\} = \{F(t_i)\}, \quad (9.4)$$

As a result, q and p are determined, which are in contact:

$$F_n = k_n(u_n^q - u_n^p - \Delta_n) \neq 0; \quad F_s = k_s(u_s^q - u_s^p - \Delta_s) \neq 0, \quad (9.5)$$

where Δ is the parameter of the iteration process in compliance with the Newton–Raphson procedure.

Under internal and external frictions, the dissipative matrix $[D]$ has a general view as:

$$[D] = \alpha[M] + \beta[K], \quad (9.6)$$

Here α and β are the coefficients characterizing the internal and external frictions, respectively.

Let us confine to considering energy dissipation due to internal friction, then Eq. (9.6) takes the following view:

$$[D] = \beta[K]. \quad (9.7)$$

With the vibration decrement δ , which is independent of the strain amplitude, coefficient β during vibrations of the blade by j -th mode with frequency ω_j is determined as:

$$\beta_j = \frac{\delta_j}{2\pi^2\omega_j}, \quad (9.8)$$

where ω_j is the resonant j -th mode of the blade vibrations.

The total system of nonlinear differential Eq. (9.1) is solved in its integration by the Newmark method (Zienkiewicz 1972). It implies the partition of time T on N steps: $\Delta t = T/N$. Then, for each time element $0, \Delta t, 2\Delta t, \dots, T$ there is an approximate solution considering the solution for the preliminary time value at each half-step:

$$\begin{cases} \{\dot{u}\}_{t+\Delta t} = \{\dot{u}\}_t + [(1-\lambda)\{\dot{u}\}_t + \lambda\{\dot{u}\}_{t+\Delta t}]\Delta t; \\ \{u\}_{t+\Delta t} = \{u\}_t + \{\dot{u}\}_t\Delta t + [(\frac{1}{2}-\psi)\{\dot{u}\}_t + \psi\{\ddot{u}\}_{t+\Delta t}]\Delta t, \end{cases} \quad (9.9)$$

where ψ, λ are the parameters defining accuracy and stability of integration.

The next step in solving the problem is harmonic analysis, for which the fast Fourier transformation procedure is used:

$$u(t) = \sum_{j=1}^{\infty} A_{(j)} \cos(\omega_j t - \phi_j), \quad (9.10)$$

Here $A_{(j)}, \omega_j, \phi_j$ are the amplitude, frequency and phase shift corresponding to the j -th harmonic of the Fourier transformation.

9.4 Results of the Computational Experiments

Using the developed FE models, computational investigations were performed to determine the influence of the considered nonlinearities on the characteristics of forced vibrations of the blades of the turbine machine assemblies. The calculations were carried out assuming the first flexural mode of vibrations.

A set of blades was chosen to study the nonlinearity effect due to the contact in the shrouded joint. The blades are made of heat-resistant nickel alloy with the following mechanical characteristics: $E = 1.9 \times 10^{11}$ Pa; $\rho = 8570$ kg/m³; $\mu = 0.3$. Moreover, it was assumed that the set consists of identical blades. Therefore, only in-phase vibrations are observed during kinematic excitation.

Harmonic displacement $Q_0 \sin(\omega t)$ of the end elements of the blade airfoil to the plane rotation of the rotor wheel along axis $0y$ (amplitude Q_0 varied in the range from 0.01 to 0.1 mm) was used to model the kinematic (in-phase) excitation of the blade vibrations. The frequency of the driving force ω varied in the range of the spectrum of natural frequencies of the blade vibrations.

In accordance with the outlined method of calculating forced vibrations, the time dependences of the displacements in node A (see Fig. 9.1a) were obtained. From the

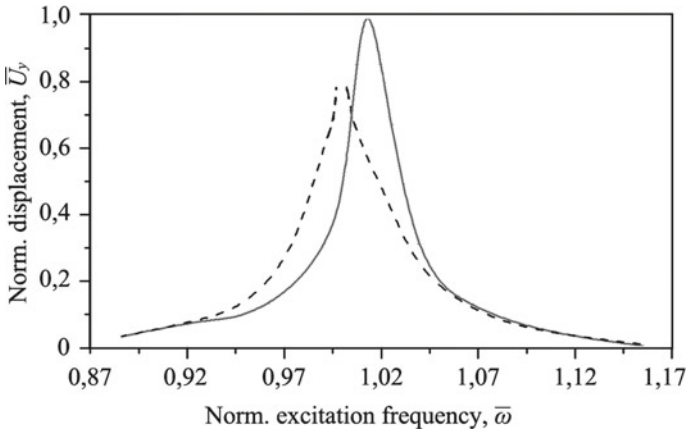


Fig. 9.3 Amplitude-frequency characteristics of the displacements along axis Oy for nonlinear (solid lines) and linearized (dashed lines) models of the blades

results of harmonic analysis of these dependencies, which characterize the steady-state vibration mode, the amplitude-frequency characteristics (AFC) of the set of blades were constructed (see Fig. 9.3). Here, for comparison, the data obtained in the linear setting are also presented.

The following conclusions can be drawn:

1. The AFC obtained using nonlinear and linearized computational models is practically identical in the in-phase excitation of vibrations of the blades, which is consistent with the data in Larin (2010). However, the level of maximum displacement amplitudes obtained in the linear settlement is 20% lower.
2. The excitation frequency, when the maximum displacement amplitude is attained, is 5% lower for the linearized calculation model, which is explained by the system stiffness variation.

Based on the calculations results, the AFC of the blades in the variation of amplitude Q_0 of the kinematic displacement of the root section were determined (see Fig. 9.4).

For a more detailed analysis, the values of the logarithmic decrement of vibrations δ were determined. Figure 9.5 illustrates its dependence on the excitation amplitude Q_0 .

As seen from the results, with the increase of the excitation amplitude Q_0 within the selected range of its values, there is a linear character of the increase in the amplitude of the displacement of the blades. Here, the level of energy dissipation in the set of blades decreases more than twice with the increase of Q_0 to 0.05 mm; however, at $Q_0 \geq 0.05$ mm, it does not change practically. This is due to the significant decrease of the relative displacements of the contact surfaces between the shrouded flanges, which also reduces its efficiency as the structural damper.

Fig. 9.4
Amplitude-frequency characteristics of displacements along axis Oy at $Q_0 = 0.01$ (1), 0.05 (2), 0.07 (3), and 0.1 mm (4)

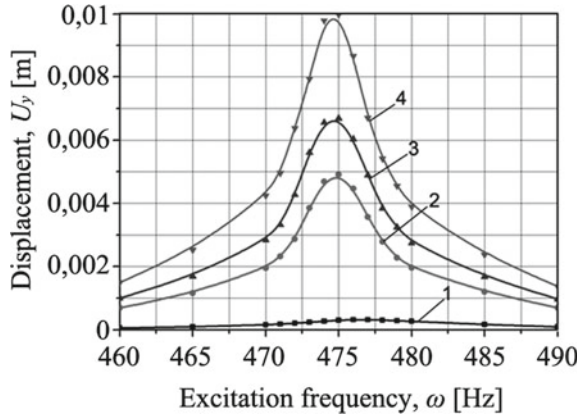
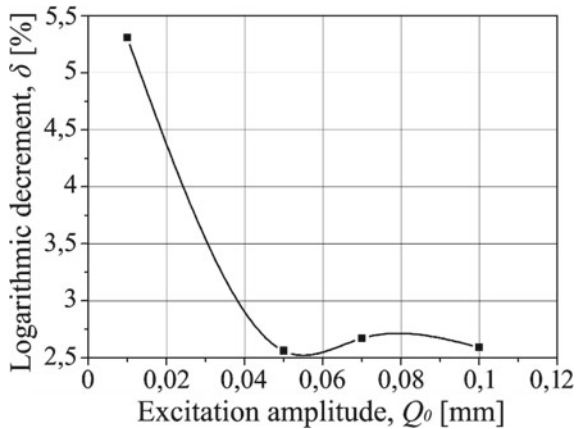


Fig. 9.5 Dependence of the logarithmic decrement of vibrations on the excitation amplitude



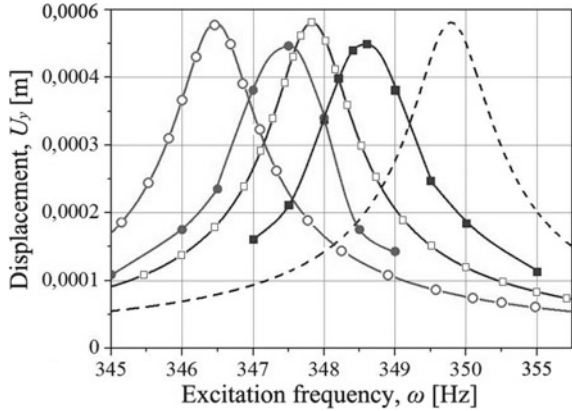
Next, consider the results of the calculation experiments on the determination of nonlinearity due to the presence of fatigue crack in the blade airfoil.

The two locations of the crack were investigated: on the suction side and leading edge of the blade airfoil at the height of $T = 0.1L$ (see Fig. 9.2). Its size was 10% of the cross-sectional area of the airfoil. To simplify the numerical calculations, only the blade airfoil was considered.

A titanium alloy with the following technical characteristics was selected as the material of the blade under investigation: $E = 1.15 \times 10^{11}$ Pa; $\rho = 4500$ kg/m³; $\mu = 0.3$.

The forced vibrations were excited via the harmonic displacement $Q_0 \sin(\omega t)$ of the end elements along axis Oy , which denotes the first flexural mode of vibrations within the plane of its minimum stiffness. The displacement amplitude was $Q_0 = 0.01$ mm.

Fig. 9.6
 Amplitude-frequency characteristics of the blade airfoil with open (○, □) and breathing cracks (●, ■) on the suction side (○, ●) and leading edge (□, ■). Dashed line denotes the undamaged airfoil of the blade



The AFC of the blade airfoil were determined in the presence of open and breathing cracks, which are shown in Fig. 9.6. For comparison, it also illustrates the frequency response of an undamaged airfoil.

Analysis of the data implies an insignificant decrease (less than 1%) in the frequency of vibrations of the blade with cracks, which correspond to the maximum amplitude of vibrations, as compared with the undamaged blade. At the same time, the level of the maximum vibration amplitudes of an undamaged airfoil with an open crack is also almost identical, and for the airfoil with a breathing crack, it is 10% lower. This can be explained by the fact that, due to the complex geometry of the blade airfoil, the crack type affects its stiffness considerably. It can be concluded that the model of an open crack, which does not consider the system nonlinearity, does not allow one to reliably estimate the level of vibrations of the object in question.

9.5 Conclusions

From the performed experiments, the following conclusions were drawn:

- In the in-phase excitation, the character of the AFC obtained using the nonlinear and linearized calculation models is almost identical. However, here, the difference in the level of the maximum amplitudes is 20%.
- The blade damage in the form of the model with a breathing crack allows one to describe the level of the maximum vibration amplitudes more accurately, as well as their corresponding frequencies, as compared with the model having an open crack. This fact enhances the efficiency of the model for the diagnostics of the presence of fatigue cracks of the blades.

References

- Dimarogonas, A.D.: Vibration of cracked structures—a state of the art review. *Eng. Fract. Mech.* **55**(5), 831–857 (1996)
- Huang, B.W., Kuang, J.H.: Variation in the stability of a rotating blade disk with a local crack defect. *J. Sound Vib.* **294**, 486–502 (2006)
- Larin, O.O.: Forced vibrations of bladings with the random technological mistuning. *Proc. ASME Turbo Expo*, 667–672 (2010)
- Matveev, V.V., Boginich, O.E., Yakovlev, A.P.: Approximate analytical method for determining the vibration-diagnostic parameter indicating the presence of a crack in a distributed-parameter elastic system at super- and subharmonic resonances. *Strength Mater.* **42**(5), 528–543 (2010)
- Onishchenko, E.A., Zinkovskii, A.P., Kruts, V.A.: Determination of the vibration diagnostic parameters indicating the presence of a mode I crack in a blade airfoil at the main, super- and subharmonic resonances. *Strength Mater.* **50**(3), 369–375 (2018)
- Petrov, E.P., Ewins, D.J.: Effects of damping and varying contact area at blade-disk joints in forced response analysis of bladed disk assemblies. *J. Turbomachinery* **128**(2), 403–410 (2006)
- Rzadkowski, R., Kwapisz, L., Drewczynski, M., Szczepanic, R., Rao, J.S.: Free vibrations analysis of shrouded bladed discs with one loose blade. *Task Q.* **10**(1), 83–95 (2007)
- Savchenko, K., Zinkovskii, A., Tokar, I.: Determination of contact interaction influence on forced vibrations of shrouded blades. *Proc. 25th Int. Congress Sound Vibr. (ICSV 25)* **5**, 2635–2640 (2018)
- Savchenko, K.V., Zinkovskii, A.P., Rzadkowski, R.: Effect of the contact surfaces orientation in the shrouded flanges and level of vibration excitation in the rotor blades on their vibration stress state. *Strength Mater.* **52**(2), 205–213 (2020)
- Shen, M.H.H., Chu, Y.C.: Vibrations of beams with a fatigue crack. *Comput. Struct.* **45**(1), 79–93 (1992)
- Siewert, C., Panning, L., Wallaschek, J., Richter, C.: Multiharmonic forced response analysis of a turbine blading coupled by nonlinear contact forces. *J. Eng. Gas Turbines Power* **132**(8), 1–9 (2010)
- Soliman, E.S.M.M.: Investigation of crack effects on isotropic cantilever beam. *J Fail. Anal. Preven.* **19**, 1866–1884 (2019)
- Szwedowicz, J., Visser, R., Sextro, W., Masserey, P.A.: On nonlinear forced vibration of shrouded turbine blades. *J. Turbomachinery* **130**(1), 11–18 (2008)
- Wriggers, P. (ed.) *Computational Contact Mechanics*. Springer-Verlag, Berlin, Heidelberg (2006)
- Zienkiewicz, O.C. (ed.): *Finite Element Method in Engineering Science*. McGraw-Hill Inc. (1972)
- Zinkovskii, A., Savchenko, K., Ya, K.: Influence of modeling of contact interaction conditions on spectrum of natural vibration frequencies of blade assembly. *Proc. 23rd Int. Congress Sound Vibr. (ICSV 23)* **1**, 289–293 (2016)
- Zucca, S., Firrone, C.M., Gola, M.M.: Numerical assessment of friction damping at turbine blade root joints by simultaneous calculation of the static and dynamic contact loads. *Nonlinear Dyn.* **67**, 1943–1955 (2012)

Part III
Nonlinear Dynamics of Discrete Systems

Chapter 10

Influence of Linear and Nonlinear Electromechanical Couplings on Vibration Absorber–Harvester System



Krzysztof Kecik and Arkadiusz Smagala

Abstract This paper presents analysis of the electromechanical coupling problem in the pendulum absorber–harvester system. The system consists of an oscillator with the attached pendulum tuned mass absorber. In an absorber, a special mechanism consisting of the oscillating magnet in the coil is applied. It uses electromagnetic induction effect for energy harvesting. We have compared the response behavior and recovered energy of the absorber–harvester system with the fixed, linear and nonlinear electromechanical coupling models. These models have been developed using experimental results of the electromechanical coupling determination. The obtained results show that the recovered energy depends on the electromechanical coupling models, but the vibration mitigation effect does not depend on them.

Keywords Energy harvesting · Vibration mitigation · Pendulum · Magnetic levitation · Electromechanical coupling

10.1 Introduction

The presence of mechanical vibration is an important problem in many engineering applications. Usually, we want to reduce the vibration to an acceptable level. For this purpose, additional special isolators between the vibrating machine and the excitation source are applied. Another solution is the structural modification to shift the unwanted oscillation away from the resonance or dissipate vibration by external devices (Lu et al. 2016; Sun and Jahangiri 2018). The vibration energy harvester is a device that converts mechanical energy to electrical energy via a special transduction mechanism. Energy harvester has to be a viable alternative to batteries for low-power electronic devices. The mechanical energy is derived from ambient energy (wind,

K. Kecik (✉) · A. Smagala
Department of Applied Mechanics, Lublin University of Technology, 20-618 Lublin, Poland
e-mail: k.kecik@pollub.pl

A. Smagala
e-mail: a.smagala@pollub.pl

solar, thermal, kinetic energy, etc.). Wiercigroch (2005) patented the concept of energy extraction from sea waves.

A very promising technique in engineering is the simultaneous vibration mitigation and energy harvesting. The methodology of the dynamical vibration absorber and energy harvester is similar. Energy recovery from the dynamical vibration absorbers will give the added advantage of harvesting energy while unwanted vibrations are suppressed. The energy harvesters require transducer mechanisms, usually be it electromechanical, piezoelectric or electrostatic. The vibration absorber–harvester system should be designed to maximize the energy harvesting while maintaining the effectiveness of vibration suppression.

There are numerous papers that describe energy harvesters, microgenerators, microelectromechanical systems (MEMS generators) for converting mechanical energy to electricity (Williams and Yates 1996; Mitcheson 2004; Lueke et al. 2011). In general, the vibration absorber–harvester system combines absorption ability and harvesting capability. Ali and Adhikari (2013) have investigated the vibration absorber design integrated with a piezoelectric stack harvester for both vibration reduction and energy recovery. They showed that with proper parameters, the energy harvesting and vibration control are possible. Hassan (2014) presented a mass-spring absorber as an energy harvester. The “harvesting frequency” at which the maximum amplitude of the absorber depends only on the absorber’s mass was defined. Kecik (2021) proposed a pendulum absorber-harvester system for energy harvesting and vibration mitigation. The electromechanical coupling coefficient was modeled as the high-complicated nineteenth-degree nonlinear function of the magnet position. The obtained results prove that both vibration mitigation and energy harvesting could be achieved. Comparison of the vibration absorber and the vibration absorber–harvester was demonstrated. Dipak et al. (2013) have presented the possibility of harnessing vibration energy from the linear vibration absorber with a piezoelectric energy harvester. They have optimized the system parameters for simultaneous vibration mitigation and energy recovery. In the papers of Davies and Mc Dowell (2016,2017), the prototype device for simultaneous vibration absorption and energy harvesting has demonstrated. Authors have used a system with the post–buckled beam spring. The piezo elements over the beam for energy harvesting were attached. Rasil Raj and Santhosh (2019) have studied two degrees of freedom nonlinear system used for vibration mitigation and energy harvesting simultaneously. Multi-harmonic balance method (MHBM) along with arc length continuation for frequency response analysis was used.

In general, the electromagnetic energy harvesters are based on the induced voltage in a coil when a magnet moves relative to it (the change in magnetic flux is either due to having a fixed coil and a moving magnet, or the opposite). The induced voltage (well–known as electromotive force) is proportional to the velocity of the relative motion and the number of turns of the coil. There are two basic types of transducer mechanisms in terms of the relative displacement. The first is the mechanism of lateral motion between the magnet and the coil. The second type is based on the magnet motion in of the coil terminal (or in and out). The harvester efficiency depends largely on the architecture of the transduction mechanism and the electromechanical

coupling. Therefore, the simple method to increase the harvesting efficiency is higher harvester size (higher magnet, more coil windings). As reported by Beeby (2007) the electromagnetic generators perform better on macro-scale than on micro-scale.

In the literature, the electromechanical coupling can be modeled as a constant value, because the magnetic flux density is treated as uniform (Stephen 2006; Mann and Sims 2010). Stephen derived the coupling coefficient parameter and its influence on the optimum load resistance. Mann and Sims have assumed the coupling as the constant including the coil inductance. O'Donnell et al. (2007) also reported a similar approach but neglected the coil inductance. Moreover, the author showed that the induced current of the harvester is equivalent to an additional damping called "electrical damping". This assumption simplifies analysis and the current flow equation was reduced. Cepnik et al. (2011) used the time-optimized simulation of the electromagnetic coupling by analytical calculation. Some papers have shown an experimentally determined coupling coefficient (Liu and Garrett 2005). Kecik (2017) demonstrated some differences in the experimental determination of the electromechanical coupling during the static and dynamic tests. Other methods are expressing the magnetic flux density by elliptic integrals (Spreemann 2008) or by finite element method (Zuo et al. 2010). Mosch and Fischerauer (2019) have presented an interesting review paper describing different methods for coupling coefficient measurement. Additionally, they have recommended some methods for determination of the electromechanical coupling coefficient and the optimum load resistance for the maximum power harvesting.

In this paper, we present a frequency response analysis of the absorber–harvester system with four different electromechanical couplings: fixed model, linear model and two nonlinear models. All models were determined based on the experiment dynamic tests. The main aim is to show the differences between various electromechanical models and estimate how these models influence the vibration mitigation and energy harvesting. The obtained results show that the modification in the coupling coefficient by changing the magnet–coil position does not influence the vibration suppression, but influences the energy harvesting.

10.2 Absorber-Harvester Architecture

In this section, we present the architecture of the vibration absorber-harvester system. This system was originally designed as the pendulum tuned mass absorber (Kecik 2015). Next, the modification and adding the magnet–coil harvester allows for energy recovery during the operation of the absorber. The main problem seems how the added harvester influences the vibration mitigation.

10.2.1 Model of Vibration Absorber System with Energy Harvester

Figure 10.1 shows the schematic diagram of the proposed dynamic pendulum vibration absorber with energy harvesting component. It consists of three main subsystems: the main system (I), the tuned mass absorber (II) and the magnetic levitation harvester (III). The primary system (mass m_1) is suspended on the classical suspension consisting of a linear spring with stiffness k_1 and a damper with damping coefficient c_1 . This system is excited in a kinematic way with the amplitude k_2x_0 , where k_2 is the linear stiffness of the excitation's spring and x_0 is its end displacement. Frequency of the harmonic excitation is denoted by ω . The tuned mass damper has mass m_2 and length l . The pendulum to the main system is attached. The pivot's damping is assumed to be linear and denoted by c_2 . The subsystem can absorb the energy from the main system and the vibrations of the primary system are suppressed. The third harvester subsystem is mounted in the pendulum structure. It consists of the levitating magnet (m_3) in the coil (Fig. 10.1c). The levitating magnet is suspended between two repulsive arranged magnets. The magnetic levitation system in the literature as the strongly mechanical nonlinear oscillator is assumed. The magnetic forces

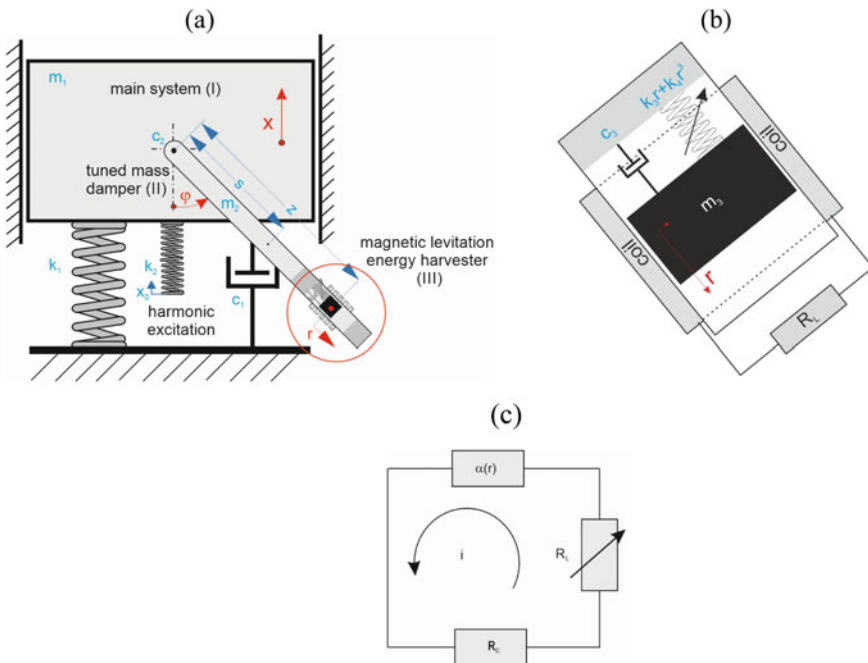


Fig. 10.1 Absorber–harvester scheme (a), the electromechanical energy harvester installed in the tuned mass absorber structure (b) and the energy harvester circuit diagram (c). The pendulum motion causes vibration mitigation of the main system and the current is induced in the coil winding

usually are treated as nonlinear springs (Mann and Sims 2009). The detailed description of the experimental absorber–harvester system and the magnetic levitation part is presented by Kecik (2021).

The motion of the pendulum causes vibration mitigation of the main system and causes the magnet to oscillate in the coil and finally the current is induced. Note that the energy is recovered for the pendulum swinging (non–trivial solution) and for the pendulum rest (semi–trivial solution). The electrical circuit consists of the coil terminal with the resistance R_C and the resistor with a load resistance R_L . This circuit dissipates the produced energy across the load resistor and it is not capable of storing energy. The electromechanical coupling parameter $\alpha(r)$ couples mechanical and electrical subsystems. The electromagnetic harvester can be modeled as a mechanical nonlinear oscillator. The total system has four degrees of freedom: the displacement of the main system (x), the pendulum angular displacement (φ), the levitating magnet displacement (r) and the induced current (i). The equations of motion are derived from Lagrange approach. The kinetic and potential energies in the paper of Kecik (2021) are defined. The equations of motion are:

$$\begin{aligned} & (m_1 + m_2 + m_3)\ddot{x} + c_1\dot{x} + (k_1 + k_2)x \\ & = k_2x_0 \sin \omega t - \left(m_2 \frac{l}{2} + m_3(z + r) \right) [\ddot{\varphi} \sin \varphi + \cos \varphi^2] \\ & + m_3(2\dot{r}\dot{\varphi} \sin \varphi - \ddot{r} \cos \varphi), \end{aligned} \quad (10.1)$$

$$(I_0 + m_3(z + r)^2)\ddot{\varphi} + c_2\dot{\varphi} + (\ddot{x} + g)[m_2s + m_3(z + r)] \sin \varphi + 2m_3\dot{\varphi}\dot{r}(z + r) = 0. \quad (10.2)$$

$$m_3\ddot{r} - m_3[\ddot{x} \cos \varphi + \dot{\varphi}^2(z + r)] + c_3\dot{r} + k_3r + k_4r^3 - m_3g \cos \varphi + \alpha(r)i = 0, \quad (10.3)$$

$$L\dot{i} + i(R_L + R_C) = \alpha(r)\dot{r}. \quad (10.4)$$

Here, I_0 denotes the pendulum mass moment of inertia, z is the magnet's position vs. the pendulum pivot, and L is the coil inductance. Equation (10.4) is the electrical differential equation characterizing the current flow in the circuit (Fig. 10.1c). These equations of motion are strongly nonlinear and additionally coupled by inertial terms leading to so-called autoparametric systems. Therefore, there is an energy transfer between different subsystems.

10.2.2 Electromechanical Coupling Modeling

As mentioned earlier, the electromechanical coupling coefficient $\alpha(r)$ of the transduction mechanism couples the mechanical and electrical systems (Eqs. 10.3 and 10.4). This parameter characterizes the ability to convert mechanical vibration energy into

electricity. The electromechanical transducer mechanisms generally differ in size, architecture and output performance. Therefore, the electromechanical coupling is determined in various ways. In our case, the transducer architecture consists of a cylindrical magnet oscillating inside a coil (or oscillating outside the coil).

In the literature, the electromechanical coupling in the magnet–coil system is often assumed as the constant value due to the low coil inductance. Then the equation of induced current (Eq. 10.4) is reduced and the electromechanical coupling represents only an additional damping term (Stephen 2006; Mosch and Fischerauer 2019).

$$L \approx 0, \quad i = \frac{\alpha \dot{r}}{R_L + R_C}, \quad \alpha i = \frac{\alpha^2 \dot{r}}{R_L + R_C}. \quad (10.5)$$

This means that the induced current equations are omitted. As reported by Kecik (2017) this approach is correct provided that the constant value of the electromechanical coupling coefficient is properly chosen. To find the electromechanical coupling function (parameter), one can start by examining how the induced voltage in the coil terminal is related to the velocity of the magnet. For this aim, the dynamic test of the moving magnet through the coil was applied. Applying Kirchhoff's voltage law yields (Kecik 2017)

$$\alpha(r) = \frac{L\dot{i} + i(R_L + R_C)}{\dot{r}}. \quad (10.6)$$

Finally, the electromechanical coupling function in Fig. 10.2 is obtained. The black line means the experimental electromechanical coupling coefficient relative to the magnet position in the coil. The dashed lines show the coil ends. As we can see, this function is strongly nonlinear and its value depends on the magnet's position. The maximal $\alpha(r)$ value of 80 Vs/m close to the coil's end is obtained. For small oscillations (close to the coil's center) the function is linear.

Therefore, the first proposed model is linear that depends on the magnet position in the coil (blue circle in Fig. 10.2). This model has simply form

$$\alpha(r) = \alpha_{11}r, \quad (10.7)$$

where α_{11} is the parameter estimated from the experiment. Generally, this model for the small magnet oscillation close to the coil's center is designed.

The second electromechanical coupling model is the nonlinear (called nonlinear I) that depends also on the magnet position in the coil according to the square polynomial function

$$\alpha(r) = \alpha_{21} + \alpha_{22}r + \alpha_{23}r^2. \quad (10.8)$$

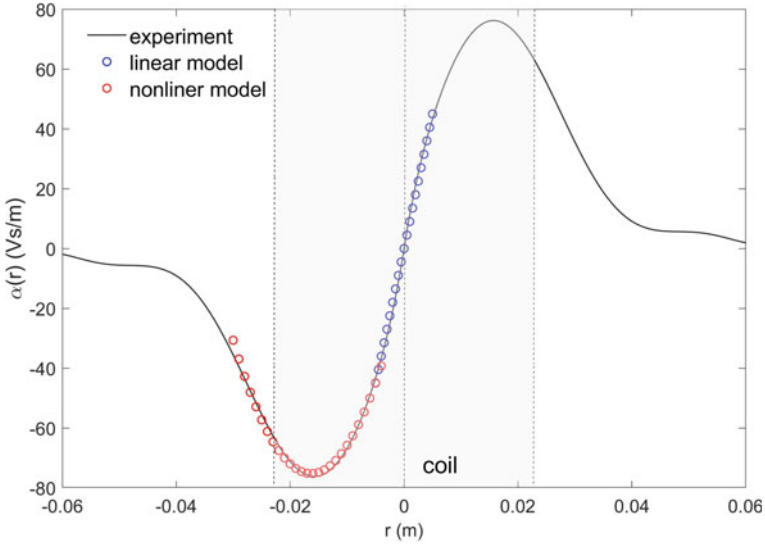


Fig. 10.2 Electromechanical coupling coefficient in function of the magnet position obtained from the experiment (black line). For the magnet oscillation close to the coil’s center the electromechanical coupling can be described by the linear function (blue circle), for the magnet oscillation close to the coil’s end the electromechanical coupling is a nonlinear function (red circle)

Parameters α_{21} , α_{22} , and α_{23} are obtained by the curve fitting technique (red circles in Fig. 10.2). This model is dedicated to the magnet oscillation close to the coil’s end.

The strongly nonlinear polynomial model (called nonlinear II) based on the full shape of the experimental electromechanical coupling function (black line in Fig. 10.2) has been proposed by Kecik (2019). This polynomial nonlinear model has the form

$$\alpha(r, d) = a_0(r - d) + \sum_{i=1}^9 a_i(r - d)^{2i+1}, \tag{10.9}$$

where d is the position magnet versus the coil. The coefficients a_1 – a_9 are determined by the curve fitting technique. This model can be used for all magnet coil positions.

10.3 Results

10.3.1 Parameters Identification

The equations governing the model appear as fully implicit ordinary differential equations. Therefore, the numerical continuation method (Auto07) and verification with the solver ode15i (MATLAB) which can handle fully implicit differential equations were used. The parameters of the absorber-harvester system have been estimated from the laboratory rig. Most of these are readily measurable (mass, length, stiffness, resistance, inductance), others had to be identified (damping and electromechanical coupling). The damping coefficients have been estimated from well-known logarithmic decrement of the damping method. The identified system parameters are: $m_1 = 0.55$ kg, $m_2 = 0.3$ kg, $m_3 = 0.1$ kg, $c_1 = 12$ Ns/m, $c_2 = 0.03$ Nsm/rad, $c_3 = 0.085$ Ns/m, $z = 0.15$ (m), $k_1 = 600$ N/m, $k_2 = 800$ N/m, $k_3 = 400$ N/m, $k_4 = 260$ kN/m³, $I = 0.004$ kgm², $L = 1.5$ H, $R_L = 1$ k Ω , $R_C = 1$ k Ω . The electromechanical coupling parameters are: $\alpha = 75$ Vs/m, $\alpha_{11} = 9000$ Vs/m², $\alpha_{21} = -12.07$ Vs/m, $\alpha_{22} = 7751$ Vs/m², $\alpha_{22} = 237,700$ Vs/m³. The parameters of the nonlinear model II are listened by Kecik (2019). The amplitude of kinematic excitation equals $x_0 = 0.035$ m.

10.3.2 Comparison of Electromechanical Coupling Models

At the beginning, the comparison of the frequency response curves of the main system (Fig. 10.3a), the absorber (Fig. 10.3b), the harvester (Fig. 10.3c) and the induced current (Fig. 10.3d) for all coupling models are shown. The black color means the constant coupling model (Eq. 10.5), the purple line is the result of the linear coupling model (Eq. 10.7), the red color shows the nonlinear I model (Eq. 10.8), the yellow line denotes the nonlinear II model (Eq. 10.9) and the green triangles are the experimental results.

The marked circle points mean the period doubling bifurcation that causes the destabilization of the semi-trivial solution and the pendulum starts to oscillate from rest. The continuous and dashed lines are stable and unstable solutions, respectively.

From all diagrams, it can be seen that all electromechanical coupling models practically do not influence the main system (Fig. 10.3a) and the absorber (Fig. 10.3b) oscillation. However, the magnet dynamics and the induced current are different for each model. This suggests that the electromechanical coupling influences the harvester only. Therefore, the increase of energy recovery without loss of vibration mitigation effectiveness is possible by simple modification in the magnet coil configuration. As we can see, for the small pendulum's oscillation the induced currents for all analyzed models agree with the experiment. However, for higher oscillations, the induced current is better described by the nonlinear I and II models.

Interestingly, for some frequency ranges, the recovered current is higher if the pendulum was swinging (constant, nonlinear I and nonlinear II models close to

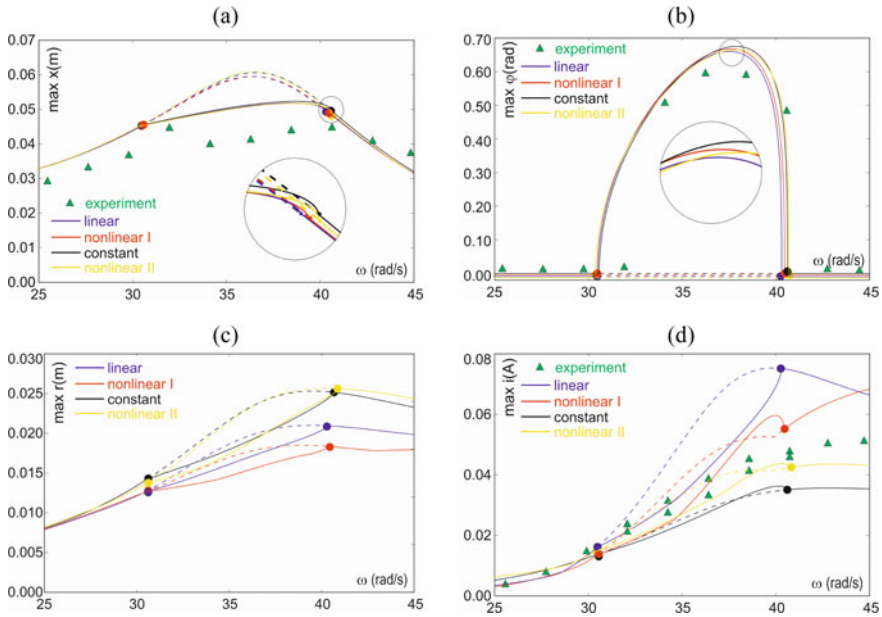


Fig. 10.3 Absorber–harvester responses with constant, linear and nonlinear electromechanical coupling models: main system (a), the tuned mass damper (b), the harvester (c) and the induced current (d). The continuous line means the stable response while the dashed line denotes an unstable solution. The marked circle points are the period doubling bifurcations that cause destabilization and motion of the tuned mass absorber

frequency of $\omega \approx 40$ rad/s). This means that the harvester recovered more energy if the pendulum is swinging. In other words, this means that activation of the absorber improves energy harvesting.

10.3.3 Analysis of Linear Electromechanical Coupling Model

The detailed analysis of influence of the linear electromechanical coupling coefficient model on the energy harvesting and vibration maximal amplitudes is presented in Fig. 10.4. Three different values of parameter α_{11} have been compared. The black line shows result for $\alpha_{11} = 100$ Vs/m, the purple line for $\alpha_{11} = 5000$ Vs/m and the red line for $\alpha_{11} = 10,000$ Vs/m. Analysis of Fig. 10.4a, b indicates small changes in the primary system and the absorber responses. Only at the high value of coefficient α_{11} the absorber amplitude is slightly less.

Of course, the highest recovered current is obtained for high coefficient α_{11} . As we can see, the modification of the linear electromechanical coupling model strongly influences the induced current. Interestingly, the harvester’s mass executes smaller oscillations (the pendulum also vibrates less), but the induced current is higher.

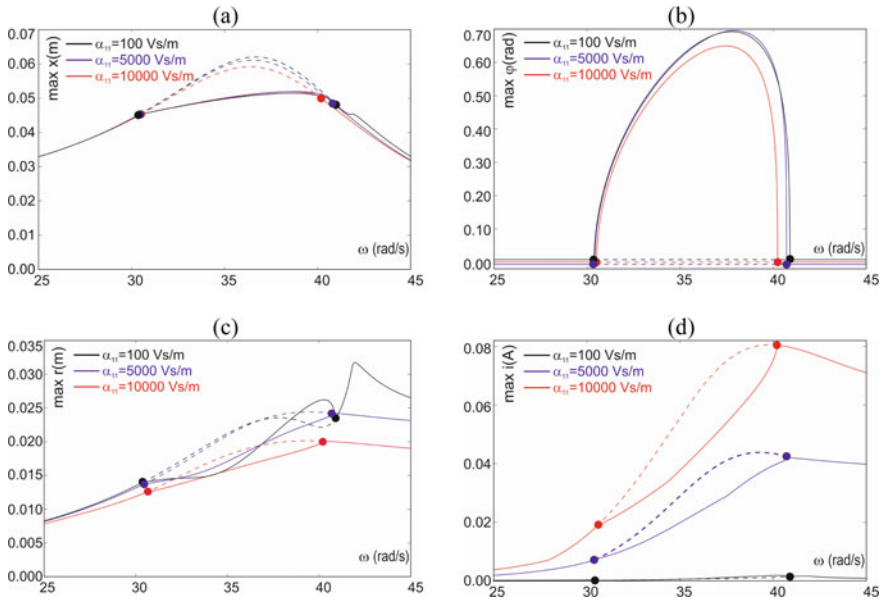


Fig. 10.4 Influence of the linear electromechanical coupling on: main system (a), the tuned mass damper (b), the levitating magnet (c) and the induced current (d). The continuous line means the stable response while the dashed line is an unstable solution. The marked points are the period doubling bifurcations that cause destabilization and motion of the tuned mass absorber

10.3.4 Analysis of Nonlinear Electromechanical Coupling Model

The nonlinear model I is dedicated to the magnet’s oscillation close to the coil end. As we can see in Fig. 10.2, in this position, the electromechanical coupling reaches the highest value and the coupling function is strongly nonlinear. Therefore, the linear model rather should not be used for the energy harvesting analysis if the magnet vibrates near the end of the coil and can leave it.

In Fig. 10.5a we show the influence of the nonlinear electromechanical coupling model I. The main parametric resonance is located close to $\omega \approx 30\text{--}40$ rad/s. We change the parameters α_{21} , α_{22} and α_{23} and compare with the nonlinear model I from Fig. 10.3 (red line). It is clear, that the change of α_{21} , α_{22} and α_{23} practically does not affect the primary system vibrations. Additionally, no significant influences on the absorber (pendulum) amplitudes were observed (Fig. 10.5b).

However, we note again that these parameters influence the induced current (Fig. 10.5d) and the magnet oscillation amplitude (Fig. 10.5c). In general, the increase values of α_{21} , α_{22} and α_{23} cause higher induced current, but the magnet harvester amplitude may increase or decrease.

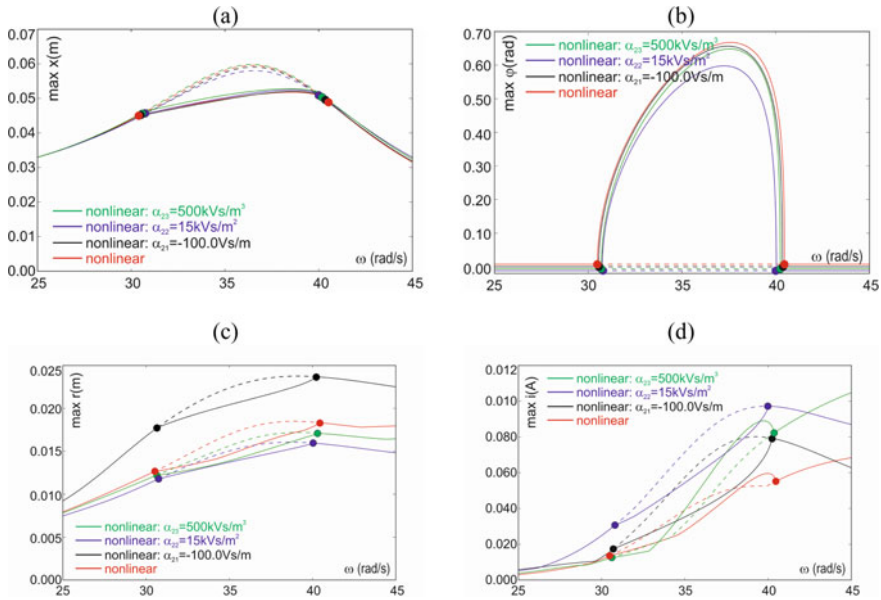


Fig. 10.5 Influence of the nonlinear electromechanical coupling model I on: main system (a), the tuned mass damper (b), the levitating magnet (c) and the induced current (d). The continuous line means the stable response while the dashed line is an unstable solution. The marked points are the period doubling bifurcations that cause destabilization and motion of the tuned mass absorber

The obtained results suggest that the modification of the levitating magnet position can be an easy way to increase the recovered energy while maintaining the effectiveness of vibration reduction.

Because the polynomial nonlinear model II is complicated and has as many as nine coefficients, therefore their influence has not been studied here. Moreover, Kecik (2021) reported the detailed analysis of the nonlinear model II and its influence on the unstable region.

10.4 Conclusions

This work is devoted to simultaneous vibration mitigation and energy harvesting. The main aim of the research is to recover energy from the dynamic vibration absorber without reducing its vibration reduction efficiency. Therefore, we propose the control of energy harvesting via simple modification of the magnet–coil position. Then, we have not observed the reduction in the effectiveness of vibration.

The different modeling of the electromechanical coupling in the vibration absorber–harvester system is proposed. Electromechanical coupling model variants have been estimated based on the experiment test. The linear and nonlinear models

have been compared with the most used approach (constant value). The experimental test shows that the maximal value of the electromechanical coupling coefficient close to the coil's end was obtained. In this position, the electromechanical coupling is a strongly nonlinear function.

The obtained results confirmed that the modification of the electromechanical coupling by the magnet–coil position practically does not influence the vibration mitigation. The linear and nonlinear models influence the harvester only. However, for small oscillations (below 0.01 m of the magnet's amplitude) all models give similar results. The electromechanical coupling description is essential especially for higher vibration amplitudes.

The next step will be modification of the electromechanical coupling models by design and optimization of the oscillating magnet by applying the special stock of magnets and separators.

Acknowledgements The research was financed in the framework of the project: Theoretical–experimental analysis possibility of electromechanical couplings shaping in energy harvesting systems, no. DEC-2019/35/B/ST8/01068, funded by the National Science Centre, Poland.

References

- Ali, S.F., Adhikari, S.: Energy harvesting dynamic vibration absorbers. *J. Appl. Mech.* **80**(4), 041004 (2013)
- Beeby, S.P., Tudor, M.J., Torah, R.N., Roberts, S., O'Donnell, T., Roy, S.: Experimental comparison of macro and micro scale electromagnetic vibration powered generators. *Microsyst. Tech.* **3**, 1647–1653 (2007)
- Cepnik, C., Radler, O., Rosenbaum, S., Strohla, T., Wallrabe, U.: Effective optimization of electromagnetic energy harvesters through direct computation of the electromagnetic coupling. *Sens. Actuator A-Phys* **167**, 416–421 (2011)
- Davis, R.B., McDowell, M.D.: Combined Euler column vibration isolation and energy harvesting. *Smart Mater Struct.* **26**(5), 055001 (2017)
- Davis, R.B., McDowell, M.D.: Simultaneous vibration isolation and energy harvesting: simulation and experiment. In: Kerschen, G. (eds.) *Nonlinear Dynamics. Conference Proceedings of the Society for Experimental Mechanics Series*, vol. 1, 305–315. Springer (2016)
- Dipak, S., Rajarathinam, M., Ali, S.F.: Energy harvesting dynamic vibration absorber under random vibration, *IEEE International Conference on Control Applications (CCA)*, 1241–1246 (2013)
- Hassan, G.A.: Optimal design of a vibration absorber-harvester dynamic system. *Int. j. Res. Eng. Techn* **3**(6), 325–329 (2014)
- Kecik, K.: Simultaneous vibration mitigation and energy harvesting from a pendulum-type absorber. *Commun. Nonlinear Sci.* **92**, 105479 (2021)
- Kecik, K., Mitura, A., Lenci, S., Warminski, J.: Energy harvesting from a magnetic levitation system. *Int. j. Nonlinear Mech.* **94**, 200–206 (2017)
- Kecik, K.: Dynamics and control of an autoparametric system. *Int. j. Nonlinear Mech.* **70**, 63–72 (2015)
- Kecik, K.: Architecture and optimization of a low-frequency maglev energy harvester. *Int. J. Struct. Stab. Dyn.* **19**(8), 1950097 (2019)
- Lu, Z., Wang, D., Masri, S.F., Lu, X.: An experimental study of vibration control of wind excited high-rise buildings using particle tuned mass dampers. *Smart Struct. Syst.* **18**(1), 93–115 (2016)

- Liu, J., Garrett, S.: Characterization of a small moving-magnet electrodynamic linear motor. *J. Acoust. Soc. Am* **118**(4), 2289–2294 (2005)
- Lueke, J., Moussa, W.A.: MEMS-based power generation techniques for implantable biosensing applications. *Sensors* **11**, 1433–1460 (2011)
- Madhav, Ch., Faruque, S.A.: Harvesting energy from vibration absorber under random excitations. *IFAC-PapersOnLine* **49**(1), 807–812 (2016)
- Mann, B.P., Sims, N.D.: Energy harvesting from the nonlinear oscillations of magnetic levitation. *J. Sound Vib.* **319**(1–2), 515–530 (2009)
- Mann, B., Sims, N.: On the performance and resonant frequency of electromagnetic induction energy harvesters. *J. Sound. Vib* **329**(1–2), 1348–1361 (2010)
- Mitcheson, P.D., Miao, P., Stark, B.H., Yeatman, E.M., Holmes, A.S., Green, T.C.: MEMS electrostatic micropower generator for low frequency operation. *Sensors Actuators A* **115**, 523–529 (2004)
- Mosch, M., Fischerauer, G.: Comparison of methods to measure the coupling coefficient of electromagnetic vibration energy harvesters. *Micromachines* **10**(12), 826 (2019)
- O'Donnell, T., Saha, C., Beeby, S., Tudor, J.: Scaling effects for electromagnetic vibrational power generators. *Microsyst. Technol.* **13**, 1637–1645 (2007)
- Rasil Raj, P.V., Santhosh, B.: Parametric study and optimization of linear and nonlinear vibration absorbers combined with piezoelectric energy harvester. *Int. J. Mech. Sci.* 268–279 (2019)
- Spreemann, D., Hoffmann, D., Folkmer, B., Manoli, Y.: Numerical optimization approach for resonant electromagnetic vibration transducer designed for random vibration. *J. Micromech. Microeng.* **18**(1), 104001 (2008)
- Stephen, N.: On energy harvesting from ambient vibration. *J. Sound. Vib* **293**(12), 409–425 (2006)
- Sun, C., Jahangiri, V.: Bi-directional vibration control of offshore wind turbines using a 3D pendulum tuned mass damper. *Mech. Syst. Signal Process.* **105**, 338–360 (2018)
- Wiercigroch, M.: Wave energy extraction via parametric pendulum (patent pending, 2005)
- Williams, C.B., Yates, R.B.: Analysis of a micro-electric generator for microsystems. *Sens. Actuators A Phys.* **52**(1–3), 8–11 (1996)
- Zuo, L., Scully, B., Shestani, J., Zhou, Y.: Design and characterization of an electromagnetic energy harvester for vehicle suspensions. *Smart Mater. Struct.* **19**(4), 045003 (2010)

Chapter 11

Crisis-Induced Intermittency and Other Nonlinear Dynamics Phenomena in Vibro-impact System with Soft Impact



Victor Bazhenov, Olga Pogorelova, and Tatiana Postnikova

Abstract The dynamic behavior of a platform-vibrator with shock is studied. It is the main molding equipment in the production of precast concrete elements and is widely used in the construction industry for compacting and molding large concrete products. Its mathematical model corresponds to a two-body 2-DOF vibro-impact system with a soft impact. This model has several peculiar properties. Comparing a soft impact simulation with a linear force and a nonlinear contact force in accordance with the Hertzian contact theory showed that it is preferable to use the Hertz force. When various control parameters are changing, the model demonstrates interesting phenomena, inherent in non-smooth nonlinear discontinuous systems, namely, sustained (permanent) and transient chaos, boundary and interior crises, crisis-induced intermittency, coexisting regimes in the hysteresis zone. The ranges of control parameters in which unwanted modes can be implemented are shown.

Keywords Platform-vibrator · Vibro-impact · Mold with concrete · Soft impact · Hysteresis · Crisis · Intermittency · Chaotic · Time series · Lyapunov exponent

11.1 Introduction

The vibro-impact system with soft impact is a mathematical model of a platform-vibrator with shock that is widely used in the construction industry for the production of precast concrete elements. But their operational efficiency, the choice of design parameters, the effect on the machine dynamics of the concrete mix (first liquid and then gradually hardening) and other problems are still being discussed at present

V. Bazhenov · O. Pogorelova · T. Postnikova (✉)
Kyiv National University of Construction and Architecture, 31, Povitroflotskiy avenu, Kyiv,
Ukraine
e-mail: posttan@ukr.net

V. Bazhenov
e-mail: vikabazh@ukr.net

O. Pogorelova
e-mail: pogos13@ukr.net

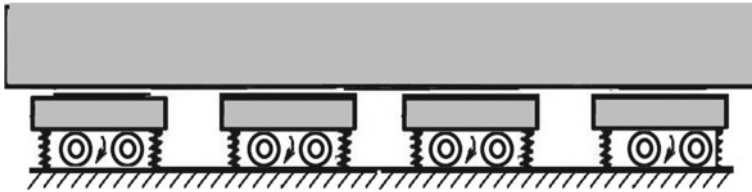


Fig. 11.1 Schematic diagram of platform-vibrator with four blocks

(Vasiliev 2019; Nazarenko et al. 2017a, b, 2019). A schematic diagram of vibration equipment that implements the shock-vibration technology for concrete mixtures compaction and reinforced products molding is shown in Fig. 11.1.

The shock-vibration platform of the block type consists of separate blocks on which rubber plate limiters are fixed. Two general vibration exciters with periodic excitation are installed on each block. The mold with concrete mix is installed on the stops without fastening. But the platform table is equipped with stops that prevent the mold from sliding and rotating. For volumetric compaction, this machine uses vertically directed mold vibrations. A mold with concrete, which has a huge mass, breaks off the stops for a very short distance. The platform table and the mold with concrete move separately for a very short time. Then the mold falls with a shock onto a rubber gasket attached to the table. The mold collides with the limiters with oncoming movement. Then it comes off again and falls on the gasket and so on. The vibro-impact movement is accompanied by a soft, even very soft, impact due to the softness, flexibility of the rubber gasket. These peculiar properties give the reason to consider the mechanical system as an unusual vibro-impact system.

The special attention was paid to the way for simulating the soft impact. The systems with a soft impact are discussed in Andraeus et al. (2013), Fu et al. (2020). In Andraeus et al. (2013), the authors simulate an impact by interposing a linear spring between the bodies at their contact point.

When varying the control parameters, this model exhibits many phenomena inherent in nonlinear systems. The exciting frequency, the technological mass of the mold with concrete, and the stiffness of the vibro-isolating spring were chosen as control parameters. The model demonstrated permanent and transient chaos; boundary and interior crises; crisis-induced intermittency; jump phenomena of hysteresis, where coexisting regimes existed. To identify the observed modes, the generally accepted techniques were used, namely, the graphs of time series, trajectories in phase space, Poincaré maps, Fourier spectra, the largest Lyapunov exponents, and wavelet characteristics, which were obtained using Continuous Wavelet Transform.

Many phenomena of nonlinear dynamics were discovered in 70s and 80s of the twentieth century (Grebogi et al. 1983, 1987; Lorenz 1972; Pomeau and Manneville 1980). At present, they are widely discussed in the world scientific literature (Wang et al. 2016; Danca 2016; Mishra et al. 2020; Noël and Kerschen 2017). Well-known authors (Elaskar 2018; Elaskar and del Río 2017; Macau 2019; Lai and Tél 2011) have

written several comprehensive monographs. Many works consider the emergence of chaotic and chaos-related events and their analysis in different dynamical systems in various fields of science (Bhalekar et al. 2012; Macek 2015).

In authors' opinion, the study of the manifold of nonlinear phenomena in a specific vibro-impact system may be interesting from three points of view. Firstly, it adds information to fundamental knowledge about phenomena that occur in nonlinear dynamical systems. Secondly, it shows the behavior of a specific vibro-impact system (a platform-vibrator with shock) with varying different control parameters. Thirdly, it allows us to point out at what values of the control parameters an undesirable and possibly dangerous state, such as permanent and transient chaos and chaos-related events, can occur.

Thus, the goals of this paper are:

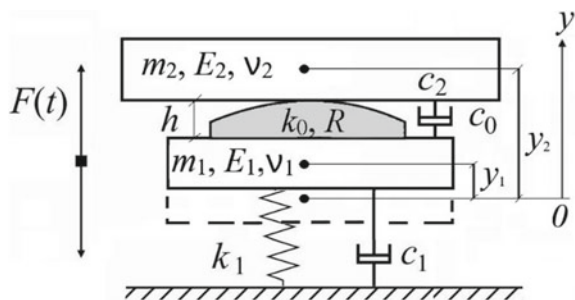
- To show that it is preferable to simulate a soft impact using the nonlinear Hertz force;
- Clearly, graphically, and persuasively show the manifold of the nonlinear dynamics phenomena that can occur in the specific vibro-impact system (a platform-vibrator with shock) when varying the control parameters.

11.2 Brief Description of Platform-Vibrator Mathematical Model

The two-mass platform-vibrator with shock is one of the successful solutions for vibration equipment that implements shock-vibration technology for concrete mixtures compaction and reinforced products molding. The creation of a platform-vibrator mathematical model was described in detail in Bazhenov et al. (2020). Now the basic statements required to understand its dynamical behavior will be repeated.

The accepted simplified design scheme of the platform-vibrator with shock is shown in Fig. 11.2. Since the limiters on the platform table prevent the mold from sliding and turning, the movement is only vertical. The exciting force is $F(t) = P \cos(\omega t + \phi_0)$, and its period is $T = 2\pi / \omega$.

Fig. 11.2 Design scheme of a platform-vibrator with shock. The platform table with a fastened rubber gasket is attached to the base with a linear vibro-isolating spring. The mold with concrete is installed on the gasket without fastening



A platform table with mass m_1 is attached to the base by a linear vibration isolating spring with a stiffness k_1 and a linear dashpot with a damping factor c_1 . The exciting external periodic force $F(t)$ is generated by electric motors mounted under the table. An elastic rubber gasket with thickness h and stiffness k_0 is attached to the table. A linear dashpot with a damping factor c_0 is placed between the table and the mold. A mold with concrete of mass m_2 is installed on the gasket, but is not fastened either to the gasket or to the table.

The machine starts its movement when the electric motors begin their work. This motion has several peculiar properties. First, the table and the mold move vertically together. Then the mold with huge mass comes off from the gasket for a very short distance and “bounce”. The table and the mold are moving separately until the mold falls down onto the rubber gasket. A soft impact occurs. The bodies move together again until the mold comes off the gasket and so on. The mathematical model corresponds to the two-body 2-DOF vibro-impact system with a soft impact. It is a strongly nonlinear non-smooth discontinuous system.

In the two-body model, the masses are concentrated in the mass centers of both bodies. The parameters y_1 and y_2 represent the coordinates of these centers for the lower body (a platform table) and the upper body (a mold with concrete) respectively in the selected coordinate system. The origin of the y coordinate is chosen in the table center in a state of static equilibrium.

To compose the motion equations, let us consider the forces acting on the system bodies. The elastic forces are:

- in the spring— $F_{k1} = k_1 \Delta l_1 = k_1(y_1 - \lambda_{st})$;
- in the rubber gasket— $F_{k0} = k_0 \Delta l_0 = k_0[h - (y_2 - y_1)]$.

Here λ_{st} is the static deformation of the spring, $\lambda_{st} = (m_1 + m_2)g/k_1$; g is the acceleration due to gravity; $[h - (y_2 - y_1)]$ is the bodies' rapprochement, further it will be noted as z .

The damping forces are taken to be proportional to the first degree of velocity: $F_{damp1} = c_1 \dot{y}_1$, $F_{damp0} = c_0 \dot{y}_1$. The influence of the concrete mixture can be taken into account as some additional damping— $F_{damp2} = c_2 \dot{y}_2$.

There are three states of the platform-vibrator: the initial joint movement of both bodies, the separate movement in the case of loss of contact between them, and the joint movement during the impact due to the mold falling onto the gasket.

The basic law of dynamics gives the following equations of the primary joint movement:

$$\begin{aligned} \ddot{y}_1 &= g\chi - \omega_1^2 y_1 - \omega_2^2 \chi [h - (y_2 - y_1)] \\ &\quad - 2\dot{y}_1(\xi_1 \omega_1 - \xi_0 \omega_2 \chi) + \frac{1}{m_1} F(t) \\ \ddot{y}_2 &= -g + \omega_2^2 [h - (y_2 - y_1)] - 2\omega_2(\xi_2 \dot{y}_2 + \xi_0 \dot{y}_1) \end{aligned} \quad (11.1)$$

The initial conditions are:

$$\text{at } t = 0 \text{ there are } \phi_0 = 0, y_1 = 0, \dot{y}_1 = 0, y_2 = h - \lambda_0, \dot{y}_2 = 0. \quad (11.2)$$

Here λ_0 is the static deformation of the gasket, $\lambda_0 = m_2 g / k_0$.

After the finish of the primary joint movement, the platform-vibrator performs a vibro-impact motion. The basic law of dynamics gives the following equations of this movement:

$$\begin{aligned} \ddot{y}_1 &= g\chi - \omega_1^2 y_1 - 2\xi_1 \omega_1 \dot{y}_1 + \frac{1}{m_1} F(t) \\ &+ H(z) \left\{ 2\xi_0 \omega_2 \chi \dot{y}_1 - \omega_2^2 \chi [h - (y_2 - y_1)] - \frac{1}{m_1} F_{con}(z) \right\} \\ \ddot{y}_2 &= -g - 2\xi_2 \omega_2 \dot{y}_2 + \\ &+ H(z) \left\{ \omega_2^2 [h - (y_2 - y_1)] - 2\xi_0 \omega_2 \dot{y}_1 + \frac{1}{m_2} F_{con}(z) \right\} \end{aligned} \quad (11.3)$$

Here the standard notations are introduced:

$$\begin{aligned} \frac{k_1}{m_1} &= \omega_1^2, \quad \frac{k_0}{m_2} = \omega_2^2, \quad \frac{c_0}{m_2} = 2\xi_0 \omega_2, \quad \frac{c_1}{m_1} = 2\xi_1 \omega_1, \\ \frac{c_2}{m_2} &= 2\xi_2 \omega_2, \quad \frac{m_2}{m_1} = \chi. \end{aligned} \quad (11.4)$$

$H(z)$ is the Heaviside function relatively the bodies' rapprochement $z = h - (y_2 - y_1)$.

$$H(z) = \begin{cases} 1, & z \geq 0 \\ 0, & z < 0 \end{cases} \quad (11.5)$$

$F_{con}(z)$ is the contact interactive force that simulates an impact and acts only during an impact. It also depends on the bodies' rapprochement z . Since the impact of the mold with concrete on the rubber gasket attached to the table is soft one, the problem of a soft impact simulation and choice of the type of contact force $F_{con}(z)$ in this system is very important. This problem will be discussed in the next Sect. 11.3.

The main numerical parameters were taken in accordance with the technical literature (Gusev et al. 1986). Some parameters were chosen in such a way that the created model would meet the requirements for a real machine. In particular, the damping ratios ξ_1, ξ_2, ξ_0 should remain in the range $0 \leq \xi \leq 1$ (Sönerlind 2019). The parameters have to provide firstly, a steady-state T -periodic oscillatory process with one impact per cycle after a transient period; secondly, the oscillation amplitude of the mold close to the required 0.8–1 mm; thirdly, a satisfactory value of the asymmetric acceleration coefficient. The parameters that meet these requirements have been selected through many numerical experiments and are shown in Table 11.1.

Table 11.1 Parameters of platform-vibrator with shock

Mass of table m_1 , kg	7400	Damping ratio of dashpot in spring ξ_1	0.5
Mass of mold with concrete m_2 , kg	15,000	Damping ratio of dashpot in gasket ξ_0	0.02
Stiffness of rubber gasket k_0 , Nm^{-1}	3.0×10^8	Damping ratio in concrete mixture ξ_2	0.03
Stiffness of spring k_1 , Nm^{-1}	2.6×10^7	Elastic modulus of mold E_2 , Nm^{-2}	2×10^{11}
Thickness of gasket h , m	0.0275	Elastic modulus of rubber gasket E_1 , Nm^{-2}	$3.5 \cdot 10^6$
Poisson's ratio of mold ν_2	0.3	Amplitude of exciting force P , N	$2.44 \cdot 10^5$
Poisson's ratio of rubber gasket ν_1	0.4	Frequency of exciting force ω , Hz	25
Radius of gasket R , m	5		

11.3 Soft Impact Simulation

Soft impact simulation, based on the classical theory of impact, called stereomechanics, is not successful (Bazhenov et al. 2013). It is known that, in accordance with this theory, at the impact moment, the displacements equality and the reversals in the colliding bodies' velocities are fixed. The change in velocities is calculated using Newton coefficient of restitution. The impact is considered as instantaneous; the velocities change by jump; local deformations in the contact area are not allowed. However, in fact, a soft impact is not instantaneous; its duration is quite long.

It is more expedient to simulate a soft impact using an interactive contact force, which can be linear or nonlinear. This force acts only during the impact, the rest of the time it is absent. Local deformations of the contact surfaces are permissible; you can see the bodies' penetration into each other.

11.3.1 With Linear Force

In Andreaus et al. (2013), the authors admit the presence of elastic deformations at the contact upon an impact of finite duration. It is achieved by interposing a concentrate spring between the bodies at their contact point, simulating their deformability at the interaction zones. The influence of the rigidity of the contact spring on the system response is examined.

The linear force is similar to the elastic one, that is, a virtual linear spring with rigidity k is interposed between the colliding bodies. The hardness of the impact is measured by the k parameter. Numerical investigations allow to examine the effect of spring rigidity on the system response.

$$F_{\text{con}}(z) = kz(t), \tag{11.6}$$

where $z(t)$ is the rapprochement of the bodies, $z = h - (y_2 - y_1)$, when $(y_2 - y_1) \leq h$.

Five values of the virtual spring rigidity k are considered. All the system parameters and parameters of the exciting force are the same in all numerical experiments. The results of these experiments are shown in Fig. 11.3 and 11.4. The impact duration becomes shorter; the bodies penetrate into each other less with an increase in the rigidity of the virtual spring k , since the impact becomes more rigid (Fig. 11.3).

On the other hand, the higher the rigidity k of the virtual spring, the greater the contact force between the two bodies (Fig. 11.4).

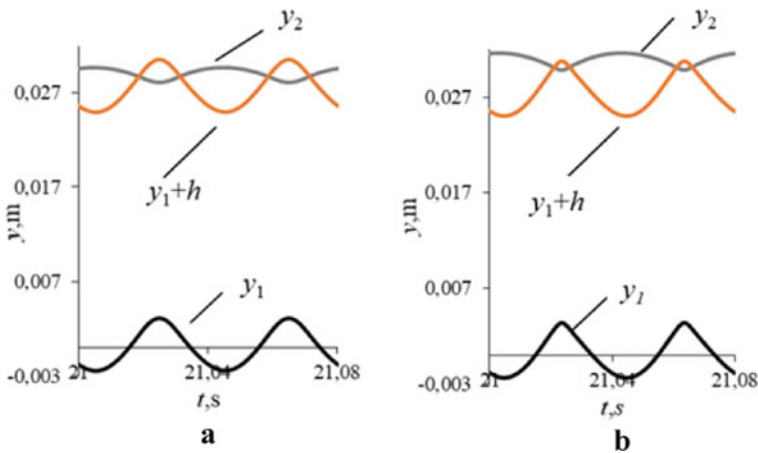


Fig. 11.3 Time histories for the smallest and the largest values of k coefficient in linear contact force: **a** $k = 1.5 \times 10^6$ N/m, **b** $k = 1.5 \times 10^9$ N/m. The larger k , the shorter the impact duration and the less the bodies' penetration into each other, because the impact becomes more rigid

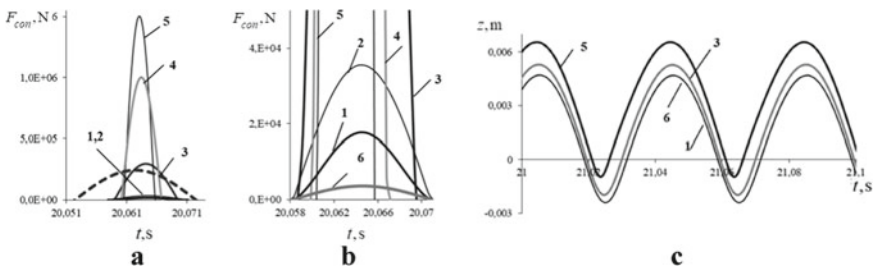


Fig. 11.4 **a, b** contact forces; **c** distance between bodies, when impact simulating by: 1 Hertz force; linear force with: 2 $k = 1.5 \times 10^7$ N/m; 3 $k = 1.5 \times 10^8$ N/m; 4 $k = 8.0 \times 10^8$ N/m; 5 $k = 1.6 \times 10^9$ N/m; 6 - $k = 1.5 \times 10^6$ N/m; the exciting force $F(t)$ is shown by the dotted line.

The acceleration of the upper body in its lowest position varies significantly with increasing spring rigidity. The ratio of this acceleration to the acceleration of the upper body in the uppermost position is important for the platform-vibrator with shock. The magnitude of this ratio affects the quality of the concrete compaction. Thus, these experiments show a strong dependence of the vibro-impact system response on the spring rigidity k .

11.3.2 With Nonlinear Hertz's Force

The nonlinear contact Hertzian force, according to the quasi-static contact Hertz's theory, is used to simulate a soft impact.

$$F_{\text{con}}(z) = K[z(t)]^{3/2}, K = \frac{4}{3} \frac{q}{(\delta_1 + \delta_2)\sqrt{A+B}},$$

$$\delta_1 = \frac{1 - \nu_1^2}{E_1\pi}, \delta_2 = \frac{1 - \nu_2^2}{E_2\pi} \quad (11.7)$$

Here $z(t)$ is the rapprochement of the bodies, as before, $z = h - (y_2 - y_1)$, when $(y_2 - y_1) \leq h$; ν_i and E_i —are Poisson's ratios and Young's moduli of elasticity for both bodies; A, B, q —are constants characterizing the local geometry of the contact zone. The gasket surface is flat, but here it is advisable to consider it as a sphere of the large radius R . Then in the collision of a plane (mold) and a sphere (rubber gasket) $A = B = 1/2R, q = 0.318$.

The contact impact forces are shown in Fig. 11.4a, b in different scales. These are the linear contact forces with different values of the coefficient k and a nonlinear contact Hertz force. A strong increase in the linear contact force and a decrease in the duration of the impact with increasing spring stiffness k are clearly seen. The contact Hertz force is less and corresponds to a soft impact.

The dependence of the distance between bodies $z = [(y_2 - y_1) - h]$ on time, when simulating an impact by linear forces with different values of the virtual spring rigidity k and a nonlinear Hertz contact force is shown in Fig. 11.4c. Both the penetration of the bodies into each other, and the impact duration decrease with increasing the virtual spring rigidity k . In the case of the Hertz force, the curve 1 almost merges with the curve 6 for a soft impact at $k = 1.5 \times 10^6 \text{ N/m}$.

The use of both the nonlinear Hertzian contact force and the linear force provides the motion law along the entire time axis, including the impact phase. It is possible to determine local deformations in the contact area and mutual bodies' penetration. But the mechanical characteristics of colliding bodies are taken into account by the coefficient K in (11.7); this coefficient is quite definite. While different values of the coefficient k in (11.6) give different responses of the vibro-impact system; this coefficient is not well defined. Therefore, a soft impact simulation by a nonlinear Hertz

contact force in accordance with his quasi-static contact theory seems preferable. However, the limitations of this theory should be considered.

This problem formulation, namely the integration of the movement Eqs. (11.3) with the parameters values given in Table 11.1, and the use of the nonlinear Hertz force (11.7) as the contact interactive force $F_{\text{con}}(z)$ provides a fairly good coincidence of results with experiment (see Sect. 11.4). This made it possible to observe many interesting phenomena inherent in non-smooth nonlinear systems when the control parameter is varied.

11.4 About the Model Verification and Validation

The described model is focused on the vibro-impact platform *SMZH-538* (*СМЖ-538* by Ukrainian)—a platform with a non-fixed mold and only vertical oscillations. For its simplified model, the characteristics have been got that have been confirmed experimentally. The following experimental data obtained during the design and operation of this low frequency machine are presented in Nazarenko et al. (2017a; b):

- After the overlocking, a periodic mode with one impact per cycle is established in the platform-vibrator.

A steady-state T -periodic one-impact regime is established in model after the transient process finish. Direct numerical integration of stiff differential Eq. (11.1), and then (11.3) with $F_{\text{con}}(z)$ according to (11.7) gives a complete movement picture, which is shown in Fig. 11.5. A primary joint motion from the equilibrium position before the first separation (up to the vertical line I), a short transient process (up to the line II), and then the T -periodic one-impact regime are well visible.

- The oscillation amplitude of the mold with concrete should be 0.8–1 mm (Nazarenko et al. 2017a, b; Gusev et al. 1986).

After direct numerical integration of stiff differential Eq. (11.3), the oscillatory amplitude for non-harmonic vibrations is calculated hereinafter with the simple formula.

$$A_{\text{max}} = \frac{y_{\text{max}} - y_{\text{min}}}{2} \quad (11.8)$$

The amplitude of the mold with concrete in steady-state T -periodic one-impact regime is 0.79 mm.

- The coefficient of asymmetric acceleration should be ~ 4 .

This coefficient is the ratio of the lower acceleration to the upper acceleration. The lower acceleration w_L is the acceleration of the mold with concrete at its lowest

Fig. 11.5 The movement of the model bodies from the equilibrium position

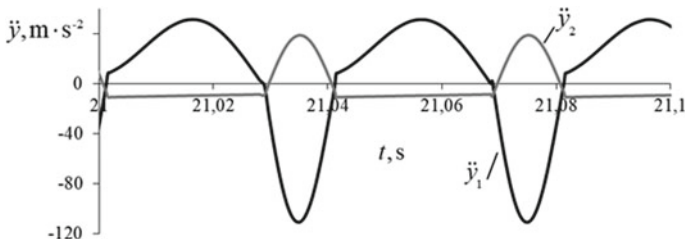
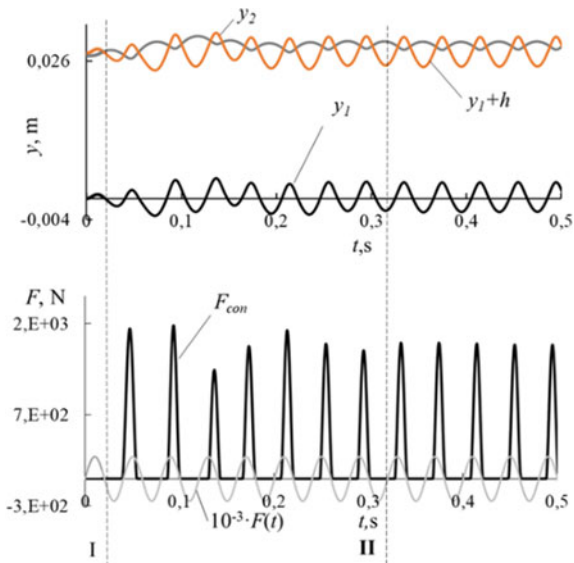


Fig. 11.6 The accelerations of both model bodies

position; the upper acceleration w_U is the mold acceleration at its highest position. For the described vibro-impact system, it is $\frac{w_L}{w_U} = 3.6$ (Fig. 11.6).

The coincidence of the vibro-impact system response with the experiment gives ground to believe that the created model may adequately characterize the operation of the vibro-impact platform with shock.

11.5 Coexisting Regimes—Hysteresis

The model exhibits coexisting regimes, i.e., the hysteresis effect (jump phenomenon) under different initial conditions when the control parameter varies. This phenomenon is observed under different control parameters, namely, exciting frequency, technological mass of the mold with concrete, and stiffness of the

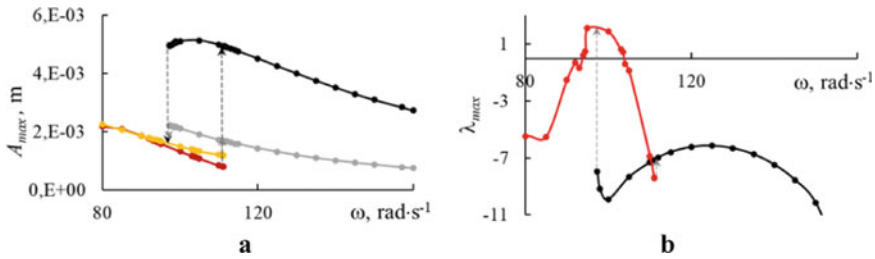


Fig. 11.7 Dependence on the exciting frequency ω : **a** the oscillatory amplitude A_{max} ; **b** the largest Lyapunov exponent λ_{max}

vibro-isolating spring. The dynamical systems in general and nonlinear systems in particular may typically have the coexisting solutions at certain fixed parameter values.

11.5.1 When the Exciting Frequency Ω is Varied

The platform-vibrator with shock is a low frequency machine. It often operates with an exciting frequency $\omega = 157\text{rad}\cdot\text{s}^{-1}$ (25 Hz). Does the model show any nonlinear phenomena with a change in the exciting frequency? Yes, at a lower exciting frequency, the model exhibits the presence of coexisting regimes in the hysteresis zone.

Figure 11.7 clearly shows the hysteresis effect in a narrow range of low values of the exciting frequency, which is the control parameter. Direct numerical integration of stiff differential Eq. (11.3) with different initial conditions and the oscillatory amplitude calculation with formula (11.8) give the graph in Fig. 11.7a. The black and gray curves correspond to the main periodic (1,1)-regime¹ for the lower and the upper bodies, respectively. The yellow and red curves show the amplitude-frequency responses for these bodies under other initial conditions.

The graph of the largest Lyapunov exponent λ_{max} , computed by Benettin’s algorithm, is shown in Fig. 11.7b. On the lower black curve, it corresponds to the main periodic (1,1)-regime, its sign is negative. On the upper red curve, it corresponds to the coexisting modes. The largest Lyapunov exponent λ_{max} has a positive sign in a narrow frequency range. One can assume that a chaotic mode occurs in this frequency range. The chaotic regime at $\omega = 95 \text{ rad}\cdot\text{s}^{-1}$ will be shown further in Fig. 11.12.

¹ (n,m)-regime is the mode with period nT and m impacts per cycle.

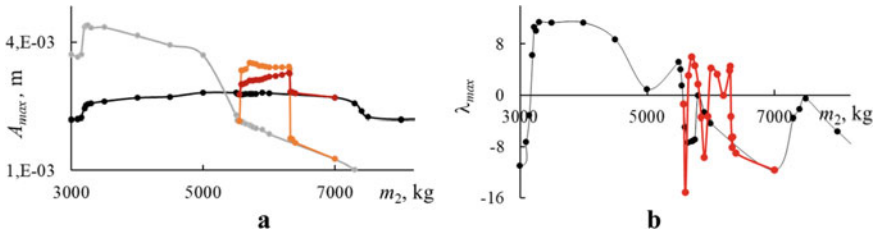


Fig. 11.8 Dependence on the technological mass of the upper body m_2 : **a** the oscillatory amplitude A_{max} ; **b** the largest Lyapunov exponent λ_{max}

11.5.2 When the Technological Mass m_2 is Varied

The platform-vibrator with shock is used for compaction and molding large concrete products (up to 15,000–18,000 kg). How will the model behave if the product is not so large?

The control parameter is technological mass of the upper body m_2 . When it varies, the coexisting regimes are again observed in narrow hysteresis zone (Fig. 11.8). As before, the black and gray curves in Fig. 11.8a correspond to the main periodic (1,1)-regime for the lower and the upper bodies, respectively. The yellow and red curves show the dependence of the amplitudes on the mass m_2 in coexisting modes under other initial conditions.

In Fig. 11.8b the gray curve with black markers corresponds to the main regime, the red curve—to the coexisting regimes. For the small masses, the largest Lyapunov exponent λ_{max} is positive even in the main mode; this means that chaotic motion may occur in this range.

The coexisting regimes alternate several times in a narrow parameter range, which follows from the change in the sign of the largest Lyapunov exponent. There are periodic windows in this parameter range. Exactly within the periodic windows, the transient chaos can occur. It will be shown below in Sect. 11.6.

11.5.3 When the Stiffness of Vibro-isolating Spring k_1 is Varied

The control parameter is the stiffness of vibro-isolating spring k_1 . The parameters of the stiffness in general and the stiffness of vibro-isolating spring in particular strongly affect the platform-vibrator dynamic behavior. The nonlinear effects are observed in the model at very low values of the vibro-isolating spring stiffness. When it is small, one can watch the coexisting regimes in the hysteresis zone (branches I, II, III, IV in Fig. 11.9a), which were obtained by direct integration of stiff Eq. (11.3) under different initial conditions. In Fig. 11.9b, the black curve corresponds to the branch I, the red curve—to the branch II. The curves for branches III and IV coincide with

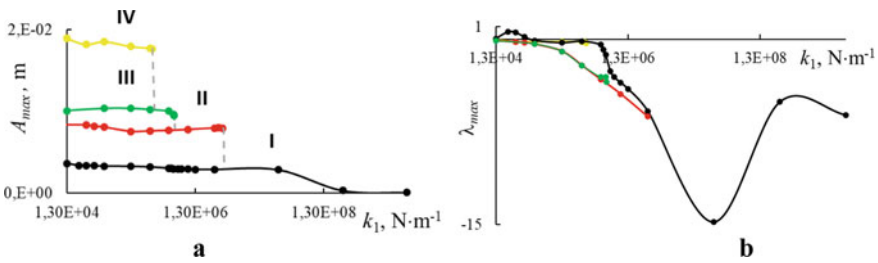


Fig. 11.9 Dependence on the stiffness of vibro-isolating spring k_1 : **a** the oscillatory amplitude for platform table A_{max} ; **b** the largest Lyapunov exponent λ_{max}

the red curve. For very small parameter values, the largest Lyapunov exponent is positive; a chaotic regime can arise.

As an example, four different regimes for small value $k_1 = 2.6 \cdot 10^4 \text{ Nm}^{-1}$ in I, II, III, IV branches are shown in Fig. 11.10. The phase trajectories are very close one to another at each period of the external force and almost merge in the (3,1)-regime in the IV branch. But the contact force graph clearly shows that the regime has a periodicity of $3T$ and 1 impact per cycle. The external force $F(t)$ is shown on a reduced scale. The red dots on the phase trajectories are Poincaré sections: n dots for an nT -periodic mode, and an undefined set of dots for a chaotic signal. Fourier spectra have frequencies that are multiples of ω/n for nT -periodic regime. A chaotic signal produces a broad continuous spectrum.

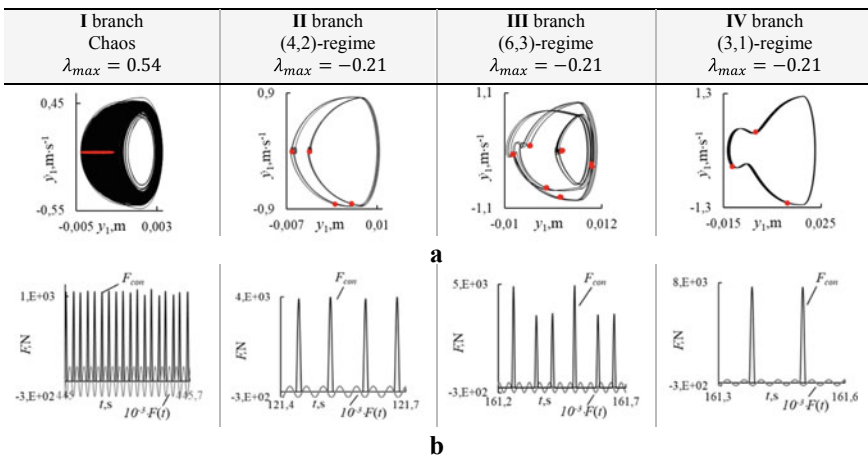


Fig. 11.10 **a** Phase trajectories with Poincaré maps; **b** Hertz contact force in coexisting regimes at $k_1 = 2.6 \times 10^4 \text{ Nm}^{-1}$.

11.6 Interior Crisis. Crisis-Induced Intermittency

A crisis is a bifurcation event in which a chaotic attractor and its basin of attraction suddenly disappear or suddenly change in size as some control parameter is varied. The term crisis in dynamical systems was first introduced in (Grebogi et al. 1983). The interior crisis leads to the sudden widening of a chaotic attractor (Lai and Tél 2011), that is, to a sudden increase (or decrease) in its size. Following an interior crisis, a crisis-induced intermittency is observed. This type of intermittency is characterized by permanent jumps between two chaotic attractors (Kapitaniak and Bishop 1999).

An interior crisis and crisis-induced intermittency were watched, when there was a sudden discontinuous change in the chaotic attractor with a change in the technological mass of the upper body m_2 . Interior crisis and crisis-induced intermittency develop little by little starting from periodic movement with a mass $m_2 = 5600$ kg and ending with the intermittency by Pomeau and Manneville (1980) with a mass $m_2 = 3200$ kg. This development is observed when the control parameter changes in the opposite direction, that is, when it decreases. First, you can see the alternation of the chaos of different sizes during the interior crisis. Then the chaos between bursts expands and becomes more “smooth” (with smaller amplitude difference). At last, the intermittency with sufficiently wide regions of approximately periodic movement is well seen (Fig. 11.11).

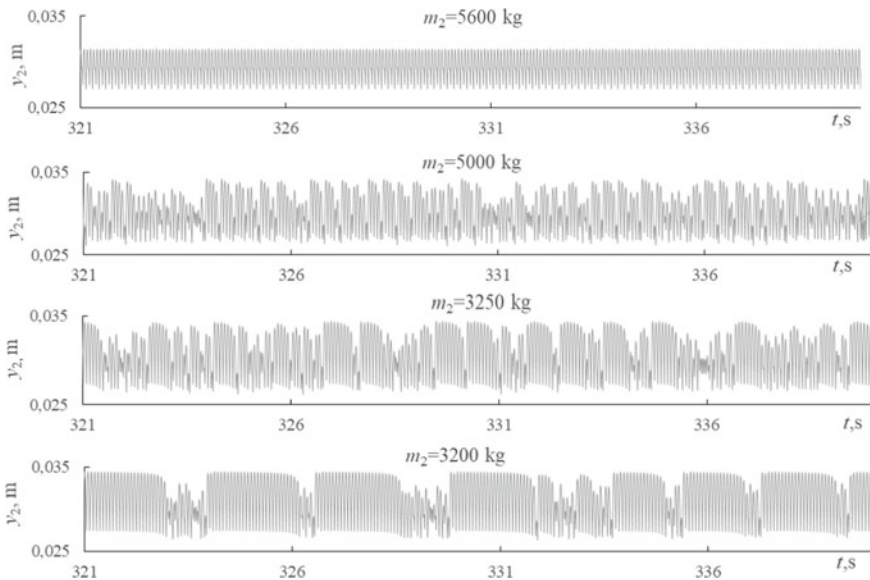


Fig. 11.11 Development of crisis-induced intermittency (for the upper body) with a change in control parameter m_2

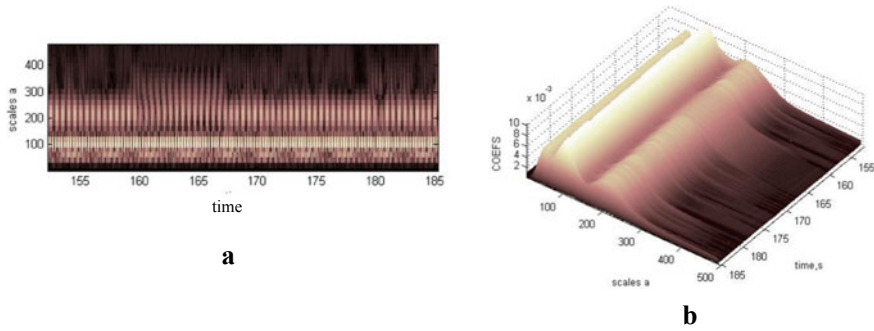


Fig. 11.12 Wavelet characteristics for chaotic motion at $\omega = 95 \text{ rad}\cdot\text{s}^{-1}$: **a** projection of wavelet surface; **b** surface of wavelet coefficients. The largest Lyapunov exponent is positive $\lambda_{\max} = 2.12$. See also Fig. 11.8b

11.7 Permanent and Transient Chaos

11.7.1 *Permanent (Sustained) Chaos*

Chaotic motion was observed with a change in each of the three control parameters. When the exciting frequency ω was chosen as the control parameter, chaotic movement was watched in a narrow range of the low frequencies. The typical form of phase trajectories with Poincaré maps, a broad continuous Fourier spectrum, a fractal structure of Poincaré maps, and a specific form of wavelet characteristics confirmed its chaoticity. The route to chaos on its left border was very similar to the transition through a period doubling, that is, Feigenbaum route. On the right border, the chaotic attractor suddenly disappeared, which is typical of a boundary (exterior) crisis.

One can see the chaoticity of this movement very clearly using drawings of wavelet characteristics (Fig. 11.12). In the drawing of wavelet surface projection, in addition to a bright light strip for high frequency, there are many bursts for the lower frequencies, which change over time. The “mountain ranges” of different heights correspond to these frequencies on the wavelet coefficients surface. Their heights are not constant in time. The wavelet characteristics were constructed using Continuous Wavelet Transform with Morlet wavelet in MATLAB software (MathWorks).

With a change in the technological mass m_2 , the chaotic motion was implemented in the range of small masses and in the hysteresis zone (Fig. 11.8).

11.7.2 *Transient Chaos*

The appearance of chaos with a finite lifetime is known as transient chaos. When a transient chaos is observed in the system, the trajectory is chaotic initially for some

time and then becomes periodic (Bhalekar et al. 2012). In Lai and Tél (2011), the authors note that a typical occurrence of the transient chaos is in the periodic windows inside the chaotic region.

Indeed, the transient chaos was observed exactly in the region of the periodic windows, when the technological mass m_2 was chosen as a control parameter (see also Fig. 11.8b).

When the initial conditions correspond to permanent chaos for $m_2 = 6000$ kg, the transient chaos was got in a narrow range of the control parameter values. Chaotic vibrations, arising at certain system parameters values, degenerate into a periodic subharmonic (2,2)-regime after some time. Time series, contact force, and phase trajectories for $m_2=6330$ kg are shown in Fig. 11.13. The figures of the time series (Fig. 11.13a) and the contact force (Fig. 11.13b) clearly show how the chaotic regime suddenly turns into a periodic one. The phase trajectories corresponding to a periodic motion are shown in red in Fig. 11.13c, d. Analysis of the largest Lyapunov exponent λ_{max} over a quite long time helps to determine the existence of transient chaos. Its sign is positive for the phase of chaotic motion, then, after a long procedure, the exponent converges to a negative value, which is typical for periodic movement. Figure 11.14 clearly shows how after some time the largest Lyapunov exponent λ_{max} crosses the abscissa axis and becomes negative. It is worth to emphasize once more that the value of the control parameter remains the same.

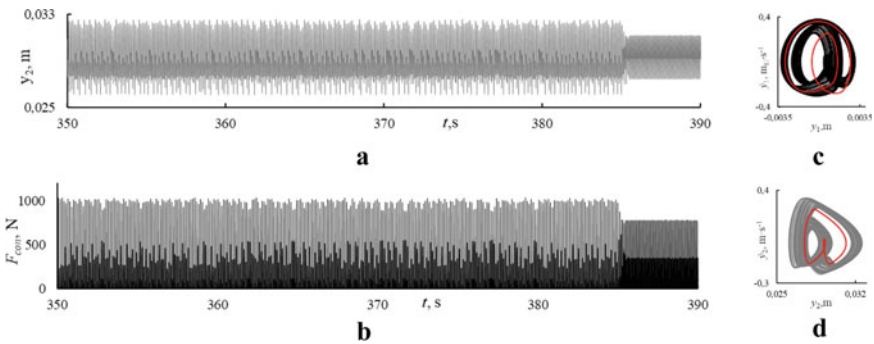


Fig. 11.13 **a** Time histories; **b** Hertz contact force; **c, d** phase trajectories in transient chaos at $m_2 = 6330$ kg.

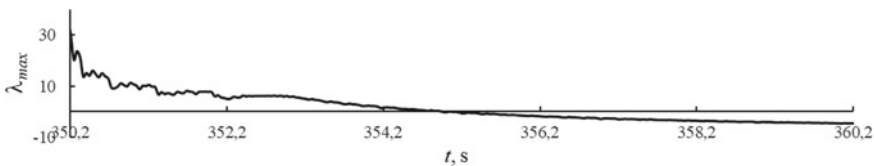


Fig. 11.14 Convergence of the largest Lyapunov exponent to negative value during the transient chaos: $m_2 = 6330$ kg, start from permanent chaos at $m_2 = 6000$ kg

Table 11.2 Average lifetime of transient chaos $\langle T \rangle$, (s)

Mass m_2 (kg)	6300	6310	6320	6330	6340	6350	6360	6370	6380	6390	6400
$\langle T \rangle$, (s)	773	304	97	28	10	5.8	3.6	1.5	2.0	1.8	1.3

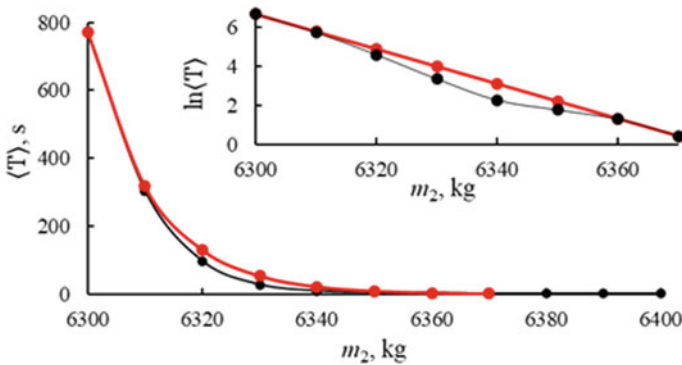


Fig. 11.15 Dependence of average chaotic transient lifetime $\langle T \rangle$ on m_2 on a linear–linear plot and on a logarithmic versus linear scale (inset). All points are the result of averaging 12 realizations

The transient chaos lifetime sensitively depends on both the control parameter value and the initial conditions. The sensitive dependence of the transient chaos on the initial conditions brightly demonstrates “the butterfly effect”, that is, the main feature of chaotic dynamics.

The average transient chaos lifetime for different control parameter values is shown in Table 11.2. It is the result of averaging twelve realizations obtained for different initial conditions. The average transient lifetime obeys an exponential law (Fig. 11.15), which is typical for many chaotic systems.

The average transient lifetime obeys an exponential law $\langle T \rangle \approx C e^{-\kappa m_2}$ where $\kappa > 0$. Then, in a logarithmic versus linear scale, there is a straight line with slope $-\kappa$; the escape rate $\kappa = 0.089$. The red curve on linear–linear plot and the red straight line on a log–linear plot were plotted according to the exponential law and the equation of the straight line, respectively.

11.8 Conclusions

For this unusual vibro-impact system with a soft impact, which is a mathematical model of a platform-vibrator with shock, the following has been established.

- It is preferable to simulate a soft impact in this model by the nonlinear contact Hertzian force.

- Many phenomena inherent in a nonlinear non-smooth discontinuous dynamical system occur when the control parameter is varied. For this model of a vibro-impact system, these nonlinear events were detected for the first time. The exciting frequency, the technological mass of the upper body, and the stiffness of the vibro-isolating spring were chosen as control parameters.
- The model demonstrated: the permanent and transient chaos, boundary and interior crises, crisis-induced intermittency, coexisting regimes in the hysteresis zone under different initial conditions.
- A sensitive dependence of the transient chaos on both the control parameter value and the initial conditions was demonstrated. The average transient lifetime obeys an exponential law, which is typical to many chaotic systems.
- The ranges of control parameters, in which unwanted chaos-related events may be implemented, are in the regions of small control parameters values and are visible on numerous graphs.

We hope in the future to study in more detail the model dynamical behavior when the spring stiffness changes.

References

- Andreas, U., Chiaia, B., Placidi, L.: Soft-impact dynamics of deformable bodies. *Continuum Mech. Thermodyn.* **25**(2–4), 375–398 (2013). <https://doi.org/10.1007/s00161-012-0266-5>
- Bazhenov, V.A., Pogorelova, O.S., Postnikova, T.G.: Comparison of two impact simulation methods used for nonlinear vibroimpact systems with rigid and soft impacts. *J. Nonlinear Dyn.* (2013). <https://doi.org/10.1155/2013/485676>
- Bazhenov, V.A., Pogorelova, O.S., Postnikova, T.G.: Creation of mathematical model of platform-vibrator with shock, designed for concrete products compaction and molding. *Strength Mater. Theor. Struct.* **104**, 103–116 (2020). <https://doi.org/10.32347/2410-2547.2020.104.103-116>
- Bhalekar, S., Daftardar-Gejji, V., Baleanu, D., Magin, R.: Transient chaos in fractional Bloch equations. *Comput. Math. Appl.* **64**(10), 3367–3376 (2012). <https://doi.org/10.1016/j.camwa.2012.01.069>
- Danca, M.F.: Hidden transient chaotic attractors of Rabinovich-Fabrikant system. *Nonlinear Dyn.* **86**, 1263–1270 (2016). <https://doi.org/10.1007/s11071-016-2962-3>
- Elaskar, S., Río Del, E.: *New Advances on Chaotic Intermittency and its Applications*. Springer International Publishing (2017). <https://doi.org/10.1007/978-3-319-47837-1>
- Elaskar, S.: *Studies on Chaotic Intermittency*. PhD Thesis, Universidad Politécnica de Madrid (2018)
- Fu, S., Liu, Y., Chávez, J.P.: Discontinuous bifurcation of a soft-impact system. *Int. j. Bifurcation Chaos* **30**(09), 2050132 (2020). <https://doi.org/10.1142/S0218127420501321>
- Grebogi, C., Ott, E., Yorke, J.A.: Crises, sudden changes in chaotic attractors, and transient chaos. *Phys. D* **7**(1–3), 181–200 (1983). [https://doi.org/10.1016/0167-2789\(83\)90126-4](https://doi.org/10.1016/0167-2789(83)90126-4)
- Grebogi, C., Ott, E., Romeiras, F., Yorke, J.A.: Critical exponents for crisis-induced intermittency. *Phys. Rev. A* **36**(11), 5365–5380 (1987). <https://doi.org/10.1103/physreva.36.5365>
- Gusev, B.V., Nazarenko, I.I., Shmigalsky, V.N.: Recommendations on Vibration Forming of Reinforced Concrete Products (1986) (in Russian). www.gostrf.com/normadata/1/4294847/4294847727.htm
- Kapitaniak, T., Bishop, S.R.: *The Illustrated Dictionary of Nonlinear Dynamics and Chaos*. Wiley (1999). <https://doi.org/10.1002/rnc.560>

- Lai, Y.C., Tél, T.: *Transient Chaos: Complex Dynamics on Finite Time Scales*, vol. 173. Springer Science & Business Media (2011). <https://doi.org/10.1007/978-1-4419-6987-3>
- Lorenz, E.: Predictability: does the flap of a butterfly's wing in Brazil set off a tornado in Texas? *J. Sci. Educ. RESONANCE* **20**(3), 261–263 (1972). www.ias.ac.in/article/fulltext/reso/020/03/0260-0263
- Macau, E.E. (ed.): *A Mathematical Modeling Approach from Nonlinear Dynamics to Complex Systems*. Springer International Publishing (2019). <https://doi.org/10.1007/978-3-319-78512-7>
- Macek, W.M.: Intermittency in the Generalized Lorenz Model. *Chaotic Modeling Simul. (CMSIM)* **4**, 323–328 (2015)
- MathWorks. Wavelet Toolbox. www.mathworks.com/help/wavelet/
- Mishra, A., Leo Kingston, S., Chittaranjan, H., Kapitaniak, T., Feudel, U., Dana, S.K.: Routes to extreme events in dynamical systems: Dynamical and statistical characteristics. *Chaos Interdiscip. J. Nonlinear Sci.* **30**(6), 063114 (2020). <https://doi.org/10.1063/1.5144143>
- Nazarenko, I.I., et al.: Investigation of vibration machine movement with a multimode oscillation spectrum. *Eastern-Euro. j. Enterprise Technol.* **6**(1), 28–36 (2017a). <https://doi.org/10.15587/1729-4061.2017.118731>
- Nazarenko, I., Dedov, O., Dyachenko, O., Sviderskyi, A.: Ohlyad i analiz vibratsiynoho obladnannya dlya formuvannya ploskykh zalizobetonykh vyrobiv (Review and analysis of vibrating equipment for the formation of flat reinforced concrete products). *Mining Constr. Road Melioration Mach.* **90**, 49–58 (2017b) (in Ukrainian). <https://gbdmm.knuba.edu.ua/article/view/143522>
- Nazarenko, I.I., Rukhinskyi, M.M., Sviderskyi, A.T., Kobylanska, I.M., Harasim, D., Kalizhanova, A., Kozbakova, A.: Development of energy-efficient vibration machines for the building-and-construction industry. *Przeglad Elektrotechniczny.* **1**(4), 55–61 (2019). <https://doi.org/10.15199/48.2019.04.10>
- Noël, J.P., Kerschen, G.: Nonlinear system identification in structural dynamics: 10 more years of progress. *Mech. Syst. Signal Process.* **83**, 2–35 (2017). <https://doi.org/10.1016/j.ymssp.2016.07.020>
- Pomeau, Y., Manneville, P.: Intermittent transition to turbulence in dissipative dynamical systems. *Commun. Math. Phys.* **74**(2), 189–197 (1980). <https://doi.org/10.1007/BF01197757>
- Sönnerlind, H.: COMSOL Blog. Damping in structural dynamics: theory and sources. COMSOL Multiphys. (2019). www.comsol.com/blogs/damping-in-structural-dynamics-theory-and-sources/
- Vasiliev, V.G.: Vybor optimalnykh parametrov vibratsionnogo formovaniia Zhelezobetonykh izdeliy (Selection of optimal parameters of vibration molding of reinforced concrete products). *Dig. J. Techn. Technol. Transp.* **S13** (2019) (in Russ.). https://transport-kgasu.ru/index.php?option=com_content&view=article&id=10&Itemid=2
- Wang, G., Lai, Y.-C., Grebogi, C.: Transient chaos—a resolution of breakdown of quantum-classical correspondence in optomechanics. *Sci. Rep.* **6**, 35381 (2016). <https://doi.org/10.1038/srep35381>

Part IV
Interaction of Structures and Flow

Chapter 12

Aeroelastic Interactions Between Plates and Three-Dimensional Inviscid Potential Flows



**Konstantin V. Avramov, Darkhan S. Myrzaliyev,
and Kazira K. Seitkazenova**

Abstract The method for analysis of dynamic interactions between plates and three-dimensional, potential, inviscid gas is suggested. The system of the singular integral equations with respect to aerodynamic derivatives of the pressure drop is obtained. The numerical method for the singular integral equations solutions is suggested. Loss of the plate dynamic stability is analyzed numerically.

Keywords Singular integral equation · Inviscid gas · Dynamic instability · Aerodynamic derivative

12.1 Introduction

The singular integral equations with respect to a circulation density are used basically to analyze aeroelasticity of plates in three-dimensional potential flow. In this case, the vorticity shed from the trailing edge of the plate and wake formation are considered. This leads to significant computational burden. The calculations of the plate transient responses reduce to the analysis of the characteristic exponents, which is transformed to high dimension eigenvalue problem (Tang et al. 1999a, b).

K. V. Avramov (✉)

National Academy of Science of Ukraine, Podgorny Institute for Mechanical Engineering,
Kharkiv, Ukraine

e-mail: kvavramov@gmail.com

National Technical University “Kharkiv Polytechnic Institute”, Kharkiv, Ukraine

Department of Technical Systems, Kharkiv National University of Radio Electronics, Kharkiv,
Ukraine

D. S. Myrzaliyev · K. K. Seitkazenova

Department of Mechanics and Engineering, M. Auezov South Kazakhstan State University,
Shimkent, Republic of Kazakhstan

e-mail: darkhan-m7@mail.ru

K. K. Seitkazenova

e-mail: kseitkazi@mail.ru

In this paper, the singular integral equations with respect to the pressure drop are suggested. The pressure drop outside the plate is equal to zero. Therefore, the wake is not considered. The mechanical steady-state vibrations can be analyzed using single harmonic approximation in time of plate pressure drop. The characteristic exponents are calculated to analyze dynamic stability of the plate. Assuming, that the gas is three-dimensional, potential, inviscid and incompressible, the system of the singular integral equations with respect to the pressure drop is derived. The numerical method for the solutions of the obtained singular integral equations system is suggested.

Now the results of others researchers in this field are considered. The singular integral equation with respect to pressure acting on the plate was derived by Albano and Rodden (1969). The series of spatial functions is used to approximate a pressure. The vortex method is used to analyze the aerodynamics of wings by Katz (1985). Morino et al. (1975) suggested the method to predict the flowing of finite thickness curved surfaces. Morino and Kuo (1974) derived the integro-differential equation to describe the plate interaction with the compressible gas flow. Djojodihardjo and Widnall (1969) suggested the numerical approach to solve the singular integral equation with respect to a circulation density. Hess (1975) proposed the new method to analyze a gas flowing of three-dimensional bodies. Landahl and Stark (1968) investigated different types of the singular integral equations with respect to both a circulation density and a pressure. The advantages and shortcomings of these integral equations were discussed. Strganac and Mook (1990) analyzed the wings flowing at arbitrary angle of attack. The vortex method was used to solve the aerodynamic problem. Mook and Dong (1994) suggested the methods for calculations of incompressible flows past airfoils and their wakes. The properties of the wake behind airfoils were considered. Eloy et al. (2007) assumed that the flutter mode is two-dimensional but the potential flow is assumed to be three-dimensional. Using the Galerkin method and the Fourier transformations, the flutter mode is predicted. Preidikman and Mook (1998) analyzed the dynamics of the rigid plate with two degrees of freedoms. The method of discrete vortices was applied to predict the wind loads acting on the plate. The self-sustained vibrations of a wing are absorbed using the saturation phenomenon (Hall et al. 2001). Three-dimensional vortex lattice method was applied to describe the aerodynamic problem. Watanabe et al. (2002) discussed different methods for the paper flutter analysis. Both the Navier-Stokes equations simulations and the potential flow analysis were considered to calculate unsteady lift forces. The authors concluded that the potential theory was enough to predict the paper flutter. Guo and Paidoussis (2000) analyzed the plate stability. The Fourier transformation was used to solve the Laplace equation with respect to the velocity potential. Ellen (1972) considered the clamped plate flowing by an incompressible gas. The pressure drop is described by the integral of the plate displacements. The plate divergence was analyzed analytically. Kornecki et al. (1976) and Huang (1995) considered flutter of cantilever plates using Theodorsen theory. Shayo (1980) analyzed the linear vibrations of the plate interacting with moving gas. The singular integral equations with respect to the pressure acting on the lifting surface were treated in the book (Dowell et al. 1995). The self-sustained vibrations of the plates with geometrical nonlinearity flowing by gas were studied in the papers (Attar and

Dowell 2003; Tang et al. 1999b; Tang and Dowell 2002; Tang et al. 1999a). The vortex lattice method was used to simulate a potential stream. The pressure drop on the vibrating plate was analyzed in the paper (Breslavsky 2011). The almost periodic and the chaotic vibrations of the plates with internal resonances flowing by gas were considered in the paper (Avramov 2012). The method of discrete vortices for inviscid potential flows analysis was treated in the books (Belotserkovskii and Lifanov 1993; Lifanov et al. 2004).

Thus, the singular integral equations with respect to a circulation density are generally used to describe the interactions of thin-walled structures with a stream. Due to the wake formation, transients are observed and analyzed mandatory. Numerical analysis of these motions leads to significant computational burden.

The system of the singular integral equations with respect to the aerodynamic derivatives of the plate pressure drop is derived in this paper. Then there is no necessity to account the wake shed from the trailing edge. In this case, the numerical analysis of the plate vibrations in gas flow is simpler than the analysis, which is used the singular integral equations with respect to a circulation density. The numerical method for the solution of the singular integral equations with respect to the aerodynamic derivatives of the pressure drop is suggested. Validity of the plates dynamic stability analysis is verified by comparison with the results of others researchers.

Many models of plate vibrations in stream exist. The plates of wing-type are described by 2D models (Tang et al. 1999a, b). The plates of flag-type are described by 1D models (Eloy et al. 2007; Tang and Dowell 2002). The general method for analysis of plate stability in stream is suggested in this paper.

12.2 Equations of Plate Motions

The flexural vibrations of the rectangular plates in stream (Fig. 12.1) are analyzed. Transversal vibrations of the plates are described by the function $w(x, y, t)$, which satisfies the following partial differential equation:

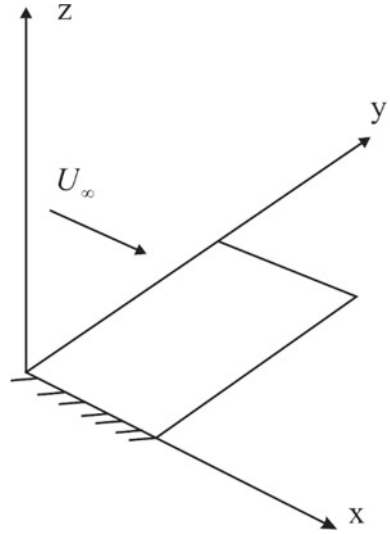
$$\frac{h^2}{12} \nabla^4 w + \frac{1 - \nu^2}{E} \left(\rho \ddot{w} + c \dot{w} + \frac{\Delta p(x, y, t)}{h} \right) = 0, \quad (12.1)$$

where $\nabla^4 w = \frac{\partial^4 w}{\partial x^4} + 2 \frac{\partial^4 w}{\partial x^2 \partial y^2} + \frac{\partial^4 w}{\partial y^4}$; $\ddot{w} = \frac{\partial^2 w}{\partial t^2}$; h is plate thickness; E , ν are Young's modulus and the Poisson's ratio; ρ is the material density; c is the coefficient of the material damping; $\Delta p(x, y, t)$ is a pressure drop on the plate.

The plate dynamics is expanded by using the eigenmodes $\psi_j(x, y)$:

$$w(x, y, t) = \sum_{j=1}^{N_1} q_j(t) \psi_j(x, y), \quad (12.2)$$

Fig. 12.1 Sketch of the system



where $q_j(t)$ are the generalized coordinates of the plate. It is assumed, that the plate vibrations are single harmonic:

$$q_j(t) \approx \gamma_j \cos(\omega t) + \delta_j \sin(\omega t); \quad j = 1, \dots, N_1. \tag{12.3}$$

12.3 System of Singular Integral Equations with Respect to Aerodynamic Derivatives of Pressure Drop

The plate is streamed by three-dimensional, potential, inviscid and incompressible gas. On significant distance from a plate, the flow has constant velocity U_∞ , which is parallel to x axis. The projections of the flow velocities on x, y, z axes are denoted by $u(x, y, z, t); v(x, y, z, t); w(x, y, z, t)$, respectively. The velocity potential $\varphi(x, y, z, t)$ satisfies the following equations: $u = U_\infty + \frac{\partial \varphi}{\partial x}; v = \frac{\partial \varphi}{\partial y}; w = \frac{\partial \varphi}{\partial z}$. The velocity potential and pressure $p(x, y, z, t)$ satisfy the Laplace equations:

$$\nabla^2 \varphi = 0; \quad \nabla^2 p = 0, \tag{12.4}$$

where $\nabla^2 \varphi = \frac{\partial^2 \varphi}{\partial x^2} + \frac{\partial^2 \varphi}{\partial y^2} + \frac{\partial^2 \varphi}{\partial z^2}$.

The boundary conditions for the Laplace equation (12.4) are considered. The Sommerfeld radiation condition is fulfilled:

$$\lim_{x^2+y^2+z^2 \rightarrow \infty} \text{grad } \varphi = 0. \tag{12.5}$$

The no penetration boundary condition satisfies on the plate surface:

$$\left. \frac{\partial \varphi}{\partial z} \right|_{z=0} = \frac{\partial w}{\partial t} + U_\infty \frac{\partial w}{\partial x}. \quad (12.6)$$

The pressure drop

$$\Delta p(x, y, t) = p(x, y, z)|_{z=0^+} - p(x, y, z)|_{z=0^-}$$

is equal to zero outside the plate on the plane $z = 0$. The pressure drop is equal to zero on the plate boundary ∂S :

$$\Delta p|_{\partial S} = 0. \quad (12.7)$$

The aerodynamic derivatives (Belotserkovskii and Lifanov 1993; Lifanov et al. 2004) are used to calculate the flow perturbations induced by the plate vibrations:

$$\varphi(x, y, z, t) = \sum_{j=1}^{N_1} \left[\varphi_j^{(0)}(x, y, z) q_j(t) + \varphi_j^{(1)}(x, y, z) \dot{q}_j(t) \right]; \quad (12.8)$$

$$p(x, y, z, t) = \sum_{j=1}^{N_1} \left[p_j^{(0)}(x, y, z) q_j(t) + p_j^{(1)}(x, y, z) \dot{q}_j(t) \right]. \quad (12.9)$$

Following (Belotserkovskii and Skripach 1975), the functions $\varphi_j^{(0)}(x, y, z)$, $\varphi_j^{(1)}(x, y, z)$, $p_j^{(0)}(x, y, z)$, $p_j^{(1)}(x, y, z)$ satisfy the Laplace equations:

$$\nabla^2 \varphi_j^{(k)} = 0; \quad (12.10)$$

$$\nabla^2 p_j^{(k)} = 0; \quad k = 0, 1; \quad j = 1, \dots, N_1. \quad (12.11)$$

Index j indicates the number of eigenmode, which induce the pressure drop. The solutions of Eqs. (12.10, 12.11) satisfy the boundary conditions (12.5, 12.6, 12.7). The solutions of Eq. (12.11) take the following form (Dowell et al. 1995):

$$p_j^{(k)}(x, y, z) = \frac{1}{4\pi} \int \int_S \Delta p_j^{(k)}(x_1, y_1) \left[\frac{\partial}{\partial z_1} \left(\frac{1}{r} \right) \right]_{z_1=0} dx_1 dy_1, \quad (12.12)$$

where $r = \sqrt{(x - x_1)^2 + (y - y_1)^2 + (z - z_1)^2}$; S is region of the plate middle plane; $\Delta p_j^{(k)}(x_1, y_1) = p_j^{(k)}(x_1, y_1, z_1)|_{z_1=0^+} - p_j^{(k)}(x_1, y_1, z_1)|_{z_1=0^-}$ are aerodynamic derivatives of the plate pressure drop; x_1, y_1, z_1 are integration variables.

Bernoulli's equation is used in the following form:

$$p(x, y, z) = -\rho_\infty \left(\frac{\partial \varphi(x, y, z, t)}{\partial t} + U_\infty \frac{\partial \varphi(x, y, z, t)}{\partial x} \right), \quad (12.13)$$

where ρ_∞ is a gas density. Equations (12.8, 12.9) is substituted into Eq. (12.13). As a result, the following system of the partial differential equations is obtained:

$$\begin{aligned} U_\infty \frac{\partial \varphi_j^{(0)}}{\partial x} - \omega^2 \varphi_j^{(1)} &= -\frac{p_j^{(0)}}{\rho_\infty}; \\ U_\infty \frac{\partial \varphi_j^{(1)}}{\partial x} + \varphi_j^{(0)} &= -\frac{p_j^{(1)}}{\rho_\infty}. \end{aligned} \quad (12.14)$$

The method of constants variation is used to solve Eq. (12.13). The solution of this system takes the following form:

$$\begin{aligned} \varphi_j^{(0)}(x, y, z) &= B_j^{(1)}(x, y, z) \exp\left(i \frac{\omega}{U_\infty} x\right) + B_j^{(2)}(x, y, z) \exp\left(-i \frac{\omega}{U_\infty} x\right); \\ \varphi_j^{(1)}(x, y, z) &= \frac{i}{\omega} B_j^{(1)}(x, y, z) \exp\left(i \frac{\omega}{U_\infty} x\right) - \frac{i}{\omega} B_j^{(2)}(x, y, z) \exp\left(-i \frac{\omega}{U_\infty} x\right), \end{aligned} \quad (12.15)$$

where i is the imaginary unit. Equation (12.15) is substituted into (12.14). As a result, it is derived:

$$\begin{aligned} 2U_\infty \rho_\infty \frac{\partial B_j^{(1)}(x, y, z)}{\partial x} &= \left[i\omega p_j^{(1)}(x, y, z) - p_j^{(0)}(x, y, z) \right] \exp\left[-i \frac{\omega}{U_\infty} x\right]; \\ 2U_\infty \rho_\infty \frac{\partial B_j^{(2)}(x, y, z)}{\partial x} &= -\left[i\omega p_j^{(1)}(x, y, z) + p_j^{(0)}(x, y, z) \right] \exp\left[i \frac{\omega}{U_\infty} x\right]. \end{aligned} \quad (12.16)$$

The integration of Eq. (12.16) is carried out using the Sommerfeld conditions (12.5). The results are substituted into (12.15). It is obtained:

$$\begin{aligned} \varphi_j^{(1)}(x, y, z) &= -\frac{1}{U_\infty \rho_\infty \omega} \int_{-\infty}^x \left[\omega p_j^{(1)}(\xi, y, z) \cos\left(\frac{\omega}{U_\infty}(\xi - x)\right) \right. \\ &\quad \left. + p_j^{(0)}(\xi, y, z) \sin\left(\frac{\omega}{U_\infty}(\xi - x)\right) \right] d\xi; \\ \varphi_j^{(0)}(x, y, z) &= \frac{1}{U_\infty \rho_\infty} \int_{-\infty}^x \left[-p_j^{(0)}(\xi, y, z) \cos\left(\frac{\omega}{U_\infty}(\xi - x)\right) \right. \\ &\quad \left. + \omega p_j^{(1)}(\xi, y, z) \sin\left(\frac{\omega}{U_\infty}(\xi - x)\right) \right] d\xi. \end{aligned} \quad (12.17)$$

The expansions (12.8, 12.9) are substituted into the boundary condition (12.6). As a result, the time-independent boundary conditions are obtained:

$$\left. \frac{\partial \varphi_j^{(0)}}{\partial z} \right|_{z=0} = U_\infty \frac{\partial \psi_j}{\partial x}; \quad (12.18)$$

$$\left. \frac{\partial \varphi_j^{(1)}}{\partial z} \right|_{z=0} = \psi_j. \quad (12.19)$$

The solution (12.12) is substituted into Eq. (12.17) and the result is substituted into (12.8, 12.9). As a result, the following system of the singular integral equations is obtained:

$$\begin{aligned} 4\pi U_\infty^2 \rho_\infty \frac{\partial \psi_j(x, y)}{\partial x} &= -\omega \iint_S \Delta p_j^{(1)}(x_1, y_1) K_S(x - x_1, y - y_1) dx_1 dy_1 \\ &\quad + \iint_S \Delta p_j^{(0)}(x_1, y_1) K_C(x - x_1, y - y_1) dx_1 dy_1; \\ 4\pi U_\infty \rho_\infty \omega \psi_j(x, y) &= \omega \iint_S \Delta p_j^{(1)}(x_1, y_1) K_C(x - x_1, y - y_1) dx_1 dy_1 \\ &\quad + \iint_S \Delta p_j^{(0)}(x_1, y_1) K_S(x - x_1, y - y_1) dx_1 dy_1, \end{aligned} \quad (12.20)$$

where

$$\begin{aligned} K_C(x - x_1, y - y_1) &= - \int_{-\infty}^{x-x_1} \frac{\cos \frac{\omega(\lambda+x_1-x)}{U_\infty}}{[\lambda^2 + (y - y_1)^2]^{3/2}} d\lambda; \\ K_S(x - x_1, y - y_1) &= - \int_{-\infty}^{x-x_1} \frac{\sin \frac{\omega(\lambda+x_1-x)}{U_\infty}}{[\lambda^2 + (y - y_1)^2]^{3/2}} d\lambda. \end{aligned} \quad (12.21)$$

The kernels $K_C(\tilde{x}, \tilde{y})$ and $K_S(\tilde{x}, \tilde{y})$ satisfy the following relations:

$$\lim_{\substack{\tilde{x} \rightarrow 0 \\ \tilde{y} \rightarrow 0}} K_C(\tilde{x}, \tilde{y}) = \infty; \quad \lim_{\substack{\tilde{x} \rightarrow 0 \\ \tilde{y} \rightarrow 0}} K_S(\tilde{x}, \tilde{y}) = -\infty.$$

The following dimensionless variables and parameters are used:

$$\chi = \frac{\omega a}{U_\infty}; \quad \bar{\lambda} = \frac{\lambda}{a}; \quad \bar{x}_1 = \frac{x_1}{a}; \quad \bar{y}_1 = \frac{y_1}{b}; \quad \bar{x} = \frac{x}{a}; \quad \bar{y} = \frac{y}{b};$$

$$r = \frac{a}{b}; \tau = \omega t; \vartheta_i = \frac{q_i}{h};$$

$$K_S = \frac{a \bar{K}_S}{b^3}; K_C = \frac{a \bar{K}_C}{b^3}; \Delta \bar{p}_j^{(1)} = \frac{\omega a \Delta p_j^{(1)}}{\rho_\infty U_\infty^2}; \Delta \bar{p}_j^{(0)} = \frac{a \Delta p_j^{(0)}}{\rho_\infty U_\infty^2}, \quad (12.22)$$

where χ is the Strouhal number. The system of the singular integral Eq. (12.20) with respect to the dimensionless variables takes the following form:

$$\iint_{\bar{S}} \left[-\Delta \bar{p}_j^{(1)}(\bar{x}_1, \bar{y}_1) \bar{K}_S(\bar{x} - \bar{x}_1, \bar{y} - \bar{y}_1) + \Delta \bar{p}_j^{(0)}(\bar{x}_1, \bar{y}_1) \bar{K}_C(\bar{x} - \bar{x}_1, \bar{y} - \bar{y}_1) \right]$$

$$d\bar{x}_1 d\bar{y}_1 = \frac{\partial \psi_j(\bar{x}, \bar{y})}{\partial \bar{x}} \frac{4\pi}{r^2}; \quad (12.23)$$

$$\iint_{\bar{S}} \left[-\Delta \bar{p}_j^{(1)}(\bar{x}_1, \bar{y}_1) \bar{K}_S(\bar{x} - \bar{x}_1, \bar{y} - \bar{y}_1) + \Delta \bar{p}_j^{(0)}(\bar{x}_1, \bar{y}_1) \bar{K}_C(\bar{x} - \bar{x}_1, \bar{y} - \bar{y}_1) \right]$$

$$d\bar{x}_1 d\bar{y}_1 = \frac{\partial \psi_j(\bar{x}, \bar{y})}{\partial \bar{x}} \frac{4\pi}{r^2}; \quad (12.24)$$

$$\bar{K}_S(\bar{x} - \bar{x}_1, \bar{y} - \bar{y}_1) = - \int_{-\infty}^{\bar{x} - \bar{x}_1} \frac{\sin \chi (\bar{\lambda} + \bar{x}_1 - \bar{x})}{[r^2 \bar{\lambda}^2 + (\bar{y} - \bar{y}_1)^2]^{3/2}} d\bar{\lambda};$$

$$\bar{K}_C(\bar{x} - \bar{x}_1, \bar{y} - \bar{y}_1) = - \int_{-\infty}^{\bar{x} - \bar{x}_1} \frac{\cos \chi (\bar{\lambda} + \bar{x}_1 - \bar{x})}{[r^2 \bar{\lambda}^2 + (\bar{y} - \bar{y}_1)^2]^{3/2}} d\bar{\lambda},$$

where \bar{S} is the region of the plate middle plane with respect to dimensionless coordinates.

The kernels of the singular integral Eqs. (12.23, 12.24) satisfy the following relations:

$$\frac{\partial}{\partial \bar{x}} \bar{K}_S(\bar{x} - \bar{x}_1, \bar{y} - \bar{y}_1) = -\chi \bar{K}_C(\bar{x} - \bar{x}_1, \bar{y} - \bar{y}_1);$$

$$\frac{\partial}{\partial \bar{x}} \bar{K}_C(\bar{x} - \bar{x}_1, \bar{y} - \bar{y}_1) = -[r^2(\bar{x} - \bar{x}_1)^2 + (\bar{y} - \bar{y}_1)^2]^{-3/2} + \chi \bar{K}_S(\bar{x} - \bar{x}_1, \bar{y} - \bar{y}_1). \quad (12.25)$$

Equation (12.23) is differentiated with respect to \bar{x} and the result is substituted into Eq. (12.24). As a result, the following singular integral equation is derived:

$$\iint_{\bar{S}} \frac{\Delta \bar{p}_j^{(1)}(\bar{x}_1, \bar{y}_1) d\bar{x}_1 d\bar{y}_1}{[r^2(\bar{x} - \bar{x}_1)^2 + (\bar{y} - \bar{y}_1)^2]^{3/2}} = - \frac{8\pi \chi}{r^2} \frac{\partial \psi_j(\bar{x}, \bar{y})}{\partial \bar{x}}. \quad (12.26)$$

The index j indicates on the number of eigenmode, which induced the pressure. Equation (12.24) is differentiated with respect to \bar{x} and the result is substituted into (12.23). As a result, the following singular integral equation is derived:

$$\iint_{\bar{s}} \frac{\Delta \bar{p}_j^{(0)}(\bar{x}_1, \bar{y}_1) d\bar{x}_1 d\bar{y}_1}{[r^2(\bar{x} - \bar{x}_1)^2 + (\bar{y} - \bar{y}_1)^2]^{3/2}} = \frac{4\pi}{r^2} \left[\chi^2 \psi_j(\bar{x}, \bar{y}) - \frac{\partial^2 \psi_j(\bar{x}, \bar{y})}{\partial \bar{x}^2} \right]. \quad (12.27)$$

Thus, the system of the singular integral equations with respect to the aerodynamic derivatives (12.26, 12.27) is derived. Equations (12.26) and (12.27) are solved independently. The vortex method (Belotserkovskii and Lifanov 1993; Lifanov et al. 2004) is used to solve these equations. If the solution of this system is obtained, the pressure drop on the plate is obtained using Eq. (12.9).

The system (12.26, 12.27) has several advantages in comparison with the frequently used singular integral equations with respect to the circulation density. The wake shed from the trailing edge is taken into account, if the system of singular integral equations with respect to the circulation density is solved. Then the plate transients are analyzed mandatory.

12.4 Finite Degrees of Freedom Model of Plates Vibrations

Equations (12.2) and (12.9) are substituted into (12.1). The Galerkin method is applied. As a result, the linear dynamical system with respect to the generalized coordinates $\vartheta_1, \vartheta_2, \dots$ is derived. This dynamical system with respect to the dimensionless variables (12.22) takes the following form:

$$\sum_{j=1}^{N_1} R_{ij} (\chi^2 \vartheta_j'' + \alpha \chi^2 \vartheta_j' + \chi_1^2 \Omega_j^2 \vartheta_j) + \varepsilon \sum_{j=1}^{N_1} (A_{ij} \vartheta_j + B_{ij} \vartheta_j') = 0; \\ i = 1, \dots, N_1, \quad (12.28)$$

where

$$\vartheta_j' = \frac{d\vartheta_j}{d\tau}; \\ R_{ij} = \iint_{\bar{s}} \psi_j(\bar{x}, \bar{y}) \psi_i(\bar{x}, \bar{y}) d\bar{x} d\bar{y}; \\ A_{ij} = \iint_{\bar{s}} \bar{p}_j^{(0)}(\bar{x}, \bar{y}) \psi_i(\bar{x}, \bar{y}) d\bar{x} d\bar{y};$$

$$B_{ij} = \iint_{\bar{s}} \bar{p}_j^{(1)}(\bar{x}, \bar{y}) \psi_i(\bar{x}, \bar{y}) d\bar{x} d\bar{y};$$

$$\Omega_j = \frac{\omega_j}{\omega_1}; \quad \chi_1 = \frac{\omega_1 a}{U_\infty}; \quad \varepsilon = \frac{a \rho_\infty}{h \rho}; \quad \alpha = \frac{c}{\omega \rho}.$$

Stability analysis of the plate equilibrium is reduced to the investigations of the trivial equilibrium of the dynamical system (12.28). The characteristic exponents $\tilde{\lambda}$ are calculated to analyze this stability. The solution of the system (12.28) has the following form:

$$[\vartheta_j, \vartheta'_j] = [Q_j, V_j] \exp(\tilde{\lambda} t); \quad j = 1, \dots, N_1, \quad (12.29)$$

where Q_j, V_j are unknown parameters. The characteristic exponents are determined from the eigenvalue problem:

$$\begin{pmatrix} \mathbf{C}^{(1)} & \mathbf{C}^{(2)} \\ -\chi^2 \mathbf{E} & 0 \end{pmatrix} \begin{pmatrix} \mathbf{V} \\ \mathbf{Q} \end{pmatrix} = -\lambda_1 \begin{pmatrix} \mathbf{V} \\ \mathbf{Q} \end{pmatrix}, \quad (12.30)$$

where (\mathbf{E}) is identity matrix;

$$\begin{aligned} \lambda_1 &= \chi^2 \tilde{\lambda}; \\ \mathbf{C}^{(1)} &= \varepsilon \mathbf{R}^{-1} \mathbf{B} + \alpha \chi^2 \mathbf{E}; \\ \mathbf{C}^{(2)} &= \varepsilon \mathbf{R}^{-1} \mathbf{A} + \chi_1^2 \mathbf{\Omega}^2; \\ \mathbf{\Omega}^2 &= \text{diag}(\Omega_1^2; \dots; \Omega_{N_1}^2); \\ \mathbf{Q} &= [Q_1, \dots, Q_{N_1}]; \quad \mathbf{V} = [V_1, \dots, V_{N_1}]; \\ \mathbf{A} &= \{A_{ij}\}; \quad \mathbf{B} = \{B_{ij}\}; \quad \mathbf{R} = \{R_{ij}\}. \end{aligned}$$

The values of the system parameters, where the Hopf bifurcation are observed, are called critical. Now the approach for the critical parameters calculation is considered. The parameter χ is preset with the step h_χ : $\chi^{(j)} = \chi_0 + j h_\chi$. For every value of $\chi^{(j)}$ the system of the singular integral Eqs. (12.26, 12.27) is solved. Using the results of the system (12.26, 12.27) solution, the finite degrees of freedom dynamical system (12.28) is obtained numerically. The critical values of the parameter χ_1 are calculated. If the system has critical parameters, two characteristic exponents are complex conjugate with zero real parts: $\tilde{\lambda}_{1,2} = \pm i \tilde{\Omega}$. As a result of the calculations, the curve on the plane (χ, χ_1) is obtained. Only one point on this curve has the critical parameters (χ, χ_1) .

The approach for determination of this point is considered. On the boundary of stability, the frequency of the system (12.28) vibrations is $\tilde{\omega} = 1$. As follows from Eq. (12.30), the following relation satisfies at the Hopf bifurcation:

$$\tilde{\Omega} = \chi^2.$$

This additional equation is used to obtain the critical parameters of the system (12.28).

12.5 Numerical Methods of Singular Integral Equation Solution

The singular integral Eqs. (12.26, 12.27) are solved independently. The numerical methods for their solution are identical.

The plate is split into n vertical and N horizontal bands. As a result, the plate consists of $n N$ rectangles (Fig. 12.2). The vertexes of these rectangles have the following coordinates: $x_k = k h_x$; $k = 1, \dots, n$; $y_p = p h_y$; $p = 1, \dots, N$. The region of the rectangle $k + n(p - 1)$ is determined as:

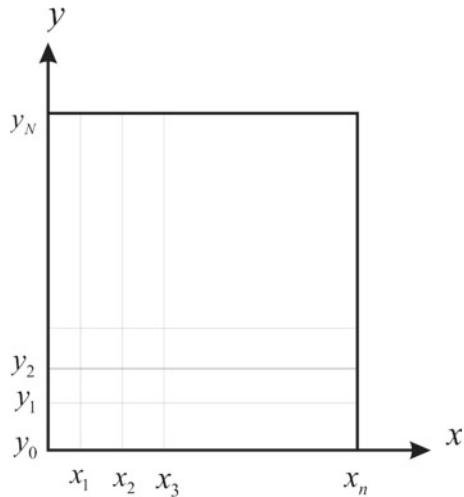
$$S_{k+n(p-1)} = \{ (x, y) \in R^2 \mid x_{k-1} < x < x_k; y_{p-1} < y < y_p \}. \tag{12.31}$$

The gravity center of the rectangle is denoted by (ξ_k, η_p) .

The rectangles are so small, that the functions $\Delta \bar{p}_j^{(1)}(\bar{x}_1, \bar{y}_1)$ and $\Delta \bar{p}_j^{(0)}(\bar{x}_1, \bar{y}_1)$ are assumed constants on them. These constants values are equal to the functions in the rectangles gravity centers:

$$\begin{aligned} \Delta \bar{p}_{0,j}^{[k+n(p-1)]} &= \Delta \bar{p}_j^{(0)}(\xi_k, \eta_p); \\ \Delta \bar{p}_{1,j}^{[k+n(p-1)]} &= \Delta \bar{p}_j^{(1)}(\xi_k, \eta_p). \end{aligned}$$

Fig. 12.2 The diagram of the plate discretization



The integral (12.26) is expressed as the sum of the integrals on all rectangles $S_{k+n(p-1)}$. Then Eq. (12.26) is satisfying in the collocation points (ξ_l, η_m) ; $l = 1, \dots, n$; $m = 1, \dots, N$. As a result, the following system of linear algebraic equations with respect to $\Delta \bar{p}_{1,j}^{[\mu]}$; $\mu = 1, \dots, nN$ is derived:

$$\sum_{k=1}^n \sum_{p=1}^N A_{l+n(m-1), k+n(p-1)} \Delta \bar{p}_{1,j}^{[k+n(p-1)]} = B_{l+n(m-1)}^{(1,j)}; \quad (12.32)$$

$$l = 1, \dots, n; m = 1, \dots, N,$$

where

$$\begin{aligned} A_{l+n(m-1), k+n(p-1)} &= \frac{\sqrt{(\eta_m - y_p)^2 + r^2(\xi_l - x_{k-1})^2}}{(\eta_m - y_p)(\xi_l - x_{k-1})} \\ &- \frac{\sqrt{(\eta_m - y_p)^2 + r^2(\xi_l - x_k)^2}}{(\eta_m - y_p)(\xi_l - x_k)} \\ &+ \frac{\sqrt{(\eta_m - y_{p-1})^2 + r^2(\xi_l - x_k)^2}}{(\eta_m - y_{p-1})(\xi_l - x_k)} \\ &- \frac{\sqrt{(\eta_m - y_{p-1})^2 + r^2(\xi_l - x_{k-1})^2}}{(\eta_m - y_{p-1})(\xi_l - x_{k-1})}; \\ B_{l+n(m-1)}^{(1,j)} &= -8\pi \chi \frac{\partial \psi_j(\bar{x}_l, \bar{y}_m)}{\partial \bar{x}}. \end{aligned}$$

Thus, the solution of the singular integral Eq. (12.26) is reduced to the system of linear algebraic Eq. (12.32). The singular integral Eq. (12.27) is approximated by the following system of linear algebraic equations:

$$\begin{aligned} \sum_{k=1}^n \sum_{p=1}^N A_{l+n(m-1), k+n(p-1)} \Delta \bar{p}_{0,j}^{[k+n(p-1)]} &= B_{l+n(m-1)}^{(0,j)}; \\ B_{l+n(m-1)}^{(0,j)} &= 4\pi \left[\chi^2 \psi_j(\bar{x}_l, \bar{y}_m) - \frac{\partial^2 \psi_j(\bar{x}_l, \bar{y}_m)}{\partial \bar{x}^2} \right]. \end{aligned}$$

12.6 Results of Numerical Analysis

Validation of the plate aeroelasticity by the system of the singular integral Eqs. (12.25, 12.26) and the numerical method for their solution is the main goal of stability numerical analysis. Dynamic stability of the plate (Fig. 12.3) is investigated numerically. This plate is analyzed in the paper (Tang et al. 2003). 1D model is used to analyze such plates in the papers (Eloy et al. 2007; Tang and Dowell 2002). However, 2D model is used to investigate this plate here. The following numerical values of the parameters are used:

$$E = 70.56 \cdot 10^9 \text{ Pa}; \quad \rho = 2.84 \cdot 10^3 \text{ kg/m}^3;$$

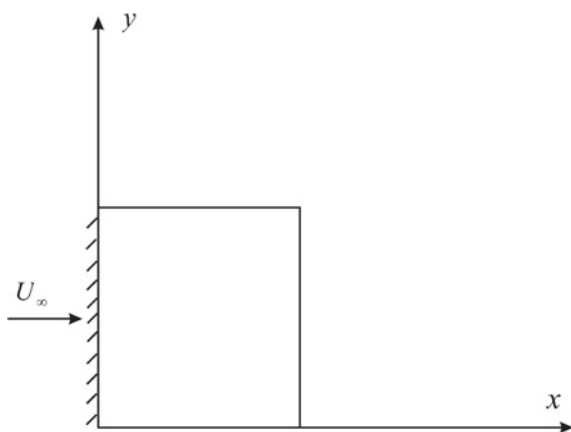
$$\rho_\infty = 1.43 \text{ kg/m}^3; \quad \nu = 0.3; \quad h = 0.39 \cdot 10^{-3} \text{ m}; \quad b = 0.127.$$

Figure 12.4 shows the first four modes of the plate vibrations at $r = 4$. Aerodynamic derivatives of the pressure, which are induced by these eigenmodes, are shown in Figs. 12.5 and 12.6.

Loss of the plate dynamic stability is analyzed. The critical stream velocity U_∞ and the vibrations frequency ω are calculated. The plate with $r = 2.12$ is considered. The critical stream velocity U_∞ and the plate vibrations frequency ω are calculated using the approach from Sect. 12.4. It is obtained: $U_\infty = 30.52 \text{ m/s}$; $\omega = 124 \text{ rad/s}$. The results of the calculations of the structure, which is treated in the paper (Tang et al. 2003), are $U_\infty = 29.5 \text{ m/s}$; $\omega = 141.3 \text{ rad/s}$. Thus, the results, which are published here, and the data from the paper (Tang et al. 2003) are close.

Changing the plate aspect ratio r , the loss of the plate dynamic stability is analyzed. Figure 12.7 shows the dependence of the critical stream velocity on the plate aspect ratio. The flutter onset frequency versus the plate aspect ratio is presented in Fig. 12.8. If the plate is lengthen, the stream velocity and the flutter onset frequency are

Fig. 12.3 Sketch of the plate



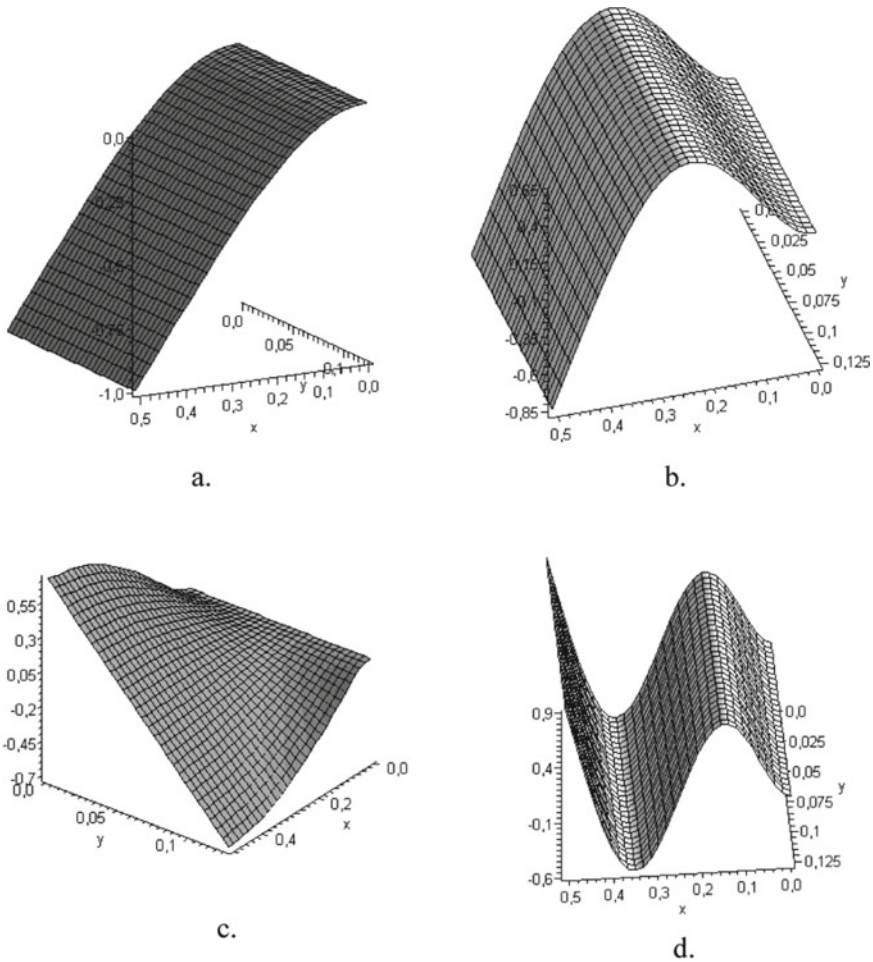


Fig. 12.4 The eigenmodes of the plate at $r = 4$. Figures **a**, **b**, **c**, **d** show the first, the second, the third and the fourth vibrations eigenmodes of the plate with the following parameters: $E = 70.56 \cdot 10^9$ Pa; $\rho = 2.84 \cdot 10^3$ kg/m³; $\rho_\infty = 1.43$ kg/m³; $\nu = 0.3$; $h = 0.39 \cdot 10^{-3}$ m; $b = 0.127$

decreased. The calculations results from the paper (Tang et al. 2003) are shown by point on Figs. 12.7 and 12.8.

The influence of damping coefficient α on parameters of flutter is analyzed. The results of analysis are shown in Figs. 12.9 and 12.10. Figure 12.9 shows the dependence of damping coefficient on critical stream velocity and Fig. 12.10 shows the dependence of flutter onset frequency on damping coefficient.

The data of stability analysis are obtained by 2D model and the results of 1D model analysis (Tang et al. 2003) are close.

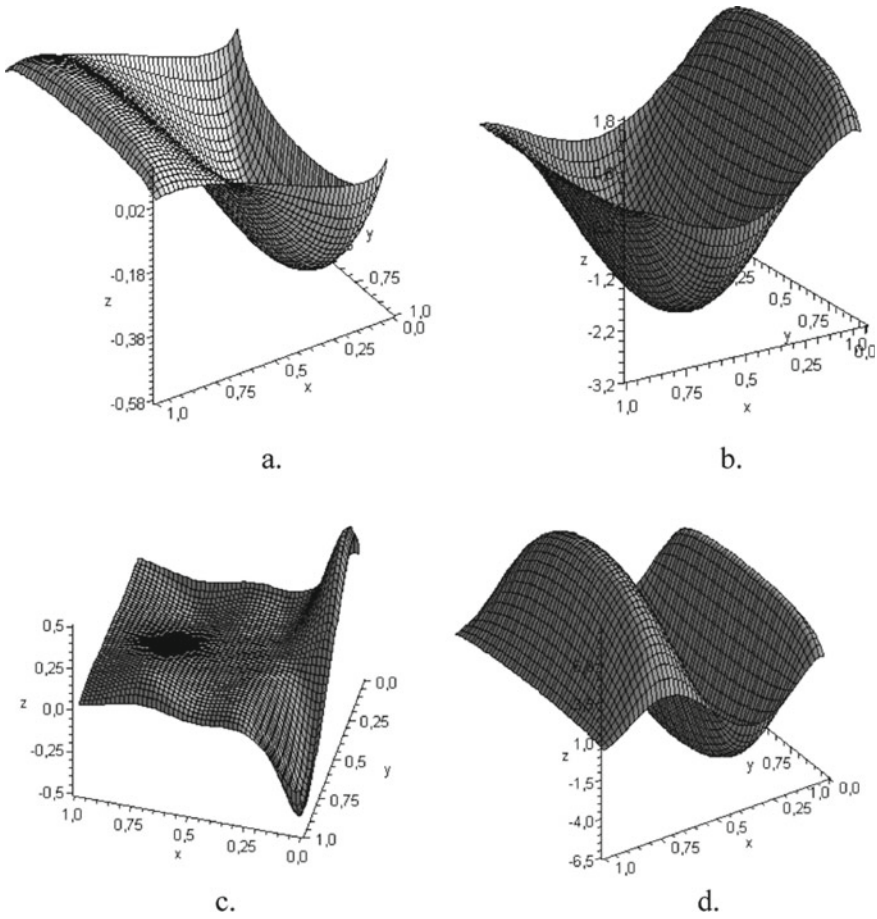


Fig. 12.5 The aerodynamic derivatives of the general coordinates. Figures **a**, **b**, **c**, **d** shows the aerodynamic derivatives induced by the first, the second, the third and the fourth eigenmodes of the plate with the following parameters: $E = 70.56 \cdot 10^9$ Pa; $\rho = 2.84 \cdot 10^3$ kg/m³; $\rho_\infty = 1.43$ kg/m³; $\nu = 0.3$; $h = 0.39 \cdot 10^{-3}$ m; $b = 0.127$

Dynamic stability of the plate (Fig. 12.1) is considered. The stream is parallel to x axis. The side $y = 0$ is clamped and all others sides are free. Aeroelastic stability of such plates is studied in the papers (Tang et al. 1999b; Avramov 2012). This system has the following numerical values of parameters:

$$a = b = 0.3 \text{ m}; h = 0.001 \text{ m}; E = 0.69 \cdot 10^{11} \text{ Pa};$$

$$\nu = 0.3; \rho = 2.7 \cdot 10^3 \frac{\text{kg}}{\text{m}^3}; \alpha = 0.005.$$

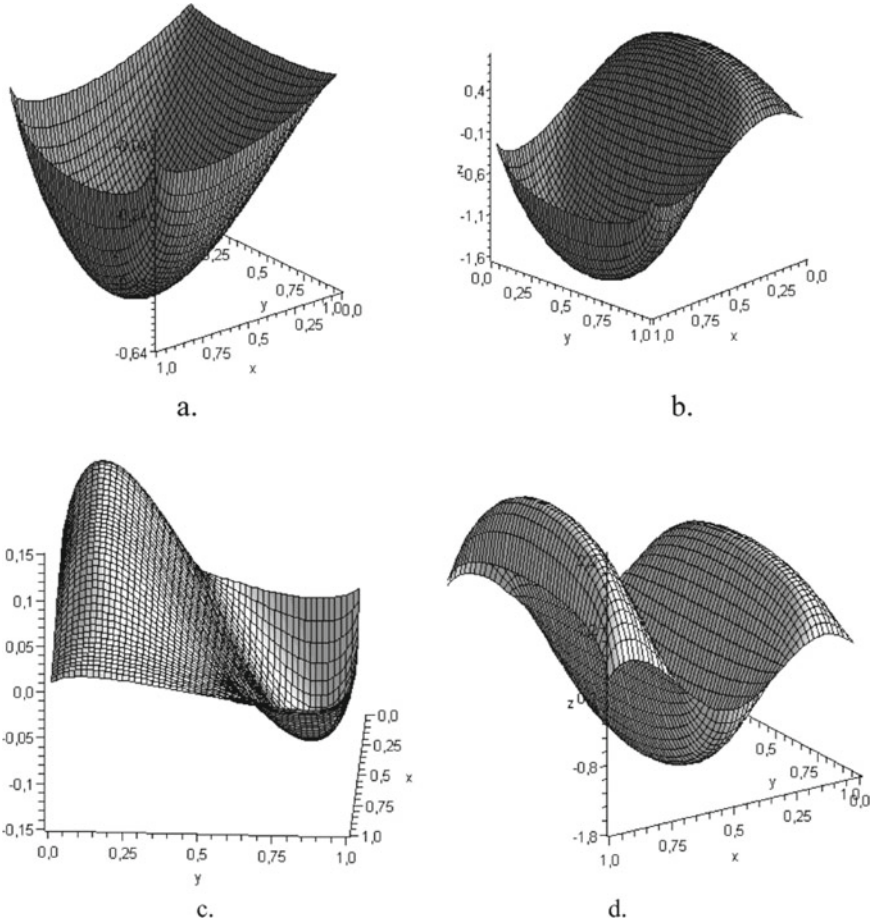


Fig. 12.6 The aerodynamic derivatives of the general velocities. Figures **a, b, c, d** show the aerodynamic derivatives induced by the first, the second, the third and the fourth eigenmodes with the following parameters: $E = 70.56 \cdot 10^9$ Pa; $\rho = 2.84 \cdot 10^3$ kg/m³; $\rho_\infty = 1.43$ kg/m³; $\nu = 0.3$; $h = 0.39 \cdot 10^{-3}$ m; $b = 0.127$

For the considered parameters the critical velocity is obtained: $V_\infty = 39.76$ m/s. The plate frequency for the critical system parameters is $\omega = 86.13$ rad/s. The following values of the plate critical velocity and frequency are published in Tang et al. (1999b): $V_\infty = 42.00$ m/s ; $\omega = 84.85$ rad/s. The results, which are published here, and the data from the paper (Tang et al. 1999b) are close.

Only dynamic instability of the plate is treated in this paper. The nonlinear vibrations of the structure (Avramov 2002, 2003, 2009; Avramov and Mikhlin 2004) are not considered.

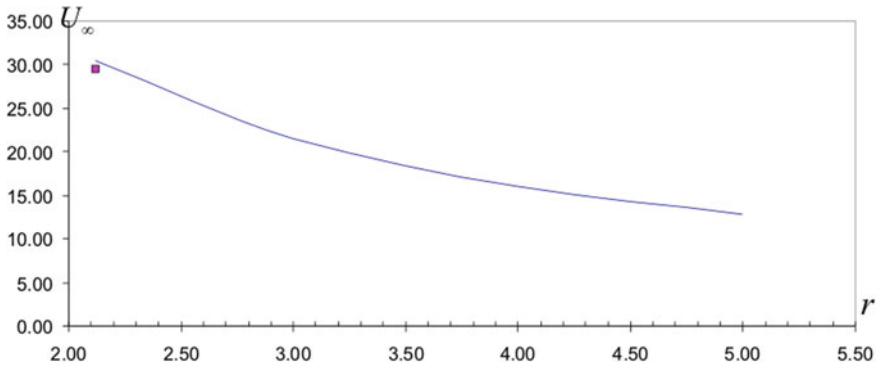


Fig. 12.7 The dependence of the critical stream velocity on the plate aspect ratio. The plate has the following parameters: $E = 70.56 \cdot 10^9$ Pa; $\rho = 2.84 \cdot 10^3$ kg/m³; $\rho_{\infty} = 1.43$ kg/m³; $\nu = 0.3$; $h = 0.39 \cdot 10^{-3}$ m; $b = 0.127$

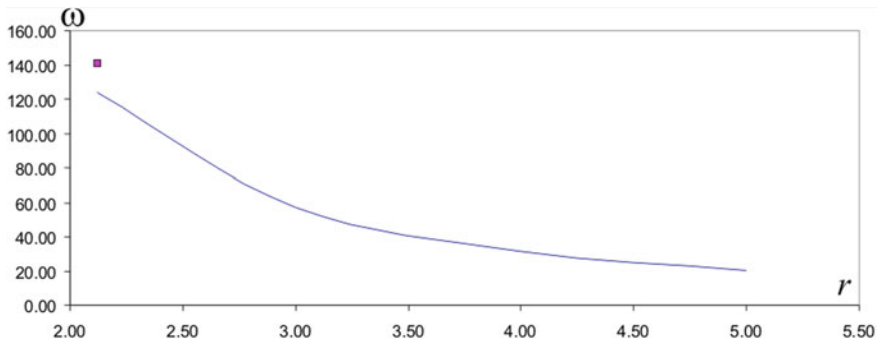


Fig. 12.8 The dependence of flutter onset frequency on the plate aspect ratio. The plate with the following parameters is considered: $E = 70.56 \cdot 10^9$ Pa; $\rho = 2.84 \cdot 10^3$ kg/m³; $\rho_{\infty} = 1.43$ kg/m³; $\nu = 0.3$; $h = 0.39 \cdot 10^{-3}$ m; $b = 0.127$

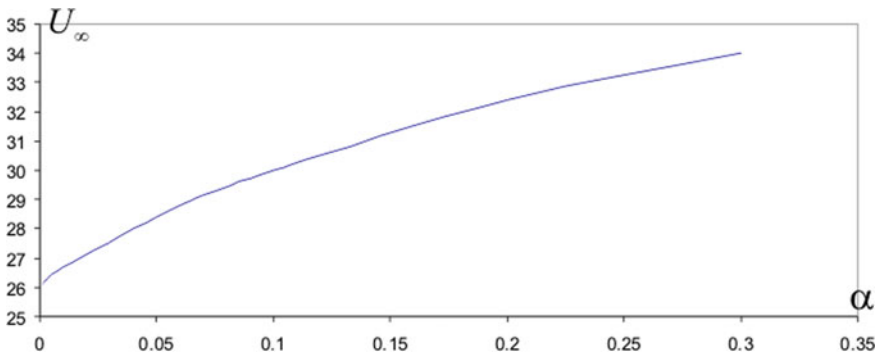


Fig. 12.9 The dependence of damping coefficients on critical stream velocity

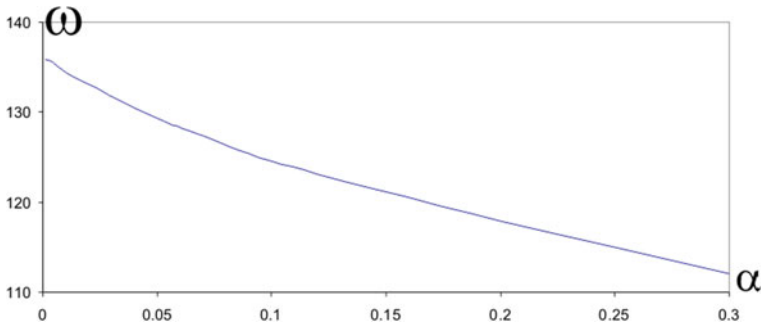


Fig. 12.10 The dependence of flutter onset frequency on the damping coefficient

12.7 Conclusions

The system of the singular integral equations with respect to the aerodynamic derivatives of pressure drop is suggested this paper. This system is very suitable for aeroelastic analysis, as there is unnecessary to analyze the wake shed from the trailing edge. Moreover, the approach for numerical solutions of the singular integral equations, based on the vortex method, is suggested.

For verification of the obtained system of singular integral equations and the method of their solution, the dynamic stability of several plates, which are treated in the previous papers, is analyzed. The obtained results are consistent with the data published by other researches.

The suggested system of singular integral equations will be used to analyze bifurcations and stability of nonlinear self-sustained vibrations of plates flowing by gas, using the modern methods of nonlinear dynamics.

Funding This study was particularly funded by National Research Foundation of Ukraine (grant number 128/02.2020).

References

- Albano, E., Rodden, W.P.: A doublet-Lattice method for calculating lift distributions on oscillating surfaces in subsonic flows. *AIAA J.* **7**, 279–285 (1969)
- Attar, P.J., Dowell, E.H.: A theoretical and experimental investigation of the effects of a steady angle of attack on the nonlinear flutter of a delta wing plate model. *J. Fluids Struct.* **17**, 243–259 (2003)
- Avramov, K.V.: Nonlinear beam oscillations excited by lateral force at combination resonance. *J. Sound Vib.* **257**, 337–359 (2002)
- Avramov, K.V.: Bifurcations of parametric oscillations of beams with three equilibrium. *Acta Mech.* **164**, 115–138 (2003)

- Avramov, K.V.: Nonlinear modes of parametric vibrations and their applications to beams dynamics. *J. Sound Vib.* **322**, 476–489 (2009)
- Avramov, K.V., Mikhlin, Y.V.: Forced oscillations of a system containing a snap-through truss, close to its equilibrium position. *Nonl. Dyn.* **35**, 361–379 (2004)
- Avramov, K.V., Strel'nikova, E.A., Pierre, C.: Resonant many-mode periodic and chaotic self-sustained aeroelastic vibrations of cantilever plates with geometrical nonlinearities in incompressible flow. *Nonlinear Dyn.* **70**, 1335–1354 (2012)
- Belotserkovskii, S.M., Lifanov, I.K.: *Method of discrete vortices*. CRC Press, New York (1993)
- Belotserkovskii, S.M., Skripach, B.K.: *Aerodynamic derivatives of aircrafts and wings at subsonic flows*. Nauka, Moscow (1975). (in Russian)
- Breslavsky, I.D., Strel'nikova, E.A., Avramov, K.V.: Dynamics of shallow shells with geometrical nonlinearity interacting with fluid. *Comput. Struct.* **89**, 496–506 (2011)
- Djojodihardjo, R.H., Widnall, S.E.: A numerical method for the calculation of nonlinear, unsteady lifting potential flow problems. *AIAA J.* **7**, 2001–2009 (1969)
- Dowell, E.H., Curtiss, H.C., Scanlan, R.H., Sisto, F.: *A modern course in aeroelasticity*. Kluwer Academic Publishers, New York (1995)
- Ellen, C.H.: Stability of clamed rectangular plates in uniform subsonic flow. *AIAA J.* **10**, 1716–1717 (1972)
- Eloy, C., Souilliez, C., Schouveiler, L.: Flutter of a rectangular plate. *J. Fluids Struct.* **23**, 904–919 (2007)
- Guo, C.Q., Paidoussis, M.P.: Stability of rectangular plates with free side-edges in two-dimensional inviscid channel flow. *ASME J. Appl. Mech.* **67**, 171–176 (2000)
- Hall, B.D., Mook, D.T., Nayfeh, A.H., Preidikman, S.: Novel strategy for suppressing the flutter oscillations of aircraft wings. *AIAA J.* **39**, 1843–1850 (2001)
- Hess, J.L.: Review of integral-equation techniques for solving potential-flow problems with emphasis of the surface-source method. *Comput. Methods Appl. Mech. Eng.* **5**, 145–196 (1975)
- Huang, L.: Flutter of cantilevered plates in axial flow. *J. Fluids Struct.* **9**, 127–147 (1995)
- Katz, J.: Calculation of the aerodynamic forces on automotive lifting surfaces. *ASME J. Fluids Eng.* **107**, 438–443 (1985)
- Kornecki, A., Dowell, E.H., O'Brein, J.: On the aeroelastic instability of two-dimensional panels in uniform incompressible flow. *J. Sound Vib.* **47**, 163–178 (1976)
- Landahl, M.T., Stark, V.J.E.: Numerical lifting-surface theory—problems and progress. *AIAA J.* **6**, 2049–2060 (1968)
- Lifanov, I.K., Poltavskii, L.N., Vainikko, G.M.: *Hypersingular integral equations and their applications*. A CRC Press Company, New York (2004)
- Mook, D.T., Dong, B.: Perspective: numerical simulations of wakes and blade-vortex interaction. *ASME J. Fluids Eng.* **116**, 5–21 (1994)
- Morino, L., Kuo, C.C.: Subsonic potential aerodynamic for complex configurations: a general theory. *AIAA J.* **12**, 191–197 (1974)
- Morino, L., Chen, L.T., Suci, E.O.: Steady and oscillatory subsonic and supersonic aerodynamics around complex configuration. *AIAA J.* **13**, 368–374 (1975)
- Preidikman, S., Mook, D.T.: On the development of a passive-damping system for wind-excited oscillations of long-span bridges. *J. Wind Eng. Ind. Aerodyn.* **77&78**, 443–456 (1998)
- Shayo, L.K.: The stability of cantilever panels in uniform incompressible flow. *J. Sound Vib.* **68**, 341–350 (1980)
- Strganac, T.W., Mook, D.T.: Numerical model of unsteady subsonic aeroelastic behavior. *AIAA J.* **28**, 903–909 (1990)
- Tang, D., Dowell, E.H.: Limit cycle oscillations of two-dimensional panels in low subsonic flow. *Int. J. Non-Linear Mech.* **37**, 1199–1209 (2002)
- Tang, D., Henry, J., Dowell, E.H.: Limit cycle oscillations of delta wing models in low subsonic flow. *AIAA J.* **37**, 1355–1362 (1999a)

- Tang, D., Dowell, E.H., Hall, K.C.: Limit cycle oscillations of a cantilevered wing in low subsonic flow. *AIAA J.* **37**, 364–371 (1999b)
- Tang, D.M., Yamamoto, H., Dowell, E.H.: Flutter and limit cycle oscillations of two-dimensional panels in three-dimensional axial flow. *J. Fluids Struct.* **17**, 225–242 (2003)
- Watanabe, Y., Isogai, K., Suzuki, S., Sugihara, M.: A theoretical study of paper flutter. *J. Fluids Struct.* **16**, 543–560 (2002)

Chapter 13

Hydroelastic Vibrations of Circular Sandwich Plate Under Inertial Excitation



Dmitry V. Kondratov, Lev I. Mogilevich, Victor S. Popov,
and Anna A. Popova

Abstract In this paper, a bending vibrations problem for a circular sandwich plate, which is the top wall of a narrow channel, under the action of inertial excitation was considered. We assumed the channel bottom wall is an absolutely rigid disk mounted on a vibrating foundation and considered the case when the circular sandwich plate was a three-layered disk formed by two metal face sheets and a lightweight incompressible core located between them. Due to the channel axial symmetry, the axisymmetric problem was studied. To describe the dynamics of the circular sandwich plate, we used the equations obtained in the framework of the zig-zag hypothesis for the normal in the plate cross-section. As part of the study, we assumed the channel was filled with a viscous incompressible liquid, and its movement was studied as a creeping one. We had formulated the coupled hydroelasticity problem for the circular sandwich plate under vibration acceleration of the channel foundation. Taking into account the channel narrowness, the dynamics equations for the viscous liquid were solved and the stresses acting on the circular sandwich plate from the liquid side were found. As a result, we obtained the equation for bending hydroelastic vibrations of the circular sandwich plate. The solution of this equation was found by the variables separation method. The hydroelastic response of the circular sandwich plate for the main mode of vibrations was determined. The study of this response was carried out for the sandwich plate with face sheets made of duralumin and a fluoroplastic core. The hydroelastic responses for the sandwich plate and the single-layered plate were compared.

D. V. Kondratov · V. S. Popov (✉)

Institute of Precision Mechanics and Control, Russian Academy of Sciences, 24, Rabochaya street, Saratov 410028, Russia

e-mail: vic_p@bk.ru

D. V. Kondratov

e-mail: kondratovdv@yandex.ru

L. I. Mogilevich · V. S. Popov · A. A. Popova

Department of Applied Mathematics and System Analysis, Yuri Gagarin State Technical University of Saratov, 77, Politechnicheskaya street, Saratov 410054, Russia

e-mail: mogilevich@info.sgu.ru

A. A. Popova

e-mail: anay_p@bk.ru

Keywords Hydroelasticity · Sandwich plate · Viscous incompressible fluid · Vibration

13.1 Introduction

Plates and beams are the main structural elements of various structures and they are usually applied for mathematical modeling of the complex mechanical systems behavior (Amabili 2008). Currently, sandwich plates and beams are widely used in civil engineering, mechanical engineering, and other industries. These structural elements possess a number of important properties, such as protection from aggressive environments, high energy absorption, impact resistance, noise and vibration reduction, etc. (Birman and Kardomateas 2018). Modern installations of transport systems are subject to intense vibration loads with a wide range of frequencies and high intensity of impact and at the same time are their sources. The reliability and service life of modern high power density products are largely determined by the vibration level of its assemblies and parts. Therefore, various vibration damping systems based on hydrodynamic dampers and vibration dampers are widely used in mechanical engineering and instrument making. In this regard, it becomes urgent to study the dynamics of the interaction of elastic sandwich structures that are part of hydrodynamic dampers and supports with a working fluid. Thus, already at the design stage of vibration damping systems, there is a need to calculate and assess the behavior of a sandwich plate—liquid system under dynamic loads, and this is associated with the formulation and solution of the dynamic problem of hydroelasticity of a hydrodynamic damper, which includes an elastic sandwich structure. Thus, we can say that the presented research topic is relevant for the modern development of technology.

Well-known classical theories such as Euler-Bernoulli beam theory and Kirchhoff-Love plate theory applied to the study of single-layered beams and plates are not suitable for sandwich ones. Therefore, to describe their behavior, zig-zag theories are used that take into account a piecewise form of transverse stress and displacement fields for multilayered structure (Carrera 2003; Gorshkov et al. 2005; Tessler 2015). For example, in Starovoitov et al. (2018), Starovoitov and Leonenko (2019) the study of thermoelastic deformation for elastic and elastoplastic three-layer circular plates possessing asymmetry across its thickness was carried out. The authors obtained the equilibrium equations for sandwich plates with the incompressible core using Lagrange variational principle and the zig-zag hypothesis for the normal in the plate cross-section.

On the other hand, in recent decades, interest in the problems of hydroelasticity for single-layered plates has not diminished. Among these problems, we can distinguish studies for plates interacting with an ideal and viscous liquid. For example, in one of the first papers (Lamb 1921), free vibrations of a clamped circular plate with an ideal liquid located on one side of it were considered. In Amabili and Kwak (1996), the results of Lamb (1921) are generalized on the basis of a study of the coupled

hydroelasticity problem for a circular plate with various edge conditions, in particular, for both free-edge, simply supported and clamped plates, as well as for supported plates with an elastic moment edge constraint. The free hydroelastic vibrations of circular and annular plates interacting with an ideal fluid either bounded by a free surface or by a solid wall are investigated in Amabili (1996). The paper of Amabili (2001) deals with the vibrations of a circular plate resting on a sloshing liquid-free surface. The author considered the case of an ideal incompressible fluid, the domain of which is limited by a rigid cylinder and a rigid flat bottom. Hydroelastic vibrations of container walls formed by a cylindrical shell and a circular plate are investigated in Amabili (1997, 2000). In these papers, the hermetic and open tanks filled with an ideal liquid are investigated. Hydroelastic vibrations of a circular plate immersed in an ideal liquid, having a free surface and located in a cylindrical tank were theoretically and experimentally investigated in Askari et al. (2013). In Askari et al. (2020), a new approach to mathematical modeling for fluid-coupled vibration of axisymmetric plate structures with asymmetries was proposed. The authors determined the mode shapes of the vibrating plate with asymmetries without fluid and in turn, they used them to study vibrations of the fluid-coupled plate structure. Mathematical modeling of the hydroelastic behavior of the circular plate which is the pipeline end seal and contacting with an ideal liquid filled the pipeline was carried out in Velmisov and Pokladova (2019). Results of the experimental study of the rectangular plate's natural vibrations for both in the air or on the liquid-free surface were presented in (Bochkarev et al. 2020). Bochkarev and Lekomtsev (2016) are devoted to the research of the hydroelastic stability for two parallel rectangular plates forming a narrow channel and interacting with a flowing ideal fluid in it.

Among the papers devoted to the hydroelasticity problems for plates interacting with a viscous liquid, the following can be distinguished. Kozlovsky (2009) generalizes the well-known study of Lamb (1921) taking into account the viscosity of a liquid located on one side of the circular plate. The dynamics and stability of the plate separating two viscous liquids were investigated in Velmisov and Ankilov (2017). Plane problems of hydroelastic vibrations for rectangular plates forming the walls of a narrow channel filled with a viscous liquid and resting on an elastic foundation were studied in Mogilevich et al. (2016, 2017), Tulchinsky and Gat (2019). Mogilevich et al. (2018) was devoted to the study of longitudinal and transverse hydroelastic vibrations of the wall of narrow tapered channel resting on vibrating foundation and filled with viscous liquid.

Currently, we can point there are few studies for the hydroelastic behavior of composite plates. For instance, the natural vibrations of composite cantilevered plates interacting with air and in water were studied in Kramer et al. (2013), Liao et al. (2019). Grushenkova et al. (2015), Mogilevich et al. (2017), Chernenko et al. (2019) consider the issues of the hydroelastic response of three-layer beams and plates interacting with a viscous liquid layer and being the walls of narrow channels, including cases of taking into account the elastic properties of the foundation on which they are placed. However, among the abovementioned papers, there are no investigations devoted to hydroelastic vibrations of a circular sandwich plate interacting with a viscous liquid layer and installed on a vibrating foundation. The article is the

first to solve the associated problem of hydroelastic vibrations of a round sandwich plate, installed on a vibrating foundation, interacting with a layer of a viscous incompressible fluid.

13.2 The Problem Statement

Let us consider a mechanical system consisting of two coaxial disks parallel to each other, between which there is a layer of viscous incompressible liquid. The disks have a radius R (see Fig. 13.1). The bottom disk is absolutely rigid, and the top one is a circular three-layer plate, clamped along its contour. We assume the presence of an end cavity filled with the same liquid in which constant pressure is maintained. Therefore, the liquid can freely flow from the narrow channel formed by two disks into the end cavity. The system is placed on a vibrating foundation. Thus, the sandwich plate can vibrate due to the foundation vibration. We introduce a cylindrical coordinate system $r\theta z$, the pole O of which is connected with the center of the top surface of the bottom disk. Due to the axial symmetry, we will next focus on the study of the axisymmetric problem. In the introduced coordinate system, the foundation oscillates along the z -axis with an amplitude z_m . We assume that the distance between the disks is $h_0 \ll R$, and the amplitude of elastic deflections of the circular sandwich plate w_m is significantly less than the liquid layer thickness, i.e., $w_m \ll h_0$.

Let us assume the foundation vibration law has the form $z_f = z_m f(\omega t)$, where $f(\omega t) = \sin(\omega t)$, ω is the oscillation frequency. Then the foundation acceleration is

$$\ddot{z}_f = z_m d^2 f(\omega t) / dt^2 = -z_m \omega^2 f(\omega t).$$

Further, the foundation acceleration amplitude is represented in units of gravity g , i.e., we assume that $z_m = kg/\omega^2$, where k is the vibration overload coefficient.

The sandwich plate is a three-layer structure consisting of two face sheets and a core between them. The face sheets bear the load bulk, and the core enables the three-layer structure to work together. The core material is rigid and lightweight, i.e.,

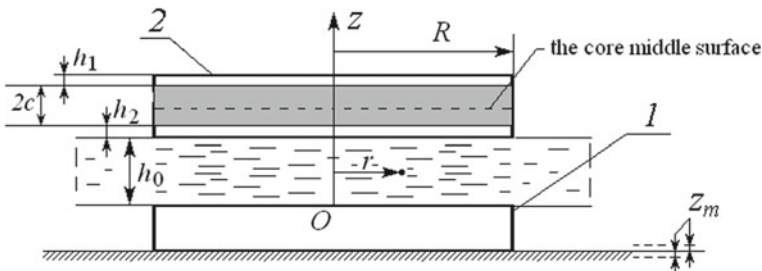


Fig. 13.1 Oscillatory mechanical system: 1—absolutely rigid disk, 2—circular sandwich plate

we neglect the core work in the tangential direction. We consider the kinematics of the circular sandwich plate in the approach proposed in Gorshkov et al. (2005), i.e., we assume that the top and bottom face sheets obey the Kirchhoff hypotheses, and the normal to the middle surface of the deformed core remains straight, but rotates by an angle φ . In other words, we use the zig-zag hypothesis for the normal. In addition, we will study bending vibrations of the sandwich plate, i.e., exclude from consideration the inertial forces of the plate in the radial direction. In this case (Gorshkov et al. 2005; Starovoitov et al. 2018; Starovoitov and Leonenko 2019), the stress-strain state of the sandwich plate is completely described by means of radial displacement u and deflection of the core middle surface w , as well as the rotation angle of the normal φ . The dynamics equations of the circular sandwich plate (Gorshkov et al. 2005), taking into account the reference-frame acceleration, i.e., the foundation acceleration, can be written in the form

$$\begin{aligned}
 L_2 \left(a_1 u + a_2 \varphi - a_3 \frac{\partial w}{\partial r} \right) &= -q_{zr}, \\
 L_2 \left(a_2 u + a_4 \varphi - a_5 \frac{\partial w}{\partial r} \right) &= 0, \\
 L_3 \left(a_3 u + a_5 \varphi - a_6 \frac{\partial w}{\partial r} \right) - M_0 \left(\frac{\partial^2 w}{\partial t^2} + \ddot{z}_f \right) &= -q_{zz}, \\
 L_2(g) = \frac{\partial}{\partial r} \left[\frac{1}{r} \frac{\partial}{\partial r} (rg) \right], L_3(g) = \frac{1}{r} \frac{\partial}{\partial r} [rL_2(g)], \\
 a_1 = h_1 K_1^+ + h_2 K_2^+ + 2c K_3^+, a_2 = c (h_1 K_1^+ - h_2 K_2^+) \\
 a_3 = h_1 \left(c + \frac{1}{2} h_1 \right) K_1^+ - h_2 \left(c + \frac{1}{2} h_2 \right) K_2^+, \\
 a_4 = c^2 \left(h_1 K_1^+ + h_2 K_2^+ + \frac{2}{3} c K_3^+ \right), \\
 a_5 = c \left(h_1 \left(c + \frac{h_1}{2} \right) K_1^+ + h_2 \left(c + \frac{h_2}{2} \right) K_2^+ + \frac{2}{3} c^2 K_3^+ \right), \\
 a_6 = h_1 \left(c^2 + ch_1 + \frac{h_1^2}{3} \right) K_1^+ \\
 + h_2 \left(c^2 + ch_2 + \frac{h_2^2}{3} \right) K_2^+ + \frac{2c^3}{3} K_3^+, \\
 K_k^+ = K_k + \frac{4}{3} G_k, k = 1, 2, 3, M_0 = \rho_1 h_1 + \rho_2 h_2 + \rho_3 2c. \tag{13.1}
 \end{aligned}$$

Here u is a radial plate displacement; w is a plate deflection; φ is a rotation angle of deformed normal in the plate core; q_{zr} and q_{zz} are shear and normal liquid stresses acting on the top plate surface, respectively. G_k is a shear modulus of the k -th layer; K_k is a bulk modulus of the k -th layer; ρ_k is a density of the k -th layer material. The expressions for a_1, \dots, a_6 were obtained in Gorshkov et al. (2005).

The boundary conditions for Eq. (13.1) are

$$u = \varphi = w = \frac{\partial w}{\partial r} = 0 \text{ at } r = R, \quad (13.2)$$

and the condition of limited deflection on the symmetry axis

$$r \frac{\partial w}{\partial r} = 0 \text{ at } r = 0. \quad (13.3)$$

Following (Loitsyanskii 1966), we consider the viscous incompressible liquid motion in a narrow channel as a creeping one and neglect gravity. In this case, the dynamics equations of the viscous liquid are the Navier-Stokes equations, in which the local and convective terms of inertia are neglected, but take into account the reference-frame acceleration. These equations are written together with the continuity equation. As a result, we obtain

$$\begin{aligned} \frac{1}{\rho} \frac{\partial p}{\partial r} &= \nu \left(\frac{\partial^2 V_r}{\partial r^2} + \frac{1}{r} \frac{\partial V_r}{\partial r} + \frac{\partial^2 V_r}{\partial z^2} - \frac{V_r}{r^2} \right), \\ \ddot{z}_f + \frac{1}{\rho} \frac{\partial p}{\partial z} &= \nu \left(\frac{\partial^2 V_z}{\partial r^2} + \frac{1}{r} \frac{\partial V_z}{\partial r} + \frac{\partial^2 V_z}{\partial z^2} \right), \\ \frac{\partial V_r}{\partial r} + \frac{1}{r} V_r + \frac{\partial V_z}{\partial z} &= 0. \end{aligned} \quad (13.4)$$

Here V_r and V_z are liquid velocity projections on the coordinate system axes, p is the liquid pressure, ν is the kinematic viscosity coefficient of the liquid, ρ is the liquid density.

Since the model of a viscous incompressible fluid is used, then the boundary conditions for Eq. (13.4) are the non-slip conditions

$$\begin{aligned} V_r &= 0, \quad V_z = 0, \quad \text{at } z = 0, \\ V_r &= \frac{\partial u}{\partial t}, \quad V_z = \frac{\partial w}{\partial t}, \quad \text{at } z = h_0 + w. \end{aligned} \quad (13.5)$$

and conditions for the pressure at the channel edge and the symmetry axis

$$p = p_0 - \rho \ddot{z}_f (z - h_0/2) \text{ at } r = R, \quad (13.6)$$

$$r \frac{\partial p}{\partial r} = 0 \text{ at } r = 0. \quad (13.7)$$

The stresses $-q_{zz}$, $-q_{zr}$ in the right-hand sides of Eq. (13.2) are viscous liquid stresses, i.e., they have the form (Loitsyanskii 1966)

$$\begin{aligned} -q_{zr} &= -\rho \nu \left(\frac{\partial V_z}{\partial r} + \frac{\partial V_r}{\partial z} \right) \Big|_{z=h_0+w}, \\ -q_{zz} &= \left(-p + 2\rho \nu \frac{\partial V_z}{\partial z} \right) \Big|_{z=h_0+w}. \end{aligned} \quad (13.8)$$

13.3 Solving the Hydroelasticity Problem

Let us designate the amplitudes of radial displacement, deflection, and rotation angle of the normal for the sandwich plate as u_m , w_m , φ_m , respectively. Next, we take into account that $w_m \ll h_0$ and $h_0 \ll R$ and introduce small parameters of the problem and dimensionless variables

$$\psi = \frac{h_0}{R} \ll 1, \lambda = \frac{w_m}{h_0} \ll 1, \zeta = \frac{z}{h_0}, \xi = \frac{r}{R}, \tau = \omega t. \quad (13.9)$$

The functions included in the equations are represented as

$$\begin{aligned} V_z &= w_m \omega U_\zeta(\xi, \zeta, \tau), \quad V_r = \frac{w_m \omega R}{h_0} U_\xi(\xi, \zeta, \tau), \\ p &= p_0 + \frac{\rho v w_m \omega}{h_0 \psi^2} P(\xi, \zeta, \tau) - \rho h_0 \ddot{z}_f(\zeta - 1/2), \\ w &= w_m W(\xi, \tau), \quad u = u_m U(\xi, \tau), \quad \varphi = \varphi_m \Phi(\xi, \tau). \end{aligned} \quad (13.10)$$

Taking into account (13.9), (13.10) into Eq. (13.4), we obtain

$$\begin{aligned} \frac{\partial P}{\partial \xi} &= \frac{\partial^2 U_\xi}{\partial \zeta^2} + \psi^2 \left(\frac{\partial^2 U_\xi}{\partial \xi^2} + \frac{1}{\xi} \frac{\partial U_\xi}{\partial \xi} - \frac{U_\xi}{\xi^2} \right), \\ \frac{\partial P}{\partial \zeta} &= \psi^2 \left[\psi^2 \left(\frac{\partial^2 U_\zeta}{\partial \xi^2} + \frac{1}{\xi} \frac{\partial U_\zeta}{\partial \xi} \right) + \frac{\partial^2 U_\zeta}{\partial \zeta^2} \right], \\ \frac{\partial U_\xi}{\partial \xi} + \frac{1}{\xi} U_\xi + \frac{\partial U_\zeta}{\partial \zeta} &= 0. \end{aligned} \quad (13.11)$$

Neglecting the terms of order ψ in these equations (van Dyke, 1975), we write the equations for the dynamics of a thin layer of a viscous liquid

$$\begin{aligned} \frac{\partial P}{\partial \xi} &= \frac{\partial^2 U_\xi}{\partial \zeta^2}, \\ \frac{\partial P}{\partial \zeta} &= 0, \\ \frac{\partial U_\xi}{\partial \xi} + \frac{1}{\xi} U_\xi + \frac{\partial U_\zeta}{\partial \zeta} &= 0. \end{aligned} \quad (13.12)$$

Note that according to the second equation, pressure is a function of the radial coordinate and time, i.e., we further assume $P(\xi, \tau)$.

The boundary conditions (13.5) in dimensionless form are

$$U_\xi = 0, \quad U_\zeta = 0 \text{ at } \zeta = 0,$$

$$U_\xi = \psi \frac{u_m}{w_m} \frac{\partial U}{\partial \tau}, \quad U_\zeta = \frac{\partial W}{\partial \tau} \text{ at } \zeta = 1 + \lambda W.$$

In the problem under consideration, we assume $u_m/w_m = O(1)$, so up to ψ and λ (van Dyke, 1975), the boundary conditions (13.5)–(13.7) are written as

$$\begin{aligned} U_\xi &= 0, \quad U_\zeta = 0 \text{ at } \zeta = 0, \\ U_\xi &= 0, \quad U_\zeta = \frac{\partial W}{\partial \tau} \text{ at } \zeta = 1, \\ P &= 0 \text{ at } \xi = 1, \\ \xi \frac{\partial P}{\partial \xi} &= 0 \text{ at } \xi = 0. \end{aligned} \tag{13.13}$$

By solving Eq. (13.12) bearing in mind boundary conditions (13.13), we obtained

$$\begin{aligned} U_\xi &= \frac{\partial P}{\partial \xi} \frac{\zeta(\zeta - 1)}{2}, \\ U_\zeta &= \frac{1}{\xi} \frac{\partial}{\partial \xi} \left(\xi \frac{\partial P}{\partial \xi} \right) \left(\frac{3\zeta^2 - 2\zeta^3}{12} \right), \\ P &= -12 \int_\xi^1 \left[\frac{1}{\xi} \int_0^\xi \xi \frac{\partial W}{\partial \tau} d\xi \right] d\xi. \end{aligned} \tag{13.14}$$

Taking into account above, we write the stresses (13.8) as

$$\begin{aligned} -q_{zr} &= -\frac{\rho v w_m \omega}{h_0 \psi} \frac{\partial U_\xi}{\partial \zeta} \Big|_{\zeta=1}, \\ -q_{zz} &= -p_0 + \rho h_0 \ddot{z}_f / 2 - \frac{\rho v w_m \omega}{h_0 \psi^2} P. \end{aligned} \tag{13.15}$$

It can be noted that $q_{zr}/q_{zz} = O(\psi)$, i.e., $q_{zz} \gg q_{zr}$. Therefore, we assume $q_{zr} = 0$ and substituting (13.9), (13.10), (13.14), (13.15) into Eq. (13.1), we obtain

$$\begin{aligned} L_2 \left(a_1 u_m U + a_2 \varphi_m \Phi - \frac{a_3 w_m}{R} \frac{\partial W}{\partial \xi} \right) &= 0, \\ L_2 \left(a_2 u_m U + a_4 \varphi_m \Phi - \frac{a_5 w_m}{R} \frac{\partial W}{\partial \xi} \right) &= 0, \\ L_3 \left(a_3 u_m U + a_5 \varphi_m \Phi - \frac{a_6 w_m}{R} \frac{\partial W}{\partial \xi} \right) - M_0 \omega^2 \left(w_m \frac{\partial^2 W}{\partial \tau^2} + \frac{\ddot{z}_f}{\omega^2} \right) & \\ = -p_0 + \rho h_0 \ddot{z}_f / 2 + 12 \frac{\rho v w_m \omega}{h_0 \psi^2} \int_\xi^1 \left[\frac{1}{\xi} \int_0^\xi \xi \frac{\partial W}{\partial \tau} d\xi \right] d\xi. & \end{aligned} \tag{13.16}$$

with $L_2(g) = \frac{\partial}{R^2 \partial \xi} \left[\frac{1}{\xi} \frac{\partial}{\partial \xi} (\xi g) \right]$, $L_3(g) = \frac{\partial}{\xi R \partial \xi} [\xi L_2(g)]$.

Using the first and second Eq. (13.16) we find

$$\begin{aligned} u &= u_m U = \frac{b_1}{R} w_m \frac{\partial W}{\partial \xi}, \\ \varphi &= \varphi_m \Phi = \frac{b_2}{R} w_m \frac{\partial W}{\partial \xi}. \end{aligned} \quad (13.17)$$

where $b_1 = \frac{a_4 a_3 - a_2 a_5}{a_1 a_4 - a_2^2}$, $b_2 = \frac{a_1 a_5 - a_2 a_3}{a_1 a_4 - a_2^2}$. Substituting (13.17) in (13.16), we obtain the bending hydroelastic vibrations equation for the circular sandwich plate due to the foundation vibration

$$\begin{aligned} &L_3 \left(D_s \frac{w_m}{R} \frac{\partial W}{\partial \xi} \right) + M_0 \omega^2 \left(w_m \frac{\partial^2 W}{\partial \tau^2} + \frac{\ddot{z}_f}{\omega^2} \right) \\ &= p_0 - \rho h_0 \ddot{z}_f / 2 - 12 \frac{\rho \nu w_m \omega}{h_0 \psi^2} \int_{\xi}^1 \left[\frac{1}{\xi} \int_0^{\xi} \xi \frac{\partial W}{\partial \tau} d\xi \right] d\xi. \end{aligned} \quad (13.18)$$

Here we use the following notation $D_s = [a_6 - a_3 b_1 - a_5 b_2]$. Note that if D_s is understood as the flexural rigidity $D = Eh^3/(12(1-\mu^2))$ and $m_0 = \rho_p h$ is assumed then we make the transition to a homogeneous single-layered circular plate of thickness h , the material of which has a young's modulus E , Poisson's ratio μ and density ρ_p .

Taking into account the boundary conditions (13.2), (13.3) we offered the solution of (13.18) as the eigenfunctions series for the Sturm-Liouville problem

$$w = w_m \sum_{k=1}^{\infty} (R_k^0 + R_k(\tau)) \left[\frac{J_0(\beta_k \xi)}{J_0(\beta_k)} - \frac{I_0(\beta_k \xi)}{I_0(\beta_k)} \right], \quad (13.19)$$

with R_k^0 , Q_k^0 , T_k^0 mean the coefficients, corresponding to the static pressure p_0 and R_k , Q_k , T_k are the time functions, corresponding to the foundation vibrations, J_0 , J_1 are the Bessel function of the first kind, I_0 , I_1 are the modified Bessel function, β_k is eigenvalue determined from the solution of the equation $I_1(\beta_k)/I_0(\beta_k) = -J_1(\beta_k)/J_0(\beta_k)$ (Gorshkov et al. 2005).

By substituting (13.19) in (13.18) we get

$$\begin{aligned} &w_m \sum_{k=1}^{\infty} (R_k^0 + R_k(\tau)) \frac{D_s \beta_k^4}{R^4} \left[\frac{J_0(\beta_k \xi)}{J_0(\beta_k)} - \frac{I_0(\beta_k \xi)}{I_0(\beta_k)} \right] \\ &+ M_0 w_m \omega^2 \sum_{k=1}^{\infty} \frac{d^2 R_k}{d\tau^2} \left[\frac{J_0(\beta_k \xi)}{J_0(\beta_k)} - \frac{I_0(\beta_k \xi)}{I_0(\beta_k)} \right] \\ &+ M_0 \ddot{z}_f = p_0 - \rho h_0 \ddot{z}_f / 2 \end{aligned}$$

$$- 12 \frac{\rho v w_m \omega}{h_0 \psi^2} \sum_{k=1}^{\infty} \frac{1}{\beta_k^2} \left[\frac{J_0(\beta_k \xi)}{J_0(\beta_k)} + \frac{I_0(\beta_k \xi)}{I_0(\beta_k)} - 2 \right] \frac{dR_k}{d\tau}. \tag{13.20}$$

In the obtained Eq. (13.20), there are terms other than eigenfunctions, therefore, we performing the re-decompositions these terms in the form of eigenfunctions series. As a result, we obtain the following equations

$$\begin{aligned} & w_m \sum_{k=1}^{\infty} (R_k^0 + R_k(\tau)) \frac{D_s \beta_k^4}{R^4} \left[\frac{J_0(\beta_k \xi)}{J_0(\beta_k)} - \frac{I_0(\beta_k \xi)}{I_0(\beta_k)} \right] \\ & + M_0 w_m \omega^2 \sum_{k=1}^{\infty} \frac{d^2 R_k}{d\tau^2} \left[\frac{J_0(\beta_k \xi)}{J_0(\beta_k)} - \frac{I_0(\beta_k \xi)}{I_0(\beta_k)} \right] \\ & = (p_0 - \ddot{z}_f (M_0 + \rho h_0 / 2)) \\ & \times \sum_{k=1}^{\infty} \frac{2}{\beta_k} \frac{J_1(\beta_k)}{J_0(\beta_k)} \left[\frac{J_0(\beta_k \xi)}{J_0(\beta_k)} - \frac{I_0(\beta_k \xi)}{I_0(\beta_k)} \right] \\ & - 12 \frac{\rho v w_m \omega}{h_0 \psi^2} \left(\sum_{k=1}^{\infty} \left(\sum_{i=1}^{k-1} \frac{4}{(\beta_i^4 - \beta_k^4) \beta_k \beta_i} \left[\beta_k^3 \frac{J_1(\beta_i)}{J_0(\beta_i)} - \beta_i^3 \frac{J_1(\beta_i)}{J_0(\beta_i)} \right] \right. \right. \\ & \times \left. \left[\frac{J_0(\beta_i \xi)}{J_0(\beta_i)} - \frac{I_0(\beta_i \xi)}{I_0(\beta_i)} \right] \frac{dR_k}{d\tau} \right. \\ & + \left. \frac{1}{\beta_k^2} \left[\frac{J_1^2(\beta_k)}{J_0^2(\beta_k)} - \frac{4}{\beta_k} \frac{J_1(\beta_k)}{J_0(\beta_k)} \right] \left[\frac{J_0(\beta_k \xi)}{J_0(\beta_k)} - \frac{I_0(\beta_k \xi)}{I_0(\beta_k)} \right] \frac{dR_k}{d\tau} \right. \\ & + \left. \sum_{i=k+1}^{\infty} \frac{4}{(\beta_i^4 - \beta_k^4) \beta_k \beta_i} \left[\beta_k^3 \frac{J_1(\beta_i)}{J_0(\beta_i)} - \beta_i^3 \frac{J_1(\beta_k)}{J_0(\beta_k)} \right] \right. \\ & \times \left. \left. \left[\frac{J_0(\beta_i \xi)}{J_0(\beta_i)} - \frac{I_0(\beta_i \xi)}{I_0(\beta_i)} \right] \frac{dR_k}{d\tau} \right) \right). \tag{13.21} \end{aligned}$$

Further, we assume $k = 1, 2, \dots, n, i = 1, 2, \dots, n$ and equating in (13.21) the coefficients at the same eigenfunctions we define the expressions for R_k^0

$$R_1^0 = p_0 \frac{2R^4}{D_s} \frac{J_1(\beta_1)}{J_0(\beta_1) \beta_1^5 w_m}, \dots, R_n^0 = p_0 \frac{2R^4}{D_s} \frac{J_1(\beta_n)}{J_0(\beta_n) \beta_n^5 w_m}, \tag{13.22}$$

and also we obtain the system of linear ordinary differential equations for determining $R_k(\tau)$

$$\begin{aligned} & w_m \frac{D_s \beta_1^4}{R^4} R_1(\tau) + M_0 w_m \omega^2 \frac{d^2 R_1(\tau)}{d\tau^2} \\ & = -\ddot{z}_f (M_0 + \rho h_0 / 2) \frac{2}{\beta_1} \frac{J_1(\beta_1)}{J_0(\beta_1)} \end{aligned}$$

$$\begin{aligned}
 & - 12 \frac{\rho \nu w_m \omega}{h_0 \psi^2} \left[\frac{1}{\beta_1^2} \left[\frac{J_1^2(\beta_1)}{J_0^2(\beta_1)} - \frac{4}{\beta_1} \frac{J_1(\beta_1)}{J_0(\beta_1)} \right] \frac{dR_1(\tau)}{d\tau} \right. \\
 & + \left. \sum_{i=2}^n \frac{4}{(\beta_i^4 - \beta_1^4) \beta_1 \beta_i} \left[\beta_1^3 \frac{J_1(\beta_i)}{J_0(\beta_i)} - \beta_i^3 \frac{J_1(\beta_1)}{J_0(\beta_1)} \right] \frac{dR_i(\tau)}{d\tau} \right], \\
 & \dots\dots\dots, \\
 & w_m \frac{D_s \beta_\ell^4}{R^4} R_\ell(\tau) + M_0 w_m \omega^2 \frac{d^2 R_\ell(\tau)}{d\tau^2} \\
 & = -\ddot{z}_f (M_0 + \rho h_0 / 2) \frac{2}{\beta_\ell} \frac{J_1(\beta_\ell)}{J_0(\beta_\ell)} \\
 & - 12 \frac{\rho \nu w_m \omega}{h_0 \psi^2} \left[\sum_{i=1}^{\ell-1} \frac{4}{(\beta_i^4 - \beta_\ell^4) \beta_\ell \beta_i} \left[\beta_\ell^3 \frac{J_1(\beta_i)}{J_0(\beta_i)} - \beta_i^3 \frac{J_1(\beta_\ell)}{J_0(\beta_\ell)} \right] \frac{dR_i(\tau)}{d\tau} \right. \\
 & + \left. \frac{1}{\beta_\ell^2} \left[\frac{J_1^2(\beta_\ell)}{J_0^2(\beta_\ell)} - \frac{4}{\beta_\ell} \frac{J_1(\beta_\ell)}{J_0(\beta_\ell)} \right] \frac{dR_\ell(\tau)}{d\tau} \right. \\
 & + \left. \sum_{i=\ell+1}^n \frac{4}{(\beta_i^4 - \beta_\ell^4) \beta_\ell \beta_i} \left[\beta_\ell^3 \frac{J_1(\beta_i)}{J_0(\beta_i)} - \beta_i^3 \frac{J_1(\beta_\ell)}{J_0(\beta_\ell)} \right] \frac{dR_i(\tau)}{d\tau} \right], \\
 & \dots\dots\dots, \\
 & w_m \frac{D_s \beta_n^4}{R^4} R_n(\tau) + M_0 w_m \omega^2 \frac{d^2 R_n(\tau)}{d\tau^2} \\
 & = -\ddot{z}_f (M_0 + \rho h_0 / 2) \frac{2}{\beta_n} \frac{J_1(\beta_n)}{J_0(\beta_n)} \\
 & - 12 \frac{\rho \nu w_m \omega}{h_0 \psi^2} \left[\sum_{i=1}^{n-1} \frac{4}{(\beta_i^4 - \beta_n^4) \beta_n \beta_i} \left[\beta_n^3 \frac{J_1(\beta_i)}{J_0(\beta_i)} - \beta_i^3 \frac{J_1(\beta_n)}{J_0(\beta_n)} \right] \frac{dR_i(\tau)}{d\tau} \right. \\
 & + \left. \frac{1}{\beta_n^2} \left[\frac{J_1^2(\beta_n)}{J_0^2(\beta_n)} - \frac{4}{\beta_n} \frac{J_1(\beta_n)}{J_0(\beta_n)} \right] \frac{dR_n(\tau)}{d\tau} \right]. \tag{13.23}
 \end{aligned}$$

Thus, by setting the number for retained terms of the series, we can find the desired coefficients R_k^0 and solving the system of Eq. (13.23) to find the functions $R_k(\tau)$, thereby determining the deflections of the circular sandwich plate.

For instance, consider the steady-state harmonic oscillations of the circular sandwich plate on the main mode, i.e., we assume $k = 1, i = 1$ and write Eqs. (13.22), (13.23) as

$$R_1^0 = p_0 \frac{2R^4}{D_s} \frac{J_1(\beta_1)}{J_0(\beta_1) \beta_1^5 w_m}, \tag{13.24}$$

$$w_m \frac{D_s \beta_1^4}{R^4} R_1(\tau) + M_0 w_m \omega^2 \frac{d^2 R_1(\tau)}{d\tau^2}$$

$$\begin{aligned}
 &+ 12 \frac{\rho v w_m \omega}{h_0 \psi^2} \frac{1}{\beta_1^2} \left(\frac{J_1^2(\beta_1)}{J_0^2(\beta_1)} - \frac{4}{\beta_1} \frac{J_1(\beta_1)}{J_0(\beta_1)} \right) \frac{dR_1(\tau)}{d\tau} \\
 &= -\ddot{z}_f (M_0 + \rho h_0 / 2) \frac{2}{\beta_1} \frac{J_1(\beta_1)}{J_0(\beta_1)}. \tag{13.25}
 \end{aligned}$$

Taking into account that for harmonic oscillations $d^2 R_n(\tau) / d\tau^2 = -R_n(\tau)$ and solving (13.25), we obtain

$$\begin{aligned}
 R_1(\tau) &= kg(M_0 + \rho h_0 / 2) \frac{2}{w_m \beta_1} \frac{J_1(\beta_1)}{J_0(\beta_1)} \\
 &\times \frac{1}{\sqrt{(D_s \beta_1^4 / R^4 - M_0 \omega^2)^2 + (K_1 \omega)^2}} \sin(\tau + \theta),
 \end{aligned}$$

where $K_1 = 12 \frac{\rho v}{h_0 \psi^2} \frac{1}{\beta_1^2} \left(\frac{J_1^2(\beta_1)}{J_0^2(\beta_1)} - \frac{4}{\beta_1} \frac{J_1(\beta_1)}{J_0(\beta_1)} \right)$, $tg\theta = \frac{K_1 \omega}{M_0 \omega^2 - (D_s \beta_1^4 / R^4)}$.

As a result, we present the deflections of the circular sandwich plate on the main mode of oscillation as

$$\begin{aligned}
 w &= p_0 \frac{2R^4}{D_s} \frac{J_1(\beta_1)}{J_0(\beta_1) \beta_1^5} \left[\frac{J_0(\beta_1 r / R)}{J_0(\beta_1)} - \frac{I_0(\beta_1 r / R)}{I_0(\beta_1)} \right] \\
 &+ kg(M_0 + \rho h_0 / 2) A(r, \omega) \sin(\omega t + \theta). \tag{13.26}
 \end{aligned}$$

Writing (13.26), we introduced the frequency-dependent distribution function of the deflection amplitudes for the circular sandwich plate

$$\begin{aligned}
 A(r, \omega) &= \frac{2}{\beta_1} \frac{J_1(\beta_1)}{J_0(\beta_1)} \frac{1}{\sqrt{(D_s \beta_1^4 / R^4 - M_0 \omega^2)^2 + (K_1 \omega)^2}} \\
 &\times \left[\frac{J_0(\beta_1 r / R)}{J_0(\beta_1)} - \frac{I_0(\beta_1 r / R)}{I_0(\beta_1)} \right]. \tag{13.27}
 \end{aligned}$$

Expression (13.27) allows us to find the hydroelastic response of the circular sandwich plate at its main mode vibration due to the foundation vibration. To do this, it is sufficient to consider the ratio of the function $A(r, \omega)$ to its value at $\omega = 0$, i.e., we have defined the hydroelastic response as

$$\alpha(\omega) = A(r, \omega) / A(r, 0) = \frac{R^4}{D_s \beta_1^4} \frac{1}{\sqrt{(D_s \beta_1^4 / R^4 - M_0 \omega^2)^2 + (K_1 \omega)^2}}, \tag{13.28}$$

where $A(r, 0) = \frac{2R^4}{D_s} \frac{J_1(\beta_1)}{J_0(\beta_1) \beta_1^5} \left[\frac{J_0(\beta_1 r / R)}{J_0(\beta_1)} - \frac{I_0(\beta_1 r / R)}{I_0(\beta_1)} \right]$.

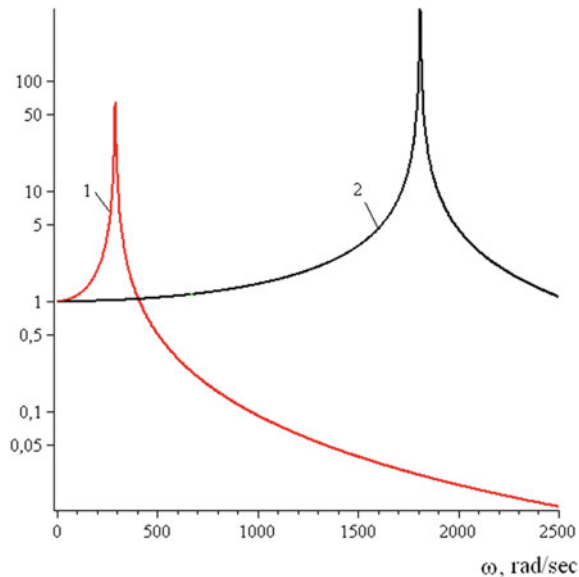
13.4 Calculation Results

As an example, we carried out a numerical study for the hydroelastic response of the circular sandwich plate, the face sheets of which are made of duralumin and the core is made of fluoroplastic. We examined the channel with the following parameters (Gorshkov et al. 2005): $R = 0.3$ m, $h_0/R = 0.04$, $h_1/R = 0.005$, $h_2/R = 0.0075$, $c/R = 0.01$, $\rho = 10^3$ kg/m³, $\rho_1 = \rho_2 = 2.7 \times 10^3$ kg/m³, $\rho_3 = 2.15 \times 10^3$ kg/m³, $K_1 = K_2 = 8 \times 10^3$ Pa, $K_3 = 4.7 \times 10^9$ Pa, $G_1 = G_2 = 2.67 \times 10^{10}$ Pa, $G_3 = 9 \times 10^7$ Pa, $\nu = 10^{-6}$ m²/s.

In addition, we calculated the hydroelastic response for the single-layered circular plate of similar geometric dimensions made of duralumin. The calculation results are shown in Fig. 13.2.

We have formulated the coupled hydroelasticity problem for the circular sandwich plate placed on a vibrating foundation. In the framework of this problem, the equation of bending vibrations of the circular sandwich plate interacting with the viscous liquid layer under the reference-frame acceleration is derived. Using the separation of variables, the system of ordinary differential equations is obtained, which makes it possible to study the hydroelastic response of the plate. It can be noted that for steady-state harmonic oscillations, this equation system is transformed into the system of algebraic equations that can be solved by known methods. We presented the solution for the main mode of harmonic vibrations and determined an analytical expression for plate deflections (13.26). This made it possible to consider the frequency-dependent distribution function of the sandwich plate deflections (13.27), which completely determines its stress-strain state, and also makes it possible to find the frequency

Fig. 13.2
Amplitude-frequency responses for bending vibrations of the circular plate on the main mode: 1—the circular sandwich plate (the face sheets material is duralumin, the core material is fluoroplastic), 2—the circular homogeneous single-layered plate (the plate material is duralumin)



response of the sandwich plate. We note that the first term of solution (13.26) can be represented as $p_0 A(r, 0)$, i.e., $A(r, 0)$ is the static deflection of the plate under the uniformly distributed load 1 Pa. We obtained the frequency response of the circular sandwich plate to the reference-frame acceleration as the ratio $A(r, \omega)/A(r, 0) = \alpha(\omega)$. Our calculations of $\alpha(\omega)$ showed a significant difference between the resonant frequencies of the sandwich plate from a homogeneous single-layered plate of the same geometric dimensions and made of the face sheets material. In particular, as follows from Fig. 13.2, for the sandwich plate, a shift of the resonance frequency to the low-frequency region and a decrease in the response amplitude is observed in comparison with a homogeneous single-layered plate.

13.5 Summary and Conclusion

The problem of hydroelasticity of a multilayer plate on a vibrating base is formulated and a method for its solution is presented. The obtained analytical solution determines the hydroelastic response of a round sandwich plate to the main vibration mode. The presented analytical solution can be the main one for the development of scientific software products for simulating similar problems of hydroelasticity. Thus, the results obtained in this work can be used to analyze the dynamic response of a circular sandwich plate interacting with the viscous liquid layer under inertial excitation. The developed model can make it possible to design highly efficient and low-power mechanical vibrators for various technological processes. For example, vibrators for creating optimal conditions and accelerating the impregnation of porous products with liquid and others.

Acknowledgements The study was funded by Russian Foundation for Basic Research (RFBR) according to the projects No. 18-01-00127-a and No. 19-01-00014-a.

References

- Amabili, M.: Effect of finite fluid depth on the hydroelastic vibrations of circular and annular plates. *J. Sound Vib.* **193**(4), 909–925 (1996). <https://doi.org/10.1006/jsvi.1996.0322>
- Amabili, M.: Shell-plate interaction in the free vibrations of circular cylindrical tanks partially filled with a liquid: the artificial spring method. *J. Sound Vib.* **199**(3), 431–452 (1997). <https://doi.org/10.1006/jsvi.1996.0650>
- Amabili, M.: Vibrations of fluid-filled hermetic cans. *J. Fluids Struct.* **14**(2), 235–255 (2000). <https://doi.org/10.1006/jfls.1999.0267>
- Amabili, M.: Vibrations of circular plates resting on sloshing liquid: solution of the fully coupled problem. *J. Sound Vib.* **245**(2), 261–283 (2001). <https://doi.org/10.1006/jsvi.2000.3560>
- Amabili, M., Kwak, M.K.: Free vibrations of circular plates coupled with liquids: revising the Lamb problem. *J. Fluids Struct.* **10**(7), 743–761 (1996). <https://doi.org/10.1006/jfls.1996.0051>
- Amabili, M.: *Nonlinear Vibrations and Stability of Shells and Plates*. Cambridge University Press, New York, (2008). <https://doi.org/10.1017/CBO9780511619694>

- Askari, E., Jeong, K.-H., Amabili, M.: Hydroelastic vibration of circular plates immersed in a liquid-filled container with free surface. *J. Sound Vib.* **332**(12), 3064–3085 (2013). <https://doi.org/10.1016/j.jsv.2013.01.007>
- Askari, E., Jeong, K.-H., Ahn, K.-H., Amabili, M.: A mathematical approach to study fluid-coupled vibration of eccentric annular plates. *J. Fluids Struct.* **98**, (2020). <https://doi.org/10.1016/j.jfluidstructs.2020.103129>
- Birman, V., Kardomateas, G.A.: Review of current trends in research and applications of sandwich structures. *Compos. B Eng.* **142**, 221–40 (2018). <https://doi.org/10.1016/j.compositesb.2018.01.027>
- Bochkarev, S.A., Lekomtsev, S.V.: Numerical investigation of the effect of boundary conditions on hydroelastic stability of two parallel plates interacting with a layer of ideal flowing fluid. *J. Appl. Mech. Tech. Phys.* **57**(7), 1254–1263 (2016). <https://doi.org/10.1134/S002189441607004X>
- Bochkarev, S.A., Kamenskikh, A.O., Lekomtsev, S.V.: Experimental investigation of natural and harmonic vibrations of plates interacting with air and fluid. *Ocean Eng.* **206**, 10734 (2020). <https://doi.org/10.1016/j.oceaneng.2020.107341>
- Carrera, E.: Historical review of zig-zag theories for multilayered plates and shells. *Appl. Mech. Rev.* **56**(3), 287–308 (2003). <https://doi.org/10.1115/1.1557614>
- Chernenko, A., Kondratov, D., Mogilevich, L., Popov, V., Popova, E.: Mathematical modeling of hydroelastic interaction between stamp and three-layered beam resting on Winkler foundation. *Stud. Syst. Decis. Control* **199**, 671–681 (2019). https://doi.org/10.1007/978-3-030-12072-6_54
- Gorshkov, A.G., Starovoitov, E.I., Yarovaya, A.V.: *Mechanics of Layered Viscoelastoplastic Structural Elements*. Fizmatlit, Moscow (2005)
- Grushenkova, E.D., Mogilevich, L.I., Popov, V.S., Rabinsky, L.N., Kuznetsova, E.L.: Mathematical model of three-layer plate interaction with viscous incompressible liquid layer under foundation vibration. *Appl. Math. Sci.* **9**(109–112), 5551–5559 (2015). <https://doi.org/10.12988/ams.2015.57482>
- Kozlovsky, Y.: Vibration of plates in contact with viscous fluid: Extension of Lamb’s model. *J. Sound Vib.* **326**(332–339) (2009). <https://doi.org/10.1016/j.jsv.2009.04.031>
- Kramer, M.R., Liu, Z., Young, Y.L.: Free vibration of composite plates in air and in water. *Compos. Struct.* **95**, 254–263 (2013). <https://doi.org/10.1016/j.compstruct.2012.07.017>
- Lamb, H.: On the vibrations of an elastic plate in contact with water. *Proc. Roy. Soc. A* **98**, 205–216 (1921). <https://doi.org/10.1098/rspa.1920.0064>
- Liao, Y., Garg, N., Martins Joaquim, R.R.A., Young, Y.L.: Viscous fluid structure interaction response of composite hydrofoils. *Compos. Struct.* **212**, 571–585 (2019). <https://doi.org/10.1016/j.compstruct.2019.01.043>
- Loitsyanskii, L.G.: *Mechanics of Liquids and Gases*. Pergamon Press, Oxford (1966)
- Mogilevich, L.I., Popov, V.S., Popova, A.A., Christoforova, A.V., Popova, E.V.: Mathematical modeling of three-layer beam hydroelastic oscillations. *Vibroeng. Procedia* **12**, 12–18 (2017). <https://doi.org/10.21595/vp.2017.18462>
- Mogilevich, L.I., Popov, V.S., Popova, A.A., Christoforova, A.V.: Mathematical modeling of hydroelastic walls oscillations of the channel on Winkler foundation under vibrations. *Vibroeng. Procedia* **8**, 294–299 (2016)
- Mogilevich, L.I., Popov, V.S., Popova, A.A.: Interaction dynamics of pulsating viscous liquid with the walls of the conduit on an elastic foundation. *J. Mach. Manuf. Reliab.* **46**(1), 12–19 (2017). <https://doi.org/10.3103/S1052618817010113>
- Mogilevich, L.I., Popov, V.S., Popova, A.A.: Longitudinal and transverse oscillations of an elastically fixed wall of a wedge-shaped channel installed on a vibrating foundation. *J. Mach. Manuf. Reliab.* **47**(3), 227–234 (2018). <https://doi.org/10.3103/S1052618818030093>
- Starovoitov, E.I., Leonenko, D.V.: Deformation of an elastoplastic three-layer circular plate in a temperature field. *Mech. Compos. Mater.* **55**(4), 503–512 (2019). <https://doi.org/10.1007/s11029-019-09829-6>

- Starovoitov, E.I., Leonenko, D.V., Tarlakovskii, D.V.: Thermoelastic deformation of a circular sandwich plate by local loads. *Mech. Compos. Mater.* **54**(3), 299–312 (2018). <https://doi.org/10.1007/s11029-018-9740-x>
- Tessler, A.: Refined zigzag theory for homogeneous, laminated composite, and sandwich beams derived from Reissner’s mixed variational principle. *Meccanica* **50**(10), 2621–2648 (2015). <https://doi.org/10.1007/s11012-015-0222-0>
- Tulchinsky, A., Gat, A.D.: Frequency response and resonance of a thin fluid film bounded by elastic sheets with application to mechanical filters. *J. Sound Vib.* **438**, 83–98 (2019). <https://doi.org/10.1016/j.jsv.2018.08.047>
- van Dyke, M.: *Perturbation methods in fluid mechanics*. Parabolic Press, Stanford, CA (1975)
- Velmisov, P.A., Ankilov, A.V.: Dynamic stability of plate interacting with viscous fluid. *Cybern. Phys.* **6**(4), 262–270 (2017)
- Velmisov, P.A., Pokladova, Y.V.: Mathematical modelling of the “Pipeline – pressure sensor” system. *J. Phys: Conf. Ser.* **1353**(1), (2019). <https://doi.org/10.1088/1742-6596/1353/1/012085>

Chapter 14

Effect of Finite Vessel Stiffness on Transition from Two-Dimensional Liquid Sloshing to Swirling: Reduced-Order Modeling



Dar Zusman and Oleg V. Gendelman

Abstract Liquid sloshing in partially filled tanks is rather complex. Thus, reduced-order dynamical models are often used in attempt to describe the dynamics of the contained liquid. One of the most important sloshing phenomena is the transition from two-dimensional to three-dimensional motion, including swirling. This paper addresses a reduced-order model that describes this transition, with one substantial addition—it considers finite stiffness of the vessel itself. Most classical models were obtained under the assumption of infinite stiffness of the vessel and therefore neglected the interaction between the sloshing liquid and the tank structural modes. However, this interaction was proven to be extremely significant. This paper suggests a reduced-order model of the sloshing liquid in a tank with finite stiffness and analyzes the model in conditions of simple horizontal harmonic forcing. The effect of vessel stiffness on the transition from two-dimensional to three-dimensional motion is studied.

Keywords Liquid sloshing · Reduced-order models · Swirling

14.1 Introduction

Vessels filled with liquid are widely used over the world, from containers used to store different chemicals in factories, to fuel tanks in aircrafts, missiles or rockets. Resonant excitations of the free surface of the liquid may cause a well-known effect called liquid sloshing. This kind of excitation, in particular, can take place in either liquid cargo or stationary tanks exposed to earthquakes. During the slosh motion, hydraulic pressures and impacts are applied to the vessel's inner walls. These, in turn, may alter the dynamics of the system and its stability significantly, and thus, may have a tremendous effect on its robustness (Farid and Gendelman 2016). Failure of

D. Zusman · O. V. Gendelman (✉)

Faculty of Mechanical Engineering, Technion, Israel Institute of Technology, Haifa 32000, Israel
e-mail: ovgend@technion.ac.il

D. Zusman

e-mail: darzus77@gmail.com

tanks which contain hazardous liquids might lead to severe pollution or even loss of human lives. Therefore, the ability to predict the dynamics and the resulting stresses is crucial.

When the tank is excited, different response regimes can take place. In order to have a better understanding of sloshing dynamics, various phenomenological models have been presented over the years. Numerous studies assumed the vessel walls to be rigid, and hydrodynamic pressures were separated into "impulsive" and "convective" decoupled components (Jolie et al. 2013). In the mid-1950s, Housner (1957, 1963) formulated a simplified two-dimensional mechanical model consisting of equivalent masses. Following Housner's work, Dodge (1966) and Abramson (1966) suggested two equivalent mechanical models to simulate two-dimensional sloshing response: a spring-mass system and a pendulum. They derived the values of different parameters for both types of models and for different tank shapes.

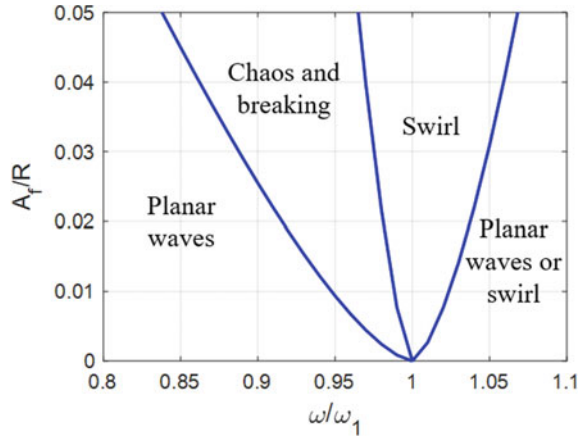
More models intended to describe three-dimensional behavior including swirling (also referred to as rotary sloshing by Ibrahim et al. 2005) in rigid tanks have also been introduced. The most popular one is that of a horizontally forced spherical pendulum, which was first presented by Miles (1961, 1984a, 1984b). Kana (1989) developed a model of a compound pendulum (a spherical pendulum coupled with a simple linear pendulum). Bauer (1966) developed a different nonlinear model, which includes a sliding mass point on a parabolic surface with an attached nonlinear spring, represented by high exponent. Additional analytical work concerning swirling was conducted by Faltinsen and Timokha (e.g., Faltinsen et al. 2003, 2005, 2006), who developed a multimodal approach to rotary sloshing in a square base tank. Faltinsen et al. (2016) developed a similar approach for a cylindrical tank. These studies showed, inter alia, that with increasing liquid level, the characteristics of the two-dimensional steady-state response change from hard to soft. In a rectangular tank with liquid depth h and breadth b , this transition occurs in the critical depth of $h^* \approx 0.3368b$. In a cylindrical tank with radius R , this transition occurs in $h^* \approx 0.5059R$. It should be noted that in cylindrical tanks, the swirling keeps a hardening response for $h^* \geq 0.2R$.

Experimental studies have also been carried out, such as the one presented by Royon-Lebeaud and Hopfinger (2007). They described the bounds of steady-state wave motion in a cylinder according to bifurcation points β_i first determined by Miles (1984b). For a tank with radius R and natural frequency ω_1 , which is forced with excitation amplitude A_f and frequency ω , these lines are given by:

$$\frac{A_f}{R} = \frac{1}{1.684} \left[\frac{(\omega/\omega_1)^2 - 1}{\beta_i} \right]^{3/2} \quad (14.1)$$

where $i = 2, 3, 4$ and $\beta_2 = -0.36$, $\beta_3 = -1.55$ and $\beta_4 = 0.735$. These bounds are plotted in Fig. 14.1. It is shown that in the vicinity of resonance ($\omega/\omega_1 = 1$), the liquid becomes nonplanar and starts to swirl. Chaos was exhibited in excitation frequencies on the left side of resonance.

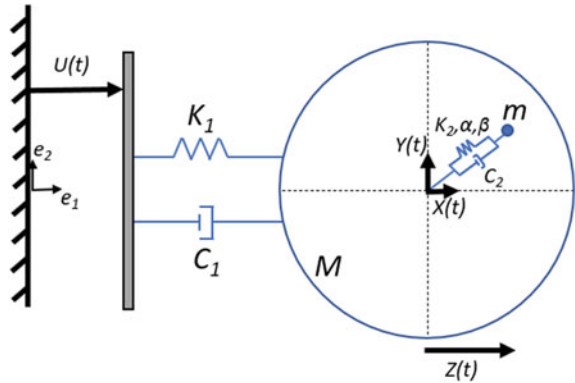
Fig. 14.1 Phase diagram of dimensionless forcing amplitude A_f/R versus frequency ratio ω/ω_1 . Bounds of steady-state wave motion were determined according to Miles (1984b) and Royon-Lebeaud and Hopfinger (2007)



In 1964, a major earthquake took place in Alaska and caused great damage to the oil tanks. The main conclusion from this event was that the flexibility of the tank plays a substantial role in the seismic performance of liquid storage tanks. It was stated that the vibrations of the tank are always coupled with the vibrations of the free surface of the contained liquid (Barton and Parker 1987). Since then, additional considerable efforts were invested in understanding the response of flexible tanks. For example, Bauer et al. (1967) showed that the natural frequency of a container with flexible walls increases with the decrease of liquid depth. Further analytical work concerning the hydrodynamic forces induced in a seismically excited flexible tank was presented by Veletsos (1974), Fischer (1979), Balendra et al. (1982), Parkus (1982), Tedesco et al. (1989), Fischer and Rammerstorfer (1999) and many others. These investigations revealed that the hydraulic forces in flexible tanks are considerably higher than those in rigid tanks. Moreover, studies dealing with this nonlinear coupling such as those of Ibrahim and Barr (1975a, and 1975b) and Ibrahim (1976) indicated that conditions of internal resonance may lead to amplified response.

Following these findings, Haroun and Housner (1981) developed a generalized model for two-dimensional sloshing, based on Housner's model from the 1960s, that takes tank wall flexibility into account. Moreover, Zou and Wang (2015) studied the effects of tank wall stiffness and filling ratio on the coupled sloshing modes, by modeling the wall as a flexible bulkhead. They found that a higher filling ratio and smaller bending stiffness of the bulkhead cause a stronger coupling effect, leading to a decrease in water wave frequencies. These two models are intended to describe two-dimensional sloshing in flexible tanks.

Fig. 14.2 Scheme of the suggested equivalent mechanical model for rotary sloshing in a flexible vessel



14.2 Description of the Model

14.2.1 Introducing the Model

The suggested ROM consists of a mass m which is mounted in a cylindrical container with horizontal displacement Z . The mass m represents the first liquid sloshing mode mass, whereas mass M is the total mass of the container-liquid system. A dashpot with damping coefficient C_2 and a nonlinear spring with linear, cubic and quintic stiffness coefficients K_2, α and β , respectively, are attached to the sloshed mass. A linear spring with stiffness coefficient K_1 and a dashpot with damping coefficient C_1 attach the container to an oscillating wall with horizontal displacement U and represent the structure's elasticity. U is considered to be harmonic, with displacement amplitude P and frequency ω . The model is schematically shown in Fig. 14.2.

As the main purpose of the model is to provide a general insight into the formation of rotary motion in non-rigid containers, it is designed to be as simple as possible. For this reason, the model is formulated as a top view of the container. Practically, planar waves (linear sloshing) are two-dimensional, and swirling is three-dimensional. However, in the model discussed in this study, planar waves will be expressed as one-dimensional motion and swirling as two-dimensional. Furthermore, it is assumed that the dimensions of the container are big enough so that mass m does not impact with the tank walls.

14.2.2 Equations of Motion

The equations of motion governing the system are developed according to Lagrange formalism. The kinetic and potential energies, T and V , are expressed as:

$$T = \frac{1}{2}M(U_t + Z_t)^2 + \frac{1}{2}m[(U_t + Z_t + X_t)^2 + Y_t^2] \tag{14.2}$$

$$V = \frac{1}{2}K_1Z^2 + \frac{1}{2}K_2\ell^2 + \frac{1}{4}\alpha\ell^4 + \frac{1}{6}\beta\ell^6 \quad (14.3)$$

Here, ℓ is the geometrical length $\ell = \sqrt{X^2 + Y^2}$. The Lagrangian is given by:

$$L = T - V = \frac{1}{2}M(U_t + Z_t)^2 + \frac{1}{2}m[(U_t + Z_t + X_t)^2 + Y_t^2] - \frac{1}{2}K_1Z^2 - \frac{1}{2}K_2\ell^2 - \frac{1}{4}\alpha\ell^4 - \frac{1}{6}\beta\ell^6 \quad (14.4)$$

The damping is described by Rayleigh's dissipation function:

$$D = \frac{1}{2}C_1Z_t^2 + \frac{1}{2}C_2(X_t^2 + Y_t^2) \quad (14.5)$$

Using (14.4) and (14.5) and applying some simple manipulations, one obtains the following non-dimensional equations of motion:

$$x_{\tau\tau} + (1 + \mu)\left[1 + \gamma(x^2 + y^2) + \chi(x^2 + y^2)^2\right]x + (1 + \mu)c_2x_\tau - \mu\kappa z - c_1z_\tau = 0$$

$$y_{\tau\tau} + \left[1 + \gamma(x^2 + y^2) + \chi(x^2 + y^2)^2\right]y + c_2y_\tau = 0$$

$$z_{\tau\tau} - \mu\left[1 + \gamma(x^2 + y^2) + \chi(x^2 + y^2)^2\right]x - \mu c_2x_\tau + \mu\kappa z + c_1z_\tau = F \sin(\Omega\tau) \quad (14.6)$$

where $x = X/w$, $y = Y/w$ and $z = Z/w$, w is a factor of normalization of length, subscripts τ represent differentiation with respect to normalized time, and the non-dimensional parameters governing the system dynamics are defined as follows:

$$\omega_0^2 = \frac{K_2}{m}, \Omega = \frac{\omega}{\omega_0}, F = \frac{P\Omega^2}{w}, \mu = \frac{m}{M}, \kappa = \frac{K_1}{K_2},$$

$$\gamma = \frac{\alpha w^2}{K_2}, \chi = \frac{\beta w^4}{K_2}, c_1 = \frac{C_1}{M\omega_0^2}, c_2 = \frac{C_2}{m\omega_0^2} \quad (14.7)$$

It is noteworthy that the parameter κ is used as a measure of tank flexibility. Specifically, $\kappa \rightarrow \infty$ corresponds to the case of a perfectly rigid tank.

14.3 Numerical Study

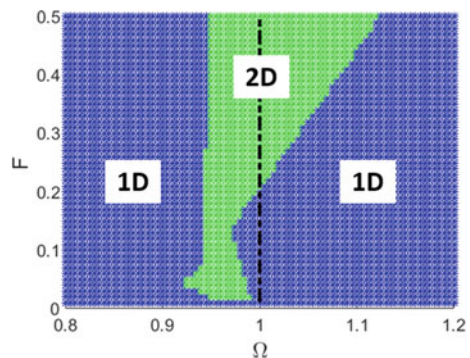
14.3.1 Effect of Finite Vessel Stiffness on the Critical Excitation Amplitude

Preliminary numerical study showed that 2D motion, which is related to swirling, is formed merely in the vicinity of primary resonance ($\Omega = 1$). These results are encouraging as they are consistent with all past studies treated rotary sloshing. Figure 14.3 presents an example of a typical phase diagram of (14.6), in which simulations resulting in one-dimensional (1D) and two-dimensional (2D) motion are plotted in different colors, for different values of excitation amplitudes and excitation frequencies.

At this point, the comparison to Fig. 14.1 is called for. In accordance with Fig. 14.1, excitations with frequencies higher than resonance are required to be stronger in order for a rotary motion to transpire. Nevertheless, there is also a remarkable difference between this work and past analyzes. Previous studies showed that in frequencies slightly lower than resonance, chaotic motion is much likely to take place. In contrast with these findings, in the current model, chaos is exhibited only in specific cases (which will be discussed later on). One may witness this difference when comparing Figs. 14.3 and 14.1. Even so, it is important to bear in mind that the model suggested in this work is very simple and is not destined to fully describe the properties of three-dimensional dynamics in tank-liquid systems.

More numerical study was targeted at discovering whether there is a correlation between degree of vessel stiffness and formation of the 2D response. For this matter, additional simulations were performed to find the critical value of the excitation amplitude, F , in which the system response changes from one to two-dimensional, for various parameter sets. It was found that generally, as the flexibility of the vessel increases, so does the value of the excitation amplitude needed for the swirling regime to be formed. This trend is evident in Fig. 14.4. Nonetheless, some kind of spikes about the values $35 \leq \kappa \leq 45$ can also be exhibited in this figure. Interestingly, it

Fig. 14.3 Classification of response dimensions for different excitation amplitudes and excitation frequencies. Each point represents a simulation resulted in two-dimensional (green) or one-dimensional (blue) response. Simulation results are presented for $\mu = 0.2$, $\kappa = 50$, $c_1 = 0.07$, $c_2 = 0.01$, $\gamma = -0.15$ and $\chi = 0.025$



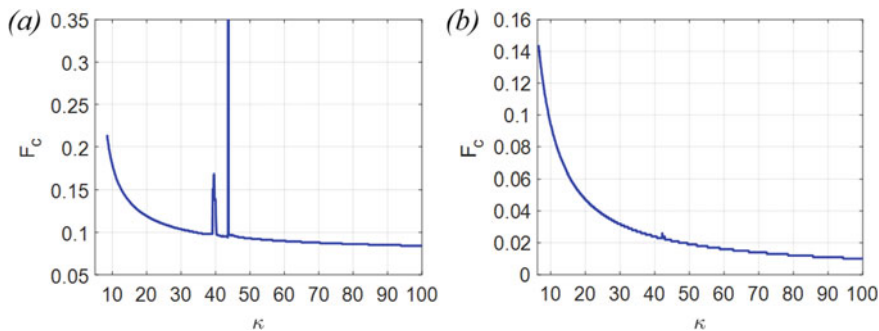


Fig. 14.4 Critical excitation amplitude, F_C , in which the system dynamics change from one-dimensional to two-dimensional response, for different values of κ : **a** $\Omega = 1$; **b** $\Omega = 0.98$. Simulation results are presented for $\mu = 0.2$, $c_1 = 0.001$, $c_2 = 0.001$, $\gamma = -0.06$ and $\chi = 0.01$

turns out that in this narrow parameter range, unstable chaotic motion is observed. This phenomenon takes place in the vicinity of 3:1 internal resonance, which will be discussed in Sect. 14.3.3.

14.3.2 Effect of Finite Vessel Stiffness and Finite Liquid Depth on the Sloshing Modes

The natural frequencies of (14.6) can be easily obtained by performing linearization about the trivial equilibrium point: $\bar{X}_s = (x, y, z, x_\tau, y_\tau, z_\tau) = 0$:

$$\begin{aligned} \omega_1^2 &= \frac{1}{2} \left[\mu(\kappa + 1) + 1 + \sqrt{[\mu(\kappa + 1) + 1]^2 - 4\mu\kappa} \right] \\ \omega_2^2 &= \frac{1}{2} \left[\mu(\kappa + 1) + 1 - \sqrt{[\mu(\kappa + 1) + 1]^2 - 4\mu\kappa} \right] \\ \omega_3^2 &= 1 \end{aligned} \tag{14.8}$$

Figure 14.5 displays the frequencies ω_1 and ω_2 versus κ for different values of μ . In this figure, the effect of tank flexibility and filling ratio on the sloshing modes is demonstrated: Higher flexibility of the tank or a higher filling ratio (which corresponds to smaller values of μ) leads to a decrease in the natural frequencies. As κ reaches infinity, which corresponds to the case of a rigid tank, the natural frequency ω_2 gets closer to unity, which is the modal frequency of the uncoupled system. These results are consistent with results of previous works.

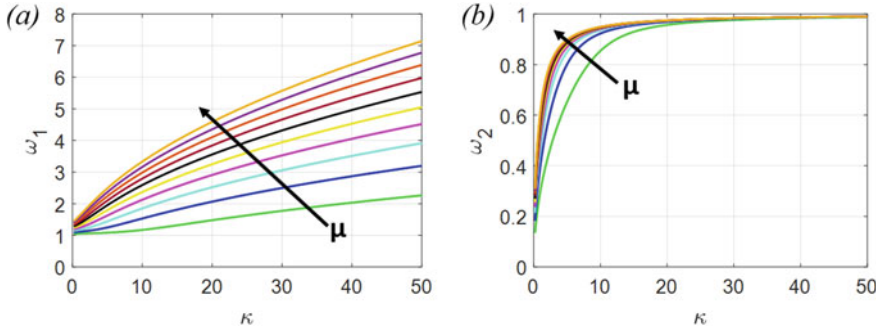


Fig. 14.5 Natural frequencies ω_1 (a) and ω_2 (b) versus κ for different values of μ . The following values of μ are presented: $\mu = 0.1, \mu = 0.2, \mu = 0.3, \mu = 0.4, \mu = 0.5, \mu = 0.6, \mu = 0.7, \mu = 0.8, \mu = 0.9, \mu = 1$

14.3.3 3:1 Internal Resonance

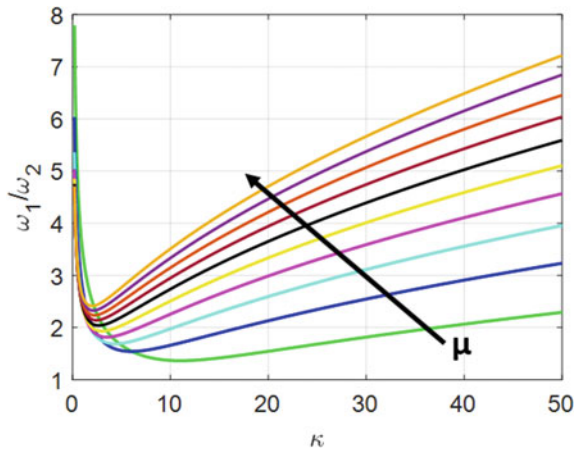
Following (14.8), the condition for 3:1 internal resonance can be determined by values of κ and μ that uphold:

$$9\mu^2\kappa^2 + 2\mu(9\mu - 41)\kappa + 9(\mu + 1)^2 = 0 \tag{14.9}$$

Clearly, the 3:1 internal resonance is obtained for different combinations of κ and μ (see Fig. 14.6). For example, for a mass ratio of $\mu = 0.2$, 3:1 this resonance is obtained for $\kappa \approx 42.8$.

To examine the effect of 3:1 internal resonance on system response, different numerical simulations have been carried out, in the vicinity of the internal resonance and far from it. All parameter values remained constant, except for κ which varied

Fig. 14.6 Natural frequencies ratio vs. κ for different values of μ . The following values of μ are presented: $\mu = 0.1, \mu = 0.2, \mu = 0.3, \mu = 0.4, \mu = 0.5, \mu = 0.6, \mu = 0.7, \mu = 0.8, \mu = 0.9, \mu = 1$



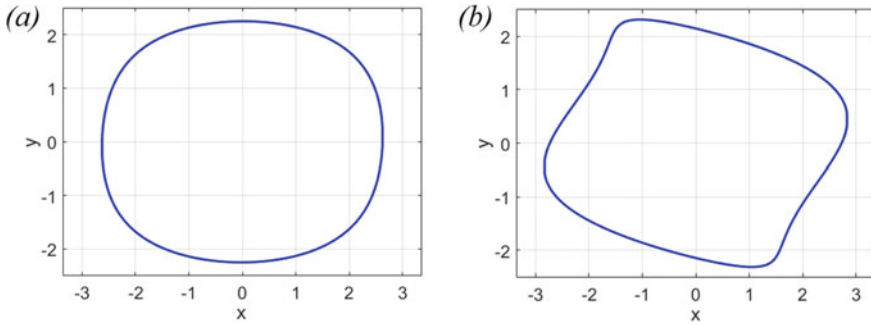


Fig. 14.7 Effect of 3:1 internal resonance in configurational space, $\mu = 0.2$. **a** System response for $\kappa = 45$, far from 3:1 internal resonance. **b** System response for $\kappa = 42.8$, at 3:1 internal resonance. Simulation results are presented for $\Omega = 1$, $F = 0.28$, $c_1 = 0.03$, $c_2 = 0.01$, $\gamma = -0.15$ and $\chi = 0.025$

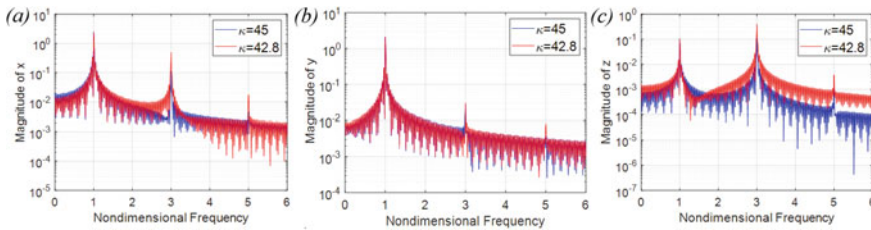


Fig. 14.8 Effect of 3:1 internal resonance - $\mu = 0.2$. FFT of x (a), y (b) and z (c) signals, for $\kappa = 45$ (blue) and $\kappa = 42.8$ (red). Simulation results are presented for $\Omega = 1$, $F = 0.28$, $c_1 = 0.03$, $c_2 = 0.01$, $\gamma = -0.15$ and $\chi = 0.025$

to study its impact. Fast Fourier transforms (FFT) were performed to exemplify the significance of the modes. It is shown that far from 3:1 internal resonance, the first mode is substantially more dominant than the others. As κ approaches the value that corresponds to 3:1 resonance, the following mode is amplified. To illustrate this point, numerical results are presented in Figs. 14.7 and 14.8. It is noteworthy that in the vicinity of 3:1 internal resonance, the system exhibited a chaotic response. This type of response will be discussed in Sect. 14.3.4.2.

14.3.4 Effect of Finite Vessel Stiffness on the Formation of Chaotic Response

Numerical exploration revealed the existence of unstable regimes in two cases: for very flexible tanks and in the vicinity of 3:1 internal resonance. These regimes were characterized as chaotic by evaluating the Lyapunov exponents— asymptotic quantities commonly used to describe the rate of convergence or separation of two close

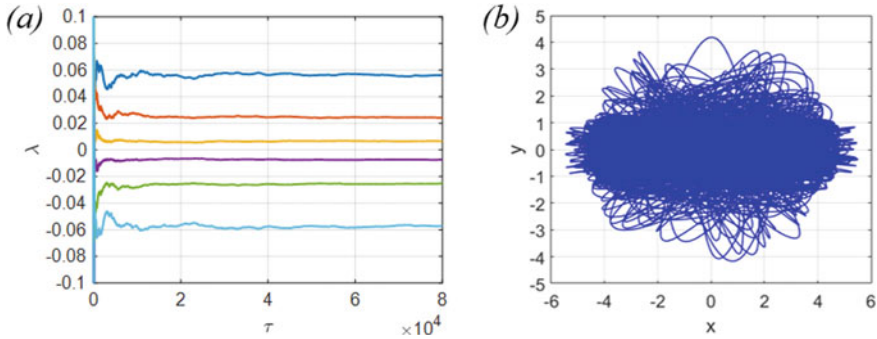


Fig. 14.9 Chaos in very flexible tanks. **a** Evolution of Lyapunov exponents; **b** System response. Simulation results are presented for $\Omega = 1$, $F = 0.278$, $\mu = 0.2$, $\kappa = 8$, $c_1 = 0.001$, $c_2 = 0.001$, $\gamma = -0.06$ and $\chi = 0.01$

trajectories and thus indicate chaotic behavior. If we consider an initial deviation from a specific trajectory, $\bar{\delta}(0)$, and describe its evolution by:

$$\bar{\delta}(t) = e^{\lambda t} \bar{\delta}(0) \tag{14.10}$$

Then, the Lyapunov exponents are defined as:

$$\Lambda = \lambda = \lim_{t \rightarrow \infty} \frac{1}{t} \ln \left(\frac{\|\bar{\delta}(t)\|}{\|\bar{\delta}(0)\|} \right) \tag{14.11}$$

A dynamical system with at least one positive Lyapunov exponent is considered chaotic. In this work, the Lyapunov exponents are calculated with the help of Govorukhin (2004), which is based on an algorithm suggested by Wolf et al. (1985).

14.3.4.1 Chaos in Very Flexible Tanks

Chaos was exhibited for small values of κ and for relatively small damping coefficients. An example is illustrated in Fig. 14.9, which shows there are three positive exponents.

14.3.4.2 Chaos in the Vicinity of Internal Resonance

Simulations which were carried out in the vicinity of 3:1 internal resonance revealed the existence of an unstable regime in a narrow range of parameter sets (see Fig. 14.4). The formation of this regime is demonstrated in Fig. 14.10. Positive Lyapunov exponents indicate chaotic behavior, as shown in Fig. 14.11.

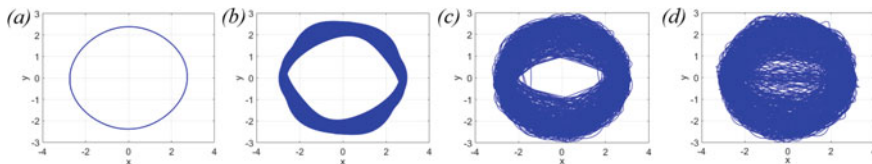
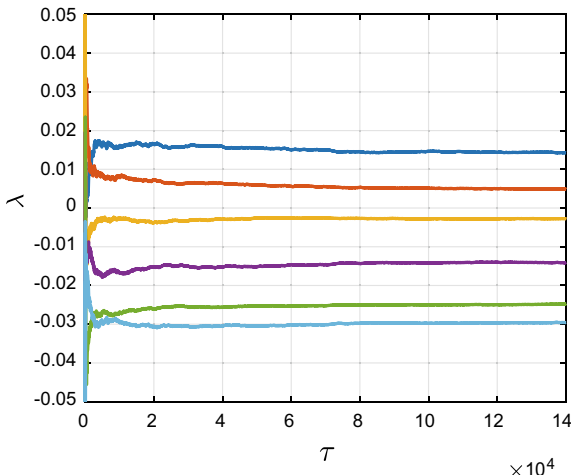


Fig. 14.10 Formation of chaotic response when approaching 3:1 internal resonance with $\mu = 0.2$. Linear stiffness parameter value: from left to right: $\kappa = 35, \kappa = 38, \kappa = 39, \kappa = 39.42$. Simulation results are presented for $\Omega = 1, F = 0.28, c_1 = 0.03, c_2 = 0.01, \gamma = -0.15$ and $\chi = 0.025$

Fig. 14.11 Evolution of Lyapunov exponents in the vicinity of 3:1 internal resonance with $\mu = 0.2$. Simulation results are presented for $\Omega = 1, F = 0.28, \kappa = 39.42, c_1 = 0.03, c_2 = 0.01, \gamma = -0.15$ and $\chi = 0.025$



14.4 Analytical Treatment

In order to study the transition from one-dimensional to two-dimensional response, we firstly focused on one-dimensional motion. This means that (14.6) can be reduced to:

$$\begin{aligned}
 x_{\tau\tau} + (1 + \mu)(1 + \gamma x^2 + \chi x^4)x + (1 + \mu)c_2 x_\tau - \mu \kappa z - c_1 z_\tau &= 0 \\
 z_{\tau\tau} + \mu \kappa z - \mu(1 + \gamma x^2 + \chi x^4)x - \mu c_2 x_\tau + c_1 z_\tau &= F \sin(\Omega\tau) \quad (14.12)
 \end{aligned}$$

Supposing that the first harmonic is the most dominant allows us to use the ansatz:

$$\begin{aligned}
 x &= \alpha_x \cos(\Omega\tau) + \beta_x \sin(\Omega\tau) \\
 z &= \alpha_z \cos(\Omega\tau) + \beta_z \sin(\Omega\tau) \quad (14.13)
 \end{aligned}$$

where $\alpha_x, \beta_x, \alpha_z$ and β_z are slowly varying amplitudes ($\alpha_j = \alpha_j(\varepsilon\tau), \beta_j = \beta_j(\varepsilon\tau)$). Differentiation of (14.13) while neglecting insignificant terms ($O(\varepsilon^2)$) yields:

$$\begin{aligned}
x_\tau &= [\alpha_{x\tau} + \beta_x \Omega] \cos(\Omega\tau) + [\beta_{x\tau} - \alpha_x \Omega] \sin(\Omega\tau) \\
x_{\tau\tau} &= [2\Omega\beta_{x\tau} - \Omega^2\alpha_x] \cos(\Omega\tau) - [2\Omega\alpha_{x\tau} + \Omega^2\beta_x] \sin(\Omega\tau) \\
z_\tau &= [\alpha_{z\tau} + \beta_z \Omega] \cos(\Omega\tau) + [\beta_{z\tau} - \alpha_z \Omega] \sin(\Omega\tau) \\
z_{\tau\tau} &= [2\Omega\beta_{z\tau} - \Omega^2\alpha_z] \cos(\Omega\tau) - [2\Omega\alpha_{z\tau} + \Omega^2\beta_z] \sin(\Omega\tau) \quad (14.14)
\end{aligned}$$

As a first step, in order to find the fixed points, amplitude derivatives of (14.14) are eliminated ($\alpha_{x\tau} = \beta_{x\tau} = \alpha_{z\tau} = \beta_{z\tau} = 0$). Substituting (14.13) and (14.14) to (14.12) and balancing the harmonics yield the following equations:

$$\begin{aligned}
& -\Omega^2\alpha_x + (1 + \mu) \left[1 + \frac{3}{4}\gamma(\alpha_x^2 + \beta_x^2) + \frac{5}{8}\chi(\alpha_x^2 + \beta_x^2)^2 \right] \\
& \quad \alpha_x + (1 + \mu)\Omega c_2\beta_x - \mu\kappa\alpha_z - \Omega c_1\beta_z = 0 \\
& -\Omega^2\beta_x + (1 + \mu) \left[1 + \frac{3}{4}\gamma(\alpha_x^2 + \beta_x^2) + \frac{5}{8}\chi(\alpha_x^2 + \beta_x^2)^2 \right] \\
& \quad \beta_x - (1 + \mu)\Omega c_2\alpha_x - \mu\kappa\beta_z + \Omega c_1\alpha_z = 0 \\
& -\Omega^2\alpha_z - \mu \left[1 + \frac{3}{4}\gamma(\alpha_x^2 + \beta_x^2) + \frac{5}{8}\chi(\alpha_x^2 + \beta_x^2)^2 \right] \\
& \quad \alpha_x - \Omega\mu c_2\beta_x + \mu\kappa\alpha_z + \Omega c_1\beta_z = 0 \\
& -\Omega^2\beta_z - \mu \left[1 + \frac{3}{4}\gamma(\alpha_x^2 + \beta_x^2) + \frac{5}{8}\chi(\alpha_x^2 + \beta_x^2)^2 \right] \\
& \quad \beta_x + \Omega\mu c_2\alpha_x + \mu\kappa\beta_z - \Omega c_1\alpha_z = F \quad (14.15)
\end{aligned}$$

(14.15) may yield up to five different combinations of α_x , β_x , α_z and β_z . Each combination represents a possible stationary solution of (14.12). Mathematically, some of these solutions can be complex. We are interested only in the real solutions. Stationary solutions will be denoted by subscript "s" further on in this work.

In order to determine whether the solutions of (14.15) are locally stable, one should analyze the response to small perturbations. In order to perform this analysis, slow-flow equations need to be obtained. For this matter, (14.14) is reexamined. Substitution of (14.13) and (14.14) to (14.12) yields:

$$\begin{aligned}
\alpha_{x\tau} &= A_{11}\alpha_x + A_{12}\beta_x + A_{13}\alpha_z + A_{14}\beta_z \\
& \quad + \left[1 + \frac{3}{4}\gamma(\alpha_x^2 + \beta_x^2) + \frac{5}{8}\chi(\alpha_x^2 + \beta_x^2)^2 \right] (B_{11}\alpha_x + B_{12}\beta_x) + C_{11} \\
\beta_{x\tau} &= -A_{12}\alpha_x + A_{11}\beta_x - A_{14}\alpha_z + A_{13}\beta_z \\
& \quad + \left[1 + \frac{3}{4}\gamma(\alpha_x^2 + \beta_x^2) + \frac{5}{8}\chi(\alpha_x^2 + \beta_x^2)^2 \right] (-B_{12}\alpha_x + B_{11}\beta_x) + C_{21} \\
\alpha_{z\tau} &= A_{21}\alpha_x + A_{22}\beta_x + A_{23}\alpha_z + A_{24}\beta_z \\
& \quad + \left[1 + \frac{3}{4}\gamma(\alpha_x^2 + \beta_x^2) + \frac{5}{8}\chi(\alpha_x^2 + \beta_x^2)^2 \right] (B_{21}\alpha_x + B_{22}\beta_x) + C_{31} \\
\beta_{z\tau} &= -A_{22}\alpha_x + A_{21}\beta_x - A_{24}\alpha_z + A_{23}\beta_z \\
& \quad + \left[1 + \frac{3}{4}\gamma(\alpha_x^2 + \beta_x^2) + \frac{5}{8}\chi(\alpha_x^2 + \beta_x^2)^2 \right] (-B_{22}\alpha_x + B_{21}\beta_x) + C_{41} \quad (14.16)
\end{aligned}$$

Coefficients A_{ij} , B_{ij} , C_{ij} are defined in the Appendix. The Jacobian matrix of (14.16) can be derived and defined as follows:

$$J_{SF_{\bar{x}=\bar{x}_s}} = \begin{bmatrix} J_{11} & J_{12} & A_{13} & A_{14} \\ J_{21} & J_{22} & -A_{14} & A_{13} \\ J_{31} & J_{32} & A_{23} & A_{24} \\ J_{41} & J_{42} & -A_{24} & A_{23} \end{bmatrix} \quad (14.17)$$

where coefficients J_{ij} are expressed as follows:

$$\begin{aligned} J_{11} &= A_{11} + S_1(B_{11}\alpha_{x_s} + B_{12}\beta_{x_s})\alpha_{x_s} + S_2B_{11} \\ J_{21} &= -A_{12} + S_1(-B_{12}\alpha_{x_s} + B_{11}\beta_{x_s})\alpha_{x_s} - S_2B_{12} \\ J_{31} &= A_{21} + S_1(B_{21}\alpha_{x_s} + B_{22}\beta_{x_s})\alpha_{x_s} + S_2B_{21} \\ J_{41} &= -A_{22} + S_1(-B_{22}\alpha_{x_s} + B_{21}\beta_{x_s})\alpha_{x_s} - S_2B_{22} \\ J_{12} &= A_{12} + S_1(B_{11}\alpha_{x_s} + B_{12}\beta_{x_s})\beta_{x_s} + S_2B_{12} \\ J_{22} &= A_{11} + S_1(-B_{12}\alpha_{x_s} + B_{11}\beta_{x_s})\beta_{x_s} + S_2B_{11} \\ J_{32} &= A_{22} + S_1(B_{21}\alpha_{x_s} + B_{22}\beta_{x_s})\beta_{x_s} + S_2B_{22} \\ J_{42} &= A_{21} + S_1(-B_{22}\alpha_{x_s} + B_{21}\beta_{x_s})\beta_{x_s} + S_2B_{21} \end{aligned} \quad (14.18)$$

and:

$$\begin{aligned} S_1 &= \frac{3\gamma}{2} + \frac{5\chi(\alpha_{x_s}^2 + \beta_{x_s}^2)}{2} \\ S_2 &= 1 + \frac{1}{2}(\alpha_{x_s}^2 + \beta_{x_s}^2)S_1 \end{aligned} \quad (14.19)$$

Eigenvalues of (14.17) can be calculated for each set of α_{x_s} , β_{x_s} , α_{z_s} and β_{z_s} . Fixed solutions which yield Jacobian eigenvalues that lie in the open left half plane (OLHP) will be defined as stable.

Figure 14.12 is an example of a bifurcation diagram which displays some of the possible solutions of (14.15), for varying values of excitation amplitudes. Adjacent fixed points which formed continua are represented by continuous curves or branches. A branch comprising stable fixed points is considered stable, whereas a branch consisting of unstable solutions is considered unstable. Solid and dashed lines represent stable and unstable branches, respectively. In order to evaluate the accuracy of these branches, numerical simulation results of the full system, (14.6), for the same parameter sets, are also plotted. Different initial conditions were examined.

It seems that generally, for the same set of parameters, different initial conditions may yield up to two different solutions, which are located on two different branches. When the excitation amplitude is varied, the solutions “jump” between branches. For relatively small excitation amplitudes and about the critical amplitude, there is a satisfactory correspondence between the full numerical solution and the branches

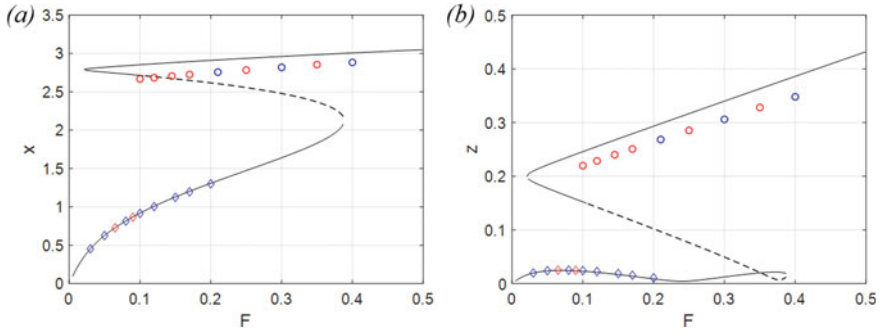


Fig. 14.12 Comparison between numerical simulation results and solutions obtained by harmonic balancing for $\kappa = 20$ and $\Omega = 1$. The black line represents the stable (solid) and unstable (dashed) analytical solutions. The diamonds and circles represent full numerical simulation results: Diamonds represent 1D response, whereas circles represent 2D response. Different colors represent different initial conditions. Simulation results are presented for $\mu = 0.2$, $c_1 = 0.07$, $c_2 = 0.01$, $\gamma = -0.15$ and $\chi = 0.025$

obtained by the harmonic balance. This means that the first harmonic is the dominant one in these cases. However, as the excitation amplitude increases and becomes greater than the critical excitation amplitude, this fit becomes poor, and the branches fail to predict the system response. This is also true concerning all cases in which more than one mode takes part in the dynamics. This point is emphasized in Figs. 14.13 and 14.14.

In addition, Figs. 14.15, 14.16 and 14.17 present three types of frequency responses. For small excitation amplitudes, we get a softening effect, whereas for relatively larger excitation amplitudes, we get a hardening effect. This finding is

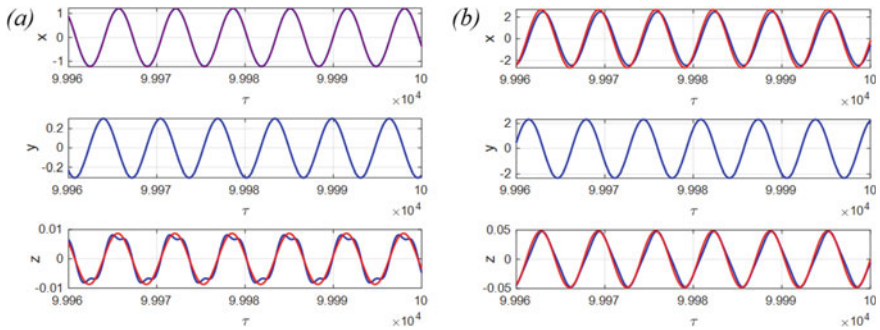


Fig. 14.13 Time series comparison between numerical simulation results (blue) and the analytical solution (red), for $\kappa = 70$ and $\Omega = 0.97$. The significance of the second mode is not reflected in the HB solution for z for some initial conditions. Simulation results are presented for $F = 0.1$, $\mu = 0.2$, $c_1 = 0.03$, $c_2 = 0.01$, $\gamma = -0.15$ and $\chi = 0.025$. **a** Initial conditions: $x_0 = 0.5$, $x_{\tau_0} = y_0 = y_{\tau_0} = z_0 = z_{\tau_0} = 0$; **b** Initial conditions: $x_0 = 2.5$, $x_{\tau_0} = y_0 = y_{\tau_0} = z_0 = z_{\tau_0} = 0$

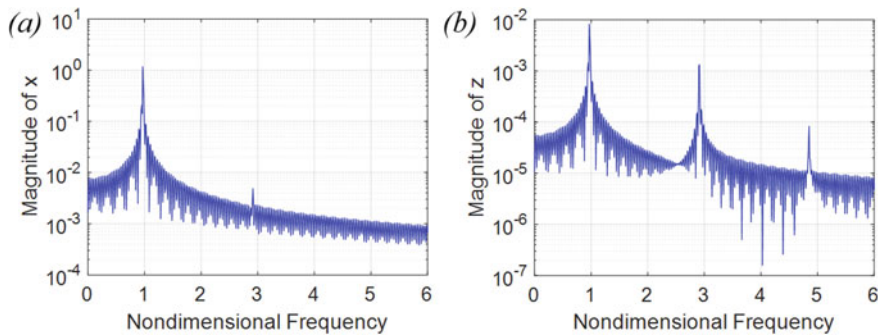


Fig. 14.14 FFT diagrams of x (a) and z (b), with the same parameter set and initial conditions as for Fig. 14.13a

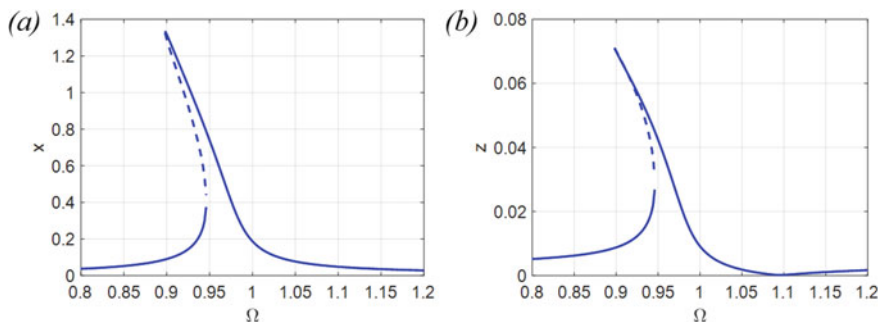


Fig. 14.15 Frequency response graph for $F = 0.01$. Softening nonlinearity is exhibited. Results are presented for $\mu = 0.2$, $\kappa = 20$, $c_1 = 0.07$, $c_2 = 0.01$, $\gamma = -0.15$ and $\chi = 0.025$

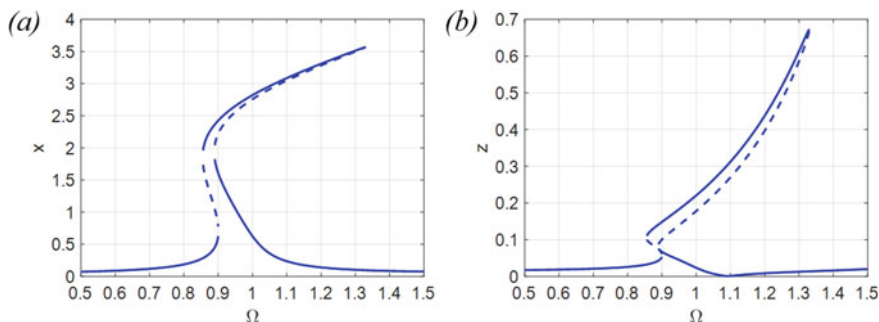


Fig. 14.16 Frequency response graph for $F = 0.05$. A sort of combination of softening and hardening nonlinearities is exhibited. Results are presented for $\mu = 0.2$, $\kappa = 20$, $c_1 = 0.07$, $c_2 = 0.01$, $\gamma = -0.15$ and $\chi = 0.025$

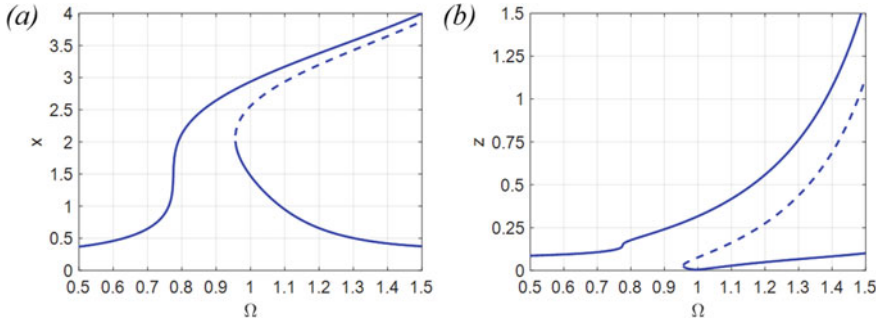


Fig. 14.17 Frequency response graph for $F = 0.25$. Hardening nonlinearity is exhibited. Results are presented for $\mu = 0.2$, $\kappa = 20$, $c_1 = 0.07$, $c_2 = 0.01$, $\gamma = -0.15$ and $\chi = 0.025$

consistent with previous analytical works, which argued that planar waves are related to softening nonlinearity and swirling—to hardening nonlinearity.

For intermediate values of the excitation amplitudes, we get a sort of combination of softening and hardening response. There is a possible reason for this unique shape: In the previous sections, it was found that the critical excitation amplitude is much lower for frequencies in the vicinity of primary resonance, than those for resonant frequencies. Thus, there is a wide range of excitation amplitudes which are strong enough to cause 2D motion in the vicinity of resonance, but not strong enough to trigger this bifurcation at resonance. This makes as reasonable for both softening and hardening characteristics to exist in the same frequency response graph.

14.5 Discussion and Concluding Remarks

This work is aimed at describing the transition between two-dimensional liquid sloshing and three-dimensional swirling motion, in a flexible cylindrical tank, under external horizontal excitation. For this matter, a reduced-order model was introduced.

It was shown that rotary sloshing in flexible containers is formed in the case of higher excitation amplitudes. This finding is reasonable. In the general case in which the liquid-tank system is horizontally excited, the liquid has to obtain a critical amount of energy to bifurcate to the swirling motion. In flexible containers, some of this energy is converted to a strain energy. Thus, more energy is required to enter the system to form the rotary sloshing.

Further numerical exploration revealed the existence of chaos in very flexible tanks with relatively small damping coefficients and in the vicinity of internal resonance. This regime was validated by determination of positive Lyapunov exponents and simulations of the system with different initial conditions.

One-dimensional motion was assumed (i.e., $y = 0$), and simple harmonic balancing was performed. It was demonstrated that in most cases, balancing the first harmonic provides a satisfactory agreement with numerical simulations of the

full system. However, it was found to be inaccurate in relatively high excitation amplitudes or in any case where additional modes become significant.

The considered model succeeds in predicting the features of fluid-structure interaction in coupled liquid-tank systems. It also succeeds in exhibiting softening nonlinearity of planar waves and hardening nonlinearity of rotary waves, in accordance with previous works. The model makes it possible to study the dependence of the transition to the swirling on the vessel stiffness, a subject which, as far as we know, has yet to be studied. Moreover, it allows to reveal more interesting dynamical phenomena of liquid sloshing which take place in very flexible tanks.

Acknowledgements The authors are grateful to PAZY Foundation (grant 298/18) for financial support.

Appendix

$$A_{11} = -\frac{c_2\Omega^2[4(\mu+1)\Omega^2+c_1^2]}{16\Omega^4+[4(\mu+1)^2c_2^2+8\mu c_1c_2+4c_1^2]\Omega^2+c_1^2c_2^2}$$

$$A_{12} = -\frac{\Omega\{8\Omega^4+[4(\mu+1)^2c_2^2+6\mu c_1c_2+2c_1^2]\Omega^2+c_1^2c_2^2\}}{16\Omega^4+[4(\mu+1)^2c_2^2+8\mu c_1c_2+4c_1^2]\Omega^2+c_1^2c_2^2}$$

$$A_{13} = -\frac{\Omega^2\{-4\Omega^2c_1+[c_1^2-4\mu\kappa(1+\mu)]c_2-4\mu\kappa c_1\}}{16\Omega^4+[4(\mu+1)^2c_2^2+8\mu c_1c_2+4c_1^2]\Omega^2+c_1^2c_2^2}$$

$$A_{14} = \frac{2\Omega\{[c_1c_2(1+\mu)+c_1^2-4\mu\kappa]\Omega^2+\mu\kappa c_1c_2\}}{16\Omega^4+[4(\mu+1)^2c_2^2+8\mu c_1c_2+4c_1^2]\Omega^2+c_1^2c_2^2}$$

$$A_{21} = -\frac{\mu c_2\Omega^2[-4\Omega^2+c_1c_2]}{16\Omega^4+[4(\mu+1)^2c_2^2+8\mu c_1c_2+4c_1^2]\Omega^2+c_1^2c_2^2}$$

$$A_{22} = \frac{2\Omega^3\mu c_2[(1+\mu)c_2+c_1]}{16\Omega^4+[4(\mu+1)^2c_2^2+8\mu c_1c_2+4c_1^2]\Omega^2+c_1^2c_2^2}$$

$$A_{23} = -\frac{4\Omega^4c_1+[c_1(1+\mu)c_2^2+4c_2\mu^2\kappa+4\mu\kappa c_1]\Omega^2+\mu\kappa c_1c_2^2}{16\Omega^4+[4(\mu+1)^2c_2^2+8\mu c_1c_2+4c_1^2]\Omega^2+c_1^2c_2^2}$$

$$A_{24} = - \frac{\{8\Omega^4 + [2(1 + \mu)^2 c_2^2 + 6\mu c_1 c_2 + 4c_1^2 - 8\mu\kappa]\Omega^2 - c_2^2(2\kappa\mu^2 - c_1^2 + 2\mu\kappa)\}\Omega}{16\Omega^4 + [4(\mu + 1)^2 c_2^2 + 8\mu c_1 c_2 + 4c_1^2]\Omega^2 + c_1^2 c_2^2}$$

$$B_{11} = - \frac{[4(1 + \mu)^2 c_2 + 4\mu c_1]\Omega^2 + c_1^2 c_2}{16\Omega^4 + [4(\mu + 1)^2 c_2^2 + 8\mu c_1 c_2 + 4c_1^2]\Omega^2 + c_1^2 c_2^2}$$

$$B_{12} = - \frac{2A_{11}}{\Omega c_2}$$

$$B_{21} = \frac{2A_{22}}{\Omega c_2}$$

$$B_{22} = - \frac{2A_{21}}{\Omega c_2}$$

$$C_{11} = - \frac{F c_1 A_{22}}{\Omega^2 c_2 \mu}$$

$$C_{21} = - \frac{F c_1 A_{21}}{\Omega^2 c_2 \mu}$$

$$C_{31} = - \frac{2[(1 + \mu)^2 c_2^2 + \mu c_1 c_2 + 4\Omega^2]\Omega F}{16\Omega^4 + [4(\mu + 1)^2 c_2^2 + 8\mu c_1 c_2 + 4c_1^2]\Omega^2 + c_1^2 c_2^2}$$

$$C_{41} = \frac{[(1 + \mu)c_2^2 + 4\Omega^2]c_1 F}{16\Omega^4 + [4(\mu + 1)^2 c_2^2 + 8\mu c_1 c_2 + 4c_1^2]\Omega^2 + c_1^2 c_2^2}$$

References

- Abramson, H.N.: The Dynamic Behavior of Liquids in Moving Containers. NASA Spec. Publ. 106 (1966)
- Balendra, T., Ang, K.K., Paramasivam, P., Lee, S.L.: Seismic design of flexible cylindrical liquid storage tanks. *Earthq. Eng. Struct. Dyn.* **10**, 477–496 (1982)
- Barton, D.C., Parker, J.V.: Finite element analysis of the seismic response of anchored and unanchored liquid storage tanks. *Earthq. Eng. Struct. Dyn.* **15**, 299–322 (1987)
- Bauer, H.F.: Nonlinear mechanical model for the description of propellant sloshing. *AIAA J.* **4**, 1662–1668 (1966)

- Bauer, H.F., Hsu, T.-M., Wang, J.T.-S.: Liquid Sloshing in Elastic Containers. NASA CR-882 (1967)
- Dodge, F.T.: Analytical Representation of Lateral Sloshing by Equivalent Mechanical Models. The Dynamic Behavior of Liquids in Moving Containers. NASA SP-106. (1966)
- Faltinsen, O.M., Rognebakke, O.F., Timokha, A.N.: Resonant three-dimensional nonlinear sloshing in a square-base basin. Part 2. Effect of higher modes. *J. Fluid Mech.* **523**, 199–218 (2005)
- Faltinsen, O.M., Rognebakke, O.F., Timokha, A.N.: Resonant three-dimensional nonlinear sloshing in a square-base basin. Part 3. Base ratio perturbations. *J. Fluid Mech.* **551**, 93–116 (2006)
- Faltinsen, O.M., Rognebakke, O.F., Timokha, A.N.: Resonant three-dimensional nonlinear sloshing in a square-base basin. *J. Fluid Mech.* **487**, 1–42 (2003)
- Faltinsen, O.M., Lukovsky, I.A., Timokha, A.N.: Resonant sloshing in an upright annular tank. *J. Fluid Mech.* **804**, 608–645 (2016)
- Farid, M., Gendelman, O.V.: Internal resonances and dynamic responses in equivalent mechanical model of partially liquid-filled vessel. *J. Sound Vib.* **379**, 191–212 (2016)
- Fischer, D.: Dynamic fluid effects in liquid-filled flexible cylindrical tanks. *Earthq. Eng. Struct. Dyn.* **7**, 587–601 (1979)
- Fischer, F.D., Rammerstorfer, F.G.: A refined analysis of sloshing effects in seismically excited tanks. *Int. J. Press. Vessel. Pip.* **76**, 693–709 (1999)
- Govorukhin, V.: Calculation Lyapunov Exponents for ODE. MATLAB Central File-Exchange (2004)
- Haroun, M.A., Housner, G.W.: Seismic design of liquid storage tanks. *J. Tech. Coun. ASCE.* **107**, 191–207 (1981)
- Housner, G.W.: Dynamic pressures on accelerated fluid containers. *Bull. Seismol. Soc. Am.* **47**, 15–35 (1957)
- Housner, G.W.: The dynamic behavior of water tanks. *Bull. Seismol. Soc. Am.* **53**, 381–387 (1963)
- Ibrahim, R.A.: Multiple internal resonance in a structure-liquid system. *J. Eng. Ind.* **98**, 1092 (1976)
- Ibrahim, R.A., Barr, A.D.S.: Autoparametric resonance in a structure containing a liquid, part I: Two mode interaction. *J. Sound Vib.* **42**, 159–179 (1975a)
- Ibrahim, R.A., Barr, A.D.S.: Autoparametric resonance in a structure containing a liquid, part II: Three mode interaction. *J. Sound Vib.* **42**, 181–200 (1975b)
- Ibrahim, R.A.: *Liquid Sloshing Dynamics: Theory and Applications.* (2005)
- Jolie, M., Hassan, M.M., El Damatty, A.A.: Assessment of current design procedures for conical tanks under seismic loading. *Can. J. Civ. Eng.* **40**, 1151–1163 (2013)
- Kana, D.D.: Validated spherical pendulum model for rotary liquid slosh. *J. Spacecr. Rockets.* **26**, 188–195 (1989)
- Miles, J.W.: Stability of forced oscillations of a spherical pendulum **2**, 21–32 (1961)
- Miles, J.: Resonant motion of a spherical pendulum. *Phys. D Nonlinear Phenom.* **11**, 309–323 (1984a)
- Miles, J.W.: Resonantly forced surface waves in a circular cylinder. *J. Fluid Mech.* **149**, 15–31 (1984b)
- Parkus, H.: Modes and frequencies of vibrating liquid-filled cylindrical tanks. *Int. J. Eng. Sci.* **20**, 319–326 (1982)
- Royon-Lebeaud, A., Hopfinger, E.J.: Liquid sloshing and wave breaking in circular and square-base cylindrical containers. *J. Fluid Mech.* **577**, 467–494 (2007)
- Tedesco, J.W., Landis, D.W., Kostem, C.N.: Seismic analysis of cylindrical liquid storage tanks. *Comput. Struct.* **32**, 1165–1174 (1989)
- Veletos, A.S.: Seismic effects in flexible liquid storage tanks. In: *Proceedings of the 5th World Conference on Earthquake Engineering*, pp. 630–639 (1974)
- Wolf, A., Swift, J.B., Swinney, H.L., Vastano, J.A.: Determining Lyapunov exponents from a time series. *Phys. D.* 285–317 (1985)
- Zou, C., Wang, D.: A simplified mechanical model with fluid—structure interaction for rectangular tank sloshing under horizontal excitation. *Adv. Mech. Eng.* **7**, 1–16 (2015)

Part V
Longtime Behavior of Engineering
Structures

Chapter 15

Analysis of Creep, Shrinkage, and Damage in Armored Concrete Dome at Static and Seismic Loading



Dmytro Breslavsky and Aleksandr Chuprynin

Abstract The main approaches and methods for studying creep and long-term strength of thin-walled structures made of concrete and reinforced concrete are considered. A mathematical formulation and a method for solving the creep-damage problem of thin-walled concrete elements under short-term and long-term loading, which makes it possible to determine their bearing capacity and long-term strength, are presented. An example of calculations the resistance to dynamic loading and long-term strength of a reinforced concrete dome is given.

Keywords Creep · Damage · Shrinkage · Concrete dome · Static and seismic loading

15.1 Introduction

With proper operation, reinforced concrete structures can serve indefinitely without reducing the bearing capacity. This is due to the fact that, unlike most other materials, the strength of concrete increases over time. However, with design errors, irreversible creep strains can increase significantly over time and reach critical values (Neville 1973). Microcracks and initial voids can appear in the concrete before any loads are applied (Baron and Sautgry 1982). The brittle fracture that occurs as a result of the growth of internal damage is highly dependent on the load type. At the same time, the rate of the damage accumulation increases at the last stages of loading the structure, eventually leading to the appearance of macroscopic defects or cracks (Lemaitre and Chaboche 1994).

It is well known that concrete has a strain delay effect, which determines its long-term mechanical behavior (Ulm et al. 2013) and the long-term strength of structures

D. Breslavsky (✉)

Department of Computer Modelling of Processes and Systems, National Technical University "Kharkiv Polytechnic Institute", Kharkiv 61002, Ukraine
e-mail: brdm@kpi.kharkov.ua

A. Chuprynin

Department of Theoretical and Building Mechanics, O.M. Beketov National University of Urban Economy, Kharkiv 61002, Ukraine

(Tanabe et al. 2013). Ensuring reliable and safe operation of building concrete and reinforced concrete structures, in particular, those that correspond to the models of plates and shells, necessitates the development of adequate models, calculations using which can confirm the fact of safe operation during the design period.

Creep models for concrete should take into account several important phenomena that significantly affect the behavior of structures during long-term operation (Sellier et al. 2016). When constructing the constitutive equations, the characteristic of the water content varying in concrete is of great importance, which, in turn, depends on operational factors, such as temperature and humidity of the environment, as well as the contact area of the structure with open air (Rossi et al. 2012; Jennings et al. 2013). Analysis of experimental results on long-term deformation of concrete makes it possible to formulate the corresponding constitutive equations that describe its creep and shrinkage, to determine the values of constants included in them (Hubler et al. 2015; RILEM 2015). For specific materials often used in thin-walled building structures, data were obtained on their sensitivity to creep and shrinkage (Bazant 2000). These data are processed in order to concretize the constitutive equations (Torrenti and Le Roy 2018) based on data that determine the influence of various factors on the rate of creep and shrinkage of concrete. The influence of temperature (Gernay 2012) and relative humidity on concrete aging (Gawin et al. 2007) is considered separately.

Analysis of the experimental data allows us to formulate recommendations for refining the existing calculation methods (Sakata et al. 2008). In the calculations of structures made of concrete and reinforced concrete, much attention has recently been paid to the investigation of the creep mechanism in the course of changes in the structure of the material over time, especially during drying and loading, which can ultimately lead to failure (Pignatelli et al. 2016). In addition, attention is paid to material tests not only for uniaxial loading, but also for biaxial loading, which also reflects the properties of a complex material—reinforced concrete (Charpin et al. 2018).

Thus, the improvement of methods for calculating reinforced concrete structural elements of complex shapes is one of the priority tasks arising in the design of buildings and structures (Mancinelli 1989; Bari 2000; Widiyanto 2006). The paper is devoted to the analysis of the long-term strength and creep of thin-walled reinforced concrete elements, the solution of which makes it possible to formulate recommendations necessary for the design of structures with a given resource, including taking into account possible seismic effects. The formulated constitutive equations include strains caused by creep and shrinkage of concrete and also describe the processes of damage accumulation in it. The problem is solved by the finite element method (FEM) combined with the finite difference method for solving the initial problem. The problem of creep of a reinforced concrete dome is considered as an example.

15.2 Problem Statement and Constitutive Equations

15.2.1 Problem Description

Let us consider the mathematical formulation of the problem of long-term deformation of thin-walled reinforced concrete structures, taking into account the possibility of dynamic effects due to seismic activity. Focusing on the calculation method, a conical shell of revolution is considered under arbitrary non-axisymmetric loading, which determines the shape of the finite element used. The classical approach of the theory of thin shells with finite deflections is applied to the physically nonlinear problem of deformation, including the description of the complex action of shrinkage together with creep and damage under static and dynamic action.

Let us consider an open conical shell. We use the equations of the Donnell shell theory (Donnell 1933) and use the assumption, that plane section are initially normal to the middle surface remain plane and normal to it, which is valid for thin shells (Volmir 1974). We consider the case when the deflections of the shell are commensurate with its thickness. So, for the coordinates $x_1 \equiv x$, $x_2 \equiv \varphi$, $x_3 \equiv z$, the static equations are obtained for the stress resultants reduced to the middle surface: transverse Q_{ii} , longitudinal N_{ij} and shear forces $N_{x\theta}$, $N_{\theta x}$; bending moments M_{ii} and moments $M_{x\varphi}$, $M_{\varphi x}$; $Q_{ii} = \int_{-h/2}^{h/2} \sigma_{zi} dz$, $i = x, \varphi$, $N_{ij} = \int_{-h/2}^{h/2} \sigma_{ij} dz$, $M_{ij} = \int_{-h/2}^{h/2} \sigma_{ij} z dz$, $i, j = x, \varphi$. These equations do not neglect the projections of the membrane forces on the middle surface, which may turn out to be significant during long-term creep deformation (Volmir 1974).

For the formulation of geometric equations, the deformed state is considered under the assumption that deflections can reach values of the same order of magnitude as the shell thickness, taking into account the assumption of an inextensible and incompressible material in the direction perpendicular to the median surface (Volmir 1974; Breslavsky et al. 2019). Strains in the shell can be described in terms of the deformation of the middle surface. Taking this into account, the linear (ε_{xx} , $\varepsilon_{\phi\phi}$) and angular ($\varepsilon_{x\phi}$) components of the deformed state are presented as the sum of the linear and nonlinear components.

Physical equations express the relationship between the stress $\underline{\underline{\sigma}}$ and strain $\underline{\underline{\varepsilon}}$ tensors. In the FE formulation of problems in the shell theory, it is customary to introduce the corresponding vectors that describe the stress and deformed states. We represent the stress vector in the following form: $\underline{\underline{\sigma}} = (N_{xx}, N_{\phi\phi}, N_{x\phi}, M_{xx}, M_{\phi\phi}, M_{x\phi})^T$. Using the accepted assumptions, the strains of an arbitrary point of the solid can be expressed through the values of strains of its middle surface $\varepsilon_{xx}^{[0]}$, $\varepsilon_{\phi\phi}^{[0]}$, $\varepsilon_{x\phi}^{[0]}$ and the varying in the corresponding curvatures (k_{xx} , $k_{\phi\phi}$, $k_{x\phi}$). We introduce a strain vector defined at the points of the middle surface of the shell: $\underline{\underline{\varepsilon}} = (\varepsilon_{xx}^{[0]}, \varepsilon_{\phi\phi}^{[0]}, \varepsilon_{x\phi}^{[0]}, k_{xx}, k_{\phi\phi}, k_{x\phi})^T$. Then we represent the physical equations as follows ($i, j = x, \varphi$; $k, l = x, \varphi$):

$$\sigma_{ij} = \bar{b}_{ijkl} \cdot (\varepsilon_{kl}^0 - c_{kl} - \varepsilon_{kl}^{(V)}) + z \cdot \bar{d}_{ijkl} \cdot (k_{kl} - \bar{k}_{kl}) \quad (15.1)$$

where c_{kl} is the components of the tensor of creep strains, $\varepsilon_{kl}^{(V)}$ is volumetric strains caused by temperature varying and concrete shrinkage. Specifying these equations will allow us to determine the forces and moments reduced to the middle surface (Breslavsky et al. 2019):

$$N_{ij} = b_{ijkl} \varepsilon_{kl}^{(l)} + N_{ij}^{(n)} - N_{ij}^{(V)} - N_{ij}^{(C)}, \quad M_{ij} = d_{ijkl} \chi_{kl} - M_{ij}^{(V)} - M_{ij}^{(C)} \quad (15.2)$$

where $\bar{b}_{ijkl} = b_{ijkl} / h$, $\bar{d}_{ijkl} = 12 \cdot d_{ijkl} / h^3$,

$$b_{ijkl} = B \cdot \left[\delta_{ik} \delta_{jl} \cdot \frac{(1-\nu)}{2} + \nu \cdot \delta_{ij} \delta_{kl} \right], \quad B = \frac{Eh}{(1-\nu^2)},$$

$$d_{ijkl} = D \cdot \left[\delta_{ik} \delta_{jl} \cdot \frac{(1-\nu)}{2} + \nu \cdot \delta_{ij} \delta_{kl} \right], \quad D = \frac{Eh^3}{12(1-\nu^2)}.$$

Here E is Young's modulus, ν is Poisson's ratio, δ_{ij} is Kronecker's delta, h is the shell thickness. Equation (15.2) contains both linear (l) and nonlinear (n) quadratic terms (Breslavsky et al. 2019), which allow us to decompose the strain state into linear and nonlinear parts: $\varepsilon_{ij}^{[0]} = \varepsilon_{ij}^{(l)} + \varepsilon_{ij}^{(n)}$.

In Eq. (15.2), the components of forces and moments depend on the nonlinear components of elastic strains as well as volume changes and creep process. They are defined as follows (Breslavsky et al. 2019): $N_{ij}^{(n)}$, $N_{ij}^{(C)}$, $N_{ij}^{(V)}$ are the components of membrane forces, which are caused by geometrically nonlinear strain components, irreversible creep strains, and changes in volume in the material, respectively; $M_{ij}^{(C)}$ and $M_{ij}^{(V)}$ are the moments reduced to the middle surface, determined by the influence of creep and volume changes.

15.2.2 Constitutive Equations

Let us represent volumetric strain in the following form (Bazant et al. 1993):

$$\varepsilon_{kl}^{(V)} = \varepsilon_{kl}^{(T)} + \varepsilon_{kl}^{(R)}, \quad \varepsilon_{ij}^{(T)} = \alpha_{ij} \Delta T, \quad \varepsilon_{ij}^{(R)} = \varepsilon_0^{(R)} \delta_{ij}, \quad \alpha_{ij} = \alpha_0 \delta_{ij}. \quad (15.3)$$

where $\varepsilon_{kl}^{(T)}$, $\varepsilon_{kl}^{(R)}$ are the temperature and shrinkage strains, α_0 is the coefficient of thermal expansion of concrete, $\varepsilon_0^{(R)}$ is the shrinkage mean strain (is proportional to the first invariant of shrinkage strain tensor). Currently, research shows that the shrinkage rate depends on many structural, technological, and physicochemical factors. In the design and strain analysis, the method of calculating shrinkage is often used, in which the strain components are calculated by the formula from EN 1992-2-1:

$$\varepsilon_{kl}^{(R)} = \varepsilon_{kl}^d + \varepsilon_{kl}^a \quad (15.4)$$

where $\varepsilon_{kl}^d = \beta_{ds} \varepsilon_{\infty}^d \delta_{kl}$ is the part of shrinkage, which is caused due to the evaporation of moisture from concrete (for waterproofing reinforced concrete structures $\beta_{as} \rightarrow 0$); $\varepsilon_{kl}^a = \beta_{as} \varepsilon_{\infty}^a \delta_{kl}$ is part caused by solidification processes (DIN EN 1992-1-1:2005-10); $\beta_{ds} = \frac{(t-t_s)}{0.04\sqrt{h_0^3+(t-t_s)}}$ is the function which reflects the shrinkage development in time; ε_{∞}^d is shrinkage limit value caused by evaporation of moisture; t is concrete age; t_s is age of concrete at the time of the finishing the wet storage period; $h_0 = \frac{2A_c}{u}$ (here A_c , u are the area and perimeter of the section of the element); $\beta_{as} = 1 - \exp(0.2t^{0.5})$ is the function of the shrinkage development in time; ε_{∞}^a is limit value of shrinkage caused by solidification processes.

The relationship between the components of the stress deviator at a point of the solid (taking into account that, according to the accepted hypotheses, the stresses on the areas parallel to the median surface are small compared to other stresses) and creep strains, taking into account the damageability of the material, are specified by the constitutive equations. Damage parameter ω (Lemaitre and Chaboche 1994) ($0 < \omega < 1$) can be considered as a characteristic of the inhomogeneity of a substance caused by the accumulation of hidden defects. For many materials, the hypothesis of isotropic damage is quite acceptable, which says that cracks and cavities with different orientations are uniformly distributed in all directions. The quantitative assessment of damage, as well as for any physical variable associated with the determination of the internal variables chosen to describe the phenomenon, is carried out indirectly, by investigations the properties of materials and the laws of its deformation.

The effect of long-term loading on the creep of concrete and reinforced concrete is taken into account based on the theory of aging. For this, obtained experimental curves are used and so-called isochrones are built for concretes of various classes. Each isochronous diagram corresponds to a certain moment of time t , and for each specific loading time the relationship between stress and strain “ $\sigma - \varepsilon$ ” is established, which can be represented in a form similar to Hooke’s law: $\varepsilon(t) = \frac{\sigma(t)}{E(t)}$. The normative values of the parameters for the “ $\sigma - \varepsilon$ ” diagram and their calculated values are known for different classes of concrete, depending on the compressive strength (Shmukler et al. 2010). At $t = 0$, the isochronous diagrams are conventional short-term deformation diagrams. For an arbitrary point of the solid under creep conditions, equations of state, that reflect the response of the system to the effect of the load and the environment, are formulated. At an arbitrary point in time, strains in concrete can be described by a dependence of the form (Prandtl 1925):

$$\varepsilon(\sigma, t) = \frac{\sigma(t)}{E(t)} (1 + C_0^*(t, \tau)) \quad (15.5)$$

where t is the time value at which the strain is determined; τ is the moment of time at which the load was applied; $C_0^*(t, \tau)$ is the creep measure, which designates the creep strain at time t from the action of an unit stress applied at time τ . The measure of creep can be determined by the following relationship:

$$C_0^*(t, \tau) = \xi \cdot \theta(\tau) \cdot (1 - e^{-\varphi(t-\tau)}) \tag{15.6}$$

where $\xi = [1.3 - 0.79 \cdot e^{-0.404m_0}] \cdot [1.27 - 0.01334 \cdot (\Phi - 40)] \cdot [1 + 0.0482 \cdot e^{(T-20)}]$ is the parameter that describes the conditional age of concrete; (m_0 is the part of structure in %, which is in contact with air (for waterproofing reinforced concrete structures $m_0 \rightarrow 0$); Φ is relative humidity; T is average working temperature; $\theta(\tau) = A_1/\tau + C_0$ is the function that reflects concrete aging; $A_1 = 0.7$ day, $C_0 = 0.5$ are the experimental constants (Klovnich 2009); φ [day⁻¹] is the coefficient allowing explicit time allocation in state equations, and which for concrete of various classes is varied from 2.2 to 2.5. The functions proposed here are constructed due to the condition of minimizing the number of approximating constants, which are determined from basic standard experiments.

When calculating the long-term strength, expressions (15.5-15.6) can be transformed taking into account the accumulated damage to estimate the time until the structure failure. In this case, the constitutive equations, which are written for the creep strains and damage parameter rates, are used. In practical calculations, taking into account the fact that the loads can change during operation, the creep equation should be represented using the hardening law. For a complex stress state (Rabotnov 1969):

$$\dot{c}_{ij} c_i^{\hat{\alpha}} = B \frac{(\sigma_i)^n}{(1 - \omega)^k} \sigma_{ij} \tag{15.7}$$

$$\dot{\omega} = D \frac{(\sigma)^m}{(1 - \omega)^l} \tag{15.8}$$

where c_{ij} is the components of irreversible creep strain and c_i the is von Mises equivalent creep strain; $\omega(t)$ is scalar damage parameter, $\omega(0)=0$, $\omega(t^*)=\omega^*$; ω^* is the value of the damage parameter at the moment of time t^* (the finish of the process of hidden damage accumulation). Here B, D, n, k, m, l and $\hat{\alpha}$ are constants describing the behavior of an isotropic material under prolonged loading.

In the case of presence of additional vibrational loading on the structure, for example due to seismic actions, Eqs. (15.7–15.8) take form (Rabotnov 1969; Breslavsky et al. 2014):

$$\dot{c}_{ij} c_i^{\hat{\alpha}} = BH(A) \frac{(\sigma_i)^n}{(1 - \omega)^k} \sigma_{ij} \tag{15.9}$$

$$\dot{\omega} = DK(A) \frac{(\sigma)^m}{(1 - \omega)^l} \tag{15.10}$$

where $A = \sigma_i^{(a)}/\sigma_i$ is the stress cycle asymmetry coefficient, σ_i is the von Mises equivalent stress, calculated by use of static stress components, σ_i^a is the von Mises equivalent stress, calculated by use of amplitude stress components;

$H(A) = \int_0^1 (1 + A \sin(2\pi\xi))^n d\xi$, $K(A) = \int_0^1 (1 + A \sin(2\pi\xi))^r d\xi$, are the functions reflecting the influence of the cyclic component of the load on the rate of accumulation of strains and damage parameters, respectively (Breslavsky et al. 2014).

15.2.3 Method of Numerical Modeling

In problems of the creep theory, the FEM equations include additional forces and moments from irreversible creep and volumetric strains, in particular, from concrete shrinkage. At an arbitrary point in time, the creep and shrinkage strains are assumed to be known. Using the standard FEM procedure (Zienkiewicz et al. 2014; Breslavsky et al. 2017), a system of differential equations for the vector of generalized nodal displacements is obtained. It is solved using finite difference procedures (Breslavsky et al. 2019). At each time step, the components of the vectors of displacements, strains, stresses, and damage parameters are determined. The number of nodes and, accordingly, elements in the scheme of spatial discretization of the investigated solid according to the FEM should be chosen so as to ensure the adequacy of the real process to the computational models. In calculations of creep and long-term strength in shells, such a correspondence is selected by numerical experiments from the analysis of the possibility of obtaining the effect of stress redistribution at points of the shell surface. In the calculations, the *SCC* software package (Breslavsky et al. 2014; Breslavsky et al. 2017) was used. It was designed for numerical simulation of creep-damage processes in thin shells of revolution under asymmetric loading. A comprehensive check of the method was also carried out by comparing the numerical results with the experimental ones obtained during a full-scale experiment on the creep of a reinforced concrete slab for 3 months (Shmukler et al. 2010).

15.3 Numerical Simulation of Spherical Dome Loaded by Long-Term Static and Seismic Actions

The presented approach and method were used to analyze the stress–strain state of a dome, the middle surface of which is a part of a sphere of the corresponding radius. As a design scheme, a shell that deforms under its own weight and, possibly, additional load, was used. The dome is rigidly clamped around the base circumference.

A shell of thickness h , round in plan (with a base diameter $d = 10$ m), made of reinforced concrete is considered. In the calculations, the lifting height and the external load perceived by the shell varied. Figure 15.1 shows the considered shell with its division into finite elements: 20 along the generatrix and 20 along the circumference direction. This number of elements is established by preliminary calculations to ensure adequate accuracy.

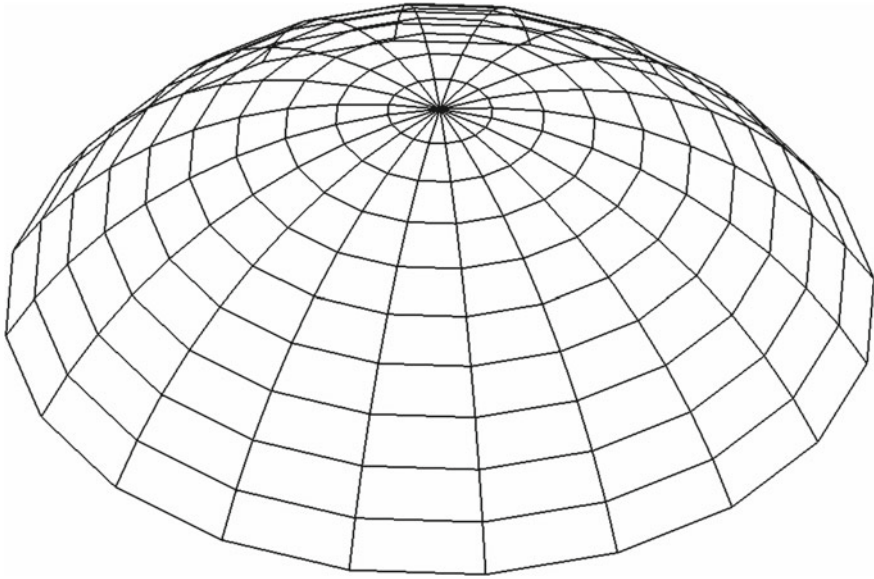


Fig. 15.1 FE model of spherical dome

A shell with a thickness of $h = 20$ cm (1/50 of the dimensions in the plane) made of reinforced concrete B40 was considered. Its mechanical characteristics: elastic modulus $E = 3.6 \times 10^4$ MPa, Poisson's ratio $\nu = 0.16$, mass density $\rho = 1.9 \cdot 10^3$ kg/m³.

For such a shell, the radius of the sphere is equal to: $R = \frac{\hat{h}}{2} + \frac{d^2}{8\hat{h}}$, where \hat{h} is the height of the dome, d is the size in plan, which corresponds to the opening angle of the sphere, which is determined by the formula: $\alpha = 2 \arccos\left(1 - \frac{\hat{h}}{R}\right)$. For practical use in the design of buildings and structures, the value of the reduced height is used in the analysis: $\tilde{h} = \frac{\hat{h}}{d}$, i.e., height divided into the base size.

In this formulation, let us consider the deformation of the considered shell during long-term operation for 100 years. According to the above scheme, the shape of the dome was selected using numerical modeling. The criterion of the minimum von Mises stress and, consequently, the minimum damage accumulation is used.

The values of shrinkage and creep constants in Eqs. (15.3–15.4) and (15.7–15.10) are determined after processing experimental curves (Handbook 2003, Shmukler et al. 2010) of B40 concrete (C32/40 according to EN 206-1) at an average temperature of 20 °C and waterproofing of the structure:

$$B = 1.443 \times 10^{-11} \text{ (MPa)}^{-n}/(\text{h}); D = 7.402 \times 10^{-11} \text{ (MPa)}^{-m}/(\text{h}); \hat{\alpha} = 1.437; n = 2.198; m = 1.489; k = 3.142; l = 2.096; \varepsilon_{\infty}^a = 0.00025.$$

The performed calculations of long-term deformation indicate that a dome with a minimum level of damage accumulation can be selected based on an estimate of the magnitude of the von Mises stress at the initial time moment. So, after set of

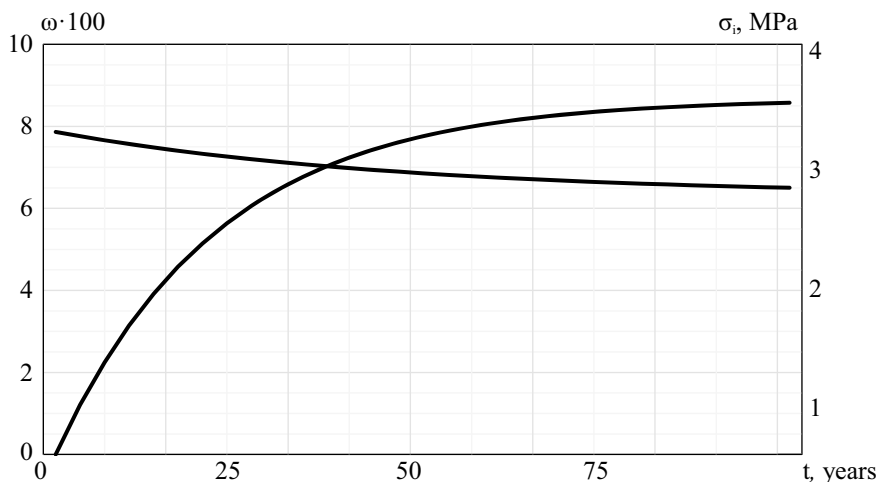


Fig. 15.2 Maximum values of von Mises equivalent stress σ_i and damage parameter ω versus time. Unloaded dome

the calculations we obtained, that the minimum von Mises stress will be at $\bar{h} = 0.242$. For such a shell, the dependence of the magnitude of the maximum von Mises equivalent stress σ_i (during the entire period of operation this value is concentrated in supports area) and the maximum value of the damage parameter ω on time is shown (Fig. 15.2).

These data indicate a fairly moderate redistribution of stresses during the period of operation. In addition, the accumulated value of damage for the considered time does not exceed 0.1. This allows us to assume that the calculated results obtained can with a sufficient degree of accuracy confirm the absence of the risk of cracking in the calculation period.

Analysis of the results shows that due to the flatness of the shell, the difference in the stress level for shells of different curvature is insignificant. Bending moments appear only in the part of the shell that is in contact with the supports. Most of the shell material is usually subjected only to longitudinal compressive forces. At the base of the shell, shear forces and bending moments reach values that can no longer be neglected. This causes the appearance of significant stresses in these places.

Similar dependencies are observed in the case when the dome is loaded. Let us analyze the deformation of the dome under the action of the structure's own weight and the same loading $q = 1.0p$, where p is the shell's own weight per unit area (Fig. 15.3). In the calculations, as well as for operation only under its own weight, the value of lifting height was varied. It was found that the lowest von Mises stress will be in the shell, the relative height of which is $\bar{h} = 0.222$. A similar result was also obtained for a dome under the action of its own weight of the structure and a twice loading that, $q = 2.0p$. It has been established that the lowest von Mises stress will be in the dome, the relative height of which is $\bar{h} = 0.189$ (Fig. 15.4). Additional

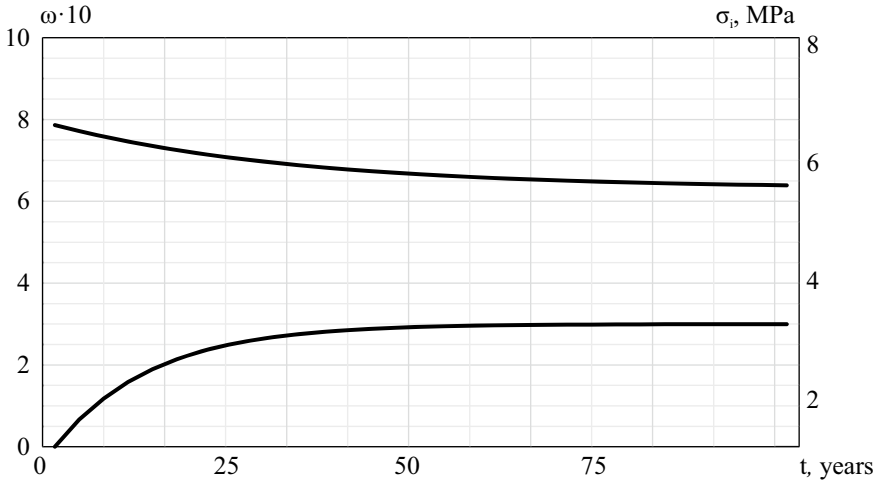


Fig. 15.3 Maximum values of von Mises equivalent stress σ_i and damage parameter ω versus time. $q = 1.0p$

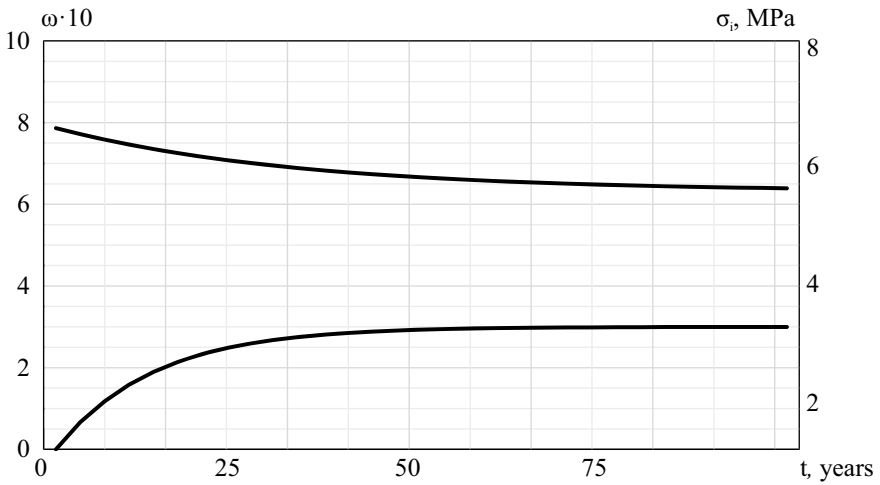


Fig. 15.4 Maximum values of von Mises equivalent stress σ_i and damage parameter ω versus time. $q = 2.0p$

loading leads to a significant increase in damage accumulation and moderate stress redistribution. And at load $q = 2.0p$, the damage parameter for 100 years reaches the 0.7, which is close to the critical value.

When designing buildings and structures, in addition to analyzing the long-term strength under static load, it is also necessary to take into account the possibility of dynamic loading at some points in time. Such loads can arise, in particular, during

Table 15.1 Values of damage parameters after 100 years of operation and additional dynamic loading

Vertical acceleration (m/s ²)	The level of basic loading		
	$q=0 p$	$q=1.0 p$	$q=2.0 p$
0.5	0.113	0.245	>1
1.0	0.147	0.485	>1
2.0	0.231	>1	>1

earthquakes. Moreover, the structure itself must withstand such loading at any period of operation. Since the level of damage in the material grows over time (Figs. 15.2, 15.3, and 15.4), it is obvious that the most dangerous moment of loading with additional dynamic action will be at the end of the design period (near the time of 100 years).

Let us consider the problem of vibration loading of the shell caused by oscillations of the Earth's surface during seismic impacts at the end of its operation. To simplify the analysis at this stage, we will consider one-harmonic oscillations passing continuously for 0.5 h. Such loading can be considered as close to the limiting one (in reality, oscillations occur periodically).

We consider the oscillations of the dome with a frequency which is far from the resonance values, while analyzing the loading by the base load of various intensities. The value of the additional loading is chosen to implement various values of vertical accelerations, which are 0.5, 1.0, and 2.0 m/s². These values of accelerations occur during earthquakes of 7, 8, and 9 points, respectively (SP 14.13330. 2014). Table 15.1 shows the maximum values of the damage parameter that occur after the described dynamic impact. Dark gray filling in a Table 15.1 shows cells that correspond to the critical value of the damage parameter and, accordingly, to the destruction of the dome.

15.4 Conclusions

The presented method for analyzing the long-term strength of concrete structural elements in the form of shells of revolution makes it possible to assess the possibility of their destruction under static and dynamic loads. Obtained by processing experimental data such as creep and shrinkage curves, the effect of moisture for different grades of concrete and the constants included in the proposed constitutive equations are obtained. Using numerical simulation, the best configurations of spherical domes from the point of view of long-term strength have been obtained. The assessment of the possibility of destruction of fairly old structures, which are subjected to short-term dynamic impact, is carried out. It is shown that, in this case, at some rather

high levels of external loads, concrete destruction is possible, despite the safety of the dome operation under static loading.

References

- Bari, M.S.: Punching shear strength of slab-column connections—a comparative study of different codes. *Journal of the Institution of Engineers* **80**(4), 163–168 (2000)
- Baron, J., Sautgrey, R.: *Le Béton Hydraulique*. Presses de l'ENPC, Paris (1982)
- Bazant, Z.P., Baweja, S.: Creep and shrinkage prediction model for analysis and design of concrete structures: model B3. In: Al-Manaseer, A. (Ed.) *Adam Neville Symposium: Creep and Shrinkage-Structural Design Effects*, ACI SP-194. Am. Concrete Institute, Farmington Hills, Michigan, pp. 1–83 (2000)
- Bazant, Z.P., Xi, Y.-P., Baweja, S., Carol, I.: Preliminary guidelines and recommendations for characterizing creep and shrinkage in structural design codes. In: Bazant, Z.P., Carol, I. (eds.) *Proceedings of 5th International RILEM Symposium on Creep and Shrinkage of Concrete (ConCreep 5)*, held at U.P.C., Barcelona, September, E & FN Spon, London (1993), pp. 805–829
- Breslavsky, D.V., Korytko, Y.N., Tatarinova, O.A.: Design and Development of Finite Element Method Software. *Pidruchnyk NTU «KhPI»*, Kharkiv, Ukraine (2017) (in Ukrainian)
- Breslavsky, D., Morachkovsky, O., Tatarinova, O.: Creep and damage in shells of revolution under cyclic loading and heating. *Int. J. Nonlinear Mech.* **66**, 87–95 (2014)
- Breslavsky, D., Chuprynin, A., Morachkovsky, O., Tatarinova, O., Pro, W.: Deformation and damage of nuclear power station fuel elements under cyclic loading. *J. Strain Anal. Eng. Des.* **54**(5–6), 348–359 (2019)
- Charpin, L., Pape, Y.L., Coustabeau, E., Toppani, E., Heinfing, G., Le Bellego, C., Masson, B., Montalvo, J., Courtois, A., Sanahuja, J., de Reviron, N.: A 12 year EDF study of concrete creep under uniaxial and biaxial loading. *Cem. Concr. Res.* **103**, 140–159 (2018)
- DIN EN 1992-1-1:2005-10, Eurocodez «Design of concrete structures. Part 1: General Rules and Rules for Building» Commition of European Communities (2005)
- Donnel, L.H.: Stability of Thin-Walled Tubes Under Torsion. NACA report No.479 (1933)
- EN 1992-2-1, Eurocodez «Desing of concrete structures. Part 1: General Rules and Rules for Building»—Commition of European Communities (1991)
- Gawin, D., Pesavento, F., Schrefler, B.A.: Modelling creep and shrinkage of concrete by means of effective stresses. *Mater. Struct.* (2007)
- Gernay, T.: Effect of transient creep strain model on the behavior of concrete columns subjected to Heating and Cooling. *Fire Technol.* **48**(2), 313–329 (2012)
- Handbook for the Design of Prestressed Reinforced Concrete Structures Made of Heavy Concrete (to SP 52-102-2003). Tsniipromzdaniy, Moscow, Russia (2005) (In Russian)
- Hubler, M.H., Wendner, R., Bazant, Z.P.: Comprehensive database for concrete creep and shrinkage: analysis and recommendations for testing and recording. *ACI Mater. J.* **112**(4), 547–558 (2015)
- Jennings, H., Masoero, E., Pinson, M., Strelakova, E.G., Bonnaud, P.A., Manzano, H., Ji, Q., Thomas, J.J., Pellenq, R.J.M., Ulm, F.J., Bazant, M.Z., Van Vliet, K.J.: Water isotherms, shrinkage and creep of cement paste: hypotheses, models and experiments. *Mechanics and Physics of Creep, Shrinkage, and Durability of Concrete*, American Society of Civil Engineers (2013), pp. 134–141
- Klovanich, S.F.: *Finite Element Method in Nonlinear Mechanics of Reinforced Concrete*. Zaporozhye, Ukraine: IPO Zaporozhye (2009) (In Russian)
- Lemaitre, J., Chaboche, J.-L.: *Mechanics of Solid Materials*. Cambridge University Press, Cambridge (1994)
- Mancinelli, P.A.: Acrylic HMPA base provides adhesion and stability features. *Adhesive Age* **32**(10), 18–23 (1989)
- Neville, A.M.: *Properties of Concrete*. Wiley, New York (1973)

- Pignatelli, I., Kumar, A., Alizadeh, R., Le Pape, Y., Bauchy, M., Sant, G.: A Dissolution-precipitation mechanism is at the origin of concrete creep in moist environments. *J. Chem. Phys.* **145**(5) (2016)
- Prandtl, L.: Spannungsverteilung in plastischen Körpern. *Proc. 1st Int. Congr. Appl. Mech.* 43–54 (1925)
- Rabotnov, Y.N.: *Creep Problems in Structural Members*. North-Holland, Amsterdam (1969)
- RILEM Technical Committee TC-242-MDC (Z.P. Bazant, chair). RILEM draft recommendation: TC-242-MDC multi-decade creep and shrinkage of concrete: material model and structural analysis. *Mater. Struct.* **48**(4), 753–770 (2015)
- Rossi, P., Tailhan, J.-L., Le Maou, F., Gaillet, L., Martin, E.: Basic creep behavior of concretes investigation of the physical mechanisms by using acoustic emission. *Cem. Concr. Res.* **42**(1), 61–73 (2012)
- Sakata, K., Ayano, T., Imamoto, K., Sato, Y.: Database of creep and shrinkage based on Japanese researches. *Creep, Shrinkage and Durability Mechanics of Concrete and Concrete Structures: Proceedings of ConCreep 8*. Taylor & Francis (2008), pp. 1253–1274
- Sellier, A., Multon, S., Bufo-Lacarrière, L., Vidal, T., Bourbon, X., Camps, G.: Concrete creep modelling for structural applications: non-linearity, multi-axiality, hydration, temperature and drying effects. *Cement Concr. Res.* **79**, 301–315 (2016)
- Shmukler, V.S., Chuprynin, A.A., Abbasi, R.H.: New method of full-scale tests. *Concr. Reinf. Concr. Ukraine* **5**, 13–24 (2010). (In Russian)
- SP 14.13330.2014. Construction in seismic areas SNiP II-7-81*. The Ministry of Construction, Moscow, Russia (2014) (In Russian)
- Tanabe, T., Ono, S., Morimoto, H., Nakamura, H., Ishikawa, Y.: Development of comprehensive platform for the estimation of volume change and damage in cement. *Mechanics and Physics of Creep, Shrinkage, and Durability of Concrete*, American Society of Civil Engineers (2013), pp. 412–420
- Torrenti, J.M., Le Roy, R.: Analysis of some basic creep tests on concrete and their implications for modeling. *Struct. Concr.* **22** (2018)
- Ulm, F.J., Jennings, M.H., Roland, J.M.P.: *Mechanics and physics of creep, shrinkage, and durability of Concrete* (ASCE). Ninth International Conference on Creep, Shrinkage, and Durability Mechanics (CONCREEP-9) Cambridge, Massachusetts, United States September 22–25, 2013, American Society of Civil Engineers, Boston (2013)
- Volmir, A.S.: *The Nonlinear Dynamics of Plates and Shells*, Foreign Technology Division. Wright-Patterson Air Force Base, USA (1974)
- Widianto: *Rehabilitation of Reinforced-Concrete Slab-Column Connections for Two-Way Shear*. PHD Dissertation University of Texas at Austin, Austin, TX (2006)
- Zienkiewicz, O.C., Taylor, R.L., Wood, D.D.: *The Finite Element Method for Solid and Structural Mechanics*. Butterworth-Heinemann (2014)

Chapter 16

Stress–Strain State of Nuclear Reactor Core Baffle Under the Action of Thermal and Irradiation Fields



Dmytro Breslavsky, Alyona Senko, Oksana Tatarinova, Victor Voevodin,
and Alexander Kalchenko

Abstract The paper describes the method for numerical simulation of stress–strain state variation in the structural elements of nuclear reactor under creep and swelling conditions. The mathematical statement of the initial–boundary value creep problem is presented. The constitutive equations account the radiation swelling, creep, and damage accumulation in reactor steel. The nonlinear system of differential equations is linearized by use of time integration schemes. The boundary problem, which appears at each time step, is solved by the finite element method. Nuclear reactor’s baffle initially is considered as a 3D solid object, and subsequently, the problem is reduced to 2D one. The long-term deformation and hidden damage accumulation processes are considered for simplified problem of baffle’s operation without shutdowns.

Keywords Reactor core baffle · Stress–strain state · Irradiation creep · Swelling · Damage

D. Breslavsky (✉) · A. Senko · O. Tatarinova
Department of Computer Modelling of Processes and Systems, National Technical University
“Kharkiv Polytechnic Institute”, Kharkiv 61002, Ukraine
e-mail: brdm@kpi.kharkov.ua

A. Senko
e-mail: alyonassenko@gmail.com

O. Tatarinova
e-mail: ok.tatarinova@gmail.com

V. Voevodin · A. Kalchenko
Institute of Solid-State Physics, Materials Science and Technologies, National Scientific Center
‘Kharkiv Institute On Physics and Technics’ NAS of Ukraine, Kharkiv 61002, Ukraine
e-mail: voyev@kipt.kharkov.ua

A. Kalchenko
e-mail: kalchenko@kipt.kharkov.ua

16.1 Introduction

One of the most important problems of modern power engineering is ensuring the durability of existing nuclear reactors in compliance with the necessary safety measures. Increasing the life time of a reactor comparing to the value specified during design requires effective methods and software for predicting the deformation level and ensuring long-term strength.

Development of such calculation methods that require the formulation, justification, and comprehensive verification of the constitutive equations, in which the relation between the components of strains arising from the combined action of thermal force and radiation fields and stresses at a point of the solid, is reflected. The first step was analysis the behavior of structural materials under the influence of neutron fluxes under prolonged loading. Such work has continued since the beginning of the use of nuclear reactors (Ma 1983).

The main experimental facts and approaches to the construction of constitutive equations, suitable for use in solving problems of solid mechanics, are described in Aktaa and Schmitt (2006), Duderstadt and Hamilton (1976), Andersson-Östling and Sandström (2009), Garner (2012), Likhachev and Pupko (1975), Kiselevsky (1977), Ma (1983), Takakura et al. (2009), Margolin et al. (2006), Margolin et al. (2012), and others.

Strains of radiation creep and radiation swelling are the main components of the total strain tensor, which cause their growth with time, for relatively low-temperature operating modes of WWER-type reactors. Experimental data show that, in most cases, the relationship between the components of the tensor of radiation creep rates and stresses is linear or close to it (Foster et al. 2003; Ma 1983; Gorokhov et al. 2020). To construct the constitutive equations describing the process of radiation swelling, experimentally obtained dependences for the strain components or their rates on the temperature and neutron fluence are used (Garner 2012; Kalchenko et al. 2010; Kalchenko et al. 2013). Recently, there have been attempts to take into account the effect of the stress state on the swelling strains growth Margolin et al. (2012). Similar equations can be used in a simplified analysis of the swelling processes at a point of a loaded body under a complex stress state. Their use in the calculations of structural elements can lead to double consideration of the effect of the level and sign of stresses: the first time due to direct consideration in the equation and the second time due to the effect of stress redistribution on the current level of total strain when the strain compatibility condition is ensured. It is well known that radiation swelling strains are inherently volumetric (Likhachev and Pupko 1977). In this regard, it seems necessary to take it into account using the equations obtained for free swelling (e.g., Kalchenko et al. 2013) in the same way as calculating temperature strains, which are also volumetric.

To construct an effective scheme for the analysis of long-term deformation of elements of reactor in-vessel components, it is necessary to take into account the time variation of the main factors: stress redistribution, accumulation of strains, and hidden damage in the material (Lemaitre and Chaboche 1994). Such an account is only

possible when formulating the problem as a boundary–initial value one (Likhachev and Pupko 1977; Breslavsky et al., 2019; Gorokhov et al. 2020).

Most of the elements used in the construction of a nuclear reactor have a complex geometric shape. Due to this, the finite element method (FEM) is most widely used in calculations (Zienkiewicz et al., 2014). Nordlund (2019) in his review of methods for computer modeling of radiation effects in materials noted that FEM is currently used not only in solving problems of mathematical physics (heat transfer, solid mechanics, etc.), but also when simulating the effects of radiation exposure on the long-term behavior of structures.

The use of the ANSYS software package for modeling the thermo-physical properties of reactors and fuel assemblies and individual elements of research nuclear reactors considered in Piro and Williams (2015). They note that the use of such a powerful FE modeling tool makes it possible to assess the real properties of processes without carrying out costly field experiments when designing new nuclear power station equipment.

A model that is able to provide a macroscopic estimate of the stresses caused by irradiation using information on the distribution of radiation defects produced by high-energy neutrons in the microstructure of materials developed in Dudarev et al. (2018). The analytical solutions are compared to the FE solution.

Creep problems can be solved in the ANSYS software package, but the package does not have tools for modeling the stress redistribution under the influence of radiation swelling and damage accumulation. This feature is implemented in the FEM Creep software package (Breslavsky et al. 2017).

The paper discusses a method for calculating radiation creep and swelling, used to analyze the level of deformation and the possibility of fracture of the core baffle of a WWER-type nuclear reactor. The formulation of an initial–boundary value problem describing the processes of strain accumulation of radiation creep and swelling as well as the hidden damage in the material of the baffle is described. A finite difference method is used to solve the initial problem, and at each time step, the resulting boundary value problem is solved by use of the FEM scheme. The results of numerical simulation of the strain and damage accumulation in the baffle cross section are presented.

16.2 Solution Procedure

16.2.1 Problem Statement

Let us consider a solid with a volume Ω and surface area S . To describe the processes of temperature – stress and radiation deformation of isotropic materials, we use a system of differential equilibrium equations written in tensor form (Lemaitre and Chaboche 1994)

$$\frac{d\sigma_{ij}}{dx_j} = P_i \quad i, j = 1, 2, 3 \quad \sigma_{ij} = \sigma_{ij}(u_i), \quad (16.1)$$

where u_i are the components of displacement vector, σ_{ij} are the stress tensor components, P_i is the vector of volume forces. Cartesian coordinate system x_i , $i = 1, 2, 3$ is used.

Let us restrict ourselves to the case of small strains that occur in most structural elements. To determine the components of the strain tensor, the Cauchy equations are used

$$\varepsilon_{ij} = \frac{1}{2}(u_{i,j} + u_{j,i}). \quad (16.2)$$

It is postulated (Lemaitre and Chaboche 1994) that at each moment of time the total strain tensor can be represented as a sum of the tensors of elastic, thermal, radiation creep, and swelling strains:

$$\varepsilon_{ij} = e_{ij}^e + e_{ij}^T + c_{ij} + e_{ij}^{sw}, \quad (16.3)$$

and for any time moment Hooke's law is applicable:

$$\sigma_{ij} = (\hat{\lambda}\delta_{ij}\delta_{kl} + \hat{\mu}(\delta_{ik}\delta_{jl} + \delta_{il}\delta_{jk}))(\varepsilon_{kl} - e_{kl}^T - c_{kl} - e_{kl}^{sw}), \quad (16.4)$$

where δ_{ij} is Kronecker's delta, $\hat{\lambda}$, $\hat{\mu}$ are Lamé constants: $\hat{\lambda} = \frac{\nu E}{(1+\nu)(1-2\nu)}$; $\hat{\mu} = \frac{E}{2(1+\nu)}$. E is Young modulus, ν is Poisson ratio.

The components of the temperature strain tensor are dependent on the temperature difference $\Delta T = T - T_0$

$$e_{ij}^T = \alpha_{\text{expan}} \Delta T \delta_{ij}, \quad (16.5)$$

where α_{expan} is the coefficient of thermal expansion $^{\circ}K^{-1}$, T, T_0 are current and initial temperature values, $T = T(x_i)$.

The radiation swelling strain tensor describes the dependence of the occurrence of strains as the function of the integral neutron fluence, temperature, and time. The integral fluence Φ describes the interaction of charged particles with the microstructure of the material being irradiated and depends on a number of factors: their energy, spectral density, fluence density, etc. The functional dependence of the tensor of the strain rate of radiation swelling from the rate of the integral fluence function has the form

$$\dot{e}_{ij}^{sw} = \frac{1}{3} \dot{S}_{\Phi}(\dot{\Phi}, t, T) \delta_{ij}. \quad (16.6)$$

At present, the functional expression for the radiation swelling function S_ϕ is obtained experimentally, by the processing of the obtained data using the mathematical methods, for example, the least squares method. In the calculations, we use the model obtained in Kalchenko et al. (2013):

$$S_\phi = (0.25 - 0.022 \ln k)\varphi(D - 103 + 0.1T - 2.6 \ln k) \exp\left(-\frac{(T - 690 - 15.5 \ln k)^2}{2(12.3 - 1.9 \ln k)^2}\right), \quad (16.7)$$

where D is damaging dose, $\phi(x)$ is Heaviside function: $\phi(x) = x\theta(x)$; $\theta(x) = 1$, $x > 0$; $\theta(x) = 0$, $x \leq 0$; k is the dose rate, dpa/s.

To describe the processes of radiation creep, accompanied by the accumulation of hidden damage, which arises as a result of the action of temperature stress and radiation factors, the constitutive equations with Norton law and the Rabotnov–Kachanov model for scalar damage parameter ω were applied (Lemaitre and Chaboche 1994):

$$\dot{c}_{ij} = \frac{3}{2} \frac{B\sigma_i^{n-1} S_{ij}}{(1-\omega)^l} \exp\left(-\frac{Q_c}{T}\right), \quad Q_c = \frac{U_c}{R}, \quad (16.8)$$

$$\dot{\omega} = \frac{D\sigma_i^r}{(1-\omega)^l} \exp\left(-\frac{Q_d}{T}\right), \quad Q_d = \frac{U_d}{R}, \quad (16.9)$$

Here S_{ij} are the components of stress deviator, σ_i is the von Mises equivalent stress, B , D , n , m , r , l are the constants, obtained experimentally in creep and long-term strength tests, U_c and U_d are the values of activation energies for processes of radiation creep and damage accumulation, R is Boltzmann constant.

Radiation creep usually runs by linear mechanisms: $\dot{\varepsilon}_i = \tilde{B}\sigma_i$, ε_i is the von Mises equivalent strain, \tilde{B} is the radiation creep constant (Ma 1983).

It is considered that on some part of the surface S_1 the boundary conditions in the form of a given displacements which is a function of time are specified. On a part of the surface S_2 , there are boundary conditions in the form of traction:

$$u|_{S_1} = u_0, \quad \sigma_{ij}n_j|_{S_2} = h_j. \quad (16.10)$$

At the initial moment of time, the damage parameters as well as creep and radiation swelling strains have zero values

$$\omega(0) = 0, \quad e_{ij}^c(0) = 0, \quad e_{ij}^s(0) = 0. \quad (16.11)$$

16.2.2 Solution of Heat Conductivity Problem

To obtain the temperature distribution, it is necessary to solve the problem of heat conductivity. In the proposed approach, this is the problem of stationary thermal conductivity (Lemaitre and Chaboche 1994), solved for the moment of finishing the temperature distribution in the baffle.

The core baffle of the WWER-1000 reactor (Fig. 16.1) is a monolithic cylindrical structure with an outer diameter of 3470 mm, and the inner surface of which in cross section repeats the configuration of the core. It has 90 longitudinal channels for cooling. The total height of the baffle in the reactor is made up of five elements at a height of 4070 mm. The height of each element is 814 mm.

The core baffle is an important element of the nuclear reactor, and it provides the necessary thermal power mode of its operation. The baffle of WWER reactors operating at nuclear power plants in Ukraine is made of 18Cr10NiTi austenitic steel. In this regard, we will pay attention to the results of experimental studies and the constructed equations of state for steels of this type.

The following physical and mechanical properties of above-mentioned steel in the range of operating temperatures of the baffle 710 K–573 K were used: density 7900 kg/m³, coefficient of linear thermal expansion $1.75 \times 10^{-5} \text{ K}^{-1}$, specific heat 500 J/(kg K), thermal conductivity coefficient 43 W/(m K).

According to the approach in Troyanov et al. (1998), as a boundary condition the surface temperature distribution was set. It is considered that on the baffle internal surface, there is a constant temperature of 710 K, and for external surfaces, it is 670 K. Cooling channels have the temperature 573 K.

Fig. 16.1 Configuration of the core baffle

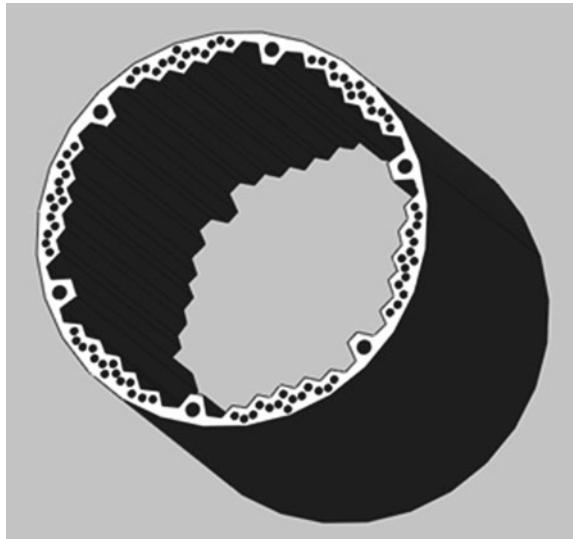
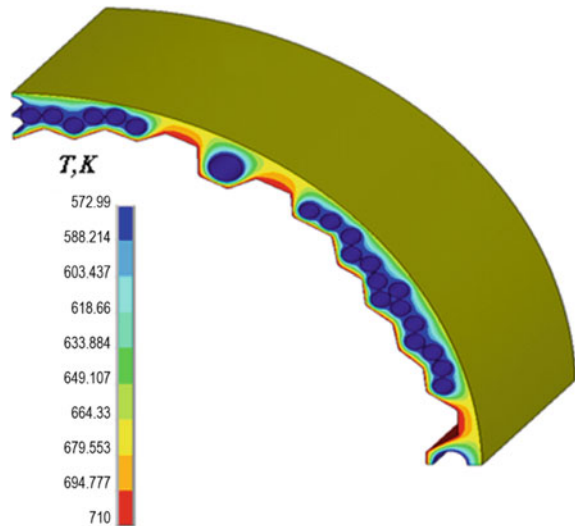


Fig. 16.2 Temperature distribution in the baffle cross section (at a distance of 0.1 m from its upper edge)



The problem was solved in a general three-dimensional statement. Due to the symmetry of the baffle, the calculation model was built for its one-fourth part. Based on the results of numerical experiments on the analysis of their convergence, a FE model with 82,290 elements and 392,105 nodes was chosen.

Based on the data of numerical investigations, it has been established that the temperature field in the baffle is practically unchanged along its height. As an example, Fig. 16.2 shows the temperature distribution in the cross section, which is located at a distance of 0.1 m from baffle upper edge.

The invariance of the temperature field along the height of the baffle means that in further simulation it is possible to proceed to the calculation model originating from the two-dimensional problem formulation. The same conclusion was obtained in Troyanov et al. (1998).

16.2.3 FEM Calculation Scheme

As explained in the previous subsection, we will formulate the problem as a plane strain problem. It is described by the mathematical formulation (16.1)–(16.11) for $i, j = 1, 2$. We will solve it using FEM.

Resolving system of equations has the following form (Breslavsky et al. 2017, 2019; Altenbach et al. 2020):

$$[K]\{\dot{u}\} = \{\dot{F}\} + \{\dot{F}^c\} + \{\dot{F}^{sw}\}$$

$$\begin{aligned}
\{\dot{F}\} &= \sum_{N_\beta} \int_{V_\beta} [N^p]^T \cdot \{\dot{P}\} dV + \sum_{N_\beta} \int_{S_2^\beta} [N^p]^T \{\dot{h}\} dV \\
&\quad + \sum_{N_\beta} \int_{V_\beta} [\bar{B}]^T [C] \{\dot{\varepsilon}^T\} dV \\
\{\dot{F}^{sw}\} &= \sum_{N_\beta} \int_{V_\beta} [\bar{B}]^T [C] \{\dot{\varepsilon}^{sw}\} dV \\
\{\varepsilon\} &= \{\varepsilon^e\} + \{\varepsilon^T\} + \{c\} + \{e^{sw}\} \\
\{\dot{F}^c\} &= \sum_{N_\beta} \int_{V_\beta} [\bar{B}]^T [C] \{\dot{c}\} dV; \\
\{\dot{c}\} &= \frac{3}{2} B \frac{\sigma_i^{n-1}}{(1-\omega^r)^k} \exp\left(-\frac{Q_c}{T}\right) [\hat{C}] \{\sigma\}, \quad Q_c = \frac{U_c}{R}; \\
\dot{\omega} &= D \frac{\sigma_i^m}{(1-\omega^r)^k} \exp\left(-\frac{Q_d}{T}\right), \quad Q_d = \frac{U_d}{R}, \\
\omega(0) &= \omega_0, \quad \omega(t_*) = \omega_*.
\end{aligned} \tag{16.12}$$

Here K is the stiffness matrix of system; u is global vector of nodal displacements; F is the vector of nodal loads caused by surface and volume forces and temperature strains; F^{sw} is nodal loads caused by radiation swelling strains; F^c is nodal loads caused by radiation creep strains; \bar{B} is the matrix differentiation operator; C is the matrix of elastic constants; N is a matrix of shape functions; β is finite element number; V_β is the volume of the finite element; \sum_{N_β} is summation over all

finite elements; S_2^β is the surface area of a finite element that is under a traction (Zienkiewicz et al. 2014). Matrix $[\hat{C}]$ has the following form:

$$[\hat{C}] = \begin{bmatrix} 1 & -1/2 & 0 \\ -1/2 & 1 & 0 \\ 0 & 0 & 3 \end{bmatrix}.$$

A triangular three-nodal finite element is used in the calculations. Its degrees of freedom are six components of the displacement rate vector.

Let us consider the specification of the constitutive equations associated with the description of the effects arising from irradiation.

To describe radiation creep, we use the linear dependence of the strain rate on stresses (Ma 1983). For 08Kh18N10T steel in the operating temperature range of the baffle 573–710 K [47] $n = 2$, $B = 1.214 \cdot 10^{-12} \text{ (MPa}^{-1}\text{) \cdot h}^{-1}$.

In the case when the distribution law of the radiation dose along the radius is known, it is possible to introduce it into the calculation model. For steel 08Kh18N10T in the range of working temperatures of the baffle, the following data obtained in

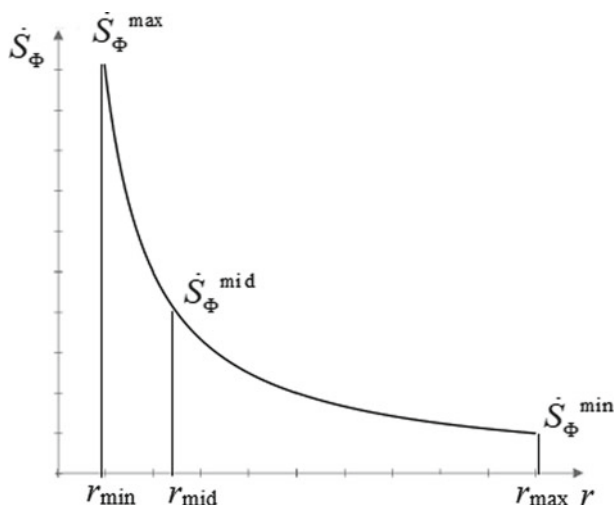


Fig. 16.3 Dependence of dose accumulation rate on radius

OKB “GIDROPRESS” are known (Margolin et al. 2012). In this regard, it is possible to enter into the calculation the function of the dependence of the radiation swelling strain on the baffle radius r , which is hyperbolic in the first approximation (Fig. 16.3):

$$\dot{S}_\Phi = \hat{A} \frac{\dot{S}_\Phi}{r}, \quad (16.13)$$

where \hat{A} is a coefficient.

To describe the process of accumulation of hidden damage for relation (9) according to the data in Takakura et al. (2009), which shows a graph of long-term strength for irradiated steel of the type that is being analyzed, the value of the constants was determined: $k = m = 15.52$; $D = 9.55 \cdot 10^{-48} \text{ MPa}^{-m}/\text{h}$, $Q_d = 1023 \text{ K}$.

16.3 Results of Numerical Simulation

The calculations were performed for a simplified case. It was assumed that core baffle works without any reactor’s shutdowns during 60 years. This case may be regarded as limiting, because in time intervals of shutdowns the deformation may be considered as negligible. From the other hand, the cyclic character of loading and heating can essentially accelerate the deformation process.

16.3.1 Deformation of a Thick Tube of Equivalent Dimensions

To understand the processes occurring during long-term deformation of the baffle, we first consider the results of numerical simulation of a simpler structure—a thick-walled tube with the same outer radius as the baffle. The inner radius was specified by the average values of its points on the inner surface.

This model makes it possible to identify the main factors affecting the processes of stress redistribution and strain growth in structure. This is primarily the role of temperature strains and strains of radiation swelling on the outer and inner sides of the tube.

Calculations are carried out using FEM; therefore, if the degree of discretization is insufficient, especially in the areas of cooling holes, it will be impossible to accurately determine the magnitude of their influence on the overall deformation process.

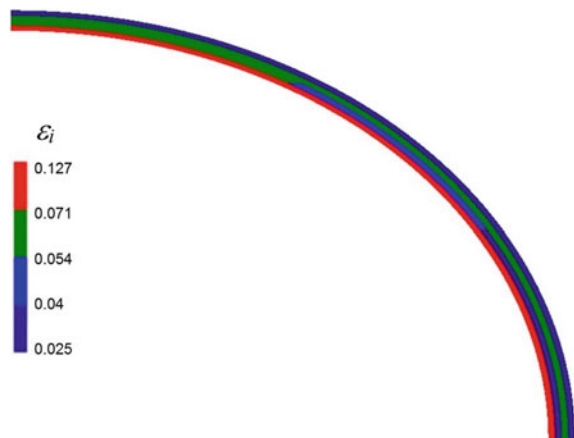
The influence of design features (geometry at the inner radius, cooling holes) will be considered additionally when analyzing the complete geometric model of the baffle.

Let us consider the results of calculations for the case when the maximum dose, which was accumulated over 60 years, is 104 dpa (linear interpolation from the data provided in Margolin et al. (2012)).

The calculation results show that under free swelling [without taking into account the dependence of the dose on the radius like (16.13)], the maximum of the von Mises equivalent strains obtained is 14.5%. At the same time, when the dose distribution along the radius is taken into account, the maximum values of the von Mises equivalent strains are 12.7%. (Fig. 16.4).

Analyzing the results, we can make conclusion that in the case of consideration the dose dependence from the radius, the maximum level of strains is observed at the inner radius, where there is a maximum dose (Fig. 16.4). With completely free

Fig. 16.4 Distribution of total von Mises strains in a tube cross section, $t = 60$ years



swelling, the maximum strains are at the outer radius, which does not agree with the experimental data.

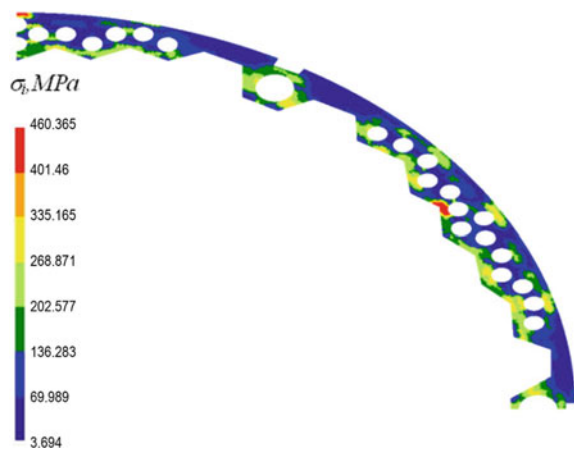
16.3.2 Long-Term Behavior of Core Baffle

Next, we consider the cross section of the baffle, assuming that any of those that are spaced from the edges work similarly. As a result of its symmetry, we construct a FE model for the one-fourth part of the section. As boundary conditions: we set the possibility of free displacement of the ends in the direction x_1 (at $x_2 = 0$) and x_2 (at $x_1 = 0$).

After the convergence study (the maximum number of elements was 135,697), a FE model, which was selected for simulations, had 72,264 elements. The results of calculating the stress state of the baffle, carried out in the FEM Creep (Breslavsky et al. 2017) and ANSYS software packages, are shown in Fig. 16.5 in the form of the von Mises stress distribution over the cross section. The calculation data differ by 2–3%. The distribution map shows that the highest stress values are observed in the vicinity of the holes and internal lugs of the section and range from 136 to 401 MPa. The maximum stresses take place in the region of transition from lugs to holes, and their values reach 460–461 MPa. Let us note that similar distributions were obtained in Margolin et al. (2012), Troyanov et al. (1998), where the maximum von Mises stress values are in the range of 440–460 MPa.

Numerical simulation of the process of long-term deformation of the baffle was carried out, and the strain fields were determined over its cross section at different times. The following conclusions in Troyanov et al. (1998) were confirmed in general: in the first 20 years of operation, the main contribution to the deformation process is made by radiation creep, and in the following years, the radiation swelling is dominant.

Fig. 16.5 Distribution of von Mises equivalent stress over baffle cross section, $t = 0$



As an example, we present the cross-sectional distributions of the von Mises equivalent strains. Such distribution for $t = 30$ years with accumulated dose of 52 dpa is shown in Fig. 16.6. Figure 16.7 presents similar data for $t = 60$ years, and accumulated dose is 104 dpa.

The performed numerical calculations and the results obtained using the KIPT radiation swelling model (Kalchenko et al. 2013) show that the maximum von Mises strain values over 60 years will be approximately 14%.

Using the approaches of the continuum damage mechanics (CDM, Lemaitre and Chaboche 1994) in order to estimate the long-term behavior of the baffle under conditions of initial non-uniform heating, radiation creep and swelling, a damage

Fig. 16.6 Distribution of von Mises equivalent strains over baffle cross section, accumulated dose 52 dpa, $t = 30$ years

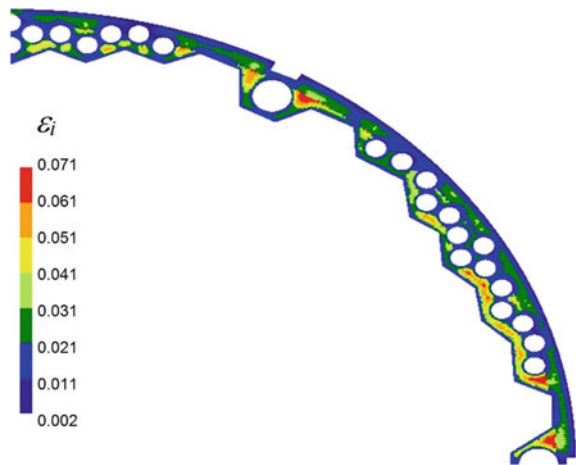


Fig. 16.7 Distribution of von Mises equivalent strains over baffle cross section, accumulated dose 104 dpa, $t = 60$ years

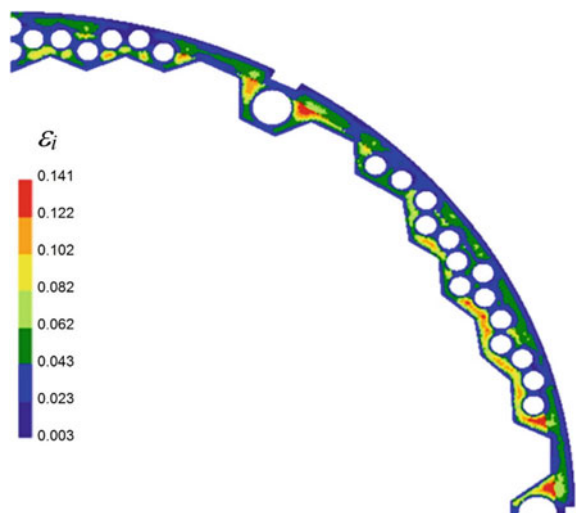
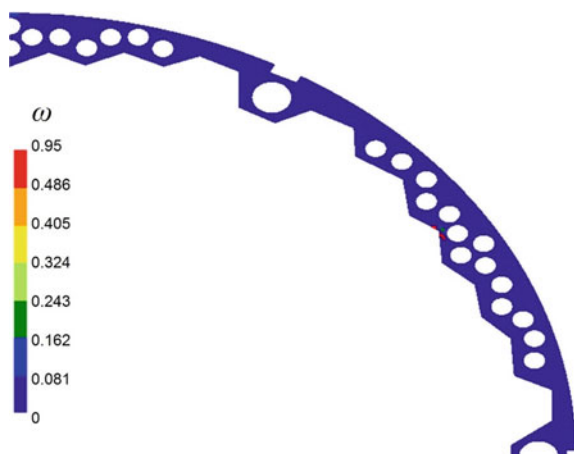


Fig. 16.8 Distribution of damage parameter over baffle cross section, accumulated dose 81 dpa, $t = 47$ years



kinetic equation with the implemented dependence on temperature (16.9) was added to the system of governing equations. The data of numerical modeling are presented in Fig. 16.8, where the distribution of the damage parameter over the section of the baffle for the case of the maximum dose 81 dpa, accumulated over 47 years, is shown. Numerical modeling has demonstrated that after 47 years of operation in the sectional zone of the baffle, located between the 9th and 10th holes from the bottom side of Fig. 16.8 and in which high stress values take place (Fig. 16.5), the accumulation of hidden damage ends and a crack nucleus appears.

It can be seen from the damage distribution that in this zone, in contrast to others, the damage parameter reaches a critical value ($\omega^* = 0.95$). This means that macroscopic defects appear in the areas marked by red.

This conclusion correlates with the results in Margolin et al. (2012) which provided data on the analysis of the possibility of initiation of the fracture of the baffle using the IASCC model (Takakura et al. 2009).

16.4 Conclusions

The paper presents a solution method and the results of computer simulation of the processes of the stress–strain state varying and the accumulation of hidden damage in the core baffle of a WWER-type nuclear reactor. The simplified problem of the baffle operation during 60 years without shutdowns was considered as an example of the method application. The values of stresses, strains, and damage parameters, distributed over the cross section of the baffle, were obtained. The location of possible occurrence of a macroscopic defect was established.

The homogeneous temperature distribution along the baffle's height was confirmed. This made it possible to use a two-dimensional formulation using the plane strain model.

When comparing the results obtained from the numerical simulation data for the equivalent tube and for the baffle, it was determined that in the latter a little more strains occur than in the tube, by about 1%. This can be explained by the satisfaction of strain compatibility condition in the vicinity of the holes and borders of the baffle. Such a comparison can be considered as verification of the results obtained for a cross section of complex geometry. It was found that the maximum value of the von Mises equivalent strain, which is about 14% at the maximum radiation dose 104 dpa, takes its place near the inner zones of the baffle section.

Calculations carried out using the CDM approach revealed the possibility of occurrence, in about 47 years, of a small macroscopic defect. The zone of its occurrence corresponds to the stress concentrator in the area of the cooling hole. The time and place of occurrence correlate with the data reported in Margolin et al. (2012) using the IASCC model (Takakura et al. 2009).

Further studies should focus on the refinement of constitutive equations for radiation swelling as well as on taking into consideration the cyclic character of baffle's operation.

References

- Aktaa, J., Schmitt, R.: High temperature deformation and damage behavior of RAFM steels under low cycle fatigue loading: experiments and modelling. *Fusion Eng. Des.* **81**(19), 2221–2231 (2006)
- Altenbach, H., Breslavsky, D., Mitielov, V., Tatarinova, O.: Short term transversally isotropic creep of plates under static and periodic loading. In: Naumenko, K., Krüger, M. (Eds.) *Advances in Mechanics of High Temperature Materials. Advanced Structured Materials*. Springer, Berlin (2020), vol. 117, pp. 181–211
- Andersson-Östling, H.C.M., Sandström, R.: Survey of creep properties of copper intended for nuclear waste disposal. Swedish Nuclear Fuel and Waste Management Co. Technical Report TR-09-32 (2009)
- Breslavsky, D.V., Korytko, Y.N., Tatarinova, O.A.: Design and Development of Finite Element Method Software. Kharkiv, Ukraine (2017) (in Ukrainian)
- Breslavsky, D., Chuprynin, A., Morachkovsky, O., Tatarinova, O., Pro, W.: Deformation and damage of nuclear power station fuel elements under cyclic loading. *J. Strain Anal. Eng. Des.* **54**(5–6), 348–359 (2019)
- Dudarev, S.L., Mason, D.R., Tarleton, E., Ma, P.W., Sand, A.E.: A multi-scale model for stresses, strains and swelling of reactor components under irradiation. *Nucl. Fus.* **58**(12) (2018)
- Duderstadt, J.J., Hamilton, L.J.: *Nuclear Reactor Analysis*. Wiley, Hoboken (1976)
- Foster, J.P., Bunde, K., Porter, D.L.: Irradiation creep of annealed 304L stainless steel at low dose levels. *J. Nucl. Mater.* **317**(2), 167–174 (2003)
- Garner, F.A.: Radiation damage in austenitic steels. In: Konings, R.J.M. (Ed.) *Comprehensive Nuclear Materials*, vol. 4, pp. 33–95 (2012)
- Gorokhov, V.A., Kapustin, S.A., Churilov, Y.A., Igumnov, L.A.: Modeling deformation of materials and structures of nuclear power engineering subjected to thermal-radiation effects. *Continuum Mechanics and Thermodynamics* (2020) <https://doi.org/10.1007/s00161-020-00946-5>
- Gulenko, A.G., Margolin, B.Z., Buchatskii, A.A., Nuzhdov, A.A.: Construction of theoretical curves of the long-term strength for neutron-irradiated austenitic steels Kh18N9 and 08Kh16N11M3. *Inorg. Mater. Appl. Res.* **9**(6), 1254–1262 (2018)

- Kalchenko, A.S., Bryk, V.V., Lazarev, N.P., Voevodin, V.N., Garner, F.A.: Prediction of void swelling in the baffle ring of WWER-1000 reactors for service life of 30–60 years. *J. Nucl. Mater.* **437**, 415–423 (2013)
- Kalchenko, A.S., Bryk, V.V., Lazarev, N.P., Neklyudov, I.M., Voevodin, V.N., Garner, F.A.: Prediction of swelling of 18Cr10NiTi austenitic steel over a wide range of displacement rates. *J. Nucl. Mater.* **399**, 114–121 (2010)
- Kiselevsky, V.N.: Varying of Mechanical Properties of Steels and Alloys Under Radioactive Irradiation. Kyiv (1977) (In Russian)
- Lemaitre, J., Chaboche, J.-L.: *Mechanics of Solid Materials*. Cambridge University Press, Cambridge (1994)
- Likhachev Yu, S., Pupko, V.D.: *Strength of Fuel Elements for Nuclear Reactors*. Moscow (1975) (In Russian)
- Ma, B.M.: *Nuclear Reactor Materials and Applications*. Van Nostrand Reinhold Company, New York (1983)
- Margolin, B.Z., Gulenko, A.G., Kursevich, I.P., Buchatskii, A.A.: Modeling for fracture in materials under long-term static creep loading and neutron irradiation. Part 1. A physico-mechanical model. *Strength Mater.* **38**(3), 221–233 (2006)
- Margolin, B., Fedorova, V., Sorokin, A.: The mechanisms of material degradation under neutron irradiation for WWER internals and methods for structural integrity assessment. In: International Conference «Structural Integrity and Life of NPP Equipment», Kiev (2012)
- Piro, M., Williams, A.: Fueling research reactors. *Ansys Advantage IX* **2**, 51–53 (2015)
- Takakura, K., Nakata, K., Kubo, N., Fujimoto, K., Sakima, K.: IASCC evaluation method of irradiated cold worked 316SS baffle former bolt in PWR primary water. In: Proceedings of the ASME Pressure Vessels and Piping Division Conference PVR, PVP2009-77279 (2009)
- Troyanov, V.M., Likhachev, I.M., Khmelevsky, M.Ya., Tsofin, V.I., Shary, N.V., Yuremenko, V.P., Shamardin, V.K., Neustroyev, V.S., Prokhorov, V.I.: Evaluation and analysis of thermo-mechanical behavior of in-vessel components elements of WWER reactors with consideration of irradiation effects. Collected papers of 5th Interindustry Conference on Reactor Building, Dimitrovgrad **2**(1), 3–18 (1998) (In Russian)
- Zienkiewicz, O.C., Taylor, R.L., Wood, D.D.: *The Finite Element Method for Solid and Structural Mechanics*. Butterworth-Heinemann (2014)

Chapter 17

Application of Data-Driven Yield Surface to Prediction of Failure Probability for Centrifugal Pump



Mariya Shapovalova and Oleksii Vodka

Abstract The modern world is often faced with the problem of the equipment design lifetime ending. Researches related to determines the residual lifetime, extension of service life, and prediction of failure-free operation is important, especially when it comes to equipment for nuclear and thermal power plants. Such interest is associated with the difficult economic situation, high cost of equipment and its components, requirements for safe working conditions, etc. The main objective of this work is to study the probability of the centrifugal pump failure-free operation. Attention is paying to the water elbow part of a centrifugal pump. Finding the probability of model failures is based on data-driven yield surface application. Takes into account the different behavior of composite materials under tensile and compressive loads, which is analyzed at the micro-level using the finite element method. Going beyond the yield surface indicates the possibility of transition into a plastic state. The proposed method of analysis of a centrifugal pump type WD 16/25 leads to predict the probability of failure during normal operation and in hydro testing mode. Consideration of the influence of corrosion-erosive processes and uniform thinning of the water pump elbow wall, an analysis of the probability of failure-free operation in time is carried out.

Keywords Microstructure · Yield surface · Probability · Finite element method · Failure

M. Shapovalova (✉) · O. Vodka
Department of Dynamics and Strength of Machines, National Technical University “Kharkiv Polytechnic Institute”, Kharkiv, Ukraine
e-mail: MiShapovalova@gmail.com

O. Vodka
e-mail: oleksii.vodka@khp.edu.ua

17.1 Introduction

It's important to predict the failures, especially when it comes to the equipment of nuclear and thermal power plants. The limited financial resources do not allow the renewal of power units, the design lifetime of which is almost exhausted. Therefore, the research deals with predicting the probability of non-failure operation, the assessment of the residual lifetime (Kelin et al. 2019), and extend the design lifetime (Kahlman 2016; Verhuelsdonk 2005), which are in demand and relevant nowadays. During operation, pumping units under the influence of corrosion and erosion inevitably encounter thinning of the housing walls. The negative effects of redistribution of mechanical stresses in the structure are required close attention. It is also necessary to take into account the various modes of operation of the pump, such as normal operating conditions and hydro testing, which is provided by the relevant standards to calculate the strength of the pump equipment (IEC 60041:1991; ISO/TR 17766:2005; ISO 9906:2012).

There are various methods to assess the unit's lifetime. In some works, the reliability and probability of failure are assessed (Cheng et al. 2016; Patel et al. 2005). Other ones are based on deterministic models (Jacobs et al. 2018). The authors use the principle of stress state determination to estimate the operational life. In this work, it is proposed to evaluate the failure-free operation of the pump based on the yield surface data-driven approach. Nowadays, a data-driven approach helps to analysis of the collected data and scientifically make decisions. Widely used in artificial intelligence, engineering (Siddiq 2020; Lvov and Kostromytska 2020), strategy, marketing, policy, medicine, etc.

On the one hand, materials science and modern microscopy have contributed to the development of methods for predicting material properties based on their internal structure. On the other hand, the traditional sciences of continuum mechanics, the theory of elasticity, the theory of vibrations, and reliability provide ample opportunities for multilevel modeling and analysis of materials. During the construction of the model, such a connection leads to the loss of a significant part of the information accumulated during the experimental research. Therefore, the technology of obtaining as complete information on the micro-level as possible and transferring it to the macro model is important, will contribute to the expansion and improvement of existing methods.

As a bridge of communication between the micro and macro levels, approaches based on obtaining large data sets (data mining), and subsequent statistical processing (data science) can serve, which allow obtaining, accumulating, and processing significant amounts of data. The revealed dependences and probabilistic characteristics of the microstructure were used in further modeling of the material—to help improve the quality, accuracy, and completeness of the analysis.

Investigation of the probabilistic characteristics of the anisotropic materials yield surface (Banabic et al. 2010; Shapovalova and Vodka 2019a, b), makes it possible to describe the behavior of a structure under a complex stress state. Computer modeling for predicting material behavior is an alternative to such an approach. The main

principle proposed in this article is to predict possible macro failure of the model based on the study of processes at the micro-level. To evaluate the probability of failure-free operation in the time of the waste dynamic pump (WD 16/25) during normal operation and hydro test mode.

17.2 Objectives

The main objective of this study is to use the yield surface data-driven approach to determine the failure-free probability of a centrifugal pump. This objective requires the completion of such tasks:

- construction of a geometric model of the waste dynamic pump (WD 16/25); the simulation of the uniform casing walls thinning process under the influence of erosion effects; meshing the model with finite elements; calculating the stress-strain state at the normal operating conditions and hydro-testing;
- apply the previously obtained material properties (modulus of elasticity) to the most critical pump unit (the water elbow part of the pump); to use a method for assessing the probability of plastic stress occurrence, based on data-driven yield surface application.

17.3 Modeling of Centrifugal Pump WD 16/25

The centrifugal pump WD 16/25 is designed for pumping waste, industrial, domestic contaminated, and waste liquids. The analysis takes into account various operating conditions such as normal operating conditions (NOC) and hydro testing (HT) mode. The geometric model of the pump is presented in Fig. 17.1, and consists of: 1—inlet branch, 2—outlet branch, 3—water pump elbow, 4—shaft, 5—motor, 6—stand, 7—bearing, 8—supports, 9—bolts (M8, M12, M14, M16).

According to studies of the pump under similar operating conditions (Kelin et al. 2020), based on the requirements of the standard for strength analyzes (IEC 60041:1991; ISO/TR 17766:2005), a uniform thinning of the walls of the pump elbow is assumed. This thinning corresponds to 18 years of operation with an average running time of 135 h per year (equal to 0.5% thinning per year). A three-dimensional geometric model of complete and partial wall thinning at 0 and 9% is shown in Fig. 17.2.

A finite element (FE) mesh based on linear FE of hexagonal and tetrahedral shapes is applied to the geometric model. The grid used for calculations is shown in Fig. 17.3.

For the calculations, the physical and mechanical characteristics of the material are used for the entire model (steel 20), except for the water pump elbow (orthotropic material, the mechanical properties of which are obtained earlier during the analysis of an artificially generated statistically equivalent material (Shapovalova and Vodka 2020). The corresponding data for the test materials are presented in Table 17.1.

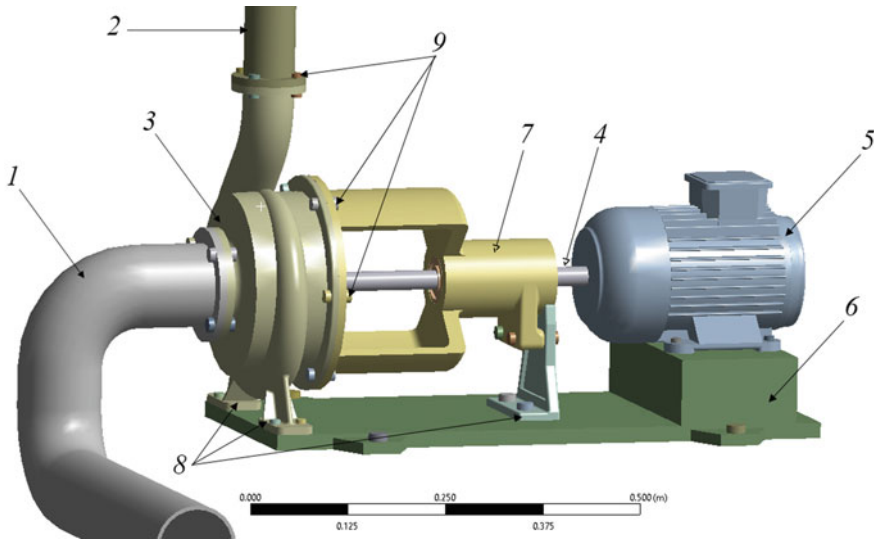


Fig. 17.1 The geometric model of the WD 16/25 pump

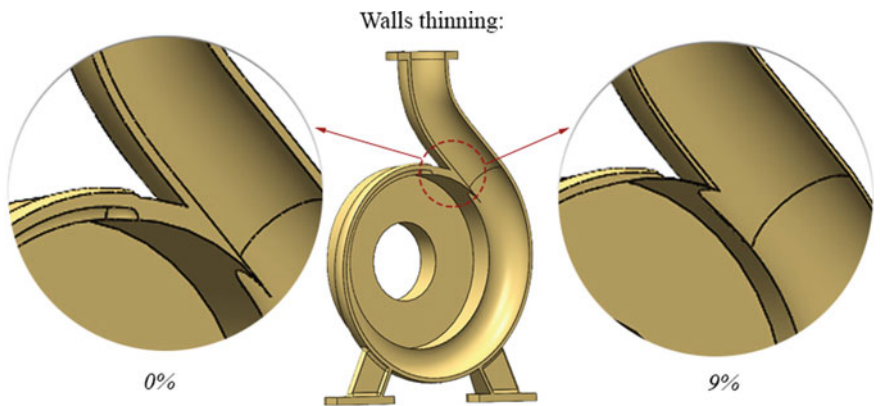


Fig. 17.2 The water elbow part of the pump walls thinning at 0 and 9%

According to strength standards by PNAE G-7-002-86 or similar standards ASME Boiler and Pressure Vessel Code, Vol. III, the nominal allowable stress for elements of equipment and pipelines loaded with internal pressure is selected as the minimum of the following values:

$$[\sigma] = \min\{\sigma_B/2.6; \sigma_{0.2}/1.5\} \tag{17.1}$$

where σ_B —tensile strength; $\sigma_{0.2}$ —yield strength.

To calculate the stress–strain state, the boundary conditions are set:

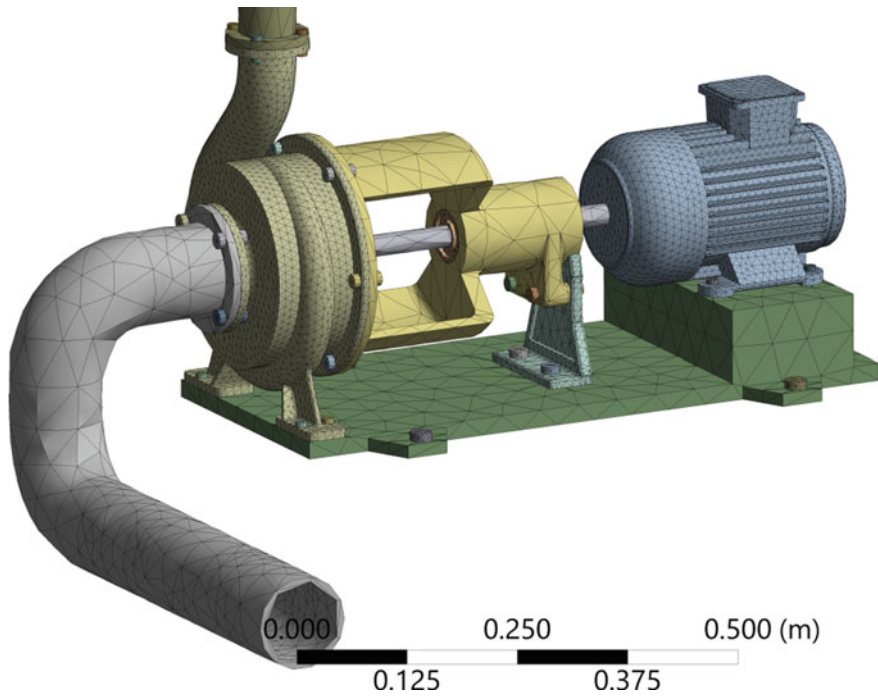


Fig. 17.3 Finite element mesh of the model (general view)

Table 17.1 Mechanical properties of the materials

Elastic modulus, E , GPa	Poisson ratio, ν	Shear module, G , GPa	Ultimate tensile strength, (σ_B) , MPa	Yield strength, $(\sigma_{0.2})$, MPa	Allowable stress, (σ) , MPa	
<i>Steel 20</i>						
200	0.30	79.30	402	216	144	
Artificial microstructure with concentration of inclusions $\psi = 0.100$ (Shapovalova and Vodka 2020)						
$E_x = E_y = E_z$	$\nu_x = \nu_y = \nu_z$	$G_x = G_y = G_z$	Macrolevel ^a		Micro-level	Macrolevel
186.16	0.31	68.93	350	220	3.3	135

^aMacrolevel data taken from cast iron material properties

- surface adjacent to the floor—rigid fixation;
- volumetric force—gravity (acceleration of gravity $g = 9.8 \text{ m/s}^2$);
- the tightening torque of the bolts in the absence of passport data takes according to Table 17.2;

Table 17.2 Standard forces of tightening

Standard size	Preload force, kN	Standard size	Preload force, kN
M8	3.17	M14	10.10
M12	7.38	M16	20.90

- inlet and outlet nozzles are connected to fragments of pipelines, which are modeled to the nearest support. A rigid fixation is set in the axial direction for the working fluid supply pipe and its outlet pipe, and elastic supports with a rigidity of 0.1 N/m are placed in the plane perpendicular to the axis of these pipes;
- internal pressure during normal operation $p = 0.2452$ MPa is set in the volume and the outlet pipe; under the condition of hydro testing, the pressure is increasing to 1.5 times ($p = 0.3678$ MPa) and is set in water pump elbow, in the inlet, and outlet pipes.

According to the result in Fig. 17.4, the maximum stresses occur in the water elbow part of the pump. Therefore, in this part of the model, it is advisable to assess the probability of plastic deformations. The von Mises equivalent stresses are shown in Fig. 17.5 under NOC and during HT mode for the nominal model and at 9% of the elbow walls thinning. According to the results of the calculation (Fig. 17.5a–c), the strength condition is satisfied (the maximum stress value is less than the limit value

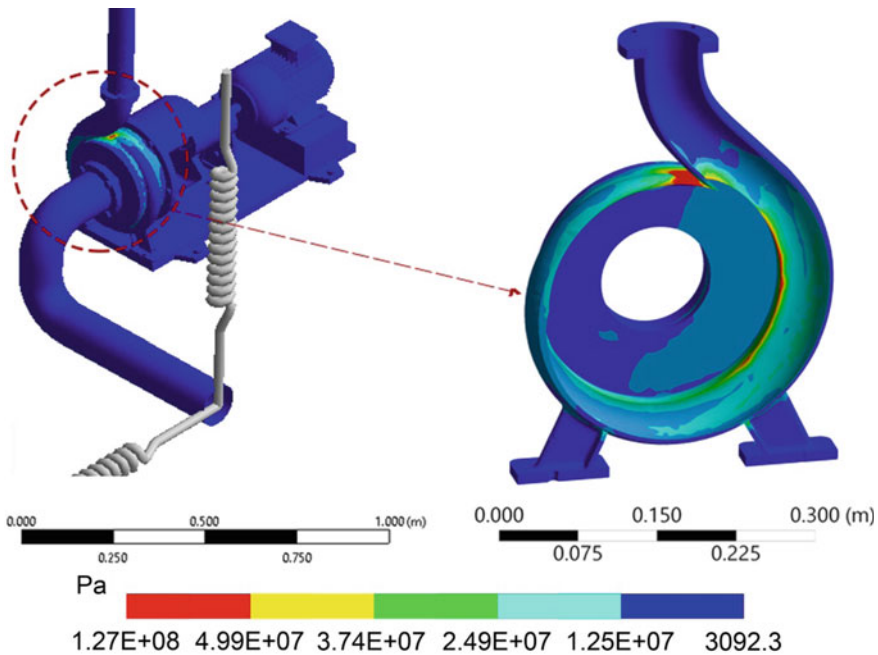


Fig. 17.4 Distribution of equivalent von Mises stresses (Pa), under NOC, at 9% wall thinning

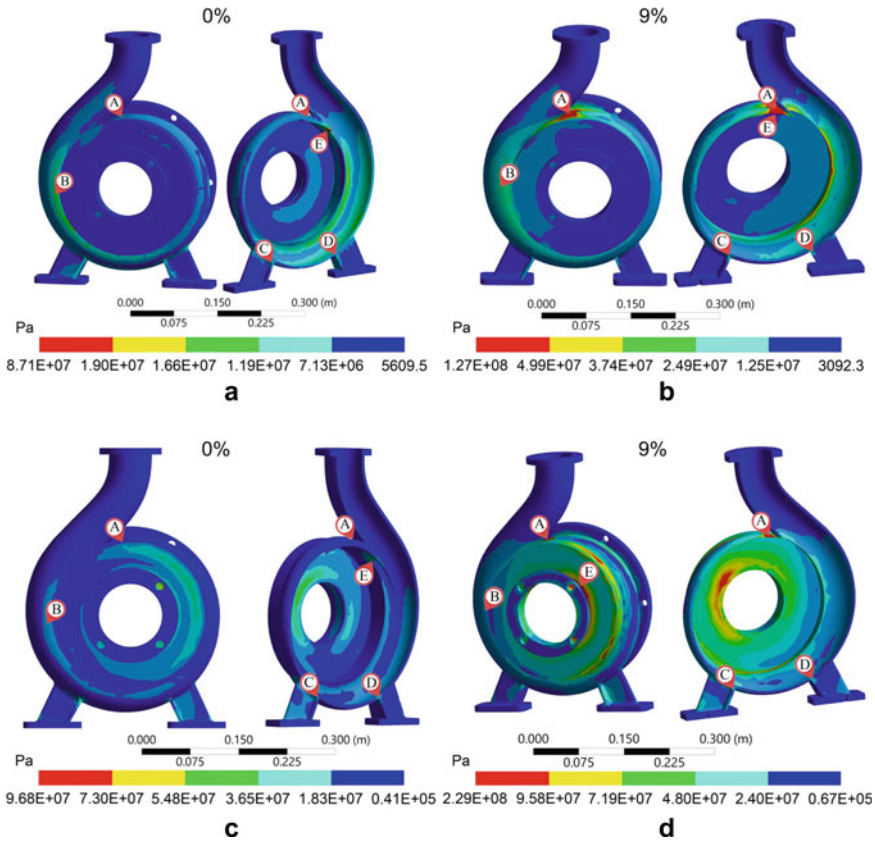


Fig. 17.5 Von Mises equivalent stress (Pa): **a** under NOC at 0% walls thinning; **b** under NOC at 9% walls thinning; **c** under HT mode at 0% walls thinning; **d** under HT mode at 9% walls thinning

$[\sigma] = 135 \text{ MPa}$). During HT mode (Fig. 17.5d) with wall thinning up to 9% in the model arise stresses exceeding the permissible ones (the maximum stress value $[\sigma] = 229 \text{ MPa}$), which indicates the occurrence of plastic deformations of the model at the macrolevel. This is unacceptable according to the standards for this type of equipment (IEC 60041:1991; ISO 9906:2012).

For the analysis of the water elbow part of the pump, five control points are selected, which corresponds: *A*—the upper part of the housing near the outlet; *B*—the outer part of the elbow, which passes into the outlet; *C*, *D*—points of contact water pump elbow with supports; *E*—point with maximum stress in the model.

The dependence of the principal's stress on the water pump elbow walls thinning during the normal operation condition and the hydro test mode in control points are shown in Fig. 17.6.

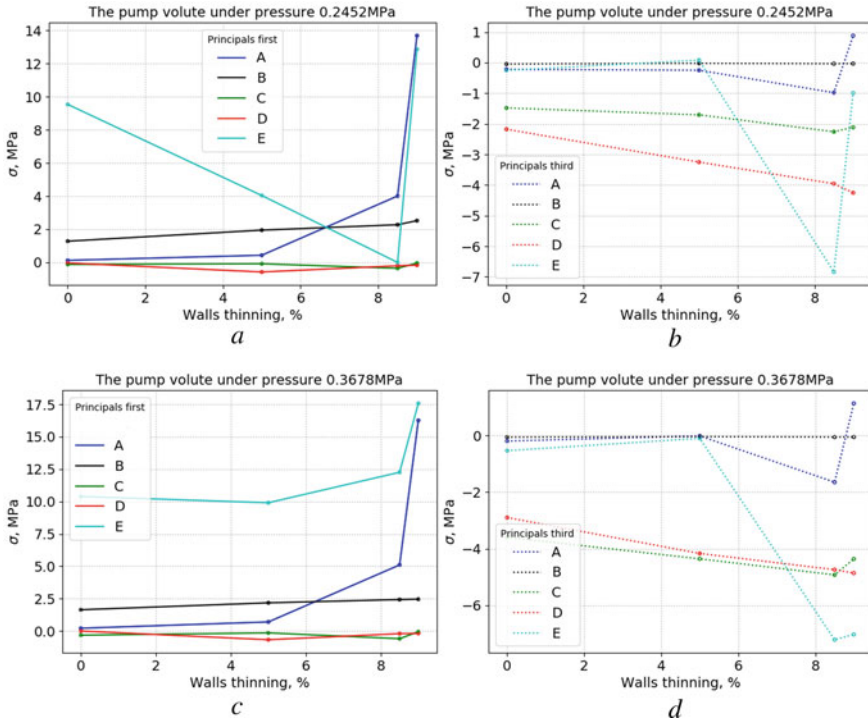


Fig. 17.6 The dependence of the principals stress on the elbow walls thinning: **a** the first principals stress under NOC; **b** the third principals stress under NOC; **c** the first principals stress under HT mode; **d** the third principals stress under HT mode

17.4 Application of Data-Driven Yield Surface to Prediction of Failure Probability for Centrifugal Pump

The proposed technology for studying the occurrence of plastic deformations involves several stages. At the first step, an artificial microstructure of a statistically equivalent material is created for the analysis of the stress–strain state. Artificial microstructure generation is implemented by establishing the dependence between the size and concentration of inclusions (Shapovalova and Vodka 2019a, b, 2020). The information about the quantity and size of inclusions located on a plane is collecting by using computer vision technology. The mathematical expectation data $M[R]$ and the variance $D[R]$ of the radii inclusions dependence on the concentration have been obtained.

The location is followed by a uniform distribution and the size of inclusions is followed to a normal distribution function of concentration. Concentration (ψ) is defined as the ratio of the area of the inclusion to the area of the sample. For this study, the concentration of inclusions is equal to $\psi = 0.100$.

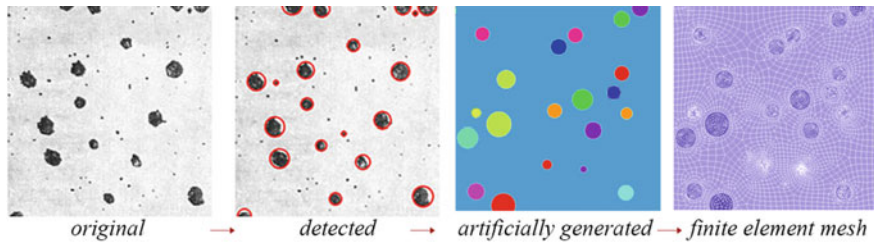


Fig. 17.7 Microstructure research process

The finite element model construction is based on the artificial generated geometric model of the spheroidal graphite cast iron microstructure. To create the mesh grid, a two-dimensional 8-node finite element with two degrees of freedom in each node is used (Zienkiewicz 1971). For calculation, it is assumed that the main matrix of the investigate sample is isotropic ferrite and the inclusions are an orthotropic graphite material. The corresponding materials properties and elastic constants are given in Table 17.1. Various material properties and their resistance to tension and compression are taken into account. An example of the initial image of the nodular cast iron microstructure, the recognized inclusions, the artificial statistically equivalent generated microstructure, and the mesh of the model are shown in Fig. 17.7.

The next step for the probability of pump failure investigation is the yield surface calculation. One of the tasks of materials engineering is to establish the loading conditions that cause plastic deformation. This is important to determine the load combination which leads to a transition from the elastic to the plastic. In the case of uniaxial loading, this task is not particularly difficult. It is enough to have a relation between stress and strain. Such data can be obtained from experiments on simple tension and compression. However, for materials that are in multi-dimensional stress state conditions, plasticity predicting requires additional information. In the case of a three-dimensional stress state, determining the yield surface is a difficult task. This is due to several technical difficulties caused on the one hand by the complexity of the experimental environment, and on the other hand, by the huge number of samples that need to be tested. This problem is especially acute for composite and heterogeneous materials. To solve this problem, computer simulation methods are used.

In this work to construct the yield surface, the model is considered under different loadings. One of the typical load cases for concentration $\psi = 0.100$ is shown in Fig. 17.8. The model is represented by a square plate with a side— l . The deformation is set equal to $\varepsilon_\rho = \Delta/l = 10^{-5}$, then the displacement is calculated by (2):

$$\begin{aligned} U_x &= \varepsilon_\rho l \cos \Theta \\ U_y &= \varepsilon_\rho l \sin \Theta \end{aligned} \quad (17.2)$$

where U_x, U_y —displacement along the corresponding axis, $\theta = (0 \dots 360)^\circ$ the angle changes in a range, with a step in 3.6° .

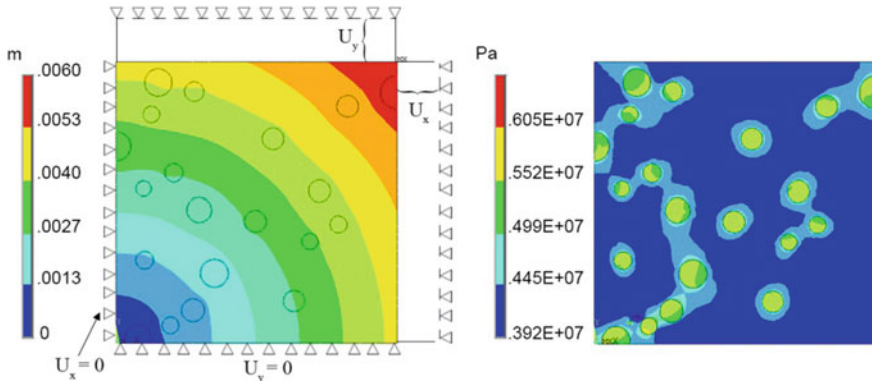


Fig. 17.8 Displacement (m) and von Mises equivalent stress (Pa) for the microstructure model, $\psi = 0.100$

Computer simulation methods are used to calculate the yield surface in a multidimensional stress state. This approach uses the hypothesis of yield strength under difficult loading conditions (Larin et al. 2018; Wu et al. 2020). Finding the yield surface is based on the hypothesis of the maximum distortion energy theory (the Huber-von Mises-Hencky hypothesis), (Ambartsumian 1967). According to it, plastic strains of a sample in a complex stress state occurs when the specific formation energy becomes equal to or exceeds the specific formation energy of the material under the action of a uniaxial stress state.

For statistical equivalent artificial generate microstructure which is consists of two types of materials (ferrite and graphite), the maximum stresses are found. For graphite, the tensile and compressive strengths differ significantly, therefore, separately for each type of stress state, the ratios maximum stresses to the corresponding allowable tensile strength are found. The yield surface is determined by the ratio of the principal stresses to the safety factor (Shapovalova and Vodka 2020). The calculation results of 250 random typical implementations of the yield surface are presented graphically in Fig. 17.9.

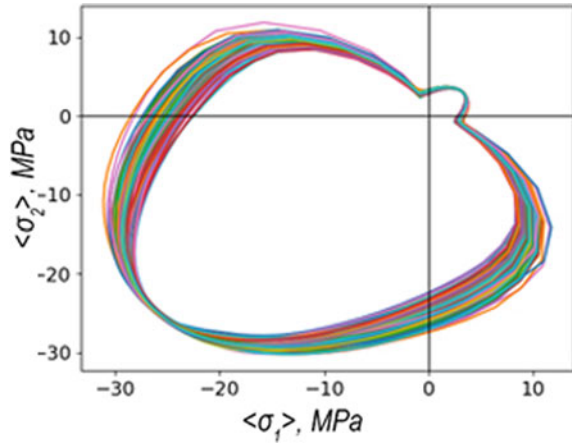
The accumulated statistical information on possible yield surface variants helps to determine the area of stress impact. The construction of a line passing through the origin of the coordinates with control points along it is used (Fig. 17.10). The theta angles that correspond to the loading trajectory are calculated according to (3).

$$\operatorname{tg} \Theta = \frac{\sigma_2}{\sigma_1} \quad (17.3)$$

where σ_1 and σ_2 —the principal stresses.

Information about the number of the yield surfaces that have fallen into the control points along the line is obtained. This method allowing to define the inverse cumulative distribution function, which in turn determines the parameters of descriptive

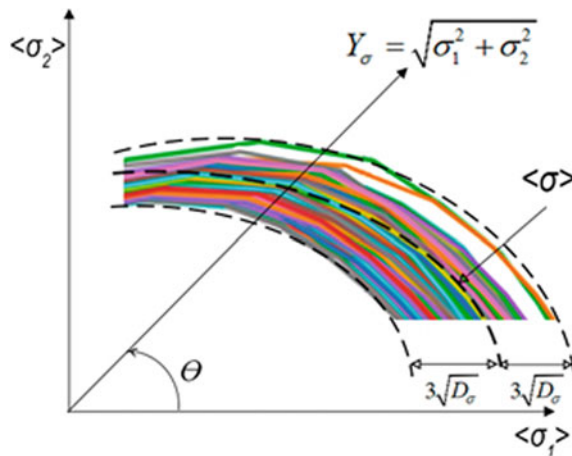
Fig. 17.9 Typical implementations of the yield surface arrangement for $\psi = 0.100$



statistics as mathematical expectation (mean), and variance of the random radius function.

In the third step of investigating pump failure-free operation probability, the micro material analysis technology is applied. The material properties for the generated microstructure from Table 17.1 are used, the finite element method is applied for the model with different modes of operation. The probability of failure-free operation in five control points of the water elbow part of the pump depending on the walls thinning under NOC and HT modes are shown in Fig. 17.11. The probability of microplastic deformations at the control points increases even when the walls are thinned by 1%, and tend to 1 already at 4% thinning (Fig. 17.11, a). Which corresponds approximately to 8 years of normal operation. During hydro testing, the probability of microplastic deformations increases to 1 even at thinning close to 2% (Fig. 17.11b), which corresponds to 3–4 years of equipment operation. The

Fig. 17.10 Bounds on the yield surface stress



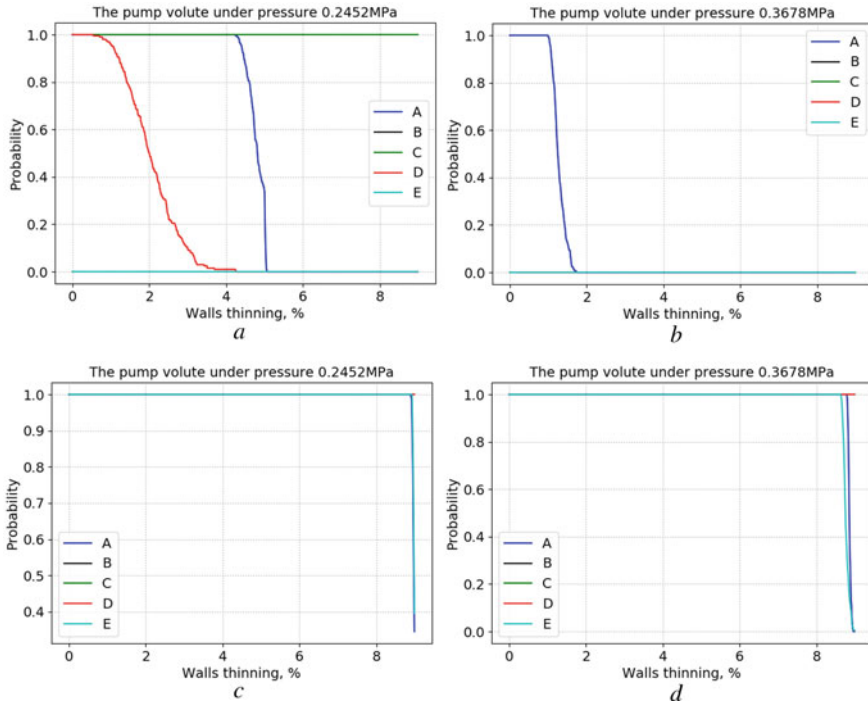


Fig. 17.11 The probability of failure-free operation of the pump depending on the elbow walls thinning: **a** for NOC at the micro-level; **b** for HT mode at the micro-level; **c** for NOC at the macrolevel; **d** for HT mode at the macrolevel

occurrence of plastic deformations at the micro-level can lead to the development of cracks and structural failure at the macro level. Consequently, such areas require careful study and control over the entire life of the equipment.

The criterion for strength at the macrolevel is the yield stress $\sigma_{0.2}$, which already implies 0.2% plastic deformation. The score for an artificially generated structure assumes 0% plastic deformation, and it's much less. But in practice, the $\sigma_{0.2}$ criterion is used. According to Table 17.1, the passport data to comparing the strength criterion are taken for a similar material by which an equivalent structure is created (spheroidal cast iron 35). Therefore, a transition coefficient is introduced, which corresponds to the expansion of the yield surface curve at the macro level without changing its shape. The results for the control points at NOC and under HT mode are shown in (Fig. 17.11c, d). The results of macroplastic deformation probability in the model occur when the wall thinning is close to 9%, which corresponds to 17–18 years of equipment operation.

Visualization of the entire model plastic deformation probability implemented by using the pyansys (Kaszynski 2020) library (Fig. 17.12). For the case of normal operating conditions with 0% wall thinning, the probability at the macro level and the

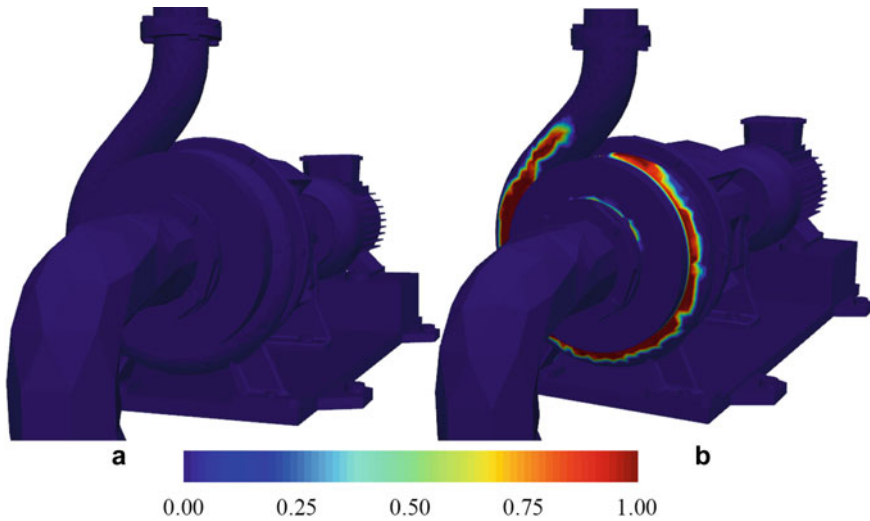


Fig. 17.12 The probability of plastic deformation in the pump under NOC with 0% walls thinning, visualized by pyansys library (Kaszynski 2020). **a** Probability of macroplastic deformation; **b** probability of microplastic deformation

micro-level is different. This corresponds to the onset of microplastic deformations, which do not significantly affect the macrolevel.

17.5 Conclusions

The paper discusses steps at studying the probability of the centrifugal pump failure-free operation with data-driven yield surface application. The construction of a geometric model of the WD 16/25 pump was carried out taking into account the uniform thinning of the body walls under the influence of corrosive effects. Distributions of equivalent stresses in the pump construction elements under normal operating conditions and hydro-testing mode are obtained. To the most critical pump unit (the elbow part of the pump) applying previously obtained material properties. The investigation of the elbow part of a centrifugal pump is based on the microstructure estimation of the material for obtaining information about the state and predicting the probabilistic characteristics. A set of yield surfaces is determined from an artificially generated statistically equivalent material structure using the finite element method. Takes into account the different behavior of composite materials under tensile and compressive loads. Going beyond the yield surface indicates the possibility of transition into a plastic state. Understanding the processes in the structure at the micro-level allows one to predict possible macro destruction of the model in advance. The results of the work show the probability of failure-free operation in the time of the pump during normal operation and hydro test mode.

Acknowledgements This work has been supported by the Ministry of Education and Science of Ukraine in the framework of the realization of the research project «Development of methods of computational intelligence in problems of synthesis of characteristics of responsible elements, increase of reliability and efficiency of innovative equipment» (State Reg. Num. 0121U100730).

References

- Ambartsumian, S.: Theory of Anisotropic Plates. Nauka, Moscow (1967). (in Russian)
- ASME Boiler and Pressure Vessel Code, vol. III, 2019 Edition. ASME. Retrieved 8 July 2019
- Banabic, D., Barlat, F., Cazacu, O., et al.: Advances in anisotropy and formability. *Int. J. Mater. Form.* **3**, 165–189 (2010). <https://doi.org/10.1007/s12289-010-0992-9>
- Cheng, Q., Wang, S., Yan, C.: Robust optimal design of chilled water systems in buildings with quantified uncertainty and reliability for minimized life-cycle cost. *Energy Build.* **126**, 159–169 (2016). <https://doi.org/10.1016/j.enbuild.2016.05.032>
- IEC 60041:1991, Field acceptance tests to determine the hydraulic performance of hydraulic turbines, storage pumps, and pump-turbines (1991), p. 436
- ISO/TR 17766:2005, Centrifugal pumps handling viscous liquids (2005), p. 35
- ISO 9906:2012, Rotodynamic pumps—Hydraulic performance acceptance tests—Grades 1, 2 and 3, IDT (2012), p. 59
- Jacobs, J., Mathews, M., Kleingeld, M.: Failure prediction of mine de-watering pumps. *Failure Anal. Prevent.* **18**(4), 927–938 (2018). <https://doi.org/10.1007/s11668-018-0488-3>
- Kahlman, L.: Extending the life of pumps and fans. *World Pumps.* **2016**(7–8), 32–33 (2016). [https://doi.org/10.1016/S0262-1762\(16\)30167-5](https://doi.org/10.1016/S0262-1762(16)30167-5)
- Kaszynski, A.: Pyansys: Python Interface to MAPDL and Associated Binary and ASCII Files (Version 0.43.2). Zenodo (2020). <https://doi.org/10.5281/zenodo.4009467>
- Kelin, A., Larin, O., Naryzhna, R., Trubayev, O., Vodka, O., Shapovalova, M.: Mathematical modelling of residual lifetime of pumping units of electric power stations. In: *Integrated Computer Technologies in Mechanical Engineering. Advances in Intelligent Systems and Computing*, vol. 1113 (2020), pp. 271–288. https://doi.org/10.1007/978-3-030-37618-5_24
- Kelin, A., Larin, O., Naryzhna, R., Trubayev, O., Vodka, O., Shapovalova, M.: Estimation of residual life-time of pumping units of electric power stations. In: *IEEE 14th International Conference on Computer Sciences and Information Technologies (CSIT)*, Lviv, Ukraine, vol. 1 (2019), pp. 153–159. <https://doi.org/10.1109/STC-CSIT.2019.8929748>
- Larin, O., Kelin, A., Naryzhna, R., Potopalska, K., Trubayev, O.: Analysis of the pump strength to extend its lifetime. *Nucl. Radiat. Safety* **3**(79), 30–35 (2018). [https://doi.org/10.32918/nrs.2018.3\(79\).05](https://doi.org/10.32918/nrs.2018.3(79).05)
- Lvov, G., Kostromytska, O.: A data-driven approach to the prediction of plasticity in composites. *Integrated computer technologies in mechanical engineering. Adv. Intell. Syst. Comput.* **1113**, 3–10 (2020). https://doi.org/10.1007/978-3-030-37618-5_1
- Patel, S., Allaire, P., Wood, H., Throckmorton, A., Tribble, C., Olsen, D.: Methods of failure and reliability assessment for mechanical heart pumps. *Artif. Organs* **29**(1), 15–25 (2005). <https://doi.org/10.1111/j.1525-1594.2004.29006.x>
- Shapovalova, M., Vodka, O.: A data-driven approach to the prediction of spheroidal graphite cast iron yield surface probability characteristics. In: *Integrated Computer Technologies in Mechanical Engineering. ICTM 2020. Lecture Notes in Networks and Systems*, vol. 188 (2020), pp. 565–576. https://doi.org/10.1007/978-3-030-66717-7_48
- Shapovalova, M., Vodka, O.: Image microstructure estimation algorithm of heterogeneous materials for identification their chemical composition. In: *IEEE 2nd Ukraine Conference on Electrical and Computer Engineering (UKRCON)*. Institute of Electrical and Electronics Engineers Inc., Ukraine, Lviv (2019a), pp. 975–979. <https://doi.org/10.1109/UKRCON.2019.8879861>

- Shapovalova, M., Vodka, O.: Computer methods for constructing parametric statistically equivalent models of high-strength cast iron microstructure to analyze its elastic characteristics. In: Notes of the Tavrida National Univ. V.I. Vernadsky. Series: Technical Sciences, vol. 6(1) (2019b), pp. 179–187 (in Ukrainian). <https://doi.org/10.32838/2663-5941/2019.6-1/33>
- Siddiq, A. (2020). Data-driven finite element method: theory and applications. Proc. Inst. Mech. Eng. Part C J. Mech. Eng. Sci. <https://doi.org/10.1177/0954406220938805>
- Verhuelsdonk, B.: Increasing the operational lifetime of rotary lobe pumps. World Pumps **2005**(468), 42–44 (2005). [https://doi.org/10.1016/S0262-1762\(05\)70750-1](https://doi.org/10.1016/S0262-1762(05)70750-1)
- Wu, B., Wang, H., Taylor, T., Yanagimoto, J.: A non-associated constitutive model considering anisotropic hardening for orthotropic anisotropic materials in sheet metal forming. Int. J. Mech. Sci. **169**, 105320 (2020). <https://doi.org/10.1016/j.ijmecsci.2019.105320>
- Zienkiewicz, O.: The Finite Element Method in Engineering Science. McGraw-Hill, London (1971)

Part VI

Rotating Systems

Chapter 18

Self-synchronization of Rotational Regimes of Vibro-exciter on Oscillatory Systems



Arkadiy I. Manevich

Abstract The steady-state synchronous rotations of vibro-exciter (unbalanced rotors), mounted on a linear oscillator (elastic base) and driven by different rotating torques, are studied employing the proposed in our previous work analytical procedure. The obtained solution which is validated in the numerical simulation yields to essential corrections in characteristics of the synchronized regimes in comparison with some previous works. Stability of the synchronized motions is studied, and a new stability criterion is proposed and discussed.

Keywords Vibro-exciter · Synchronized regimes · Stability

18.1 Introduction

Synchronization of rotating bodies on elastic support has been discovered in the middle of the twentieth century and since that time has found various technical applications. It seems that the first theoretical analysis of interaction of vibration and rotation, in particular, vibrational retardation of rotation, and explanations of effects caused by this interaction can be found in Rocard (1949); Mazet (1955); Kononenko (1969); Blekhman (1971). Systematic and extensive studies have been conducted, among others, by I.I. Blekhman, his co-workers and followers and have been summarized in Blekhman (1999). However, the solution for the problem of self-synchronization of several vibro-exciter, presented in this monograph, suffers with some drawbacks; in particular, it misses the Sommerfeld effect (in distinction on presented there solutions for oscillatory systems with one vibrator or rotator), and therefore, it leads to inexact characteristics of synchronized modes.

Note also that during last decades, the results of theoretical investigation and numerical simulation of the Sommerfeld effect in different systems can be found

Professor Arkadiy I. Manevich died on February, 8, 2021.

A. I. Manevich (✉)
Department of Theoretical and Computational Mechanics,
Dniepr National University, Dniepr 49010, Ukraine

in numerous publications. For review of these investigations, we refer to Balthazar et al. (2003, 2018).

In Manevich (2018, 2020), the problems of vibrational maintenance and retardation of rotation in oscillatory systems with one vibrator or rotator are considered, and a straightforward analytical procedure has been proposed for description of stationary synchronous oscillation—rotation regimes. This approach, which accounts for the nonlinear interaction of rotation and oscillation without unjustified introduction of small parameters and associated with them asymptotic procedures, nicely correlates to numerical simulations.

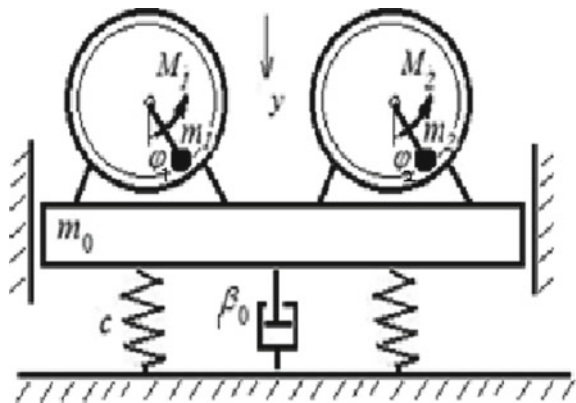
In the present work, a similar approach is employed to study the self-synchronization of a multiple vibrators on a linear oscillator. The obtained solution has some fundamental differences from one presented in Blekhman (1999), and in particular, it entirely agrees with the Sommerfeld effect and with results of the numerical simulation.

18.2 The Model and Governing Equations

The mechanical system consists of a few vibro-exciter with masses m_k ($k = 1, \dots, s$), installed on an common elastic base—linear oscillator of mass m_0 with springs of total stiffness c and viscous friction coefficient β_0^* . We adopt that the oscillator moves only in the vertical direction. The rotors are driven by rotating moments M_k and are considered as physical pendulums with radius of inertia r and reduced length l_c (see Fig. 18.1, where for the simplicity, only two vibro-exciter are shown).

The Lagrangian and the Rayleigh dissipative function in terms of displacement y of the mass m_0 and the angles of rotation φ_k (with account of viscous friction in the oscillating base and in the vibro-exciter) are written as follows:

Fig. 18.1 Mechanical system under consideration



$$L = \frac{m}{2} \left(\frac{dy}{dt} \right)^2 + \sum_k \frac{m_s r^2}{2} \left(\frac{d\varphi_k}{dt} \right)^2 - l_c \sum_k m_k \frac{dy}{dt} \frac{d\varphi_k}{dt} \sin \varphi_k - \frac{cy^2}{2} - gl_c \sum_k m_k (1 - \cos \varphi_k) \quad (18.1)$$

$$\Phi = \frac{\beta_0}{2} \left(\frac{dy}{dt} \right)^2 + \sum_k \frac{\beta_k}{2} \left(\frac{d\varphi_k}{dt} \right)^2$$

where $m = m_0 + \sum_{k=1}^s m_k$. Equations of motion in dimensionless variables $\tau = \omega_0 t$, $Y = y/l_c$, $\omega_0 = \sqrt{c/m}$ are presented as follows:

$$\frac{d^2 Y}{d\tau^2} + \beta_0^* \frac{dY}{d\tau} + Y - \sum_k \mu_k \left(\frac{d^2 \varphi_k}{d\tau^2} \sin \varphi_k + \left(\frac{d\varphi_k}{d\tau} \right)^2 \cos \varphi_k \right) = 0 \quad (18.2)$$

$$\mu_k \frac{d^2 \varphi_k}{d\tau^2} + \beta_k^* \frac{d\varphi_k}{d\tau} + \mu_k \left(p^2 - \eta^2 \frac{d^2 Y}{d\tau^2} \right) \sin \varphi_k = M_k^* \left(\frac{d\varphi_k}{d\tau} \right), \quad (k = 1, \dots, s) \quad (18.3)$$

where

$$\mu_k = \frac{m_k}{m}, \quad p = \frac{\omega_p}{\omega_0}, \quad \omega_p = \frac{\sqrt{gl_c}}{r}, \quad \eta = \frac{l_c}{r}, \quad \beta_0^* = \frac{\beta_0}{m\omega_0}, \quad \beta_k^* = \frac{\beta_k}{mr^2\omega_0}, \quad M_k^* = \frac{M_k}{mr^2\omega_0^2} \quad (18.4)$$

Here, ω_0 is the natural frequency of the oscillator with pendulum vibro-exciter, and ω_p is the partial frequency of the pendulum on immovable base. Parameter p specifies the relationship between the partial frequencies of the pendulum and the main body (base). The time is normalized by period of natural oscillations of the main body (with vibrators fixed on it), so the normalized frequency $\omega = 1$ corresponds to oscillations with natural frequency ω_0 .

In this system, different characteristic time scales can be indicated, which are determined by the following frequencies:

1. Natural frequency of the main body with the fixed pendulums,
2. Natural frequency of the unbalanced pendulum swinging ω_p (the natural frequency is the same for each identical pendulum), and
3. Frequencies (or average angular velocities of rotation) of the rotors on the immobile base, which depends on relationships between the rotating moments and damping moments in the rotors.

In general case, “quick” and “slow” motions cannot be separated.

18.3 Solution in the First Approximation: Averaged Synchronous Regimes

18.3.1 Averaged Characteristics of the Synchronous Regimes

18.3.1.1 Averaged Equations

We are seeking stationary regimes of synchronous rotation of the rotors-vibrators and oscillation of the base (1:1 stationary synchronous rotation-oscillation regimes, or SSRO-regimes). The problem is solved in two stages. At the first stage, the averaged (per period) characteristics of stationary synchronous modes are determined. Solution of Eq. (18.2) is sought in the form of harmonic oscillations, and Eqs. (18.3) for the rotors are satisfied in integral sense (i.e., rotation of the rotors is assumed uniform):

$$Y = a \cos \omega \tau; \quad \varphi_k = \sigma_k(\omega \tau + \gamma_k) \quad (k = 1, \dots, s), \quad (18.5)$$

where $\sigma_k = \pm 1$, depending on the directions of rotation of the k th rotor;

Equation (18.2) after substitution of (18.5) is reduced to the following form:

$$\left[a(1 - \omega^2) - \sum_k \mu_k \omega^2 \cos \gamma_k \right] \cos \omega \tau + (-\beta_0^* a \omega + \sum_k \mu_k \omega^2 \sin \gamma_k) \sin \omega \tau = 0 \quad (18.6)$$

Equation (18.3) for averaged (over the period) steady-state rotations yields the equalities:

$$\frac{\omega}{2\pi} \int_0^{2\pi/\omega} [\sigma_k \beta_k^* \omega + \mu_k (p^2 + \eta^2 a \omega^2 \cos \omega \tau) \sigma_k \sin(\omega \tau + \gamma_k) - M_k^*] d\tau = 0 \quad (k = 1, \dots, s) \quad (18.7)$$

We come to a set of $s + 2$ transcendental equations for the synchronous frequency ω , amplitude of the base oscillations a , and phases of the each rotor rotation γ_k (with respect to oscillations of the base):

$$a(1 - \omega^2) - \omega^2 \sum_k \mu_k \cos \gamma_k = 0 \quad (18.8a)$$

$$-\beta_0^* a \omega + \omega^2 \sum_k \mu_k \sin \gamma_k = 0 \quad (18.8b)$$

$$-\beta_k^* (\omega_k - \sigma_k \omega) + 0.5 \eta^2 \sigma_k \mu_k a \omega^2 \sin \gamma_k = 0. \quad (k = 1, \dots, s) \quad (18.8c)$$

where $\omega_k = M_k^*/\beta_k^*$ are the partial angular velocities of the rotors (speeds of their stationary rotation on a fixed base). The quantity

$$V_k = -0.5\sigma_k\eta^2\mu_k a \omega^2 \sin \gamma_k \quad (18.9)$$

is the average value (over the period) of the normalized moment of the translational inertia force applied to the k th rotor from the oscillating base. In the literature, it is called “vibrational moment” (Blekhman 1999); (in dimensional form vibrational moment (18.9) is multiplied by $m r^2 \omega_0$). Equation (18.8c) has a meaning of balancing the averaged moments of friction forces, the external moment, and the vibrational moment for each rotor.

Stationary synchronous regimes of rotors rotations—oscillations of the base exist if there are real roots to the transcendental set of Eqs. (18.8). Numerical simulation have shown that, and it is typical for n-DOF nonlinear systems, for given parameters of the system ($\mu_k, \beta_0^*, \beta_k^*, \eta$) and given ω_k (i.e., driving moments), several stationary synchronous modes can exist that differ by frequency, amplitude and also by phase relationships (in particular, for system with two vibrators, we can obtain up to six modes, as it will be shown in the examples presented below). It does not seem possible to determine an exact number of synchronous modes in such systems, but this problem will be discussed in the next sub-section.

18.3.1.2 Solution for the Averaged Modes

Expressing the $\sin \gamma_k$ from (18.8c), namely

$$\sin \gamma_k = \frac{2\beta_k^*(\sigma_k \omega_k - \omega)}{\eta^2 \mu_k a \omega^2} \quad (k = 1, \dots, s) \quad (18.10)$$

we obtain from (18.8b) the relationship between the base oscillation amplitude and the synchronous frequency ω of the 1:1 SSRO-regimes that we can write in two following forms:

$$\omega = \frac{\sum_k \beta_k^* \sigma_k \omega_k}{0.5\beta_0^* \eta^2 a^2 + \sum_k \beta_k^*}, \quad a^2 = \frac{2}{\beta_0^* \eta^2 \omega} \sum_k \beta_k^* (\sigma_k \omega_k - \omega), \quad (18.11)$$

First Formula (18.11) principally differs from analogous relation given in Blekhman (1999, Chap. 7). It includes the term in the denominator, which depends on the oscillation amplitude a accounting for the effect of vibrations of the base on rotation of the rotors (energy loss in vibrations), i.e., the Sommerfeld effect for the system under consideration. The absence of this term in solution for self-synchronized vibroexciters obtained in Blekhman (1999, see expressions (7.2.47) and (7.2.54) there), which is caused by oversimplified expression for the “vibrational moment,” leads to incorrect assertions. Namely, it is stated that the synchronous frequency cannot

be less than the minimal of the partial angular velocities, and that the sum of vibrational moments on all vibro-exciters equal to zero, and a number of other wrong conclusions. We should underline that the numerical simulation described below (see Sect. 4.2) convincingly confirms expressions (18.11).

Excluding from the set (18.8) a , γ_k ($k = 1 - s$) by using of (18.10) and the second formula (18.11), we obtain equation for the synchronous frequency in dependence on the partial angular velocities ω_s (normalized rotating moments):

$$2(1 - \omega^2) \sum_k \beta_k^* (\sigma_k \omega_k - \omega) - \omega \sum_k \text{sign}(\cos \gamma_k) \sqrt{2\omega^3 \eta^2 \mu_k^2 \sum_k \beta_0^* \beta_k^* (\sigma_k \omega_k - \omega) - 4(\beta_0^* \beta_k^*)^2 (\sigma_k \omega_k - \omega)^2} = 0 \quad (18.12)$$

Equations (18.12), (18.11), and (18.10) entirely determine the averaged 1:1 SSRO-regimes in the system. Different combinations of signs in front of the radical are possible in Eq. (18.12), depending on signs of $\cos \gamma_k$, as well as two options for the direction of rotation of each rotor. For each of the options, several solutions can take place. Thus, for given parameters of the system μ_k , β_0^* , β_k^* , η , at given ω_k (i.e., torques), a few stationary synchronous modes (SSRO) can exist, differing in frequency, amplitude, and phase relationships. Their number is determined by the number of real roots of Eq. (18.12).

As the right-hand side in (18.10) cannot exceed unity by modulus, the following constraint from below on the amplitude of the support oscillation for SSRO-regimes follows from (18.10):

$$a \geq a_{\min} = \max_k \left| \frac{2\beta_k^* (\sigma_k \omega_k - \omega)}{\eta^2 \mu_k \omega^2} \right| \quad (18.13)$$

18.3.1.3 Phase Angles and Mechanism of the Self-synchronization

Let us consider the physical meaning of different signs of $\sin \gamma_k$ and $\cos \gamma_k$. Since phase angles of the rotors γ_k are defined with respect to oscillations of the support (see (18.5), condition $\sin \gamma_k > 0$ (or $0 \leq \gamma_k \leq \pi$) means that the rotation of this rotor is ahead of the support oscillations in phase, and if $\sin \gamma_k < 0$ ($-\pi \leq \gamma_k \leq 0$), then the rotor lags behind the support oscillations. Let, for definiteness, $\sigma_k = 1$. As is seen from expression (18.10), $\sin \gamma_k$ is positive if the partial angular velocity of the k th rotor and ω_k is greater than the synchronous frequency ω . In this case, vibration moment (18.9) (transmitted from the oscillating support to the k th rotor) is negative, the rotor transfers part of its energy to the oscillator, slowing down the own rotation (in comparison with the case of the rigid support, its angular velocity decreases from ω_k to ω). For those vibrators whose partial angular velocity ω_k lesser than the

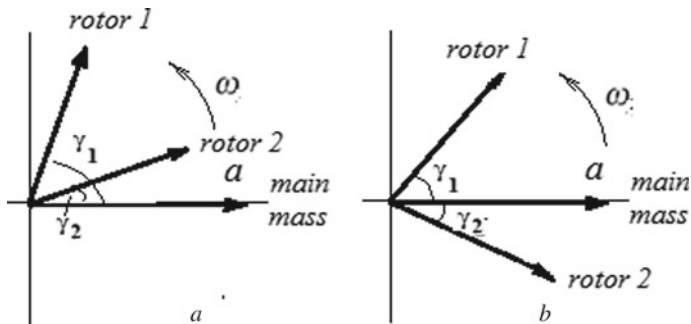


Fig. 18.2 Possible phase relations in case of two vibrators

synchronous frequency ω , the picture will be opposite, $\sin \gamma_k < 0$, the vibrational moment V_k is positive, and it accelerates rotation of the rotor by the energy of the support (such rotors operate in the generator mode). Due to this, redistribution of energy the self-synchronization occurs: vibrators with large partial angular velocities slow down, those with small ones are accelerated until velocities of all the rotors become equal.

Thus, namely the sign of $\sin \gamma_k$ determines whether the k th rotor is accelerated or retarded by the vibrations of the base. All rotors that are phase-ahead of the support oscillations transmit energy to the oscillations, and those lagging in phase receives energy from the oscillations.

In the particular case of one rotor on an elastic support, when the source of motion is a rotating torque (vibrational retardation of rotation), the rotation of the rotor is always ahead of the oscillation of the support in phase ($0 \leq \gamma_k \leq \pi$). When the source of motion is the support oscillations (vibrations maintenance of rotation), then the pendulum rotation lags behind the oscillations in phase ($-\pi \leq \gamma_k \leq 0$). In the case of two rotors on an elastic support, when the source of motion is torques (on two or one rotor), either both rotors operate in the engine mode or one of them (with a lower torque) operates in the generator mode (Fig. 18.2a, b).

As for $\cos \gamma_k$, their signs determine whether the angle γ_k is acute or obtuse. In the first case, we can conditionally say that the rotor rotates “in phase” with oscillation of the support, and in the second case, it rotates “in out-of-phase.”

In conclusion of the section, we note that Eq. (18.8) for SSRO-regimes takes into account the interaction of rotation and oscillation (centrifugal inertia forces from the rotors in the equation of support oscillations and translation inertia forces in equations of the rotors). Therefore, they determine the *exact* values of the *averaged* characteristics of synchronous motions of the system, namely synchronous frequency, amplitude of oscillations, and phase angles. To the contrary, the solutions obtained in the first approximation of the small parameter method do not take into account the centrifugal inertia forces.

18.3.2 Stability of the Synchronous Regimes in the First Approximation

Exploration of the stability of obtained averaged regimes requires the analysis of non-stationary motions. Such analysis for a system with one vibrator has been performed in Manevich (2020). In this paragraph, a similar analysis is carried out for the system of several vibro-exciter on the elastic base. The differential equation determining the *averaged* angular velocity for *non-stationary rotation* of the rotors yields from Eq. (18.3) after substituting $Y = a \cos \omega\tau$, $\varphi_k = \sigma_k(\omega\tau + \gamma_k)$ and averaging for period (here, ω is a slowly varying function):

$$\frac{\omega}{2\pi} \int_0^{2\pi/\omega} \left[\sigma_k \mu_k \frac{d\omega}{d\tau} + \sigma_k \beta_k^* \omega + \mu_k (p^2 + a\eta^2 \omega^2 \cos \omega\tau) \sigma_k \sin(\omega\tau + \gamma_k) - M_k^* \right] d\tau = 0$$

$$(k = 1, \dots, s) \quad (18.14)$$

Accounting equalities for average quantities: $\langle \cos \omega\tau \sin(\omega\tau + \gamma_k) \rangle = 0.5 \sin \gamma_k$, $\langle p^2 \sin(\omega\tau + \gamma_k) \rangle = 0$ and expressions $\omega_k = M_k^*/\beta_k^*$, after multiplying by σ_k , we come to the differential equation:

$$\mu_k \frac{d\omega}{d\tau} = \beta_k^* (\sigma_k \omega_k - \omega) - 0.5 \mu_k \eta^2 a \omega^2 \sin \gamma_k, \quad (k = 1, \dots, s) \quad (18.15)$$

(for stationary regimes right-hand sides (RHS) in (18.15) vanish by virtue of Eq. (18.8c)). Equations (18.14) and (18.15) are similar to Eq. (18.19) and (18.20) from Manevich (2020). But now, we should consider a coherent movement of the ensemble of rotors. We summarize Eq. (18.15) for all the rotors and obtain equation

$$\frac{d\omega}{d\tau} \sum_k \mu_k = \sum_k \sigma_k \beta_k^* \omega_k - \omega \sum_k \beta_k^* - 0.5 \eta^2 a \omega^2 \sum_k \mu_k \sin \gamma_k \quad (18.16)$$

Supposing that the regime of motion is quasi-static, we assume that phase angles γ_k have time to change in accordance with Eq. (18.8a and 18.8b). Then, following relationships yield from (18.8a and 18.8b) are presented:

$$\sum_s \mu_s \sin \gamma_s = \frac{\beta_0^*}{\omega} a, \quad \sum_s \mu_s \cos \gamma_s = \frac{1 - \omega^2}{\omega^2} a \quad (18.17)$$

With account of the first Formula (18.17), Eq. (18.16) takes the form

$$\frac{d\omega}{d\tau} \sum_k \mu_k = \sum_k \sigma_k \beta_k^* \omega_k - \omega \sum_k \beta_k^* - 0.5 \beta_0^* \eta^2 a^2 \omega \quad (18.18)$$

Amplitude a can be expressed in terms of ω from (18.17) (here, the lower index “*” indicates that the quantities $\gamma_j - \gamma_k$ are computed for the considered stationary synchronous regime):

$$a^2 = \frac{\omega^4 \sum_{j=1}^s \sum_{k=1}^s \mu_j \mu_k \cos(\gamma_j - \gamma_k)_*}{(1 - \omega^2)^2 + \beta_0^{*2} \omega^2} \quad (18.19)$$

Denote the right-hand side of (18.18) by $\Phi(\omega)$ (it corresponds to the non-stationary regimes). Then, Eq. (18.18) is written as

$$\frac{d\omega}{d\tau} \sum_k \mu_k = \Phi(\omega) \quad \Phi(\omega) \equiv M_{\text{sum}}(\omega) - F(\omega), \quad M_{\text{sum}}(\omega) = \sum_k \sigma_k \beta_k^* \omega_k, \quad (18.20)$$

$$F(\omega) = \omega \sum_k \beta_k^* - V(\omega), \quad V(\omega) = -0.5\omega\beta_0^* \eta^2 a^2, \quad (18.21)$$

Here, M_{sum} is the algebraic sum of the normalized rotating moments applied to the rotors. Function $V(\omega)$ can be considered as a complete moment of translational inertia forces acting from the oscillating base to the ensemble of rotors. Equation (18.20) together with expressions (18.21) generalizes Eq. (18.21) obtained in Manevich (2020) for the case of several vibro-exciter.

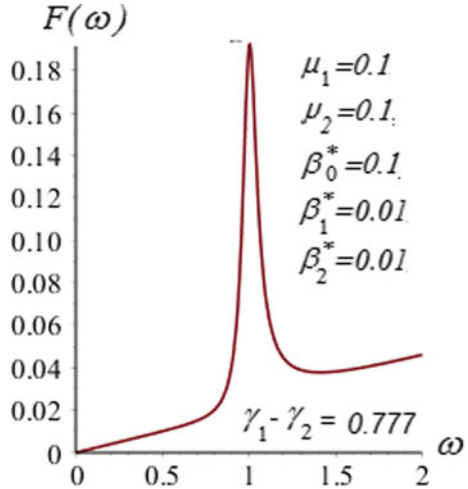
Then, the stability criterion for given stationary motion $\omega = \omega_*$, $\gamma_j - \gamma_k = (\gamma_j - \gamma_k)_*$ with respect to disturbances in frequency ω is reduced to a negativity condition for derivative of the right-hand side in Eq. (18.20): $\Phi'(\omega)|_* < 0$ (where amplitude a depends on ω in accordance to (18.19)). In case of the constant rotating moments ($\omega_k = \text{const}$), we come to the following stability condition:

$$[F'(\omega)]_* > 0, \quad \text{or} \quad \sum_k \beta_k^* - [V'(\omega)]_* > 0 \quad (18.22)$$

This criterion is similar to those obtained in several works for the problem of vibration retardation of rotation in oscillatory systems with *one vibrator*, including Blekhman (1999) and Manevich (2020), but function $V(\omega)$ here has more general sense. As it was noted in Manevich (2020), condition of type (18.22) is not a sufficient condition of stability, because it is obtained for the averaged regimes; it does not take into account the non-uniformity of rotation. In addition, in the case of several vibrators, “summary” Eq. (18.16) is not equivalent to set of s equations (18.15), and only special perturbations of the averaged regimes are accounted for (there was assumed that at deviations of the synchronous frequency the deviations of the phase angles of all the rotors are the same). So condition (18.22) is a necessary condition of stability.

Typical shape of $F(\omega)$ is presented in Fig. 18.3 for a system with two vibro-exciter (for given parameters of the system). The condition (18.22) is violated on

Fig. 18.3 Function $F(\omega)$ determining the necessary condition of stability for averaged SSRO-regimes (case of two vibrators)



the descending portion of the curve $F(\omega)$ in the post-resonance frequency diapason (close to the resonance).

18.4 Solution in the Second Approximation: Non-uniform Synchronous Regimes

18.4.1 Analytical Solution

Non-uniformity of the rotation is caused by translational inertia forces generated by vibration of the base and gravity forces related to the eccentricities of the rotors. These non-uniform rotations can be determined for each rotor at given oscillation of the support independently on others rotors since both abovementioned factors do not depend explicitly on their motions. So in the second approximation, we may consider separately rotation of the k th rotor, using the approach and results of the previous analytical solution for systems with one rotor (Manevich 2020). But in view of some distinctions in statements of the problem, we have to present briefly general stages of the analysis. We are seeking solution of Eqs. (18.2) and (18.3) in the form

$$Y = a \cos \omega \tau, \quad \varphi_k(\tau) = \sigma_k(\omega \tau + \gamma_k + \psi_k(\tau)) \quad (k = 1, \dots, s), \quad (18.23)$$

with ω and γ_k obtained in the first approximation. Functions $\psi_k(\tau)$ are $2\pi/\omega$ -periodic functions with zero average value, which are assumed small with respect to unity. Substitution of (18.23) into Eq. (18.3) with $\omega_k = M_k^*/\beta_k^*$ yields the nonlinear equation for function $\psi_k(\tau)$:

$$\begin{aligned} \mu_k \frac{d^2 \psi_k}{d\tau^2} + \beta_k^* \frac{d\psi_k}{d\tau} + \mu_k (p^2 + a \eta^2 \omega_k^2 \cos \omega \tau) \sin(\omega \tau + \gamma_k + \psi_k) \\ = 0.5 a \mu_k \eta^2 \omega_k^2 \sin \gamma_k \end{aligned} \quad (18.24)$$

Linearization with account of smallness of $\psi_k(\tau)$ compared to unity reduces (18.24) to the following inhomogeneous Hill equation:

$$\begin{aligned} \mu_k \frac{d^2 \psi_k}{d\tau^2} + \beta_k^* \frac{d\psi_k}{d\tau} \\ + \psi_k \mu_k [p^2 \cos(\omega \tau + \gamma_k) + 0.5 a \eta^2 \omega^2 (\cos \gamma_k + \cos(2\omega \tau + \gamma_k))] \\ = -\mu_k p^2 \sin(\omega \tau + \gamma_k) - 0.5 a \mu_k \eta^2 \omega^2 \sin(2\omega \tau + \gamma_k) \end{aligned} \quad (18.25)$$

Solution to this equation is sought in the form of the Fourier series,

$$\psi_k = \sum_{n=1}^{\infty} (\psi_{kn}^{(1)} \cos n \omega \tau + \psi_{kn}^{(2)} \sin n \omega \tau) \quad (18.26)$$

Substitution of (18.26) into Eq. (18.25) yields to a set of linear algebraic equations for the Fourier coefficients $\psi_{kn}^{(1)}$, $\psi_{kn}^{(2)}$. The analysis showed that only four equations for coefficients at two lower harmonics $\psi_{k1}^{(1)}$, $\psi_{k1}^{(2)}$, $\psi_{k2}^{(1)}$, $\psi_{k2}^{(2)}$ are of principal importance. We come to the set

$$\mathbf{A}_k \Psi_k = \mathbf{b}_k, \quad \Psi_k = [\psi_{k1}^{(1)} \ \psi_{k1}^{(2)} \ \psi_{k2}^{(1)} \ \psi_{k2}^{(2)}]^T, \quad (18.27)$$

$$\begin{aligned} \mathbf{b}_k = \mu_k \left[-\left(\frac{p}{\omega}\right)^2 \sin \gamma_k \quad -\left(\frac{p}{\omega}\right)^2 \cos \gamma_k - \frac{1}{2} a \eta^2 \sin \gamma_k - \frac{1}{2} a \eta^2 \cos \gamma_k \right]^T \\ A_k = \mu_k \begin{bmatrix} \left(\frac{3}{4} a \eta^2 \cos \gamma_k - 1\right) \frac{\beta_k^*}{\mu_k \omega} - \frac{1}{4} a \eta^2 \sin \gamma_k & \frac{1}{2} \left(\frac{p}{\omega}\right)^2 \cos \gamma_k & -\frac{1}{2} \left(\frac{p}{\omega}\right)^2 \sin \gamma_k \\ -\frac{1}{4} a \eta^2 \sin \gamma_k - \frac{\beta_k^*}{\mu_k \omega} & \left(\frac{1}{4} a \eta^2 \cos \gamma_k - 1\right) \frac{1}{2} \left(\frac{p}{\omega}\right)^2 \sin \gamma_k & \frac{1}{2} \left(\frac{p}{\omega}\right)^2 \cos \gamma_k \\ \frac{1}{2} \left(\frac{p}{\omega}\right)^2 \cos \gamma_k & \frac{1}{2} \left(\frac{p}{\omega}\right)^2 \sin \gamma_k & \left(\frac{a \eta^2 \cos \gamma_k}{2} - 4\right) 2 \frac{\beta_k^*}{\mu_k \omega} \\ -\frac{1}{2} \left(\frac{p}{\omega}\right)^2 \sin \gamma_k & \frac{1}{2} \left(\frac{p}{\omega}\right)^2 \cos \gamma_k & -2 \frac{\beta_k^*}{\mu_k \omega} & \left(\frac{a \eta^2 \cos \gamma_k}{2} - 4\right) \end{bmatrix} \end{aligned} \quad (18.28)$$

Note that matrix \mathbf{A}_k and vector \mathbf{b}_k for each rotor depend on three dimensionless parameters of the system ($\beta_k^*/(\mu_k \omega)$, p/ω , and η^2) and parameters of the synchronous regime a , ω and γ_k . After solving the set (18.27) the solution for the angle of rotation with account of its non-uniformity takes the form

$$\begin{aligned} \varphi_k(\tau) = \omega \tau + \gamma_k + (\psi_{k1}^{(1)} \cos \omega \tau + \psi_{k1}^{(2)} \sin \omega \tau) \\ + (\psi_{k2}^{(1)} \cos 2\omega \tau + \psi_{k2}^{(2)} \sin 2\omega \tau), \quad (k = 1, \dots, s) \end{aligned} \quad (18.29)$$

(together with the averaged solution for a , ω and γ_k (18.10)–(18.12)).

At $p = 0$ matrix (18.28) disintegrates into two separate minors of the second order, and vector \mathbf{b}_k has two zero elements. Then, set of Eq. (18.27) factorizes into two sets of second order equations:

$$\mathbf{A}_{k1} \Psi_{k1} = 0, \quad \Psi_{k1} = [\psi_{k1}^{(1)} \psi_{k1}^{(2)}]^T, \\ A_{k1} = \mu_k \begin{pmatrix} \left(\frac{3}{4} a \eta^2 \cos \gamma_k - 1 \right) \frac{\beta_k^*}{\mu_k \omega} - \frac{1}{4} a \eta^2 \sin \gamma_k \\ -\frac{1}{4} a \eta^2 \sin \gamma_k - \frac{\beta_k^*}{\mu_k \omega} \left(\frac{1}{4} a \eta^2 \cos \gamma_k - 1 \right) \end{pmatrix}, \quad (18.30)$$

$$\mathbf{A}_{k2} \Psi_{k2} = \mathbf{b}_{k2}, \quad \Psi_{k2} = [\psi_{k2}^{(1)} \psi_{k2}^{(2)}]^T \\ A_{k2} = \mu_k \begin{pmatrix} \left(\frac{a \eta^2 \cos \gamma_k}{2} - 4 \right) & 2 \frac{\beta_k^*}{\mu_k \omega} \\ -2 \frac{\beta_k^*}{\mu_k \omega} & \left(\frac{a \eta^2 \cos \gamma_k}{2} - 4 \right) \end{pmatrix} \quad (18.31) \\ \mathbf{b}_{k2} = \mu_k \left[-\frac{1}{2} a \eta^2 \sin \gamma_k - \frac{1}{2} a \eta^2 \cos \gamma_k \right]^T$$

Coefficients $\psi_{k1}^{(1)}$, $\psi_{k1}^{(2)}$ become equal to zero, if $\det \mathbf{A}_{k1} \neq 0$. Then, in (18.29), only the second harmonics remain, whose coefficients $\psi_{k2}^{(1)}$, $\psi_{k2}^{(2)}$ can be easily obtained from (18.31) in closed form.

18.4.2 *Instability of Stationary Synchronous Regimes Caused by the Translational Inertia Forces*

Stability analysis of obtained solution (18.29) also is similar to that of Manevich (2020). This solution becomes unstable when the corresponding to Eq. (18.25) homogeneous Hill equation has increasing solutions that means occurrence of parametric resonance for oscillations of angular velocity of rotors. Bounds of the stability and instability zones in the system parameters space correspond to *periodic solutions* of the homogeneous Hill equation.

Here, we consider only the parametric resonance with period 2π which is caused by harmonic perturbing terms of period π in the left hand side of (18.25) (case $p = 0$). So we deal with Mathieu equation. Applying the standard technique, we obtain for the lower boundary of the first instability zone for k th rotor the following condition:

$$\Delta_k \equiv \frac{1}{4} a^2 \eta^4 \left(\cos^2 \gamma_k - \frac{1}{4} \right) - a \eta^2 \cos \gamma_k + 1 + \left(\frac{\beta_k^*}{\mu_k \omega} \right)^2 = 0 \quad (18.32)$$

With account of smallness of $(\beta_k^*/(\mu_k\omega))^2$ with respect to unity, we come to the following necessary condition of stability in terms of critical amplitude a_* :

$$a \leq a_* = \frac{1}{\eta^2} \min_k \left| \frac{4}{2 \cos \gamma_k \pm 1} \pm \left(\frac{\beta_k^*}{\mu_k\omega} \right)^2 \right| \quad (18.33)$$

Note that, as a rule, for many realistic values of the system parameters, dimensionless critical amplitude a_* is very close to $4/3$.

18.5 Results of the Numerical Analysis and Comparison with the Numerical Simulation

As a basic variant for numerical analysis of the obtained analytical solution, there was considered the system of two vibrators on oscillatory system with following parameters: $\mu_1 = \mu_2 = 0.1$, $\beta_1^* = \beta_2^* = 0.01$, $p = 0$, $\eta = 1$. The direction of rotation of both the rotors was taken to be the same. The value of the partial angular frequency for the first rotor was taken equal to $\omega_1 = 1$ (this corresponds to the application to this rotor of torque, which would rotate the rotor on an immovable support with a resonant angular velocity (equal to the natural oscillation frequency of the real support with the fixed rotors). The value of the partial angular frequency ω_2 (and, respectively, the value of torque M_2) for the second rotor is varied over a wide range, from 0 to 7.0.

18.5.1 The Averaged Characteristics of the Synchronous Regimes

First, consider results of the averaged solution presented in Sect. 2.1. Two values of ω_2 were chosen for the numerical simulation, namely 0.6 and 4.0 (i.e., ratios of the torques M_2/M_1 were equal to 0.6 and 4). Table 18.1 presents characteristics of the SSRO-modes obtained from Eqs. (18.10)–(18.12), for the different combinations of signs of cosines for the phase angles (denoted *sgn1* and *sgn2*)—synchronous frequency ω , vibration amplitude of the support a , phase angles γ_1 , γ_2 , and also values of function $F'(\omega)$ (see (18.21)) determining the necessary condition of stability (18.22) for SSOR-regimes. The last column indicates stability or instability of the synchronous regimes in the numerical simulation with the original set of nonlinear Eqs. (18.2) and (18.3).

As is seen from Table 18.1, there exist two SSOR-regimes in case $\omega_2 = 0.6$ and six regimes at $\omega_2 = 4.0$. The signs of angles γ_1 , γ_2 show that in both regimes at $\omega_2 = 0.6$ the first rotor (with larger torque) operates in engine mode and the second rotor—in generator mode. Both these regimes are pre-resonance ($\omega < 1$) and differ

Table 18.1 Characteristics of the synchronous stationary modes in system with parameters: $\mu_1 = 0.1, \mu_2 = 0.1, \beta_0^* = 0.1, \beta_1^* = 0.01, \beta_2^* = 0.01$

ω_2	sgn1, sgn2	ω	a	γ_1	γ_2	$F'(\omega)$	Stability in numerical simulations
0.6	++	0.7253	0.2030	0.5405	-0.2368	0.0407	Stable
	+-	0.7912	0.0667	1.5741	-1.1572	-1.836	Unstable
4.0	++	0.9210	0.8281	0.0225	1.0688	0.810	Stable
	+-	0.9753	0.7908	0.00657	2.2072	0.404	Unstable
	-+	1.0229	0.7600	-3.1362	0.8461	-0.515	Unstable
	--	1.1657	0.6767	-3.1057	2.4773	-0.169	Unstable
	--	2.1750	0.2445	-2.9370	2.8205	0.021	Unstable
	--	2.4846	0.0497	-1.8290	1.7330	0.034	Stable

with sign of $\cos \gamma_1$ (acute angle with respect to the base oscillation in the first mode and obtuse—in the second one).

At $\omega_2 = 4.0$ the second rotor (now with larger torque) in all regimes operates as engine; the first rotor is also operates as engine in both pre-resonance regimes and in generator mode—in four post-resonance regimes ($\omega > 1$). All these regimes have different combinations of the phase angles with different signs of sines and cosines for each rotor. Physically, this means a transfer from engine mode to generator one and (conditionally) transfer from in phase to out-of-phase rotation with respect to the base oscillation, for each rotor.

The numerical simulations (these simulations dealing with non-uniform motions are described below) excellently confirm the characteristics of the SSOR-regimes presented in Table 18.1.

As for stability of the SSOR-regimes, in those three cases, when the criterion (18.22) was violated ($F'(\omega) < 0$), these regimes are found to be unstable. Nevertheless, in other cases, when $F'(\omega) > 0$, two modes (of five) are proved to be unstable. This confirms that inequality (18.22) is necessary but not sufficient condition of stability of synchronous regimes in the systems under consideration.

18.5.2 Verification by Numerical Simulation

The obtained solution in the second approximation [with account of non-uniform rotation (18.23) and (18.29)] was verified by numerical simulation with the primary set of governing Eqs. (18.2) and (18.3). The initial conditions were set using the analytical solution for the averaged steady-state regimes (18.29):

$$\begin{aligned}
 Y(0) &= a, \quad \dot{Y}(0) = 0 \quad \varphi_k(0) = \sigma_k \left(\gamma_k + \psi_{k1}^{(1)} + \psi_{k2}^{(1)} \right) \\
 \dot{\varphi}_k(0) &= \sigma_k \omega \left(1 + \psi_{k1}^{(2)} + 2\psi_{k2}^{(2)} \right) \quad (k = 1 - s)
 \end{aligned}
 \tag{18.34}$$

Due to putting rather exact initial conditions, the SSOR-regimes were established in the numerical simulation very quickly.

Typical results for stable SSOR-modes for the same system ($\mu_1 = \mu_2 = 0.1, \beta_0^* = 0.1, \beta_1^* = \beta_2^* = 0.01, p = 0$) at $\omega_1 = 1, \omega_2 = 4.0$ (normalized torques on two rotors $M_1^* = 0.01$ and $M_2^* = 0.04$) are presented in Fig. 18.4. We take the first pre-resonance mode with normalized synchronous frequency $\omega = 0.9210$, which is presented in Table 18.1 (third line). In Fig. 18.4, there are constructed the time dependences for oscillation of the support $Y(a)$, angles of rotation of the rotors φ_1, φ_2 (*b, c*), their angular velocities $\dot{\varphi}_1, \dot{\varphi}_2$ (*d, e*), and phase curve $\dot{\varphi}_1 - Y$ (*f*). Black curves describe the numerical simulation results; red and blue points and curves describe the analytical solution.

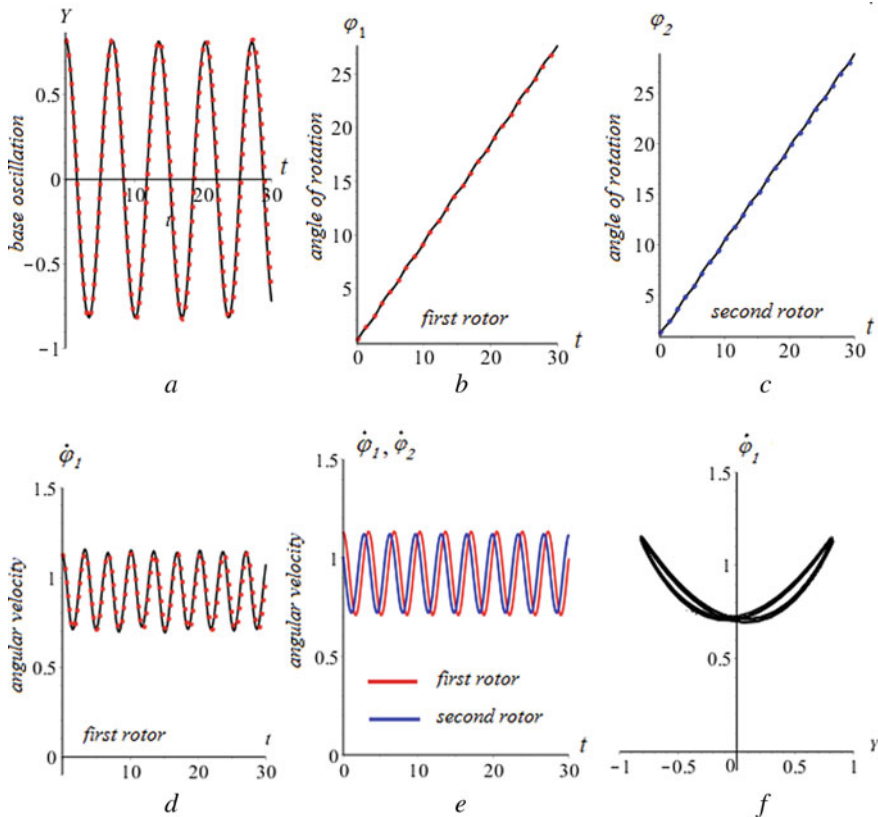


Fig. 18.4 Comparison of the analytical results and the numerical simulation for system $\mu_1 = \mu_2 = 0.1, \beta_0^* = 0.1, \beta_1^* = \beta_2^* = 0.01, p = 0$ with two rotors excited by the torques corresponding to partial angular velocities $\omega_1 = 1, \omega_2 = 4.0$, pre-resonance mode with synchronous frequency $\omega = 0.9210$; (**a**) the base oscillation; (**b, c**) angles of rotation; (**d, e**) angular velocities of the rotors; *f*-phase curve $\dot{\varphi}_1 - Y$. Black curves—numerical simulation, red and blue points and curves—the analytical solution (red—rotor 1, blue—rotor 2)

As it can be seen from Fig. 18.4, the stationary synchronous oscillation-rotation modes are actually established in the system, and practically, from the very beginning, this indicates that the accepted initial conditions are very close to the actual conditions for these modes. The theoretical solution in Fig. 18.4a–d is shown by dots, since the corresponding curves almost completely merge with the curves obtained in the numerical simulation. The complete synchronization of rotation of the vibrators is clearly visible, especially in Figs. 18.4e, we can see not only the mean values of angular velocities are equal but also the deviations from the mean value, as well as a constant phase shift between the rotors. The oscillation of the angular velocity (Fig. 18.4d, e) relatively to the mean value has a frequency equal to the doubled frequency of the base oscillations, in accordance with the formula (18.29) (at $p = 0$ the first harmonics are absent). The phase curve f shows the synchronization of the support oscillation and rotation of the vibrators (in average per period).

Practically, the same good agreement of the analytical predictions and the numerical simulation was observed for other stable synchronous modes, at least for $p = 0$ (some small discrepancies appear at not too small p -values).

In case of unstable regimes, there were observed different pictures. Figure 18.5 shows the results for the same system in case $\omega_1 = 1$, $\omega_2 = 0.6$ ($M_1^* = 0.01$ and $M_2^* = 0.006$); for the pre-resonance mode with synchronous frequency $\omega = 0.7912$ (this case is presented in the second line of Table 18.1).

At the initial interval (approximately up to $t = 40$), the predicted synchronous regime is realized, but then it loses stability, and synchronization of two rotors is violated.

18.5.3 Checking the New Stability Criterion (18.33)

For checking the obtained in Sect. 3.2 the stability criterion (18.33), detecting instability of SSRO-regimes caused by the translational inertia forces, we consider the same system $\mu_1 = \mu_2 = 0.1$, $\beta_1^* = \beta_2^* = 0.01$, $p = 0$ at rotating torques corresponding to partial angular velocities $\omega_1 = 1$, $\omega_2 = 4.0$ ($M_1^* = 0.01$ and $M_2^* = 0.04$). However, parameter of the viscous friction for the base β_0^* , which has principal effect on amplitudes of the base oscillations, was varied from 0.1 to 0.035. For each value of β_0^* , we take the pre-resonance synchronous regime with minimal synchronous frequency (presented for $\beta_0^* = 0.1$ in the third line of Table 18.1 and in Fig. 18.4).

Table 18.1 provides characteristics of the averaged synchronous regimes, obtained analytically, namely synchronous frequency ω , amplitude of the base oscillation a , phase angles γ_k . In the last four columns, values of function $F'(\omega)$ are given (see (18.21)) governing the necessary condition of stability (18.22), and Δ_k represents values (18.32) for detecting change of sign of the minimal Δ_k -value indicating on occurrence of the rotational instability. In the last column, results of checking stability in the numerical simulation are presented.

The values $F'(\omega)$ are positive in all the cases, i.e., necessary stability condition (18.22) is satisfied. As is seen from Table 18.2, angles γ_1 are very small, $\cos \gamma_1$ -values

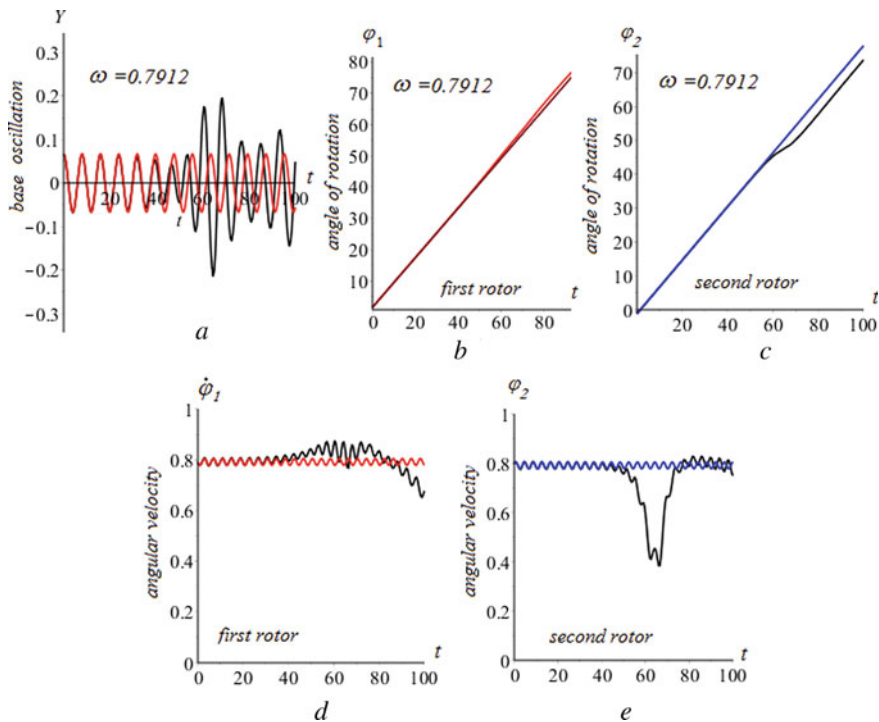


Fig. 18.5 Results of the numerical simulation for the system $\mu_1 = \mu_2 = 0.1$, $\beta_0^* = 0.1$, $\beta_1^* = \beta_2^* = 0.01$, $p = 0$ with two rotors excited by the torques corresponding to partial angular velocities $\omega_1 = 1$, $\omega_2 = 0.6$; pre-resonance synchronous mode with frequency $\omega = 0.7912$; **a** the base oscillation; **b, c** angles of rotation; **d, e** angular velocities of the rotors; black curves—numerical simulation, red and blue curves—analytical solution (red—rotor 1, blue—rotor 2). Initial conditions: $Y(0) = a = 0.0667$, $\dot{Y}(0) = 0$, $\varphi_1(0) = 1.5824$, $\varphi_2(0) = -1.1646$, $\dot{\varphi}_1(0) = 0.790$, $\dot{\varphi}_2(0) = 0.7973$

Table 18.2 Characteristics of synchronous pre-resonance modes and their stability ($\mu_1 = \mu_2 = 0.1$, $\beta_1^* = \beta_2^* = 0.01$, $p = 0$, $\omega_1 = 1$, $\omega_2 = 4.0$) at different values of the friction parameter for the base β_0^*

β_0^*	Frequency ω	Amplitude a	Phase angles		$F'(\omega)$	Δ_1	Δ_2	Stability by numerical simulation
			γ_1	γ_2				
0.10	0.9210	0.8281	0.0225	1.0688	0.810	0.310	0.61	Stable
0.06	0.9270	1.0635	0.0160	0.7374	0.922	0.160	0.31	Stable
0.05	0.9307	1.1614	0.0138	0.6562	0.978	0.103	0.21	Stable
0.04	0.9356	1.2930	0.0114	0.5721	1.056	0.032	0.12	Unstable
0.038	0.9367	1.3254	0.0109	0.5548	1.064	0.015	0.092	Unstable
0.037	0.9373	1.3425	0.0106	0.5460	1.074	0.007	0.080	Unstable
0.036	0.9379	1.3603	0.0104	0.5372	1.085	-0.002	0.068	Unstable
0.035	0.9386	1.3788	0.0101	0.5283	1.107	-0.011	0.056	Unstable
0.030	0.9420	1.4850	0.0088	0.4827	1.170	-0.060	-0.009	Unstable

are very close to 1, and the critical value of the normalized amplitude according to (18.33) is close to 1.35.

As we can see at Table. 18.2, with decreasing β_0^* amplitude a increases and approaches 1.35 at $\beta_0^* \approx 0.0365$. At this β_0^* -value, Δ_1 changes its sign. The onset of instability in the numerical simulation is detected a little earlier (approximately at $\beta_0^* = 0.04$), when Δ_1 becomes very small.

Comparison of the analytical predictions and the numerical simulation is presented in Fig. 18.6 for two β_0^* -values—0.05 and 0.035 (results for $\beta_0^* = 0.1$ were shown above in Fig. 18.4). In Fig. 18.6a–c angular velocities for two rotors and the phase curve at $\beta_0^* = 0.05$ and in Fig. 18.6d–f—these quantities at $\beta_0^* = 0.035$ are shown. In case $\beta_0^* = 0.05$, the synchronous mode remains stable, but coincidence of the analytical (color points and curves) and numerical (black curves) results is not so precise as for $\beta_0^* = 0.1$. There appear harmonics with double period in numerical time-dependencies of angular velocities of two rotors (these harmonics have the same frequency as oscillation of the support). In the case of $\beta_0^* = 0.035$ (Fig. 18.6d–f),

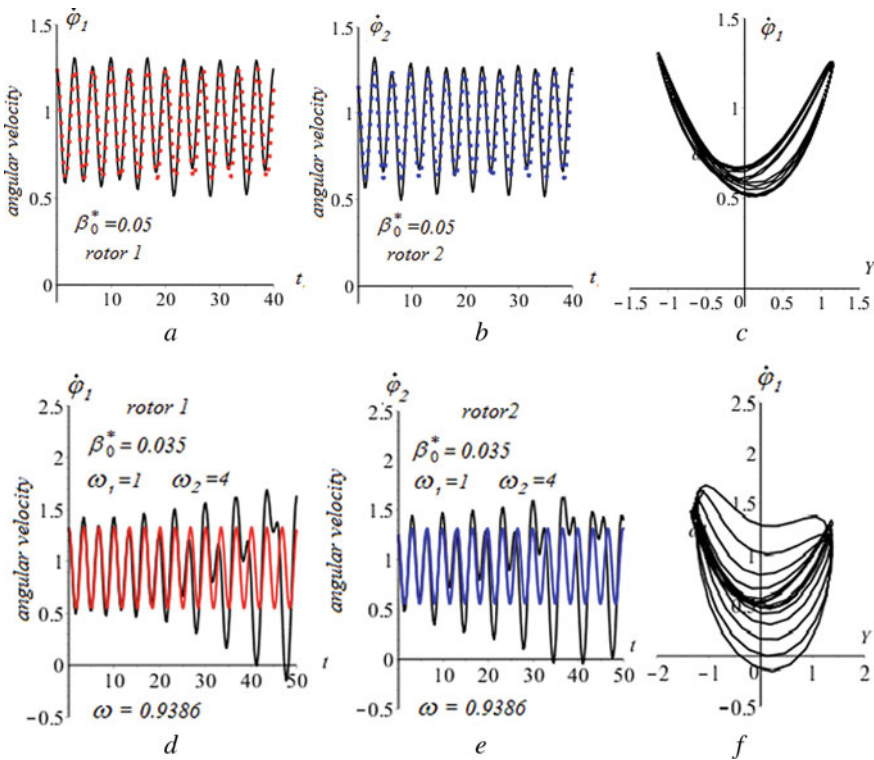


Fig. 18.6 Results of the analytical solution and numerical simulation for system $\mu_1 = \mu_2 = 0.1$, $\beta_1^* = \beta_2^* = 0.01$, $p = 0$ at $\omega_1 = 1$, $\omega_2 = 4.0$, figures **a, b, c** for $\beta_0^* = 0.05$; **d, e, f**—for $\beta_0^* = 0.035$; **a, b, d, e**—angular speeds of rotors 1, 2; **c, f**—phase curves. Black curves—numerical simulation, color points and curves—analytical solution

the onset of parametric resonance for oscillations of the angular velocity because of increasing amplitudes of the double period harmonics is clearly visible. The phase curve (Fig. 18.6f) shows gradual violation of the periodicity.

Stability criterion (18.33) in this case is well agreed with the numerical simulation. But more extensive computations, in particular, for other SSOR-regimes in the considered systems, show that this criterion is not sufficient. So the problem of stability of synchronous regimes in systems under consideration remains open.

18.6 Conclusions

An analytical investigation of stationary synchronized regimes in the oscillatory system with a few vibrators is presented. It is shown that the analytical procedure proposed in previous author's papers for problems of vibrational retardation, and maintenance of rotation in oscillatory systems with one rotator is very efficient also in analysis of synchronization of several vibro-exciter on elastic base. This procedure in the first approximation gives the exact description of averaged characteristics of the synchronized modes with account of the centrifugal inertia forces in rotors, unlike the proposed earlier asymptotic procedures based on assumption of smallness of these forces. Already on this stage, the mechanism of synchronization of rotors is clearing up. Certain phase relations between the rotations of the rotor and oscillation of the base secures the necessary energy exchange between all elements of the system.

The obtained solution essentially corrects the characteristics of the synchronized regimes in comparison with a few previous works, in particular, to Blekhman (1999).

In the second approximation, the presented solution results in analytical description of non-uniform rotation of vibro-exciter caused by interaction of the rotation and oscillation. Both the solutions (for averaged modes and for actual non-uniform motions) are validated by the numerical simulation with very high accuracy.

It is shown that stability criteria based on analysis of averaged synchronous modes are not sufficient. The stationary synchronous regimes in systems with several rotors can become unstable because of the parametric resonance for oscillations of the rotors velocity generated by the translational inertia forces from the base. A new stability criterion is obtained based on the refined solution in the second approximation. This criterion is similar to one obtained earlier for one rotator-oscillator systems, but in a case of several rotors, the occurrence of instability is more probable due to larger number of rotors. In the same time, this criterion also is not sufficient one, so the problem of stability of the synchronized modes in case of several rotors remains open.

References

- Balthazar, J.M., Mook, D.T., Weber, H.I., et al.: An overview on non-ideal vibrations. *Meccanica* **38**, 613–621 (2003)
- Balthazar, J.M., et al.: An overview on the appearance of the Sommerfeld effect and saturation phenomenon in non-ideal vibrating systems (NIS) in macro and MEMs scales. *Nonl. Dyn.* **93**(1), 19–40 (2018)
- Blekhman, I.I.: *Synchronization of Dynamic Systems*. Nauka, Moscow (1971). (in Russian)
- Blekhman, I.I.: *Vibrational Mechanics: Nonlinear Dynamic Effects, General Approach, Applications*. World Scientific, Singapore (1999)
- Kononenko, V.O.: *Vibrating Systems with Limited Power Supply*. Scripta Technica, Inc., New York (1969). (Russian ed.: Moscow: Nauka, 1964)
- Mazet, R.: *Mecanique vibratoire*. Libr. politechn. Ch. Beranger, Paris (in French, 1955)
- Manevich, A.I.: An oscillator-rotator system: vibrational maintenance of rotation, stationary synchronous regimes, stability, *Vibration Mitigation*. *J. Sound Vib.* **437**(22), 223–241 (2018)
- Manevich, A.I.: Stability of synchronous regimes in unbalanced rotors on elastic base. In: *Proceedings of the Institution of Mechanical Engineers, Part C. Journal of Mechanical Engineering Science*, 14 p. Online first (2020). <https://doi.org/10.1177/0954406220920325>
- Rocard, Y.: *Dynamique Generale des Vibrations*. Masson, Paris (1949)

Chapter 19

Stability Analysis of Rotor Motion in Nonlinear Systems with Passive and Active Magnetic Bearings



Gennadii Martynenko

Abstract The paper proposes an approach to analyzing the stability of rotor motion in systems and machines with passive and active magnetic bearings. The rotor dynamics is mathematically described using the Lagrange–Maxwell magnetomechanical system of differential equations. It contains unknown components namely generalized coordinates and flux linkages in coils of electromagnets of active magnetic bearings. This system of equations is nonlinear due to nonlinearity of magnetic forces in the bearings. Complexity of this system makes difficult the analysis of motion stability in non-resonant and resonant modes using analytical and semi-analytical methods. Therefore, an analytical–numerical–graphical approach based on simulation modeling and stability analysis by vibrograms, spectrograms, phase trajectories and Poincare sections is proposed. This algorithm was tested in the analysis of dynamic behavior of a rotor of a laboratory rig in radial passive and axial active magnetic bearings. Validation was performed by comparing calculated and experimental results. Advantages of the approach include accuracy of analytical–numerical modeling of various dynamic modes, ability to analyze stability of rotors of complex magnetomechanical systems, as well as numerical and visual representation of nonlinear phenomena of rotor dynamics.

Keywords Rotor dynamics · Magnetic bearings · Mathematical simulation · Nonlinear phenomena

19.1 Introduction

Rotor systems with magnetic bearings (MBs) of various types (Yonnet 1978; Zhang and Zhu 2017) are widely used in practice (Maslen and Schweitzer 2009). Permanent magnet passive magnetic bearings (PMBs) are used as rotor supports in wind turbines with vertical axis (Mahmoud et al. 2020, 2019), flywheel energy storage systems (Amiryar and Pullen 2020; Wen et al. 2020), pumps (Chen et al. 2019; Prusa et al.

G. Martynenko (✉)

Department of Dynamics and Strength of Machines, National Technical University “Kharkiv Polytechnic Institute”, Kharkiv, Ukraine
e-mail: gmartynenko@ukr.net

2018), bearingless motors (Kato et al. 2020; Yuan et al. 2020) and other small-medium sizes rotor machines and systems. Active magnetic bearings (AMBs) are currently used in almost all fixed rotor machines and systems. They are installed in industrial machines such as compressors (Anantachaisilp and Lin 2020), turbines and generators (Grönman et al. 2020; Khatri et al. 2020; Pilotto and Nordmann 2019), pumps (Bangcheng et al. 2020; Barbosa Moreira and Thouverez 2020) and motors (Żokowski et al. 2020).

When developing or modernizing rotor systems and machines with MBs, approaches and tools for a variant assessment of their dynamic state are required. They should have the ability to perform parametric calculations at low cost of resources and time. The dynamic characteristics can be determined from the results of the modal (Čorović and Miljavec 2020; Martynenko and Martynenko 2020a), harmonic (Chalageri et al. 2020; Martynenko and Martynenko 2020b) and spectral analyses (Xiang et al. 2020). Their accurate determination allows achieving the high quality of created or modified rotary machines, namely the strength of structural elements (Martynenko 2020c; Martynenko et al. 2020b), dynamics stability (Martynenko 2016), reliability (Rusanov et al. 2018), performance and other parameters.

When developing rotor machines and units, an actual issue is the mathematical modeling of rotor dynamics taking into account various nonlinearities in the system. They are mainly due to nonlinear force characteristics of the magnetic field (Martynenko and Martynenko 2019; Santra et al. 2017). To simulate the dynamics of rotors in the magnetic field, numerical methods (e.g., finite element or finite difference ones) (Ran et al. 2018) and analytical approaches (Ebrahimi et al. 2018) can be used. In the first case, when using general-purpose software systems, the analysis of stability of rotor motion can be performed according to the Campbell diagram (Matsushita et al. 2017, 2019). It shows the dependence of critical velocities on rotational speed with an assessment of stability according to cylindrical or conical precession by the roots of the characteristic equation. However, such an analysis is linear and does not take into account the features of nonlinear dynamic processes (Lacarbonara et al. 2020; Worden and Tomlinson 2019). However, this nonlinear behavior is also characteristic of rotor systems (Nan et al. 2020), including the ones with magnetic bearings (Zhang et al. 2020). In the second case, simplified mathematical models of rotor dynamics are used to assess stability using approximate analytical mathematical methods for analyzing nonlinear oscillatory systems. In this instance, although the nonlinear properties of the rotor system with MPs are taken into account (Wu et al. 2018), this accounting is very limited. Often this fact does not allow relying on the accuracy of the analysis for the synthesis of such a mechatronic rotor system. In this case, in order to increase reliability of modeling of the nonlinear phenomena and assess stability of rotor motion in magnetic fields, it is possible to use analytical approaches (Martynenko 2018) and graphoanalytical methods (Ebrahimi et al. 2017).

For example, Qiao and Tang (2020) consider the influence of the gyroscopic effect on the dynamics of a high-speed electrospindle in active magnetic bearings. The analysis is performed for a simplified system with four degrees of freedom and on the

basis of the real part of the characteristic equation roots. The work (Xia et al. 2019) is devoted to the analysis of the stability of the gyroscope rotor with a magnetic bearing using pseudo-linear equivalent transformation and extended double-frequency Bode diagram. To ensure stability control in sliding mode and control based on Lyapunov's theory are used in (Mystkowski 2019). Soni et al. (2020) uses Floquet-Liapunov theory on stability of periodic system to analyze the stability of the rotor motion in the AMBs, taking into account the mobility of the system base. This allows the response under parametric excitation in such machines as an aircraft turbo engine or a ship propeller shaft to be assessed. The analysis of the rotor motion in passive magnetic bearings using numerical simulation is proposed in Goleman et al. (2018). Numerical calculations and a graphical approach to the analysis of the behavior of elements of rotary machines are presented in Zhao et al. (2016). It involves the use of several methods, including the construction of graphs of control point motions as well as trajectories, wavelet transform and others. Cui et al. (2018) proposes a method for evaluating vibration resistance based on the standard ISO14839 for rotating equipment elements with AMBs.

The approaches given as examples are quite acceptable in the case of a simplified, often linearized, mathematical description of the rotor dynamics in magnetic bearings of passive and active types. But they are practically not applicable in the case of a full accounting of the nonlinear relationship of electrical, magnetic and mechanical processes that are inherent in rotary systems with magnetic bearings. This work is devoted to filling this gap.

19.2 Object and Aim of Research

19.2.1 Analyzed Design and Initial Data

The numerical-graphical approach to the study of the motion stability of rotors in magnetic bearings of various types involves the construction of a mathematical model of the system dynamics, the use of numerical methods for solving, numerical and graphical representation of processes and the analysis of these results to assess the rotor motion stability in various operating modes. Its essence can be described most fully and clearly when considering a specific rotor system with magnetic bearings, which comprehensively manifests its nonlinear properties. Such a system can be a complete magnetic suspension of the rotor in two different types of bearings.

Therefore, the paper considers a nonlinear controlled mechatronic electromagneto-mechanical system with a rotor in passive and active magnetic bearings (Martyntenko and Ulianov 2019; Martyntenko et al. 2020a). Two radial passive MBs consist of ring permanent magnets with an axial magnetization. The axial active magnetic bearing for stabilizing the rotor in an axial direction uses an automatic control system which utilizes an original control algorithm. This system is implemented as a laboratory rig and is a prototype of complete passive-active magnetic

suspensions of small and medium-sized rotors such as compressors, expanders, and engines. It is presented in Fig. 19.1. Figure 19.2 shows the control system of the axial AMB and the rotor calculation scheme.

Both radial PMB has the following dimensions of the rings (Fig. 19.2): diameters of an outer fixed (stator) ring $D_1 = 58$ mm and $D_2 = 40$ mm, and an inner movable (rotary) ring $D_3 = 29$ mm and $D_4 = 15$ mm, a thickness of both the rings $H = 10.5$ mm. The rings are made of an NdFeB alloy with a residual induction of $B_r = 1.07$ T and a coercive force $H_c = 808,000$ A/m. The axial magnetization of the rings provides the rotor with self-centering due to repulsive forces. The power characteristics of the PMBs are shown in Fig. 19.2. Axial AMP has the following parameters: electromagnet (EM) inner and outer diameters are 0.12 and 0.05 m, each EM length in the axial direction is 0.021 m, winding inner and outer diameters are 0.1 and 0.072 m, an amount of turns is 300, resistance of windings is $r_c = 5 \Omega$,

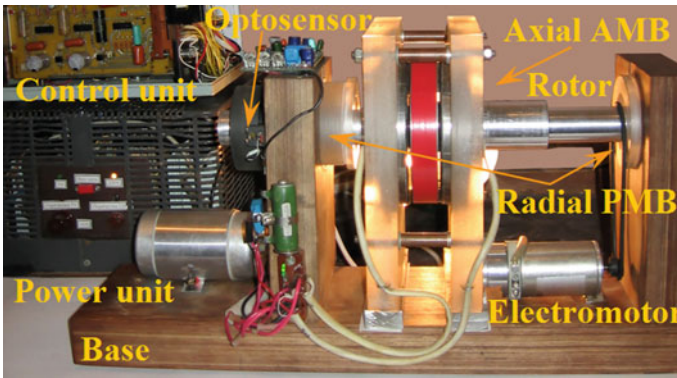


Fig. 19.1 The model rotor in the radial PMBs and the axial AMB—the appearance of the laboratory rig

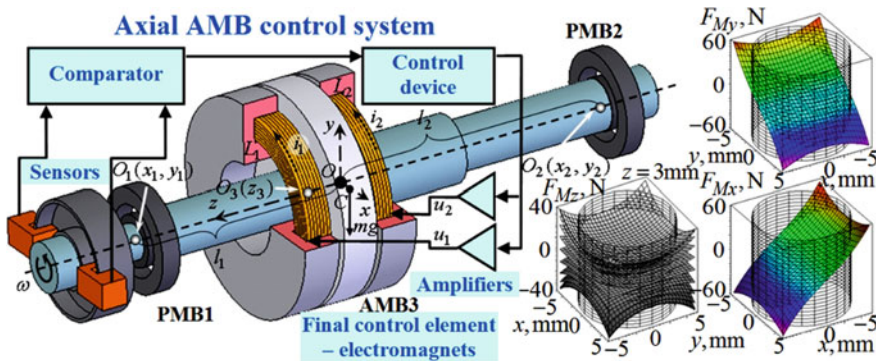


Fig. 19.2 The model rotor in the radial PMBs and the axial AMB—the control system diagram, design model and force characteristics of the PMB within the gaps

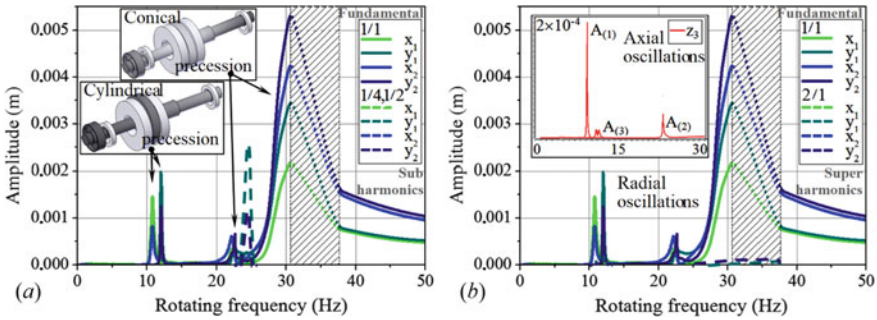


Fig. 19.3 Experimental amplitude-frequency characteristic of the rotor and the dependence of the amplitudes of multiple harmonics on the excitation frequency (rotation): **a** fundamental harmonic with subharmonics and **b** fundamental harmonic with superharmonics

thickness of the disk is 0.02 m, a nominal clearance on each side is $\delta_a = 0.003$ m (Martynenko and Martynenko 2019), and the parameters of the control system and law are: control frequency—300–400 Hz, voltage $U_0 = 24$ V, the rest are given in (Martynenko and Ulianov 2019). The range of rotor operational rotational speeds is from 0 to 3000 rpm.

The fact that the structure includes the PMBs with permanent magnets made of rare-earth materials, as well as the axial AMB with a relatively large air gap, generates pronounced nonlinear effects. Their analysis and influence on the rotor motion stability are the purpose of this work.

The experimental dependences of the amplitudes of the fundamental and multiple harmonics are presented in Fig. 19.3 (Martynenko 2018). They characterize the dynamic nonlinear behavior of the “rotor in the MBs” system in the operating frequency range. Dependencies of fundamental harmonics are amplitude-frequency characteristics (AFCs). Only the fundamental harmonics and subharmonics with different multiplicity are presented in (a) and only the fundamental harmonics and superharmonics are shown in (b) to improve the legibility of the graphs in Fig. 19.3 for the comparative analysis of nonlinear resonances.

Confirmation of the nonlinear behavior of the system is the presence of sub- and superharmonic oscillations and resonances, as well as the connection between radial and axial oscillations of the rotor. Figure 19.3 indicates that the amplitudes of subharmonics exceed the amplitudes of the fundamental frequency and are more dangerous in some modes.

19.2.2 Research Objectives

The object of the research is the dynamic behavior of a rotating rotor excited by its own imbalance, taking into account nonlinear relationships of electrical, magnetic and mechanical phenomena in the considered mechatronic system. The complex

mathematical description of the nonlinear rotor dynamics of such a system makes it almost impossible to use standard methods (asymptotic, small parameter, harmonic balance, normal forms, etc.) for analyzing the stability of its motion. Therefore, the proposed analytical–numerical–graphical approach aims to evaluate the stability of different operational modes.

19.3 Mathematical Modeling of the Nonlinear Rotor Dynamics in Magnetic Bearings

Since preliminary studies in the range of possible deviations of the rotational speed showed that the rotor vibrates only as a rigid body, a mathematical model can be built for a rigid rotor. If in some system the rotor is flexible, then the principle of constructing a mathematical model and research technique is the same with the increased number of degrees of freedom and equations.

19.3.1 Formation of a System of Electromechanical Equations

It is known that the Lagrange–Maxwell equations are used to describe the dynamic behavior of electromechanical systems. One of the forms of their notation is similar to the Routh equations in mechanics and has the form (Maslen and Schweitzer 2009; Routh 2018, 2012):

$$\begin{cases} \frac{d}{dt} \frac{\partial T}{\partial \dot{q}_j} - \frac{\partial T}{\partial q_j} + \frac{\partial \Pi}{\partial q_j} + \frac{\partial D}{\partial \dot{q}_j} = -\frac{\partial W}{\partial q_j} + Q_j \quad (j = 1, \dots, M); \\ \frac{\partial \Psi_k}{\partial r} + \sum_{s=1}^N r_{Cks} \frac{\partial W}{\partial \Psi_s} = E_k \quad (k = 1, \dots, N), \end{cases} \quad (1)$$

where T —kinetic energy; Π —potential energy; q_j —generalized mechanical coordinates; Q_j —non-potential generalized forces; D —dissipative function; M —number of mechanical generalized coordinates; W —magnetic field energy; Ψ_k —induction fluxes (flux linkages), r_{Cks} —active resistances of electrical circuits; E_k —algebraic sum of external electromotive forces; i_k —contour currents; N —number of closed unbranched contours, and $\Psi_k = \partial W / \partial i_k$, $i_k = \partial W / \partial \Psi_k$.

The kinetic energy of the rotor should be substituted into these equations. Its expression is written in terms of generalized coordinates. In the case of a rigid rotor, there are five of these coordinates. A fixed Cartesian coordinate system $Oxyz$ is introduced in the design scheme (Fig. 19.3). In this case of a rotor with a disk, the coordinates x_0, y_0, z_0 of the pole O and Euler angles ψ, ϑ, φ can be specified as the

generalized coordinates q_0 of the rigid body, and generalized velocities are the first time derivatives of these quantities. Then the expression for kinetic energy has the form:

$$T = \frac{1}{2} [m v_0^2 + 2m(v_0 \times \omega) \cdot r'_C + \omega \Theta^0 \omega] \quad (2)$$

here v_0 —velocity of the pole O ; ω —angular velocity of the body (the rotor); r'_C —the radius vector OC of the center of inertia of the body in the system of moving axes starting at the pole O ; Θ^0 —the tensor of inertia of the body at this point.

Then the formation of a system of equations requires: representing the expressions for the projections of the body angular velocity ω onto the axes $O\xi\eta\zeta$ connected with the body and the expressions for the projections on the same axes of the velocity vector v_0 of the pole O ; further considering the radius vector projection r'_C on the axes $O\xi\eta\zeta$ and the tensor of inertia of the rotor with the disk in the pole O ; making the transition to the fixed coordinate system $Oxyz$, and simplifying by replacing trigonometric functions by power series with keeping terms up to the third order for preservation of nonlinearities in the representations. For the convenience of determining and monitoring the position of the rotor in the MBs, the second group of generalized coordinates $q = (x_1, y_1, x_2, y_2, z_3)$ can be used in addition to the first one q_0 . These are the coordinates x and y of the points O_1 and O_2 (Fig. 19.3) in the fixed coordinate system and the coordinate z of some point O_3 placed on the rotor axis. Points O_1 and O_2 are the centers of rotor supporting sections in the radial direction, i.e., the centers of mass of journals of the radial PMBs, and the point O_3 is the center of a rotor supporting section in the axial direction, i.e., the center of mass of the axial AMB disk.

In the case of a flexible rotor, lateral vibrations of the axis are considered. Then, either a larger number of degrees of freedom is introduced, or a continual approach is used (Van Osch 2006).

In the case of a rigid rotor for the mathematical description of the rotor dynamics (Fig. 19.3) uses a nonlinear differential equation system (NDES) relative to generalized coordinates (displacements of support sections centers, points of disks-to-shaft attachments) and fluxes in coils of AMB electromagnets (Martynenko 2018). Such a system is formed on the basis of the Lagrange-Maxwell Eqs. (19.1) taking into account (19.2) and has the form (19.3).

In (19.3), m is a rotor overall mass; J_1 and J_3 are rotor moments of inertia; l_1 , l_2 and l_3 are distances from the coordinate system center to centers of the radial and axial supporting sections ($l_1 + l_2 = l$); members $-\partial\Pi/\partial q_j$ are potential forces—magnetic forces in the PMBs; $P_{qj} = -\partial W/\partial q_j$ are electromagnetic reactions of the AMB; $H_q(t)$ are external periodic loads caused by the dynamic rotor imbalance; Q_j are other non-potential generalized forces; $f'_{qj}(q_i)$, $f''_{qj}(q_i)$ are nonlinear members of the equations of motion, caused by inertia forces and a potential field of the second and third order; b_{x_1, \dots, z_3} are viscosity coefficients; $r_{c_1, \dots, N}$ are active resistances in winding circuits; $u_{c_1, \dots, N}$ are control voltages supplied to the AMB windings, the value of which is formed in accordance with the adopted control law; Ψ_{ck} are the

fluxes of induction (flux linkage); $W(\Psi_{c1}, \dots, \Psi_{cN}, x_1, \dots, z_3)$ is the magnetic field energy of the AMB.

$$\left\{ \begin{array}{l} (ml_2^2 + J_1)\ddot{x}_1/l^2 + (ml_1l_2 - J_1)\ddot{x}_2/l^2 + \omega J_3(\dot{y}_1 - \dot{y}_2)/l^2 \\ \quad + b_{x_1}\dot{x}_1 + f_{x_1}'' + f_{x_1}''' = -\partial \Pi / \partial x_1 - \partial W / \partial x_1 + Q_{x_1} + H_{x_1}(t); \\ (ml_1^2 + J_1)\ddot{x}_2/l^2 + (ml_1l_2 - J_1)\ddot{x}_1/l^2 - \omega J_3(\dot{y}_1 - \dot{y}_2)/l^2 \\ \quad + b_{x_2}\dot{x}_2 + f_{x_2}'' + f_{x_2}''' = \partial \Pi / \partial x_2 - \partial W / \partial x_2 + Q_{x_2} + H_{x_2}(t); \\ (ml_2^2 + J_1)\ddot{y}_1/l^2 + (ml_1l_2 - J_1)\ddot{y}_2/l^2 - \omega J_3(\dot{x}_1 - \dot{x}_2)/l^2 \\ \quad + b_{y_1}\dot{y}_1 + f_{y_1}'' + f_{y_1}''' = -\partial \Pi / \partial y_1 - \partial W / \partial y_1 + Q_{y_1} + H_{y_1}(t); \\ (ml_1^2 + J_1)\ddot{y}_2/l^2 + (ml_1l_2 - J_1)\ddot{y}_1/l^2 + \omega J_3(\dot{x}_1 - \dot{x}_2)/l^2 \\ \quad + b_{y_2}\dot{y}_2 + f_{y_2}'' + f_{y_2}''' = -\partial \Pi / \partial y_2 - \partial W / \partial y_2 + Q_{y_2} + H_{y_2}(t); \\ m\ddot{z}_3 + b_{z_3}\dot{z}_3 + f_{z_3}'' + f_{z_3}''' = -\partial \Pi / \partial z_3 - \partial W / \partial z_3 + Q_{z_3} + H_{z_3}(t); \\ \partial \Psi_{c1} / \partial t + r_{c1} \partial W / \partial \Psi_{c1} = u_{c1}(x_1, \dots, z_3, \dot{x}_1, \dots, \dot{z}_3, i_1, \dots, i_N); \\ \dots \\ \partial \Psi_{cN} / \partial t + r_{cN} \partial W / \partial \Psi_{cN} = u_{cN}(x_1, \dots, z_3, \dot{x}_1, \dots, \dot{z}_3, i_1, \dots, i_N). \end{array} \right. \quad (3)$$

The expression of the magnetic energy of an AMB is recorded on the basis of the analysis of magnetic circuits taking into account the magnetic resistances all sections of magnetic cores (Martynenko 2020a, b). The nonlinear force characteristics of the PMBs are included in the right-hand sides of the equations of motion, which represent the first part of the DES. There are members depending on the flux linkages here too. The second part of the system consists of the first-order differential equations for the flux linkages. These equations correspond to the second Kirchhoff law for magnetic circuits and are a representation of the total current law for each electrical circuit of the system (each winding of the AMB). The right-hand side of these equations contains terms that depend on the generalized coordinates. This is the AMB control law ($u_{c1, \dots, cN}$), in which both generalized coordinates and generalized velocities can be present.

19.3.2 Solving the Nonlinear Differential Equation System

The analytical solution of such a complex NDES (19.3) does not exist at the moment, as well as a stability analysis based on analytical methods of the nonlinear vibrations theory is impossible. Therefore, the following technique aims to evaluate the dynamic behavior and stability of the rotor in the range from zero to the nominal rotation speeds. The solution of the NDES for frequencies selected with a certain step in a given frequency range is performed by the 7th order Runge–Kutta method with checking the uniqueness of the solution (the ambiguity of the solution is determined and excluded by multiple calculations at each frequency, performed under different initial conditions).

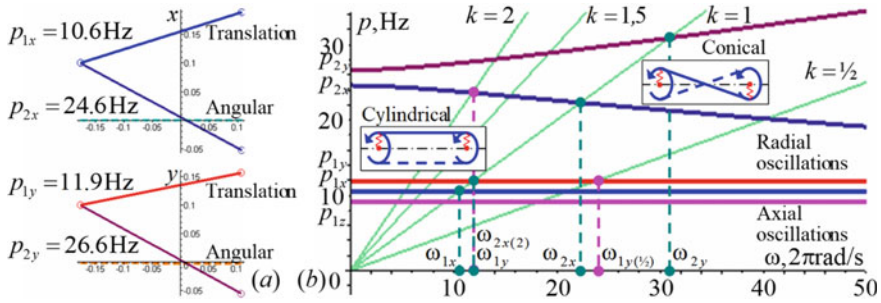


Fig. 19.4 The results of the linear rotor dynamics analysis: natural frequencies and forms of the non-rotating rotor (a); Campbell diagram (b)

19.4 Numerical-Graphical Analysis of Rotor Motion Stability in Magnetic Bearings

19.4.1 Estimation of the Parameters of the Linearized Oscillatory System

The calculation of the parameters of rigid rotor natural vibrations was performed using a linearized system of equations without taking into account damping. Natural forms and frequencies are presented in Fig. 19.4a. Force characteristics of PMBs are axisymmetric. However, the values of the first natural frequencies (NFs) p_{1x} , p_{1y} and second ones p_{2x} , p_{2y} are different. This bifurcation of the resonance at the fundamental frequency is observed due to the fact that the stiffness values in PMB1 and PMB2 in the x and y directions correspond to the static equilibrium position of the rotor, taking into account the force of gravity. Figure 19.4a shows it by dashed lines in absolute units. First (without nodes) and second (with one node) NFs in both directions are identical and correspond to cylindrical and conical precessions. The Campbell diagram (Fig. 19.4b) precises the critical speeds ω_{1x} , ω_{1y} and ω_{2x} , ω_{2y} considering the gyroscopic moment. It is found that at $\omega_{1x} < \omega < \omega_{1y}$ and $\omega_{2x} < \omega < \omega_{2y}$, rotor unbalance causes the backward precession, and at the other values of ω —the forward one.

19.4.2 Simulation of the Nonlinear Dynamics of a Rotor in Magnetic Bearings

The results of computational studies of forced vibrations are solutions at stationary sections for generalized coordinates x_1, y_1, x_2, y_2, z_3 in the range of angular velocities of 0–100 π rad/s. These solutions were performed for a given number of frequency

values within the range. Their number was selected based on the possible fundamental, sub- and super resonances, and the Campbell diagram allows predicting their presence (Fig. 19.4b).

There are vibrograms of vertical and horizontal motion of centers of the rotor supporting sections, their motion trajectory within the gaps of the radial PMB and vibrograms of the axial motion of the center of the rotor supporting section in the axial AMB formed and visualized for each frequency. For some of the frequencies, they are shown in Figs. 19.5, 19.6 and 19.7. These are the four graphs in the top row. The first graph shows the horizontal displacements of the centers of the radial bearing sections of the rotor (O_1 and O_2 , see Fig. 19.2) depending on time $x_1(t)$ and $x_2(t)$. The time interval corresponds to the steady-state oscillatory process. The second graph shows the dependence of the vertical displacements of the same points on time $y_1(t)$ and $y_2(t)$. In both of these figures, horizontal straight lines indicate possible extreme deviations, that is, air gaps in the PMBs. On the y -axis, the maximal displacements are smaller due to the downwardly shifted static equilibrium position. This is due to the action of gravity on the rotor. The third graph shows the motion orbits of the points (O_1 and O_2 , see Fig. 19.2) for the same time range. The fourth graph shows dependencies of displacements of the center of the axial supporting rotor section (O_3 , see Fig. 19.2) depending on time $z_3(t)$. These graphs, in contrast to the previous ones, are not scaled by the value of the axial clearance due to the smallness of the amplitudes of axial vibrations.

Values of dangerous resonant frequencies in Figs. 19.5, 19.6 and 19.7 are highlighted with a background color that matches the color of the dotted lines of the corresponding mode in the Campbell diagram (Fig. 19.4). Figs. 19.5, 19.6 and 19.7 represent the results of calculations in three subranges of the considered range $0-50 \times 2\pi$ rad/s (see Fig. 19.4a). The first subrange $9-12.5 \times 2\pi$ rad/s (Fig. 19.5) contains the first fundamental bifurcated resonance. The second subrange $21-23.5 \times 2\pi$ rad/s (Fig. 19.6) contains the first frequency of the second fundamental resonance. The third subrange $23.5-34 \times 2\pi$ rad/s (Fig. 19.7) contains the subresonance with multiplicity $\frac{1}{2}$ and the second frequency of the second bifurcated resonance. This is the most dangerous frequency region in the studied range with the highest amplitudes.

The vibrograms and motion trajectories allowed to analyze the nature of motion and amplitudes of oscillations in non-resonant modes for the rotor of the laboratory rig. The magnitudes of the amplitudes, which are much smaller than the gaps during the movement of cylindrical and conical precession types, testified to the stability of the rotor motion for these modes. Identifying the stability of the rotor motion in the entire range of study requires an in-depth analysis at resonant frequencies (critical speeds), which contain sub- and superharmonic vibrations. To do this, it is proposed to analyze the spectrograms of lateral vibrations, phase trajectories and Poincare sections. There are four graphs for each frequency in Figs. 19.5, 19.6 and 19.7 in the bottom row. The spectrograms shown in the first and second of these four graphs in the amplitude-frequency coordinates $A_{x1}(f)$, $A_{x2}(f)$ и $A_{y1}(f)$, $A_{y2}(f)$ are the spectral expansions of dependences $x_1(t)$, $x_2(t)$ and $y_1(t)$, $y_2(t)$, respectively. It is done using Fast Fourier Transform. The constant component at zero frequency was excluded from consideration. It corresponds to a shift in the position of static equilibrium. The

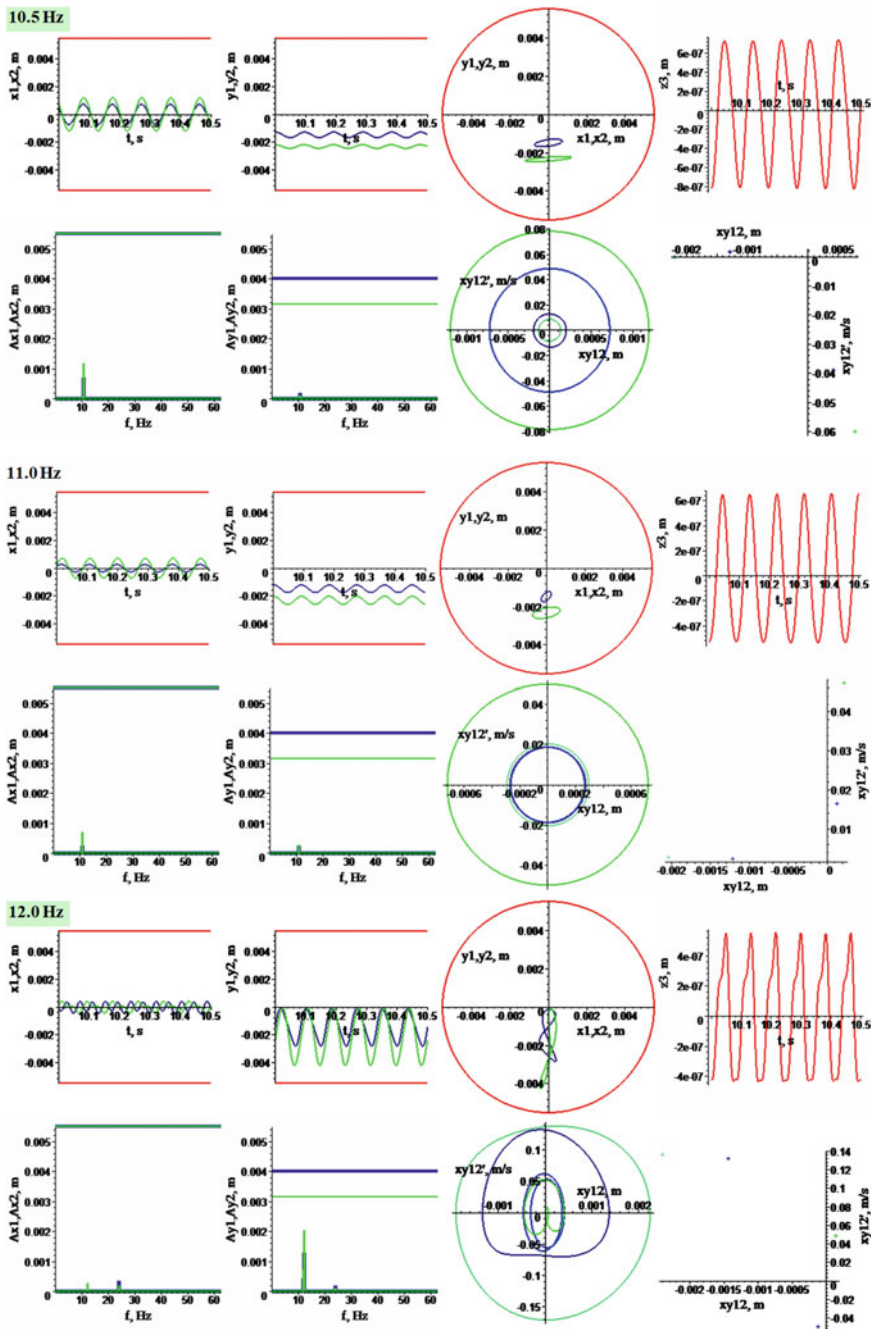


Fig. 19.5 Results of the nonlinear rotor dynamics analysis in the frequency range in the first fundamental bifurcated resonance region

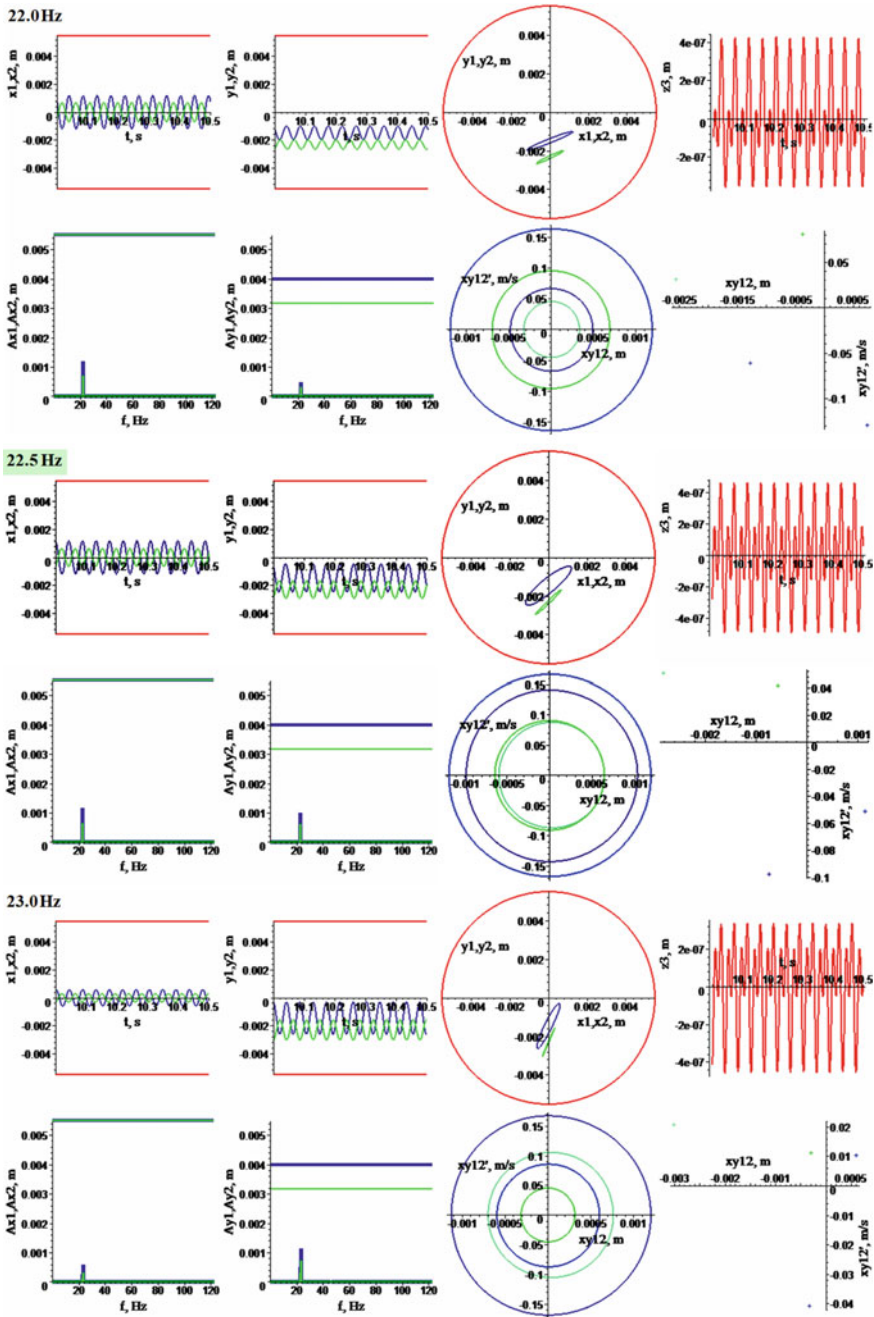


Fig. 19.6 Results of the rotor dynamics nonlinear analysis in the frequency range in the region of the first frequency of the second fundamental resonance

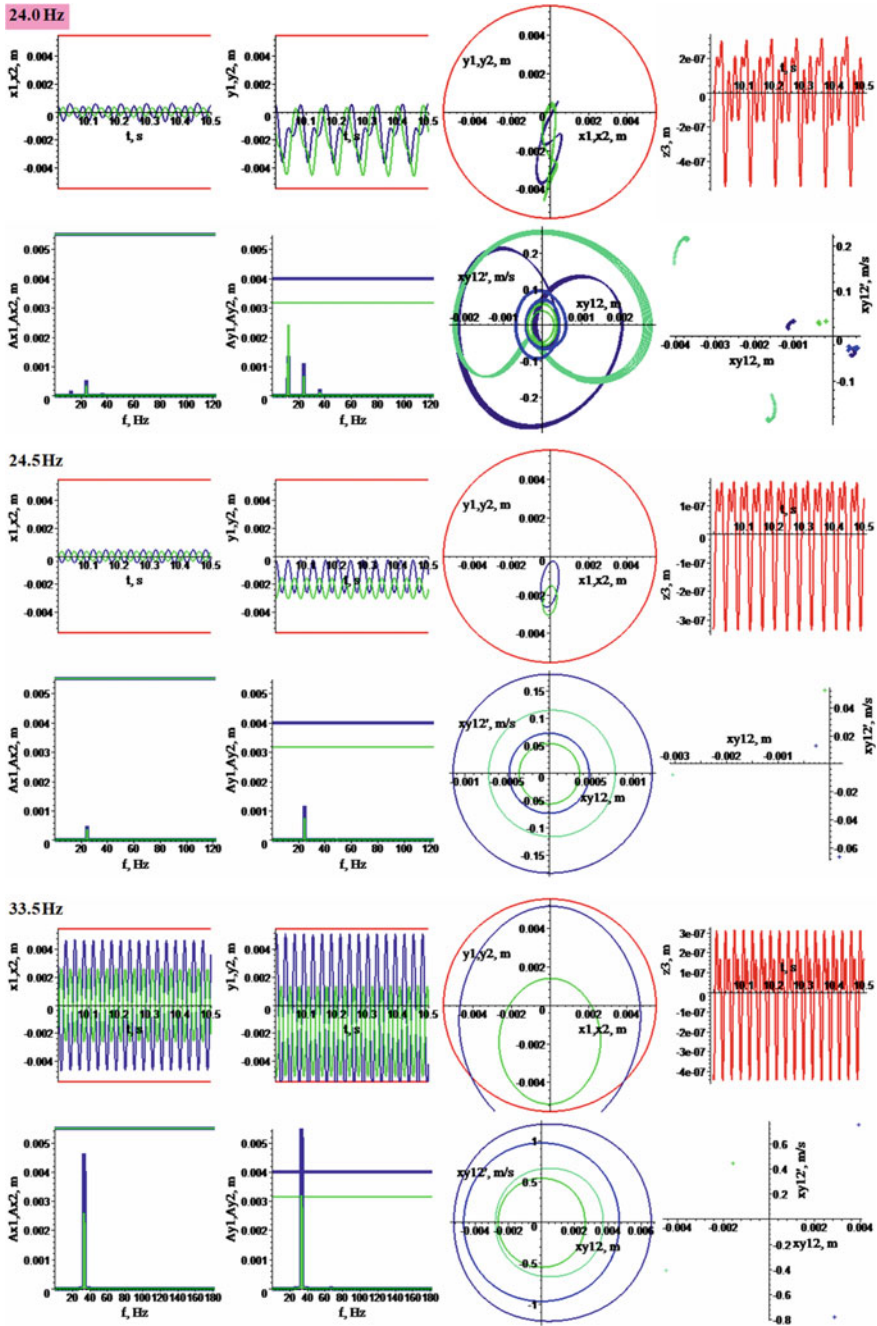


Fig. 19.7 Results of the nonlinear rotor dynamics analysis in the frequency range in the region of subresonance with a factor of $\frac{1}{2}$ and the second frequency of the second bifurcated resonance

third graph is the phase plane on which the phase trajectories $\dot{x}_1(x_1)$, $\dot{x}_2(x_2)$, $\dot{y}_1(y_1)$ and $\dot{y}_2(y_2)$ are depicted. The fourth graph is the Poincare sections (stroboscopic images for the period of an external force).

19.4.3 Stability Rating of the Rotor Motion in MBs Using Numerical and Graphical Data

For such an analysis, the proposed method suggests to generate and visualize signal spectra, phase trajectories and Poincare sections at each of the problematic frequencies. The latter were obtained on the basis of the stroboscopic examination method, which is a special case of the Poincare point mappings method. An analysis of these results allows to comprehensively evaluate the stability of a periodic polyharmonic oscillatory process. An analysis of the radial vibrations (precession motion) of the rotor of the laboratory rig in resonance modes made it possible to determine that the rotor executes both harmonic vibrations with a fundamental frequency (with a rotational speed) and sub- and superharmonic vibrations. The assessment was performed on the basis of signal spectra, as well as phase trajectories and Poincare sections. It testified to the stability of the rotor. Thus, singular points of the “center” type were observed on the phase trajectories, and the Poincare sections were either stroboscopic points for each of the radial generalized coordinates (there was a rational ratio of the periods of vibrations and an impact—in this case they were simply equal), or the form of the trajectories corresponded to stable resonant orbits.

19.4.4 Validation of the Proposed Approach to the Stability Analysis

Validation of the proposed method was performed by comparing the calculated and experimental data presented in the form of amplitude-frequency characteristics and dependences of the amplitudes of sub- and superharmonics on the frequency of excitation (rotation).

Figure 19.8 shows the calculated dependences of amplitudes of the fundamental (AFC) and multiple harmonics of lateral vibrations on excitation (rotational) frequency. Subharmonics and superharmonics together with the fundamental harmonics are presented in different pictures (a) and (b) in Fig. 19.3 for a better perception. They are built on the basis of spectrograms by combining them along the frequency axis. Figure 19.8 have the following notation: $A_{(1)}$ —amplitudes of the first harmonics, $A_{(1/n)}$, $A_{(n)}$ —amplitudes of sub- and superharmonics, where the value in parentheses is a multiplicity of harmonics frequency to the fundamental frequency ω_0 , and the dashed lines show skeletal curves. Critical speeds of the rotating rotor are designed by ω_{1x} , ω_{1y} , ω_{2x} , ω_{2y} (see Fig. 19.4b).

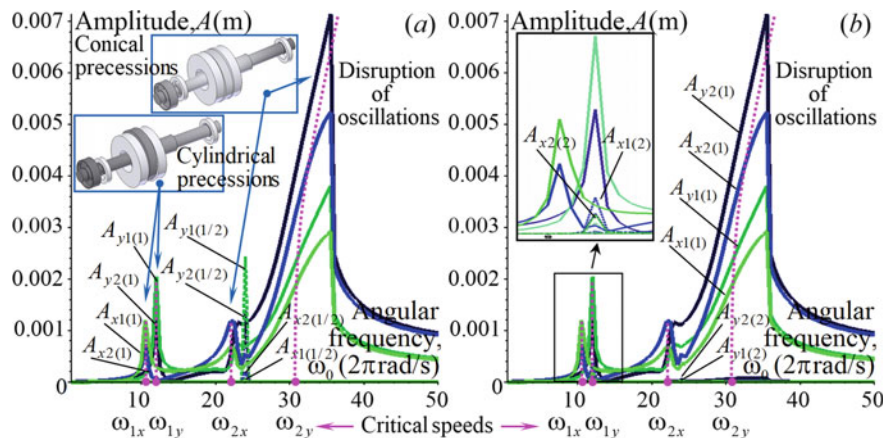


Fig. 19.8 The calculated dependences of amplitudes of the fundamental and multiple harmonics of lateral vibrations on excitation (rotational) frequency: **a** of the fundamental and subharmonics, **b** of the fundamental and superharmonics

Comparison of these dependencies with the same experimentally obtained results gives a sufficient degree of coincidence both in terms of the qualitative reflection of the phenomena and in terms of quantitative indicators (values of the fundamental and multiple resonance frequencies, vibration amplitudes). This confirms the reliability of the proposed approach. Some discrepancy between the oscillation amplitudes in the shaded region in Fig. 19.3 is explained by the fact that additional damping was introduced to avoid collisions during the passage of the second resonance in the experiment.

19.5 Conclusions

The paper showed that the proposed approach to analytical modeling allows a correct numerical study of the spatial nonlinear oscillation excitation mechanisms of rotating rotors in magnetic bearings of different types to be performed. It enables clarification of the conditions for the existence of various resonance modes inherent in such the systems, as well as simulation of super-, subharmonic and combined oscillations. Visualization of nonlinear processes and characteristics underlies the analysis of the stability of the rotor motion in various modes.

Studies were performed for a real rotor system with passive and active magnetic bearings and demonstrated the possibility of recognizing and evaluating various nonlinear phenomena of rotor dynamics. Validation based on experimental data confirmed the correctness of the simulation.

The proposed approach to assessing the stability of motion is applicable to other rotary systems with periodic excitations, which contain elements with a complex

form of the mathematical description of their dynamic behavior in terms of the analytical analysis.

References

- Amiryar, M.E., Pullen, K.R.: Analysis of standby losses and charging cycles in flywheel energy storage systems. *Energies* **13**, 4441 (2020). <https://doi.org/10.3390/en13174441>
- Anantachaisilp, P., Lin, Z.: Fractional-order surge control of active magnetic bearings suspended compressor. *Actuators* **9**, 75 (2020). <https://doi.org/10.3390/act9030075>
- Bangcheng, H., Zan, H., Xu, Z., Xu, L., Tong, W., Shiqiang, Z.: Loss estimation, thermal analysis, and measurement of a large-scale turbomolecular pump with active magnetic bearings. *IET Electr. Power Appl.* **14**, 1283–1290 (2020). <https://doi.org/10.1049/iet-epa.2020.0037>
- Barbosa Moreira, A.B., Thouverez, F.: Influence of blade flexibility on the dynamic response simulation of a turbomolecular pump on magnetic bearings. *J. Eng. Gas Turbines Power.* **142**, 041004 (2020). <https://doi.org/10.1115/1.4044733>
- Chalageri, G.R., Bekinal, S.I., Doddamani, M.: Dynamic and harmonic analysis of pillar drilling machine spindle supported by hybrid bearing set. In: *AIP Conference Proceedings*, (2020), p. 020008
- Chen, G., Yao, L., Zheng, R., Zhang, L., Ding, J.: Design and implementation of a novel passive magnetically levitated nutation blood pump for the ventricular-assist device. *IEEE Access* **7**, 169327–169337 (2019). <https://doi.org/10.1109/ACCESS.2019.2955027>
- Čorović, S., Miljavec, D.: Modal Analysis and rotor-dynamics of an interior permanent magnet synchronous motor: an experimental and theoretical study. *Appl. Sci.* **10**, 5881 (2020). <https://doi.org/10.3390/app10175881>
- Cui, H.B., Zhou, J., Dong, J.Y., Jin, C.W.: Case study on vibration stability of rotating machinery equipped with active magnetic bearings. *Zhejiang Daxue Xuebao (Gongxue Ban)/J. Zhejiang Univ. (Eng. Sci.)* **52**, 635–640 (2018). <https://doi.org/10.3785/j.issn.1008-973X.2018.04.004>
- Ebrahimi, R., Ghayour, M., Khanlo, H.M.: Nonlinear dynamic analysis and experimental verification of a magnetically supported flexible rotor system with auxiliary bearings. *Mech. Mach. Theory.* **121**, 545–562 (2018). <https://doi.org/10.1016/j.mechmachtheory.2017.11.018>
- Ebrahimi, R., Ghayour, M., Mohammad Khanlo, H.: Chaotic vibration analysis of a coaxial rotor system in active magnetic bearings and contact with auxiliary bearings. *J. Comput. Nonlinear Dyn.* **12**, 031012 (2017). <https://doi.org/10.1115/1.4034869>
- Goleman, R., Jerzy, S., Gizewski, T., Bak, P., Krzysztof, W.: Numerical analysis of a rotor axis stability with a passive magnetic bearing system. In: *2018 14th Selected Issues of Electrical Engineering and Electronics (WZEE)*. IEEE (2018), pp. 1–4
- Grönman, A., Nerg, J., Sikanen, E., Sillanpää, T., Nevaranta, N., Scherman, E., Uusitalo, A., Uzhegov, N., Smirnov, A., Honkatukia, J., Sallinen, P., Jastrzebski, R.P., Heikkinen, J., Backman, J., Pyrhönen, J., Pyrhönen, O., Sopanen, J., Turunen-Saaresti, T.: Design and verification of a hermetic high-speed turbogenerator concept for biomass and waste heat recovery applications. *Energy Convers. Manag.* **225**, 113427 (2020). <https://doi.org/10.1016/j.enconman.2020.113427>
- Kato, H., Komori, M., Asami, K., Sakai, N.: Development of one-axis active controlled bearingless motor working at extremely low temperature. *J. Adv. Mech. Des. Syst. Manuf.* **14**, JAMDSM0034–JAMDSM0034 (2020). <https://doi.org/10.1299/jamdsm.2020jamdsm0034>
- Khatri, R., Hawkins, L.A., Ortiz Neri, M., Cangiolli, F., Biliotti, D.: Design and prototype test data for a 300 kW active magnetic bearings-supported turbine generator for natural gas pressure letdown. *J. Eng. Gas Turbines Power.* **142**, 011007 (2020). <https://doi.org/10.1115/1.4045277>
- Lacarbonara, W., Balachandran, B., Ma, J., Tenreiro Machado, J.A., Stepan, G. (eds.): *Nonlinear Dynamics of Structures, Systems and Devices*. Springer International Publishing, Cham (2020)

- Mahmoud, M.S., Ueno, S., Jiang, C.: Stiffness analysis of vertical-axis wind turbines rotors using permanent magnet attractive type passive magnetic bearings. In: 2019 12th Asian Control Conference (ASCC). IEEE, Kitakyushu-shi (2019), pp. 1222–1227
- Mahmoud, M.S., Ueno, S., Jiang, C.: Power reduction and resonance avoidance of maglev vertical axis wind turbines using attractive type passive magnetic bearings. *Mech. Eng. J.* **7**, 20-00043-20-00043 (2020). <https://doi.org/10.1299/mej.20-00043>
- Martynenko, G.: Resonance mode detuning in rotor systems employing active and passive magnetic bearings with controlled stiffness. *Int. J. Automat. Mech. Eng.* **13**, 3293–3308 (2016). <https://doi.org/10.15282/ijame.13.2.2016.2.0274>
- Martynenko, G.: Accounting for an interconnection of electrical, magnetic and mechanical processes in modeling the dynamics of turbomachines rotors in passive and controlled active magnetic bearings. In: 2018 IEEE 3rd International Conference on Intelligent Energy and Power Systems (IEPS 2018), pp. 326–331. IEEE, Kharkiv (2018)
- Martynenko, G.: Practical application of the analytical method of electromagnetic circuit analysis for determining magnetic forces in active magnetic bearings. In: 2020 IEEE Problems of Automated Electrodrive. Theory and Practice (PAEP 2020), pp. 1–4. IEEE, Kremenchuk (2020a)
- Martynenko, G.: Analytical method of the analysis of electromagnetic circuits of active magnetic bearings for searching energy and forces taking into account control law. In: 2020 IEEE KhPI Week on Advanced Technology (KhPIWeek 2020), pp. 86–91. IEEE, Kharkiv (2020b)
- Martynenko, G., Martynenko, V.: Numerical determination of active magnetic bearings force characteristics taking into account control laws based on parametric modeling. In: 2019 IEEE International Conference on Modern Electrical and Energy Systems (MEES 2019), pp. 358–361. IEEE, Kremenchuk (2019)
- Martynenko, G., Martynenko, V.: Modeling of the dynamics of rotors of an energy gas turbine installation using an analytical method for analyzing active magnetic bearing circuits. In: 2020 IEEE KhPI Week on Advanced Technology (KhPIWeek 2020), pp. 92–97. IEEE, Kharkiv, Ukraine (2020a)
- Martynenko, G., Martynenko, V.: Rotor dynamics modeling for compressor and generator of the energy gas turbine unit with active magnetic bearings in operating modes. In: 2020 IEEE Problems of Automated Electrodrive. Theory and Practice (PAEP 2020), pp. 1–4. IEEE, Kremenchuk (2020b)
- Martynenko, G., Ulianov, Y.: combined rotor suspension in passive and active magnetic bearings as a prototype of bearing systems of energy rotary turbomachines. In: 2019 IEEE International Conference on Modern Electrical and Energy Systems (MEES 2019), pp. 90–93. IEEE, Kremenchuk (2019)
- Martynenko, G.Y., Marusenko, O.M., Ulyanov, Y.M., Rozova, L. V.: The use of information technology for the design of a prototype engine with rotor in magnetic bearings. In: Nechyporuk, M., Pavlikov, V., Kritskiy, D. (eds.) *Advances in Intelligent Systems and Computing*, vol. 1113, pp. 301–309. Springer, Cham (2020a)
- Martynenko, V.: Analysis of strength and bearing capacity of the auxiliary mine ventilation fan connected to the rotor of its electrical drive. In: 2020 IEEE KhPI Week on Advanced Technology (KhPIWeek 2020), pp. 19–23. IEEE, Kharkiv, Ukraine (2020c)
- Martynenko, V., Hrytsenko, M., Martynenko, G.: Technique for evaluating the strength of composite blades. *J. Inst. Eng. Ser. C* **101**, 451–461 (2020b). <https://doi.org/10.1007/s40032-020-00572-9>
- Maslen, E.H., Schweitzer, G. (eds.): *Magnetic Bearings. Theory, Design, and Application to Rotating Machinery*. Springer, Berlin (2009)
- Matsushita, O., Tanaka, M., Kanki, H., Kobayashi, M., Keogh, P.: *Vibrations of Rotating Machinery: Volume 1. Basic Rotordynamics: Introduction to Practical Vibration Analysis*. Springer Japan, Tokyo (2017)
- Matsushita, O., Tanaka, M., Kanki, H., Kobayashi, M., Keogh, P.: *Vibrations of Rotating Machinery: Volume 2. Advanced Rotordynamics: Applications of Analysis, Troubleshooting and Diagnosis*. Springer Japan, Tokyo (2019)

- Mystkowski, A.: Lyapunov sliding-mode observers with application for active magnetic bearing operated with zero-bias flux. *J. Dyn. Syst. Meas. Control.* **141**, 041006 (2019). <https://doi.org/10.1115/1.4041978>
- Nan, G., Zhang, Y., Zhu, Y., Guo, W.: Nonlinear dynamics of rotor system supported by bearing with waviness. *Sci. Prog.* **103**, 003685042094409 (2020). <https://doi.org/10.1177/0036850420944092>
- Van Osch, M.M.E.: Rotor Dynamics of a Centrifugal Pump. Technische Universiteit Eindhoven Faculteit Werktuigbouwkunde, Divisie Thermo Fluids Engineering, Sectie Proces Technologie, Eindhoven (2006)
- Pilotto, R., Nordmann, R.: Vibration control of a gas turbine-generator rotor in a combined cycle system by means of active magnetic bearings. In: Cavalca, K., Weber, H. (eds.) *Mechanisms and Machine Science*, pp. 520–533. Springer, Cham (2019)
- Prusa, R., Huzlik, R., Haban, V.: Design of passive magnetic axial bearing for seal-less pump. In: 2018 18th International Conference on Mechatronics—Mechatronika (ME 2018), pp. 1–6. IEEE, Brno, Czech Republic (2019)
- Qiao, X., Tang, X.: The stability of magnetic levitation milling system based on modal decoupling control. *Shock Vib.* **2020**, 1–9 (2020). <https://doi.org/10.1155/2020/7839070>
- Ran, S., Hu, Y., Wu, H.: Design, modeling, and robust control of the flexible rotor to pass the first bending critical speed with active magnetic bearing. *Adv. Mech. Eng.* **10**, 168781401875753 (2018). <https://doi.org/10.1177/1687814018757536>
- Routh, E.J.: *The Advanced Part of a Treatise on the Dynamics of a System of Rigid Bodies, Being of a Treatise on the Whole Subject, With: Numerous Examples*, vol. 2 (Classic reprint series). Forgotten Books, London (2012)
- Routh, E.J.: *The Elementary Part of a Treatise on the Dynamics of a System of Rigid Bodies, Vol. 1: Being Part I. of a Treatise on the Whole Subject, with Numerous* (Classic reprint series). Forgotten Books, London (2018)
- Rusanov, A., Martynenko, G., Avramov, K., Martynenko, V.: Detection of accident causes on turbine-generator sets by means of numerical simulations. In: 2018 IEEE 3rd International Conference on Intelligent Energy and Power Systems (IEPS 2018), pp. 51–54. IEEE (2018)
- Santra, T., Roy, D., Choudhury, A.B.: Calculation of passive magnetic force in a radial magnetic bearing using general division approach. *Prog. Electromagn. Res. M* **54**, 91–102 (2017). <https://doi.org/10.2528/PIERM16120602>
- Soni, T., Dutt, J.K., Das, A.S.: Parametric stability analysis of active magnetic bearing supported rotor system with a novel control law subject to periodic base motion. *IEEE Trans. Ind. Electron.* **67**, 1160–1170 (2020). <https://doi.org/10.1109/TIE.2019.2898604>
- Wen, T., Xiang, B., Zhang, S.: Optimal control for hybrid magnetically suspended flywheel rotor based on state feedback exact linearization model. *Sci. Prog.* **103**, 003685042095138 (2020). <https://doi.org/10.1177/0036850420951389>
- Worden, K., Tomlinson, G.R.: *Nonlinearity in Structural Dynamics: Detection, Identification and Modelling*. CRC Press (2019)
- Wu, R.Q., Zhang, W., Yao, M.H.: Nonlinear dynamics near resonances of a rotor-active magnetic bearings system with 16-pole legs and time varying stiffness. *Mech. Syst. Signal Process.* **100**, 113–134 (2018). <https://doi.org/10.1016/j.ymssp.2017.07.033>
- Xia, C., Cai, Y., Ren, Y.: stability analysis for a rotor system in a magnetically suspended control and sensitive gyroscope with the Lorentz force magnetic bearing rotation. *Proc. Inst. Mech. Eng. Part I J. Syst. Control Eng.* **233**, 548–557 (2019). <https://doi.org/10.1177/0959651818800913>
- Xiang, L., Yang, Y., Zhang, Y., An, C., Ye, F.: Research on nonlinear dynamics of a rotor based on full spectrum analysis. *Dongli Gongcheng Xuebao/Journal Chinese Soc. Power Eng.* **40**, 556–563 (2020). <https://doi.org/10.19805/j.cnki.jcspe.2020.07.006>
- Yonnet, J.-P.: Passive magnetic bearings with permanent magnets. *IEEE Trans. Magn.* **14**, 803–805 (1978). <https://doi.org/10.1109/TMAG.1978.1060019>
- Yuan, Y., Ma, Y., Guo, S., Yang, F., Xu, B.: Suspension performance analysis of a novel bearingless motor. *Electron. Lett.* **56**, 132–134 (2020). <https://doi.org/10.1049/el.2019.3011>

- Zhang, W., Wu, R.Q., Siriguleng, B.: Nonlinear vibrations of a rotor-active magnetic bearing system with 16-pole legs and two degrees of freedom. *Shock Vib.* **2020**, 1–29 (2020). <https://doi.org/10.1155/2020/5282904>
- Zhang, W., Zhu, H.: Radial magnetic bearings: an overview. *Results Phys.* **7**, 3756–3766 (2017). <https://doi.org/10.1016/j.rinp.2017.08.043>
- Zhao, X.W., Xu, X.L., Zhao, W.X., Jiang, Z.L.: Extraction methods for numerical and graphical features of long course eccentric fault of rotating machinery. *Beijing Ligong Daxue Xuebao/Transact. Beijing Inst. Technol.* **36**, 893–898 (2016). <https://doi.org/10.15918/j.tbit1001-0645.2016.09.003>
- Żokowski, M., Falkowski, K., Kurnyta-Mazurek, P., Henzel, M.: Control of bearingless electric machines dedicated for aviation. *Aircr. Eng. Aerosp. Technol.* **92**, 27–36 (2020). <https://doi.org/10.1108/AEAT-11-2018-0293>

Chapter 20

Computational–Experimental Evaluation of Stiffness Response in Elastic Supports of Rotor Systems



Mykola M. Tkachuk, Andriy Grabovskiy, Mykola A. Tkachuk, and Olexandr Shut

Abstract The paper contains analysis of stiffness response in elastic supports found in rotor systems such as superchargers of heavy-duty engines. A particular design of flexible bushings in the form of a circular ring with grooves is considered. Several computational models for the evaluation of their response are proposed. The numerical results were obtained for various numbers of inner and outer flanges that serve as contact points. The elastic bushing displays stiffer response for wider groove arcs and larger number of flanges. It has been shown that the elastic response of the ring is linear up to a certain displacement limit. Once the initial gap in the grooves is closed, the bushing becomes essentially rigid. The obtained numerical results are compared with the experimental data, which display good agreement. It can be concluded that the force–displacement response is essentially nonlinear due to the contact. This nonlinearity is expected to have profound effect on rotor dynamics.

Keywords Rotor system · Elastic bushing · Finite element analysis · Contact interaction · Complementary energy principle

20.1 Introduction

Analysis and control of vibrational characteristics are crucial for the design of machine components that have rotating parts (Rao 1996). The choice of elastic supports has a great effect on the rotational dynamics (Kelson et al. 1982). The

M. M. Tkachuk (✉) · A. Grabovskiy · M. A. Tkachuk · O. Shut
Department of Theory and Computer-Aided Design of Mechanisms and Machines, National Technical University “Kharkiv Polytechnic Institute”, Kharkiv, Ukraine
e-mail: m.tkachuk@tmm-sapr.org

A. Grabovskiy
e-mail: Grabovskiy@tmm-sapr.org

M. A. Tkachuk
e-mail: myk.tkachuk@gmail.com

O. Shut
e-mail: misapr@tmm-sapr.org

critical velocity strongly depends on the transverse stiffness of these supports more. That is why adjustment of these parameters is the principal method of detuning rotor systems away from resonance. Nevertheless, this solution is not universality efficient. Often the moderation of vibrations in a broad spectrum of operational regimes is not successful by standard methods. The real response of elastic supports to the displacements of the shaft turns out to play nontrivial role. It may display significant nonlinearity, which requires further analysis.

Unsolved problems of rotor dynamics can be found in heavy-duty engines that have a supercharger with is a dual-drive design. This means that the torque coming from the crankshaft of the engine and the exhaust turbine drives the compressor simultaneously. This inevitably causes abrupt power ripple in the dynamic system. In such circumstances, the properties of the rotor support system become even more important than in the traditional cases.

20.2 Literature Overview

Numerous models of rotor systems (Rao 1996; Kelson et al. 1982; Martynenko 2016a, b; Neilson and Barr 1988) have been developed up to this point. The focus is set on the critical rotational velocities and vibration damping. Coupled bending and torsional vibrations of a rotor system with nonlinear friction are studied in Hua et al. (2017, 2015), Shi et al. (2013). Parametrical instability of a flexible rotor system is described in Mutra and Srinivas (2016), Han and Chu (2015), Avramov et al. (2015), Matthew and Glavatskih (2015). Passive and active magnetic bearings are proposed for amplitude moderation of turbochargers in resonance.

Despite the abundant research effort, the studies did not cover all actual problems. In particular, this concerns turbocompressors of high-power engines with high-speed rotations. The cantilever design of the impeller installation poses new challenges due to the heavyweight of the disk and size limitations regarding the shaft length and support distance.

This contribution addresses several important issues for the impeller design shown in Fig. 20.1. A known method of vibration damping by means of elastic bushing is analyzed for this rotary unit. The contact response of the flexible ring in bearing supports was analyzed in lie with the approach proposed in Tkachuk et al. (2020, 2021). The ultimate effect of the stiffness on the dynamical characteristics of the studied rotor system is further evaluated.

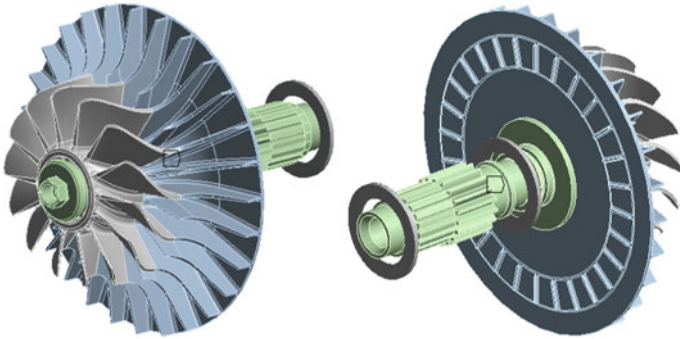


Fig. 20.1 Cantilever installation of the impeller

20.3 The Design of the Flexible Ring with Intermeshed Inner and Outer Flanges

The compressor may have unconventional configuration of supports. The considered design includes an additional elastic bushing between the rolling bearings and the rigid socket of the housing. Each of the elements of this structure has its elastic characteristics. These characteristics can be determined either by numerical computations or experimentally. However, at the design stage, it is important to have information on the dependence of the force–displacement characteristics on the variable parameters. In particular, it concerns the elastic insert, as it is the element that allows one to control the ultimate properties of the elastic support. This contribution elaborates on computational and experimental evaluation of elastic response of this structural element.

The elastic insert is a cylindrical thin ring with a set of grooves machined along the inner and outer surfaces. The center of each groove on one side of the ring is placed exactly between the centers of two other grooves on the opposite side. The arch of the groove is much larger than the width of each of the narrow flanges. This creates a set of alternating contacts between the busing and the bearing on inner side and the insert and the socket on the other side upon which the ring is rested. The section of the ring between the edges of two adjacent flanges deforms elastically as a curved beam, thus providing the flexibility of the entire structural element. As a result, the slender elastic ring is far more compliant to radial displacements than the rest of the structure, in particular the bearings themselves. The variable design parameters are the width and thickness of the ring, number of grooves and their depth as well as the amount of gap or pretension in the assembly. The computer geometrical model of a ring with 10 grooves on each side is shown in Fig. 20.2.

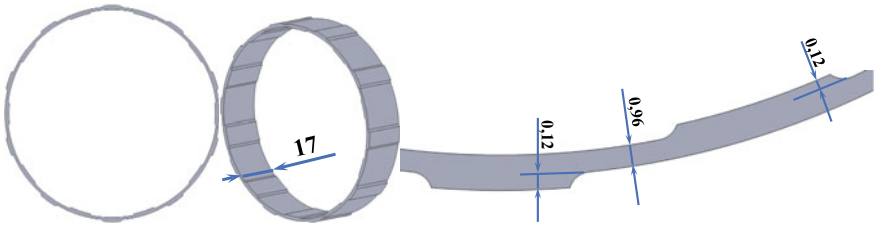


Fig. 20.2 CAD model of an elastic ring with 10 grooves (mm)

20.4 Computational Models for the Elastic Ring

Given the presence of contact interaction in the elastic support its response turns out to be essentially nonlinear. Three types of models are developed for the analysis of deformations.

The first model considers the elastic ring as a curved beam ring of variable thickness. The Euler–Bernoulli approximation is applied to describe the elastic response of the beam. The radial displacements of this beam are constrained by contacts from the both sides of the insert. The deformations occur in the form of transverse bending and linear extension. A variational complementary energy principle is formulated for this system. The optimality conditions provide a set of equations and inequalities that determine the unknown internal stresses in the elastic ring as well as the unknown contact reactions. The obtained solution is used to acquire the thought—for force–displacement curve for the response of the elastic insert.

The other two types of models are created in commercial finite element modeling software in 2D in plane stress formulation and in full 3D statement with various types of contact in the analysis.

20.5 Numerical Evaluation of Elastic Supports Stiffness and Critical Velocities

Two major factors are analyzed numerically in this study. Firstly, the stiffness of the elastic response of the flexible ring in contact with the bearing and the rotor housing is evaluated. The parametric study of number of grooves on the elastic ring with respect to the resulting stiffness is performed. Secondly, the critical velocities of the rotor for the obtained support stiffness values are assessed.

20.5.1 Stiffness of Elastic Supports for Various Number of Grooves on the Elastic Ring

The appropriate choice of geometrical parameters of the flexible ring is required in order to get the exact stiffness in elastic supports. The number of grooves on each side of the ring is considered in the range between 3 and 10 for the given width and height of narrow flanges presented in Fig. 20.2. The model for the contact of this flexible bushing with stator housing and the bearing is presented in Fig. 20.3. The deformations in the journal and the rotor housing are disregarded, and thus, they are defined as two rigid bodies. Correspondingly, they can be introduced in a simplified form as two cylindrical rings. Two pairs of contacts are introduced on the inner and outer sides of the ring. The finite element model of this system is shown in Fig. 20.4. The loading is introduced kinematically as a rigid translation w of the bearing in the range 0–0.15 mm.

The deformed shape and the stress distribution in the elastic ring for various number of grooves are shown in Figs. 20.5, 20.6, 20.7, 20.8, 20.9, 20.10, 20.11 and 20.12. The corresponding reaction force P to radial displacement w diagrams are shown for small and large numbers of grooves in Fig. 20.13.

The results obtained simultaneously by the three models display excellent consistency. In particular, it is established that the curve “force P —radial displacement w ” has two characteristic sections. The first corresponds to the elastic bending of thin parts of the elastic insert while being only partially supported by contacts outside of the cutout grooves. The plot clearly demonstrates the linear nature of the response in

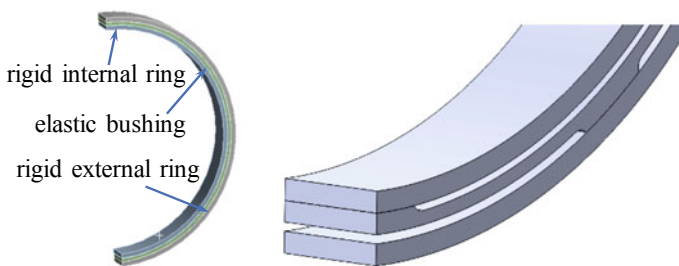


Fig. 20.3 Contact of the elastic bushing with the stator housing and the bearing

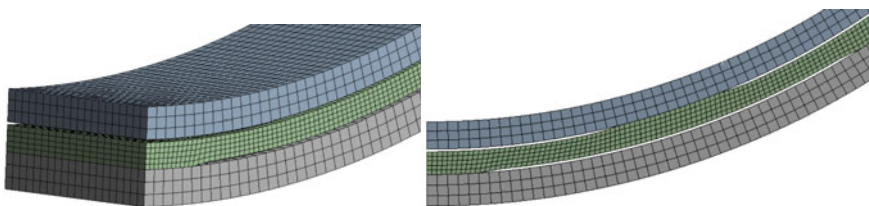


Fig. 20.4 Finite element model of the elastic ring in contact with two rigid cylindrical bodies

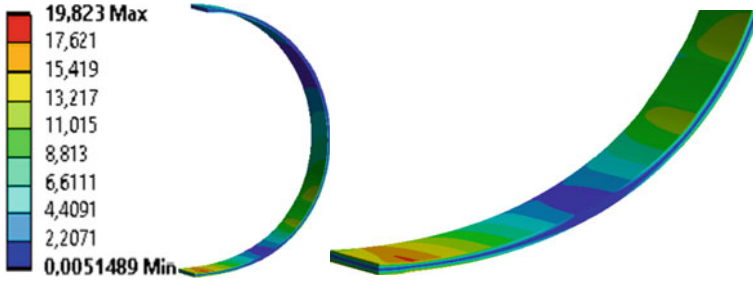


Fig. 20.5 Von Mises stress (MPa) distribution in the deformed configuration of the elastic ring with 3 grooves at radial displacement $w = 0.15$ mm

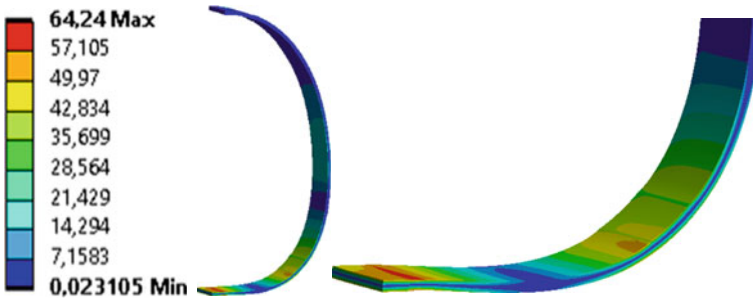


Fig. 20.6 Von Mises stress (MPa) distribution in the deformed configuration of the elastic ring with 4 grooves at radial displacement $w = 0.15$ mm

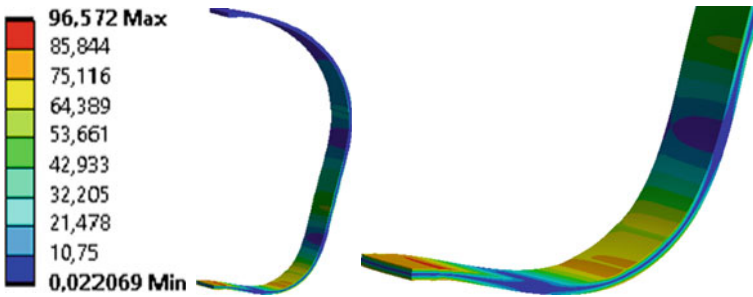


Fig. 20.7 Von Mises stress (MPa) distribution in the deformed configuration of the elastic ring with 5 grooves at radial displacement $w = 0.15$ mm

this regime determined by relation $dP = c_1 dw$, where the stiffness c_1 is determined by the bending stiffness of the segments of the ring. The other type of response is observed when the gap in the grooves is closed. When this happens, the system gets abruptly much stiffer transferring to the other elastic regime with $dP = c_2 dw$, where the much greater stiffness $c_2 \gg c_1$ is defined by the compression of the

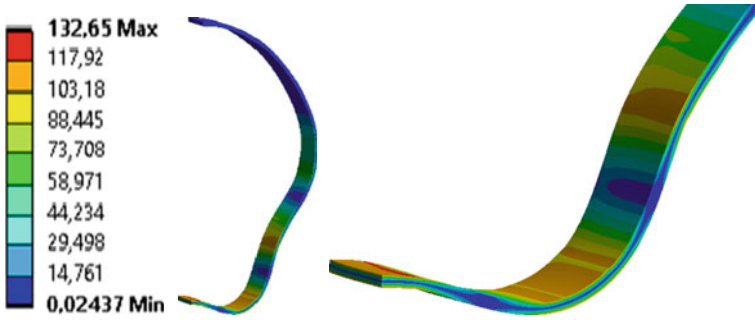


Fig. 20.8 Von Mises stress (MPa) distribution in the deformed configuration of the elastic ring with 6 grooves at radial displacement $w = 0.15$ mm

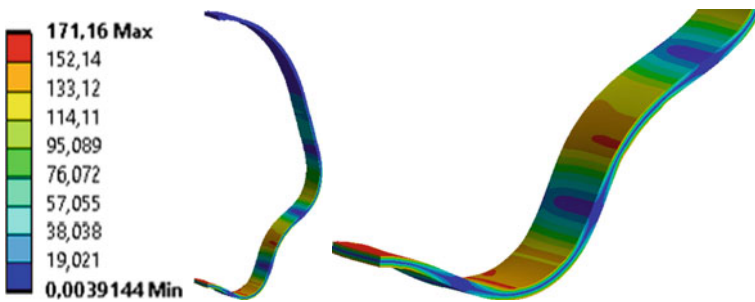


Fig. 20.9 Von Mises stress (MPa) distribution in the deformed configuration of the elastic ring with 7 grooves at radial displacement $w = 0.15$ mm

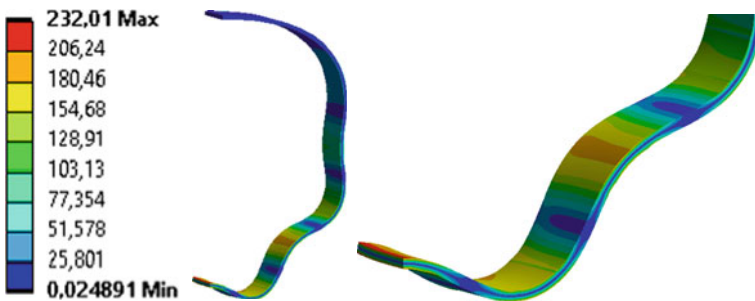


Fig. 20.10 Von Mises stress (MPa) distribution in the deformed configuration of the elastic ring with 8 grooves at radial displacement $w = 0.15$ mm

insert between the bearing and the housing. The transition occurs at a very small displacement increment interval.

Besides, there might be a portion with zero response $P \equiv 0$ on the force–displacement curve in case there is an initial gap between the elastic bushing and either the

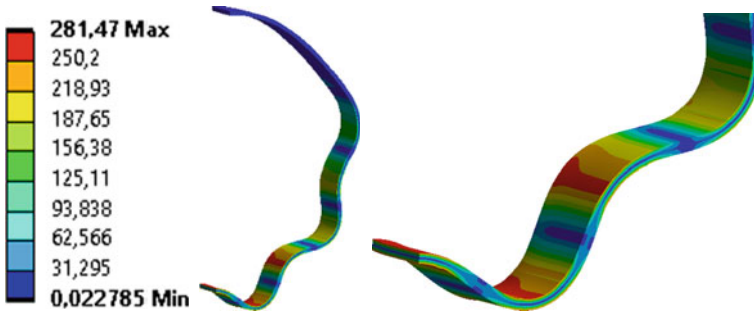


Fig. 20.11 Von Mises stress (MPa) distribution in the deformed configuration of the elastic ring with 9 grooves at radial displacement $w = 0.15$ mm

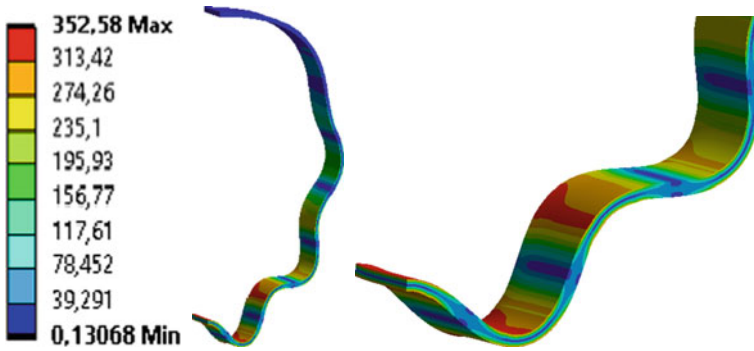


Fig. 20.12 Von Mises stress (MPa) distribution in the deformed configuration of the elastic ring with 10 grooves at radial displacement $w = 0.15$ mm

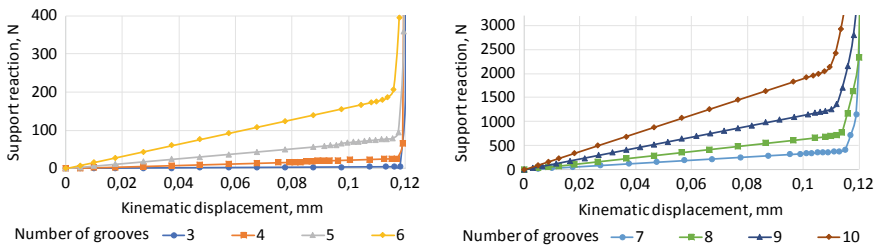
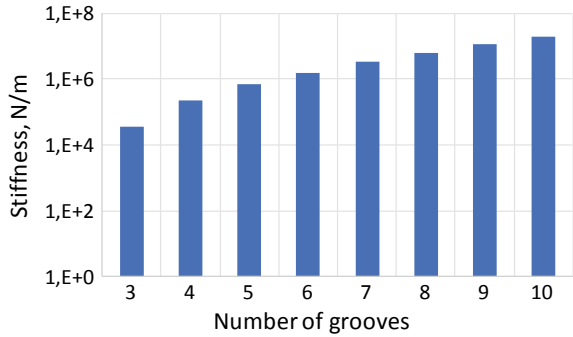


Fig. 20.13 Reaction force P to radial displacement w diagrams are shown for small (*left*) and large (*right*) numbers of grooves

bearing or the housing or both. It continues until this gap is not closed by the displacement $w \leq \delta$. To the contrary, if there is a pretension Δ , the ring is permanently in contact with other parts in the assembly. Furthermore, its response becomes stiffer with a shorter first section on the force–displacement curve.

Fig. 20.14 Stiffness c_1 of the elastic ring depending on the number of grooves



The stiffness of the elastic ring for small oscillations depends on the number of grooves and flanges as can be seen in Fig. 20.14. The variation of this parameter that is essential for rotor dynamics spans over three orders of magnitude. Hence, it provides broad control over the desired characteristics of the rotor system. In particular, critical velocities of the cantilever impeller can be detuned from operational range of the supercharger by the appropriate choice of the ring geometry as illustrated next.

20.5.2 Critical Rotation Velocities of the Cantilever Rotor Depending on the Stiffness of the Elastic Supports

The rotor shown in Fig. 20.1 weighs 2.58 kg, largely due to a massive rotor. Although it is made of aluminum, it is much heavier than the steel shaft not to mention its moment of inertia. The finite element model of the assembly with approximately 140 thousand nodes is shown in Fig. 20.15.

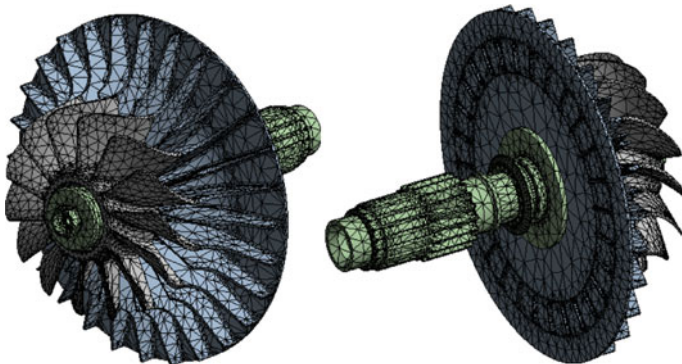


Fig. 20.15 Finite element model of the cantilever impeller

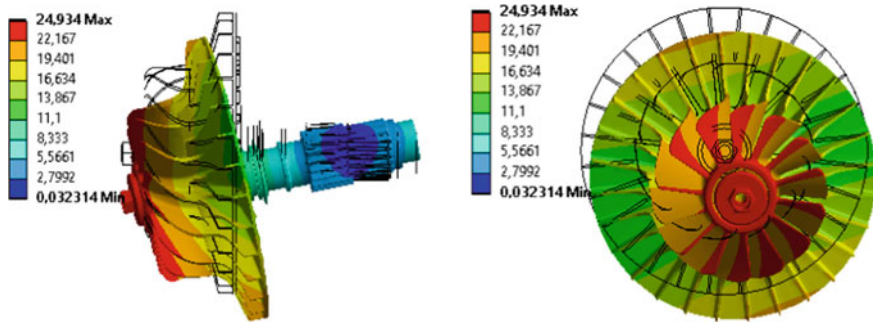


Fig. 20.16 First eigenform of the rotor for the nominal stiffness of bearings $c_1^0 = 6.36 \times 10^6$ N/m

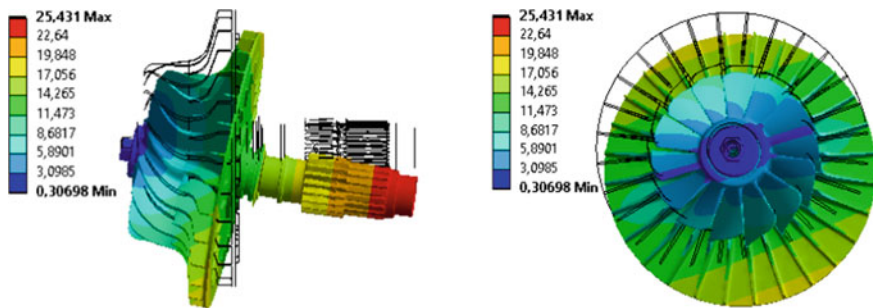


Fig. 20.17 Second eigenform of the rotor for the nominal stiffness of bearings $c_1^0 = 6.36 \times 10^6$ N/m

The first and the second eigenforms of the rotor for the nominal stiffness of bearings $c_1^0 = 6.36 \times 10^6$ N/m are shown in Figs. 20.16 and 20.17. The compliance of the bearings even without the additional damping of the flexible bushing has the decisive effect on the first two oscillation modes. As can be noted that they are essentially translational. The disk and the shaft perform rigid body motion with negligible deformations.

The introduction of the flexible bushing decreases dramatically the stiffness of the elastic supports. According to the analysis of the compliance of the ring insert the resulting stiffness values below the nominal value $c_1 < c_1^0 = 6.36 \times 10^6$ N/m are considered. The dependence of eigenfrequencies on this variable parameter is given in Figs. 20.18 and 20.19. It can be seen that the eigenfrequencies and accordingly the critical rotational velocities vary significantly for the support stiffness values in the range 10^2 – 10^6 N/m and level out at the support response approaching the rigid limit.

Fig. 20.18 First eigenfrequency and critical rotational velocities (backward and forward whirl), Hz as function of support stiffness, N/m

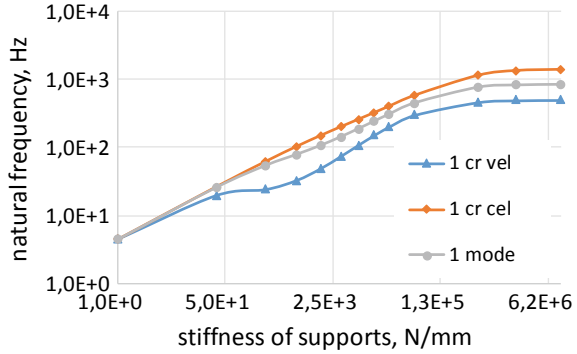
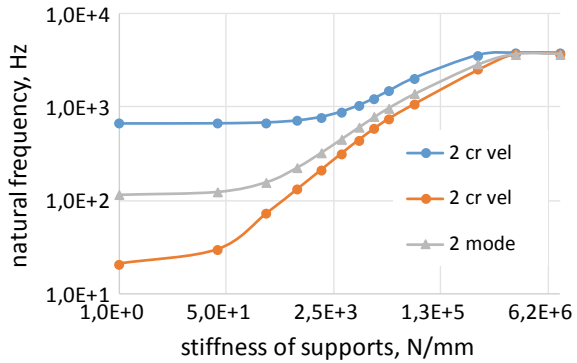


Fig. 20.19 Second eigenfrequency and critical rotational velocities (backward and forward whirl), Hz as function of support stiffness, N/m



20.6 Experimental Measurement of Elastic Support Stiffness

The stiffness of the elastic support with a flexible ring bushing for an actual design of the supercharged engine was measured experimentally in addition to the performed numerical analysis. The experimental installation is shown in Fig. 20.20.

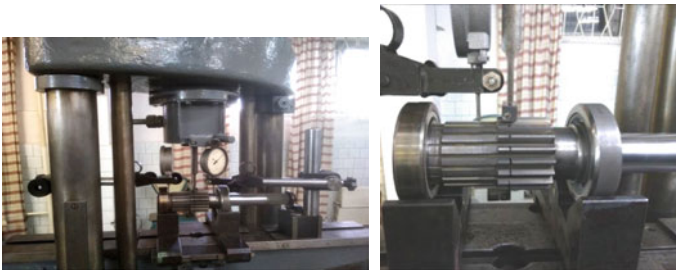
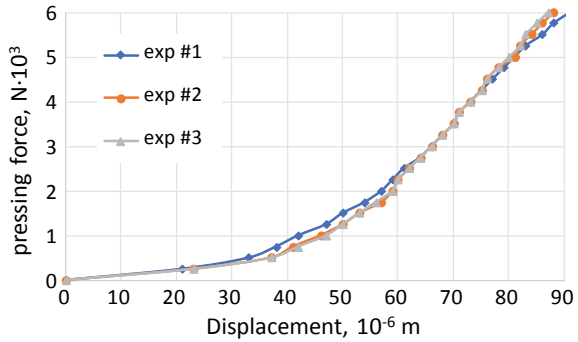


Fig. 20.20 Experimental installation for measurement of elastic support stiffness

Fig. 20.21 Experimentally measured force–displacement curve for the elastic support with a flexible bushing with **10** grooves



The obtained relation between the radial force P and the displacement w for the flexible ring with 10 grooves is shown in Fig. 20.21. The measured elastic response agrees well with the computational model. The loading curve contains the initial section with low stiffness succeeded by a transition to significantly stiffer response.

The test run of the rotor with the control of disk tip displacements was performed as well. The excessive amplitudes of lateral oscillations have been detected on certain rotational velocities. This confirms the existence of critical regimes in the system that correlates with the estimates of eigenfrequencies obtained from the numerical analysis.

20.7 Results Analysis

Comparison between the numerical and computational results displays good agreement. The response of the flexible bushing is essentially nonlinear when lateral displacements exceed the initial gap in the grooves of the ring. The stiffness of the elastic ring depends besides its thickness on the number of grooves as well as the height and the width of the flanges. The compliance of the flexible ring exceeds significantly the deformations of the other parts of the supports. The resulting stiffness in turn has effect on the critical rotational velocities of the cantilever impeller.

20.8 Conclusions

1. The experimental and computational studies have established the essentially nonlinear response of the elastic supports of a rotor with a bushing in the form of a flexible ring with intermeshed grooves on opposite sides. This nonlinearity needs to be accounted for in the rotor dynamics model.

2. The compliance of the flexible ring is typically higher than the compliance of the journal bearings. Thus, the former mainly determines the ultimate stiffness of the elastic supports.
3. The stiffness of the elastic ring depends strongly on the number of grooves and flanges. The larger is the stiffer which is the response of the ring in contact with the stator housing and the bearing.
4. Critical velocities depend greatly on the stiffness of the elastic supports. Controlling this crucial parameter through rational choice of elastic ring geometry is an effective way to influence the dynamics of the studied cantilever rotor setup. In particular, it can be detuned from resonance by separating the operational range of rotational velocities from the first two critical velocities.

The obtained functional and parametric dependence enters the equations of dynamics of the studied rotor system. As noticed, this nonlinear response in supports can be approximated by a piece-wise linear. Accordingly, after analyzing the solutions of differential equations, the influence of the varying parameters on the vibrations is determined. In particular, it is possible to determine the amplitudes of steady-state oscillations of the rotor system and the subharmonic modes. It also enables qualitative and quantitative analysis of the behavior of the nonlinear studied rotor system. Phase portraits, Poincaré maps and repetition rates are used for this purpose. The latter enables to evaluate more accurately the multiplicity of the subharmonic mode, especially for the case of numerical integration of the differential equations of motion of the rotary system under study.

References

- Avramov, K., Shulzhenko, M., Borysiuk, O., Pierre, C.: Influence of periodic excitation on self-sustained vibrations of one disk rotors in arbitrary length journals bearings. *Int. J. Non-Linear Mech.* **77**, 274–280 (2015)
- Han, Q., Chu, F.: Parametric instability of flexible rotor-bearing system under time-periodic base angular motions. *Appl. Math. Model.* **39**(15), 4511–4522 (2015)
- Hua, C., Rao, Z., Ta, N., Zhu, Z.: Nonlinear dynamics of a rub-impact rubber bearing-rotor system with Stribeck friction model. *J. Mech. Sci. Technol.* **29**(8), 3109–3119 (2015)
- Hua, C., Cao, G., Rao, Z., Ta, N., Zhu, Z.: Coupled bending and torsional vibration of a rotor system with nonlinear friction. *J. Mech. Sci. Technol.* **31**, 2679–2689 (2017)
- Kelson, A.S., Cymanskii, H.P., Yakovlev, B.H.: *Dynamics of Rotor-Bearing Systems*. Nauka, Moscow (1982)
- Martynenko, G.: Resonance mode detuning in rotor systems employing active and passive magnetic bearings with controlled stiffness. *Int. J. Automot. Mech. Eng.* **13**, 3293 (2016)
- Martynenko, G.: Application of nonlinear models for a well-defined description of the dynamics of rotors in magnetic bearings. *Eureka: Phys. Eng.* **3**, 3–12
- Matthew, C., Glavatskih, S.: Nonlinear dynamic behaviour of vertical and horizontal rotors in compliant liner tilting pad journal bearings: some design considerations. *Tribol. Int.* **82**, 142–152 (2015)
- Mutra, R.R., Srinivas, J.: Vibration analysis of a support excited rotor system with hydrodynamic journal bearings. *Procedia Eng.* **144**, 825–832 (2016)

- Neilson, R.D., Barr, A.D.S.: Dynamics of a rigid rotor mounted on discontinuously non-linear elastic supports. *Proc. Inst. Mech. Eng. Part C: J. Mech. Eng. Sci.* **202**(5), 369–376 (1988)
- Rao, J.S.: *Rotor dynamics*. New Age International (1996)
- Shi, M.L., Wang, D.Z., Zhang, J.G.: Nonlinear dynamic analysis of a vertical rotor-bearing system. *J. Mech. Sci. Technol.* **27**(1), 9–19 (2013)
- Tkachuk, M.M., Grabovskiy, A., Tkachuk, M.A., Saverska, M., Hrechka, I.: A semi-analytical method for analys of contact interaction between structural elements along aligned surfaces. *Eastern-European J. Enterprise Technol.* **1/7**(103), 16–25 (2020)
- Tkachuk, M.M., Grabovskiy, A., Tkachuk, M.A., Zarubina, A., Lipeyko, A.: Analysis of elastic supports and rotor flexibility for dynamics of a cantilever impeller. *J. Phys: Conf. Ser.* **1741**(1), 012043 (2021)

Part VII
Satellites and Spacecrafts

Chapter 21

A Brief Analysis of Artificial Satellites Solar Panels Deployment Considering a Nonlinear Dynamic Model



Rafael Avanço, Raibel Arias, José Manoel Balthazar, Ângelo Marcelo Tusset, Maurício Aparecido Ribeiro, Frederic Conrad Janzen, and Átila Madureira Bueno

Abstract The present analysis is focused on the nonlinear dynamics of a solar panel opening during the trajectory of a satellite around the Earth, analyzing the dynamics between energy sources and structural response that must not be ignored in real engineering problems. The governing equations were obtained with the Lagrangian function and the results were found using the Runge–Kutta method for integration. These results were found using two different models. One of them considers the panel directly connected to a DC motor and the other considers a torsion spring connected to the motor shaft and the solar panel. As a result, we obtained the time series of the mathematical model proposed.

Keywords Simplified model · Solar panel · Nonlinear dynamics · Vibrations

R. Avanço · R. Arias

Federal University of Maranhão, Campus Balsas, Balsas, State of Maranhão, Brazil

e-mail: avancorafael@gmail.com

R. Arias

e-mail: raibel.jac1@gmail.com

J. M. Balthazar (✉)

UNESP-Universidade Estadual Paulista, Bauru, SP, Brazil

e-mail: jmbaltha@gmail.com

Â. M. Tusset · M. A. Ribeiro · F. C. Janzen

Federal University of Technology, Ponta Grossa, Paraná, Brazil

e-mail: a.m.tusset@gmail.com

M. A. Ribeiro

e-mail: mau.ap.ribeiro@gmail.com

F. C. Janzen

e-mail: fcjanzen@utfpr.edu.br

Á. M. Bueno

UNESP-Universidade Estadual Paulista, Sorocaba, SP, Brazil

e-mail: atila@sorocaba.unesp.br

21.1 Introduction

The study of non-ideal vibrations, that is, when the source of energy is influenced by the response of the system, has been considered a major challenge in theoretical and practical engineering research (Balthazar et al. 2003). This phenomenon was called limited power supply in Kononenko (1969), when the source of energy was affected by the system vibrated, so-called non-ideal. When the energy source is not affected by the vibratory system, the case is considered ideal energy source (IS) and it is called non-ideal energy source (RNIS) or limited power supply when the energy source is affected by the system. The relevance of non-ideal effects in the mechanical systems was studied in Krasnopolskaya and Shvets (1990) and Krasnopolskaya and Shvets (1992), when a numerical analysis of a pendulum vibrated by a DC motor was performed. These results demonstrated the change from regular motion of the pendulum to the chaotic motion due to this interaction between the pendulum and the motor. A pendulum horizontally excited by limited power supply was studied in Avanço et al. (2018). It was considered a case of limited power supply, on the one hand by the characteristics of a particular energy source, and on the other hand, limited by the dependence of the motion of the vibrated system on the motion of the energy source. The results of pendulum motion cover chaotic motion, regular rotation and oscillation with quasiperiodic motions.

The connection in non-ideal systems is expressed by a system of differential equations of motion of the mechanical system and the electro-mechanical equations of the energy source. For non-ideal dynamical systems, someone must add an equation that describes how the energy source supplies the energy to the mechanical system. In order to review different theories on this subject, see Balthazar et al. (2003), Balthazar et al. (2018) and Cveticanin et al. (2018).

It is also known that Solar Panels are used in space applications and they are important in structures like satellites. Space solar power satellite (SSPS) is a tremendous *energy* system that collects and converts solar power to electric power in space, and then transmits the electric power to earth wirelessly. Design for any satellite includes its electrical power needs and the system to supply them. However, its dynamics and control of the position is a challenging work, because the flexibility leads the system to vibrate in larger amplitudes (Cveticanin et al. 2018; Omidi and Mahmoodi 2015).

In this book chapter, two simplified models of a solar panel are analyzed, one of them directly connected to a DC motor and the other considering a torsion spring linked to the axis of the motor and the solar panel. It is announced that a preliminary discussion of this note was reported in Fenili (2000) and Porro et al. (2004). Therefore, we will extend these preliminary results.

This chapter was organized as follows. In Sect. 21.2 we present the non-ideal model for the dynamics in the opening of the simplified solar panel and the ideal model for the dynamics of the simplified model of solar panel. In Sect. 21.3, we will show the numerical results from the non-ideal and ideal model of the solar panel. In Sect. 21.4 we present the concluding remarks and future works. So, finally we present some acknowledgments and list the main bibliographic references used.

21.2 The Non-ideal and Ideal Model for the Simplified Solar Panel

Figure 21.1a illustrates the adapted model used here and in Fig. 21.1b we show the reference systems and variables considered in this problem. In the considered non-ideal model there is a torsion spring connected between the DC motor and the solar panel. The deflection of this spring is given by the difference of angle θ_2 and θ_m , where θ_m is the angle of the motor and θ_2 is angle of the panel with the satellite. The satellite describes a circular orbit and therefore the potential gravitational energy is not considered. The motion occurs in circular plane where is contained the center of mass of the Earth. The spin of the satellite is neglected in the calculus.

21.2.1 The Non-ideal (RNIS) and Ideal (IS) Model for the Dynamics in the Opening of the Simplified Solar Panel

The Lagrangian function is written taking the kinetic energy of the main mass of satellite and the kinetic energy of translation and rotation for the solar panel. The term m_1 represents the mass of the main body of the satellite, I_2 the moment of inertia of the solar panel and m_2 the mass of the solar panel. The kinetic energy of the satellite is given by B_1 and the kinetic energy of the solar panel is B_2 , these energies are present in Eqs. (21.1) and (21.2):

$$B_1 = \frac{1}{2}m_1(\dot{x}_1^2 + \dot{y}_1^2) \tag{21.1}$$

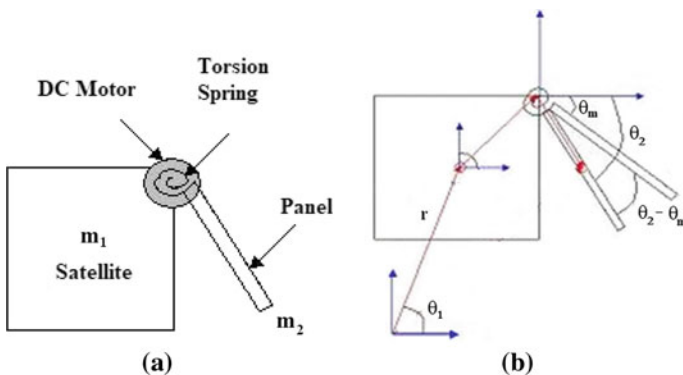


Fig. 21.1 Adapted from Porro et al. (2004). **a** Satellite with its parts, **b** Angles and position of the satellite-related with Earth center

$$B_2 = \frac{1}{2}m_2(\dot{x}_2^2 + \dot{y}_2^2) + \frac{1}{2}I_2\dot{\theta}_2^2 \quad (21.2)$$

The moment of inertia of solar panel I_2 referenced by its center is determined according to its length l :

$$I_2 = \frac{1}{12}m_2l^2 \quad (21.3)$$

The position of satellite is given by coordinates x_1 and y_1 depending on the angle θ_1 , that is the angular position of the satellite around the Earth.

$$\begin{aligned} x_1 &= r \cdot \cos \theta_1 \\ y_1 &= r \cdot \sin \theta_1 \end{aligned} \quad (21.4)$$

In Eq. (21.5) the coordinates x_2 and y_2 give the position of the center of the solar panel. The symbol w represents the width and h is the height of the satellite. The angle θ_2 was previously mentioned in Fig. 21.1.

$$\begin{aligned} x_2 &= x_1 + \frac{w}{2} + \frac{l}{2} \sin \theta_2 \\ y_2 &= y_1 + \frac{h}{2} - \frac{l}{2} \cos \theta_2 \end{aligned} \quad (21.5)$$

The potential energy U in Eq. (21.6) is determined by the deflection in torsion spring with elastic constant k .

$$U = \frac{1}{2}k(\theta_2 - \theta_m)^2 \quad (21.6)$$

The Lagrangian function in Eqs. (21.7) and (21.8) considers the translation of the satellite around the Earth. The gravitational potential energy is not taken into account because the orbit is circular and therefore it is not affected.

$$L = B_1 + B_2 - U \quad (21.7)$$

The Lagrangian equation may be written in the form presented in Eq. (21.8) after the derivation was applied in Eqs. (21.4) and (21.5).

$$\begin{aligned} L &= \frac{1}{2}m_1r^2\dot{\theta}_1^2 + \frac{1}{2}m_2r^2\dot{\theta}_1^2 + \frac{1}{8}m_2l^2\dot{\theta}_2^2 + \frac{1}{2}m_2rl\dot{\theta}_1\dot{\theta}_2\sin(\theta_2 - \theta_1) \\ &\quad + \frac{1}{2}I_2\dot{\theta}_2^2 - \frac{1}{2}k(\theta_2 - \theta_m)^2 \end{aligned} \quad (21.8)$$

The Lagrangian equations are derived from the Lagrangian function related to the coordinates θ_1 and θ_2 :

$$\begin{aligned} \frac{d}{dt} \frac{\partial L}{\partial \dot{\theta}_1} - \frac{\partial L}{\partial \theta_1} &= Q_{\theta_1} \\ \frac{d}{dt} \frac{\partial L}{\partial \dot{\theta}_2} - \frac{\partial L}{\partial \theta_2} &= Q_{\theta_2} \end{aligned} \tag{21.9}$$

In Eq. (21.10) the differential equations of motion are found without non-conservative generalized forces in the right-hand side of equation. In the present analysis, the generalized coordinates are the angles θ_1 and θ_2 . When the generalized coordinates are angles, the generalized forces are given by torques acting in these angles. In the non-ideal model (RNIS) the generalized forces Q_{θ_1} and Q_{θ_2} are equal to zero, because the force of the spring is included in the potential energy in the Lagrangian system. The DC motor is externally acting over the angle θ_m and the force from the spring comes according to the potential energy in the spring deflection given by the difference in the angles θ_2 and θ_m . If the torsion spring is not considered in the Lagrangian system and treated as an external force, the same final equation would be found. The differential equation for the angle θ_m is described by Eq. (21.14) determined through torque balance.

$$\begin{aligned} m_1 r^2 \ddot{\theta}_1 + m_2 r^2 \ddot{\theta}_1 + \frac{1}{2} m_2 r l \ddot{\theta}_2 \sin(\theta_2 - \theta_1) + \frac{1}{2} m_2 r l \dot{\theta}_2^2 \cos(\theta_2 - \theta_1) &= 0 \\ \frac{1}{4} m_2 l^2 \ddot{\theta}_2 + \frac{1}{2} m_2 r l \ddot{\theta}_1 \sin(\theta_2 - \theta_1) - \frac{1}{2} m_2 r l \dot{\theta}_1^2 \cos(\theta_2 - \theta_1) + I_2 \ddot{\theta}_2 & \\ + k(\theta_2 - \theta_m) &= 0 \end{aligned} \tag{21.10}$$

The electric equation of the motor in Eq. (21.11) shows the voltage set given by the symbol V . The armature inductance is the term L , and the resistance is given by R_a . The electric current is the i_a , K_E is the electric constant of the motor and $\dot{\theta}_m$ is the angular speed of the motor. The derivative of the current is isolated in the left-hand side of the Eq. (21.12).

$$V = L \frac{di_a}{dt} + R_a i_a + K_E \cdot \dot{\theta}_m \tag{21.11}$$

$$\frac{di_a}{dt} = \frac{V}{L} - \frac{R_a i_a}{L} - \frac{K_E \dot{\theta}_m}{L} \tag{21.12}$$

The mechanical equation of the DC motor is determined by the torques acting over the rotor. The constant of torque is symbolized by the term K_T , the moment of inertia of the rotor by the term I_m , the angular acceleration with the term $\ddot{\theta}_m$ and the term c_m is the viscous friction neglected in the present analysis. The reason for ignoring the viscous friction is the absence of gravitational field. According to Budynas and Nisbett (2014), the Petroff equation determines the viscous friction based on same parameters, including the shaft radial load that in the present problem is equal to zero.

$$I_m \ddot{\theta}_m = -k \cdot (\theta_m - \theta_2) + K_T i_a - c_m \dot{\theta}_m \quad (21.13)$$

$$\ddot{\theta}_m = \frac{-k(\theta_m - \theta_2)}{I_m} + \frac{K_T i_a}{I_m} - \frac{c_m \dot{\theta}_m}{I_m} \quad (21.14)$$

21.2.2 Ideal (IS) Model for the Dynamics of the Simplified Model of the Solar Panel

The results from the ideal case (IS) consider the motor directly connected to the joint where the panel is opened. The Lagrangian equations do not consider the spring as used in the non-ideal model. Then, in Eq. (21.15), the Lagrangian function does not contain the potential energy of the spring.

$$L = \frac{1}{2} m_1 r^2 \dot{\theta}_1^2 + \frac{1}{2} I_1 \dot{\alpha}_1^2 + \frac{1}{2} m_2 r^2 \dot{\theta}_1^2 + \frac{1}{8} m_2 l^2 \dot{\theta}_1^2 + \frac{1}{2} m_2 r l \dot{\theta}_1^2 \dot{\theta}_2^2 \sin(\theta_2 - \theta_1) + \frac{1}{2} I_2 \dot{\theta}_2^2 \quad (21.15)$$

Applying again the derivatives for the coordinates θ_1 and θ_2 we may obtain the set of differential equations where Q_{θ_1} equals zero and Q_{θ_2} is equal to T_G . This term T_G is the torque of coupling between the motor and axis of the solar panel. The torque present is the same because it is not considered a gear ratio. Specifically, in the case, it was considered the same size for gear and pinion. Hence, the same torque and speed for both axes.

The first Lagrangian equation related to the coordinate θ_1 leads to the following differential equation:

$$m_1 r^2 \ddot{\theta}_1 + m_2 r^2 \ddot{\theta}_1 + \frac{1}{2} m_2 r l \ddot{\theta}_2 \sin(\theta_2 - \theta_1) + \frac{1}{2} m_2 r l \dot{\theta}_2^2 \cos(\theta_2 - \theta_1) = 0. \quad (21.16)$$

The second Lagrangian equation leads to Eq. (21.17) where the right-hand side stands for the external nonconservative force. The DC motor is not included in the Lagrangian system, so there is an external force represented by T_G , the torque of the gearing.

$$\frac{1}{4} m_2 l^2 \ddot{\theta}_2 + \frac{1}{2} m_2 r l \ddot{\theta}_1 \sin(\theta_2 - \theta_1) - \frac{1}{2} m_2 r l \dot{\theta}_1^2 \cos(\theta_2 - \theta_1) + I_2 \ddot{\theta}_2 = T_G. \quad (21.17)$$

The torque generated by the DC motor is represented by T_M and it is proportional to the current in the motor armature.

$$T_M = K_T \cdot i_a \quad (21.18)$$

The voltage determines the power provided to the system according to the electric equation of the DC motor. The rotor speed $\dot{\theta}_m$ is equal to the angular speed $\dot{\theta}_2$ of the opening in the solar panel in the model of ideal energy source (IS). Therefore, the symbol $\dot{\theta}_m$ is not present in Eqs. (21.15)–(21.21). For this reason, the term θ_m is replaced by θ_2 in the modeling of the ideal case.

$$V = L \frac{di_a}{dt} + R_a i_a + K_E \cdot \dot{\theta}_2 \quad (21.19)$$

The derivative of the current is given by Eq. (21.20) and may be used in the differential equations.

$$\frac{di_a}{dt} = \frac{V}{L} - \frac{R_a i_a}{L} - \frac{K_E \dot{\theta}_2}{L} \quad (21.20)$$

Through the equilibrium of the torque over the rotor in the DC motor, the equation of the angular acceleration is written:

$$I_m \ddot{\theta}_2 = -T_G + T_m - c_m \dot{\theta}_2 \quad (21.21)$$

21.3 Numerical Results from the Non-ideal (RNIS) and Ideal (IS) of the Simplified Model of the Solar Panel

The results found are time series obtained through the Runge–Kutta method of integration with 4th and 5th order published in Dormand and Prince (1980) and implemented in MatLab with the internal function ode45. The process does not demand a step size to be set. The user must choose the relative and absolute tolerances. In this analysis the relative tolerance set was 10^{-2} and the absolute tolerance 10^{-4} .

21.3.1 Results from the Non-ideal Model (RNIS) of the Simplified Model of the Solar Panel

The numerical simulations were performed with the following conditions. The mass m_1 and m_2 equal to 1 kg, r is the distance to the center of the Earth to the satellite equal to 42,000 km (Soler and Eisemann 1994), length of the solar panel l is equal to 0.5 m. The constant of torque K_T is 250×10^{-3} Nm/A. The electric constant K_E is equal to K_T . The inductance L used was 0.6×10^{-3} Henry and the armature resistance is 1.4 Ω , the moment of inertia of the solar panel I_2 is 10 kgm². The moment of inertia I_m of the rotor present in the DC motor is equal to 0.13 kg m².

The elastic constant k of this torsion spring is 300 N/rad. These parameters for DC motors are coherent with the range of values in the catalog of Maxongroup (2020), where the motor used is a 600 W.

The initial condition for $\dot{\theta}_1$ is 7.2×10^{-5} rad/s, which stands for the angular speed of the satellite around the Earth. Considering the satellite is geostationary, its speed follows the rotation speed of the Earth. The other initial conditions for θ_1 , θ_2 and $\dot{\theta}_2$ are equal to zero.

A sinusoidal signal was applied using the DC motor. The voltage pulse is half a period of a wave. The pulse in Fig. 21.2 is an input signal for the voltage in the DC motor. The period chosen was based on the natural frequency of the parameters present in the equation. The natural frequency ω_0 is approached to the formula in Eq. (21.22):

$$\omega_0 = \sqrt{\frac{k}{I_2 + \frac{1}{4}m_2l^2}} \tag{21.22}$$

In Fig. 21.3 it is plotted the angular speed of the solar panel versus the time in seconds. The symbol ω_2 is the same as $\dot{\theta}_2$, which means an angular speed with unit equal to rad/s. The angle of the solar panel along time is represented in Fig. 21.4. This figure demonstrates a continuous increase even after the pulse. The angle is likely to reach a maximum due to the energy dissipated by resistance of the armature. Figure 21.5 demonstrates the electric current i_a in Amperes versus the time t in seconds. As the pulse of voltage in Fig. 21.2, it is possible to observe a similar pulse for the current in Fig. 21.5. The angle θ_m in Fig. 21.6 and the angular speed ω_m in Fig. 21.7 demonstrate the vibration in the motor coherent with the vibration in the solar panel. It is possible to observe some oscillation of ω_2 in Fig. 21.3 but maintaining a positive speed. The vibrations in Fig. 21.7 alternates positive and

Fig. 21.2 Voltage pulse from de DC motor. V (Volts) versus $t(s)$

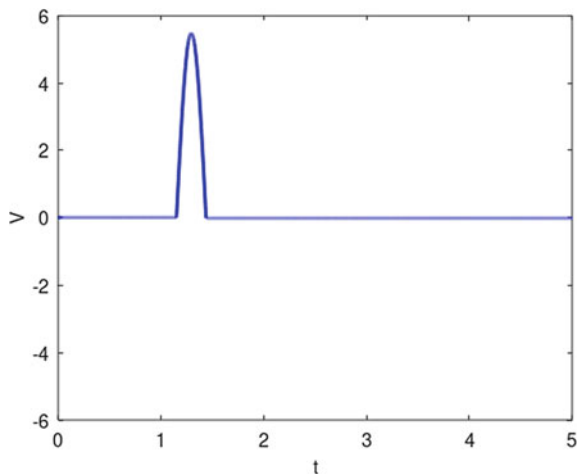


Fig. 21.3 Angular speed ω_2 versus time $t(s)$

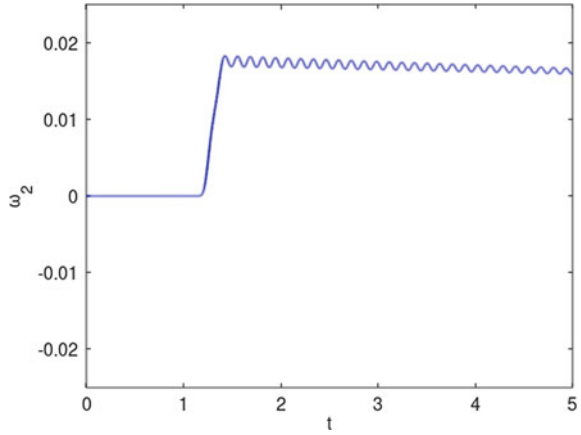


Fig. 21.4 Angle θ_2 versus time $t(s)$

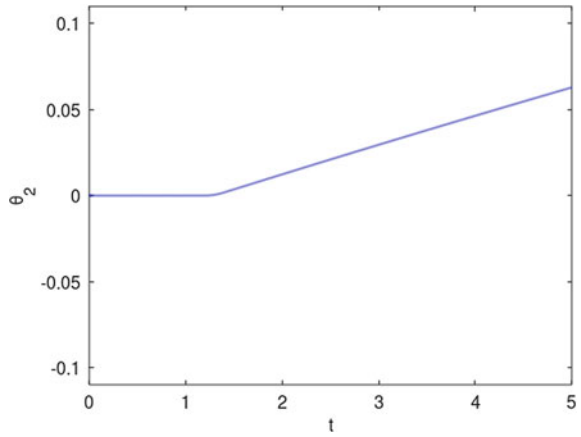


Fig. 21.5 The response in electric current in the armature i_a (A) versus time $t(s)$

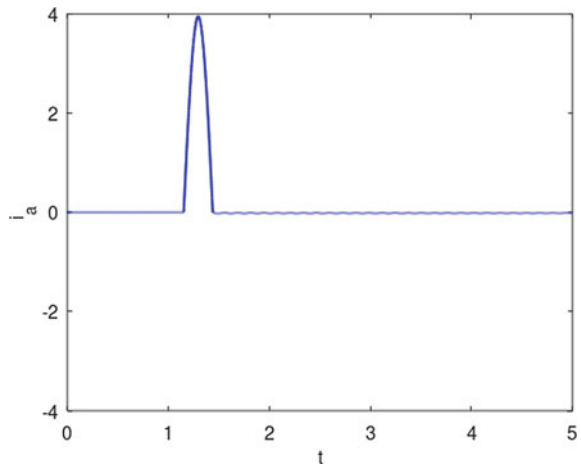


Fig. 21.6 Angle θ_m of the rotor of the DC motor versus time $t(s)$

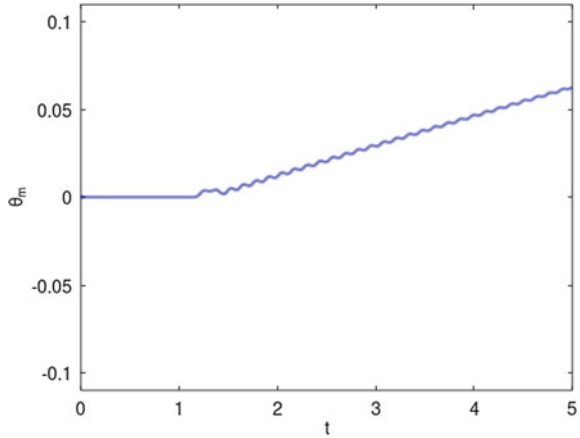
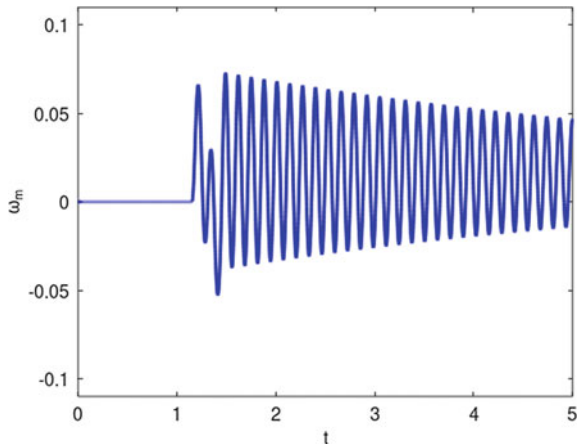


Fig. 21.7 Angular speed ω_m of the rotor of the DC motor



negative velocities for the DC motor. This behavior may be justified since the rotor in the motor has a much smaller moment of inertia when compared with the solar panel.

21.3.2 Results from the Ideal (IS) Model of the Simplified Solar Panel

The same input was set for the voltage using the ideal model (IS). The ideal model, as previously mentioned, consists of the motor spinning at the same velocity as the solar panel, due to the fact they are directed linked. Therefore, there are no more the graphics for the motor. The results of the kinematics of the motor are the same of

the solar panel. The input signal of voltage was the same that in Fig. 21.2 and the current i_A was graphically identical to that in Fig. 21.5.

A pulse in the speed is present in Fig. 21.8, where is possible to see an oscillation with a negative zone for the angular speed caused by the inductance opposing to the rise on the electric current. In Fig. 21.9, the angle increases and diminishes immediately, but the angular position goes on increasing after the pulse because of the inertia maintaining the velocity. Continue oscillations in Figs. 21.8 and 21.9 are present after the pulse because of the armature inductance.

Fig. 21.8 Angular speed of the solar panel ω_2 versus time $t(s)$

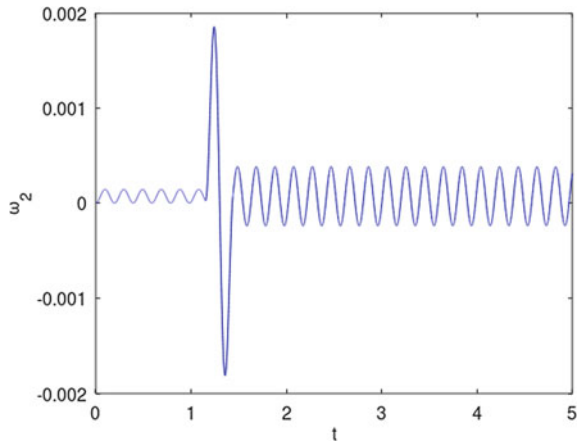


Fig. 21.9 Angle of the solar panel θ_2 versus time $t(s)$

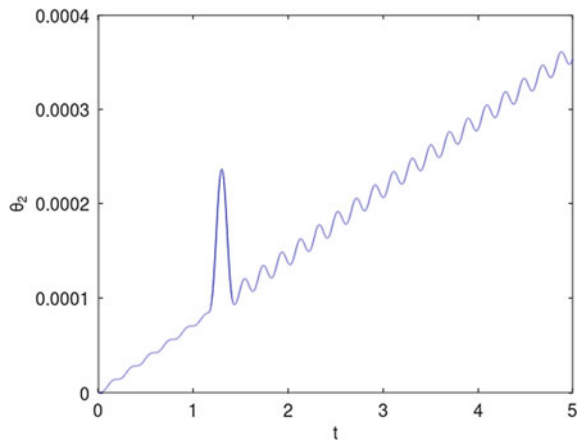
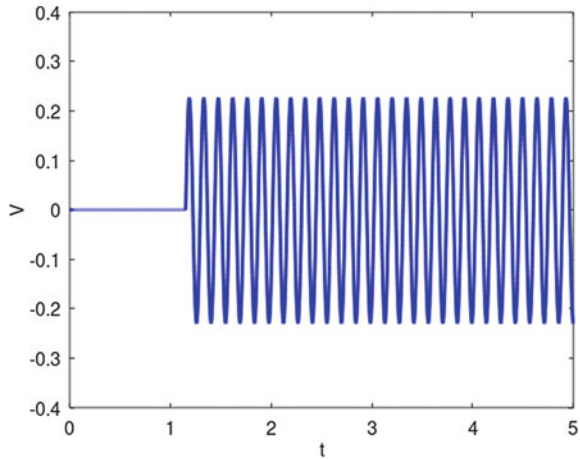


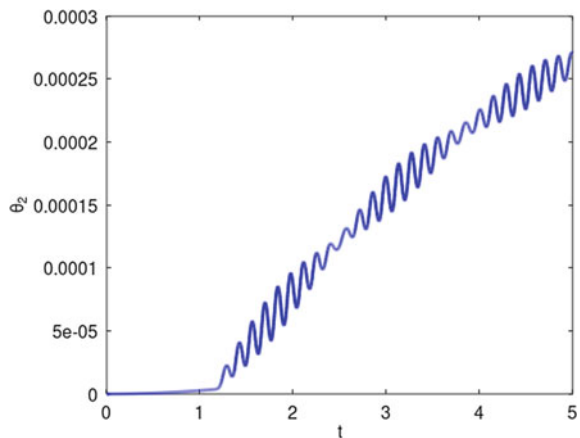
Fig. 21.10 Voltage versus time $t(s)$



21.3.3 *Non-ideal (RNIS) with Constant Sinusoidal Voltage from the Motor*

A non-ideal interaction (RNIS) physically like case treated in Sect. 3.1 is analyzed again but now with a sinusoidal input for the voltage set. The model and the initial conditions are the same used in Sect. 3.1. The unique difference is the voltage amplitude used equal to 0.23 V, which is represented in Fig. 21.10. The frequency of the tension applied is 8 times greater than the natural frequency ω_0 in Eq. (21.22). Figure 21.11 shows the increase of the angle θ_2 with the characteristic of beats in waves. Beats are caused by interference of waves. They are characterized by an *envelope* of the maxima and minima of a wave whose frequency is half the difference between the frequencies of the two original waves (Crawford Jr. 1968). Using

Fig. 21.11 Angle θ_2 of the solar panel versus time $t(s)$



trigonometry, it is possible to write in Eq. (21.23) the result of sum of two waves with the same amplitude and different frequencies f_1 and f_2 . The frequency of the envelope is equal to $(f_1 - f_2)/2$ and the wave inside the envelope has the frequency $(f_1 + f_2)/2$.

$$\cos(2\pi f_1 t) + \cos(2\pi f_2 t) = 2 \cos\left(2\pi \frac{f_1 + f_2}{2} t\right) \cdot \cos\left(2\pi \frac{f_1 - f_2}{2} t\right). \quad (21.23)$$

These beats are also observed in Fig. 21.12 where is plotted the angular speed ω_2 . In Fig. 21.13 the angle θ_m clearly demonstrates its beats as much as in Fig. 21.14 with the angular speed ω_m .

Fig. 21.12 Angular speed ω_2 versus time $t(s)$

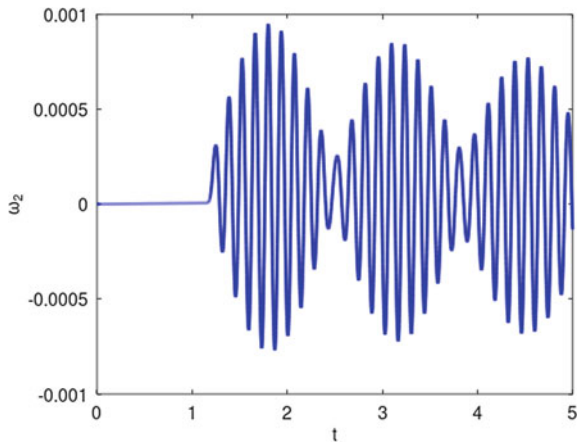


Fig. 21.13 Angular position of the rotor of the DC motor θ_m versus $t(s)$

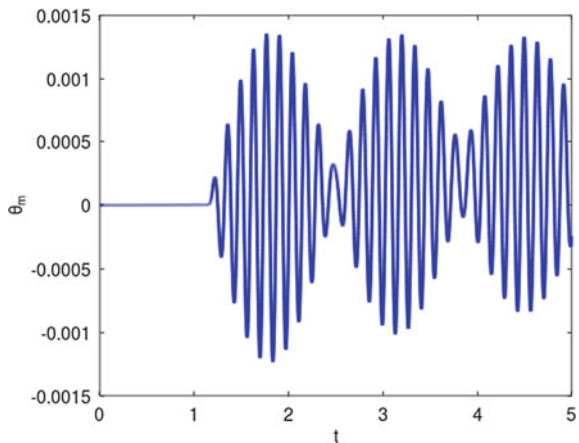
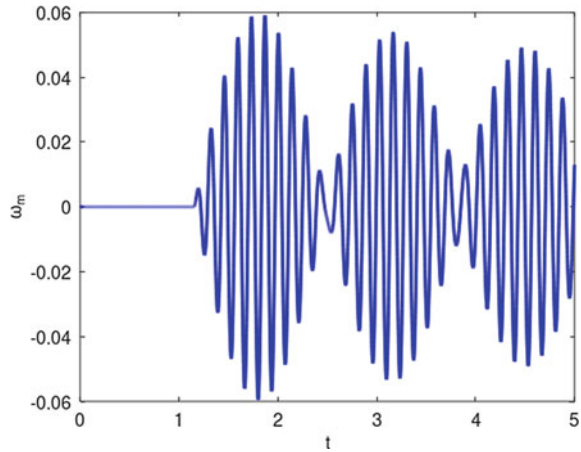


Fig. 21.14 Angular speed ω_m of the DC motor versus time $t(s)$



21.4 Conclusions

The present analysis was focused on the dynamics of the deployment of a solar panel during the trajectory of a satellite around the Earth, analyzing the dynamics between energy sources and structural response. Differences between both (IS) and (RNIS) were observed. In the Sect. 3.1, the (RNIS) case demonstrated a sequence of oscillations in the motor and solar panel linked by a spring. These oscillations were damped because of the internal resistance of the DC motor. In the Sect. 3.2, the ideal model (IS) showed results where the kinematics of the engine is the same as that of the solar panel, as shown in the graphs of the results for the IS case in Figs. 21.8 and 21.9. The angular position of motor and solar panel continues to move even after the electric pulse has ceased. In the Sect. 3.3, the (RNIS) case with sinusoidal voltage gives rise to beats in oscillations, like those we find when overlapping waves with near frequencies. There is an envelope of waves in Fig. 21.11 with an increase in the angle θ_2 . The angular speed ω_2 in Fig. 21.12 also presents these characteristics with envelope. In Figs. 21.13 and 21.14 the angle θ_m and speed ω_m have a high similarity with ω_2 in Fig. 21.12, indicating the same frequencies with differences in amplitudes. For future works, it is suggested to consider a flexible panel and analyze its deformation. Furthermore, it would be interesting to insert some dampers and springs in the coupling of the solar panel and the DC motor.

Acknowledgements The third and fourth authors are grateful for the financial support by the Brazilian Council for Scientific and Technological Development, CNPq, grants [306525/2015-1](#) and [307371/2017-4](#), respectively.

References

- Avanço, R.H., Tusset, A.M., Balthazar, J.M., et al.: On nonlinear dynamics behavior of an electro-mechanical pendulum excited by a non-ideal motor and a chaos control taking into account parametric errors. *J. Braz. Soc. Mech. Sci. Eng.* **40**, 23 (2018). <https://doi.org/10.1007/s40430-017-0955-x>
- Balthazar, J.M., Brasil, R.M.I.R.F., Weber, H.I., Fenili, A., Belato, D., Felix, J.L.P.: An overview on non-ideal vibrations. *Meccanica* **38**, 613–621 (2003)
- Balthazar, J.M., Tusset, A.M., Brasil, R.M.L.R.F., et al.: An overview on the appearance of the Sommerfeld effect and saturation phenomenon in non-ideal vibrating systems (NIS) in macro and MEMS scales. *Nonlinear Dyn.* **93**, 19–40 (2018)
- Budynas, R.G., Nisbett, K.: *Shigley's Mechanical Engineering Design*. McGraw-Hill (2014). ISBN-10:9780073398204
- Crawford Jr., F.S.: *Waves (Berkeley Physics Course, vol. 3)* McGraw-Hill (1968). ISBN 10:0070048606
- Cveticanin, L., Zukovic, M., Balthazar, J.M.: *Dynamics of Mechanical Systems with Non-Ideal Excitation*. Springer International Publishing (2018). ISBN: 978-3-319-54168-6
- Dormand, J., Prince, P.: A family of embedded Runge-Kutta formulae. *J. Comput. Appl. Math.* **6**, 19–26 (1980)
- Fenili, A.: *Modelagem Matemática e Análise dos Comportamentos Ideal e Não Ideal de Estruturas Flexíveis de Rastreamento*. Phd Thesis, UNICAMP, Campinas, SP (2000)
- Kononenko, V.O.: *Vibrating system with a limited power-supply*. Piiffe, London (1969)
- Krasnopol'skaya, T.S., Shvets, A.Y.: Chaotic interactions in a pendulum-energy-source system. *Prikl. Mekh.* **26**(5), 90–96 (1990)
- Krasnopol'skaya, T.S., Shvets, A.Y.: Chaotic oscillations of a spherical pendulum as an example of interaction with energy source. *Int. Appl. Mech.* **28**, 669–674 (1992)
- Maxongroup Ec 90 flat (2020). https://www.maxongroup.com/medias/sys_master/root/8841186181150/EN-302.pdf
- Omid, E., Mahmoodi, S.N.: Nonlinear vibration suppression of flexible structures using nonlinear modified positive position feedback approach. *Nonlinear Dyn.* **79**, 835–849 (2015). <https://doi.org/10.1007/s11071-014-1706-5>
- Porro, J.R.S.; Fenili A.; Balthazar, J.M.: *Modelagem Matemática de um Satélite Considerando a Abertura de um Painel Solar: Abordagem Ideal e Não-Ideal*. In: CONEM 2004—III Congresso Nacional de Engenharia Mecânica, Belém, PA, Brazil. In: *Proceedings of the CONEM 2004—III Congresso Nacional de Engenharia Mecânica (in portuguese)* (2004)
- Soler, T., Eisemann, D.W.: Determination of look angles to geostationary communication satellites. *J. Surveying Eng.* **120**(3), 123 (1994). [https://doi.org/10.1061/\(ASCE\)0733-9453\(1994\)120:3\(115\).ISSN0733-9453](https://doi.org/10.1061/(ASCE)0733-9453(1994)120:3(115).ISSN0733-9453)

Chapter 22

The Optimal in Terms of Fuel Consumption Approach to Reorientation of a Spacecraft Based on the Nonlinear Boundary Value Problem Solution



Valerii B. Uspenskiy, Natalia V. Shyriaieva, and Mariia V. Nekrasova

Abstract In this paper, there has been considered the nonlinear boundary problem connected with the reorientation of a rigid body along the trajectory of inertial rotation. The problem solution is offered to search in the form of decomposition in the power series. In this case to determine the problem solution, there was developed a special circulation procedure of the series and was investigated the conditions of convergence. As a result, the obtained solution can be used to calculate the initial conditions of the inertial maneuver in the onboard control system of the spacecraft. Thus, the predicted control approach would minimize fuel costs for the implementation of angular maneuvers.

Keywords Attitude control system (ACS) · Satellite · Boundary problem · Reorientation accuracy · Series inversion

22.1 Introduction

Nowadays, the most of the modern spacecrafts (SC) are characterized by a long-life span. This quality is ensured by the increased service life of all spacecraft systems. The one of the most important SC systems is the attitude control system (ACS). Despite the undoubted successes of the practical astronautics, there is still paid a considerable attention to improving the efficiency of the ACS functioning. Currently, there can be distinguished the following areas of increasing the ACS efficiency (He et al. 2020):

V. B. Uspenskiy (✉) · N. V. Shyriaieva · M. V. Nekrasova
National Technical University “Kharkiv Polytechnic Institute”, Kharkiv 61002, Ukraine
e-mail: uspensky61@gmail.com

N. V. Shyriaieva
e-mail: natalia.shyriaieva@gmail.com

M. V. Nekrasova
e-mail: masha12dec@gmail.com

- hardware improvement of the ACS, in particular, increasing the accuracy of information sensors and actuators;
- improvement of the ACS methodical and software support regarding the determination of the attitude from the measurements of the angular velocity sensors and control.

The second case has been characterized by the development of the new ways of responding effectively to the determination and control of the attitude and the implementation of these ways in the software and mathematical support of the ACS. This paper focuses on the development of the one of these methods. There were described the classical structure of the ACS, as well as problems and the modern level of solving various tasks of the SC control (Bong 2016).

The typical composition of the onboard attitude control system forms a closed loop along with information links in it (Fig. 22.1). The figure schematically shows a spacecraft, on a board of which the next blocks are located:

- the unit of gyroscopic angular velocity sensors that measure the vector of the absolute angular velocity of the spacecraft rotation $\bar{\omega}$ in projections onto the axes connected with the spacecraft. The measurement vector $\hat{\omega}$ includes the true value of the absolute angular velocity of the spacecraft rotation $\bar{\omega}$, but also contains sensor errors and a noise;

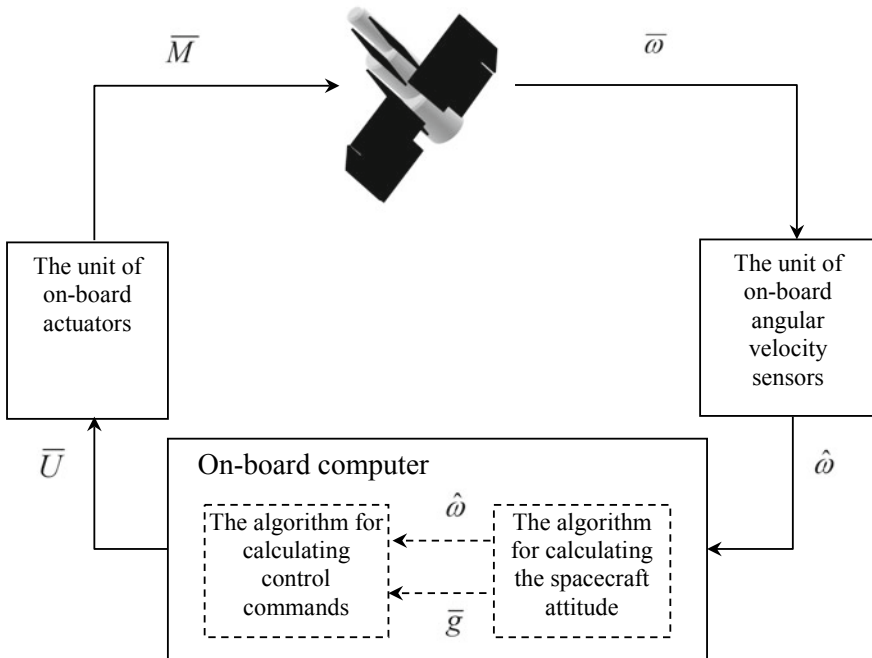


Fig. 22.1 Composition of the onboard attitude control system and information links in it

- the onboard computer in conjunction with other programs, implements the algorithm for calculating the vector of spacecraft attitude parameters \bar{g} based upon measurements $\hat{\omega}$ and the algorithm for calculating control commands \bar{U} , taking into account the current values of the actual angular velocity and attitude;
- the unit of actuators includes reaction jets, reaction wheels and control moment gyros. In the paper, there is assumed that the unit consists of low-thrust gas-jet engines, that are switched on or off by a command \bar{U} . The jet engines create a control torque \bar{M} that affects the spacecraft structure and has nonzero projections onto the three axes connected with the spacecraft. The actual angular velocity of the spacecraft rotation $\bar{\omega}$ changes under the influence of the latter.

Generally, the main purpose of the ACS is to maintain the given attitude of the spacecraft in space and to implement the reorientation of it at significant angles for the given time. At the present time, the listed problems are being solved on the basis of different theories. In particular:

- in order to solve the problem of bringing the SC into the given angular position and hold it in this position for an indefinitely long time, there have been proposed the various control laws based on the stability theory (MacKunis et al. 2016), the analytical design of the optimal controller (Gadelha de Souza and De Souza Alain 2014), as well as on artificial intelligence technologies where the systems based on fuzzy logic (Glumov et al. 2004; Salah and Bayoumi Gamal 2015; Kosari et al. 2017), and neural networks (Leeghim et al. 2009; Montenegro and Lenin 2011; MacKunis et al. 2016).
- in order to solve the problems of the SC reorientation to the significant angles in the finite (given or not given) time with an arbitrarily finite angular velocity, there has been used the concept of inverse dynamic problems (Uspenskiy 2006; Boyarko et al. 2011) and the methods of optimal control theory (Levskii 2016, 2020; Park 2018).

In terms of the achieved quality indicators, the algorithms based on the optimal solution of the reorientation problem are the most effective. Some of them are as follows:

- the algorithms optimally based on the criterion of the reorientation maneuver duration (Boyarko et al. 2011; Phogat et al. 2017; Levskii 2020);
- the algorithms optimally based on the quadratic criterion of energy consumption for the power supply of reaction wheels and control moment gyros (Zhang et al. 2011);
- the algorithms optimally based on the terms of fuel consumption or the criteria close to it (Levskii 2019).

Apparently, that the ability of the SC to perform its functions depends on the performance of the ACS. Hence, it follows that saving resources (fuel, working body) is the most important task in designing the SC control system.

The well-known solutions to the problem of the SC optimal reorientation according to the minimum fuel consumption and near-term criteria are related to

the particular cases of the SC symmetry (Levskii 2019) or particular reorientation conditions. As opposed to such solutions, there has been considered the problem of optimal reorientation for the SC with arbitrary moments of inertia and without restrictions on the angles.

It is obvious that if the planned duration of the maneuver is sufficiently long, the optimal strategy for the fuel consumption optimization will turn the SC by inertia. Therefore, the SC is accelerated to the certain angular velocity and the rotation by inertia is performed. After turning to the specified angle, the spacecraft brakes to zero velocity. Under these conditions, in order to implement this strategy, it is necessary to determine the required initial angular velocity for the planned section of inertial rotation with the aim of its further implementation using the ACS. The main requirement for the velocity is to provide the given spacecraft reorientation in space for the given time by inertial rotation. Mathematically, this is a two-point boundary value problem.

Taking into account the insignificance of dynamic influences from the external environment and low-thrust engines, the design of the spacecraft is taken as an absolutely rigid body. In this case, the solution of the indicated boundary value problem is trivial only in special cases: for a spherically symmetric rigid body or under strictly defined boundary conditions. For the real spacecraft, the general case of mass distribution is distinctive. Under these conditions, the solution of the boundary value problem presents a problem that is associated with the significant nonlinearity of differential equations and the need to obtain a high-precision solution. The expected solution of the mentioned problem in the form of formula expressions can be used in the future in the algorithm for calculating control commands in the onboard computer of the spacecraft and provide the formation of commands to turn on or off low-thrust engines, bearing in mind the actual value of the angular velocity of the spacecraft.

Thus, there has been obtained the new solution to the problem of optimal fuel consumption reorientation for the SC with arbitrary moments of inertia and without restrictions on the angles. The obtained solution is based on solving the nonlinear boundary value problem using the adapted power series method. It is shown that the further increasing of the algorithm order leads to the improvement of the decision accuracy.

22.2 Formulation of the Problem

In the considered optimal control strategy, the free rotation area is the main area on which the spacecraft is reoriented. Therefore, we determine the initial spacecraft angular velocity for this area, which will provide the required reorientation of the spacecraft in a given time.

To this end, let us consider the dynamic and kinematic equations of a rigid body free rotation (Lur'e 1961; Frolov and Shipulina 1985):

$$I_i \dot{\omega}_i - (I_j - I_k) \omega_j \omega_k = 0, \quad i, j, k = 1, 2, 3, \quad (22.1)$$

$$\dot{\bar{g}} = \left(1 - \frac{g^2}{16}\right) \cdot \bar{\omega} + \frac{1}{2}[\bar{g} \times \bar{\omega}] + \frac{1}{8}\bar{g}(\bar{g}, \bar{\omega}), \tag{22.2}$$

where $\omega_i, \omega_j, \omega_k$ are the projections of the angular velocity vector $\bar{\omega}$ on the axes associated with the spacecraft (these axes are further considered as the main axes of inertia); I_i, I_j, I_k are the main moments of inertia; $g^2 = \sum_{i=1}^3 g_i^2 = (\bar{g}, \bar{g})$; (\circ, \circ) is the vector dot product notation; $[\circ \times \circ]$ is the cross-product of vectors notation.; \bar{g} is the vector of the modified final rotation associated with the well-known vector of four normalized Rodrigue–Hamilton’s parameters, traditionally denoted as λ_0 and $\lambda_i, i = \overline{1, 3}$, by the relations (Frolov and Shipulina 1985)

$$g_i = \frac{4\lambda_i}{1 + \lambda_0}, \quad i = \overline{1, 3}. \tag{22.3}$$

The kinematic Eq. (22.2) for the vector of parameters \bar{g} was obtained by time differentiation of the ratios (22.3). There were used the known differential equations for Rodrigue–Hamilton parameters. Subsequently, the parameters were excluded from the final expressions.

Thereby, the problem of inertial maneuver is formulated in the following manner: It is required to find the initial value of the angular velocity $\bar{\omega}_0$, that will ensure the transfer of the vector \bar{g} from a known point \bar{g}_0 to a given point \bar{g}_T in time T taking into account (22.1), (22.2).

Without diminishing of generality, we shall consider that $\bar{g}_0 = 0$. This can be always done by virtually changing the position of the coordinate system against which the spacecraft orientation is measured. For this purpose, it is sufficient to take the components of the so-called mismatch quaternion $\Lambda^M(0) = [1; 0; 0; 0]$, $\Lambda^M(T) = \tilde{\Lambda}(0) \circ \Lambda(T)$ with parameters $\lambda_j, j = \overline{0, 3}$ in formulas (22.3) at time $t = 0$ and $t = T$. Here $\Lambda(0), \Lambda(T)$ are the known values of the proper quaternion characterizing the orientation of the spacecraft against to an arbitrarily given basis at time $t = 0$ and $t = T$; $\tilde{\Lambda}$ is the conjugate quaternion; \circ is the sign of the quaternion product (Branec and Shmyglevskij 1973).

The problem of inertial maneuver is a nonlinear two-point boundary value problem. What is more, there are still unknown the general methods for solving it. Therefore, in this paper the method for solving differential equations using power series was adapted.

The solution of Eqs. (22.1), (22.2) was searching in the form of Taylor series near the point $(t = 0, \bar{\omega}_0, \bar{g}_0 = 0)$ on the limited interval of variation $t \in [0, T]$:

$$\bar{\omega}(t) = \bar{\omega}_0 + \dot{\bar{\omega}}_0 \cdot t + \frac{1}{2}\ddot{\bar{\omega}}_0 \cdot t^2 + \frac{1}{6}\dddot{\bar{\omega}}_0 \cdot t^3 + \dots, \tag{22.4}$$

$$\bar{g}(t) = \bar{g}_0 + \dot{\bar{g}}_0 \cdot t + \frac{1}{2}\ddot{\bar{g}}_0 \cdot t^2 + \frac{1}{6}\dddot{\bar{g}}_0 \cdot t^3 + \frac{1}{24}\bar{g}_0^{IV} \cdot t^4 \dots \tag{22.5}$$

Considering (22.2), the consecutive calculation of derivatives $\bar{g}_0^{(m)}$, where $m = 1, 2, 3, \dots$ is an order of derivative, at time $t = 0$, allows to bind the vector $\bar{g}_0^{(m)}$ and vectors $\bar{\omega}_0^{(m-1)}, \bar{\omega}_0^{(m-2)}, \dots, \dot{\bar{\omega}}_0, \bar{\omega}_0$. Following the mentioned process of calculation, the next formula is written:

$$\bar{g}_0^{(m)} = f(\bar{\omega}_0^{(m-1)}, \bar{\omega}_0^{(m-2)}, \dots, \dot{\bar{\omega}}_0, \bar{\omega}_0) \tag{22.6}$$

In its turn, using (22.1), the following derivatives are similarly rewritten:

$$\begin{aligned} \dot{\omega}_{0i} &= \alpha_i \cdot \omega_{0j} \cdot \omega_{0k}, \\ \ddot{\omega}_{0i} &= \alpha_i \alpha_j \cdot \omega_{0j} \cdot \omega_{0k}^2 + \alpha_i \alpha_k \cdot \omega_{0i} \cdot \omega_{0j}^2, \\ \dddot{\omega}_{0i} &= \alpha_i^2 \alpha_j \cdot \omega_{0i} \cdot \omega_{0k}^3 + 4\alpha_i \alpha_j \alpha_k \cdot \omega_{0i}^2 \cdot \omega_{0j} \cdot \omega_{0k} + \alpha_i^2 \alpha_k \cdot \omega_{0j}^3 \cdot \omega_{0k}, \dots \end{aligned} \tag{22.7}$$

where $\alpha_i = \frac{(i_j - i_k)}{i}$, $(i, j, k) = (1, 2, 3)$.

Hence, it follows that the initial value of the i th component of the $(m - 1)$ order derivative of the angular velocity vector can be written as

$$\omega_{0i}^{(m-1)} = \varphi_{im}(\omega_{0i}^{S_i} \cdot \omega_{0j}^{S_j} \cdot \omega_{0k}^{S_k}),$$

where the power indexes S_i, S_j, S_k are non-negative integers and $S_i + S_j + S_k = m$; φ_{im} is linear function of its arguments for different set of powers S_i, S_j, S_k .

Substituting (22.7) into (22.6), and then the result into (22.5), the final expressions are calculated. The new expressions associate the values of vector \bar{g} at time T with the initial angular velocity $\bar{\omega}_0$:

$$\begin{aligned} g_i(T) &= \Theta_i + \frac{1}{2} \alpha_i \Theta_j \Theta_k + \frac{1}{6} \left\{ \left(\alpha_i \alpha_j - \frac{\alpha_j}{2} + \frac{1}{8} \right) \cdot \Theta_i \Theta_k^2 \right. \\ &\quad \left. + \left(\alpha_i \alpha_k + \frac{\alpha_k}{2} + \frac{1}{8} \right) \cdot \Theta_i \Theta_j^2 + \frac{\Theta_i^3}{8} \right\} \\ &\quad + \frac{1}{24} \left\{ \alpha_i \left(\alpha_i \alpha_j - \alpha_j + \frac{1}{4} \right) \cdot \Theta_j \Theta_k^3 + \alpha_i \left(\alpha_i \alpha_k + \alpha_k + \frac{1}{4} \right) \cdot \Theta_k \Theta_j^3 \right. \\ &\quad \left. + \left(4\alpha_i \alpha_j \alpha_k + \frac{3}{4} \alpha_i + \frac{1}{2} (\alpha_j + \alpha_k) \right) \cdot \Theta_i^2 \Theta_j \Theta_k \right\} + \dots, \quad i, j, k = 1, 2, 3 \end{aligned} \tag{22.8}$$

where $\bar{\Theta} = \{\Theta_1, \Theta_2, \Theta_3\}$ is unknown vector associated with the vector of the required angular velocity by the relation $\bar{\Theta} = \bar{\omega}_0 \cdot T$.

Thus, the problem of inertial maneuver was reduced to finding a vector $\bar{\Theta}$ for a given $\bar{g}(T) = \bar{g}_T$. The components of $\bar{\Theta}$ are the elements of an infinite series (22.8).

The final solution of the problem is to “convert” the series (22.8) relatively to $\bar{\Theta}$.

To realize this conversion, the vector $\bar{\Theta} = \{\Theta_1, \Theta_2, \Theta_3\}$ is searched then in the form:

$$\Theta_i = \sum_{m=1}^{\infty} h_{im}(g_{Ti}^{S_{im}} \cdot g_{Tj}^{S_{jm}} \cdot g_{Tk}^{S_{km}}), \quad i, j, k = 1, 2, 3, \tag{22.9}$$

where g_{Ti}, g_{Tj}, g_{Tk} are the components of the vector \bar{g}_T ; $h_{im}(\cdot)$ is the unknown linear form of \bar{g}_T arguments; S_{im}, S_{jm}, S_{km} are arbitrary non-negative integers such that $S_{im} + S_{jm} + S_{km} = m$.

It should be noticed that the sum (22.9) is an infinite power series, similar to the series (22.8) by the structure.

To find the linear forms h_{im} , the circulation procedure of the series (22.8) is applied. It consists of a recurring calculation of partial sums.

$$\Theta_{i[q]} = \sum_{m=1}^q h_{im}(g_{Ti}^{S_{im}} \cdot g_{Tj}^{S_{jm}} \cdot g_{Tk}^{S_{km}}) \tag{22.10}$$

at $q \rightarrow \infty$.

Assuming q as a number of ‘‘approximation’’ or iteration ($q = 2, 3, \dots$), the working formula for the recurrent procedure is obtained from (22.8) by trivially separating the first term on the right-hand side in the form

$$\begin{aligned} \Theta_{i[q]} = & g_v - \frac{1}{2}\alpha_i\Theta_{j[q-1]}\Theta_{k[q-1]} \\ & - \frac{1}{6}\left\{\left(\alpha_i\alpha_j - \frac{\alpha_j}{2} + \frac{1}{8}\right) \cdot \Theta_{i[q-1]}\Theta_{k[q-1]}^2 \right. \\ & \left. + \left(\alpha_i\alpha_k + \frac{\alpha_k}{2} + \frac{1}{8}\right) \cdot \Theta_{i[q-1]}\Theta_{j[q-1]}^2 + \frac{\Theta_{i[q-1]}^3}{8}\right\} \\ & - \frac{1}{24}\left\{\left(\alpha_i^2\alpha_k + \alpha_i\alpha_k + \frac{\alpha_i}{4}\right) \cdot \Theta_{j[q-1]}^3\Theta_{k[q-1]} \right. \\ & \left. + \left(\alpha_i^2\alpha_j - \alpha_i\alpha_j + \frac{\alpha_i}{4}\right) \cdot \Theta_{j[q-1]}\Theta_{k[q-1]}^3 \right. \\ & \left. + \left(4\alpha_i\alpha_j\alpha_k + \frac{3}{4}\alpha_i + \frac{1}{2}\alpha_j + \frac{1}{2}\alpha_k\right) \cdot \Theta_{i[q-1]}^2\Theta_{j[q-1]}\Theta_{k[q-1]}\right\} - \dots, \tag{22.11} \end{aligned}$$

$i, j, k = 1, 2, 3$

Next, consider a few steps of the iteration procedure realization.

Assume that the initial value of q is 1. Then, taking into account the first term in formula (22.11) and in accordance with (22.10), the following expression can be taken

$$\Theta_{i[1]} = g_{Ti}. \tag{22.12}$$

If $q = 2$, then it follows from (22.11)

$$\Theta_{i[2]} = g_{Ti} - \frac{\alpha_i}{2} g_{Tj} \cdot g_{Tk} \text{ for } i, j, k = 1, 2, 3; \quad (22.13)$$

if $q = 3$, then

$$\begin{aligned} \Theta_{i[3]} = & g_{Ti} - \frac{\alpha_i}{2} g_{Tj} \cdot g_{Tk} + \frac{1}{12} \left(\alpha_i \alpha_k - \alpha_k - \frac{1}{4} \right) \cdot g_{Ti} \cdot g_{Tj}^2 \\ & + \frac{1}{12} \left(\alpha_i \alpha_j + \alpha_j - \frac{1}{4} \right) \cdot g_{Ti} \cdot g_{Tk}^2 - \frac{1}{48} g_{Ti}^3, \end{aligned} \quad (22.14)$$

if $q = 4$, then

$$\begin{aligned} \Theta_{i[4]} = & g_{Ti} - \frac{\alpha_i}{2} g_{Tj} \cdot g_{Tk} + \frac{1}{12} \left(\alpha_i \alpha_k - \alpha_k - \frac{1}{4} \right) \cdot g_{Ti} \cdot g_{Tj}^2 \\ & + \frac{1}{12} \left(\alpha_i \alpha_j + \alpha_j - \frac{1}{4} \right) \cdot g_{Ti} \cdot g_{Tk}^2 - \frac{1}{48} g_{Ti}^3 \\ & + \frac{1}{24} \left(\frac{\alpha_i}{2} - \alpha_i^2 \right) \cdot g_{Tj}^3 \cdot g_{Tk} + \frac{1}{24} \left(\frac{\alpha_i}{2} + \alpha_i^2 \right) \cdot g_{Tj} \cdot g_{Tk}^3 \\ & + \frac{1}{24} \left(\alpha_i (\alpha_j - \alpha_k) - \alpha_i \alpha_j \alpha_k + \frac{\alpha_i}{2} \right) \cdot g_{Ti}^2 \cdot g_{Tj} \cdot g_{Tk}, \end{aligned} \quad (22.15)$$

and so on.

Thus, the sequence being formed for $q = 4$ is the most accurate of the above algorithm for calculation of the vector $\bar{\Theta}$ by the final value of the modified rotation vector \bar{g}_T . Adequacy of such solution is determined by the condition of the circulation vector convergence: $\lim_{q \rightarrow \infty} \|\bar{\Theta}_{[q+1]} - \bar{\Theta}_{[q]}\| = 0$. In this case, it is only possible to specify the area of the state space $Q = \{\bar{g}_T \in R^3 \mid |g_i| < 1, i = 1, 2, 3\}$. It is defined that the sufficient convergence condition is the belonging of the vector \bar{g}_T to the set Q .

The series (22.10) can be majorant by a constant sign power series, in which, $g_{\max} = \max_{i=1,3} |g_{Ti}|$, $|\Theta_{i[q]}| \leq \tilde{\Theta}_{i[q]} = \sum_{m=1}^q g_{\max}^m$. Based on the d'Alembert criterion, the limit relation $\lim_{q \rightarrow \infty} \frac{|\tilde{\Theta}_{i[q+1]} - \tilde{\Theta}_{i[q]}|}{|\tilde{\Theta}_{i[q]} - \tilde{\Theta}_{i[q-1]}|} = g_{\max} < 1$ implies the convergence of the series under consideration in the domain Q . For this reason, the series (22.10) also converges under these conditions, and absolutely. It should be noted that the set covers quite wide range of targets, up to the value of turning in 56° . The modeling shows that the analytical estimate of the convergence region is underestimated.

At the same time, the calculation of $\bar{\omega}_0 = \frac{\bar{\Theta}}{T}$ completes the solution of the inertial maneuver problem. Thus, according to the general scheme of solving the problem, the vector $\bar{\Theta}$, and consequently, the vector $\bar{\omega}_0$ are calculated with the different accuracy corresponding to the chosen value of q . Thereafter, a certain partial sum of the series (22.10) will correspond to this q . In these conditions, it is obvious that (22.10) is an algorithm of the inertial maneuver, and q is its order.

For modeling and practical use, we can recommend a fourth-order algorithm (22.15). It can also be used as a lower order algorithm. For this, it is sufficient to take into account the terms containing $g_{Ti}^{S_i} \cdot g_{Tj}^{S_j} \cdot g_{Tk}^{S_k}$ at $S_i + S_j + S_k \leq 3$.

To increase the solution accuracy of the boundary value problem when the condition of absolute convergence of the series (22.10) is violated, for example, at reorientation angles greater than 56° , one can increase more and more the order of expansion in the series (22.8) and, accordingly, increase the value of q in the series (22.10).

However, in practice, when using the algorithm in the attitude control system, taking into account the current values of time, velocity, and orientation, it is advisable to provide the periodic recalculation of the required velocity of the inertial section. It is desirable to carry out additional corrections during the maneuver, in consideration of the new value of the required velocity. In this case, the requirements to the accuracy of determining the required velocity are significantly reduced and the scope of the algorithm application, even of a low order, expands.

22.3 Results of Modeling

To investigate the convergence of the formula for calculating the required angular velocity, as well as to obtain the accuracy indicators of the algorithms, there was carried out a numerical simulation of the spacecraft reorientation process in the section of inertial rotation. In order to achieve this result, a rigid body with moments of inertia, $I_1 = 3300 \text{ kg m}^2$, $I_2 = 3000 \text{ kg m}^2$, $I_3 = 1200 \text{ kg m}^2$ was considered. Then Eqs. (22.1) and (22.2) were numerically integrated, and the following initial conditions were taken: $t = 0$, $\bar{g}(0) = 0$, $\bar{\omega}(0) = \omega_0$, where $\bar{\omega}_0 = \frac{\Theta_{|q|}}{T}$ is the required value of the initial angular velocity for the area of free rotation; $q = 1, 2, 3, 4$ is an order of the algorithm for calculating the required velocity. The simulation was carried out over time T for different set points $\bar{g}(T) = \bar{g}_T$. To analyze the influence of the algorithm order on the reorientation accuracy, the solution was constructed for various values of the parameter q . The Euler angle value $\theta(T)$ was taken as a criterion for the reorientation accuracy. The angle value corresponds to the deviation of the spacecraft actual orientation at time $t = T$. The spacecraft actual orientation was obtained through numerical integration, from the required position characterized by the value \bar{g}_T . With the ideal operation of the algorithm, such an angle at time $t = T$ should be zero. The higher its absolute value was, the lower the reorientation accuracy was obtained.

Adduce formulas for calculating the current value of the Euler angle $\theta(T)$ corresponding to the angular mismatch between the required position of the spacecraft and the current actual position. Since in this formulation the orientation of the spacecraft is characterized by the vector of kinematic parameters \bar{g} , for which there is no formula for adding turns, we will use the quaternionic representation of the orientation as an intermediate one. Under these conditions, in accordance with the definition of the Euler angle (Lur'e 1961), we have:

$$\theta(t) = 2 \cdot \arccos(\lambda_0^s(t)), \quad (22.16)$$

where $\lambda_0^s(t)$ is a scalar part of the mismatch quaternion $\Lambda^s(t) = \tilde{\Lambda}_T \circ \Lambda(t)$, calculated according to the formula for adding turns. The values of used quaternions, as a set of components, are calculated in accordance with (22.3):

$$g_T^2 = g_{T1}^2 + g_{T2}^2 + g_{T3}^2, \\ \tilde{\Lambda}_T = \frac{1}{16 + g_T^2} \cdot [16 - g_T^2; -8 \cdot g_{T1}; -8 \cdot g_{T2}; -8 \cdot g_{T3}], \quad (22.17)$$

$$g^2(t) = g_1^2(t) + g_2^2(t) + g_3^2(t), \\ \Lambda(t) = \frac{1}{16 + g^2(t)} \cdot [16 - g^2(t); 8 \cdot g_1(t); 8 \cdot g_2(t); 8 \cdot g_3(t)] \quad (22.18)$$

The dependencies $\theta(t)$ that have been calculated in this way for different orders of the algorithm are used further to demonstrate the dynamic error of the algorithms.

In order to study the influence of the reorientation angle on the accuracy of reorientation algorithms, there was carried out a series of computational experiments, where the final values of parameters \bar{g}_T are set in different ways. Let us describe the procedure for forming the final conditions.

The initial and required final orientation of the spacecraft relative to a certain reference coordinate system will be set by using the generally accepted angles of yaw $\psi(\tau)$, pitch $\beta(\tau)$, and roll $\gamma(\tau)$, $\tau = 0, T$, that have physical clarity. Then the corresponding orientation quaternions are calculated by the formula:

$$\Lambda(\tau) = \left[\cos \frac{\psi(\tau)}{2}; 0; \sin \frac{\psi(\tau)}{2}; 0 \right] \circ \left[\cos \frac{\beta(\tau)}{2}; 0; 0; \sin \frac{\beta(\tau)}{2} \right] \\ \circ \left[\cos \frac{\gamma(\tau)}{2}; \sin \frac{\gamma(\tau)}{2}; 0; 0 \right] \quad (22.19)$$

Further, the mismatch quaternion $\Lambda^M(T) = \tilde{\Lambda}(0) \circ \Lambda(T) = [\lambda_0^M; \lambda_1^M; \lambda_2^M; \lambda_3^M]$ and $g_{Ti} = \frac{4 \cdot \lambda_i^M}{1 + \lambda_0^M}$, $i = \overline{1, 3}$ are carried out. At the same time, it should be recalled that $g_{0i} = 0$.

The initial data for modeling are given in Table 22.1. The boundary conditions were set from those assumptions to consider both small reorientation angles and large ones. It is important to mention that the reorientation time in all cases was taken equal to $T = 100$ s.

Let us consider the operation of the fourth-order algorithm (22.15) in the conditions of the five tasks. The change in the Euler angle during the reorientation reflects the efficiency of the algorithm (see Figs. 22.2 and 22.3).

The above-cited results demonstrate a fairly high efficiency of the algorithm (22.15) when solving the tasks #1, #2, and #3 (Table 22.2). In the task #4, the actual orientation at the end of the maneuver differs from the required one by more

Table 22.1 Initial data for modeling

Task #	Yaw $\psi(0)$, deg.	Pitch $\beta(0)$, deg.	Roll $\gamma(0)$, deg.	Yaw $\psi(T)$, deg.	Pitch $\beta(T)$, deg.	Roll $\gamma(T)$, deg.	The initial value of Euler angle θ , deg	Vector \bar{g}_T
1	1	2	-2	-2	3	1	4.3	0.0501 -0.0525 0.0170
2	10	-10	-5	0	0	0	15.3	0.1022 -0.1819 0.1667
3	-30	45	-25	0	0	0	63.6	0.6268 0.6778 -0.6685
4	-30	45	-25	60	90	20	138.6	2.5224 0.7640 0.8338
5	-20	20	-55	60	90	20	159.6	2.7172 0.7458 1.8005

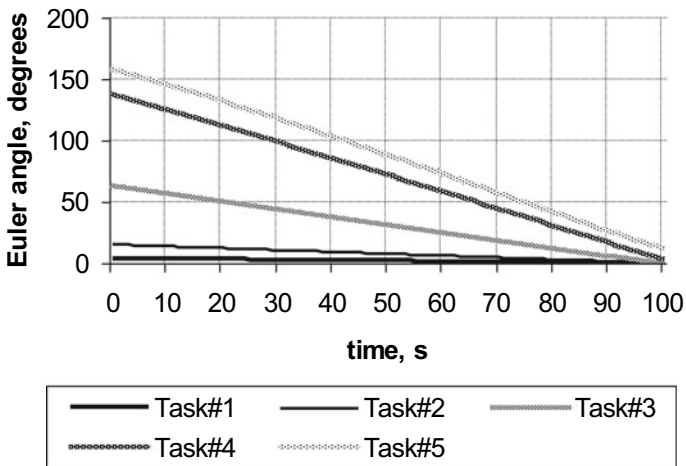


Fig. 22.2 Euler angle change during reorientation

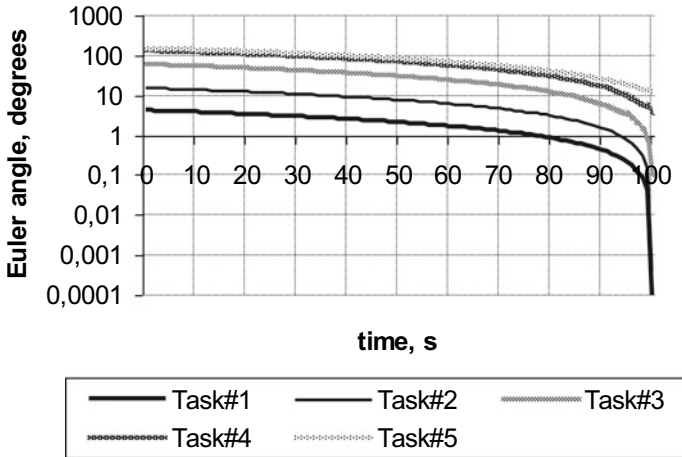


Fig. 22.3 Euler angle change on the logarithmic scale during reorientation

Table 22.2 Finite error of reorientation algorithms of different orders

Task #	The initial value of the Euler angle $\theta(0)$, deg.	The final value of the Euler angle $\theta(T)$, deg. $T = 100$ s			
		The 1-st order algorithm (22.12)	The 2-nd order algorithm (22.13)	The 3-rd order algorithm (22.14)	The 4-th order algorithm (22.15)
1	4.3	0.03	0.00	0.00	0.00
2	15.3	0.59	0.05	0.00	0.00
3	63.6	10.19	3.39	0.44	0.11
4	138.6	40.19	28.94	5.63	3.69
5	159.6	73.12	69.74	25.24	12.76

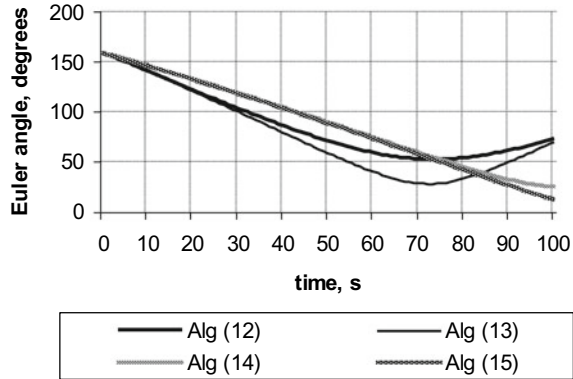
than 3.5° . In the task #5—by more than 12.5° . The difference in the efficiency of the algorithm is explained by the different initial deviation of the spacecraft orientation from the required final position. The larger this deviation, the lower the accuracy of calculating the required velocity for the truncated row, and the lower the efficiency of the algorithm.

Furthermore, Table 22.2 shows the actual values of the Euler angle at time $T = 100$ s, which determine the final error of the reorientation algorithm, for five tasks and for algorithms of different orders.

Obviously, the accuracy of solving the task increases with the increase of the algorithm order. Of the algorithms considered, the highest accuracy is for the fourth-order algorithm (22.15).

Figure 22.4 shows the change in the Euler angle when solving the task #5 by the algorithms of various orders. The ordinate of the end point, to which the various line charts come, reflects the accuracy of the corresponding algorithm.

Fig. 22.4 Euler angle change when solving the task #5 by the algorithms of various orders



It can be concluded that the algorithms of the first (Alg (22.12)) and second (Alg (22.13)) orders do not provide monotonic convergence to the final value. This is due to the fact that the order of these algorithms is insufficient for accurate reorientation at an angle of more than 150°. At the same time, the algorithms of the third and fourth orders operate effectively almost at the maximum possible angle of the initial deviation.

In the process of finalizing the analysis of the numerical simulation presented in this section, Figs. 22.5 and 22.6 were performed. The dynamics of the angular velocity in the process of reorientation of the spacecraft along the trajectory of free rotation is shown in Fig. 22.5. The dynamics of the quaternion components $\Lambda^s(t)$, tending to the value [1; 0; 0; 0] upon successful reorientation of the spacecraft is presented in Fig. 22.6. Both mentioned figures are the visualization of the task #5 solution by the fourth-order algorithm.

The figure shows $w_1 = \omega_1, w_2 = \omega_2, w_3 = \omega_3$ are projections of the angular velocity vector $\vec{\omega}$ onto the axes connected with the vehicle, calculated by integrating Eqs. (22.1) from the initial conditions obtained during the boundary value

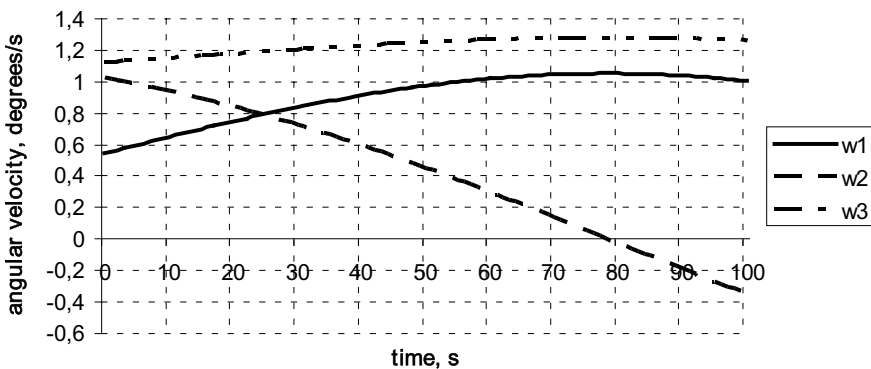


Fig. 22.5 Change of the angular velocity projections in the process of reorientation

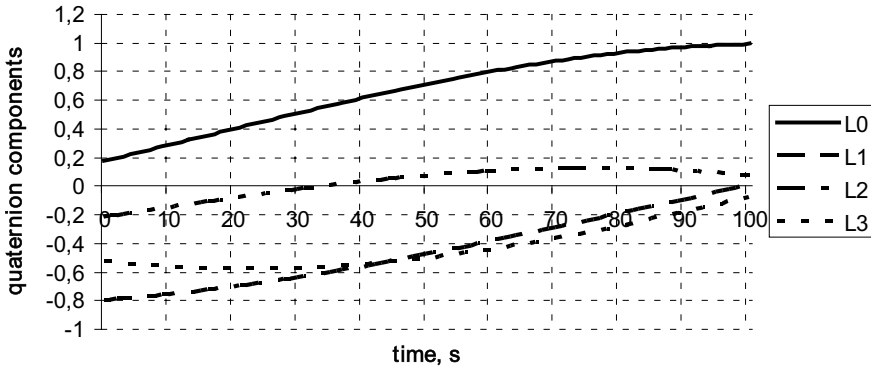


Fig. 22.6 Change of the quaternion $\Lambda^s(t)$ components in the process of reorientation

problem solution. The behavior of the projections (increasing, decreasing) is directly explained by the sign of their derivatives calculated using (22.1) for the apparatus given moments of inertia $I_1 = 3300 \text{ kg m}^2$, $I_2 = 3000 \text{ kg m}^2$, $I_3 = 1200 \text{ kg m}^2$.

In Fig. 22.6, the variables L_0, L_1, L_2, L_3 indicate the components of the previously introduced the mismatch quaternion $\Lambda^s(t) = \tilde{\Lambda}_T \circ \Lambda(t)$, computed using (22.17) and (22.18) according to the procedure described above.

In such a way, from the charts of the angular velocity of free rotation (Figs. 22.5 and 22.6), which have a fairly general form, it can be concluded that the problem of determining the initial values is not trivial. The actual behavior of the quaternion components, tending to the true final value $[1; 0; 0; 0]$, shows the efficiency of the reorientation algorithm.

22.4 Discussion of the Solution Practical Implementation

The practical implementation of the obtained solution to the boundary value problem consists in the usage of the formula (22.15) as an algorithm for calculating control commands in the onboard attitude control system of the spacecraft. The paper analyzes the methodological error of the method due to the final representation of the equations' solutions that are expanded in series. It is shown that with the high order of the algorithm, the methodical error is acceptable for a wide range of tasks. Nevertheless, with the practical usage of the inertial reversal algorithm, the additional sources of the control error will most likely occur. These include:

- a spacecraft acceleration to gain the required angular velocity of free rotation and the spacecraft deceleration at the end of the inertial section. These control stages, firstly, have a certain duration and require registration, and secondly, they lead to an unaccounted change in the actual orientation of the spacecraft;

- the parametric errors such as inaccuracy of knowledge of the spacecraft inertia moments and non-coincidence of the coordinate system, associated with the spacecraft, with the main axes of inertia;
- an error in the propulsion system;
- an inaccuracy of the angular velocity measurements and the actual orientation of the spacecraft, etc.

All of the listed factors will definitely bring an additional error in the implementation of the reorientation maneuver. The assessment of this error is not considered in this paper, since it depends on the empirical data that are having not being collected yet. However, the proposed scheme of the algorithm operation using a feedback loop on the information about the SC orientation and the possible correction of the SC velocity within the reorientation section will provide some compensation for the negative effect.

To reduce the control error under these conditions, it is necessary:

- to predict the accuracy of the reorientation maneuver,
- to recalculate the required free rotation velocity (in some cases), and
- to correct the actual velocity during the reorientation process.

Since the development and the justification of the mentioned control strategy is beyond the scope of this study, we will confine ourselves here to its informal description.

Let the actual angular velocity of the spacecraft $\hat{\omega}(t)$ and its orientation be measured at every moment of time $t \in [0; T)$. Assuming the current orientation to be the initial one, we calculate the true value of the vector \bar{g}_{T-t} , corresponding to the required position of the spacecraft in time $(T - t)$. After that, using the formula (22.8), into which the equality $\bar{\Theta} = \hat{\omega}(t) \cdot (T - t)$ is substituted, we predict the value of the vector $\hat{g}(T)$ and compare it with \bar{g}_{T-t} . When the vectors are close by the value, additional correction of the velocity is not performed, and the object continues its free rotation. If the vectors differ significantly, then using the formula (22.15) we will calculate $\bar{\Theta}_{[4]}$ and the new value of the required velocity $\bar{\omega}_0 = \frac{\bar{\Theta}_{[4]}}{T-t}$. Subsequently, with the help of low-thrust engines, the apparatus is accelerated to the required velocity. It is necessary to mention that the acceleration is controlled by comparing the required velocity with the current actual estimated (measured) velocity. Since the deviation of the actual velocity from the required one within the inertial turn area cannot be significant, the duration of such correction is insignificant.

As a justification for the described strategy convergence to the exact solution, we would like to add that the more accurate the used formula expressions are, than the smaller the reorientation angle is. Therefore, their application becomes more accurate when they approach the end point.

22.5 Conclusions

By way of conclusion, there has been solved the problem of definition of the initial angular velocity for the reorientation of a rigid body at a specified angle in a given time along the trajectory of the inertial rotation. In addition, this problem is the boundary value problem with the essential nonlinearity. The obtained solution can be used for the spacecraft orientation control system to minimize the fuel consumption. The simulation allowed to determine an order of the algorithm that is sufficient and to estimate the control accuracy for conditions close to the real ones. The main aspects of the method practical application in the spacecraft onboard control system are indicated. The aim of the aspects is the improvement of the control accuracy, regardless of the initial orientation mismatch value.

References

- Bong, W.: *Space Vehicle Dynamics and Control*, revised first edn. American Institute of Aeronautics and Astronautics, Inc. (2016) <https://doi.org/10.2514/4.103803>
- Boyarko, G., Romano, M., Yakimenko, O.: Time-optimal reorientation of a spacecraft using an inverse dynamics optimization method. *J. Guidance Control Dyn.* **34**(4), 1197–1208 (2011). <https://doi.org/10.2514/1.49449>
- Branec, V.N., Shmyglevskij, I.P.: *Primenenie kvaternionov v zadachakh orientacii tverdogo tela* (Quaternions Application for Problems on Orientation of Rigid Body). Nauka, Moskva (1973). (in Russian)
- Frolov, Y.A., Shipulina, L.V.: *Funktional'nye modeli orientacii tverdogo tela i ikh prilozheniya*. Khar'kov, NTU "KHPI" (1985). (in Russian)
- Gadelha de Souza, L.C., De Souza Alain, G.: *Satellite Attitude Control System Design considering the Fuel Slosh Dynamics*, vol. 2014, pp. 1–8. Hindawi Publishing Corporation Shock and Vibration (2014). <https://doi.org/10.1155/2014/260206>
- Glumov, V.M., Krutova, I.N., Sukhanov, V.M.: Fuzzy logic-based adaptive control system for in-orbit assembly of large space structures. *Autom. Remote Control* **65**, 1618–1634 (2004). <https://doi.org/10.1023/B:AURC.0000044271.14689.17>
- He, L., Ma, W., Guo, P., Sheng, T.: Developments of attitude determination and control system of microsats: a survey. *J. Syst. Control Eng.* **X**(XX), 1–21 (2020). <https://doi.org/10.1177/0959651819895173>
- Kosari, A., Jahanshahi, H., Razavi, S.A.: An optimal fuzzy PID control approach for docking maneuver of two spacecraft: orientational motion. *Int. J. Eng. Sci. Technol.* **20**(1), 293–309 (2017). <https://doi.org/10.1016/j.jestech.2016.07.018>
- Leeghim, H., Choi, Y., Bang, H.: Adaptive attitude control of spacecraft using neural networks. *Acta Astronaut.* **64**(7–8), 778–786 (2009). <https://doi.org/10.1016/j.actaastro.2008.12.004>
- Levskii, M.V.: On the problem of optimal spacecraft attitude control. *J. Comput. Syst. Sci. Int.* **55**, 310–330 (2016). <https://doi.org/10.1134/S1064230716010093>
- Levskii, M.V.: Optimal control of a spacecraft orientation taking into account the energy of rotation. *Mech. Solids* **54**, 144–156 (2019). <https://doi.org/10.3103/S0025654419030166>
- Levskii, M.V.: On improving the maneuverability of a space vehicle managed by inertial executive bodies. *J. Comput. Syst. Sci. Int.* **59**, 796–815 (2020). <https://doi.org/10.1134/S1064230720020094>
- Lur'e, A.I.: *Analiticheskaya mekhanika*. GIFML, Moskva (1961). (in Russian)

- MacKunis, W., Leve, F., Patre, P.M., Fitz-Coy, N., Dixon, W.E.: Adaptive neural network-based satellite attitude control in the presence of CMG uncertainty. *Aerosp. Sci. Technol.* **54**, 218–228 (2016). <https://doi.org/10.1016/j.ast.2016.04.022>
- Montenegro, S., Lenin, L.: Design of neural network for satellite's attitude control systems. *Appl. Mech. Mater.* **110–116**, 5001–5008 (2011) <https://doi.org/10.4028/www.scientific.net/AMM.110-116.5001>
- Park, Y.: Optimal control of fuzzy systems with application to rigid body attitude control. *Aerosp. Eng.* (2018). <https://doi.org/10.5772/INTECHOPEN.82181>
- Phogat, K.S., Chatterjee, D., Banavar, R.: Discrete-time optimal attitude control of a spacecraft with momentum and control constraints. *J. Guidance Control Dyn.* **41** (2017) <https://doi.org/10.2514/1.G002861>
- Salah, S.M., Bayoumi Gamal, M.El.: Adaptive robust control of satellite attitude system. *Int. Rev. Aerosp. Eng.* **8**(1), 35–42 (2015) <https://doi.org/10.15866/irease.v8i1.5322>
- Uspenskiy, V.B.: *Teoreticheskie osnovy girusilovogo upravleniya orientatsiy kosmicheskogo letatel'nogo apparata [Tekst]: monografiya/Uspenskiy, V.B.* NTU “KhPI”, Khar'kov 328 (2006). ISBN 966-593-398-1 (in Russian)
- Zhang, S., Qian, S., Zhang, L.: Optimal control techniques for spacecraft attitude maneuvers. In: *Advances in Spacecraft Technologies*, pp. 523–548 (2011). <https://doi.org/10.5772/14462>

Part VIII
Nonlinear Phenomena and Methods
of Investigation

Chapter 23

Asymptotic Methods for Soliton Excitations



Alexander Kovalev

Abstract An asymptotic method for finding the solutions for two-parameter dynamic envelope solitons in media with a different character of linear wave spectrum is demonstrated for several examples. Particular attention is paid to method of constructing such the solutions for nonlinear weakly dispersive media with a sound-type spectrum of linear waves. The features of the proposed procedure are illustrated with example of the modified Boussinesq equation.

Keywords Soliton · Dispersion · Asymptotic expansion

23.1 Introduction

In some cases, nonlinear dynamical systems with distributed parameters admit an existence of spatially localized excitations of various types or the so-called solitons (Dodd 1984; Newell 1985). In some cases, the corresponding evolution equations are completely integrable, and in mathematical sense of the word, the exact solutions of such equations are called solitons. But physical systems are mainly described by non-integrable equations, although they allow an existence of experimentally observed long-lived localized soliton-type excitations (Kivshar and Agraval 2003; Sulymenko et al. 2018). In some cases, stability of such excitations is guaranteed by choice of certain fixed boundary conditions (Menton and Sutcliffe 2004). In other cases, such solitons are excited under experimental conditions or due to thermodynamic reasons (Sulymenko et al. 2018). The soliton excitations are widely studied experimentally, and possibilities of using them in information transmission systems (optical solitons) and spintronic devices (magnetic solitons) are now being considered (Kivshar and Agraval 2003; Sulymenko et al. 2018). Great interest in solitons is shown in the study of ocean waves (“tsunamis” and “strange” waves). Usually, the equations arising in

A. Kovalev (✉)

B.I. Verkin Institute for Low Temperature Physics and Engineering of NANU, Kharkov 61103, Ukraine

e-mail: kovalev@ilt.kharkov.ua

V.N. Karazin Kharkov National University of MESU, Kharkov 61077, Ukraine

a different physical situation can be reduced to a small set of simple equations, such as the nonlinear Schrödinger equation (NSE) (23.9), the Boussinesq equation (BE) (23.13) and its modified analogue (mBE) (23.14), the Korteweg-de Vries equation (KdV) and its modification (mKdV) (23.20), the nonlinear Klein–Gordon equation (nKGE) (23.8) and its elliptic version (eKGE) (23.1). In physical applications, the so-called two-parameter dynamical solitons (or envelope solitons) play a special role. The solutions for such solitons are well known in the case of the integrable NSE, mKdV and the sinusoidal Klein–Gordon equation (SGE) (Braun and Kuvshar 2004). On the other hand, it is known that in such integrable equations as the KdV equation and the BE, the complete set of solutions, into which the initial conditions of a rather wide form decompose, consists of one-parameter dynamic solitons and linear waves. Those, there are no two-parameter solitons in this systems. The question arises about existence of envelope solitons in non-integrable systems and systems close to the integrable one. In addition, are there any approximate long-lived states of the envelope soliton type in integrable systems that do not admit exact two-parameter soliton solutions?

To explain the problem, let us give the following example. An exactly integrable BE does not allow the existence of an envelope soliton. However, at the first step of the perturbation theory based on the method of multiple time scales (Nayfeh 1981), it is reduced to the nonlinear Schrödinger equation, which allows the existence of such solitons (Newell 1985). In some cases, the reason for this discrepancy is the decay of the soliton state due to the emission of linear waves of the continuous spectrum at frequencies that are multiples of the soliton frequency, as for example in the case of KGE (Eleonskii et al. 1982, 1961). However, as it was shown by Eleonskii et al. (1982, 1961), this radiation is exponentially small. It is proportional to $\exp(-1/\varepsilon)$, where ε is a small amplitude of the soliton (Eleonskii et al. 1961, 1982; Eleonskii and Silin 1969, 1970). Therefore, we can discuss the approximate soliton excitations and construct their approximate solutions with a power law accuracy in ε . In this case, to clarify the difference between soliton solutions in various physical systems, it is necessary to construct these solutions with an accuracy greater than the basic approximation. The multi-timescale method is rather cumbersome. Therefore, it is preferable to use different versions of asymptotic expansion methods. Some of them were proposed in Eleonskii and Silin (1969, 1970) and Kosevich and Kovalev (1974) for systems with large dispersion of the dispersion law of linear waves, in particular, for nKGE and eKGE. In this paper, we will discuss briefly this question, but the main content of the paper will be devoted to the development of the soliton theory of asymptotic expansions for weakly dispersive media.

23.2 Asymptotic Method for Envelop Solitons

For the first time, an asymptotic procedure of finding the two parametric soliton solutions was developed in Eleonskii and Silin (1969, 1970) for three-dimensional stationary states of nonlinear electromagnetic field. Later, a similar procedure was

proposed in Kosevich and Kovalev (1974) for self-localized elastic antiphase oscillations with frequencies near the upper boundary for phonon spectrum. In both cases, the problem is reduced to finding the soliton solutions to nonlinear equation with an elliptic differential part. The main features of the method can be demonstrated by the example of the following simple equation

$$\ddot{u} + u'' + f(u) = 0 \tag{23.1}$$

This equation is invariant under the transformation $x' = (x - Vt)/\sqrt{V^2 - 1}$ and $t' = (t + Vx)/\sqrt{V^2 - 1}$. So it is enough to find a motionless solution for the envelope solitons. For the function $f(u)$ of the form $f = u + \alpha u^2 + \beta u^3 + \dots$ the spectrum of linear waves $\omega = \omega(k) = \sqrt{1 - k^2}$ is bounded from above by the value $\omega_0 = 1$, and soliton frequencies $\omega > \omega_0$ for $k = 0$ lie above this spectrum (see Fig. 23.1a).

Since the solution for a motionless soliton is purely periodic in time, it can be represented as the Fourier time series of the form

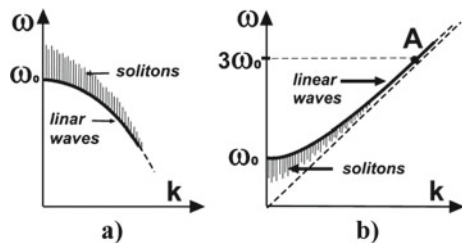
$$u = \sum_{n=0}^{\infty} A_n(x) \cos(n\omega t), \tag{23.2}$$

for amplitudes of which $A_n(x)$ the infinite set of ordinary differential equations is obtained with an infinite number of nonlinear terms in each equation. At the second step of this asymptotic procedure, the amplitudes $A_n(x)$ of the Fourier series are expanded into the infinite power series in powers of a small parameter, which is the amplitude of the soliton or the deviation of its frequency from the edge of linear wave spectrum:

$$A_0 = \sum_{m=1}^{\infty} A_{0,m+1}(x) \varepsilon^{m+1}, \quad A_n = \sum_{m=1}^{\infty} A_{n,m+n-1}(x) \varepsilon^{m+n-1}, \tag{23.3}$$

where the small parameter $\varepsilon = \sqrt{\omega^2 - 1} \ll 1$ and summation occur over all odd numbers. Substituting the expansions (23.2) and (23.3) into Eq. (23.1) and equating to zero the coefficients at different degrees of the parameter ε , we obtain an infinite system of ordinary differential and algebraic equations for the functions $A_{p,q}$ with

Fig. 23.1 a Spectrum of linear waves and region of parameters for the existence of small-amplitude two-parameter solitons (shaded in the figure) for the elliptic systems (23.1) and b for the parabolic systems (23.8)



a finite number of terms in each equation. The first index indicates the number of harmonic, and the second indicates the degree of small parameter. At the same time, it is assumed that the spatial gradients of the solution are small as well: $\partial/\partial x \sim \varepsilon$. The procedure of solving the resulting series of equations is as follows: The expressions which are proportional to ε^2 give the relations $A_{02} = -\alpha A_{11}^2/2$ and $A_{22} = \alpha A_{11}^2/6$. With these relations, the expression proportional to ε^3 leads to a closed equation for the main approximation of soliton excitation:

$$A''_{11} - A_{11} + (5\alpha^2/6 - 3\beta/4)A_{11}^3 = 0, \quad (23.4)$$

where $A' \equiv dA/d\varepsilon x$. The soliton solution to Eq. (23.4) has the standard form

$$A_{11} = \sqrt{2} \operatorname{sech}(\varepsilon x) / \sqrt{5\alpha^2/6 - 3\beta/4}. \quad (23.5)$$

Thus, up to the value ε^2 , the solution for the envelope soliton reads

$$u = \varepsilon g \frac{\cos \omega t}{ch \varepsilon x} - \varepsilon^2 \frac{\alpha g^2}{2} \frac{1}{ch^2 \varepsilon x} + \varepsilon^2 \frac{\alpha g^2}{6} \frac{\cos 2\omega t}{ch^2 \varepsilon x} \quad (23.6)$$

with the parameter $g = 2\sqrt{6}/\sqrt{10\alpha^2 - 9\beta}$. It can be seen from the expression (23.5) that soliton solution exists only if the inequality for nonlinear constants ($10\alpha^2 > 9\beta$) is satisfied. In the following steps of the procedure, for ε^4 we obtain the connections $A_{04} = aA_{11}^2 + bA_{11}^4 - \alpha A_{11}A_{13}$ and $A_{24} = cA_{11}^2 + dA_{11}^4 + \alpha A_{11}A_{13}$, where a, b, c, d are the constants. Finally, at the next step, for terms of order of ε^5 , we obtain a closed equation for A_{13} of the form

$$A''_{13} - A_{13} - 24A_{11}^2 A_{13}/g^2 = pA_{11}^3 + qA_{11}^5 \quad (23.7)$$

with the solution $A_{13} \sim 1/ch(\varepsilon x)$, $1/ch^3(\varepsilon x)$. Thus, the proposed scheme allows one to construct the soliton solutions with any power-law accuracy in the parameter ε . The main information about the soliton solution is found at the first step from the basic nonlinear equation. All other equations are the second-order linear ordinary differential equations with variable coefficients and right-hand sides. The requirement for the solution to decrease at infinity makes this procedure unique. The discussed asymptotic method is similar to the method proposed by A. Poincaré in the theory of nonlinear oscillations of finite-dimensional systems (Bogoliubov and Mitropolsky 1961; Moiseev 1969).

Since the frequencies of all harmonics of soliton solution lie above the spectrum of linear waves, there is no emission of such waves by soliton. Therefore, the found expression represents the real solution to Eq. (23.1).

A different situation arises for analogous equations of the elliptic type (see Fig. 23.1b), for example, in the case of the nonlinear Klein–Gordon equation.

$$\ddot{u} - u'' + f(u) = 0 \quad (23.8)$$

and its generalizations with higher spatial derivatives. In this case, the spectrum of linear waves $\omega = \sqrt{1 + k^2}$ is bounded from below. The asymptotic method for the soliton solutions of such systems was proposed in Kosevich and Kovalev (1974). Equation (23.8) is not exactly integrable and it is difficult to judge all its exact solutions. But usually the low-amplitude limit is considered, in which Eq. (23.8) can be approximately reduced to the exactly integrable nonlinear Schrödinger equation (NLSE). In the method of multiple time scales (Nayfeh 1981), the simplest case of Eq. (23.8) with $\alpha = 0$ and $\beta = -1$ at the first step of the procedure for the function $u = a \exp(kx - \omega t) + cc$ in terms of the effective Gardner coordinate $\xi = \varepsilon(x - kt/\omega)$ and time $\tau = \varepsilon^2 t$, where $\varepsilon = \sqrt{1 - \omega^2}$ leads to the following nonlinear Schrodinger equation (Newell 1985):

$$i a_\tau + a_{\xi\xi}/2 + 3|a|^2 a/2 = 0. \tag{23.9}$$

Its exact soliton solution is well known. In terms of initial variables of Eq. (23.8), this solution in the particular case for motionless excitations has the following form:

$$u = \varepsilon A_{11} \cos \omega t = \frac{2\sqrt{2}}{\sqrt{3}} \frac{\sqrt{1 - \omega^2} \cos \omega t}{ch\sqrt{1 - \omega^2} x}. \tag{23.10}$$

The solution for a moving solitons is obtained from (23.10) by the Galilean transformation. The region of the existence of two-parameter NLSE solitons is shown as the dashed area in Fig. 23.2a. For solitons a more natural characteristic than the wave number k is the velocity of its motion V . Therefore, in Fig. 23.2b, the region of existence of two-parameter solitons of general type is shown on the plane of velocity V and frequency $\tilde{\omega} = \omega - kV$ in a frame of reference moving with the velocity V . For linear waves in the same figure, the role of velocity is played by the group velocity $V_g = \partial\omega/\partial k$.

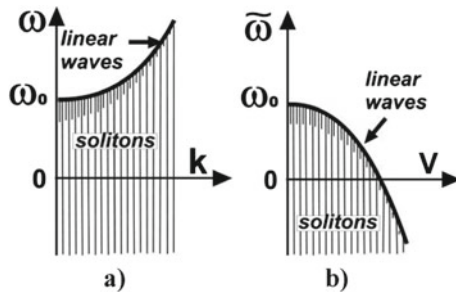


Fig. 23.2 **a** Region of the existence for two-parameter NLSE solitons (shaded) and the region of applicability of the NLSE approximation (23.10) for describing the solitons of the nonlinear Klein-Gordon Eq. (23.8) (double shaded). **b** The same is for the plain of variables $V = \partial\omega/\partial k$ (group velocity linear waves and the velocity of solitons) and $\tilde{\omega} = \omega - kV$ (the frequency in moving with V frame of reference)

But in the case of non-integrable initial Eq. (23.8), the expression (23.10) corresponds only to the first step of the asymptotic procedure for finding the solution (double-hatched area in Fig. 23.2a). The complete asymptotic procedure has the same form as (23.2, 23.3) and gives an asymptotically accurate solution with a power-law accuracy in the small expansion parameter (soliton amplitude). The peculiarity of this case is that for exactly integrable equations of type (23.8) (e.g., for the sinusoidal Klein–Gordon equation), the asymptotic power series expansions in a small parameter converge to the exact soliton solutions for two-parameter dynamic solitons. In the cases of non-integrable equations with a general form of a nonlinear force $f(u)$ or with dispersion term of the type $\sim u^{IV}$, the power expansions do not take into account the exponentially small additions of the type of $\exp(-1/\varepsilon)$, where $\varepsilon \ll 1$ is an amplitude of the soliton (Eleonskii et al. 1982, 1961). In the example under consideration with $\alpha = 0$ for the triple harmonic $\cos 3\omega t$ in the main approximation of the order of ε^3 for a stationary soliton, the algebraic relation $(9\omega^2 - 1)A_{33} + A_{11}^3/4 = 0$ arises, where all the terms are of order of ε^3 . In this case, the function A_{33}'' has a higher order of smallness ($\sim \varepsilon^5$) and is omitted in the corresponding equation. If this term is left in accordance with the Tamm–Dankov method, the equation for A_{33} will take the form

$$A_{33}'' + (9\omega^2 - 1)A_{33} + A_{11}^3/4 = 0. \quad (23.11)$$

with the solution asymptotic

$$A_{33}(+\infty) \approx \frac{8\pi}{3\sqrt{3}} \frac{\sin(\sqrt{9\omega^2 - 1}x)}{\varepsilon^3 \operatorname{ch}(\pi\sqrt{2}/\varepsilon)} \sim \sin(k(3\omega)x) \exp\left(-\frac{\sqrt{2}\pi}{\varepsilon}\right). \quad (23.12)$$

This expression describes the emission of exponentially weak wave with triple frequency from the soliton (the point A in Fig. 23.1b). Thus, asymptotic expansions generally yield only approximate solutions for the dynamic solitons. In real physical systems, such small-amplitude solitons will decay exponentially with time. However, in the case of special excitation of such solitons, for example, in optical data transmission lines or magnetic delay lines, the soliton nature of the excited pulses improves their stability in comparison with linear wave packets and makes it possible to use them in technological devices (Kivshar and Agraval 2003; Sulymenko et al. 2018). In addition, two-parameter envelope solitons in a quasi-classical approximation can be interpreted as the bound state of elementary excitations of the system (Kosevich and Kovalev 1989). In this approximation, the energy per one quasiparticle in it is smaller than the energy of a free quasiparticle. Therefore, the existence of such solitons is determined by thermodynamic reason and it gives a finite soliton contribution to thermodynamics. Thus, although the approximate solutions of nonlinear evolution equations found by asymptotic methods are not true solutions in mathematical sense, their knowledge is necessary for study of real physical systems described by equations that are not integrable in the general case.

Until now, we considered the envelope solitons in systems with a strong dispersion of the linear wave velocities. In such systems, it is easy to construct the solutions for motionless solitons and then to generalize them for moving solitons.

23.3 Asymptotic Method for Solitons in Weakly Dispersive Media

As applied to weakly dispersive media, the above method for finding soliton solutions for envelope solitons requires substantial modification. The optical waveguides, elastic media, easy-plane magnets, liquids (including superfluids), the Bose–Einstein condensates, etc., represent the examples of weakly dispersive media with a sound spectrum of elementary excitations. With an increase in the level of excitation of the nonlinear system, it becomes necessary to take into account the deviation of the wave dispersion law from linear (sound) one. In long-wavelength limit, the dependence of the wave frequency ω in the laboratory frame of reference on its wave number k can be represented in the first approximation with the wave dispersion in the form $\omega = ck + Ak^3$, where c is the sound velocity, and the dispersion of sound waves is equal to $D = \partial^2\omega/\partial k^2 = 6Ak$. In weakly dispersing media in the limit $k \rightarrow 0$, dispersion disappears ($D \rightarrow 0$), and the group velocity of linear waves $V_g = \partial\omega/\partial k = c + 3Ak^2$, together with the phase velocity $V_f = \omega/k = c + Ak^2$, tends to the value of the sound velocity (see Fig. 23.3a for the negative dispersion with $A < 0$ and Fig. 23.4a for positive dispersion with $A < 0$).

For the nonlinear waves with a stationary profile, their “nonlinear dispersion law” can be introduced as $\omega(k, a) = \omega_0(k) + N(k)a^2$, where $\omega_0(k)$ is the dispersion law of linear waves and the value $N(k) = \partial\omega(k)/\partial k$ is the nonlinearity characteristic of the system. In the situation with $DN > 0$ according to the Lighthill criterion (Whitham 1974), periodic waves (cnoidal waves) are modulation stable, and in the case $DN < 0$, they are modulation unstable in the linear limit. These cases with $DN < 0$ are presented in Figs. 23.3 and 23.4. In non-integrable systems, this fact

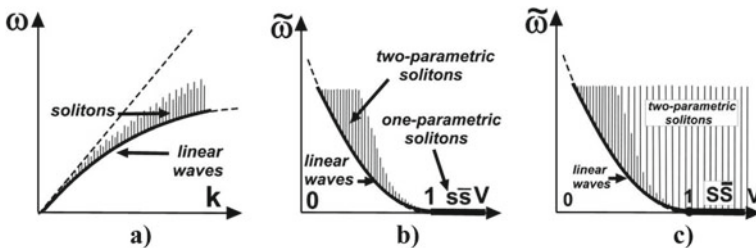
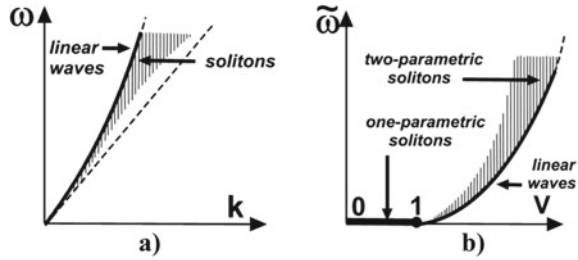


Fig. 23.3 **a** Characteristics of linear and nonlinear waves in systems with negative dispersion and “hard” nonlinearity ($\alpha > 0$ and $\beta > 0$ in the modified Boussinesq Eq. (23.14)) in the plane (ω, k) . **b** The same is for the plane $(\tilde{\omega}, V)$. **c** The same is for the modified Korteweg-de Vries equation

Fig. 23.4 **a** Characteristics of linear and nonlinear waves in systems with positive dispersion and “soft” nonlinearity ($\alpha < 0$ and $\beta < 0$) of the modified Boussinesq Eq. (23.14) in the plane (ω, k) . **b** The same is for the plane $(\tilde{\omega}, V)$



indicates the possibility for the existence of localized excitations such as envelope solitons (in dashed areas in Figs. 23.3a, b and 23.4a, b). In the low-amplitude limit, these solitons represent a “carrier wave” propagating with a velocity close to the phase velocity of linear waves, in which the amplitude of the envelope moves with a velocity close to the group velocity of these waves. Solutions for envelope solitons (or breathers) contain four parameters: carrier wave frequency ω and its wave number k , the envelope velocity V , and its amplitude a . Two of these four parameters are independent for two-parameter solitons, for which, for example, the amplitude and value of the wave vector can be chosen. The difficulty arising in systems with weak dispersion is related to the fact that only moving breathers are possible in these systems. To find the approximate solutions for them, it is necessary already at the first step of the procedure to carry out the expansions in power series in a small parameter both the shape of a soliton and its two dynamic parameters.

As examples of weakly dispersive media, let us consider elastic media and surface of a shallow water described by the Boussinesq equation and its modification:

$$\ddot{u} - u'' - \alpha u^{IV} - \gamma u'u'' - \beta u^2u'' = 0, \tag{23.13}$$

where the case $\beta = 0$ corresponds to the Boussinesq equation (BE), and the case $\gamma = 0$ corresponds to the modified Boussinesq equation (mBE), for example, for shear displacement u in an elastic medium. In dimensionless variables, the sound velocity in a medium is equal to unity. Note that we use this equation for displacements in a nonlinear elastic medium, although more often it is written for deformations of solid medium or for the height of surface displacements in a shallow water $w = \partial u / \partial x$. The sign of the so-called dispersion term u^{IV} follows from the specific type of interaction of atoms in the elastic media. With an arbitrary nature of the interaction, this term can change the sign. For example, in the case of transverse flexural vibrations of a rigid chain or plate, the dispersion term in (23.13) has the form $+\alpha u^{IV}$ (Kosevich and Kovalev 1989).

Equation (23.13) with $\beta = 0$ (BE) is completely integrable (Novikov et al. 1984). In the long-wavelength low-amplitude limit in variables similar to Gardner’s variables, it reduces to the integrable KdV equation (Gardner et al. 1968). For an arbitrary sign of the parameters, this KdV equation has only one-parameter soliton solutions and no breather solutions. The original Eq. (23.13) (BE) with $\alpha > 0$ admits two-parameter envelope solitons, but it does not have any breather solutions at $\alpha < 0$

(Tajiri and Murakami 1989). Below, we will mainly consider the MBE, since it is easier to analyze this equation within the framework of asymptotic methods than the BE. Let us demonstrate the proposed procedure using the example of the mBE or nonlinear string equation with arbitrary signs of nonlinearity and dispersion:

$$\ddot{u} - u'' - \alpha u^{IV} - \beta u^2 u'' = 0, \quad (23.14)$$

where $\alpha = \pm 1$ and $\beta = \pm 1$.

Equation (23.14) is not completely integrable and the question of the complete set of its solutions is open. It can be approximately reduced to the fully integrable mKdV equation, which admits both one-parameter and two-parameter breather-type solutions (Kosevich and Kovalev 1989) (see Fig. 23.3c). In Fig. 23.3c, the domain of two-parameter solitons (breathers) is shaded. The segment of the velocity axis with $V > c = 1$ corresponds to one-parameter solitons (S) and antisolitons (\bar{S}). For the initial Eq. (23.14) only the solutions for linear waves, one-parameter dynamic solitons (and antisolitons) and nonlinear periodic waves of a stationary profile are known. Although the mKdV equation, close to (23.14), has the breather solutions, such exact solutions for the mBE itself are unknown. Below we propose an asymptotic procedure for finding approximate solutions of the mBE for nonlinear two-parameter localized excitations of the envelope soliton type in the double-hatched area of the parameters in Fig. 23.3c.

Linear waves of the type $u = a \cos(kx - \omega t)$ have the dispersion law of sound-type $\omega = k\sqrt{1 - \alpha k^2}$ for the frequency in the laboratory frame of reference (Fig. 23.3a). For the case $\alpha < 0$, the spectrum has the Bogoliubov form (Fig. 23.4a). In long-wave approximation, which was assumed when deriving the evolutionary partial differential equations, the dependence of the group velocity $V = d\omega/dk$ on the wave number is reduced to the expression $V \approx 1 - 3\alpha k^2/2$, and the dispersion parameter $D = d^2\omega/dk^2 \approx -3\alpha k$. It is convenient to enter the frequency in the frame of reference moving with group velocity $\tilde{\omega} = \omega - kV \approx (1 - V^2)^{3/2}/\sqrt{27\alpha}$ (see Fig. 23.3b).

In addition to these linear waves, only one-parameter solitons with stationary profile are easily found. The corresponding solution reads

$$u = \pm 2\sqrt{6\alpha/\beta} \operatorname{Arth} \exp\left(\sqrt{(V^2 - 1)/\alpha}(x - Vt)\right). \quad (23.15)$$

and it has a standard soliton form. In the case of dispersion with $\alpha > 0$, which is normal for the theory of elasticity, the “fast” solitons exist only at a “hard” nonlinearity with $\beta > 0$, and their velocity $|V| > 0$ (the half-axes ($\bar{S}\bar{S}$) for solitons S and antisolitons \bar{S} in Fig. 23.3b). In the systems with the Bogoliubov spectrum ($\alpha < 0$), the “slow” solitons exist at a “soft” nonlinearity with $\beta < 0$, and their velocity $|V| < 0$ (Fig. 23.4b). The intervals of velocities values, in which one-parameter solitons exist, are complementary to the regions of group velocities of linear waves.

The question about the existence of two-parameter envelope solitons is rather complicated. The following circumstances indicate the possibility for an existence of such excitations. First of all, it is indicated by modulation instability of two-parameter nonlinear waves of a stationary profile with constant amplitude (the so-called cnoidal waves). Such excitations are described by solutions of the form

$$u = \sqrt{\frac{6\alpha}{\beta}} am\left(\sqrt{\frac{(V^2 - 1)}{\alpha(2 - q^2)}}(x - Vt), q\right) - G(x - Vt), \quad (23.16)$$

where the function $am(z, q)$ is the Jacobi elliptic amplitude and q is its modulus, the constant G is chosen from the condition of vanishing of the total deformation of the system. In the extremely nonlinear case ($q \rightarrow 1$), the solution (23.16) transforms into the soliton solution (23.15), and at small amplitudes, the solution $u \approx a \cos(kx - \omega t)$ has the form of almost harmonic waves with a “nonlinear dispersion law.” It is easily to obtain this law in the resonant approximation:

$$\omega^2 \approx k^2 - \alpha k^4 + \beta a^2 k^4 / 4 \quad (23.17)$$

From the dispersion law (23.17), it follows that under the condition $\alpha \cdot \beta > 0$ the inequality $J = (\partial^2 \omega / \partial k^2) / (\partial \omega / \partial a^2)|_{a=0} = -24\alpha / \beta k^2 < 0$ is satisfied, and according to the Lighthill criterion (Whitham 1974) for such combinations of the parameters α and β signs, the mentioned cnoidal waves (23.16) are modulation unstable. This fact can lead to the formation of envelope solitons.

In addition, Eq. (23.14) is approximately reduced to the integrable mKdV and the nonlinear Schrödinger equations, which admit exact solutions in the form of the envelope solitons (shaded areas in Figs. 23.2 and 23.3c). Indeed, representing the variable $u(x, t)$ in the form $u = a \exp(ikx - i\omega t) + cc$ and using the variables of the Gardner type $a = \varepsilon f$, $\xi = \varepsilon(x - Vt)$ and $\tau = \varepsilon^2 t$, for the value f , we obtain the nonlinear Schrödinger equation (NLSE) (Zakharov and Shabat 1972):

$$-2i\omega_0(k) f_\tau - D(k)k^2 f_{\xi\xi} - f + k^4 |f|^2 f = 0. \quad (23.18)$$

(the commonly used the NLS equation does not contain the term f , which is removed by the gauge transformation).

The retention of the dependences on the wave number k in the dispersion law of linear waves $\omega_0(k)$ and in the dispersion $D(k)$ in this Eq. (23.18) emphasizes that it is valid for arbitrary values of k , and the approximation is associated with the first step in ε of the method of multiple time scales. Parameter ε describes the smallness of the frequency deviation from the linear wave frequencies. In the long-wave approximation with $k \ll 1$, the soliton solution of Eq. (23.18) gives the solution for envelope soliton of the original Eq. (23.14) in the form

$$u = \left(2\sqrt{2\varepsilon/k^2}\right) \operatorname{sech}\left(\varepsilon(x - Vt)/\sqrt{3}k\right) \cos(kx - \omega t). \quad (23.19)$$

In the Gardner variables $\xi = \varepsilon(x - Vt)$ and $\tau = \varepsilon^2 t$ and in the same approximation, the equation for the oscillation of a nonlinear string (23.14) is also reduced to the modified KdV equation of the form

$$2u_\tau - \alpha u_{\xi\xi\xi} - \beta u_\xi^3 = 0. \quad (23.20)$$

As it is known, two-parameter soliton solutions of this equation exist only if the relation $\alpha\beta > 0$ is satisfied, which corresponds to the condition of modulation instability of cnoidal waves of the original modified Boussinesq equation. The exact two-parameter mKdV soliton solution is well known. For $\alpha = \beta = 1$ in the initial field variable, it reads

$$u = 2\sqrt{6} \operatorname{arctg} \frac{\lambda \sin(\mu\xi - \nu\tau)}{\mu \operatorname{ch}\lambda(\xi - s\tau)}, \quad (23.21)$$

where $\lambda = \sqrt{(\mu^3 - 2\nu)/3\mu}$ and $2s = 3\mu^2 - \lambda^2$. In the original variables, the solution

$$u = \left(2\sqrt{6}\kappa/k\right) \operatorname{sech}(\kappa(x - Vt)) \cos(kx - \omega t) \quad (23.22)$$

coincides with the expression (23.19). In the limit of small amplitudes (areas with double shading in Figs. 23.2 and 23.3c) solutions (23.19) and (23.21) correspond to the first step of the approximate procedure for finding soliton solutions of equations that are not exactly integrable. Two parameters of the soliton solution κ and k characterize the spatial size of the soliton envelope and the wave vector of the carrier wave. The frequency ω (in the laboratory frame of reference) and the soliton velocity V depend on parameters k and κ as follows: $\omega = k - \alpha k^3/2 + 3\beta k\kappa^2/2$ and $V = 1 - 3\alpha k^2/2 + \beta\kappa^2/2$. The first of these relations represents the nonlinear dispersion law similar to relation (23.17).

The following main steps in the method of multiple time scales are rather cumbersome. In addition, the original equations can be more varied than the ones given above, and the question remains about the existence of approximate breather solutions for them and the method for finding such the solutions. In many cases, the basic approximation is not enough, and the development of methods is required to find the solutions with greater accuracy. Therefore, it is easier to search for soliton solutions with different orders of the amplitude using the proposed methods of asymptotic expansions.

The analysis of the asymptotic procedure given above for the systems with strong dispersion suggests the necessary modernization of the method of asymptotic expansions. We are looking for a soliton solution in the form of a ‘‘carrier’’ traveling wave with frequency ω and wave number k . Its spatially localized envelope moves with a constant velocity V . The asymptotic procedure takes into account the smallness of the amplitude of the solution. However, it does not imply that the group velocity of the carrier wave V_g is close to the sound velocity and the velocity of the envelope. As it will be shown below, these velocities differ by values of the order of k^2 . In this

case at a small wave amplitude a , the soliton parameters (frequency and velocity) are close to those for the linear waves with an arbitrary wave number k . Its value is limited by the condition of long-wave consideration of the initial dynamical system, but within the framework of differential Eq. (23.14) it is arbitrary. This the soliton amplitude is the small parameter of the asymptotic expansion rather than the wave vector k .

The main principle of the proposed asymptotic procedure is the expansion of the solution in the Fourier series in harmonic functions of the moving phase of the “carrier wave” $\vartheta = kx - \omega t$ with the additional expansion of the Fourier coefficients in a power series in a small parameter associated with the amplitude of the soliton. The Fourier coefficients depend on their phase $(x - Vt)$ moving with a velocity close to the group velocity of linear waves.

Since the solution is periodic in coordinate and time in the coordinate frame of reference moving with the velocity of the envelope of a soliton V , we represent it in the form of the following expansion:

$$u(x, t) = \sum_{n=1}^{\infty'} (f_n(x - Vt) \cos n(kx - \omega t) + \varphi_n(x - Vt) \sin n(kx - \omega t)), \quad (23.23)$$

where summation, as above, is performed over positive odd integers. After substituting (23.23) into the original Eq. (23.14), we obtain the following infinite system of equations:

$$\alpha f_{nXXXX} - (V^2 - 1 + 6\alpha n^2 k^2) f_{nXX} - n^2(k^2 - \omega^2 - \alpha n^2 k^4) f_n + 4\alpha nk \varphi_{nXX} + 2n(k - \omega V - 2\alpha n^2 k^3) \varphi_{nX} + \beta P_n = 0, \quad (23.24)$$

$$\alpha \varphi_{nXXXX} - (V^2 - 1 + 6\alpha n^2 k^2) \varphi_{nXX} - n^2(k^2 - \omega^2 - \alpha n^2 k^4) \varphi_n - 4\alpha nk f_{nXX} - 2n(k - \omega V - 2\alpha n^2 k^3) f_{nX} + \beta Q_n = 0, \quad (23.25)$$

where the quantities P_n and Q_n represent the infinite series of the triple products of functions f_n and φ_n and their spatial derivatives. The explicit form of the expressions for P_n and Q_n is given in the Appendix.

The convergence of expansion (23.23) assumes a decreasing of the functions f_n and φ_n with number n . Let us introduce the expansion parameter ε . It is natural to assume that the parameter ε determines the amplitude of the soliton and the degree of localization for its envelope. However, now, for a given wave number k , the parameter ε determines not only the splitting of the soliton frequency ω from the frequency of linear waves with the same k , i.e., the value $\omega^2 - \omega_0^2(k) \sim \varepsilon^2$ with $\omega_0 \approx k - \alpha k^3/2$ (see (23.17)), but also the difference between the soliton velocity V and the group velocity of linear waves with this specified value of k : $V - V_g \sim \varepsilon^2$ with $V_g \approx 1 - 3\alpha k^2/2$. (We will verify this statement below). Let us emphasize the necessity to take into account the dispersion of linear waves (deviation from the

sound spectrum at finite values of the wave number). In addition, it is necessary to know the hierarchy of smallness for two sets of the functions f_n and φ_n . The form of the asymptotic expansion varies depending on the choice of ε : the amplitude of soliton, the amplitude of its fundamental harmonic, the region of localization or the splitting off for the frequency can be taken as a basis. But this ambiguity is of a formal nature and leads to a trivial decomposition of the solution parameters. The choice for ε is convenient and consistent in which it determines the spatial derivatives of the envelope, i.e., the functions f_n and φ_n . For it in the *main* approximation in the parameter ε , the nonlinear frequency shift is equal to $\omega^2 - \omega_0^2(k) = \gamma \varepsilon^2$, where $\gamma = \pm 1$ for a different choice of nonlinearity signs in (23.14). In this case in the linear limit in (23.24, 23.25), the coefficients for f_1 and φ_1 (but not for f_n and φ_n with $n > 1$) vanish.

The system of Eqs. (23.24, 23.25) is satisfied by the following power expansion in the small parameter ε :

$$f_n = \sum_{s=n}^{\infty'} f_{ns} \varepsilon^s, \quad \varphi_n = \sum_{s=n+1}^{\infty'} \varphi_{ns} \varepsilon^s, \tag{23.26}$$

where the prime denotes the summation through one. Because the dispersion law of linear waves has the form $\omega_0^2(k) = k^2 - \alpha k^4$, the expansion (23.26) must be supplemented with an expansion in the small parameter for nonlinear frequency shift

$$\omega^2 = k^2 - \alpha k^4 + \gamma \varepsilon^2 + N_4 \varepsilon^4 + N_6 \varepsilon^6 + \dots, \tag{23.27}$$

where $\gamma = \pm 1$, depending on dispersion and nonlinearity, and N_s are constants to be determined. In the linear limit for the group velocity of the waves we have $V_g \omega_0(k) = k - 2\alpha k^3$; i.e., the coefficients at φ_{1X} and f_{1X} in (23.24, 23.25) also vanish. Therefore, it is necessary to introduce an additional expansion in terms of a small parameter of the nonlinear shift of the group velocity or parameter:

$$\omega V = k - 2\alpha k^3 + \varepsilon^2 M_2/2 + \varepsilon^4 M_4/2 + \dots \tag{23.28}$$

(In fact, this is a series representation in terms of ε for the soliton velocity.) In this case, the quantities k and ε represent the parameters of the soliton solution. The self-consistency of the asymptotic procedure also requires the smallness of the spatial derivatives of the amplitudes f_n and φ_n . We assume that they depend on coordinates and time in the form $f_n = f_n(z)$ and $\varphi_n = \varphi_n(z)$ with $z = \varepsilon(x - Vt)$. Thus, the spatial characteristics of the envelope and the carrier wave can be considered as the parameters of the soliton.

The nonlinear terms of Eqs. (23.24, 23.25) are also expanded into series in ε . The first terms of these series for P_1 , P_3 , Q_1 , and Q_3 are given explicitly in the Appendix (see (23.46–23.49)). Substituting expressions (23.26–23.28) in (23.45–23.48) and

Eqs. (23.24, 23.25), we get an infinite system of ordinary differential equations for functions f_{ns} , φ_{ns} and coefficients N_n и M_n .

Let us demonstrate the proposed asymptotic procedure using the example of finding a solution up to the including value $\sim \varepsilon^4$:

$$u = \varepsilon f_{11} \cos \vartheta + \varepsilon^2 \varphi_{12} \sin \vartheta + \varepsilon^3 f_{13} \cos \vartheta + \varepsilon^3 f_{33} \cos 3\vartheta + \varepsilon^4 \varphi_{14} \sin \vartheta + \varepsilon^4 \varphi_{34} \sin 3\vartheta, \quad (23.29)$$

where the phase ϑ is $\vartheta = kx - \omega t$. To find the soliton solution with the specified accuracy, it is necessary to write out the equations determined by the coefficients at different harmonics $\cos(n\vartheta)$ and $\sin(n\vartheta)$ with different degrees ε^μ : $\mu = 3, 4, 5, 6$ for six functions f_{11} , f_{13} , f_{33} , φ_{12} , φ_{14} and φ_{34} . If we take into account that $\alpha^2 = 1$ and introduce the notations $S_2 = V_g^2 (M_2/k(1 - 2\alpha k^2) - \gamma/k^2(1 - \alpha k^2))$ and $d = V^2 - 1 + 6\alpha k^2 \approx \alpha k^2(3 - 2\alpha k^2)/(1 - \alpha k^2)$, then these equations can be written in the form

$$d f_{11}'' - \gamma f_{11} + (\beta k^4/4) f_{11}^3 = 0, \quad (23.30)$$

$$d f_{13}'' - \gamma f_{13} - (3\beta k^4/4) f_{11}^2 f_{13} = \alpha f_{11}^{IV} - S_2 f_{11}'' + N_4 f_{11} + 4\alpha k \varphi_{12}''' - M_2 \varphi_{12}' + \beta P_{15}(f_{11}, \varphi_{12}, f_{33}; f_{13} = 0), \quad (23.31)$$

$$72\alpha k^4 f_{33} = -(\beta k^4/4) f_{11}^3, \quad (23.32)$$

$$d \varphi_{12}'' - \gamma \varphi_{12} - \beta k^4 f_{11}^2 \varphi_{12} = 4\alpha k f_{11}''' + M_2 f_{11}' + (3\beta k^3/2) f_{11}^2 f_{11}', \quad (23.33)$$

$$d \varphi_{14}'' - \gamma \varphi_{14} - (\beta k^4/4) f_{11}^2 \varphi_{14} = \alpha \varphi_{12}^{IV} - S_2 \varphi_{12}'' + N_4 \varphi_{12} - 4\alpha k f_{13}''' + M_2 f_{13}' + M_4 f_{11}' + \beta Q_{16}(f_{11}, f_{13}, f_{33}, \varphi_{12}, \varphi_{34}; \varphi_{14} = 0), \quad (23.34)$$

$$72\alpha k^4 \varphi_{34} + 96\alpha k^3 f_{33}' + \beta Q_{34}(f_{11}, \varphi_{12}) = 0, \quad (23.35)$$

where the primes denote the derivatives with respect to the argument $z = \varepsilon(x - Vt)$. (Taking into account, the higher powers of the dispersion terms and the higher powers of the nonlinear terms in the original equation changes only the right-hand sides of these equations, which is not essential for solving the entire system of equations.) Equations (23.30–23.35), in addition to the functions of the argument z , contain three unknown constants N_4 , M_2 and M_4 , which are found from the condition of the decay of soliton solutions at infinity. (With our choice of expansions, we have $N_2 = 1$.) Equation (23.30) is the only nonlinear equation in the system. It determines the main characteristics of the soliton. The rest of the equations are the second-order linear differential equations with variable coefficients and with right-hand sides (equations for the quantities f_{1n} and φ_{1n}), and algebraic equations for the remaining quantities

f_{mn} and φ_{mn} with $m > 1$. Differential equations are of the same type and contain the same nonlinear terms $f_{11}^2 f_{1n}$ and $f_{11}^2 \varphi_{1n}$ with different numerical factors. From Eq. (23.30), it follows that for normal dispersion ($\alpha > 0$) solitons exist only for $\beta > 0$, and in this case $\gamma > 0$. Those, the soliton frequencies lie above the linear spectrum in the region of instability of nonlinear waves of a stationary profile with a constant amplitude. Similarly, for $\alpha < 0$ we have $\beta < 0$ and $\gamma < 0$. This corresponds to the results obtained above. A localized solution to Eq. (23.30) is easily found:

$$f_{11} = \left(2\sqrt{2}/k^2\right)\sqrt{\gamma/\beta}\operatorname{sech}\left(\sqrt{\gamma/d}(x - Vt)\varepsilon\right). \quad (23.36)$$

Thus, in the main approximation, the soliton solution has the following form (for simplicity, we put $\alpha = \beta = \gamma = 1$):

$$u = \left(2\sqrt{2}\varepsilon/k^2\right)\operatorname{sech}\left(\varepsilon(x - Vt)/\sqrt{d}\right)\cos(kx - \omega t), \quad (23.37)$$

which naturally coincides with the expressions (23.19) and (23.22) obtained above. (Note that $d \approx 3k^2$ for small k and $\kappa = \varepsilon/\sqrt{3}k$ in (23.22).)

The proposed asymptotic procedure is sufficient to obtain the soliton solutions with any (power-law) degree of accuracy. Substituting (23.36) into Eq. (23.32), we find for f_{33} :

$$f_{33} = -f_{11}^3/288 = -\left(\sqrt{2}/18k^6\right)\operatorname{sech}^3\left(\varepsilon(x - Vt)/\sqrt{d}\right). \quad (23.38)$$

From Eq. (23.33), we find the following expression for φ_{12} :

$$\varphi_{12} = \frac{12\sqrt{2}(d + 2k^2)}{7k^3d^{3/2}} \frac{sh\left(\varepsilon(x - Vt)/\sqrt{d}\right)}{ch^2\left(\varepsilon(x - Vt)/\sqrt{d}\right)} \quad (23.39)$$

and the value $M_2(k) = 4k/d(k)$ for the parameter M_2 from the condition of the decay of the solution φ_{12} at $x \rightarrow \pm\infty$. The solution for f_{13} of Eq. (23.31) with the known functions f_{11} , f_{33} , φ_{12} and parameter M_2 has the form $f_{13} = A\operatorname{sech}Z + B\operatorname{sech}^3Z$ with $Z = \varepsilon(x - Vt)/\sqrt{d}$. From the requirement for the absence of a resonant term in the right-hand side of Eq. (23.30), the parameter N_4 is determined: $N_4(k) = -1/d^2(k)$. Then, from the relation (23.34), the function φ_{34} is found, and from Eq. (23.34), the function φ_{14} and the coefficient M_4 are found. This completes the construction of the solution accurate to ε^4 . The nonlinear shifts of the frequency and velocity of the soliton relative to the corresponding quantities in the linear wave are determined by the formulas: $\omega \approx \omega_0(k)(1 + \beta\varepsilon^2/2\omega_0^2)$ and $V \approx V_0(k)(1 + \beta\varepsilon^2/2\omega_0^2(1 - 2k^2)(3 - 2k^2))$. In the limit of small values of k , the obtained formulas coincide with the correspondent expressions in the mKdV approximation (it is necessary to make the replacement $\varepsilon \rightarrow \kappa = \varepsilon/\sqrt{3}k$). From the

obtained formulas, it follows that the value $(\varepsilon/k)^2$ represents the real small parameter of the expansion. It follows that as the wave number k decreases, the region of validity of the obtained solution for low-amplitude envelope solitons narrows (see shaded areas in Figs. 23.1f and 23.2a).

The proposed asymptotic procedure can also be used to construct the soliton solutions for multidimensional nonlinear systems. For example, the first steps of this procedure were used to construct the solutions for soliton excitations in plates (Kovalev and Sokolova 2010) and for surface solitons (Kovalev et al. 2002).

23.4 Conclusions

In this work, the features of the asymptotic method for obtaining the solutions for two-parameter envelope solitons are studied in detail. The method is similar to the variant of asymptotic expansions in the theory of nonlinear oscillations (A. Poincaré). The main point is the expansion of the solutions in the Fourier series in terms of periodic linear waves, followed by the expansion of the amplitudes in a power series in terms of small deviations of the soliton parameters from the parameters of linear wave dispersion relation. The conditions for the existence of such excitations are analyzed, and this method is compared with other possible approaches to the problem. The main attention is paid to the features of the proposed method as applied to the nonlinear dynamics of weakly dispersive media. The peculiarities of the procedure for finding the breather solutions are demonstrated with the example of the modified Boussinesq equation.

Appendix

Explicit expressions for infinite polynomials P_n and Q_n are as follows:

$$\begin{aligned}
 P_n = & \sum_{m=1}^{\infty'} (a_m^2 - b_m^2 + A_m \Phi_{m+n} + B_m \Psi_{m+n})/2 + \sum_{m=2}^{\infty'} (A_{m+n} \Phi_m + B_{m+n} \Psi_m)/2 \\
 & + (A_1 \Phi_{n-1} + A_3 \Phi_{n-3} + \dots + A_{n-2} \Phi_2)/2 \\
 & - (B_1 \Psi_{n-1} + B_3 \Psi_{n-3} + \dots + B_{n-2} \Psi_2)/2,
 \end{aligned} \tag{23.40}$$

$$\begin{aligned}
 Q_n = & \sum_{m=1}^{\infty'} (a_m^2 - b_m^2 + A_m \Psi_{m+n} - B_m \Phi_{m+n})/2 - \sum_{m=2}^{\infty'} (A_{m+n} \Psi_m - B_{m+n} \Phi_m)/2 \\
 & + (A_1 \Psi_{n-1} + A_3 \Psi_{n-3} + \dots + A_{n-2} \Psi_2)/2 - \\
 & (B_1 \Phi_{n-1} + B_3 \Phi_{n-3} + \dots + B_{n-2} \Phi_2)/2,
 \end{aligned} \tag{23.41}$$

where the expansion coefficients of the function $\partial u/\partial x$ are denoted by

$$a_n = f'_n + kn\varphi_n, \quad b_n = \varphi'_n - knf_n, \tag{23.42}$$

and the expansion coefficients of the second derivative $\partial^2 u/\partial x^2$ are denoted by

$$A_n = f''_n - k^2n^2 f_n + 2kn\varphi'_n, \quad B_n = \varphi''_n - k^2n^2\varphi_n - 2knf'_n. \tag{23.43}$$

In addition, the following notation is introduced in formulas (23.40, 23.41):

$$\Psi_n = \sum_{s=1}^{n-1'} (a_s b_{v-s} + b_s a_{n-s})/2, \tag{23.44}$$

$$\Phi_n = \sum_{s=1}^{n-1'} (a_s a_{v-s} - b_s b_{n-s})/2 + \sum_{s=1}^{\infty'} (a_s a_{s+n} + b_s b_{s+n}). \tag{23.45}$$

Taking into account expansions (23.26), formulas (23.40, 23.41) for the first harmonics can be approximately rewritten in the form of series in powers of ε :

$$\begin{aligned} P_1 = & \varepsilon^3 P_{13} + \varepsilon^5 P_{15} + \dots = \varepsilon^3 (-k^4 f_{11}^3/4) \\ & + \varepsilon^5 (k^2 f_{11} f_{11}'^2 - k^4 f_{11} \varphi_{12}^2 - 9k^3 f_{11}^2 \varphi_{12}' \\ & + 3k^4 f_{11}^2 f_{13} - 3k^2 f_{11}^2 f_{11}'' + 3k^4 f_{33} f_{11}^2)/4 + \dots \end{aligned} \tag{23.46}$$

$$\begin{aligned} P_3 = & \varepsilon^3 P_{33} + \varepsilon^5 P_{35} + \dots = \varepsilon^3 (k^4 f_{11}^3/4) \\ & + \varepsilon^5 (-5k^2 f_{11} f_{11}'^2 - 3k^4 f_{11} \varphi_{12}^2 - 4k^3 f_{11}^2 \varphi_{12}' \\ & + 3k^4 f_{11}^2 f_{13} - k^2 f_{11}^2 f_{11}'' - 8k^3 f_{11} f_{11}' + 18k^4 f_{33} f_{11}^2)/4 + \dots \end{aligned} \tag{23.47}$$

$$Q_1 = \varepsilon^4 (k^4 f_{11}^2 \varphi_{12} + 3k^3 f_{11}^2 f_{11}'/2) + \varepsilon^6 Q_{16} + \dots, \tag{23.48}$$

$$Q_3 = \varepsilon^4 (3k^4 f_{11}^2 \varphi_{12}/4 + k^3 f_{11}^2 f_{11}') + \varepsilon^6 Q_{36} + \dots. \tag{23.49}$$

References

Bogoliubov, N.N., Mitropolsky, Y.A.: Asymptotic Methods in the Theory of Nonlinear Oscillations. Gordon & Breach, NY (1961)
 Braun, O.M., Kivshar, Y.S.: The Frenkel—Kontorova Model. Springer, UK (2004)
 Dodd, R.K., Eilbeck, J.C., Gibbon, J.D., Morris, H.C.: Solitons and Nonlinear Wave Equations. Academic Press, London (1984)

- Eleonskii, V.M., Silin, V.P.: Theory of waves that are close to exact solutions of nonlinear electrodynamics and optics, I, III. *JETP* **29**, 317–325; **30**, 262–271 (1969)
- Eleonskii, V.M., Silin, V.P.: Theory of self trapping of electromagnetic field in a nonlinear medium. *JETP* **31**, 918–929 (1970)
- Eleonskii, V.M., Kulagin, N.E., Novozhilova, N.S., Silin, V.P.: Method of asymptotic expansions and qualitative analysis of finite-dimensional models in theory of nonlinear field, pp. 1–19. Moscow, Preprint N 272 PLAN USSR (1961). (in Russian)
- Eleonskii, V.M., Kulagin, N.E., Novozhilova, N.S., Silin, V.P.: On self localization in space and time of the solutions for nonlinear equations. In: *Methods of Qualitative Theory of Differential Equations*, pp. 73–92. GSU, Gorky (1982)
- Gardner, C.S., Greene, J.P., Kruskal, M.D., Miura, K.M.: Method for solving the Korteweg-de Vries equation. *PRL* **18**, 1201–1204 (1968)
- Kivshar, Y.S., Agrawal, G.P.: *Optical Solitons*. Elsevier Science, San Diego, USA (2003)
- Kosevich, A.M., Kovalev, A.S.: Self-localization of vibrations in a one-dimensional chain. *JETP* **40**, 891–896 (1974)
- Kosevich, A.M., Kovalev, A.S.: *Introduction to Nonlinear Physical Mechanics*. Naukova Dumka, Kiev (1989). (in Russian)
- Kovalev, A.S., Sokolova, E.S.: Two-parameter dynamical solitons in thin elastic plates. *Low Temp. Phys* **36**, 3314 (2010). <https://doi.org/10.1063/1.3421088>
- Kovalev, A.S., Syrkin, E.S., Maugin, J.A.: Multidimensional and surface solitons in a nonlinear elastic medium. *Low Temp. Phys.* **28**, 452–464 (2002). <https://doi.org/10.1063/1.1491186>
- Menton, N., Sutcliffe, P.: *Topological Solitons*. Cambridge University Press, UK (2004)
- Moiseev, N.N.: *Asymptotic Methods of Nonlinear Mechanics*. Nauka, Moscow (1969). (in Russian)
- Nayfeh, A.H.: *Introduction to Perturbation Techniques*. A Wiley Interscience Publication, NY (1981)
- Newell, A.C.: *Solitons in Mathematics and Physics*. Society for Industrial and Applied Mathematics, University of Arizona (1985)
- Novikov, S.P., Manakov, S.V., Pitaevskii, L.P., Zakharov, V.P.: *Theory of Solitons. The Inverse Scattering Method*. Springer, US (1984)
- Sulymenko, O.A., Prokopenk, O.V., Teberkevych, V.S., Slavin, A.V., Serga, A.A.: Bullets and droplets: two-dimensional spin-wave solitons in modern magnonics. *LTP* **44**, 602–620 (2018)
- Tajiri, M., Murakami, Y.: On breather solutions to the Boussinesq equation. *J. Phys. Soc. Jpn.* **58**, 3585–3590 (1989)
- Whitham, G.B.: *Linear and Nonlinear Waves*. John Wiley & Sons, New York (1974)
- Zakharov, V.E., Shabat, A.B.: Exact theory of two-dimensional self-focusing and one-dimensional self-modulation of waves in nonlinear media. *JETP* **34**, 62–69 (1972)

Chapter 24

Method of Superimposed Meshes for Solving Nonlinear Dynamic Problems



Volodymyr Martynenko

Abstract The paper presents a theoretical justification and examples of applications of the previously developed method of superimposed meshes for solving continuous dynamics problems with different types of nonlinearities. The proposed method aims to benefit the relevant scientific question of an adequate modeling of anisotropic nonlinear mechanical properties of solid deformable bodies using finite element codes since there is no a universal approach to such the modeling at the moment. Rearranging the Lagrangian functional of a total energy of a deformed body shows a possibility to apply the method of superimposed meshes to modeling of a full level of anisotropy of nonlinear mechanical properties when solving dynamic problems. Consideration of the proposed solution procedure shows that the use of the method of superimposed meshes does not affect the problem scale and only influences the post processing stage. A theoretical scheme presented in the paper allows either the current tools of commercial finite element codes to be used or user subroutines to be created in order to implement the method of superimposed meshes. Presented algorithm indicates a fact that this method extends modeling capabilities of the computer-aided engineering software and user-created finite element codes.

Keywords Finite element method · Anisotropic viscoelasticity · Nonlinear dynamics · Method of superimposed meshes · Total energy · Solid deformable body

24.1 Introduction

Consideration of the nonlinear dynamics of complex solid structures is crucial for different cases; for example, when there is a need to model the opening contacts as it was discussed in Rusanov et al. (2018), when the highly nonlinear properties significantly influence the time and mode of the dynamic rupture, as it was determined in Martynenko et al. (2018), or when the nonlinear bearing properties impact the rotor

V. Martynenko (✉)

Dynamics and Strength of Machines Department, National Technical University “Kharkiv Polytechnic Institute”, Kharkiv 61000, Ukraine
e-mail: martynenko.volodymyr@gmail.com

dynamics behavior of turbomachines, as it was studied in Martynenko (2016, 2018), Martynenko and Martynenko (2019, 2020).

When modeling the nonlinear dynamic behavior of composite structural elements and machines, engineers and scientists face a number of problems related to the need of taking into account anisotropy of composite physical properties. There is a sufficiently developed mathematical apparatus for their linear elastic behavior, as evidenced by Peters (1998), but there is a lack of modeling methods for complex nonlinear properties such as plasticity, creep, and viscoelasticity.

24.1.1 The Sources of Anisotropy of Polymer Composite Properties

The dynamic viscoelastic behavior of polymer composites strongly depends on their microstructure that was shown in Kligman et al. (1981) and Nikkeshi et al. (1998), and it is also conditioned by the viscous properties of their polymer matrix which were investigated in Guo et al. 2011; Kosukegawa et al. 2008; Marin et al. 1975. The anisotropic nature of composite materials affects their fracture which was established by the explicit dynamics investigations in Radchenko and Radchenko (2012). Luo et al. 2018 performed a series of experiments and experimentally proved the crucial influence of the molecular orientation on the dynamic viscoelastic properties of polymers. Another experimental investigation of the dynamic viscoelastic behavior of a polymer for different temperatures was made in Liu et al. (2014). Free and forced vibration characteristics of sandwich plates with isotropic skins and viscoelastic core were determined in Ojha and Dwivedy (2019). The viscoelastic response of a carbon fiber reinforced polymer composite under the dynamic loading was studied in Zhang et al. 2007. The curing process also affects the dynamic viscoelastic properties of polymer composites which were discussed in Kim et al. 2010; Niu et al. 2019. Another studies of viscoelastic storage and loss moduli were carried out in the paper (Javidan and Kim 2020).

24.1.2 The Different Degrees of Anisotropy of Elastic and Viscoelastic Properties

There are several approaches to modeling of anisotropy of viscoelastic properties—from the ones in which their level of anisotropy is determined by the level of anisotropy of elastic properties to the general independent models of elastic and viscoelastic parts discussed in Skrzypek and Ganczarski (2015) and Vinson and Sierakowski (2006).

The material models in which the level of anisotropy of time-dependent viscoelastic properties corresponds to the level of anisotropy of elastic ones have

been widely used for different materials. For example, the work Lif et al. (1998) uses this model for simulations of the nonstationary response of paper sheets. Liefieith and Kolling (2007) consider this type of elasticity for its implementation while solving the explicit dynamics problem of rubber bodies.

However, there are a number of situations where the general degree of anisotropy should be taken into account. Shu and Onat (1967) first raised a question of the need for anisotropic viscoelasticity model to solve practical problems and made its formulation. Taylor et al. (2009) proved the necessity to model anisotropic viscoelasticity for biomechanical problems. Nedjar (2007) presented a method for solving nonlinear anisotropic viscoelastic models to describe the mechanical behavior of fibrous composites. Santos et al. (2011) investigated a propagation of waves in transversally isotropic viscoelastic thin plates when solving elliptic boundary value problems formulated in a space–frequency domain using the finite element (FE) Galerkin procedure. Bretin and Wahab (2011) demonstrated an applicability of Green’s functions to a solution of an anisotropic viscoelastic material model. Hwu and Chen (2011) applied the finite boundary method to the consideration of anisotropic viscoelastic plane bodies with defects. Bai and Tsvankin (2016) presented a space–time finite difference algorithm for modeling of a transversely isotropic body with a vertical axis of symmetry. Hilton (2012) proposed the fractional derivative approach to modeling of the full anisotropy of the viscoelastic materials. Nguyen et al. (2007) developed constitutive models for the anisotropic, finite deformation viscoelastic behavior of soft fiber-reinforced composites. Kuo and Hwu (2013) discussed the extended Stroh formalism for the linear anisotropic viscoelasticity modeling. Tzeng et al. (2012) applied anisotropic a viscoelastic material model to the analysis of the overwrap cylinders with its experimental validation.

24.1.3 Effects and Methods in Modeling of Nonlinear Dynamic Anisotropic Viscoelastic Properties

The dynamic viscoelastic properties of polymer composites can be essentially anisotropic which was shown in Amiri-Rad et al. (2019). They significantly affect the dissipation power of the material considered in Mika et al. (2019) and damping properties discussed in Zamani et al. (2015). The role of the nonlinear dynamic viscoelastic properties in accurate predictions of the solid body mechanics is crucial when modeling thermoforming processes of thermoplastics determined in Erchiqui et al. (2005) and loading of asphalt mixtures performed in Zhang et al. (2011).

The anisotropic dynamic viscoelastic material properties can be modeled by considering the different storage and loss moduli in different directions, as it was done for a transversally isotropic lamina in Pathan et al. (2017). Another approach to modeling of the generally anisotropic viscoelastic composite dynamics is the investigation of wave propagations in the media presented in Castaings and Hosten (2003); Hernando Quintanilla et al. (2015); Zhu et al. (2020). The dynamic fracture

of composite materials can also be estimated by the damage accumulation calculation which includes the anisotropic viscoelastic model proposed in Nciri et al. (2017).

24.1.4 The Reasons and Benefits of Using the Method of Superimposed Meshes

As it follows from the literature review, simulations of the nonlinear static and dynamics problems of the polymer composite mechanics should be performed with a careful consideration of composite anisotropic elastic and viscoelastic properties.

While the possibility to model the elastic anisotropic properties is widely developed, the general anisotropy of composite viscoelastic properties not always is taken into account due to the complexity of the resulting model.

The modern commercial finite element (FE) computer-aided engineering (CAE) codes provide users with a wide range of possibilities to solve the nonlinear problems of solid deformable bodies (SDB) of any three-dimensional shape. However, all the presented commercial FE algorithms cannot take into account any level of anisotropy of viscoelastic properties when solving nonlinear static and dynamic SDB problems. To eliminate this, the method of superimposed meshes (MSM) was proposed and tested using various computational models in Martynenko (2017) for commercial CAE codes. The necessity of modeling of independent anisotropic properties of fiber reinforced composites was proved by the numerical (Martynenko and Lvov 2017) and natural (Martynenko et al. 2019) experiments and applied to solving real problems of composite mechanics in Martynenko et al. (2020). The following paper shows the possibility to use the MSM for the solution of nonlinear dynamic problems with material nonlinearities.

24.1.5 The Insight of the MSM

The simplest application of the method of superimposed meshes can be implemented with two identical volumes created in the same place. They are consequently divided into finite element meshes—each volume with its own properties (elastic or viscoelastic). Since the algorithm for constructing a finite element (FE) meshes (mesher) works in the same manner for identical volumes with the same finite element partitioning settings, the nodes and elements of both grids are spatially identical. The next step is to merge all the nodes. Thus, the resulting nodes correspond to the elements of the elastic and viscoelastic groups at the same time, their number after merging gets twice smaller, and the number of elements remains unchanged. After this, the combined finite element model will deform together, and each of the layers of the FE mesh will make its own contribution to the energy potential. This means that the elements of each group of the material will be in the individual stress state in

the same displacement field. The resulting stress tensor field of the model is the sum of the stress tensors for each group of elements. Schematically, the methodology is shown in Fig. 24.1 (for the simplicity of representation, it deals with flat sheets of material; however, the concept works for the volumetric domains as well).

It is assumed that the usual viscoelastic model is identical to the combined model, consisting of layers of elastic and viscoelastic finite element meshes with a corresponding selection of elastic and viscoelastic parameters. Figure 24.2 shows the portions of elastic and viscoelastic elements in the combined rheological model.

Fig. 24.1 Schematic representation of the application of the method of superimposed meshes to modeling of anisotropic viscoelasticity of a square sheet of material

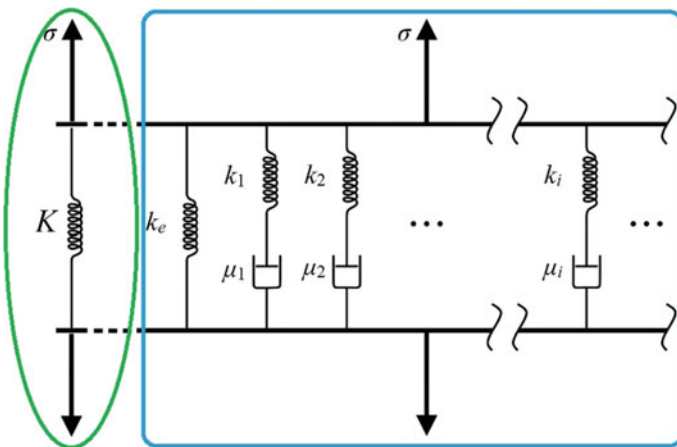
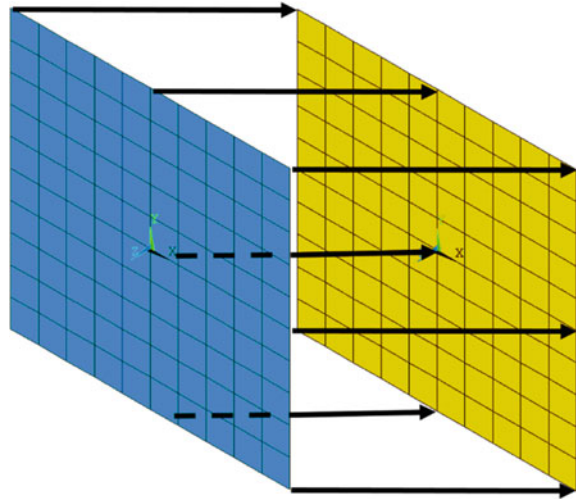


Fig. 24.2 Rheological model of the combined material connecting its elastic (green) and viscoelastic (blue) components

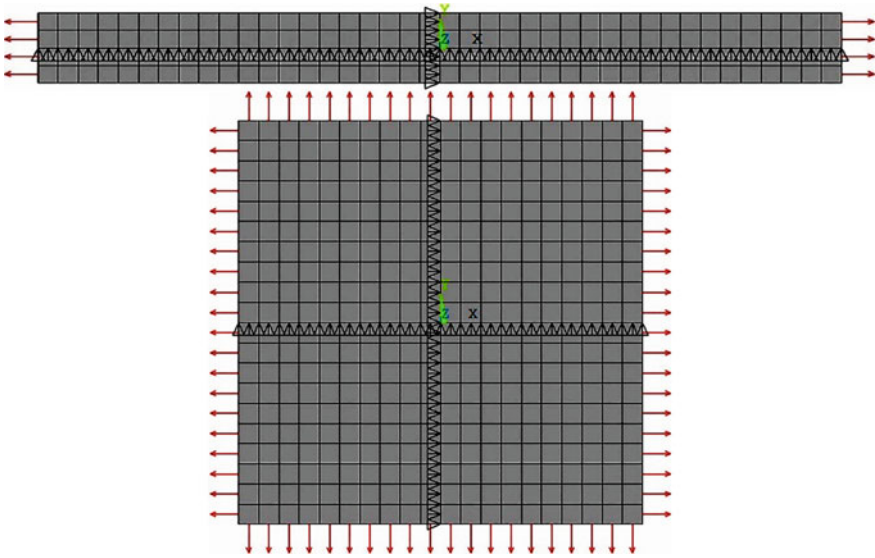


Fig. 24.3 One- and two-dimensional models for checking the correctness of applying the method of superimposed meshes

Martynenko (2017) considered a series of comparative numerical experiments on one-dimensional and two-dimensional models as shown in Fig. 24.3 for numerical confirmation of the proposed methodology which allowed it to be verified.

The current work covers the theoretical basis of the application of the MSM to solve the nonlinear dynamics problems.

24.2 Formulation of the MSM for the Elasticity Problem

24.2.1 Lagrangian Functional of the Elastic Material

The geometric relations in the three-dimensional Euclidean space with the coordinates x_1, x_2, x_3 can be written as follows:

$$\boldsymbol{\varepsilon} = \mathbf{D}\mathbf{u} \tag{24.1}$$

where $\boldsymbol{\varepsilon}$ is a strain vector; \mathbf{u} is a displacement vector; \mathbf{D} is a matrix of differential operators.

Physical relations for the case of a linear elastic body have the view:

$$\boldsymbol{\sigma} = \mathbf{C}\boldsymbol{\varepsilon} \tag{24.2}$$

where $\boldsymbol{\sigma}$ is a stress vector; \mathbf{C} is an elasticity matrix.

Then the Lagrangian functional for a three-dimensional elastic body is written in the following form:

$$W = \int_V \frac{1}{2} \mathbf{u}^T (\mathbf{D}^T \mathbf{C} \mathbf{D}) \mathbf{u} dV - \int_V \mathbf{f}^T \mathbf{u} dV - \int_{S_u} \mathbf{p}^T \mathbf{u} dS \quad (24.3)$$

where W is an elastic deformation energy; V is a volume of the elastic body; S_u is a part of an external surface of the body without deformations; \mathbf{f} is a vector of bulk loads; \mathbf{p} is a vector of surface loads.

The displacement vector is approximately represented as a linear superposition of the product of the nodal displacements of the finite element model and the orthogonal shape functions:

$$\mathbf{u} = \mathbf{n} \mathbf{U} \quad (24.4)$$

where \mathbf{n} is a shape function vector; \mathbf{U} is a nodal displacement matrix.

Application of the projection (24.4) to the functional (24.3) gives the following:

$$W = \int_V \frac{1}{2} \mathbf{U}^T (\mathbf{n}^T \mathbf{D}^T \mathbf{C} \mathbf{D} \mathbf{n}) \mathbf{U} dV - \int_V (\mathbf{f}^T \mathbf{n}) \mathbf{U} dV - \int_{S_u} (\mathbf{p}^T \mathbf{n}) \mathbf{U} dS \quad (24.5)$$

24.2.2 Subdivision into Several Finite Element Meshes

If to consider M finite element meshes, then each of them will correspond to its own energy functional:

$$W_m = \int_{V_m} \frac{1}{2} \mathbf{U}_m^T (\mathbf{n}^T \mathbf{D}^T \mathbf{C}_m \mathbf{D} \mathbf{n}) \mathbf{U}_m dV_m - \int_{V_m} (\mathbf{f}_m^T \mathbf{n}) \mathbf{U}_m dV - \int_{S_{u_m}} (\mathbf{p}_m^T \mathbf{n}) \mathbf{U}_m dS \quad (24.6)$$

where $m = 1, \dots, M$; V_m is a volume of the body with the m th FE mesh; S_{u_m} is a free-of-deformation part of the body external surface with the m th FE mesh; W_m is an elastic deformation energy of the m th FE mesh; \mathbf{U}_m is a nodal displacement matrix of the m th FE mesh; \mathbf{f}_m is a bulk load vector of the m th FE mesh; \mathbf{p}_m is a surface load vector of the m th FE mesh; \mathbf{C}_m is an elasticity matrix of the m th FE mesh.

The generally anisotropic material model can be represented by 21 coefficients of the stiffness matrix. If to denote the number of nonzero components in the stiffness matrix with M , then it will be equal to 21 for the generally anisotropic material and less than 21 for the specific cases of anisotropy (e.g., 9 for orthotropy): $M \leq 21$. To represent the anisotropic nature of the stiffness matrix \mathbf{C} , the matrices \mathbf{C}_m are

constructed by the following rules:

$$\begin{aligned}
 [\mathbf{C}_1]_{abcd} &= 0, \quad abcd \neq 1111, \quad [\mathbf{C}_1]_{1111} = C_{1111}; \\
 [\mathbf{C}_2]_{abcd} &= 0, \quad abcd \neq 1122 \text{ or } 2211, \quad [\mathbf{C}_2]_{1122} = [\mathbf{C}_2]_{2211} = C_{1122}; \\
 [\mathbf{C}_3]_{abcd} &= 0, \quad abcd \neq 1133 \text{ or } 3311, \quad [\mathbf{C}_3]_{1133} = [\mathbf{C}_3]_{3311} = C_{1133}; \\
 &\dots \\
 [\mathbf{C}_M]_{abcd} &= 0, \quad abcd \neq 1212, \quad [\mathbf{C}_M]_{1212} = C_{1212}.
 \end{aligned} \tag{24.7}$$

These matrices are positively defined, and their sum exactly coincides with the original stiffness matrix \mathbf{C} since each of the matrices \mathbf{C}_m has one or two nonzero components of the stiffness matrix \mathbf{C} :

$$\sum_{m=1}^M \mathbf{C}_m = \mathbf{C} \tag{24.8}$$

The assumption that all the M FE meshes occupy the same volume bounded by the same surface, which is analogous to creating the meshes on a single volume basis, leads to simplifications in (24.6):

$$V_m = V; \quad S_{u\ m} = S_u \tag{24.9}$$

24.2.3 Combination of Superimposed Meshes

The requirement that the nodal displacements of all finite element meshes are equal (which is analogous to merging nodes of the meshes in the finite element code) has the following form:

$$\mathbf{U}_1 = \mathbf{U}_2 = \dots = \mathbf{U}_m = \dots = \mathbf{U}_M = \mathbf{U} \tag{24.10}$$

A sum of all the expressions in system (24.6), taking into account for the requirements (24.9) and (24.10), is:

$$\begin{aligned}
 \sum_{m=1}^M W_m &= \int_V \frac{1}{2} \mathbf{U}^T \left(\mathbf{n}^T \mathbf{D}^T \left\{ \sum_{m=1}^M \mathbf{C}_m \right\} \mathbf{D} \mathbf{n} \right) \mathbf{U} dV \\
 &\quad - \int_V \left(\left\{ \sum_{m=1}^M \mathbf{f}_m^T \right\} \mathbf{n} \right) \mathbf{U} dV - \int_{S_u} \left(\left\{ \sum_{m=1}^M \mathbf{p}_m^T \right\} \mathbf{n} \right) \mathbf{U} dS
 \end{aligned} \tag{24.11}$$

Incorporating it with the rule (24.8) and considering, that:

$$\sum_{m=1}^M \mathbf{f}_m = \mathbf{f}; \quad \sum_{m=1}^M \mathbf{p}_m = \mathbf{p} \quad (24.12)$$

delivers an expression:

$$\sum_{m=1}^M W_m = \int_V \frac{1}{2} \mathbf{U}^T (\mathbf{n}^T \mathbf{D}^T \mathbf{C} \mathbf{D} \mathbf{n}) \mathbf{U} dV - \int_V (\mathbf{f}^T \mathbf{n}) \mathbf{U} dV - \int_{S_u} (\mathbf{p}^T \mathbf{n}) \mathbf{U} dS \quad (24.13)$$

If to compare it with the formula (24.5), the following conclusion can be made:

$$\sum_{m=1}^M W_m = W \quad (24.14)$$

This means that a sum of the energies of all FE meshes with merged nodes and the physical properties described by the matrices \mathbf{C}_m is equivalent to the energy of one FE mesh with the physical properties described by the matrix \mathbf{C} . The minimization of the energy of the combined FE mesh presented in the relation (24.13) is equivalent to the minimization of the energy of the initial single FE mesh shown in the relation (24.5). The energy minimization procedure is an initial step of the solution of the finite element problem in the CAE codes and the equivalence of two minimizations indicates the equivalence of all further finite element algorithms and results.

24.2.4 Total Stress–Stain State Basing on Stress–Strain States in Superimposed Meshes

According to the geometric relations (24.1), deformations of each finite element mesh are identical and determined by the joint displacements $\boldsymbol{\varepsilon}_m = \boldsymbol{\varepsilon}$, and the stresses are included in the physical relations:

$$\boldsymbol{\sigma}_m = \mathbf{C}_m \boldsymbol{\varepsilon} \quad (24.15)$$

A sum of all the expressions in the system (24.15) is:

$$\sum_{m=1}^M \boldsymbol{\sigma}_m = \left\{ \sum_{m=1}^M \mathbf{C}_m \right\} \boldsymbol{\varepsilon} \quad (24.16)$$

Comparing this relation with the relations (24.8) and (24.2) gives:

$$\boldsymbol{\sigma} = \sum_{m=1}^M \boldsymbol{\sigma}_m \quad (24.17)$$

Thus, a sum of stress tensors in all the combined finite element meshes described by the relations (24.15) is equivalent to the stress tensor of the initial single finite element mesh shown in the physical relation (24.2). On top of that, the resulting surface and bulk loads are also determined by the sum of such loads on each of the finite element meshes according to (24.12).

24.2.5 *Extension of MSM to Nonlinear Nonstationary Problems*

The functional of the total energy of an elastic body taking into account inertial and damping forces can be represented in the following form:

$$W = \int_V \frac{1}{2} \mathbf{u}^T (\mathbf{D}^T \mathbf{C} \mathbf{D}) \mathbf{u} dV - \int_V \frac{1}{2} \mathbf{u}^T \mathbf{M} \ddot{\mathbf{u}} dV - \int_V \mathbf{u}^T \mathbf{B} \dot{\mathbf{u}} dV - \int_V \mathbf{f}^T \mathbf{u} dV - \int_{S_u} \mathbf{p}^T \mathbf{u} dS \quad (24.18)$$

where \mathbf{M} is a mass matrix; \mathbf{B} is a damping matrix; $\dot{\mathbf{u}}$ is a nodal velocity vector; $\ddot{\mathbf{u}}$ is a nodal acceleration vector.

The procedure of decomposition similar to the relations (24.7) is possible for the kinetic and dissipation energy terms. Then the resultant mass and damping matrices for the combined finite element model are written as a sum of similar matrices of each mesh of the model:

$$\sum_{m=1}^M \mathbf{M}_m = \mathbf{M}, \quad \sum_{m=1}^M \mathbf{B}_m = \mathbf{B} \quad (24.19)$$

However, since the mass and damping matrices do not represent the material anisotropy in most of cases, they can be completely specified for one of the materials—the first one, for example—and set to zero for the rest of materials: $\mathbf{M}_1 = \mathbf{M}$, $\mathbf{B}_1 = \mathbf{B}$, $\mathbf{M}_m = 0$, $\mathbf{B}_m = 0$, $m = 2, \dots, M$. Note that the general view of damping is considered here. Combination of damping matrices in the case of Rayleigh damping requires additional proofs but specification of the complete damping and mass matrix for one of the materials avoids this problem at least for the mass-dependent damping.

For viscoelastic behavior, the stress dependence is written similarly to the relation (24.2):

$$\boldsymbol{\sigma} = \int_0^t \mathbf{C}(t - \xi) \frac{d}{d\xi} \boldsymbol{\varepsilon} d\xi \quad (24.20)$$

Comparison of the expressions (24.3) and (24.20) gives the potential energy of a viscoelastic body:

$$W = \int_V \frac{1}{2} \mathbf{u}^T \mathbf{D}^T \int_0^t \mathbf{C}(t - \xi) \mathbf{D} \frac{d}{d\xi} \mathbf{u} d\xi dV - \int_V \mathbf{f}^T \mathbf{u} dV - \int_{S_u} \mathbf{p}^T \mathbf{u} dS \quad (24.21)$$

The time integral in this relation introduces the necessity of the numerical solution of the integral equation. Each iteration solves a problem similar to a regular static problem, but with a matrix \mathbf{C} corresponding to a specific point in time. Obviously, it will not violate the rule (24.8), which in this case looks as follows:

$$\sum_{m=1}^M \mathbf{C}_m(t) = \mathbf{C}(t) \quad (24.22)$$

Combination of Eqs. (24.18) and (24.21) allows total energy for dynamic behavior to be obtained:

$$\begin{aligned} W = & \int_V \frac{1}{2} \mathbf{u}^T \mathbf{D}^T \int_0^t \mathbf{C}(t - \xi) \mathbf{D} \frac{d}{d\xi} \mathbf{u} d\xi dV - \int_V \frac{1}{2} \mathbf{u}^T \mathbf{M} \ddot{\mathbf{u}} dV \\ & - \int_V \mathbf{u}^T \mathbf{B} \dot{\mathbf{u}} dV - \int_V \mathbf{f}^T \mathbf{u} dV - \int_{S_u} \mathbf{p}^T \mathbf{u} dS \end{aligned} \quad (24.23)$$

This equation contains material property matrices with the relations (24.19) and (24.22) which proves an applicability of the MSM to dynamic problems with material nonlinearities.

24.3 Calculation Using the MSM

24.3.1 Benchmarking

Obviously, the additional finite elements of the superimposed meshes in comparison with the original one should increase a computational time. To determine the dependence of computational time on number of materials used in the combined material model, one-, two-, three-, four-, and five-material meshes were built for the square finite element model as shown in Fig. 24.3. The end time is 100 s, and the number

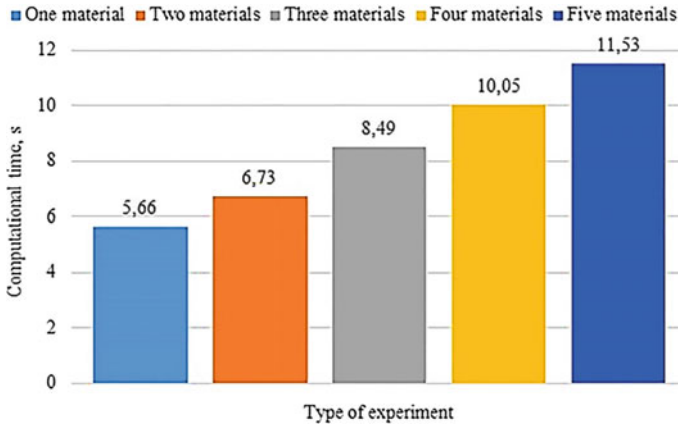


Fig. 24.4 Computational time versus number of materials dependence

of substeps is 200. The elastic properties were modeled for the one material, and viscoelastic properties were equally distributed among the rest of materials in the superimposed mesh model.

The solution process was performed using ANSYS Mechanical's direct solver using two 8-core Intel Xeon-2620 processors workstation operating at a maximum core frequency 2.4 GHz and with 128 Gb of RAM. This allowed a solution to be performed using the in-core memory mode with 16 parallel processes.

Figure 24.4 shows a dependence of a computational time on a number of materials in the combined material model.

As it follows from the diagram, the computational time increases not significantly when adding new materials to the combined material model. This is connected with the fact that the number of nodes and degrees of freedom are not increased by introduction of new superimposed meshed to the model due to merging of all added nodes with the existing ones. The total system of equations containing nodal displacements is not increased either and the solution time at each substep remains the same.

The computational time is affected by the additional equations in physical relations for the new superimposed meshes which matters only for recalculations between two substeps and is not as heavy procedure in terms of calculation time as the solution of equations containing nodal displacements. Thereby the proposed technique should not decrease the solution performance dramatically.

24.3.2 Verification

The verification of the MSM was performed using the model as shown in Fig. 24.5. The sections of the fiberglass pipeline modeled by a circular shell in a frictional

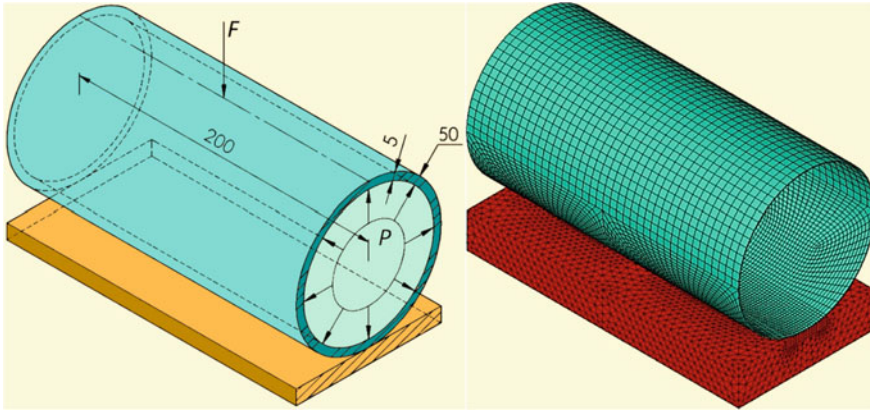


Fig. 24.5 Calculation and finite element models of the verification problem (values are in millimeters)

contact with a steel elastic foundation are fixed in the axial direction and against the rotation about the axial direction.

The model is under an action of the load in the middle of the section. The value of load is 2000 N, and it is distributed among several nodes to avoid the singularity of the point load application. The value of the internal pressure is 105 kPa.

Table 24.1 contains the input of material properties for the problem. The symmetry condition is further taken into account in two vertical planes which can be further observed in the contour plots of the Von Mises stresses—the only quarter of the initial model is displayed in Fig. 24.6.

The first calculation considers the regular one-material model of the fiberglass pipeline which incorporates both elastic and viscoelastic properties. The second calculation uses the two-material model with the merged meshes one of which is responsible for the fiberglass elastic properties and the second one represents only time-dependent properties. This simple two-material model was built to fully correspond to the regular finite element model which enables the possibility to perform further comparison of the results.

Figure 24.6a, b shows contour graphs of the displacement and von Mises equivalent stress fields, respectively, in the construction solved for isotropic viscoelasticity using the one-material shell model for the final time 100 s. Figure 24.6c, d shows similar graphs for isotropic viscoelasticity in case of the combined two-material model. The stress field is averaged for two materials of the shell in this case.

Figure 24.7a, b presents the dependencies of the vertical displacement and von Mises equivalent stress on time for the location of the point load (black curves) and point, located in the opposite top end of the pipe (gray curves) for the one-material case. The same curves for the two-material case are identical to these ones taking into account the discussed feature of the stress distribution. They are not presented due to a negligible error which is evaluated in Table 24.2.

Table 24.1 Calculation and finite element models of the verification problem (values are in millimeters)

Material	Material parameter	Designation	Value	Unit
Steel	Elastic modulus	E_s	2×10^{11}	Pa
	Poisson's coefficient	ν_s	0.26	–
	Density	ρ_s	7800	kg/m ³
Fiberglass	Elastic moduli in circumferential and axial directions	E_θ, E_z	2×10^{10}	Pa
	Elastic modulus in radial direction	E_r	8×10^9	Pa
	Shear moduli between circumferential/axial and radial directions	$G_{r\theta}, G_{rz}$	2.5×10^9	Pa
	Shear modulus between circumferential and axial directions	$G_{\theta z}$	1.5×10^9	Pa
	Poisson's ratio between circumferential and axial directions	$\nu_{\theta z}$	0.3	–
	Poisson's ratio between circumferential and radial directions/axial and radial directions	$\nu_{\theta r}, \nu_{zr}$	0.75	–
	Prony series multipliers	a_1, a_2, a_3, a_4	0.1, 0.15, 0.2, 0.3	–
	Relaxation times	$\tau_1, \tau_2, \tau_3, \tau_4$	10, 12, 15, 20	s
Density	ρ_f	2000	kg/m ³	

This table presents the total displacement values and equivalent stress in the location of the point load for the one- and two-material shell models with an evaluation of errors for the two-material case in comparison with the one-material one.

As it follows from the table and the figures above, the stress error connected with a use of the proposed combined material model is negligible and comparable with an engineering accuracy.

Note that this is just a modeling example not intended to represent all the capabilities of the MSM but to verify its adequacy in comparison with the standard finite element approaches used in the CAE software ANSYS in these case.

The further use of the MSM can then be extended to the anisotropic viscoelastic properties and dynamic problems, arising for the considered example in case of pulsations of internal pressure in the pipe.

There is a various range of applications where the nonlinear dynamics problems of anisotropic viscoelastic composites are relevant but limited by the modeling capabilities of the CAE codes, namely composite blades of fans and turbfans, casings, plane sheathing.

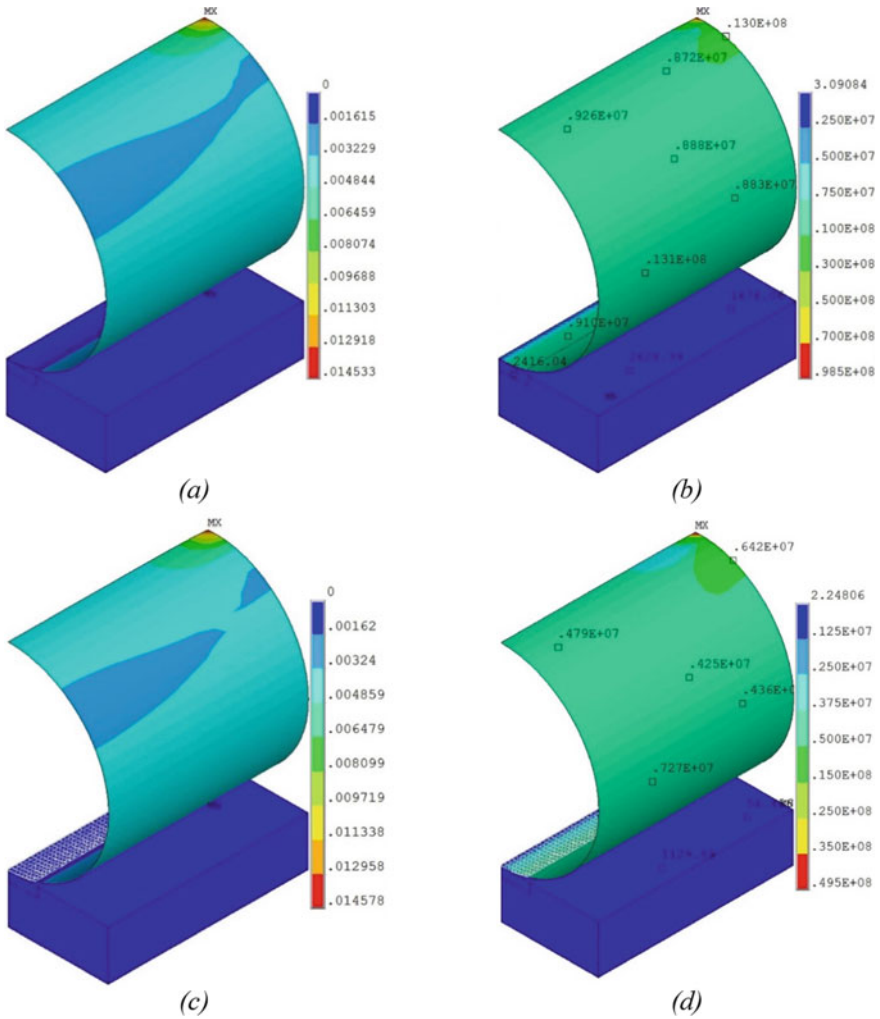


Fig. 24.6 Comparison of the results: **a** total displacement distribution for the one-material shell model, (m); **b** von Mises equivalent stress distribution for the one-material shell model, (Pa); **c** total displacement distribution for the two one-material shell model, (m); **d** von Mises equivalent stress distribution for the two-material shell model, (Pa)

24.4 Conclusions

The paper presented a theoretical justification of the method of superimposed meshes. Consideration of the energy functional of the anisotropic body for the single mesh and a set of artificially constructed meshes with merged node indicate their equivalence for both static and dynamic problems. This fact proves the identity of the further solution procedures for single and combined meshes. Since the finite element

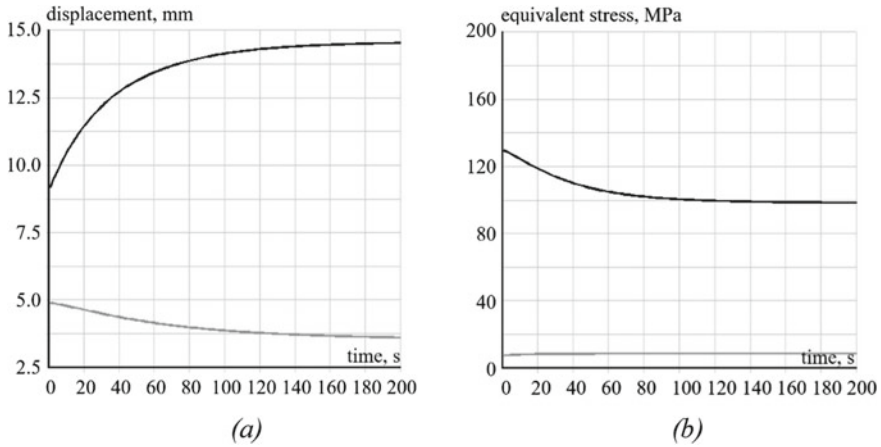


Fig. 24.7 Dependencies on time: **a** vertical displacement versus time curves; **b** equivalent stress versus time curves

Table 24.2 Equivalent stresses and relative error estimations

Case		Tot. disp., 10^{-3} m	Stress, 10^6 Pa	Relative error, %	
				Tot. disp.	Stress
One-material ANSYS test	Elastic	9.251	129.8	–	–
	Viscoelastic	5.282	31.3	–	–
	Total	14.533	98.5	–	–
Two-material ANSYS test	Elastic	9.253	130.2	< 0.1	0.3
	Viscoelastic	5.325	31.2	0.8	0.3
	Total	14.578	99	0.3	0.5

procedures used in the CAE codes are based on the minimization of the energy functional at the first step, the superimposed meshes with merged nodes allow obtaining the same result as a regular finite element mesh. On top of that, using these meshes open the opportunities to construct any level of anisotropy of viscoelastic properties for the solution of dynamic problems of polymer composites which is not available in the commercial CAE codes by default. This fact allows the MSM to be considered as an addition to the finite element method.

The proposed method of superimposed meshes allows taking into account the anisotropic viscoelastic properties of the material in the finite element codes, which reveals all the possibilities of the solution of two- and three-dimensional viscoelasticity problems, including homogeneous and multilayer shells. The method includes differences in relaxation kernels and temperature shear functions for different spatial directions. The MSM, originally designed for CAE FE codes to extend their capabilities in modeling of anisotropic viscoelasticity of materials, is not only practically but theoretically justified. This allows considering it as a modernization of the FE

method, which in some cases greatly simplifies algorithms for solving a finite element problem, especially where it is necessary to set the relaxation matrix of a viscoelastic or creeping material to make each of matrix components expressed by the hereditary function generally independent of the others. The presented approach indicates an applicability of this method to dynamic problems with material nonlinearities that enhances its capabilities significantly.

The method of superimposed meshes introduces the following benefits:

1. It provides commercial CAE codes with the possibility to solve nonlinear static and dynamic problems of solid deformable bodies with the general level of anisotropy of viscoelastic properties which is unavailable option by default.
2. It allows users of the finite element codes, either commercial or individual, to implement the anisotropic properties of the material without creation of additional user subroutines or algorithms.
3. Its simplicity in combination with a theoretical justification allows scientists and engineers to use it not only in scientific, but also in common engineering purposes for the solution of nonlinear dynamic problems of solid deformable bodies using the finite element method.
4. The high popularity of the finite element algorithms makes the MSM competitive and easy-to-use in comparison with non-FE procedures developed to solve the nonlinear problems of anisotropic viscoelastic solid deformable bodies.

References

- Amiri-Rad, A., Pastukhov, L.V., Govaert, L.E., van Dommelen, J.A.W.: An anisotropic viscoelastic-viscoplastic model for short-fiber composites. *Mech. Mater.* **137**, 103141 (2019). <https://doi.org/10.1016/j.mechmat.2019.103141>
- Bai, T., Tsvankin, I.: Time-domain finite-difference modeling for attenuative anisotropic media. *Geophysics* **81**, 163–176 (2016). <https://doi.org/10.1190/geo2015-0424.1>
- Bretin, E., Wahab, A.: Some anisotropic viscoelastic Green functions. *Contemp. Math.* **548**, 129–148 (2011)
- Castaigns, M., Hosten, B.: Guided waves propagating in sandwich structures made of anisotropic, viscoelastic, composite materials. *J. Acoust. Soc. Am.* **113**, 2622–2634 (2003). <https://doi.org/10.1121/1.1562913>
- Erchiqui, F., Gakwaya, A., Rachik, M.: Dynamic finite element analysis of nonlinear isotropic hyperelastic and viscoelastic materials for thermoforming applications. *Polym. Eng. Sci.* **45**, 125–134 (2005). <https://doi.org/10.1002/pen.20238>
- Guo, J., Hu, C.N., Huang, W.F.: Dynamic viscoelasticity of poly(ether ester) containing zinc. *Adv. Mater. Res.* **197–198**, 1263–1266 (2011). <https://doi.org/10.4028/www.scientific.net/AMR.197-198.1263>
- Hernando Quintanilla, F., Fan, Z., Lowe, M.J.S., Craster, R.V.: Guided waves' dispersion curves in anisotropic viscoelastic single- and multi-layered media. *Proc. R. Soc. A Math. Phys. Eng. Sci.* **471** (2015). <https://doi.org/10.1098/rspa.2015.0268>
- Hilton, H.H.: Generalized fractional derivative anisotropic viscoelastic characterization. *Materials (basel)* **5**, 169–191 (2012). <https://doi.org/10.3390/ma5010169>
- Hwu, C., Chen, Y.C.: Analysis of defects in viscoelastic solids by a transformed boundary element method. *Procedia Eng.* **10**, 3038–3043 (2011). <https://doi.org/10.1016/j.proeng.2011.04.503>

- Javidan, M.M., Kim, J.: Experimental and numerical sensitivity assessment of viscoelasticity for polymer composite materials. *Sci. Rep.* **10**, 1–9 (2020). <https://doi.org/10.1038/s41598-020-57552-3>
- Kim, M.H., Min, S.H., Ferracane, J., Lee, I.: Initial dynamic viscoelasticity change of composites during light curing. *Dent. Mater.* **26**, 463–470 (2010). <https://doi.org/10.1016/j.dental.2010.01.004>
- Kligman, R.L., Madigosky, W.M., Barlow, J.R.: Effective dynamic properties of composite viscoelastic materials. *J. Acoust. Soc. Am.* **70**, 1437–1444 (1981). <https://doi.org/10.1121/1.387100>
- Kosukegawa, H., Mamada, K., Kuroki, K., Liu, L., Inoue, K., Hayase, T., Ohta, M.: Measurements of dynamic viscoelasticity of poly (vinyl alcohol) hydrogel for the development of blood vessel biomodeling. *J. Fluid Sci. Technol.* **3**, 533–543 (2008). <https://doi.org/10.1299/jfst.3.533>
- Kuo, T.L., Hwu, C.: Interface corners in linear anisotropic viscoelastic materials. *Int. J. Solids Struct.* **50**, 710–724 (2013). <https://doi.org/10.1016/j.ijsolstr.2012.11.004>
- Liefelth, D., Kolling, S.: An anisotropic material model for finite rubber viscoelasticity. *LS-DYNA Adwenderforum* 25–54 (2007)
- Lif, J.O., Östlund, S., Fellers, C.: Applicability of anisotropic viscoelasticity of paper at small deformations. *Mech. Time-Depend. Mater.* **2**, 245–267 (1998). <https://doi.org/10.1023/A:1009818022865>
- Liu, B., Xu, J., Li, Y.: Constitutive investigation on viscoelasticity of polyvinyl butyral: experiments based on dynamic mechanical analysis method. *Adv. Mater. Sci. Eng.* **2014** (2014). <https://doi.org/10.1155/2014/794568>
- Luo, F., Liu, X., Yan, C., Liu, H., Dong, M., Mai, X., Shen, C., Liu, C., Zhang, J., Wang, N., Guo, Z.: Molecular orientation dependent dynamic viscoelasticity in uni-axially drawn polycarbonate. *Polym. Test.* **69**, 528–535 (2018). <https://doi.org/10.1016/j.polymertesting.2018.06.009>
- Marin, G., Labaig, J., Monge, P.: Dynamic viscoelasticity of entangled polymers. *Polymer (guildf)* **16**, 223–226 (1975). [https://doi.org/10.1016/0032-3861\(75\)90058-0](https://doi.org/10.1016/0032-3861(75)90058-0)
- Martynenko, G.: The interrelated modelling method of the nonlinear dynamics of rigid rotors in passive and active magnetic bearings. *East.-Eur. J. Enterp. Technol.* **2**, 4 (2016). <https://doi.org/10.15587/1729-4061.2016.65440>
- Martynenko, G.: Accounting for an interconnection of electrical, magnetic and mechanical processes in modeling the dynamics of turbomachines rotors in passive and controlled active magnetic bearings. In: 2018 IEEE 3rd International Conference on Intelligent Energy and Power Systems (IEPS), pp. 326–331. IEEE (2018)
- Martynenko, G., Martynenko, V.: Numerical determination of active magnetic bearings force characteristics taking into account control laws based on parametric modeling. In: 2019 IEEE International Conference on Modern Electrical and Energy Systems (MEES), pp. 358–361. IEEE (2019)
- Martynenko, G., Martynenko, V.: Rotor dynamics modeling for compressor and generator of the energy gas turbine unit with active magnetic bearings in operating modes. In: 2020 IEEE Problems of Automated Electrodrive. Theory and Practice (PAEP), pp. 1–4. IEEE (2020)
- Martynenko, V., Hrytsenko, M., Martynenko, G.: Technique for evaluating the strength of composite blades. *J. Inst. Eng. Ser. C* (2020). <https://doi.org/10.1007/s40032-020-00572-9>
- Martynenko, V.G.: An original technique for modeling of anisotropic viscoelasticity of orthotropic materials in finite element codes applied to the mechanics of plates and shells. *Mech. Mech. Eng.* **21**, 389–413 (2017)
- Martynenko, V.G., Hrytsenko, M.I., Mavrody, S.V.: Design, analysis and experimental study of static strength of composite bimetal blade of mine main ventilation fan. *Bull. Natl. Tech. Univ. «KhPI» Ser. Dyn. Strength Mach.* **1**, 20–31 (2018). <https://doi.org/10.20998/2078-9130.2018.38.152477>
- Martynenko, V.G., Lvov, G.I.: Numerical prediction of temperature-dependent anisotropic viscoelastic properties of fiber reinforced composite. *J. Reinf. Plast. Compos.* **36**, 1790–1801 (2017). <https://doi.org/10.1177/0731684417727064>

- Martynenko, V.G., Lvov, G.I., Ulianov, Y.N.: Experimental investigation of anisotropic viscoelastic properties of glass fiber-reinforced polymeric composite material. *Polym. Polym. Compos.* **27**, 323–336 (2019). <https://doi.org/10.1177/0967391119846362>
- Mika, M., Horst, T., Landgraf, R., Ihlemann, J.: Dissipation power homogenization of anisotropic linear viscoelastic composites. *ZAMM Z. Angew. Math. Mech.* **99**, 1–11 (2019). <https://doi.org/10.1002/zamm.201900193>
- Nciri, M., Notta-Cuvier, D., Lauro, F., Chaari, F., Maalej, Y.: A coupled viscoelastic-viscoplastic-damage model for short fibre reinforced composites. In: 23ème Congrès Français de Mécanique Lille, 28 Août au 1er Septembre 2017 (2017)
- Nedjar, B.: An anisotropic viscoelastic fibre-matrix model at finite strains: continuum formulation and computational aspects. *Comput. Methods Appl. Mech. Eng.* **196**, 1745–1756 (2007). <https://doi.org/10.1016/j.cma.2006.09.009>
- Nguyen, T.D., Jones, R.E., Boyce, B.L.: Modeling the anisotropic finite-deformation viscoelastic behavior of soft fiber-reinforced composites. *Int. J. Solids Struct.* **44**, 8366–8389 (2007). <https://doi.org/10.1016/j.ijsolstr.2007.06.020>
- Nikkeshi, S., Kudo, M., Masuko, T.: Dynamic viscoelastic properties and thermal properties of Ni powder-epoxy resin composites. *J. Appl. Polym. Sci.* **69**, 2593–2598 (1998). [https://doi.org/10.1002/\(sici\)1097-4628\(19980926\)69:13%3c2593::aid-app9%3e3.3.co;2-o](https://doi.org/10.1002/(sici)1097-4628(19980926)69:13%3c2593::aid-app9%3e3.3.co;2-o)
- Niu, C., Dong, X., Xiong, X., Qi, M.: Preparation and viscoelasticity of anisotropic polyurethane composites filled with TiO₂ particles. *J. Appl. Polym. Sci.* **136**, 1–3 (2019). <https://doi.org/10.1002/app.47450>
- Ojha, R.K., Dwivedy, S.K.: Dynamic analysis of sandwich plates with isotropic skins and viscoelastic core. *Int. J. Struct. Stab. Dyn.* **19** (2019). <https://doi.org/10.1142/S0219455419500330>
- Pathan, M.V., Tagarielli, V.L., Patsias, S.: Numerical predictions of the anisotropic viscoelastic response of uni-directional fibre composites. *Compos. Part A Appl. Sci. Manuf.* **93**, 18–32 (2017). <https://doi.org/10.1016/j.compositesa.2016.10.029>
- Peters, S.T.: *Handbook of Composites*. Champan & Hall (1998)
- Radchenko, A., Radchenko, P.: Modelling of fracture of anisotropic composite materials under dynamic loads. In: *Composites and Their Properties* (2012). <https://doi.org/10.5772/48157>
- Rusanov, A., Martynenko, G., Avramov, K., Martynenko, V.: Detection of accident causes on turbine-generator sets by means of numerical simulations. In: 2018 IEEE 3rd International Conference on Intelligent Energy and Power Systems, IEPS 2018—Proceedings, pp. 51–54 (2018)
- Santos, J.E., Carcione, J.M., Picotti, S.: Viscoelastic-stiffness tensor of anisotropic media from oscillatory numerical experiments. *Comput. Methods Appl. Mech. Eng.* **200**, 896–904 (2011). <https://doi.org/10.1016/j.cma.2010.11.008>
- Shu, L.S., Onat, E.T.: On anisotropic linear viscoelastic solids. In: *Proceedings of the Fourth Symposium on Naval Structures Mechanics*, pp. 203–215. Pergamon Press, London (1967)
- Skrzypek, J.J., Ganczarski, A.W.: Constitutive equations for isotropic and anisotropic linear viscoelastic materials 57–85 (2015). https://doi.org/10.1007/978-3-319-17160-9_2
- Taylor, Z.A., Comas, O., Cheng, M., Passenger, J., Hawkes, D.J., Atkinson, D., Ourselin, S.: On modelling of anisotropic viscoelasticity for soft tissue simulation: numerical solution and GPU execution. *Med. Image Anal.* **13**, 234–244 (2009). <https://doi.org/10.1016/j.media.2008.10.001>
- Tzeng, J.T., Emerson, R.P., O'Brien, D.J.: Viscoelasticity analysis and experimental validation of anisotropic composite overwrap cylinders. In: *Mechanics of Solids, Structures and Fluids*, vol. 8, p. 429. ASME (2012)
- Vinson, J.R., Sierakowski, R.L.: *Anisotropic elasticity and composite laminate theory* (2006)
- Zamani, H.A., Bodaghi, M., Aghdam, M.M., Salehi, M.: Accurate damping analysis of viscoelastic composite beams and plates on suppressive foundation. *J. Compos. Mater.* **49**, 2187–2202 (2015). <https://doi.org/10.1177/0021998314544070>
- Zhang, Y., Luo, R., Lytton, R.L.: Anisotropic viscoelastic properties of undamaged asphalt mixtures. *J. Transp. Eng.* **138**, 75–89 (2011). [https://doi.org/10.1061/\(ASCE\)TE.1943-5436.0000302](https://doi.org/10.1061/(ASCE)TE.1943-5436.0000302)

- Zhang, Z., He, C., Li, Y., Sun, Z.: Dynamic viscoelasticity of carbon fibre reinforced polymers under high load: effects of static and dynamic loads. *Polym. Polym. Compos.* **15**, 297–305 (2007). <https://doi.org/10.1177/096739110701500405>
- Zhu, F., Pan, E., Qian, Z., Luo, Z.: Waves in a generally anisotropic viscoelastic composite laminated bilayer: impact of the imperfect interface from perfect to complete delamination. *Int. J. Solids Struct.* **202**, 262–277 (2020). <https://doi.org/10.1016/j.ijsolstr.2020.05.031>

Chapter 25

New Types of Limit Sets in the Dynamic System “Spherical Pendulum—Electric Motor”



Aleksandr Shvets and Serhii Donetskyi

Abstract The nonlinear interaction of a spherical pendulum with a source of excitation of its oscillations, an electric motor of limited power, is considered. This deterministic dynamic system is nonideal in the sense of Sommerfeld–Kononenko. A number of unusual limit sets of the system, which can be both regular and chaotic, have been constructed and analyzed. It is shown that the discovered limit sets are not attractors in the traditional sense of this term. Some scenarios of transitions from regular limit sets to chaotic ones, as well as scenarios of transitions from chaotic limit sets of one type to chaotic limit sets of another type are considered.

Keywords Spherical pendulum · Nonideal excitation · Chaotic limit sets · Regular limit sets

25.1 Introduction

Various pendulum systems are classic examples of oscillatory dynamic systems. Such fundamental effects as parametric resonance (Faraday 1831; Kelvin 1982; Rayleigh 1887), high frequency stabilization of unstable equilibrium positions (Erdeli 1934; Bogolyubov 1950; Kapitsa 1951; Bogolyubov and Mitropolskii 1961; Mitropolskii 1971) and many others were found in pendulum systems. However, interest in the study of various aspects of dynamic behavior of pendulum systems is mainly explained by the fact that many effects and phenomena firstly discovered in pendulum systems, subsequently, were discovered for systems of much more complex physical nature such as rings, shells, plates and various media in cylindrical and spherical cavities. Moreover, dynamic behavior in some more complex vibrational system can be successfully mathematically described by pendulum models (Miles 1962, 1984a, b;

A. Shvets (✉) · S. Donetskyi
National Technical University of Ukraine “Igor Sikorsky Kyiv Polytechnic Institute”,
Kyiv, Ukraine
e-mail: aleksandrshvetskpi@gmail.com

S. Donetskyi
e-mail: dsvshka@gmail.com

Meron and Procaccia 1986; Crawford and Knobloch 1991; Krasnopol'skaya and Shvets 1994; Ibrahim 2005; Lukovsky 2015; Raynovskyy and Timokha 2021).

In this paper, the oscillations of a spherical pendulum are considered, the suspension point of which is excited by an electric motor of limited power. Moreover, the interaction of the oscillatory system (the pendulum itself) and the source of excitation (the electric motor) is fundamentally taken into account. Dynamical systems of this kind are called nonideal, in the sense of Sommerfeld–Kononenko, or systems with limited excitation. For the first time, the study of such systems had begun in the papers of Sommerfeld (1902a, b). And after the publication of the monograph of Kononenko (1969), the theory of systems with limited excitation had become one of the important scientific directions in the modern theory of oscillations. The theory of systems with limited excitation explores the interaction of oscillatory systems with excitation sources of their oscillations. Within the framework of this theory, it is assumed that oscillation excitation sources have a power comparable to the power consumed by the oscillatory load. In this case, operation of energy source depends on the regime of oscillation load and influence of source cannot be expressed as a predetermined explicit time function. Whereas in the traditional mathematical modeling of oscillatory systems, idealized sources of excitation of unlimited power are considered. In many cases, the “ideal” approach is fundamentally wrong, which in practice leads to gross errors in describing the dynamics for both oscillatory system and source of excitation.

The discovery of deterministic chaos stimulated the emergence of a new direction in theory of systems with limited excitation associated with the search for chaotic modes of interaction of oscillatory systems with sources of excitation. Of particular interest are those chaotic regimes whose appearance is associated with nonlinear interaction between the oscillatory system and the excitation source, and not with their autonomous properties. In publications Krasnopol'skaya and Shvets (1992), Shvets (2007), Shvets and Makaseyev (2019), the occurrence of chaotic steady-state regimes in a number of deterministic nonideal pendulum systems was described. In these systems, chaos is fundamentally impossible without taking into account the interaction between the pendulum system and the source of excitation of its oscillations.

25.2 Equations of Motion of Spherical Pendulum with the Limited Excitation

Suppose that the oscillations of a physical spherical pendulum are excited by an electric motor of limited power. The pendulum is excited through the crank mechanism. Moreover, it is assumed that the point of suspension of the pendulum moves vertically and pendulum can perform spatial oscillations. The case of parametric resonance in the system is considered, at which the speed of rotation of the electric motor shaft is close to the doubled eigenfrequency of the pendulum. In papers Krasnopol'skaya

and Shvets (1992), Shvets (2007), the equations of motion of the dynamic system “spherical pendulum—electric motor” were derived, which have the form

$$\begin{aligned}
 \frac{dy_1}{d\tau} &= Cy_1 - \left[y_3 + \frac{1}{8}(y_1^2 + y_2^2 + y_4^2 + y_5^2) \right] y_2 - \frac{3}{4}(y_1y_5 - y_2y_4)y_4 + 2y_2, \\
 \frac{dy_2}{d\tau} &= Cy_2 + \left[y_3 + \frac{1}{8}(y_1^2 + y_2^2 + y_4^2 + y_5^2) \right] y_1 - \frac{3}{4}(y_1y_5 - y_2y_4)y_5 + 2y_1, \\
 \frac{dy_3}{d\tau} &= D(y_1y_2 + y_4y_5) + Ey_3 + F, \\
 \frac{dy_4}{d\tau} &= Cy_4 - \left[y_3 + \frac{1}{8}(y_1^2 + y_2^2 + y_4^2 + y_5^2) \right] y_5 + \frac{3}{4}(y_1y_5 - y_2y_4)y_1 + 2y_5, \\
 \frac{dy_5}{d\tau} &= Cy_5 + \left[y_3 + \frac{1}{8}(y_1^2 + y_2^2 + y_4^2 + y_5^2) \right] y_4 + \frac{3}{4}(y_1y_5 - y_2y_4)y_2 + 2y_4.
 \end{aligned} \tag{25.1}$$

Here, y_1, y_2, y_4, y_5 is the phase coordinates of the system, which determine the position of the pendulum, and y_3 is the phase coordinate proportional to the speed of rotation of the motor shaft. The independent variable t is time. The system parameters that denoted by C, D, E, F depend on the reduced length of pendulum, the driving moment of the electric motor, internal moment of forces of resistance to rotation of rotor of electric motor, eigenfrequency of the pendulum, coefficient damping the resistance force of the medium in which the pendulum moves, angle of inclination of the static characteristic of electric motor, geometric parameters of the crank mechanism and so on. A detailed description of the parameters of the system (25.1) is given in Krasnopol'skaya and Shvets (1992), Shvets (2007).

The resulting system of differential equations describes a complex process of interaction of the rotation of the motor shaft (formation exciting force) and spatial oscillations of the pendulum. This system of Eq. (25.1) is nonlinear. It is impossible to write down the exact solution of this system in the form of an analytical formula.

The main aim of the research is construction and study of the possible types of limit sets of the system (25.1). Since this system is a rather complex nonlinear system of equations, then for constructing its limit sets, a whole complex of numerical methods and algorithms were used. The technique for carrying out such numerical calculations for systems with limited excitation is described in Shvets (2007), Krasnopol'skaya and Shvets (1994, 2009). We emphasize that we have created our own complex of computer programs for carrying out numerical studies on the regular and chaotic dynamics of such systems.

25.3 Results of Numerical Constructions of Limit Sets

Let us start by studying equilibrium positions. All equilibrium positions can be found by solving the system of equations, which is obtained by equalizing the right-hand side of Eq. (25.1) to zero. It can easily be verified that one of equilibrium positions

has the form

$$y_1 = 0, y_2 = 0, y_3 = -\frac{F}{E}, y_4 = 0, y_5 = 0. \tag{25.2}$$

This equilibrium position is unique in the sense that it is isolated from other equilibrium positions, i.e., there is neighborhood of this equilibrium position such that it does not contain any other equilibrium. To study stability of this equilibrium, we must study its characteristic equation which has the form

$$\left(\lambda - C - \frac{\sqrt{4E^2 - F^2}}{E}\right)^2 (\lambda - E) \left(\lambda - C + \frac{\sqrt{4E^2 - F^2}}{E}\right)^2 = 0.$$

Therefore, the equilibrium position (25.2) will be asymptotically stable under the conditions

$$C < 0 \wedge E < 0 \wedge C^2 > 4 - \frac{E^2}{F^2}. \tag{25.3}$$

Finding the rest equilibrium positions of (25.1) analytically can be cumbersome, so it can be done using various numerical methods, for example, by Newton's one. Thus, it can be numerically verified that for

$$C = -0.5, D = -2.6, E = -0.45, F = 0.5 \tag{25.4}$$

the rest of equilibrium positions belong to one family, which has the form

$$\begin{aligned} \mathbf{y}^+ &= (0.85\sqrt{6.97 - 86z^2}, 0.11\sqrt{6.97 - 86z^2}, -2.57, 7.87z, z) \\ \mathbf{y}^- &= (-0.85\sqrt{6.97 - 86z^2}, -0.11\sqrt{6.97 - 86z^2}, -2.57, 7.87z, z) \end{aligned} \quad z \in \mathbb{R} \tag{25.5}$$

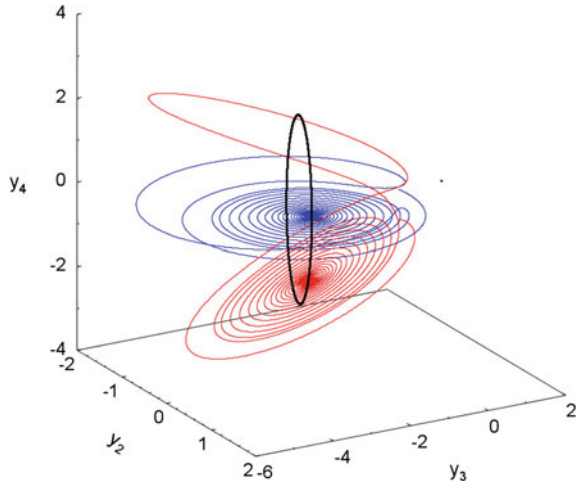
when $\{\mathbf{y}^+, \mathbf{y}^-\} \subset \mathbb{R}^5$.

This family consists of infinitely many equilibrium positions that form some closed line in the phase space. None of the equilibrium positions of this family is isolated one. Due to this, none equilibriums of the family can possibly be asymptotically stable. But instead, the whole family can exhibit attractor properties. That is, there are values of parameters such that almost any trajectory tends to some equilibrium position that belongs to family. And it is the case for values of parameters (25.4).

In addition, it is worth noting that every single representative has exactly the same Lyapunov's characteristic exponent (LCE), the signature of which has the form $< "0", "-", "-", "-", "-", ">$. This pushes us to think of family as a whole. This can be somewhat achieved by a concept of maximal attractor, which we will discuss further.

In Fig. 25.1, family of equilibrium positions that attract to itself all nearby trajectories is presented in the form of a closed line plotted in black along with isolated equilibrium in the form of a single dot plotted in black. To demonstrate that family has attraction properties, two trajectories that tend to two different representatives of

Fig. 25.1 Attractive family of equilibrium positions (closed line in black) and few trajectories that tend to its representatives (in red and blue); isolated equilibrium position (single dot in black) at $C = -0.5, D = -2.6, E = -0.45, F = 0.5$



the family are presented in red and blue. It follows from the conditions (25.3) that the isolated equilibrium is unstable.

Besides the family that exhibit attractor properties, there exist families of non-isolated equilibrium positions that do not. It means that any trajectory moves away from such family. In either case, it makes sense to talk about stability of the family as a whole, not stability of family representatives themselves. Since, as it was said, nonisolated equilibriums can not be asymptotically stable.

Consider another values of parameters

$$C = -0.5, D = -1, E = -1.4, F = 0.5. \tag{25.6}$$

For this values of parameters, family of equilibrium positions has the form

$$\begin{aligned} \mathbf{y}^+ &= (0.063\sqrt{174.078 - 4z^2}, 0.5\sqrt{174.078 - 4z^2}, -3.59, 0.127z, z) \\ \mathbf{y}^- &= (-0.063\sqrt{174.078 - 4z^2}, -0.5\sqrt{174.078 - 4z^2}, -3.59, 0.127z, z) \end{aligned} \quad z \in \mathbb{R} \tag{25.7}$$

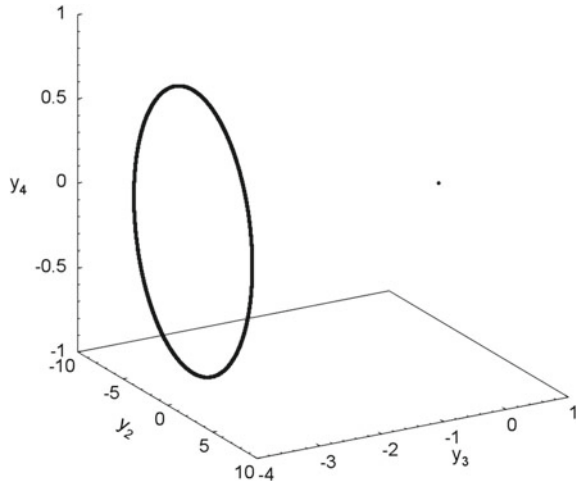
when $\{\mathbf{y}^+, \mathbf{y}^-\} \subset \mathbb{R}^5$.

Analogically to the previous family, every single representative of this one has exactly the same value of LCE, the signature of which has the form $\langle \text{“+”}, \text{“+”}, \text{“0”}, \text{“-”}, \text{“-”} \rangle$. Therefore, this family is unstable.

All equilibrium positions of the system (25.1) are plotted in Fig. 25.2

Next, we define and analyze the divergence (∇) of the vector field generated by the right-hand side of the system (25.1). Divergence can be written as

Fig. 25.2 Equilibrium positions of the system (25.1) at $C = -0.5, D = -1, E = -1.4, F = 0.5$



$$\begin{aligned} \nabla &= C - \frac{1}{4}(y_1y_2 + 3y_4y_5) + C + \frac{1}{4}(y_1y_2 + 3y_4y_5) + E \\ &+ C - \frac{1}{4}(3y_1y_2 + y_4y_5) + C + \frac{1}{4}(3y_1y_2 + y_4y_5) = 4C + E. \end{aligned}$$

Therefore, condition of dissipativity will look as follows

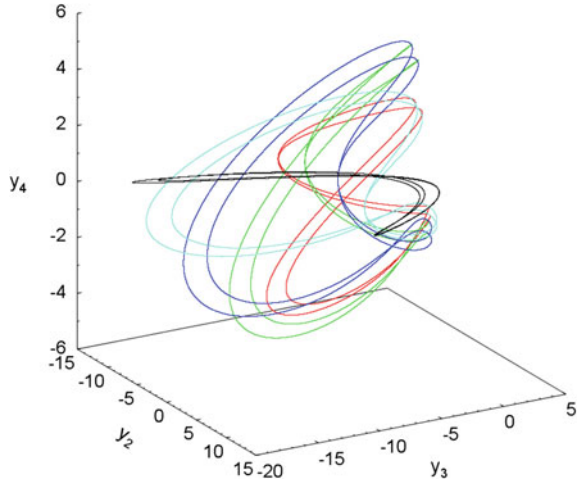
$$\nabla = 4C + E < 0. \tag{25.8}$$

And, this is true due to the physical sense of quantities included in formula (25.8). Since C (coefficient of resistance of the medium) and E (angle of inclination of the static characteristic of electric motor) are always negative. This means that the system is always dissipative, in particular for all considered values of parameters.

In the space of parameters of the system (25.1), there exist sufficiently large regions in which all equilibrium positions become unstable. As all equilibrium positions of a compact family that are everywhere densely located on a certain curve, as the isolated equilibrium position $(0, 0, -F/E, 0, 0)$ will be unstable.

Since the system (25.1) is dissipative, in the regions of instability of all equilibrium positions limit sets of other types arise. Such sets can be both regular and chaotic. Moreover, these sets form new families of limit sets and are not attractors in the traditional sense of this term. Let us consider some examples of such families. Suppose that the parameters of the system are equal: $C = -0.5, D = -1, E = -1.4, F = 0.5$. For such values of the parameters, a very unusual limit set arises in the system. This set consists of an infinite number of closed trajectories. None of the trajectories is isolated one. However, they do not intersect and do not have tangent points. Periodic solutions of the system of Eq. (25.1) correspond to each trajectory. That is, these trajectories form a family of cycles. All of these cycles exist simultaneously. Moreover, since these cycles are not isolated in the phase space, none of the cycles is a limit

Fig. 25.3 Five representatives of maximal regular attractor



cycle. All cycles have the same periods, the same spectrum of Lyapunov’s characteristic exponents, and the same finite number of fixed points in Poincare sections. In the phase space of the system (25.1), there is a sufficiently large region such that almost all trajectories starting from this region in limit ($t \rightarrow +\infty$) tend to one of the cycles of the family.

In Fig. 25.3, the projections of the phase portrait of such a limit set are shown. Each cycle is plotted in different color. Total of five cycles are shown, each of which is representative of the infinite family of cycles. We also emphasize that such limit sets are not attractors in the traditional sense of this term.

In our opinion, the most suitable term for describing such family is the concept of maximal attractor. Following (Milnor 1985; Kuznetsov 2006; Anisichenko and Vadivasova 2011; Sharkovsky 2013), we define the maximal attractor.

Definition of maximal attractor. Let the dynamical system be given by the evolution operator $T^\tau: R^n \rightarrow R^n$ and let U be the absorbing domain in R^n , that is for U the condition holds:

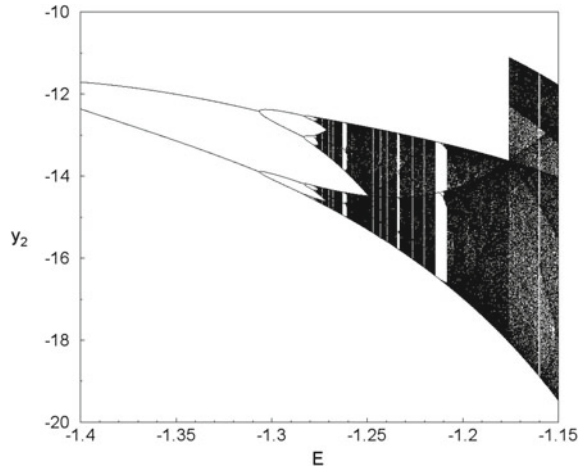
$$T^\tau U \subset U, \tau > 0.$$

The maximal attractor A_{\max} in the absorbing region U is the set

$$A_{\max} = \bigcap_{\tau > 0} T^\tau U.$$

We call some invariant set A the attractor of a dynamical system if there is an absorbing domain for which A is the maximal attractor. Basins of attraction of the attractor A is called the set B , so that all trajectories from B go to A at $t \rightarrow +\infty$.

Fig. 25.4 Phase-parametric characteristic of the system



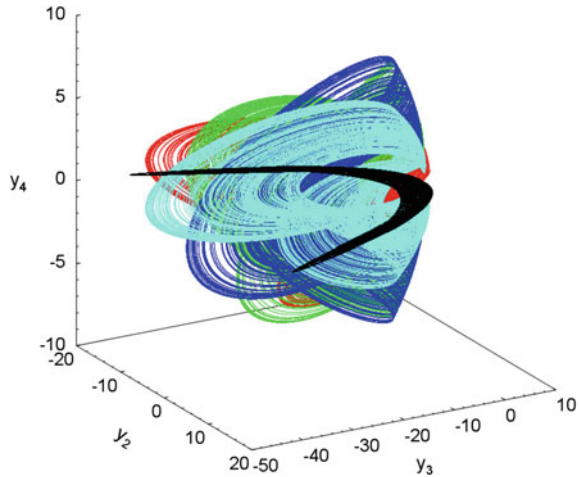
Thus, in accordance with this definition, both the family of equilibrium positions and the family of cycles are the maximal attractors of the system “pendulum-electric motor.”

With increasing parameter E , the rearrangement of the types of limit sets occurs in the system, which leads to the emergence of a chaotic limit set of very unusual structure. For a detailed study of this process, we construct a phase-parametric characteristic (“bifurcation tree”) of the system (25.1).

In Fig. 25.4, such a tree is constructed with respect to the phase variable y_2 and the parameter E . Note that bifurcation trees with respect to other phase variables have a qualitatively similar structure. We also emphasize that this tree is built relative to one of the representatives of the maximal attractor. However, for any other representative of the maximal attractor, such structure remains qualitatively unchanged and only the quantitative scale factor might change. In Fig. 25.4, separate branches of the “bifurcation tree” and their branch points are clearly visible. In the intervals of changing of the parameter E corresponding to individual branches of the “bifurcation tree,” the limit sets of the system (25.1) will be families of cycles. In turn, chaotic limit sets correspond to densely black sections of the “bifurcation tree.”

In Fig. 25.5, one of such chaotic limit sets is constructed. The arising family includes an infinite number of chaotic trajectories. It is known that the chaotic attractor in “classical” consists of an infinite number of unstable trajectories. The resulting family, at first glance, is an union of an infinite number of chaotic attractors. However, each representative of this family is not an attractor in the “classical” sense. Such chaotic family can be classified as the chaotic maximal attractor. One of the main signs of the emergence of deterministic chaos is the appearance of a positive Lyapunov’s exponent. All trajectories of the chaotic maximal attractor have the same Lyapunov’s characteristic exponents, including positive one. The signature of such a spectrum is: “+”, “0”, “0”, “-”, “-”. We emphasize that the sum of all Lyapunov’s exponents will always be negative. The Poincare sections of each trajectory

Fig. 25.5 Five representatives of maximal chaotic attractor



of the family are structurally similar chaotic sets consisting of an infinite number of points. Each representative of the chaotic maximal attractor is plotted in its own color. In total, there are five chaotic trajectories of the family are presented.

25.4 Scenarios of Transitions Between Limit Sets of Various Types

Despite the fact that maximal attractors are not attractors in the traditional sense of this term, the transition from regular maximal attractors to chaotic ones can occur in accordance with the main scenarios of chaotic dynamics, for example, according to Feigenbaum's scenario through a cascade of bifurcations of doubling the cycle period (Feigenbaum 1978, 1979) and according to the Manneville–Pomeau scenario through intermittency (Manneville and Pomeau 1980) and according to various scenarios of generalized intermittency (Krasnopol'skaya and Shvets 1994, 2009; Shvets and Sirenko 2019; Shvets and Donetskyi 2019).

The constructed phase-parametric characteristic (Fig. 25.4) allows us to understand the implementation of such scenarios. When the value of the parameter E increases, the branch points of the bifurcation tree are clearly visible on the left side of Fig. 25.4. Such branch points are period-doubling bifurcation points. At the same value of the bifurcation parameter, the period of all cycles, that form the maximal attractor, is doubled. Then, at the next bifurcation point, the period of all cycles of the maximal attractor is again doubled and so on. This endless process of period-doubling bifurcations ends with the emergence of a chaotic maximal attractor. That is, the transition from a periodic limit set to a chaotic limit set is realized according to the classical Feigenbaum's scenario.

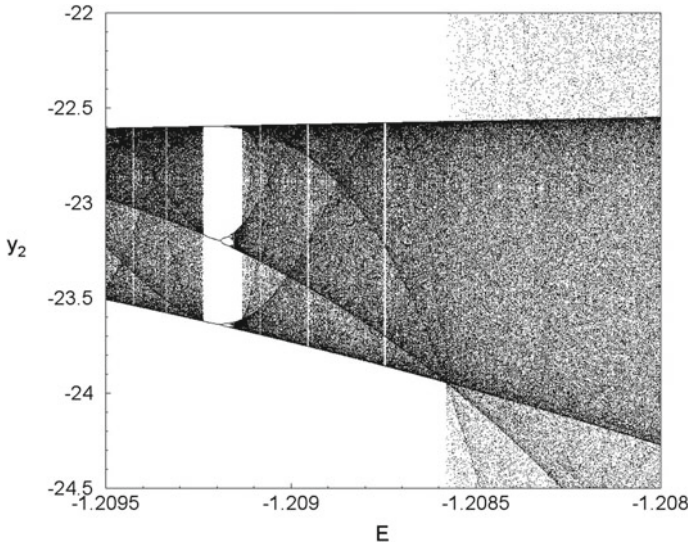


Fig. 25.6 Fragment of phase-parametric characteristic of the system

Figure 25.6 shows a fragment of the phase-parameter characteristic of the system. This fragment clearly shows a large “periodicity window” ($-1.295 < E < -1.292$) at the exit from which a transition to chaos occurs for one rigid bifurcation through intermittency. That is, the Manneville–Pomeau’s scenario is being implemented. When leaving the “periodicity window” in the direction of increasing the parameter E , a cascade of bifurcations of doubling the cycle period begins, which ends with the appearance of a chaotic maximal attractor. Then at $E \approx -1.2086$, there is a transition from the chaotic maximal attractor of one type to the chaotic maximal attractor of another type according to the scenario of generalized intermittency. This scenario is described in papers Krasnopol’skaya and Shvets (1994, 2009), Shvets and Sirenko (2019). Let us dwell in more detail on the implementation of the generalized intermittency scenario.

In Fig. 25.7a, the distribution of the invariant measure over the phase portrait projection of the representative of the chaotic maximal attractor of the system is shown. This chaotic maximal attractor appears as a result of an infinite cascade of period doubling of cycles at $E \approx -1.209$. At $E = -1.20857$, this maximal attractor disappears and chaotic maximal attractor of new type is born in the system. The distribution of the invariant measure over the projection of the phase portrait of the representative of the new chaotic maximal attractor is shown in Fig. 25.7b. The transition from one type of chaotic maximal attractor to the chaotic maximal attractor of another type occurs according to the scenario of generalized intermittency, which was described for attractors in the traditional sense of this term. At such transition, the scenario of generalized intermittency is simultaneously fulfilled for all representatives of both chaotic maximal attractors. For each representative of the new chaotic

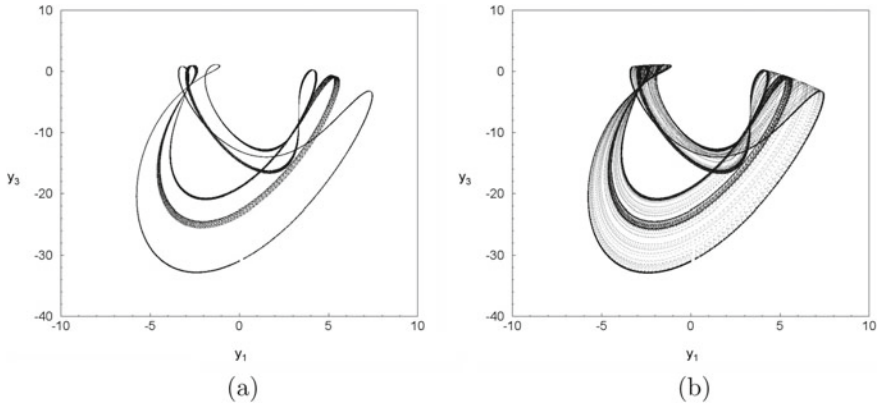


Fig. 25.7 Distribution of invariant measure at: $E = -1.209$ (a); $E = -1.20857$ (b)

maximal attractor, the motion along the trajectory consists of two alternating phases, namely rough-laminar phase and turbulent phase. In the rough-laminar phase, the trajectory makes chaotic movements in the neighborhood of the trajectories of the representative of the disappeared chaotic maximal attractor. Then, at an unpredictable moment of time, the trajectory leaves the localization region of the representative of the disappeared maximal attractor and moves to distant regions of the phase space. Rough-laminar phase corresponds to the much blacker areas in Fig. 25.7b. These areas from Fig. 25.7b are nearly the same as the distribution of the invariant measure from Fig. 25.7a. In turn, turbulent phase corresponds to much less darkened areas in Fig. 25.7b. After some time, the movement of the trajectory returns to the rough-laminar phase again. Then, trajectories switch to turbulent phase again. Such transitions are repeated an infinite number of times. Note that the duration of both rough-laminar and turbulent phases is unpredictable as are the moments of times of transition from one phase to another.

25.5 Conclusion

In the dynamic system, “spherical pendulum—electric motor of limited power” families of limit sets (maximal attractors) have been found, which can be both regular and chaotic. Despite the fact that maximal attractors are not attractors in the traditional sense of this term, it is shown that the transition from one type of maximal attractor to another occurs according to scenarios inherent in such transitions for ordinary attractors. In particular, the possibility of transition between maximal attractors of different types was established according to the scenarios of Feigenbaum, Manneville–Pomeau and through generalized intermittency. It was found that the only traditional attractor of the system is the equilibrium position (25.2).

References

- Anischenko, V.S., Vadivasova, T.E.: Lectures on Nonlinear Dynamics. R&C Dynamics, Moscow (2011). (in Russian)
- Bogolyubov, N.N.: Perturbation theory in nonlinear mechanics. Proc. Inst. Str. Mech. NAS Ukraine **14**, 9–34 (1950). (in Russian)
- Bogolyubov, N.N., Mitropolskii, Y.A.: Asymptotic Methods in the Theory of Nonlinear Oscillations. Gordon and Breach Science Publishers, New York (1961)
- Crawford, J.D., Knobloch, E.: Symmetry and symmetry-breaking bifurcations in fluid dynamics. Ann. Rev. Fluid Mech. **23**, 341–387 (1991)
- Erdeli, A.: Über die kleinen Schwingungen eines Pendels mit oszillirenden Aufhängepunkt. ZAMM **14**, 235–247 (1934)
- Faraday, M.: On a peculiar class of acoustical “figures” and on certain forms assumed by groups of particles upon vibrating elastic surfaces. Philos. Trans. R. Soc. Lond. **121**, 299–340 (1831)
- Feigenbaum, M.J.: Quantative universality for a class of nonlinear transformations. J. Stat. Phys. **19**(1), 25–52 (1978)
- Feigenbaum, M.J.: The universal metric properties of nonlinear transformations. J. Stat. Phys. **21**(6), 669–706 (1979)
- Ibrahim, R.: Liquid Sloshing Dynamics. Cambridge University Press, Cambridge (2005)
- Kapitsa, P.L.: Dynamic stability of a pendulum with oscillating point of suspension. Sov. Phys. JETP **21**, 588–597 (1951)
- Kelvin, W.: On the stability of periodic motion. Nature **46**, 384, 1190 (1892)
- Kononenko, V.O.: Vibrating System with a Limited Power-Supply. Iiffe, London (1969)
- Krasnopol'skaya, T.S., Shvets, A.Y.: Chaotic oscillations of a spherical pendulum as an example of interaction with energy source. Int. Appl. Mech. **28**, 669–674 (1992)
- Krasnopol'skaya, T.S., Shvets, A.Y.: Chaotic surface waves in limited power-supply cylindrical tank vibrations. J. Fluids Struct. **8**(1), 1–18 (1994)
- Krasnopol'skaya, T.S., Shvets, A.Y.: Dynamical chaos for a limited power supply for fluid oscillations in cylindrical tanks. J. Sound Vibr. **322**(3), 532–553 (2009)
- Kuznetsov, S.P.: Dynamical Chaos. Fizmatlit, Moscow (2006). (in Russian)
- Lukovsky, I.A.: Nonlinear Dynamics. Mathematical Models for Rigid Bodies with a Liquid. De Gruyter (2015)
- Manneville, P., Pomeau, Y.: Different ways to turbulence in dissipative dynamical systems. Phys. D Nonlinear Phenom. **1**(2), 219–226 (1980)
- Meron, E., Procaccia, J.: Low-dimensional chaos in surface waves: theoretical analysis of an experiment. Phys. Rev. A **34**, 3221–3237 (1986)
- Miles, J.W.: Stability of forced oscillations of a spherical pendulum. Quart. Appl. Math. **20**(1), 21–32 (1962)
- Miles, J.W.: Nonlinear Faraday resonance. J. Fluid Mech. **146**(2), 285–302 (1984a)
- Miles, J.W.: Resonant motion of a spherical pendulum. Phys. D **11**(3), 309–323 (1984b)
- Milnor, J.: On the concept of attractor. Commun. Math. Phys. **99**, 177–195 (1985)
- Mitropolskii, Y.A.: Method of Averaging in Nonlinear Mechanics. Naukova Dumka, Kiev (1971). (in Russian)
- Rayleigh, W.: On the maintenance of vibration by forces of double frequency. Philos. Mag. Ser. **24**(5), 145–159 (1887)
- Raynovskyy, I., Timokha, A.: Sloshing in Upright Circular Containers: Theory, Analytical Solutions, and Applications. CRC Press, London, New York (2021)
- Sharkovsky, A.N.: Attractors of trajectories and their basins. Naukova Dumka, Kiev (2013). (in Russian)
- Shvets, A.Y.: Deterministic chaos of a spherical pendulum under limited excitation. Ukr. Math. J. **59**, 602–614 (2007)

- Shvets, A., Donetskyi: Transition to deterministic chaos in some electroelastic systems. In: Skidas, C., Lubashevsky, I. (eds.) 11th Chaotic Modeling and Simulation International Conference. CHAOS 2018. Springer Proceedings in Complexity, pp. 257–264. Springer, Cham (2019)
- Shvets, A.Y., Makaseyev, A.: Chaos in pendulum systems with limited excitation in the presence of delay. In: CHAOS 2017—Proceedings: 7th Chaotic Modeling and Simulation International Conference, pp. 451–458 (2019)
- Shvets, A.Y., Sirenko, V.A.: Scenarios of transitions to hyperchaos in nonideal oscillating systems. *J. Math. Sci.* **243**(2), 338–346 (2019)
- Sommerfeld, A.: Beitrage zum dynamischen Ausbau der Festigkeitslehre. *Phys. Z.* **3**, 266–271 (1902a)
- Sommerfeld, A.: Beitrage zum dynamischen ausbau der festigkeitslehre. *Z. Ver. Dtsch. Ing.* **46**, 391–394 (1902b)

Chapter 26

Exact Solutions to the Four-Component Merola–Ragnisco–Tu Lattice Equations



Aleksandr I. Zemlyanukhin, Andrey V. Bochkarev,
and Aleksandr V. Ratushny

Abstract We construct a class of exact kink solutions of integrable four-component Merola–Ragnisco–Tu lattice equations. To this aim, a modification of the geometric series method adapted for differential-difference equations (DDE) is used. Algorithm involves the analysis of a sequence of linear ordinary differential equations (ODEs) with the same structure of homogeneous parts. Sequence of the ODE solutions forms a geometric progression, the sum of which is found using the Padé approximants and gives the exact solution to the lattice equations. The geometricity of the constructed series can be considered as a new simple and easily verified integrability criterion for DDE. The proposed approach is much simpler than existing method that requires the construction of Darboux–Bäcklund transformations of discrete Lax pairs. The accuracy of the approach is confirmed by direct numerical simulation, in which the exact solution found is used as initial condition for the integration of the lattice equations by the high-order Runge–Kutta method.

Keywords Differential-difference equation · Geometric series method · Exact solution · Padé approximant

26.1 Introduction

Currently, complicated discrete systems arising in physics, engineering, biology, etc., have attracted interest from researchers. For modeling processes in discrete systems, nonlinear differential-difference equations (DDE) and systems of such equations are often used (Cooke 1963). The list of analytically solvable nonlinear DDE contains

A. I. Zemlyanukhin (✉) · A. V. Bochkarev · A. V. Ratushny
Department of Applied Mathematics, Yuri Gagarin State Technical University of Saratov, Saratov
410054, Russia
e-mail: azemlyanukhin@mail.ru

A. V. Bochkarev
e-mail: ab2009sar@list.ru

A. V. Ratushny
e-mail: [saniam.ratushny@gmail.com](mailto:sania.ratushny@gmail.com)

only integrable models, while non-integrable systems appear most often in applications. The main methods for analyzing non-integrable systems are continualization, which leads to adequate results only in the long-wave approximation, and numerical simulation. A canonical example here is a non-integrable Fermi-Pasta-Ulam lattice, which, upon continualization, transforms into the Korteweg-de Vries equation and its higher order generalizations.

One of the common methods for constructing exact solutions to nonlinear DDE is based on the application of Darboux transformation (Xu 2015). The solution process consists of several steps. First, the Lax representation of the equation is found, and then the Darboux transformation is performed. The result is Bäcklund transformations, which are used to generate exact solutions (Kudryashov 2010). The first step of the method is often used to prove integrability of solved DDE. Unfortunately, there is currently no general method for finding the Lax representation for a given equation. Also, to build exact solutions, inverse scattering method (Ablowitz 1975), Hirota method (Silindir 2012), Riemann theta functions (Krichever 1998), Casorati determinant (Ohta 1991), Pfaffian (Tsujiimoto 1996) representations methods, along with methods of hyperbolic tangents (Baldwin 2004), truncated expansions (Ryabov 2010) and geometric series (Bochkarev 2017; Zemlyanukhin 2020; Andrianov et al. 2020) are used. Despite the large number of methods, exact solutions have not been found even for all integrable equations.

The purpose aim of this article is exact solution of the four-field integrable Merola–Ragnisco–Tu lattice (Merola et al. 1994). This lattice arose as one of the differential–difference versions of the Ablowitz–Kaup–Newell–Segur (AKNS) hierarchy (Merola et al. 1994). As is known, the most important integrable models can be obtained from this hierarchy, including the sine-Gordon, KdV and the nonlinear Schrödinger equation. We also provided numerical simulations to verify that the found traveling wave solutions retain their shape unchanged. The article is organized as follows. In the first section, the instability of constant solutions of a two-component subsystem of the original lattice is established. In the second section, this subsystem is continualized. The exact solution and the numerical simulation of the original four-field lattice are carried out in the third section. The fourth section shows how different branches of the exact solution can be combined to build a new solution of a more complex shape. Finally, the last section presents the concluding remarks.

26.2 Linear Stability Analysis of Constant Solutions

The Merola–Ragnisco–Tu system (Merola et al. 1994) consists of 4 DDEs

$$(r_n)'_t = r_{n+1} - r_n^2 s_n, \quad (26.1)$$

$$(s_n)'_t = r_n s_n^2 - s_{n-1}, \quad (26.2)$$

$$(u_n)'_t = -r_{n+1} + r_n^2 s_n + u_{n+1} - 2r_n s_n u_n - r_n^2 w_n, \tag{26.3}$$

$$(w_n)'_t = -r_n s_n^2 + s_{n-1} - w_{n-1} + 2r_n s_n w_n + s_n^2 u_n. \tag{26.4}$$

Equations (26.1) and (26.2) form an independent system for variables $r_n(t)$ and $s_n(t)$, called two-component Ragnisco–Tu system (Liu 2011). This system has trivial and constant nonzero solutions

$$s_n = r_n = 0, \tag{26.5}$$

$$s_n = \frac{1}{r_n}. \tag{26.6}$$

It is known (Khanizadeh et al. 2013) that there is a reversible transformation connecting the Ragnisco–Tu system with the nonlinear Schrödinger equation (Adler 1994), which is traditionally used to model the evolution of weakly modulated harmonic waves in continuous media with weak nonlinearity and strong dispersion. In a recent paper (Wang 2020), it was shown that an explicit one-wave solution of the Ragnisco–Tu system is unstable, and a two-wave solution retains only the phase shift, but not the waveform after interaction.

Let us show that constant solutions (26.5) and (26.6) is unstable under small periodic perturbations. Substituting

$$r_n = \varepsilon R_n(t), \quad s_n = \varepsilon S_n(t) \tag{26.7}$$

into Eqs. (26.1) and (26.2), in the leading order with respect to the small parameter ε we have

$$\begin{aligned} R'_n &= R_{n+1}, \\ S'_n &= -S_{n-1}. \end{aligned} \tag{26.8}$$

System (26.8) have solution $R_n(t) = \exp[i(dn + \omega_R t)]$, $S_n(t) = \exp[i(dn + \omega_S t)]$, where

$$\omega_R = -i \exp(id), \quad \omega_S = i \exp(-id). \tag{26.9}$$

The imaginary parts $\text{Im}(\omega_R) = -\cos d$, $\text{Im}(\omega_S) = \cos d$ of frequencies (26.9) have opposite signs, therefore, an exponential increase in time of the amplitude of small perturbations will be observed for any values of d , $d \neq \frac{\pi}{2} + \pi k$.

Substituting

$$r_n = R_0 + \varepsilon R_n(t), \quad s_n = R_0^{-1} + \varepsilon S_n(t) \tag{26.10}$$

into Eqs. (26.1) and (26.2), in the leading order with respect to ε we have system

$$\begin{aligned} R'_n &= R_{n+1} - R_0^2 S_n - 2R_n, \\ S'_n &= 2S_n + R_0^{-2} R_n - S_{n-1}, \end{aligned} \tag{26.11}$$

which reduces to the equation

$$R''_n - R'_{n+1} + R'_{n-1} + 2R_{n+1} - 4R_n + 2R_{n-1} = 0. \tag{26.12}$$

Equation (26.12) has periodic solution $R_n(t) = \exp[i(dn + \omega t)]$ under condition

$$\begin{aligned} \omega &= -\frac{i}{2}(e^{id} - e^{-id}) \pm \frac{1}{2}(8e^{id} + 8e^{-id} - e^{2id} - e^{-2id} - 14)^{1/2} \\ &= \sin d \pm \sqrt{4 \cos d - \cos^2 d - 3}. \end{aligned} \tag{26.13}$$

For any values of $d, d \neq 2\pi k$, the frequency (26.13) has a nonzero imaginary part, which is responsible for the growth of the amplitude of small perturbations. The maximum growth rate is achieved under condition $d = \pi + 2\pi k$, which corresponds to the initial perturbation of the sawtooth profile $R_n(0) = \pm \exp[i\pi n] = \pm(-1)^n$.

26.3 Continualization

Let us analyze the behavior of solutions of system (26.1), (26.2) in the long-wavelength limit when the distance h between adjacent lattice nodes tends to zero. Let us introduce the continuous coordinate z scaled in such a way that $z = nh$ at the nodes of the lattice. We assume that $r_n(t), s_n(t)$ are discrete approximations to a pair of continuous functions $r = r(z, t), s = s(z, t)$, i.e.,

$$r_n(t) = r(nh, t), \quad s_n(t) = s(nh, t) \tag{26.14}$$

and replace them in (26.1), (26.2) with the corresponding Taylor series expansions

$$\begin{aligned} r_n(t) &= r, \quad s_n(t) = s, \\ r_{n\pm 1}(t) &= r \pm h \frac{\partial r}{\partial z} + \frac{h^2}{2} \frac{\partial^2 r}{\partial z^2} \pm \frac{h^3}{6} \frac{\partial^3 r}{\partial z^3} + O(h^4), \\ s_{n\pm 1}(t) &= s \pm h \frac{\partial s}{\partial z} + \frac{h^2}{2} \frac{\partial^2 s}{\partial z^2} \pm \frac{h^3}{6} \frac{\partial^3 s}{\partial z^3} + O(h^4), \end{aligned} \tag{26.15}$$

to obtain

$$\frac{\partial r}{\partial t} = r - r^2 s + h \frac{\partial r}{\partial z} + \frac{h^2}{2} \frac{\partial^2 r}{\partial z^2} + \frac{h^3}{6} \frac{\partial^3 r}{\partial z^3} + O(h^4),$$

$$\frac{\partial s}{\partial t} = -s + rs^2 + h \frac{\partial s}{\partial z} - \frac{h^2}{2} \frac{\partial^2 s}{\partial z^2} + \frac{h^3}{6} \frac{\partial^3 s}{\partial z^3} + O(h^4). \quad (26.16)$$

Eliminating variable s from system (26.16), we write

$$\begin{aligned} & \left(\frac{\partial r}{\partial t} \right)^2 - r \frac{\partial^2 r}{\partial t^2} + 2h \left(r \frac{\partial^2 r}{\partial t \partial z} - \frac{\partial r}{\partial t} \frac{\partial r}{\partial z} \right) \\ & + h^2 \left(\left(\frac{\partial r}{\partial t} - 2r \right) \frac{\partial^2 r}{\partial z^2} + 2 \frac{\partial r}{\partial z} \frac{\partial^2 r}{\partial t \partial z} + \left(2 - \frac{3}{r} \frac{\partial r}{\partial t} \right) \left(\frac{\partial r}{\partial z} \right)^2 \right) + O(h^3) = 0. \end{aligned} \quad (26.17)$$

In the main order, we have equation

$$\left(\frac{\partial r}{\partial t} \right)^2 - r \frac{\partial^2 r}{\partial t^2} = 0, \quad (26.18)$$

solution of which

$$r = F_2 \exp(F_1 t) \quad (26.19)$$

contains two arbitrary functions $F_1 = F_1(z)$ and $F_2 = F_2(z)$. Substituting (26.19) in the next order in h :

$$r \frac{\partial^2 r}{\partial t \partial z} - \frac{\partial r}{\partial t} \frac{\partial r}{\partial z} = 0, \quad (26.20)$$

we have equation

$$\exp(4F_1 t) F_2^4 F_1' = 0 \quad (26.21)$$

with nonzero solution

$$F_1 = C = \text{const.} \quad (26.22)$$

Finally, using (26.19) and (26.22) in the equation corresponding to order of h^2 :

$$\left(2r - \frac{\partial r}{\partial t} \right) r^2 \frac{\partial^2 r}{\partial z^2} - 2 \frac{\partial r}{\partial z} r^2 \frac{\partial^2 r}{\partial t \partial z} - \left(2r - 3 \frac{\partial r}{\partial t} \right) r \left(\frac{\partial r}{\partial z} \right)^2 = 0, \quad (26.23)$$

we obtain

$$F_2^2 \exp(4F_1 t) (F_1 - 2) \left[F_2 F_2'' - (F_2')^2 \right] = 0. \quad (26.24)$$

The last equation has two nonzero solutions

$$\begin{cases} F_1 = 2, \\ F_2 = C_1 \exp(C_2 z). \end{cases} \quad (26.25)$$

It is easy to verify that the equation corresponding to order of h^3 is identically satisfied by substituting the solutions (26.19) and (26.25) into it.

The first of solutions (26.25) leads to exponential growth in time of solution (26.19) for any nonzero function $F_2(z)$. The second solution is unbounded in the spatial coordinate and is not applicable to both an infinite lattice and a finite lattice with periodic boundary conditions. Thus, a direct transition to continuous equations without preliminary scaling of the dependent and independent variables does not allow to obtain physically meaningful solution of the lattice.

26.4 Exact Solution to the System

A complete four-field integrable Merola–Ragnisco–Tu lattice can be regarded as a first-order perturbation of a two-component Ragnisco–Tu system (Xu 2010). To construct exact solutions, we use the modified geometric series method (Zemlyanukhin 2020; Andrianov et al. 2020) previously proposed by the authors for nonlinear PDEs (Bochkarev 2017). The idea of the method can be explained as follows. The linearized lattice equations have a solution in the form of an exponential function of a traveling wave variable. The solution to the original nonlinear equations is sought in the form of a series in powers of this exponential solution. Having determined the first few coefficients of this series, we require that the corresponding terms of the series form a geometric progression. The last requirement is equivalent to the coincidence of the successive diagonal Padé approximants calculated for the series (Baker and Graves-Morris 1996). The sum of the geometric progression gives an exact solution to the original nonlinear lattice equations.

A remarkable feature is that for all integrable lattices known to the authors, a geometric series in powers of the exponential function can be obtained, and the sum of the series gives exact solution (Zemlyanukhin 2021). Thus, the geometricity of the constructed series can be considered as a new simple and easily verified integrability criterion for DDE.

In the system (26.1)–(26.4) we pass to the traveling wave variable $z = dn + \omega t$:

$$-\omega r' + r_+ - r^2 s = 0, \quad (26.26)$$

$$-\omega s' + r s^2 - s_- = 0, \quad (26.27)$$

$$-\omega u' - r_+ + r^2 s + u_+ - 2rsu - r^2 w = 0, \quad (26.28)$$

$$-\omega w' - r s^2 + s_- - w_- + 2rsw + s^2 u = 0, \quad (26.29)$$

where $r = r(z)$, $r_+ = r(z + d)$, $s_- = s(z - d)$ and so on. Noting that Eqs. (26.26) and (26.27) can be solved separately, we make substitutions

$$r = \sum_{n=0}^{\infty} R_n e^{nz}, \quad s = \sum_{n=0}^{\infty} S_n e^{nz}, \tag{26.30}$$

$$r_+ = \sum_{n=0}^{\infty} R_n \delta^n e^{nz}, \quad s_- = \sum_{n=0}^{\infty} S_n \delta^{-n} e^{nz}, \tag{26.31}$$

where R_n, S_n are required coefficients and $\delta = e^d$. Equating to zero the coefficients in the resulting equations at e^{nz} , $n = 0, 1, 2, \dots$, we find

$$\begin{aligned} n = 0 : S_0 &= R_0^{-1}; \\ n = 1 : \omega &= -X + \delta - 2, S_1 = X R_1 / R_0^2; \\ n = 2 : R_2 &= (X\delta + 1) R_1^2 / [2(\delta - 1)^2 R_0], \\ &S_2 = \delta [X(\delta^2 - 4\delta + 2) - \delta] R_1^2 / [2(\delta - 1)^2 R_0^3]; \\ n = 3 : R_3 &= [X\delta(\delta - 3) - \delta - 1] R_1^3 / [4(\delta - 1)^3 R_0^2], \\ &S_3 = \delta^2 [X(\delta - 2)(\delta^2 - 5\delta + 2) - \delta(\delta - 3)] R_1^3 / [4(\delta - 1)^3 R_0^4]; \\ n = 4 : R_4 &= [X\delta(\delta^2 - 6\delta + 7) - \delta^2 + 2\delta + 1] R_1^4 / [8(\delta - 1)^4 R_0^3], \\ &S_4 = \delta^3 [X(\delta^4 - 10\delta^3 + 31\delta^2 - 32\delta + 8) - \delta(\delta^2 - 6\delta + 7)] \\ &R_1^4 / [8(\delta - 1)^4 R_0^5]; \\ &\dots \end{aligned} \tag{26.32}$$

where $X = -1 + \frac{\delta-1}{2\delta} (\delta - 1 \pm \sqrt{\delta^2 - 6\delta + 1})$.

In order to show that the series (26.30) are geometric, we make replacements $e^{nz} \rightarrow x^n$ and calculate for the obtained power series the diagonal Padé approximants $[1/1], [2/2], [3/3], \dots$. It turns out that starting from $[2/2]$, all the approximants coincide. This means that the power series are geometric and the approximants $[2/2]$ after the reverse replacement $x^n \rightarrow e^{nz}$ give exact sums of the series (26.30):

$$\begin{aligned} r &= R_0 \left(1 + \frac{(X\delta - \delta^2 + 4\delta - 2) R_1 e^{2z} + 2(\delta - 1)^2 R_0 e^z}{R_1 e^{2z} - (\delta - 1)(\delta - 3) R_0 e^z + 2(\delta - 1)^2 R_0^2 R_1^{-1}} \right), \\ s &= \frac{1}{R_0} \left(1 - \frac{\delta(X + \delta) R_1 e^{2z} - 2(\delta - 1)^2 R_0 X e^z}{\delta^2 R_1 e^{2z} - \delta(\delta - 1)(\delta - 3) R_0 e^z + 2(\delta - 1)^2 R_0^2 R_1^{-1}} \right). \end{aligned} \tag{26.33}$$

We substitute (26.33) into Eqs. (26.28), (26.29) and apply the geometric series method to them. The series for u, w are geometric and have sums

$$u = R_0^2 W_0 + \frac{a_4 e^{4z} + a_3 e^{3z} + a_2 e^{2z} + a_1 e^z}{(R_1^2 e^{2z} - 8R_0 R_1 e^z + 8R_0^2)^2},$$

$$w = W_0 + \frac{b_4 e^{4z} + b_3 e^{3z} + b_2 e^{2z} + b_1 e^z}{R_0 (R_1^2 e^{2z} - 8R_0 R_1 e^z + 8R_0^2)^2}, \tag{26.34}$$

where

$$\begin{aligned} a_4 &= R_0 R_1^4 [R_0 W_0 (\delta + 1) - 3\delta + 1], \\ a_3 &= 8R_0^2 R_1^2 [\delta R_0^2 W_1 - 2R_1 (R_0 W_0 (\delta + 1) - 2\delta + 1)], \\ a_2 &= -8R_0^3 R_1 [R_1 (9\delta - R_0 W_0 (3\delta + 11) - 11) + 2R_0^2 W_1 (\delta + 1)], \\ a_1 &= 64R_0^4 [R_0^2 W_1 - R_1 (2R_0 W_0 - \delta + 3)], \\ b_4 &= R_1^4 [R_0 W_0 (\delta - 7) + 3\delta - 17], \\ b_3 &= -8R_0 R_1^2 [R_0^2 W_1 (\delta - 6) - R_1 (2R_0 W_0 - \delta + 5)], \\ b_2 &= 8R_0^2 R_1 [2R_0^2 W_1 (\delta - 7) - R_1 (R_0 W_0 (\delta + 1) - \delta + 3)], \\ b_1 &= 64R_0^5 W_1 \end{aligned} \tag{26.35}$$

and $\delta = 3 \pm 2\sqrt{2}$. Equations (26.33), (26.34) contain 4 arbitrary constants R_0, R_1, W_0, W_1 and can be considered as a general solution of system (26.26)–(26.29). Under condition $R_0 R_1 < 0$ this solution is bounded, since the denominators of (26.33) and (26.34) not equal to zero at any value of z . The profiles of traveling kink waves at $R_0 = 1, R_1 = -10, W_0 = 1, W_1 = 20$ and $\delta = 3 + 2\sqrt{2}$ are shown in Fig. 26.1.

To verify the invariability of the traveling wave profile over time, the input system (26.1)–(26.4) was solved by the high-order Runge-Kutta method (Butcher 2008). The calculation results shown in Figs. 26.2 and 26.3 indicate that the initial deviations (see Fig. 26.1) propagate as steady-state waves.

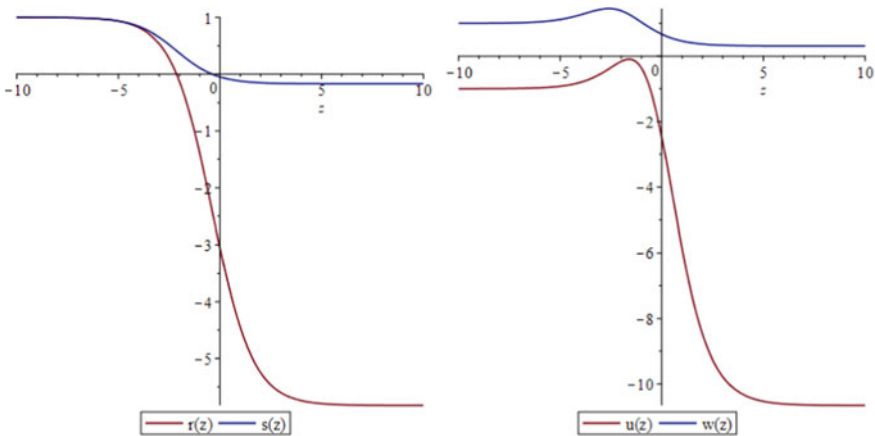


Fig. 26.1 Traveling wave profiles determined by exact solution (26.33), (26.34) at $R_0 = 1, R_1 = -10, W_0 = 1, W_1 = 20$ and $\delta = 3 + 2\sqrt{2}$

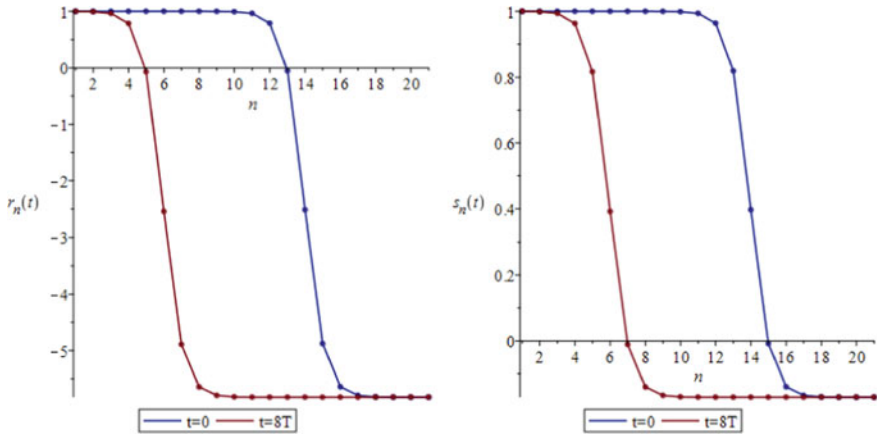


Fig. 26.2 Steady-state traveling waves for variables $r_n(t)$, $s_n(t)$

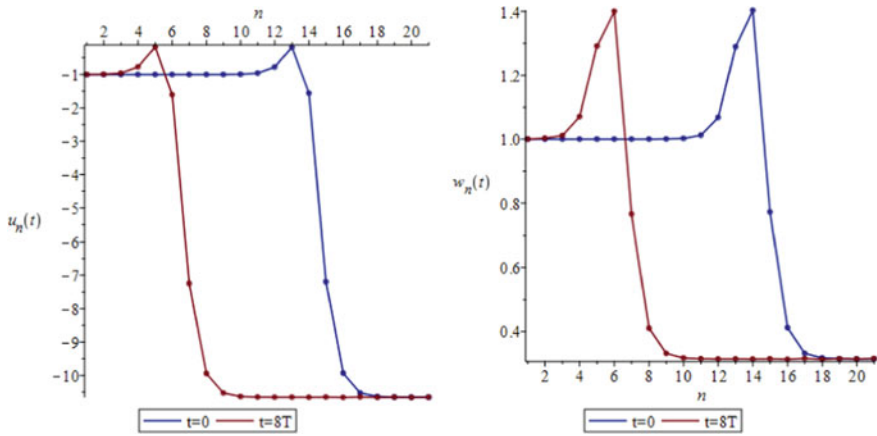


Fig. 26.3 Steady-state traveling waves for variables $u_n(t)$, $w_n(t)$

The found exact solution contains regions in which the dependent variables are practically constant. As shown in Sect. 26.1, the constant solutions of the system are unstable. This theoretical conclusion is confirmed by the results of numerical simulations. Continued observation of the traveling wave shown in Figs. 26.2 and 26.3, reveals a sawtooth disturbances, the amplitude of which grows exponentially with time (Fig. 26.4). Parameter T in Figs. 26.2, 26.3 and 26.4 denotes the time during which the wave front passing distance h .

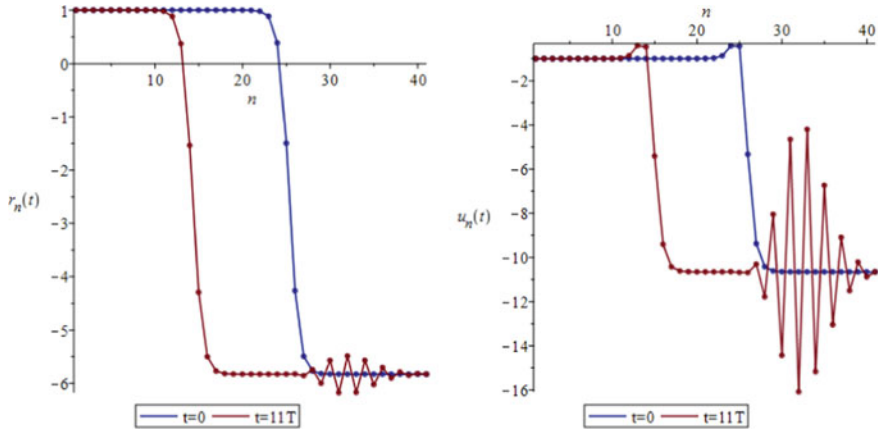


Fig. 26.4 Loss of stability

26.5 Combined Kink Wave

In the previous section, it was shown that the exact solution (26.33), (26.34) exists if parameter δ takes one of two values: $\delta_1 = 3 + 2\sqrt{2}$ or $\delta_2 = 3 - 2\sqrt{2}$. These values correspond to frequencies and wave numbers with opposite signs: $\omega_1 = -\omega_2 = 2\sqrt{2}$, $d_1 = -d_2 \approx 1.763$, therefore, the phase velocities $\frac{\omega}{d}$ of the waves in the two considered cases coincide. Taking into account that $z = dn + \omega t$, it is easy to obtain for the exact solutions (26.33), (26.34)

$$\begin{aligned} \lim_{n \rightarrow +\infty} r_1 &= -\delta_1 R_0, \quad \lim_{n \rightarrow -\infty} r_2 = -\delta_2 R_0, \quad \lim_{n \rightarrow +\infty} s_1 = -\frac{1}{\delta_1 R_0}, \quad \lim_{n \rightarrow -\infty} s_2 = -\frac{1}{\delta_2 R_0}, \\ \lim_{n \rightarrow +\infty} u_1 &= (\delta_1 R_0 W_0 - 3\delta_1 + 1)R_0, \quad \lim_{n \rightarrow -\infty} u_2 = (\delta_2 R_0 W_0 - 3\delta_2 + 1)R_0, \\ \lim_{n \rightarrow +\infty} w_1 &= -\delta_1 W_0 + \frac{1 - 3\delta_1}{R_0}, \quad \lim_{n \rightarrow -\infty} w_2 = -\delta_2 W_0 + \frac{1 - 3\delta_2}{R_0}, \end{aligned} \tag{26.36}$$

$$\begin{aligned} \lim_{n \rightarrow -\infty} r_1 &= \lim_{n \rightarrow +\infty} r_2 = R_0, \quad \lim_{n \rightarrow -\infty} s_1 = \lim_{n \rightarrow +\infty} s_2 = \frac{1}{R_0}, \\ \lim_{n \rightarrow -\infty} u_1 &= \lim_{n \rightarrow +\infty} u_2 = -R_0^2 W_0, \quad \lim_{n \rightarrow -\infty} w_1 = \lim_{n \rightarrow +\infty} w_2 = W_0, \end{aligned} \tag{26.37}$$

where variables r_1, s_1, u_1, w_1 , are obtained from (26.33), (26.34) by substitution $\delta = \delta_1$ and variables r_2, s_2, u_2, w_2 correspond to the second case $\delta = \delta_2$. Equations (26.37) allow one to construct an approximate combined solution, the shape of the left side of which is determined by functions r_2, s_2, u_2, w_2 , and the shape of the right side—by functions r_1, s_1, u_1, w_1 . The plots of the solution obtained in this way, representing a traveling wave of a constant profile, are shown in Fig. 26.5. Numerical modeling shows that, due to the instability of the constant solutions of the system

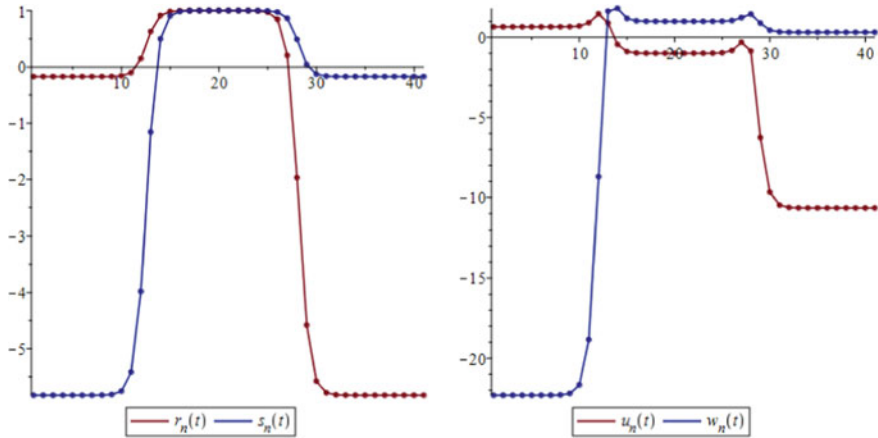


Fig. 26.5 Combined kink wave at $R_0 = 1, R_1 = -10, W_0 = 1, W_1 = 20$

under consideration, the lifetime of approximate solutions before the appearance of significant distortions is not inferior to the lifetime of the exact solution.

26.6 Conclusions

In this work, a four-field integrable lattice is investigated. Instability of constant exact solutions is shown, and the highest growth rate of the perturbation amplitude is observed for small initial perturbations of the sawtooth profile. The direct passage to the limit to a partial differential equation as a result of the continualization process does not lead to an equation whose solution is bounded in space and stable in time. An exact kink solution is found using the modified geometric series method. Numerical simulations have shown that, despite the instability of constant solutions, a traveling wave corresponding to an exact kink solution propagates for some time without changing its shape. The combination of kinks of the exact solution with increasing and decreasing slopes made it possible to construct an approximate combined solution.

The work presents an application of the modified geometric series method for constructing exact solutions of a system of nonlinear DDEs. The advantage of the method is the simplicity of its algorithmization and implementation in any modern system of symbolic calculations (e.g., in Maple). In addition, it is much easier to establish the geometricity of the power series for a given equation than to find the Lax representation for it. Thus, the geometricity of the series in exponential functions seems to be the simplest of the known criteria for integrability of DDE.

Acknowledgements The authors express their deep gratitude to Prof. Igor Andrianov for motivating discussions and thanks to the referee, whose comments allowed us to improve the quality of the article.

Funding The study was funded by RFBR, the project No. 20-01-00123.

References

- Ablowitz, M.J., Ladik, J.F.: Nonlinear differential-difference equations. *J. Math. Phys.* **16**, 598 (1975)
- Adler, V.E., Yamilov, R.I.: Explicit auto-transformations of integrable chains. *Phys. A Math. Gen.* **27**, 477–492 (1994)
- Andrianov, I., Zemlyanukhin, A., Bochkarev, A., Erofeev, V.: Steady solitary and periodic waves in a nonlinear nonintegrable lattice. *Symmetry* **12**(10), 1608 (2020)
- Baker, G.A. Jr., Graves-Morris, P.: *Padé Approximants*. Cambridge University Press, Cambridge (1996)
- Baldwin, D., Goktas, U., Hereman, W.: Symbolic computation of hyperbolic tangent solutions for nonlinear differential–difference equations. *Comput. Phys. Commun.* **162**, 203–217 (2004)
- Bochkarev, A.V., Zemlyanukhin, A.I.: The geometric series method for constructing exact solutions to nonlinear evolution equations. *Comput. Math. Math. Phys.* **57**, 1111–1123 (2017)
- Butcher, J.C.: *Numerical Methods for Ordinary Differential Equations*. Wiley, New York (2008)
- Cooke, K.L.: Differential–difference equations. In: LaSalle, J.P., Lefschetz, S. (eds.) *International Symposium on Nonlinear Differential Equations and Nonlinear Mechanics*, pp. 155–171. Academic Press, New York (1963)
- Khanzadeh, F., Mikhailov, A.V., Wang, J.P.: Darboux transformations and recursion operators for differential–difference equations. *Theor. Math. Phys.* **177**(3), 387–440 (2013)
- Krichever, I., Wiegmann, P., Zabrodin, A.: Elliptic solutions to difference non-linear equations and related many-body problems. *Commun. Math. Phys.* **193**, 373–396 (1998)
- Kudryashov, N.A.: *Metody Nelinejnoj Matematicheskoy Fiziki [Methods of Nonlinear Mathematical Physics]*. Izd. dom “Intellekt”, Dolgoprudnyj (in Russian) (2010)
- Liu, Y., Chen, D.: The exact solutions to a Ragnisco–Tu hierarchy with self-consistent sources. *Nonlinear Anal.* **74**, 5223–5237 (2011)
- Merola, I., Ragnisco, O., Tu, G.-Z.: A novel hierarchy of integrable lattices. *Inverse Prob.* **10**(6), 1315–1334 (1994)
- Ohta, Y., Hirota, R.: A discrete KdV equation and its Casorati determinant solution. *J. Phys. Soc. Jpn.* **60**, 2095 (1991)
- Ryabov, P.N.: Exact solutions of the Kudryashov–Sinelnshchikov equation. *Appl. Math. Comput.* **217**, 3585–3590 (2010)
- Silindir, B.: Soliton solutions of q-Toda lattice by Hirota direct method. *Adv. Differ. Equat.* **1**, 121 (2012)
- Tsujimoto, S., Hirota, R.: Pfaffian representation of solutions to the discrete BKP hierarchy in bilinear form. *J. Phys. Soc. Jpn.* **65**, 2797–2806 (1996)
- Wang, L.L., Song, C., Zhu, J.: Two-component generalized Ragnisco–Tu equation and the Riemann–Hilbert problem. *Theor. Math. Phys.* **205**(1), 1303–1317 (2020)
- Xu, X.-X.: Solving an integrable coupling system of Merola–Ragnisco–Tu lattice equation by Darboux transformation of Lax pair. *Commun. Nonlinear Sci. Numer. Simul.* **23**, 192–201 (2015)
- Xu, X.-X.: An integrable coupling family of Merola–Ragnisco–Tu lattice systems, its Hamiltonian structure and related nonisospectral integrable lattice family. *Phys. Lett. A* **374**, 401–410 (2010)
- Zemlyanukhin, A.I., Bochkarev, A.V.: Exact solutions and numerical simulation of the discrete Sawada–Kotera equation. *Symmetry* **12**(1), 131 (2020)
- Zemlyanukhin, A.I., Bochkarev, A.V., Orlova, A.A., Ratushny, A.V.: Geometric series method and exact solutions of differential–difference equations. In: Abramian, A.K., Andrianov, I.V., Gaiko,

V.A. (eds.) *Nonlinear Dynamics of Discrete and Continuous Systems. Advanced Structured Materials*, vol. 139, pp. 239–253 (2021)